Transactions of the ASME®

Transactions of the ASME, Journal of Heat Transfer (ISSN 0022-1481) is published bi-monthly (Feb., Apr., June, Aug., Oct., Dec.) by The American Society of Mechanical Engineers, Three Park Avenue, New York, NY 10016. Periodicals postage paid at New York, NY and additional mailing offices. POSTMASTER: Send address changes to Transactions of the ASME, Journal of Heat Transfer, c/o THE AMERICAN SOCIETY OF MECHANICAL ENGINEERS, 22 Law Drive, Box 2300, Fairfield, NJ 07007-2300. **CHANGES OF ADDRESS** must be received at Society headquarters seven weeks before they are to be effective. Please send old label and new address. **STATEMENT from By-Laws.** The Society shall not be responsible for statements or opinions advanced in papers or ... printed in its publications (B7.1, Para. 3), **COPYRIGHT** © **2002** by The American Society of Mechanical Engineers. For authorization to photocopy material for internal or personal use under those circumstances not falling within the fair use provisions of the Copyright Act, contact the Copyright Clearance Center (CCC), 222 Rosewood Drive, Danvers, MA 01923, tel: 978-750-8400, *www.copyright.com.* Request for special permission or bulk copying should be addressed to Reprints/Permission Department. **INDEXED** by Applied Mechanics Reviews and Engineering Information, Inc. Canadian Goods & Services Tax Registration #126148048.

Journal of Heat Transfer

Published Bimonthly by The American Society of Mechanical Engineers

VOLUME 124 • NUMBER 6 • DECEMBER 2002

TECHNICAL PAPERS

(Contents continued on inside back cover)

This journal is printed on acid-free paper, which exceeds the ANSI Z39.48-1992 specification for permanence of paper and library materials. ♾™
♻ 85% recycled content, including 10% post-consumer fibers.

Journal of Heat Transfer Volume 124, Number 6 DECEMBER 2002

TECHNICAL NOTES

ANNOUNCEMENTS

Theoretical Prediction of the Soil Thermal Conductivity at Moderately High Temperatures

Fabio Gori
e-mail: gori@uniroma2.it

Sandra Corasaniti

Department of Mechanical Engineering,
University of Rome "Tor Vergata",
Via di Tor Vergata, 110,
Rome, 00133, Italy

The theoretical model of the present paper assumes the unit cell of the porous medium as composed of a cubic space with a cubic solid particle at the center. The thermal conductivity is evaluated by solving the heat conduction equation with the assumption of parallel isotherms within the cubic space. The liquid water in the porous medium is distributed around the solid particle according to the phenomena of adsorption and capillarity. The thermal conductivity of the gas present within the pores takes into account the thermal conductivity of the water vapor and dry air, without enhanced vapor diffusion. The model simplifies the variation of the relative humidity, from dryness to the field capacity, with a linear increase. The predicted results, compared to experimental data, show the agreement is very good at the temperatures in the range (30–50°C) and acceptable at 70°C. At high temperature (90°C) the predictions are higher than the experiments and a better agreement could be obtained by decreasing the thermal conductivity of the gas phase. Besides, the trend of the theoretical predictions is in good agreement with the experiments also at high temperatures. [DOI: 10.1115/1.1513573]

Keywords: Conduction, Heat Transfer, Modeling, Porous Media, Thermophysical

Introduction

The prediction of the effective thermal conductivity of soils is very important in many heat and mass transfer phenomena related to ground, including waste disposal in unsaturated geologic media, geothermal energy extraction, drying problems in multiphase heat and mass transfer in porous and fractured media, enhanced oil recovery, radioactive waste storage, ground heat pumps and heat exchangers, forest fires and related problems, heat transfer from high voltage power cables, thermal soil remediation and soil behavior under forest fires. The effective thermal conductivity is dependent on a wide variety of properties related to the soil, including mineral composition of the solid particles, dry density, porosity, temperature and water content.

A soil is a multiphase porous medium. A dry or water saturated soil is a two-phases medium, composed of solid particle and gas or liquid water, respectively. A soil partially saturated by water is a three-phases medium, with the liquid water disposed among the solid particle by adsorption and capillarity [1]. In a partially saturated soil, heat and mass transfer are coupled by several mechanisms of thermally induced and water potential-induced flow of water in liquid and vapor phases [2]. If the temperature is below the freezing point, part of the water can be in the solid state and, according to the conditions in the porous medium, liquid water can coexist, as unfrozen water, with the solid ice to form a four-phases medium. Besides the large spectrum of problems identified, the interest of the present paper is focused on three-phases soils at temperatures in the range 30–90°C. Several experimental measurements are present in the literature at high temperatures [3–7]. The soils measured span many different types, varying in mineral composition, dry density, porosity and water content. Because of the large variety of experiments, the present paper focuses on the results of [3], in order to show the general agreement and the trend of the theoretical predictions.

A review of the literature has revealed that many theoretical and experimental studies have been carried out to determine the effective thermal conductivity of porous media. In the past years some experimental results measured the thermal conductivity of saturated and two-phases porous media. Theoretical models have been proposed, but the studies on the thermal conductivity of unsaturated porous media are limited.

Two recent papers [8,9] compared some modeling approaches to predict the effective thermal conductivity of high temperature soils. Two of the models tested in [8] are modifications of the original one of de Vries [4]. The third theoretical model was originally proposed in [10] for four-phases soils in partially frozen conditions and later modified for bricks [11]. A model for the thermal conductivity of unconsolidated porous medium, based on capillary pressure-saturation relation, has been proposed in [12]. A relation was obtained for the thermal conductivity of the unsaturated porous medium when $K_w/K_s \leqslant 0.2$. The stagnant thermal conductivity of spatially periodic porous media has been studied in [13]. Two models to predict the effective thermal conductivity of consolidated porous media, like cellular ceramics, have been developed in [14]. A model to determine the thermal conductivity of a bed of solid spherical particles, immersed in a static fluid, when the conductivity of the matrix solid is greater than that of the gas, has been formulated in [15].

The present paper presents a further enhancement of the model proposed in [10], with modifications that take into account the specific nature of the soil investigated, including the Permanent Wilting Point and the Field Capacity. Permanent Wilting Point is defined as the water remaining in the soil in the smallest of the micropores and around individual soil particles. Field Capacity is the water content present in the soil after a day, when rain has stopped and the irrigation water has been shut off. At this time the examination of the soil will show water has moved out of the macropores, its place has been taken by air, but the small pores remain filled with water.

Theoretical Approach

The present model is based on the assumption that the unit cell of the soil is composed of a cubic space with a cubic solid particle at the center. Figure 1 presents the cubic cell in the case of a two-phases medium where the continuous phase can be air (dry soil) or water (fully saturated soil). The main physical assumption of the cubic cell, no contact among adjoining particles, is the

Contributed by the Heat Transfer Division for publication in the JOURNAL OF HEAT TRANSFER. Manuscript received by the Heat Transfer Division July 20, 2001; revision received May 17, 2002. Associate Editor: C. T. Avedisian.

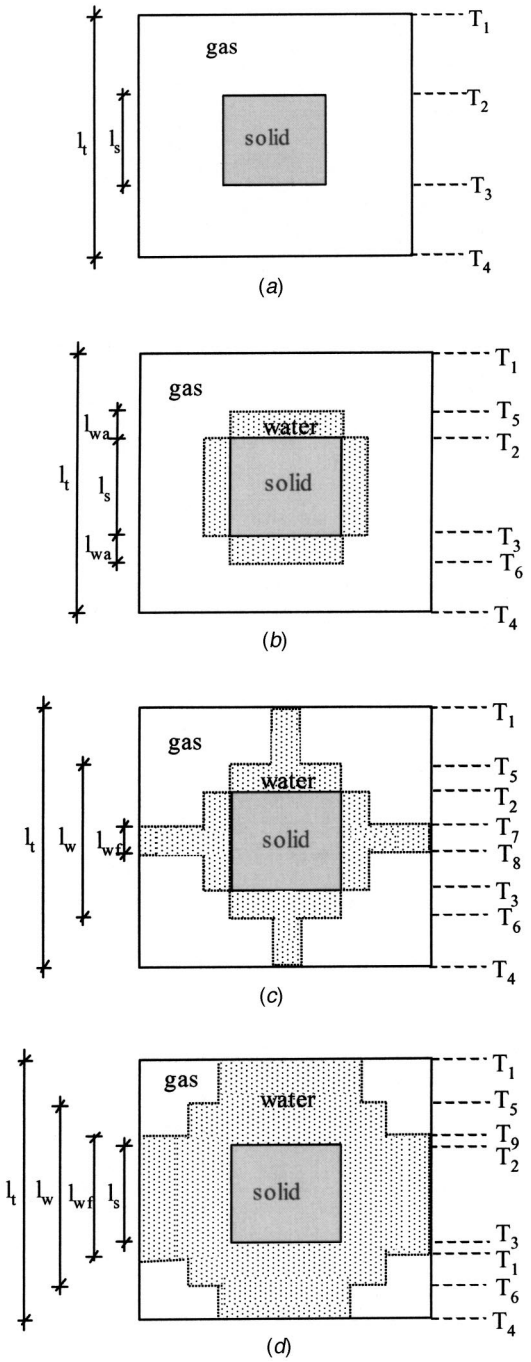

Fig. 1 (*a*) Cubic cell for two-phases dry soil; (*b*) cubic cell for three-phases soil at low water content; (*c*) cubic cell for three-phases soil in unsaturated conditions; and (*d*) cubic cell for three-phases soil near saturation conditions

answer to spherical particles with a point of contact, which is a negligible cross section for heat transfer. When water is present the major contribution to heat conduction is given by the cross section of the water bridge formed between the two particles. The porosity of the soil, ε, is taken into account by the ratio of the void volume to the total volume of the cell. The dimensions of the cubic cell, although reported in Fig. 1, do not need to be considered, because they can be expressed as ratios with the solid particle as in the following. The ratio of the lengths of the cubic cell and of the solid particle, as reported in Fig. 1, is:

$$\beta = \frac{l_t}{l_s} = \sqrt[3]{\frac{\rho_s}{\rho_d}} = \sqrt[3]{\frac{1}{1-\varepsilon}} \tag{1}$$

where ρ_s is the solid particles density and ρ_d the dry density of the soil.

The effective thermal conductivity of the unit cell can be evaluated by solving the heat conduction equation, with the assumptions of parallel isotherms or parallel heat flux lines. The parallel isotherms assumption, adopted in [10–11], is based on the hypothesis of a very high thermal conductivity in the transverse direction, while the parallel heat flux lines is valid when the thermal conductivity, in the transverse direction, is zero. Both assumptions have been tested in [16] for two-phases media.

The effective thermal conductivity of the medium has been evaluated in the present paper with the parallel isotherm hypothesis and is called K_T. For the two-phases porous medium of Fig. 1(*a*), K_T is given by:

$$\frac{1}{K_T} = \frac{\beta - 1}{K_c \cdot \beta} + \frac{\beta}{K_c \cdot (\beta^2 - 1) + K_s} \tag{2}$$

where K_c is the thermal conductivity of the gas (air and water vapor in general but water if fully saturated), and K_s the thermal conductivity of the solid particle. The first term in Eq. (2) corresponds to the thermal resistance of the gas in the cross section (l_t^2) and length $(l_t - l_s)$, while the second term is the thermal resistance of the materials gas-solid in the cross section (l_t^2) and length (l_s).

When the soil is neither dry nor fully saturated by water, water is distributed inside the cubic cell according to adsorption and capillarity. If the water content is very low, water is adsorbed around the solid particle, as assumed in Fig. 1(*b*). The adsorbed water W_c, is assumed empirically to be a fraction of the water content at the permanent wilting point W_P, according to [17], as

$$W_C = c W_P \tag{3}$$

where the constant c depends on the type of soils investigated. The present paper assumes $c \approx 0.375$ as suggested in [18]. The adsorbed water W_c, as given by Eq. (3), is the only empirical assumption of the present model.

When the water content, W, is greater than W_c, water bridges are establishes among the six solid particles surrounding the cubic cell, with the distributions assumed in Fig. 1(*c*) or 1(*d*), depending on the amount of water content. The effective thermal conductivity of the unit cell can be evaluated, with the assumption of parallel isotherms, and the expressions are reported in Appendix A.

Comparisons With Experimental Results

The soils investigated in [3] are reported in Table 1 below. The soils of Table 1 belong to three textural groups of soils: coarse, medium-fine and fine, as reported in the first column. The name of the soil is in the second column. The third column presents the range of dry density measured. The quartz content percentage is in the fourth column. The thermal conductivity of the solid particles of each soil, according to the evaluation carried out in [3], is reported in the fifth column. Volkmar soil has a thermal conductivity more than two times higher than the other soils because its quartz content is 97 percent. In the other soils the quartz content vary from 35 percent for Palouse B to 55 percent for Mokins. The sixth column shows the porosity range, corresponding to the dry densities of the third column, as evaluated in [3]. The last two columns show the Permanent Wilting Point water content W_P, and the Field Capacity W_F, as evaluated in [8]. The experimental data of [3] were found with the transient thermal probe method.

The thermal conductivity of water is assumed a function of the temperature T_C, (in °C), according to:

$$K_w = 0.569 + 1.88\ \ 10^{-3}\ \ T_C - 7.72\ \ 10^{-7}\ \ T_C^2 \tag{4}$$

Table 1 Experimental data [3]

Textural Group	Soil	ρ_d (g/cm^3)	% Quartz	K_s (W/m K)	ε	W_P (%)	W_F (%)
Coarse	L-soil	1.15 – 1.7	38	2.61	0.4 – 0.59	5.2	9.9
Coarse	Volkmar	1.27 – 1.69	97	4.71	0.362 – 0.52	8.6	15.7
Coarse	Royal	1.09 – 1.51	42.5	2.57	0.432 – 0.59	9.9	20.3
Medium - fine	Walla-Walla	0.94 – 1.52	48.4	2.53	0.429 – 0.647	9.6	26.2
Medium – fine	Palouse A	1.11 – 1.52	38.5	2.31	0.425 – 0.58	12.9	30.9
Medium – fine	Salkum	0.99 – 1.31	45.5	2.21	0.508 – 0.628	13.9	30.0
Medium - fine	Mokins	0.94 – 1.47	55	2.64	0.45 – 0.648	15.1	30.8
Fine	Palouse B	0.86 – 1.38	35	2	0.482 – 0.677	26	40.7

The thermal conductivity of air, equal to $K_a = 0.026$ W/m K at 27°C, is assumed variable with the temperature T_C, (in °C), according to the following equation:

$$K_a = 0.02408 + 0.0000792 \cdot T_C \tag{5}$$

In a partially saturated soil the thermal conductivity of the gas, present in the pore space, is due to water vapor mixed to air. The apparent thermal conductivity of the mixture of air and water vapor is then given by:

$$K_{\text{app}} = K_a + \phi \cdot K_{vs} \cdot \xi \tag{6}$$

where ϕ is the relative humidity of the gas mixture and ξ is the mass transfer enhancement factor, assumed by some investigations as $\xi > 1$, because of the phenomenon of enhanced vapor-phase diffusion. The thermal conductivity of water vapor is [8]:

$$K_{vs} = \frac{H_L \cdot D}{R_v \cdot T} \cdot \frac{p_b}{p_b - p_{vs}} \cdot \frac{dp_{vs}}{dT}; \tag{7}$$

where

$$R_v = \frac{R}{M_w}; \tag{8}$$

$$H_L = 2503 - 2.3 \cdot T_C; \tag{9}$$

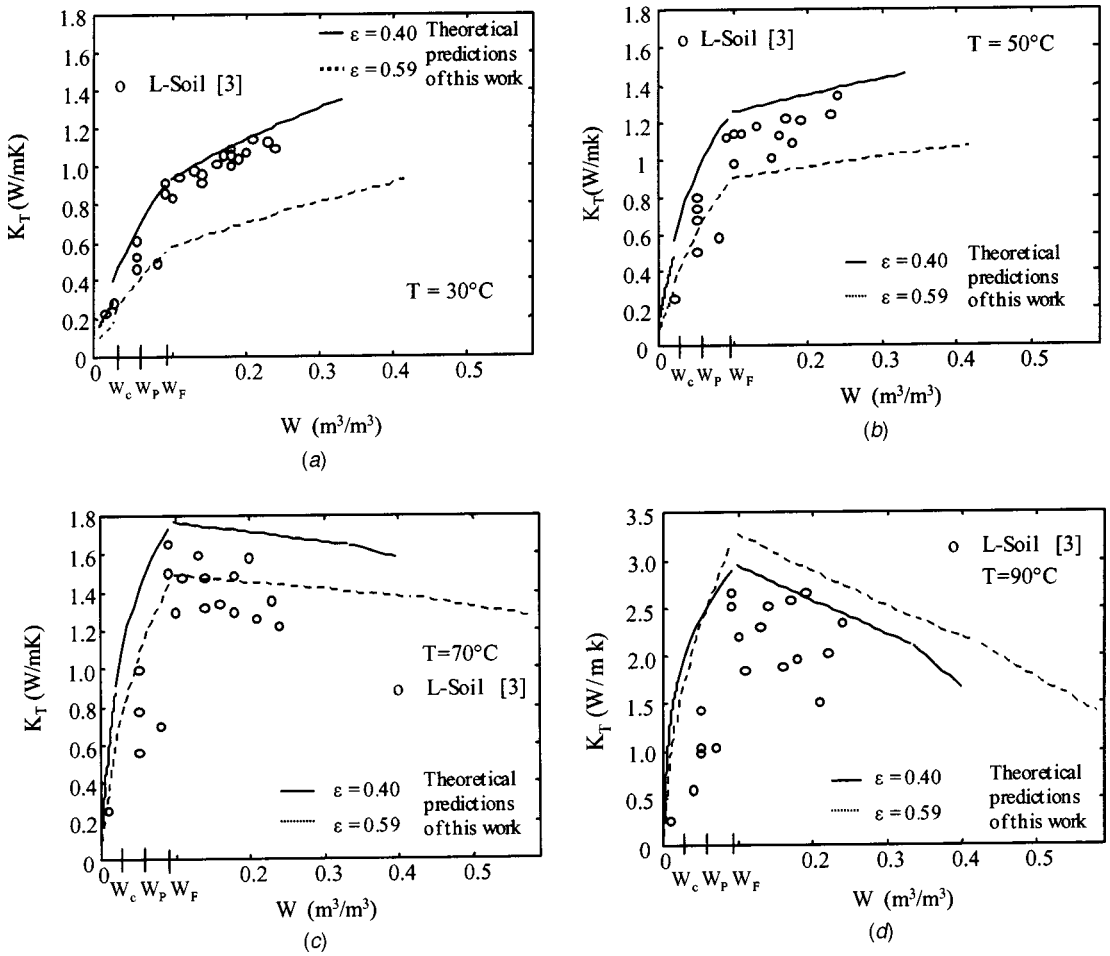

Fig. 2 (*a*) Effective thermal conductivity versus water content in *L*-soil [3]; (*b*) effective thermal conductivity versus water content in *L*-soil [3]; (*c*) Effective thermal conductivity versus water content in *L*-soil [3]; and (*d*) effective thermal conductivity versus water content in *L*-soil [3]

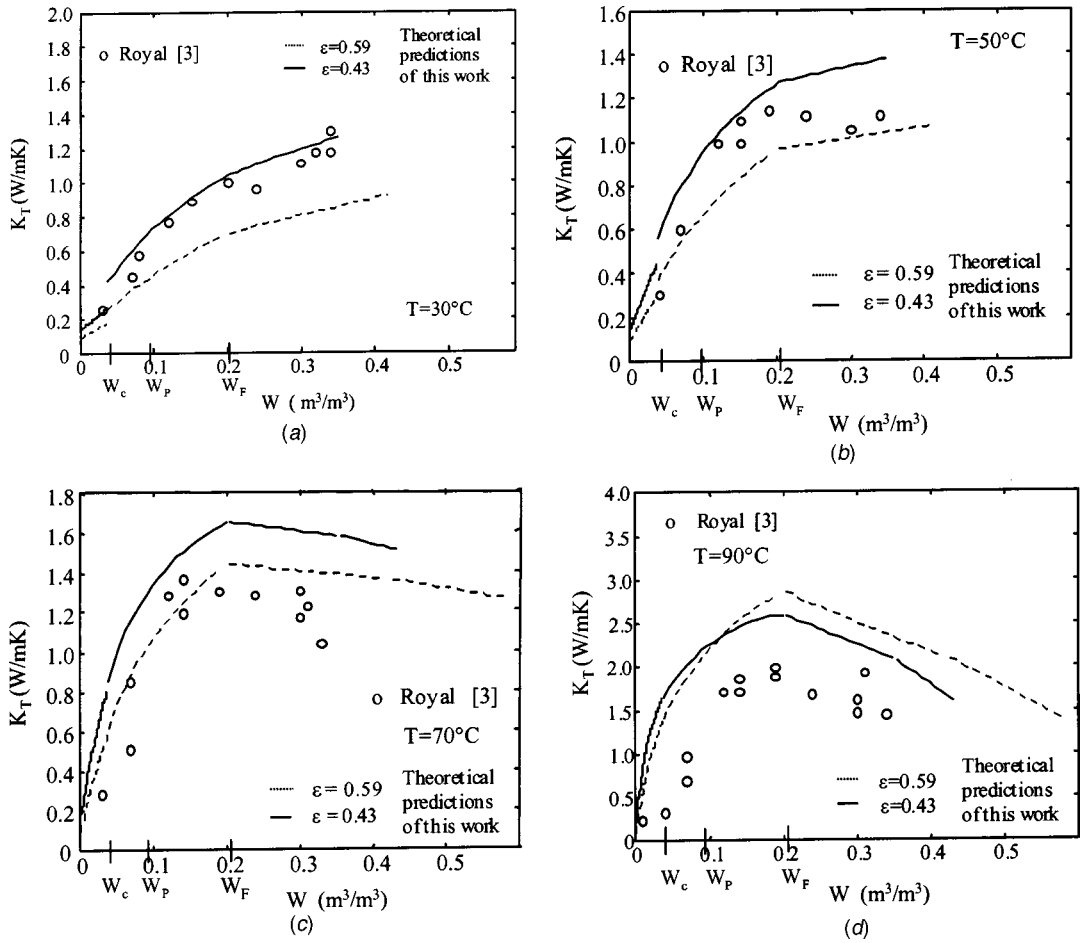

Fig. 3 (*a*) **Effective thermal conductivity versus water content in Royal soil [3]; (*b*) effective thermal conductivity versus water content in Royal soil [3]; (*c*) Effective thermal conductivity versus water content in Royal soil [3]; and (*d*) Effective thermal conductivity versus water content in Royal soil [3]**

$$D = 2.25 \cdot 10^{-5} \left[\frac{T}{273.15} \right]^{1.72}. \tag{10}$$

In the present model, on the basis of the discussion carried on in [19], the mass transfer enhancement factor ξ is assumed 1.

The Field Capacity of a soil is the condition when water has drained out of the larger pores but the small pores remain filled with water. In this situation, the air, trapped among the water bridges, contains water saturated vapor, i.e., the relative humidity, ϕ, of the gas space is equal to 1. On the other hand, $\phi = 0$ only in perfect dry conditions; i.e., with water content equal to zero. This is in agreement with [2] where the relative humidity is a function of the soil water content, according to an *s*-shaped curve, variable from zero, at zero water content, up to 100 percent, at a water content which depends on the type of soil. In order to simplify the present theoretical model, this work assumes the relative humidity as linearly variable from zero, at full dryness, to 100 percent, at the Field Capacity water content.

In summary, the thermal conductivity of the gas phase (air and water vapor) is given by Eq. (6), with $\xi = 1$, and the relative humidity is linearly variable with the water content, from dryness to field capacity, as

$$\phi = W / W_F \tag{11}$$

The linear variation is only a hypothesis which can be removed with the more correct assumption of a *s*-shaped curve, but, in a simple theoretical model like this, and with several complicated theoretical relations it seems very plausible.

Substituting the numerical values of Eq. (7–10) in Eq. (6), the apparent thermal conductivity is given by

$$K_{\text{app}} = K_a + 0.120 \cdot \phi; \quad \text{at } 30°C, \tag{12}$$

$$K_{\text{app}} = K_a + 0.335 \cdot \phi; \quad \text{at } 50°C, \tag{13}$$

$$K_{\text{app}} = K_a + 0.962 \cdot \phi; \quad \text{at } 70°C, \tag{14}$$

$$K_{\text{app}} = K_a + 4.474 \cdot \phi; \quad \text{at } 90°C, \tag{15}$$

where the thermal conductivity of dry air is variable with the temperature according to the Eq. (5). Above the Field Capacity water content, W_F, the apparent thermal conductivity of the gas is given by

$$K_{\text{app}} = K_a + K_{vs} \tag{16}$$

Figures 2–6 present the theoretical predictions of this work. Each prediction can be subdivided in four regions. The first region, extending from zero water content to W_C, given by Eq. (3), corresponds to the condition of water adsorbed around the solid particle (Fig. 1(*b*)) and it gives the lowest thermal conductivity because of the absence of water bridges between the adjoining solid particles. The first discontinuity between the first and the second region is due to the appearance of water bridges. In the second region, from W_C to W_F, water bridges are present among

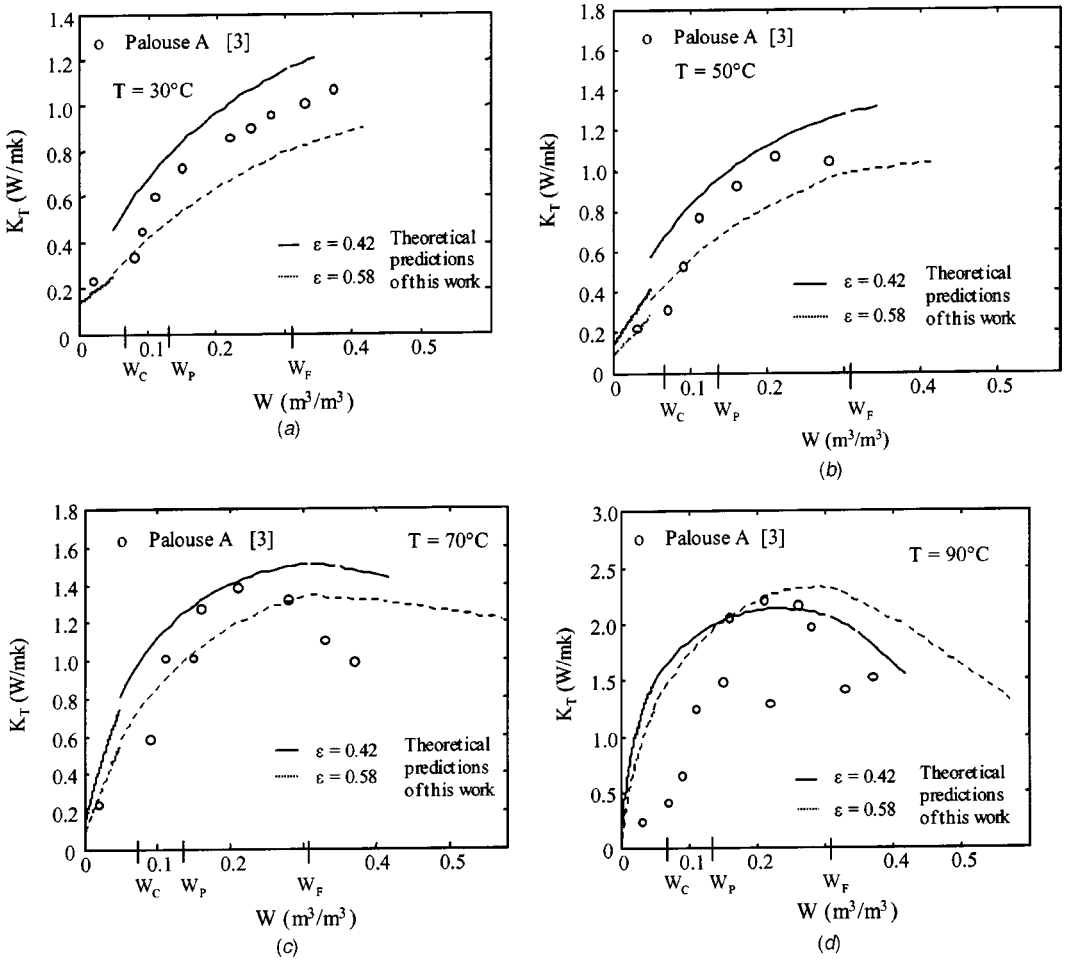

Fig. 4 (*a*) Effective thermal conductivity versus water content in Palouse A [3]; (*b*) effective thermal conductivity versus water content in Palouse A [3]; (*c*) effective thermal conductivity versus water content in Palouse A [3]; and (*d*) effective thermal conductivity versus water content in Palouse A [3]

the solid particles, due to capillarity (Fig. 1(*c*)). A continuous increase of K_T, up to the Field Capacity of the soil, W_F, is predicted because of the variation of the relative humidity, as given by Eq. (11). A second discontinuity in the model is present at the Field Capacity, W_F. The third region starts at W_F extending up to the third discontinuity, which is due to the transition from the water configuration of Fig. 1(*c*) to that of Fig. 1(*d*) and is specific of the present theoretical model. The fourth region starts at the third discontinuity and extends up to saturation. In the third and fourth regions, at the two highest temperatures (70°C and 90°C), the effective thermal conductivity decreases for $W > W_F$, because the thermal conductivity of water (at saturation) is lower than the apparent thermal conductivity given by Eq. (6).

Figures 2–3 compare the theoretical predictions of this work with the experimental measurements of two of the coarse soils of Table 1 [3]. Figure 2 shows the data for *L*-Soil, which has the smallest quartz content (38 percent), Wilting Point (5.2 percent) and Field Capacity (9.9 percent). Two theoretical predictions are reported in each figure for two porosities, which correspond to the extremes values of the dry densities of Table 1. The two predictions are in fair agreement with the experiments at 30°C (Fig. 2(*a*)) and 50°C (Fig. 2(*b*)), in the whole range of water content. The predictions are a little higher than the experiments at 70°C (Fig. 2(*c*)) and higher at 90°C (Fig. 2(*d*)). Note that the change in the slope of the predictions at the Field Capacity is in good agreement with the slope change of the experimental data [3].

Figure 3 presents the predictions and the data for Royal soil, which has a moderate quartz content (42.5 percent) and Field Capacity (20.3 percent). The predictions are in good agreement to the experiments at 30°C (Fig. 3(*a*)) and 50°C (Fig. 3(*b*)), in the complete range of water content. Indeed, the data are within the predictions obtained with the two porosities reported in Table 1 [3]. At 70°C (Fig. 3(*c*)) the predictions are in good agreement below the field capacity but somewhat higher than the experiments at higher water contents. At 90°C (Fig. 3(*d*)) the theoretical predictions are higher than the experiments in the whole range of water content. Also for Royal soil it is evident that the slope change, in the experimental as well as in the theoretical results, occurs around the field capacity (20.3 percent). Further on, at the field capacity the soil exhibits the highest thermal conductivity, for the temperatures of 70°C and 90°C.

Figures 4–5 present the theoretical predictions compared to the experimental data of two medium-fine soils of Table 1; i.e., Palouse A and Salkum. The conclusions are similar to those made with Figs. 1–2. The agreement is fairly good at the temperatures 30°C and 50°C (Figs. 4(*a*,*b*) and 5(*a*,*b*). It is acceptable at 70°C up to the Field Capacity (Fig. 4(*c*) and Fig. 5(*c*)). The predictions are higher than the experiments at 90°C (Figs. 4(*d*) and 5(*d*).

Finally Fig. 6 presents the predictions and the experiments of the only fine soil of Table 1; i.e., Palouse B. Figure 6(*a*,*b*) present a fairly good agreement. Figure 6(*c*,*d*) show the model provides higher values than the experiments with conclusions similar to the previous ones.

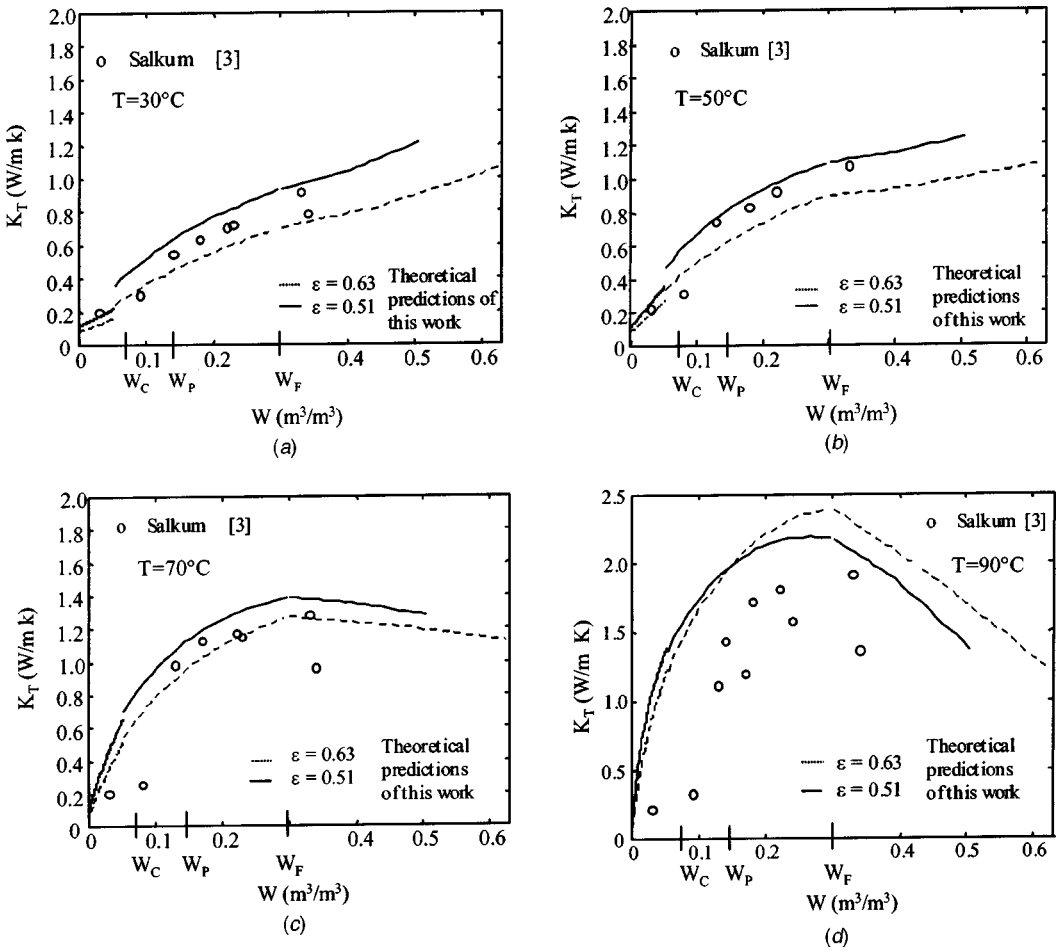

Fig. 5 (*a*) **Effective thermal conductivity versus water content in Salkum [3];** (*b*) **effective thermal conductivity versus water content in Salkum [3];** (*c*) **effective thermal conductivity versus water content in Salkum [3]; and** (*d*) **effective thermal conductivity versus water content in Salkum [3]**

Conclusions

The theoretical model, used to simulate three-phases porous soils, gives predictions in very good agreement with the experimental results at the temperatures of 30°C and 50°C. At the temperature of 70°C the agreement is fairly good from dryness to the Field Capacity. The predictions are somewhat higher than the experiments, above the field capacity. At 90°C the predictions are higher than the experiments almost everywhere and a better comparison can be obtained only with a reduced apparent thermal conductivity of the water-vapor and air mixture.

Acknowledgment

The present work was partially supported by ASI (Agenzia Spaziale Italiana).

Nomenclature

D = water vapor diffusivity in air, [m^2/s]
H_L = latent heat of condensation, [J/kg]
K = thermal conductivity, [W/m K]
l = cubic cell length, [m]
M = molecular mass, [g/mol]
p = pressure, [Pa]
R = gas constant, [J/mol K]
R_V = water vapor gas constant, [J/kg K]
T = temperature, [K]
T_C = temperature, [°C]
V = volume, [m^3]
W = water content, [m^3/m^3]
W_C = adsorbed water content, [m^3/m^3]
W_P = permanent Wilting Point, [m^3/m^3]
W_F = field Capacity, [m^3/m^3]

Greek Symbols

$\beta = l_t/l_s$ = lengths ratio $\delta = W/1-\varepsilon$
$\varepsilon = V_p/V_t$ = porosity
ϕ = air relative humidity
ρ = density, [Kg/m^3]
ξ = mass transfer enhancement factor
γ = lengths ratio
γ_f = lengths ratio

Subscripts

a = air
app = apparent
b = barometric
c = gas phase
d = dry
p = pore
s = solid particle
T = parallel isotherm
t = total
v = water vapor
vs = water vapor at saturation
w = water
wa = adsorbed water
wf = funicular water

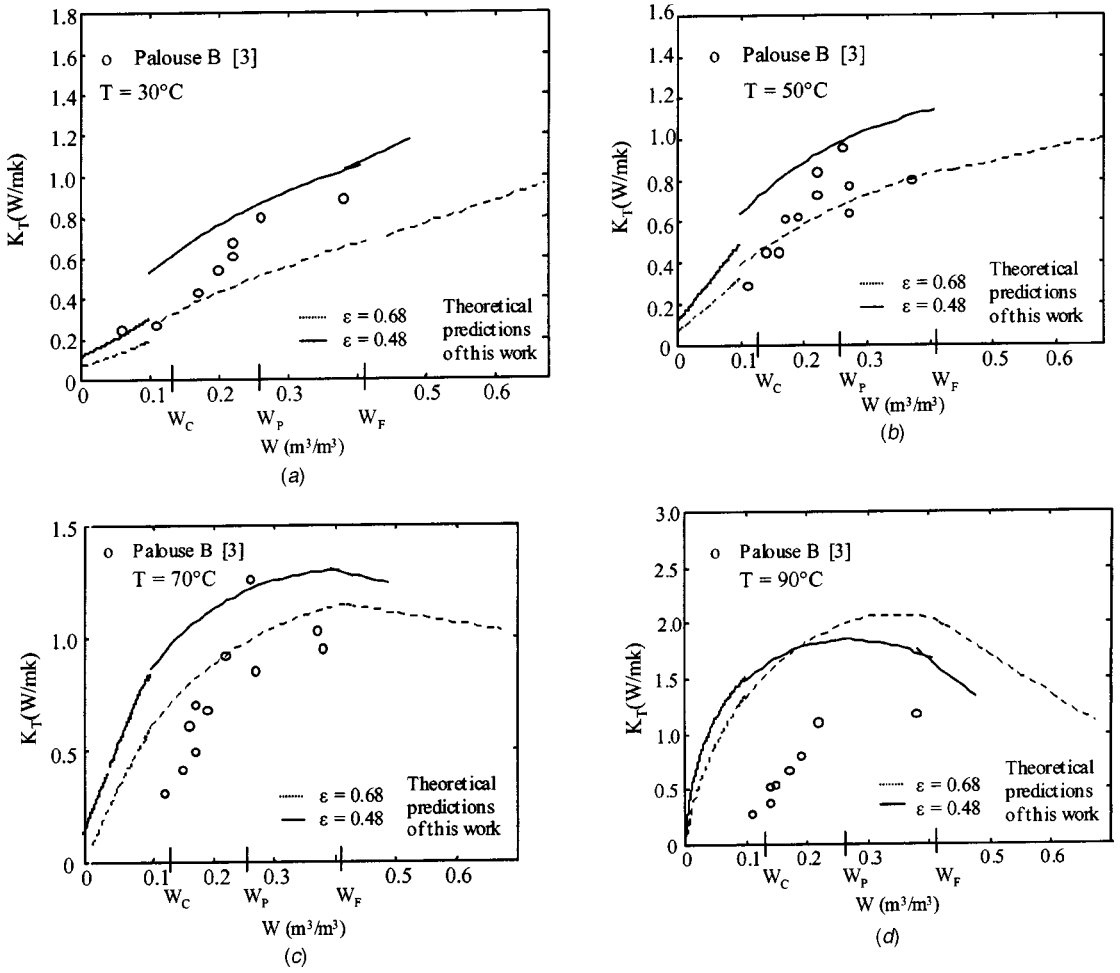

Fig. 6 (*a*) Effective thermal conductivity versus water content in Palouse B [3]; (*b*) effective thermal conductivity versus water content in Palouse B [3]; (*c*) effective thermal conductivity versus water content in Palouse B [3]; and (*d*) effective thermal conductivity versus water content in Palouse B [3].

Appendix A

If the water content is lower than W_C, the effective thermal conductivity is given by, Fig. 1(*b*);

$$\frac{1}{K_T}=\frac{\beta-1-\delta/3}{\beta\cdot K_{\text{app}}}+\frac{\beta\cdot\delta}{3[K_{\text{app}}(\beta^2-1)+K_w)]}+\frac{\beta}{K_s+\frac{2}{3}\cdot\delta\cdot K_w+K_{\text{app}}\left(\beta^2-1-\frac{2}{3}\cdot\delta\right)} \tag{A1}$$

where

$$\delta=\frac{W}{1-\varepsilon}=6\cdot\frac{l_{wa}}{l_s} \tag{A2}$$

The first term of Eq. (*A*1) is the thermal resistance of gas in the section (l_t^2) of length ($l_t-l_s-2l_{wa}$). The second term is the thermal resistance of the materials gas-water in the section (l_t^2) of length ($2l_{wa}$). The third term is the thermal resistance of the materials gas-water-solid in the section (l_t^2) of length (l_s). With reference to Fig. 1(*b*) the three terms can be looked from above to below and also on the plane on the paper.

If $W>W_c$, Fig. 1(*c*) and 1(*d*) the amount of water accumulated among the solid particles is the funicular one, V_{wf}/V_s, according to [20]. In order to simplify the model, V_{wf}/V_s is assumed linearly variable with the real porosity of the medium, between 0.183, for $\varepsilon=0.4764$, and 0.226, for $\varepsilon=0.2595$. The resulting expression is:

$$\frac{V_{wf}}{V_s}=\frac{V_{wf}}{V_p}\cdot(\beta^3-1)=\left[0.183+\frac{0.226-0.183}{0.4764-0.2595}\cdot(0.4764-\varepsilon)\right]\cdot(\beta^3-1) \tag{A3}$$

The following variables are then defined:

$$\gamma=\frac{l_w}{l_s}=\sqrt[3]{\frac{V_w}{V_s}-\frac{V_{wf}}{V_s}+1} \tag{A4}$$

and

$$\gamma_f=\frac{l_{wf}}{l_s}=\sqrt{\frac{V_{wf}/V_s}{3\cdot(\beta-\gamma)}} \tag{A5}$$

In the configuration of Fig. 1(*c*), where $\gamma_f<1$, K_T is given by:

$$\frac{1}{K_T}=\frac{\beta^2-\beta\cdot\gamma}{K_{\text{app}}\cdot(\beta^2-\gamma_f^2)+K_w\cdot\gamma_f^2}+\frac{\beta\cdot\gamma-\beta}{K_{\text{app}}\cdot(\beta^2-\gamma^2)+K_w\cdot\gamma^2}+\frac{\beta-\beta\cdot\gamma_f}{K_{\text{app}}\cdot(\beta^2-\gamma^2)+K_w\cdot(\gamma^2-1)+K_s}+\frac{\beta\cdot\gamma_f}{K_s+K_w\cdot(\gamma^2-1+2\cdot\beta\cdot\gamma_f-2\cdot\gamma\cdot\gamma_f)+A} \quad (A6)$$

where $A=K_{\text{app}}\cdot(\beta^2-\gamma^2-2\cdot\beta\cdot\gamma_f+2\cdot\gamma\cdot\gamma_f)$

The first term of Eq. (*A*6) is the thermal resistance of the materials gas-water in the section (l_t^2) of length (l_t-l_w). The second term is the thermal resistance of the materials gas-water in the section (l_t^2) of length (l_w-l_s). The third term is the thermal resistance of the materials gas-water-solid in the section (l_t^2) of length (l_s-l_{wf}). The fourth term is the thermal resistance of the materials gas-water-solid in the section (l_t^2) of length (l_{wf}). With reference to Fig. 1(*c*) the four sections can be looked from above to below and also on the plane on the paper.

For $\gamma_f>1$, Fig. 1(*d*), K_T has the following expression:

$$\frac{1}{K_T}=\frac{\beta^2-\beta\cdot\gamma}{K_{\text{app}}\cdot(\beta^2-\gamma_f^2)+K_w\cdot\gamma_f^2}+\frac{\beta\cdot\gamma-\beta\cdot\gamma_f}{K_{\text{app}}\cdot(\beta^2-\gamma^2)+K_w\cdot\gamma^2}+\frac{\beta\cdot\gamma_f-\beta}{K_{\text{app}}\cdot(\beta^2-\gamma^2-2\cdot\beta\cdot\gamma_f+2\cdot\gamma\cdot\gamma_f)+K_w\cdot(\gamma^2+2\cdot\beta\cdot\gamma_f-2\cdot\gamma\cdot\gamma_f)}+\frac{\beta}{K_s+K_w\cdot(\gamma^2-1+2\cdot\beta\cdot\gamma_f-2\cdot\gamma\cdot\gamma_f)+K_{\text{app}}\cdot(\beta^2-\gamma^2-2\cdot\beta\cdot\gamma_f+2\cdot\gamma\cdot\gamma_f)} \quad (A7)$$

The first term of Eq. (*A*7) is the thermal resistance of the materials gas-water in the section (l_t^2) of length (l_t-l_w). The second term is the thermal resistance of the materials gas-water in the section (l_t^2) of length (l_w-l_{wf}). The third term is the thermal resistance of the materials gas-water in the section (l_t^2) of length ($l_{wf}-l_s$). The fourth term is the thermal resistance of the materials gas-water-solid in the section (l_t^2) of length (l_s). With reference to Fig. 1(*d*) the four sections can be looked from above to below and also on the plane on the paper.

References

[1] Buckman, H. O., and Brady, N. C., 1975, *The Nature and Properties of Soils* Mac Millan, London.

[2] Ghildyal, B. P., and Tripathi, R. P., 1973, *Soil Physics*, Wiley, London.

[3] Campbell, G. S., Jungbauer, J. D., Bidlake, W. R., and Hungerford, R. D., 1994, ''Predicting the Effect of Temperature on Soil Thermal Conductivity,'' Soil Sci., **158**(5), (pp. 307–313).

[4] de Vries, D. A., 1963, *Thermal Properties of Soils; Physics of Plant Environment*, W. R. Van Wijk, ed., John Wiley and Sons, NY, pp. 210–235.

[5] Sepaskhah, A. R., and Boersma, L., 1979, ''Thermal Conductivity of Soils as a Function of Temperature and Water Content,'' Soil Sci. Soc. Am. J., **43**, pp. 439–444.

[6] Hopmans, J. W., and Dane, J. H., 1986, ''Thermal Conductivity of Porous Media as a Function of Water Content, Temperature and Density,'' Soil Sci., **142**(4), pp. 187–195.

[7] Hiraiwa, Y., and Kasubuchi, T., 2000, ''Temperature Dependence of Thermal Conductivity of Soils Over a Wide Range of Temperature (5–75°C),'' European Journal of Soil Science, **51**, pp. 211–218.

[8] Tarnawski, V. R., Gori, F., Wagner, B., and Buchan, G. D., 2000, ''Modeling Approaches to Predicting Thermal Conductivity of Soils at High Temperatures,'' Int. J. Eng. Res., **24**, pp. 403–423.

[9] Tarnawski, V. R., Leong, W. H., and Bristow, K. L., 2000, ''Developing a Temperature Dependent Kersten Function for Soil Thermal Conductivity,'' Int. J. Eng. Res., **24**, pp. 1335–1350.

[10] Gori, F., 1983, ''A Theoretical Model for Predicting the Effective Thermal Conductivity of Unsaturated Frozen Soils,'' *Proc. of Fourth Int. Conf. on Permafrost*, Fairbanks, AK, pp. 363–368.

[11] Gori, F., 1986, ''On the Theoretical Prediction of the Effective Thermal Conductivity of Bricks'' Proc. of Eight Int. Heat Transfer Conference, San Francisco, II, pp. 627–632.

[12] Hu, Xue-Jiao, Du, Jian-Hua, Lei, Shu-Ye, and Wang, Bu-Xuan, 2001, ''A Model for the Thermal Conductivity of Unconsolidated Porous Media Based on Capillary Pressure-Saturation Relation,'' Int. J. Heat Mass Transf., **44**, pp. 247–251.

[13] Hsu, C. T., Cheng, P., and Wong, K. W., 1995, ''A Lumped-Parameter Model for Stagnant Thermal Conductivity of Spatially Periodic Porous Media,'' ASME J. Heat Transfer, **117**, pp. 264–269.

[14] Fu, X., Viskanta, R., and Gore, J. P., 1998, ''Prediction of Effective Thermal Conductivity of Cellular Ceramics,'' Int. Comm. of Heat and Mass Transfer, **25**(2), pp. 151–160.

[15] Slavin, A. J., Londry, F. A., and Harrison, J., 2000, ''A New Model for the Effective Thermal Conductivity of Packed Beds of Solid Spheroids: Alumina in Helium Between 100 and 500°C,'' Int. J. Heat Mass Transf., **43**, pp. 2059–2073.

[16] Gori, F., Marino, C., and Pietrafesa, M., 2001, ''Experimental Measurements and Theoretical Predictions of the Thermal Conductivity of Two Phases Glass Beads,'' Int. Comm. Heat Mass Transfer, **28**, pp. 1091–1102.

[17] Tarnawski, V. R., and Leong, W. H., 2000, ''Thermal Conductivity of Soils at Very Low Moisture Content and Moderate Temperatures,'' Transport in Porous Media, **1446**, pp. 1–11.

[18] Tarnawski, V. R., and Gori, F., 2002, ''Enhancement of the Cubic Cell Soil Thermal Conductivity Model,'' Int. J. Eng. Res., **26**, pp. 143–157.

[19] Ho, C. K., and Webb, S. W., 1998, ''Review of Porous Media Enhanced Vapor-Phase Diffusion Mechanisms, Models, and Data—Does Enhanced Vapor-Phase Diffusion Exist?,'' Journal of Porous Media, **1**(1), pp. 71–92.

[20] Luikov, A. V., 1966, *Heat and Mass Transfer in Capillary-Porous Bodies*, Pergamon Press.

A Study of the Effect of Surface Metalization on Thermal Conductivity Measurements by the Transient Thermo-Reflectance Method

Mihai G. Burzo

Pavel L. Komarov

Peter E. Raad
e-mail: praad@engr.smu.edu

Department of Mechanical Engineering,
Southern Methodist University,
Dallas, TX 75275-0337

This work is a numerical and experimental investigation of the effect of the use of a metallic absorption layer on the laser-based measurements of the thermal conductivity of dielectric, semiconductor, and highly-conductive materials. The specific experimental studies, which were carried out on silicon dioxide samples, were used to validate the numerical approach and to support the findings of this investigation. The numerical and supporting experimental results reveal the presence of behaviors associated with thermally thin and thermally thick absorption layers, depending on the ratio between the thickness of the absorption layer and the heat penetration depth. It is concluded that the TTR method performs optimally when the thickness of the metalization layer falls in the transition range between the identified thermally thin and thermally thick layers. [DOI: 10.1115/1.1517265]

Keywords: Computational, Electronics, Experimental, Heat Transfer, Thin Films

1 Introduction

The performance of electronic and telecommunication devices depends heavily on electro-thermal interactions, making the knowledge of material properties fundamental to the design process. Higher performance has been achieved by significant reductions in the size of active features as well as by the introduction of innovative materials. Miniaturization leads to increased heat generation densities, which further underscores the importance of thermal analysis. But, in order for the numerical analysis to be useful in the prediction of performance and reliability of integrated circuits, accurate thermal property values are required. With the use of submicron devices came the realization that bulk and thin-film thermal properties differ markedly [1]. However, since no universal behavior is expected for these differences and since they cannot be predicted from theory [2], the properties of each material must be measured separately. Also, as films are typically layered and deposition techniques differ between manufacturers, it is important to measure the interface resistance of stacked layers [3].

There are many experimental techniques [4] that can be used to determine the thermal conductivity of thin-film and multi-layered materials, including the thermal comparator [5,6], embedded electrical resistance bridges [7,8], micro-fabricated thermocouples [9–12], IR thermography [13,14], 3-ω technique [15–17], X-ray reflectivity [18], and ac calorimetry [19–23], among others. However, the transient thermoreflectance method (TTR) [24] is preferred among experimental techniques used to determine the thermal conductivity of thin-film and multi-layered materials. The main advantage of the TTR method is that it is a non-contacting and non-destructive optical approach, both for heating a sample under test and for probing the variations of its surface temperature [19]. Because the method is noninvasive, it is attractive for the measurement of the thermal properties of thin-layer materials whose investigation by contact methods would present the difficulties of having to fabricate a measuring device into a sample, and then having to isolate and exclude the influence of that measuring device.

Of course, newly developed materials present an initial hurdle to the TTR method because of the poor availability in the open literature of required material properties. But even when available, TTR measurements of the thermal conductivity can still be hindered by less-than-desirable optical properties of the top layer material (i.e., low thermoreflectance coefficient, low reflectivity, high transparency, surface roughness), which degrade the measurement performance of a given system. More specifically, most dielectric materials have a low value of the extinction coefficient, k, which means that they are transparent to the irradiation of a heating laser. If the light penetration depth of the irradiation, $\delta_L = \lambda/4\pi k$, is larger than the layer thickness, h, the laser light cannot heat the layer under test, and thus the TTR method does not work. The next important problem is associated with the value of the thermoreflectance coefficient of the top layer material, which defines the rate of change in the reflectivity as a function of the temperature of the sample surface. This coefficient needs to be sufficiently high in order to obtain an appropriate signal-to-noise ratio in the measurements. Usually, it must be higher than 10^{-5} per Kelvin. In addition to the requirement for the thermoreflectance coefficient, the range of linear behavior between changes in reflectivity and changes in temperature has to include the range of transient temperatures experienced by the surface during the measurements. Otherwise, nonlinear effects could entirely distort the transient temperature response of a sample during analysis. Another difficulty connected with the optical properties of the top layer is the changing of those properties with time due either to long-term oxidization at room temperature or to accelerated oxidization at the higher temperatures experienced during laser irradiation pulsing. These chemical modifications of the top layer add uncertainty to the measurement procedure since they are not easily quantifiable.

In order to eliminate these difficulties, investigators have resorted to the use of a so-called metal ''absorption'' layer on top of the material under test (for instance Au in [25], and Al in [3]).

Contributed by the Heat Transfer Division for publication in the JOURNAL OF HEAT TRANSFER. Manuscript received by the Heat Transfer Division December 20, 2001; revision received July 24, 2002. Associate Editor: G. Chen.

Metal films are used because they exhibit high absorptivity and their optical properties are usually well known. Although the use of other metals as an absorption layer has not been widely considered, gold seems to be a particularly attractive material for use as an absorption film because of good stability in its refractive indexes (n and k) in a normal laboratory environment, linear dependence between reflectivity and temperature changes in the range of up to 200 K, and sufficiently high thermoreflectance coefficient.

Because of the transient nature of the laser heat source in the TTR method, the duration of a laser pulse and the wavelength of the laser light are essential parameters for analyzing the applicability of the TTR method to a particular situation. Although a number of publications have reported on the use of the TTR method for measuring different composite materials [26], a systematic investigation of the influence of the essential parameters in the TTR method on the uncertainty of the measured thermal conductivity of bulk semi-infinite layer samples has only recently been studied by the authors [27]. The present investigation represents the next step in the complexity spectrum of a sample under test, and is focused on the TTR measurements of samples that have at least two layers, one of which is the absorption layer. This work focuses on the influence of the absorption layer on the performance of the thermal conductivity measurements by analyzing the thermal response of dielectric (SiO_2), semiconductor (Si), and highly-conductive (Diamond) materials to the pulsed heating used in the TTR method. It should be pointed out, however, that the three materials considered in this investigation are representative of a wide variety of other materials for which the results obtained here would be applicable. Also, while the TTR system used in this work has a single pulse width (8.6 ns), the methodology and conclusions are largely applicable to other pulse widths and materials whose thermal behavior is governed by the one-equation Fourier heat model. The values of the thermal conductivity (K) and thermal diffusivity (α) for the materials used are as follows: Au ($K=314$ W/m-K, $\alpha=1.27\times10^{-4}$ m^2/s), Si ($K=148$ W/m-K, $\alpha=0.94\times10^{-4}$ m^2/s), SiO_2 ($K=1.4$ W/m-K, $\alpha=4.9\times10^{-7}$ m^2/s), and diamond ($K=2{,}000$ W/m-K, $\alpha=11.1\times10^{-4}$ m^2/s).

The motivation for this study arose from the discovery of a special behavior in the course of an experimental investigation of gold-covered SiO_2 samples. This interesting behavior was later confirmed by a thorough numerical analysis for samples of differing thicknesses of SiO_2 and Au. It was suspected that this behavior might be caused by the significant difference between the thermal conductivity of Au and SiO_2, or in other words, that the thermal behavior is governed by the ratio of the thermal conductivity of the underlying material and the metalization layer. To shed light on this hypothesis, numerical studies were pursued for two underlying materials for which the thermal conductivity ratio would be closer to unity (i.e., Si) and much larger than unity (i.e., Diamond). The studies led to the conclusion that the special behavior exists for any thermal conductivity ratio as will be described in the results section below.

2 Experimental Procedure

The schematic in Fig. 1 depicts the square heating and round probing spots produced by the TTR system in the SMU Submicron Electro-Thermal Sciences (SETS) Laboratory (http://www.engr.smu.edu/setsl). The source of energy in the TTR method is normally provided by a pulsed laser with short pulse duration. During each pulse, a given volume below the sample surface heats up to a temperature level above ambient due to the laser light energy absorbed into the sample. The heating area is specified by adjusting the pulsing laser aperture and the optics of the system. The depth of the volumetric heating, on the other hand, is determined by the optical penetration depth, which is a function of laser wavelength and surface material properties. The heating energy distribution through the penetration depth (δ_L)

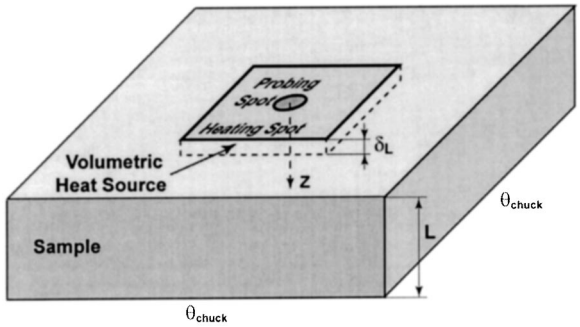

Fig. 1 Schematic of the heating and probing spot positioning on the sample

obeys an exponential decay law, as described later. After each laser pulse is completed, the sample begins to cool down to the initial ambient temperature. During this process, the probing CW laser light reflected from the sample surface at the heating spot center (probing spot on Fig. 1) is collected on a photodetector that reads the instantaneous surface reflectivity. The changes in surface reflectivity are linearly proportional to the changes in surface temperature, within a wide but finite temperature range.

The existing experimental TTR system at the SMU SETS Laboratory is depicted schematically in Fig. 2. The heating source is provided by an Nd:YAG pulsed laser whose wavelength is 532 nm, pulse width is 8.6 ns, and maximum pulse energy is 0.5 mJ. The laser power and output aperture are computer controlled, but the actual energy level delivered by each pulse is also measured by a power meter. The heating spot of the YAG was characterized by CCD imaging and fast photodiode detection, and was found to have good spatial uniformity and a Gaussian temporal distribution, namely:

$$I(t)=\frac{2F}{\tau\sqrt{\pi}}e^{-4(t-t_0)^2/\tau} \tag{1}$$

Here, F is the fluence of laser irradiation, $t_0=9.6$ ns is the time at which the intensity reaches its maximum value, and $\tau=8.6$ ns is the ''duration of the laser pulse'' (defined as the full-width of the pulse at $1/e$-height).

The probing light source is an Ar-Ion CW laser with a linearly polarized, single-mode irradiation beam at a wavelength of 488 nm. The beam is delivered to the microscope assembly via a polarization preserving, fiber optic cable with TEM_{00} mode. The microscope objective lens focuses the laser light on the sample surface concentrically with the heated spot. The probing beam reflects from the heated surface back along its optical path to the sensitive area of a pre-amplified silicon PIN photodetector (rise time$\leqslant$1 ns) through a fiber optic cable. The intensity of the reflected light depends on the reflectivity and temperature of the sample's surface. The photodetector signal, representing the variations in surface reflectivity, is acquired with an 8-bit resolution via a digital oscilloscope at a rate of 2 Giga-samples per second. Several microscope objective lenses are available, but the one used here is 20X, providing heating and probing spots whose diameters are 226 μm and 2.4 μm, respectively, on the surface of a sample under test. The sample under test is placed on a thermal chuck, capable of maintaining the bottom of the sample at an isothermal condition, in the range of 0–200°C with increments of 0.1°C. All components are computer interfaced for control and data acquisition.

3 Heat Transfer Model

The governing mathematical equation used to model the transient thermal process in the sample is the heat conduction equation [28]:

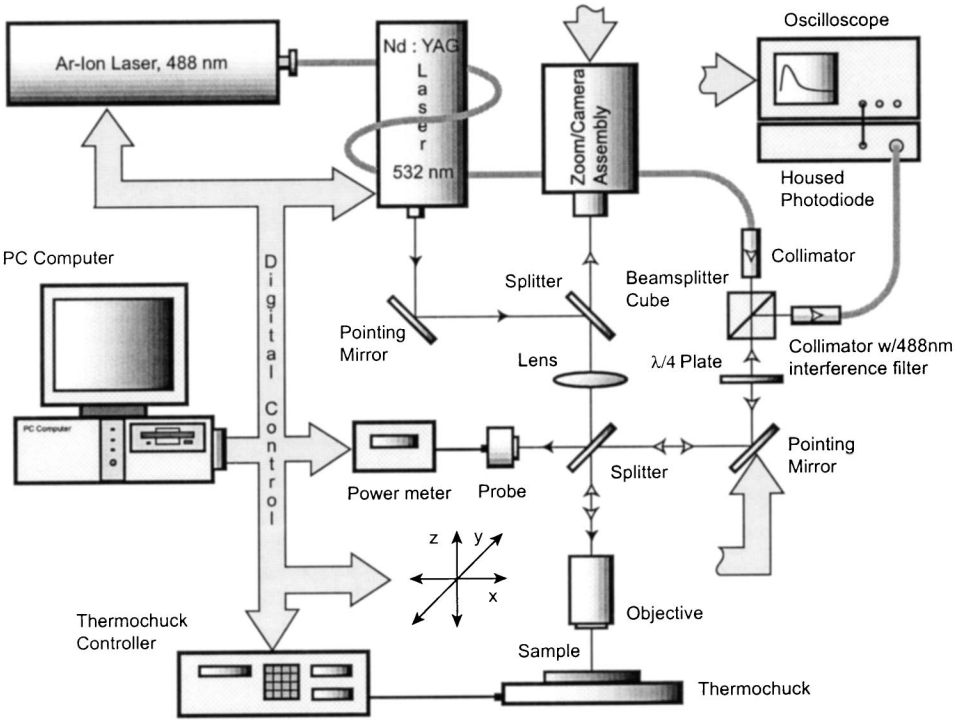

Fig. 2 Schematic of the experimental setup (http://www.engr.smu.edu/setsl)

$$\rho C_p\left(\frac{\partial\theta}{\partial t}\right)=\nabla(K\nabla\theta)+\dot{Q}(r,z,t) \tag{2}$$

where ρ is the material density, C_p is the heat capacity, K is the material thermal conductivity, and $\dot{Q}$ is the heat source term which is a function of radial position, r, depth, z, and time, t. The laser light absorbed by the sample acts as a volumetric heat source, $\dot{Q}$, such that:

$$\dot{Q}(r,z,t)=I(t)(1-R)\gamma e^{-\gamma z}\text{Flag}(r) \tag{3}$$

where $I(t)$ is defined by Eq. (1), R is the reflectivity of the top layer, γ is the absorption coefficient of the top layer, and Flag is the heat spot flag, such that:

$$\text{Flag}(r)=\begin{cases}1 & \text{inside the heating spot}\\ 0 & \text{outside the heating spot}\end{cases} \tag{4}$$

Because of the nature of the problem under consideration (heat spot, structure of the layer, etc.) cylindrical coordinates would normally be preferred. However, since the samples under study are isotropic in the θ-direction, the problem can be reduced to an axially-symmetric, two-dimensional domain. Further simplifications can be obtained by considering that the area of the heat spot is much larger than the probing spot area and that the diameter of the heating laser is much larger than the heat penetration depth, δ_H^*. In such cases, it is possible to solve a much simpler, one-dimensional problem [29,30]. The fact that the problem can be considered one-dimensional has been confirmed by initial computations (the results obtained with one-dimensional and two-dimensional cylindrical coordinates show excellent agreement). The boundary condition at $z=0$ (the upper surface of the sample) is

$$\left(\frac{\partial\theta}{\partial z}\right)_{z=0}=0 \tag{5}$$

while the boundary condition at $z=\infty$ (the lower surface of the sample) is

$$\theta_{z=\infty}=\theta_{\text{chuck}} \tag{6}$$

where θ_{chuck} is the temperature of the thermochuck and can be adjusted between 0 and 200°C. The initial condition at $t=0$ is

$$\theta_{t=0}=\theta_{\text{ambient}} \tag{7}$$

The heat equation is then discretized by the use of central finite differences for spatial derivatives and a generalized Padé-type differentiation scheme for the time derivative. The Padé based three-point-backward scheme is used because of its higher accuracy and unconditional stability. The resulting algorithm is second-order accurate in both space and time.

Initial computations of the heat penetration depth during the heat transfer process ($\Theta_0 \geqslant 0.01$), δ_H^*, indicated that the minimum required thickness (measured from the top of the sample) is 26 μm. A fine computational resolution (20 points) inside the smallest characteristic scale of the problem, which is the light penetration depth into the absorption layer, δ_L, requires that the grid size, ΔZ, be 10 Å. In order to estimate the uncertainty of the numerical simulation, a grid convergence study was conducted by obtaining nondimensional temperature responses of a representative problem with different values of ΔZ. The problem consisted of an Si substrate covered with 1 μm of SiO_2, which in turn was covered with 1.5 μm of Au. The resulting response curves are plotted in Fig. 3 and the maximum error relative to the results obtained with the smallest grid spacing, $\Delta Z=10$ Å, is shown in the legend for each grid spacing. It can be seen that not only does the temperature response curve converge, but negligible error levels of 0.04 percent are obtained at $\Delta Z=20$ Å. Therefore, all subsequent computations were conducted with a spatial step size of 10 Å.

4 Results and Discussion

The absorption layer within a substrate is depicted schematically in Fig. 4. Only three length scales are sufficient to uniquely describe the heat transfer problem during pulsed laser heating in the TTR method; namely, the thickness of the absorption layer, h;

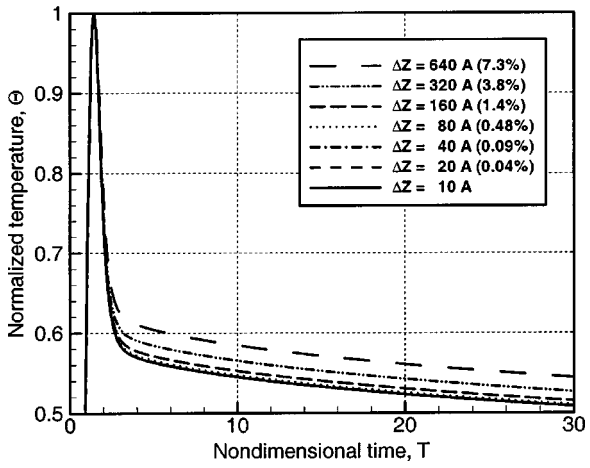

Fig. 3 Uncertainty of the numerical simulation for a Si substrate covered by 1 μm layer of SiO_2 and 1.5 μm layer of Au. Maximum relative errors at the different spatial step sizes ΔZ are shown in the brackets.

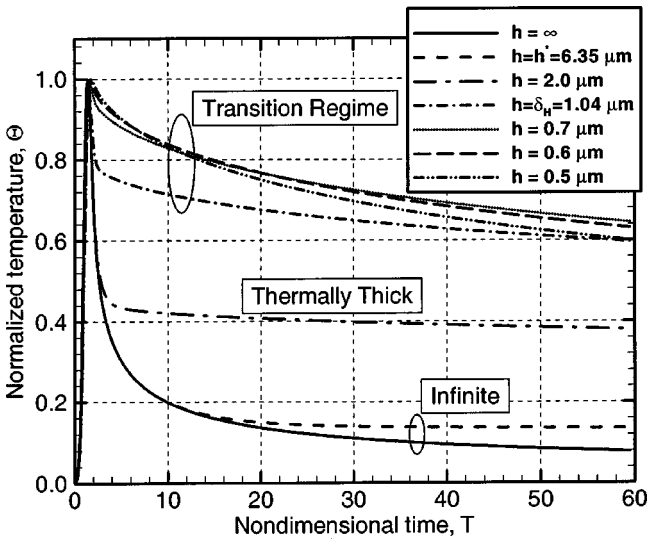

Fig. 5 *Thermally Thick Layer:* Temperature responses of a SiO_2 bulk sample covered with Au, whose thickness is higher than the heat penetration depth, δ_H

the optical penetration depth of the heating light, δ_L; and the heat penetration depth during the pulse width, δ_H. Since the only absorption layer material considered in the present article is gold, it is reasonable to assume that the heat penetration depth is much bigger than the light penetration depth, i.e., $\delta_H \gg \delta_L$ (this assumption is also applicable to all metals subjected to nanosecond-pulse laser heating). It is equally reasonable to consider that the physical thickness of the absorption layer (e.g., gold) is bigger than the light penetration depth, i.e., $h > \delta_L$. Otherwise, the top layer would be inappropriate for light energy absorption within the scope of the TTR measurement approach. Therefore, if one wishes to analyze the heat transfer process in a gold-covered sample, only two length scales need be considered: h and δ_H. After the introduction of the above reasonable limitations for the geometrical parameters of the problem, one can consider two ranges of variation for h, one larger than δ_H and the other smaller than δ_H. For the former case, when h is larger than δ_H, a practical upper limit must be placed on how thick the gold layer needs to be. To place a practical limit on the required thickness of the gold absorption layer, h^*, it is useful to think in terms of the distance traveled by a heat pulse through the sample until the temperature response falls below ten percent of its maximum value. For the case of gold, h^*_{Au} would be equal to 6.35 μm [27].

In the present work, a comparison is made between the temperature responses of two samples of thick SiO_2, one covered with a (hypothetically) infinite thickness of gold and the other with a layer of gold whose thickness is exactly $h^* = 6.35$ μm. The results of this comparison, obtained by numerical simulation, are shown as the lower two curves in Fig. 5. Some discrepancy can be observed between these two curves toward their tail ends, which is due to the influence of the SiO_2 on the heat transfer through the finite gold layer. Nevertheless, it is clear that the gold layer controls the majority of the temporal variations in temperature under the surface of the sample. Thus, the thickness h^* defines the maximum possible thickness of gold to be used as an absorption layer; thicker layers of Au will hide the influence of the thermal properties of any underlying material on the surface temperature response in the TTR method.

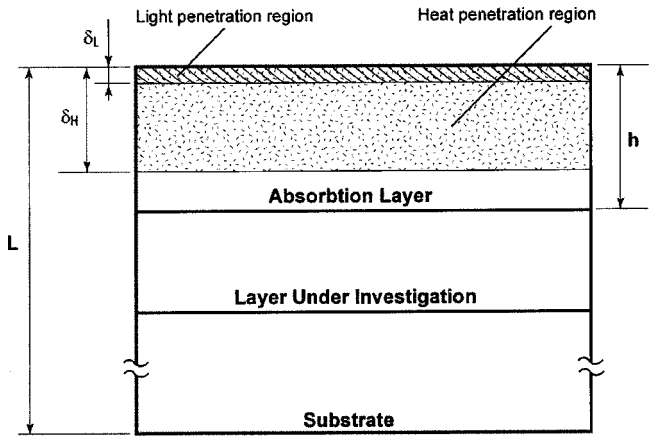

Fig. 4 Schematic of the absorption layer on the substrate

4.1 Behavior of Thermally Thick Absorption Layer for SiO_2. In categorizing the heat transfer process in a layer of material, a distinction is made between layers that are thermally thin and layers that are thermally thick. When the thickness of the absorption layer, h, is larger than the heat penetration depth, δ_H, the layer has sufficient internal thermal resistance to support temperature gradients, i.e., the gold layer behaves as a thick plate. Thus, such a class of absorption layer is referred to as thermally thick.

A typical normalized temperature response for thermally thick layers of gold ($h_{Au} = 2$ μm) is also shown in the middle part of Fig. 5. It is interesting to point out in reference to several of the curves in Fig. 5 that the temperature decay exhibits a sharp change of slope. The slope change corresponds to the time when the heat front reaches the less thermally conductive oxide layer, and is caused by the high temperature gradients developed at the interface between the highly conductive gold layer and the more resistive silicon dioxide layer. As expected, the time required for the heat front to reach the underlying oxide layer is longer for thicker absorption layers. At the upper limit, when the thickness of the absorption layer is bigger than h^*, the response shows that there is very little, if any, heat flow in the silicon dioxide layer, indicating that the bulk limit of the material has been reached.

The preceding discussion dealt with the thermal responses as the thickness of the Au absorption layer was decreased from infinity to 2 μm. While the curve for $h = \infty$ represents the lower limit for the thermal response at the surface of the sample, the four upper curves in Fig. 5 ($h = 0.5$, 0.6, 0.7, and 1.04 μm) represent the upper range. Further reductions in the thickness of the gold absorption layer will produce curves that fall below this up-

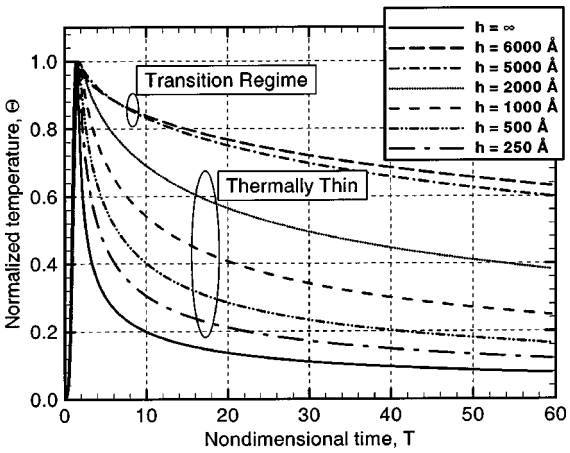

Fig. 6 ***Thermally Thin Films:*** **Temperature responses of a SiO_2 bulk sample covered with Au, whose thickness is smaller than the heat penetration depth, δ_H**

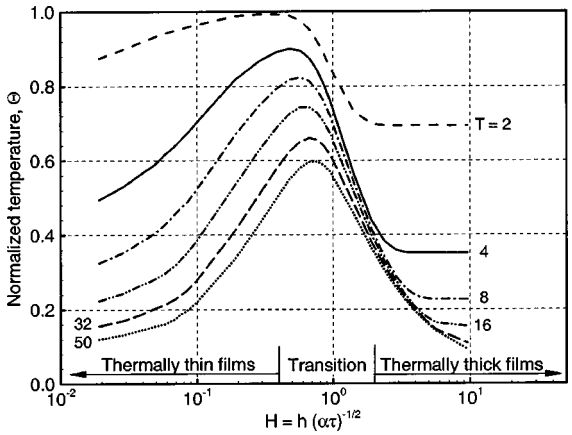

Fig. 7 Heat transfer regimes in gold covered SiO_2 samples

per range, depicting the behavior of thermally-thin absorption layers. The thermally-thin and transition regimes are discussed next.

4.2 Behavior of Thermally Thin Absorption Layer for SiO_2. When the thickness of the absorption layer is smaller than the heat penetration depth during the heating pulse, the layer has insufficient internal thermal resistance to support temperature gradients, and as a result, the instantaneous temperature field is relatively uniform throughout the material. Consequently, this type of absorption layer will be referred to as a thermally thin (also widely known as ''lumped capacity'') layer.

Characteristic temperature responses for thermally thin layers are shown in Fig. 6, bracketed from above by the curve for $h=0.6\ \mu$m and from below by the curve for $h=\infty$. The latter curve is included for reference purposes and may not necessarily represent the absolute limit for all materials. The temperature decay is visibly faster as the thickness of the absorption layer decreases and all temperature responses lie above the response for bulk gold. The light penetration depth of the heating laser, δ_L, is the lower limit for the thickness of an absorption layer. Therefore, layers thinner than δ_L are not considered since they are impractical for the TTR method.

4.3 Transition (Intermediate) Regime Limits for SiO_2. The discussion below can benefit from the use of the Fourier number defined as $\mathrm{Fo}=\alpha\tau/h^2$ where α is the thermal diffusivity of gold and τ is the pulse width of the heating laser. It turns out that the reciprocal of the square root of the Fo number (i.e., $\mathrm{Fo}^{-1/2}$) represents the ratio between the thickness of the absorption layer, h, and the heat penetration depth during a single laser pulse width, δ_H. The above-defined ratio can also be interpreted as the dimensionless thickness of the absorption layer:

$$H=\frac{h}{\sqrt{\alpha\tau}}=\frac{h}{\delta_H}=\frac{1}{\sqrt{Fo}} \tag{8}$$

The computed normalized temperature responses for gold-covered silicon dioxide are plotted in Fig. 7, where a nondimensional time based on the pulse width has been introduced, such that $T=t/\tau$. In these plots, the temperature responses from Figs. 4 and 5 are shown at specific time instances, beginning with a time equal to twice the pulse width, i.e., $T=2$, and ending with $T=50$. This view of the results makes it possible to more easily identify the three different regimes which are entirely defined by the nondimensional thickness H. Behavior consistent with the thermally thick regime appears for $H\gtrsim 2$, while behavior consistent with the thermally thin regime occurs for $H\lesssim 0.4$. A transition regime between the thermally thin and thermally thick regimes is evident. For the specific materials considered here, this transition occurs in the range of $0.4\lesssim H\lesssim 2$.

Similar numerical experiments were conducted for pulse widths equal to 86 ns and 0.86 ns, thus bracketing by an order of magnitude the 8.6 ns pulse width of the current system. The results (not shown) indicate that the transition occurs in the range of $0.4\lesssim H\lesssim 2$, exactly like for the case of the 8.6 ns pulse width.

The existence of the three regimes defined above was shown for metallized silicon dioxide samples. In the next two sections, the results are presented for Si and diamond, proving that the defined regimes can be identified for materials within a wide range of thermal conductivity.

4.4 Thermal Behavior of Gold-Covered Bulk Si and Bulk Diamond. The transient surface temperature characteristic of thermally thick and thermally thin layer regimes are presented in Figs. 8 and 9, respectively. The computed normalized temperature responses are plotted in Fig. 10 for different nondimensional time $T=t/\tau$. As previously observed for gold-covered silicon dioxide samples, behavior consistent with the thermally thick regime is evident for $H\gtrsim 2$, while behavior consistent with the thermally thin regime occurs for $H\lesssim 0.4$. Transition between the thermally thin and thermally thick regimes for the gold-covered silicon sample is clearly visible and occurs again in the range $0.4\lesssim H\lesssim 2$.

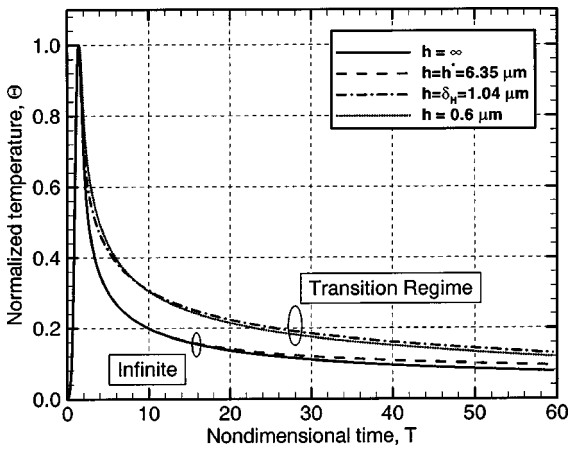

Fig. 8 ***Thermally Thick Layer:*** **Temperature responses of a Si bulk sample covered with Au, whose thickness is higher than the heat penetration depth, δ_H**

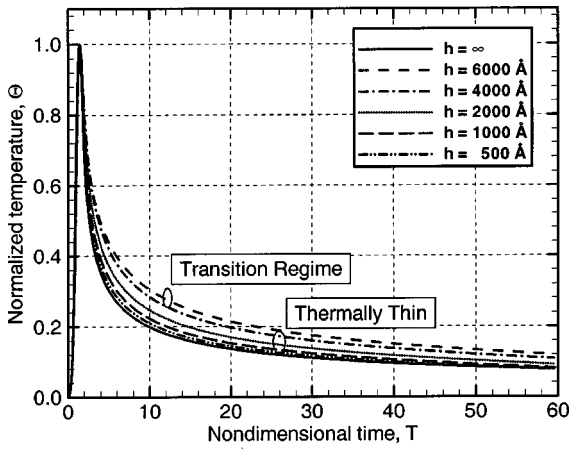

Fig. 9 ***Thermally Thin Films:*** **Temperature responses of a Si bulk sample covered with Au, whose thickness is smaller than the heat penetration depth, δ_H**

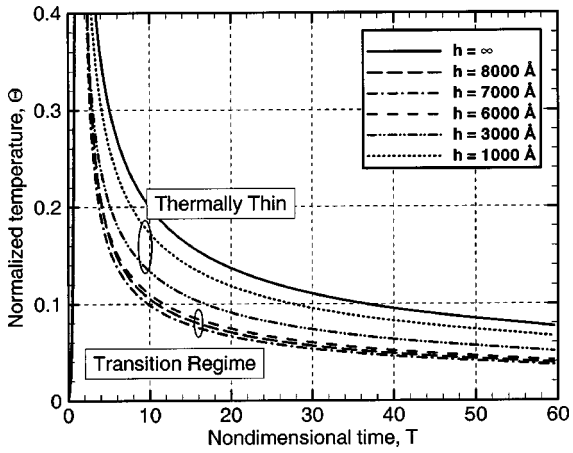

Fig. 12 ***Thermally Thin Films:*** **Temperature responses of a diamond bulk sample covered with Au, whose thickness is smaller than the heat penetration depth, δ_H**

Corresponding results for gold-covered diamond are presented in Figs. 11–13. Two major differences from the results shown above for Si and SiO_2 are observed. First, all of the transient surface temperature responses lie below the bulk gold curve (i.e., $h=\infty$). Second, increasing the thickness of Au in the thermally thin regime results in the lowering of the transient temperature curve, while increasing the thickness of Au in the thermally thick regime results in the raising of the temperature curve. The lowest curve exists in the transition regime. This behavior is the opposite of what was observed in the cases of Si and SiO_2 above. Finally, it should be noted that the behavior observed for gold-covered diamond should be expected for all combinations of underlying material and metalization cover layer whose thermal conductivity ratio is much higher than unity.

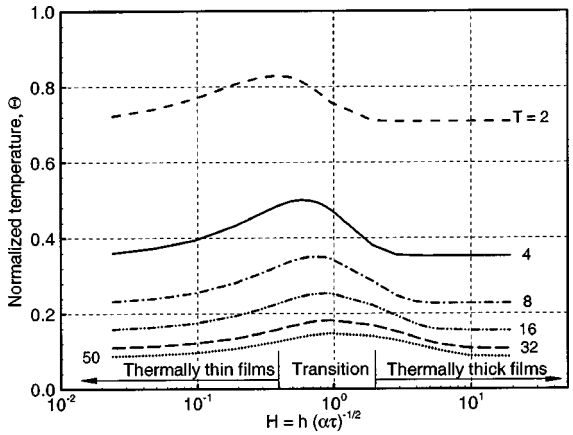

Fig. 10 Heat transfer regimes in gold covered Si samples

4.5 Experimental Results. To validate the temperature response behavior observed in the numerical results presented above for the thin and thick absorption layers, experiments were carried out for different thicknesses of the absorption layer deposited on a given semi-infinite thickness of SiO_2.

In order to determine the minimum required thickness of SiO_2 that behaves thermally as a semi-infinite material, an additional numerical investigation was carried out for seven samples of different thicknesses of SiO_2 covered by 1.5 μm of Au. The results, shown in Fig. 14, indicate that the transient surface temperature response is indistinguishable for layers of SiO_2 thicker than 5000 Å. Therefore, it was decided to thermally grow 1 μm of SiO_2 on five standard, 4-inch, silicon wafers, and then cover each of them with a metallic layer by a process of chemical vapor deposition. The actual thicknesses of SiO_2 for the five samples were measured with an ellipsometer and found to vary between 1.2 and 1.5 μm, all of which are well above the minimum required 5000 Å.

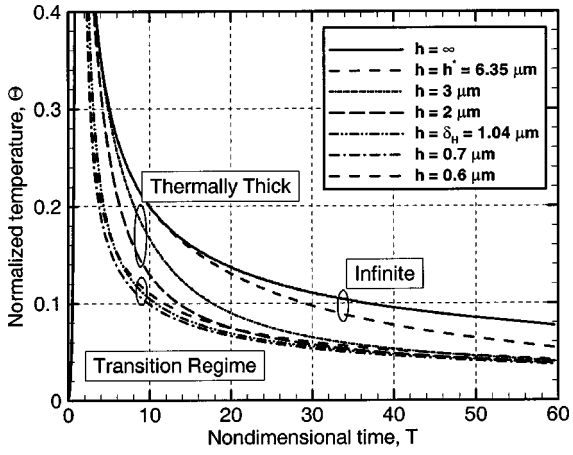

Fig. 11 ***Thermally Thick Layer:*** **Temperature responses of a diamond bulk sample covered with Au, whose thickness is higher than the heat penetration depth, δ_H**

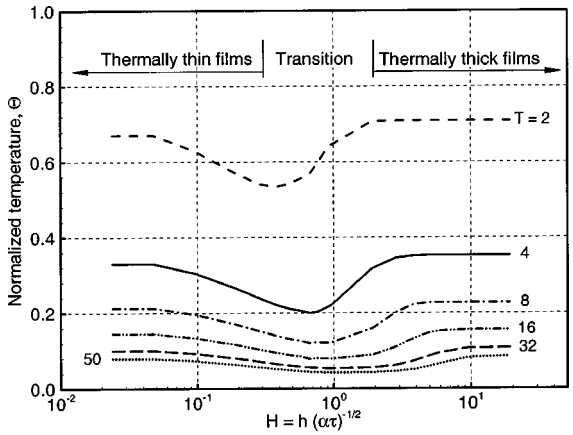

Fig. 13 Heat transfer regimes in gold covered diamond samples

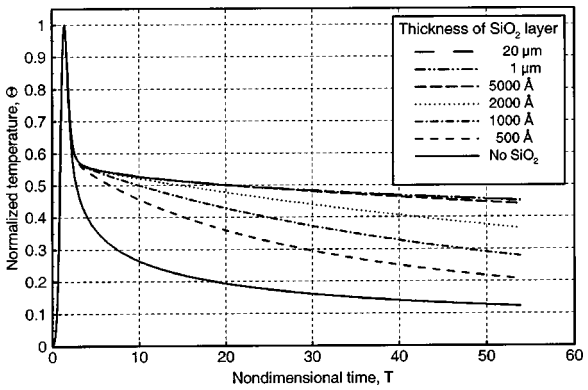

Fig. 14 Influence of the SiO_2 thickness on the normalized temperature response of the gold covered ($h_{Au}=1.5\ \mu m$) samples

As previously discussed, the metal of choice for the top layer is gold since gold is chemically stable, has known optical and thermal properties, and has a high thermal reflection coefficient. However, very large thicknesses of gold are inherently difficult and expensive to deposit. Alternatively, a thinner layer of gold was deposited on a thicker layer of aluminum, creating the desired metallic thickness while preserving the advantages of the use of gold as a surface layer. In order to assess the influence of the use of some aluminum in the metallic layer instead of using solely gold, numerical simulations were performed for the scenario of pure gold and a corresponding case of gold on top of aluminum. The simulation results indicated that as expected the differences between the temperature responses for pure gold and gold on aluminum were negligible (RMS<0.6 percent) since the two metals have similar thermal properties.

The experimental and corresponding numerical results are presented in Fig. 15. The thickness of the coating gold layer for each sample was measured by the use of a stylus profiler with an uncertainty of 5 percent (which is essentially due to the nonuniformity of the coating process rather than the low accuracy of the profiler). The thickness of the absorption layer measured by the profiler is shown in the legend of Fig. 15 for each sample as the sum of the thicknesses of the Au and the Al layers. For each sample, two temperature response curves were obtained numerically in order to bound the variations in the response that would correspond to the 5 percent uncertainty band in the metal thickness. Then, it was found that the experimental data falls within the envelope formed by two response curves. Hence, it became possible to select the best fit between the experimental data and numerical curve within the envelope for each curve. The worst average uncertainty in the curve-fitting procedure was equal to 2.2 percent and occurred for Sample 5.

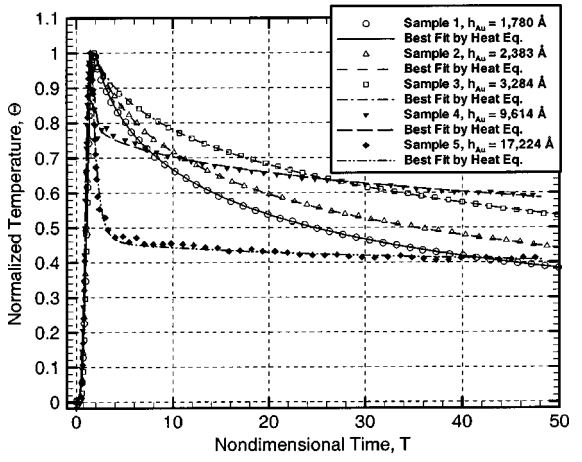

Fig. 15 Measured and computed temperature responses of a SiO_2 layer covered by different thicknesses of gold

The behavior of the temperature responses of samples 1–3 is consistent with the previously discussed behavior of thermally thin absorption layers (Fig. 15), where the gold layer thickness is considerably smaller than the heat penetration depth during the pulse, and the cooling phase of the temperature response is completely dependent on the thermal properties of SiO_2. The decrease in the level of the temperature response evident as the gold layer becomes thinner is explained by the fact that the amount of energy accumulated during the pulse decreases accordingly with the reduction of the thermal capacitance of the absorption layer.

Samples 4 and 5 exhibit a behavior consistent with the thermally thick regime whereby the diffusion of heat through the underlying oxide layer is discernable by the presence of an abrupt change of slope at small values of T ($T\cong 2.5$ for sample 4 and $T\cong 3.5$ for sample 5). In this case, both the TTR heating and the beginning of the TTR cooling phases occur within the gold layer, which is highly diffusive for the heat propagation. Thus, the initial decay of the temperature response exhibits a considerable slope, which corresponds to the TTR response of the bulk gold. Contrary to the behavior of the initial decay, the remainder of the temperature response forms a nearly "flat" curve, whose slope corresponds to the slow diffusion of the energy in the SiO_2 medium. This part of the normalized response is lower for thicker layers of gold because the accumulated energy during a pulse dissipates into the gold for thicker gold layers.

4.6 Responsivity of the TTR Method. To further assess the performance of the TTR method, it is useful to introduce a parameter whose value could directly characterize the accuracy of TTR measurements. We suggest the use of the responsivity, *Rs*, of the thermal conductivity measurement defined as $Rs=K(d\Theta/dK)_{\max}$, where T is the normalized temperature response of the sample surface and K is the thermal conductivity of the material. The responsivity *Rs* is calculated at the nondimensional time Θ where $d\theta/dK$ is maximum. Indeed, *Rs* is directly connected with the accuracy of the method by the equation $\sigma_K=Rs^{-1}\sigma_\Theta$, where σ_K is the random measurement uncertainty of the thermal conductivity, K, and σ_Θ is the random apparatus uncertainty related to detecting the temperature response. While σ_Θ depends on the apparatus signal-to-noise ratio and can be considered as a conservative value for a particular setup, the latter equation shows that the measurement uncertainty, σ_K, of the TTR technique decreases with increases in the responsivity value, *Rs*. Hence, the responsivity, *Rs*, which depends on the properties and geometry of the materials making up a sample as well as the parameters of the TTR system, can characterize the performance of the TTR method and be useful for optimizing an experiment. By numerically solving the heat equation for Θ, it is possible to compute *Rs* and to bring out an important issue that could be used to assess the performance of the TTR technique.

The influence of the thickness of the gold absorption layer on the responsivity of the thermal conductivity of three gold-covered samples (silicon, silicon dioxide, and diamond) is shown in Fig. 16. In addition, the responsivity value ($Rs=0.091$) for an uncovered bulk silicon sample is shown as a dashed horizontal line for reference purposes. For thermally-thick absorption layers, it is expected that the responsivity of the gold-covered silicon sample will be worse than the responsivity of an uncovered silicon sample because a very thick layer of gold will essentially hide the influence of the thermal properties of the underlying silicon material. In the transition and thermally-thin regimes, the responsivity of the gold-covered silicon sample is significantly higher than that of the uncovered silicon sample, except when the thickness of the gold cover becomes smaller than $h_{Au}=2{,}150$ Å ($H=0.207$). The improvement is as high as 40 percent at the specific optimal thickness of gold $h_{Au}=5{,}700$ Å, which corresponds to $H=0.558$.

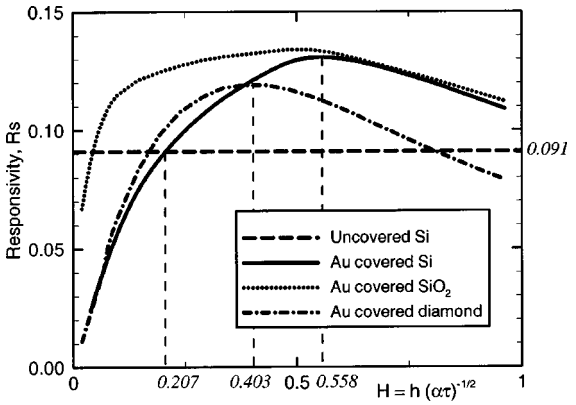

Fig. 16 Influence of thickness of Au absorption layer on the responsivity of thermal conductivity measurements for Si, SiO_2 and diamond samples

Based on this investigation, one can conclude that it is not advisable to use absorption layers that are in the thermally thin regime (i.e., $H<0.207$) since these layers result in much lower responsivity values. Furthermore, in attempting to measure lower thicknesses of the absorption layer one can expect to incur higher levels of uncertainty.

By increasing the thickness of the gold layer on an SiO_2 or diamond sample, the responsivity exhibits a similar behavior and noticeably higher *Rs* values. However, unlike silicon, SiO_2 and diamond are transparent materials; so, if it were not for the presence of the metallic layer, the heating laser would not have been able to heat the SiO_2 and diamond test samples. Therefore, it is impossible to estimate the accuracy gain resulting from the use of a gold cover for an SiO_2 or diamond sample.

4.7 Measurement Uncertainty. As described earlier, the TTR measurement procedure consists of both experimental and numerical parts. The experimental part includes heating the sample under test and detecting a change in the surface reflectivity caused by the temperature change in the heated area, while the numerical part consists of simulating the heat transfer process through the multi-layered sample. Both parts are expected to introduce errors into the respectively obtained normalized transient temperature responses. On the basis of the uncertainty analysis developed by Kline and McClintock [31] and revised later by Holman [32], the average discrepancy between the experimental data and the numerical fitting curve is given by:

$$\sigma_{\text{fit}}^2=|\sigma_{\text{exp}}^2+\sigma_{\text{num}}^2| \tag{9}$$

Here σ_{exp} and σ_{num} are the experimental and numerical uncertainties, respectively. Since systematic errors do not exist in the experimental technique, σ_{exp} is tied to the signal-to-noise ratio of the TTR system and can be estimated by calculating the standard deviation of an adequately large number of transient responses. In order to estimate σ_{num}, the responsivity, *Rs*, introduced in the previous section is used. The responsivity of the normalized transient temperature response for a small relative variation of a parameter V_i of a *j*-layer of a sample under test is

$$Rs_{i,j}=V_i\frac{\partial\Theta}{\partial V_i} \tag{10}$$

where V_i can be one of the following variables: thermal conductivity *K*, specific heat ρC_p, extinction coefficient *k*, or thickness of the layer *h*. Then, assuming that the truncation errors resulting from the discretization of the heat transfer equation are negligible as compared to those associated with the previously listed variables, the uncertainty analysis yields

$$\sigma_{\text{num}}^2=\sum_{i}^{4}\sum_{\substack{j\neq n\\ \text{if } i=K}}^{N}(Rs_{i,j}\sigma_{i,j})^2+(Rs_{K,n}\sigma_{K,n})^2 \tag{11}$$

Here, $\sigma_{i,j}$ is the relative uncertainty of parameter V_i of the layer *j* used in the numerical simulation; *N* is the number of sample layers; *n* is the particular layer under test; $\sigma_{K,n}$ is the relative uncertainty of the thermal conductivity, *K*, of the layer under test, *n*. By substituting σ_{num} into Eq. (9), the uncertainty of the TTR thermal conductivity measurement, $\sigma_{K,n}$, can be re-written as

$$\sigma_{K,n}=Rs_{K,n}^{-1}\sigma_{\Theta}=Rs_{K,n}^{-1}\left(\sigma_{\text{fit}}^2+\sigma_{\text{exp}}^2+\sum_{i}^{4}\sum_{\substack{j\neq n\\ \text{if } i=K}}^{N}(Rs_{i,j}\sigma_{i,j})^2\right)^{1/2} \tag{12}$$

As evident from Eq. (12), the uncertainty of the measurements $\sigma_{K,n}$ is directly connected to the responsivity *Rs*. Since the uncertainty σ_{Θ} is an intrinsic parameter of the TTR system, an increase in the responsivity will produce a decrease in the uncertainty of the measurements $\sigma_{K,n}$. Thus, the best uncertainty is obtained for the maximum value of responsivity *Rs*. Calculating the various terms in Eq. (12) for the present investigation reveals that the total measurement uncertainty is less than 6 percent for the five samples considered.

5 Conclusions

The influence of the thickness of a metallic absorption layer on the performance of the transient thermo-reflectance method has been investigated. The maximum practical thickness of gold that needs to be used as an absorption layer (h^*) was determined, and it was concluded that using thicker layers would hide the influence of the thermal properties of any underlying material. Conversely, the lower limit for the thickness of an absorption layer is the light penetration depth of the heating laser, δ_L, since layers thinner than δ_L do not absorb enough irradiation energy in order to generate the heat source required in the TTR method.

For thicknesses of the absorption layer between the lower and upper limits (i.e., $\delta_L<h<h^*$), the numerically and experimentally obtained transient surface temperature responses differ according to the ratio between the absorption layer thickness, *h*, and the heat penetration depth, δ_H, during a laser pulse. The two drastically different behaviors are referred to as thermally thick and thermally thin. In the thermally thick regime, a decrease of the absorption layer thickness enhances the normalized temperature response and shortens the time during which the initial rapid temperature decay takes place. In contrast, the normalized temperature response on top of a thermally thin layer exhibits the opposite behavior. Specifically, a decrease of the layer thickness leads to a lower normalized temperature response, but while lower, it remains above the temperature response for bulk gold, even at thicknesses close to δ_L. Between the thermally thick and thermally thin layers there is a range of layer thicknesses where their influence on the temperature response is minimal. The temperature response behavior associated with this range of thicknesses has been referred to as a transition regime.

The analysis performed in the present work has led to the association of the Fourier number (Fo) or the nondimensional thickness of the absorption layer (*H*) with the different regimes of the normalized temperature response behavior. The thermally thin, thermally thick, and transition regimes have been associated with $H\lesssim 0.4$, $H\gtrsim 2$, and $0.4\lesssim H\lesssim 2$, respectively.

The responsivity of the TTR measurements characterizes the performance of the TTR method, and makes it possible to recommend optimal thicknesses for a metallic absorption layer. The numerical simulations carried out for the gold-covered Si, SiO_2, and diamond samples revealed that the responsivity values in the thermally thick regime are too low for the measurements to be sufficiently accurate. The same holds true for lower values of *H* in the thermally thin regime. However, for the range $0.1\lesssim H\lesssim 2$ that

covers all of the transition regime and most of the thermally thin layer regime, the responsivity of the TTR measurements for metallized silicon dioxide and silicon samples is sufficiently high for measuring the thermal conductivity of the underlying material with acceptable uncertainty. Furthermore, the responsivity values for a metallized silicon sample exceed the responsivity value for an uncovered silicon sample over a wide range of the H parameter. And, the maximum performance of the TTR method is expected for gold covered Si and SiO_2 samples at the specific thickness of gold $h_{Au}=5700$ Å, which corresponds to $H=0.558$, while the maximum performance for gold covered diamond is observed at $H=0.403$.

Three representative materials have been selected in order to cover the wide range of thermal conductivity of electronics materials. Namely, diamond was chosen for the higher limit, silicon dioxide for the lowest, and silicon somewhat in the middle. Since the results presented here show that the optimum layer of the absorption material is obtained for the transition regime for all of the above materials, it is concluded that the above statement is valid for any material as long as it falls within the investigated range, whether its thermal conductivity is known or is to be determined. In addition to covering a wide range of materials, computations for different pulse widths (one order of magnitude smaller, 0.86 ns, and one order of magnitude larger, 86 ns, than the pulse width of the heating laser used in this work) have also shown that the analysis and the results presented in this work are applicable for a wide range of heating lasers. In other words, the transition regime identified to be in the interval of $0.4 \lesssim H \lesssim 2$ is applicable to all heating pulses in the nanosecond range. These findings indicate that the physics are similar for this wide range of materials and pulse widths.

Acknowledgments

The authors gratefully acknowledge Dr. Howard Beratan and his Raytheon colleagues at the uncooled detector branch of Raytheon in Dallas, TX, for covering the samples with oxide and metal layers.

Nomenclature

F = fluence of heating laser irradiation, J/m^2
$\mathrm{Flag}(r)$ = heating spot flag
Fo = Fourier number, $Fo=\alpha\tau/h^2$
h = thickness of the absorption layer, m
h^* = practical upper limit for the thickness of the absorption layer, m
H = nondimensional thickness of the absorption layer, m
$I(t)$ = heating irradiation intensity
K = thermal conductivity of a sample material, W/m-K
L = thickness of the sample, m
$Q_{ab}(r,z,t)$ = laser energy absorbed by a sample material
R = reflectivity of a sample surface
Rs = responsivity of the TTR method
t = time, s
t_0 = time at which heating laser intensity reaches its maximum value, s
T = nondimensional time, t/τ
z = coordinate that is normal to a sample surface, m

Greek symbols

α = thermal diffusivity of a sample material, m^2/s
γ = absorption coefficient of a sample material, m^{-1}
$\delta_L=1/\gamma$ = penetration depth of a heating laser light, m
δ_H = heat penetration depth during the pulse width, m
δ_H^* = heat penetration depth during the heat transfer process ($\Theta \geq 0.01$), m
θ = temperature of a sample, K
Θ = normalized temperature of a sample ($\theta/\theta_{\max}$)
k = extinction coefficient of a sample material
λ = wavelength of a heating laser, m
ρC_P = specific heat per unit volume, J/m^{3}K
σ_K = random apparatus uncertainty
σ_Θ = random measurement uncertainty of the thermal conductivity
τ = pulse width of a heating laser, s

Subscripts and Superscripts

ab = absorption
0 = outer boundary
r, z = direction indices

References

[1] Tien, C. L., Majumdar, A., and Gerner, F. M., eds., 1998, *Microscale Energy Transport*, Taylor and Francis, Washington, DC.
[2] Majumdar, A., 1993, "Microscale Heat Conduction in Dielectric Thin Films," ASME J. Heat Transfer , **115**, pp. 7–16.
[3] Capinski, W. S., and Maris, H. J., 1996, "Improved Apparatus for Picosecond Pump-and-Probe Optical Measurements," Rev. Sci. Instrum., **67**, pp. 2720–2726.
[4] Xu, X., Grigoropoulos, C. P., and Russo, R. E., 1995, "Transient Temperature During Pulsed Excimer Laser Heating of Thin Polysilicon films obtained by Optical Reflectivity Measurement," ASME J. Heat Transfer , **117**, pp. 17–24.
[5] Lambropoulos, J. C., and Hwang, S. S., 1993, "Thermal Properties of Thin Films," Mater. Res. Soc. Symp. Proc., **284**, pp. 133–138.
[6] Lambropoulos, J. C., Jacobs, S. D., Burns, S. J., Shaw-Klein, L., and Hwang S. S., 1989, "Thermal Conductivity of Thin Films: Measurement and Microstructural Effects," *ASME Heat Transfer Division, Thin Film Heat Transfer: Properties and Processing*, M. K. Alam, et al., eds., 1991, **184**, pp. 21–32.
[7] Tai, Y. C., Mastrangelo, C. H., and Muller, R. S., 1988, "Thermal Conductivity of Heavily Doped Low-Pressure Chemical Vapor Deposited Polycrystalline Silicon Films," J. Appl. Phys., **63**, pp. 1442–1447.
[8] Goodson, K. E., Flik, M. I., Su, L. T., and Antoniadis, D. A., 1993, "Annealing-Temperature Dependence of the Thermal Conductivity of LPCVD Silicon-Dioxide Layers," IEEE Electron Device Lett., **14**, pp. 490–492.
[9] Graebner, J. E., 1998, "Measurements of Thermal Conductivity and Thermal Diffusivity of CVD Diamond," Int. J. Thermophys., **19**, pp. 511–525.
[10] Zhao, W., Brotzen, F. R., Hehn, L., and Loos, P. J., 1998, "Interface Effect on the Transverse Thermal Conductivity of SiO2 Films Deposited on Silicon," Mater. Res. Soc. Symp. Proc., **516**, pp. 51–56.
[11] Brotzen, F. R., Loos, P. J., and Brady, D. P., 1992, "Thermal Conductivity of Thin SiO2 Films," Thin Solid Films, **207**, pp. 197–201.
[12] Griffin, A. J., Jr., Brotzen, F. R., and Loos, P. J., 1995, "The Transverse Thermal Conductivity of Thin Dielectric Films," High Temp. Mater. Sci., **33**, pp. 217–224.
[13] Shibata, H., Ohta, H., Suzuki, A., and Waseda, Y., 1991, "New Laser Flash Method for Measuring Thermal Diffusivity of Isotropic and Anisotropic Thin Films," Mater. Trans., JIM, **32**, pp. 837–844.
[14] Visser, E. P., Versteegen, E. H., and Enckevort, J. P., 1992, "Measurement of Thermal Diffusivity in Thin Films Using a Modulated Laser Technique: Application to Chemical-Vapor-Deposited Diamond Films," J. Appl. Phys., **71**, pp. 3238–3248.
[15] Cahill, D. G., and Pohl, R. O., 1987, "Thermal Conductivity of Amorphous Solids above the Plateau," Phys. Rev. B, **35**, pp. 4067–4073.
[16] Borca-Tasciuc, T., Kumar, A. R., and Chen, G., 2001, "Data Reduction in 3-ω Method for Thin-Film Thermal Conductivity Determination," Rev. Sci. Instrum., **72**, pp. 2139–2138.
[17] Moon, K., Jeong, Y. H., and Kwun, S. I., 1996, "The 3-omega Technique for Measuring Dynamic Specific Heat and Thermal Conductivity of a Liquid or Solid," Rev. Sci. Instrum., **67**, pp. 29–35.
[18] Ritley, K. A., Just, K. P., Schreiber, F., 2000, "X-ray Reflectivity Study of Solution-Deposited ZrO2 Thin Films on Self-assembled Monolayers: Growth, Interface Properties, Thermal Densification," J. Mater. Res., **15**, pp. 2706–2713.
[19] Hatta, I., 1990, "Thermal Diffusivity Measurements of Thin Films and Multilayered Composites," Int. J. Thermophys., **11**(2), pp. 293–303.
[20] Yao, T., 1987, "Thermal Properties of AlAs/GaAs Superlattices," Appl. Phys. Lett., **51**, pp. 1798–1800.
[21] Hatta, I., Yasunaga, S., Ryozo, K., and Akikazu, M., 1985, "Thermal Diffusivity Measurements of Thin Films by Means of an Calorimetric Method," Rev. Sci. Instrum., **58**, pp. 1643–1647.
[22] Stanimirovic, A. M., Maglic, K. D., Perovic, N. L., and Vukovic, G. S., 1998, "Measurement of Thermal Diffusivity of Thin Films by the AC Calorimetric Method," High Temp.-High Press., **30**(3), pp. 327.
[23] Takahashi, F., Mori, T., Hamada, Y., and Hatta, I., 2001, "Instrumentation, Measurement, and Fabrication Technology—AC Calorimetric Thermal Diffusivity Measurement in Relatively Thick Samples by a Distance-Variation Method Source," Proceedings of the Symposium on Ultrasonic Electronics, **40**, pp. 4741–4745.

[24] Tzou, D. Y., 1997, *Macro-to Microscale Heat Transfer (The Lagging Behavior)*, Taylor and Francis, Washington, DC
[25] Paddock, A., and Eesley, G. L., 1986, ''Transient Thermoreflectance From Thin Metal Films,'' J. Appl. Phys., **60**, pp. 285–290.
[26] Chen, G., Tien, C.-L., Wu, X., and Smith, J. S., 1994, ''Thermal Diffusivity Measurement of GaAs/AlGaAs Thin-Film Structures,'' ASME J. Heat Transfer, **116**, pp. 325–331.
[27] Komarov, P. L., and Raad, P. E., 2002, ''Range of Applicability of the Transient Thermo-reflectance (TTR) Method for Measuring the Thermal Conductivity of Bulk Semi-Infinite Layer Samples,'' prepared for publication.
[28] Bejan, A., 1993, *Heat Transfer*, John Wiley and Sons, New York.
[29] Kading, O. W., Skurk, H., and Goodson, K. E., 1994, ''Thermal Conduction in Metallized Silicon-Dioxide Layers on Silicon,'' Appl. Phys. Lett., **65**, pp. 1629–1631.
[30] Zhang, X., and Grigoropoulos, C. P., 1994, ''The Amplitude Technique for Measurement of Free Standing Thin Film Thermal Properties: A Comparison with other Experimental Techniques,'' *Proceedings of the ASME Heat Transfer Division, Heat Transfer in Thin Films*, **293**, ASME, New York, pp. 17–24
[31] Kline, S. J., and McClintock, F. A., 1953, ''Describing Uncertainties in Single-Sample Experiments,'' Mech. Eng. (Am. Soc. Mech. Eng.), January 1953, p. 3.
[32] Holman, J. P., 1994, *Experimental Methods for Engineers*, sixth edition, McGraw-Hill, pp. 49–65, Chap. 3.

Convective Heat Transfer in Vertical Asymmetrically Heated Narrow Channels

Yun Chin

Muthu S. Lakshminarasimhan

Qing Lu

D. Keith Hollingsworth
e-mail: hollingsworth@uh.edu

Larry C. Witte

Heat Transfer & Phase Change Laboratory,
Dept. of Mech. Engineering,
University of Houston,
Houston, TX 77204-4792

A calibrated thermochromic liquid crystal technique was used to acquire wall temperature data for laminar and turbulent forced convection in an asymmetrically heated channel. The experiments were carried out in upward flow in rectangular channels with channels spacings of 2.0, 1.0, and 0.5 mm and aspect ratios of 1:10, 1:20, and 1:40. One side was uniformly heated, and the remaining sides were approximately adiabatic. The entire surface temperature field of the heated wall was acquired in one color image, and the temperature was determined by hue-based image processing. In the laminar regime, buoyancy effects elevated the local Nusselt number to values significantly above those expected for purely forced convection in both the developing region and in the fully developed region. In the turbulent regime, the fully developed Nusselt number agreed well with previous observations, but the facility produced an unexplained linear trend in a portion of the developing region of the channel. While the channel aspect ratio affected the fully developed Nusselt number, no evidence was found that small channel spacing in itself produces Nusselt numbers that are at variance with accepted values.
[DOI: 10.1115/1.1497356]

Keywords: Channel Flow, Heat Transfer, Laminar, Mixed Convection, Turbulent

Introduction

The vertical rectangular channel with a symmetrical uniform-heat-flux boundary condition has received considerable attention in the literature. However, studies of the asymmetrical uniform-heat-flux boundary condition (here, one wall at uniform flux, the other adiabatic) are more limited, and more often theoretical and numerical than experimental. Summaries of various cases for laminar and turbulent flow are provided by Bhatti and Shah [1], Shah and Bhatti [2], and Hartnett and Kostic [3]. With the advent of interest in micro-scale thermal systems, there have been reports that single-phase convective heat transfer rates in small channels (characteristic dimension near or below 1 mm) are enhanced above classical values established for larger channels, e.g., Kamidis and Ravigururajan [4].

This study presents an experimental data set that addresses the streamwise evolution of heat transfer in channels with an asymmetrical uniform-heat-flux boundary condition, and it examines the question of heat transfer enhancement in small rectangular channels. The results concern rectangular channels with channel heights of 2.0, 1.0, and 0.5 mm. These heights correspond to aspect ratios of 1:10, 1:20, and 1:40 for the channel width of 20 mm and a length of 357 mm. One channel wall was electrically heated while the remaining walls were approximately adiabatic. The channel axis was vertical and the flow direction was upward. The working fluid was Freon-11 with a Prandtl number, Pr, of approximately 4.1. Flow rates were selected so that both the laminar and turbulent flow regions were examined. The lower flow rates were small enough that density-driven fluid motion could contribute to heat transfer. The streamwise evolution of surface temperature on the electrically heated wall was measured by hue-based liquid crystal thermography. This technique made possible surface temperature measurements with a spatial scale of less than 600 μm.

Brief Review of the Turbulent Flow Literature. The experimental studies of Sparrow et al. [5] and Tan et al. [6] of fully developed turbulent air flow in an asymmetrically heated rectangular channel yielded a fully developed value of the Nusselt number, Nu, that is about 15 percent lower than that for the symmetrically heated channel. The problem of simultaneously developing momentum and thermal profiles in a rectangular duct has received less attention. Sparrow and Cur [7] reported Nu_x for a turbulent air flow in the entrance and fully developed regions. They used a sublimation technique with an effective Pr=2.5. One wall was isothermal while the remaining three were adiabatic. They found the Nu_x for symmetrical and asymmetrical heating are identical in the initial portion of the entrance region. The fully developed value of Nu_x for the asymmetrical heating was as low as 7 percent below the value for symmetrical heating, and the thermal entrance length for asymmetric heating was about double that for symmetric heating.

A fully developed turbulent water flow through a rectangular duct with asymmetric heating was experimentally investigated by Kostic and Hartnett [8]. The two facing walls were driven at uniform-heat-flux, but at different levels. The Nu for the higher-heat-flux wall was lower than those of the lower-heat-flux wall, with the values of Nu for the symmetrical heating case falling in between. The difference in Nu between the symmetrical and asymmetrical cases increased to 8 percent as the lower-heat-flux wall approached adiabatic. This difference compares to a value of 15 percent found by Sparrow et al. [5], and the discrepancy was attributed to the higher Pr of the working fluid (water).

Brief Review of the Laminar Flow Literature. The analysis by Shah and London [9] found Nu=5.385 for fully developed, purely-forced, laminar flow in a flat duct with uniform heat flux on one side and adiabatic on the other. Maitra et al. [10] presented a theoretical and experimental study of laminar flow in a vertical annulus. Their results indicated that buoyancy effects were relatively minor when the Rayleigh number, Ra, was $<10^3$. Above this value, a steep increase in Nu occurred. The thermal entry length was much shorter than for pure forced convection, and it depended on Ra. The measured Nu followed the same trend as the theoretical analysis but were on the average 45 percent higher.

Contributed by the Heat Transfer Division for publication in the JOURNAL OF HEAT TRANSFER. Manuscript received by the Heat Transfer Division July 24, 2001; revision received May 28, 2002. Associate Editor: K. S. Ball.

Yao [11] suggested that idealized, fully developed, forced convection flows can exist only with minimum heating; therefore, it is improper to use available heat transfer predictions without considering buoyancy effects.

For fluids of intermediate Pr, the thermal entrance region involves simultaneously developing momentum and thermal boundary layers, and the resulting behavior is dependent on Pr. Few measurements are available for simultaneously developing flows in a flat duct with asymmetric heating. Heaton et al. [12] obtained an analytical solution for simultaneous development of velocity and temperature fields in a flat duct with one wall at constant heat flux and the others adiabatic. Mercer et al. [13] found that increasing buoyancy tended to increase the hydrodynamic development length but decrease the thermal development length.

Baek et al. [14] conducted a numerical analysis and an experimental study of velocity profiles for assisted convection in a vertical channel with an asymmetric uniform-wall-temperature boundary condition. The velocity distribution was observed to skew towards the heated wall and the fluid in that region accelerated as it ascended along the length of the channel. Distortion of the developed velocity profiles by asymmetric heating and enhancement of heat transfer rate on the heated wall were also reported by Aung and Worku [15]. Their results suggested that quantitative effects of buoyancy in laminar, buoyancy-aided flows in a vertical parallel-plate channel cannot be extrapolated from results available for circular tube flow. Under asymmetrical heating conditions, the effect of buoyancy causes the velocity profile to be dramatically distorted as the fluid moves through the duct. Increasing the heat flux causes the thermal development length to be shortened and the hydrodynamic development length to be elongated considerably. Aung and Worku found that for small, but significant Ra, the thermal entrance length decreases with increasing Ra, and then increases with increasing Ra at large Ra.

Experiment Apparatus and Data Reduction

Freon 11 was selected as the working fluid because its boiling point was compatible with flow-boiling experiments also carried out in this apparatus. The test section was a rectangular channel with a width of 20 mm and a length of 357 mm. Three heights, H, (channel spacings) were investigated: $H=2.0$, 1.0 and 0.5 mm. A drawing of the cross-section of channel with a detail of the surface construction is shown in Fig. 1, and a schematic of the entire apparatus is shown in Fig. 2.

The channel was machined into one face of an aluminum bar so that $H=2.0$ mm was created by the depth of the machining operation. For the 1.0 and 0.5 mm spacings, shims were attached to the non-heated wall to achieve the desired spacings. The choice of a metallic base structure for the test section was dictated by the need to hold channel dimensions fixed over a range of system pressures during the two-phase experiments referenced above. However, this choice did present challenges in the management of the thermal boundary conditions on the unheated walls. To alleviate this problem, a number of flow passages designed to approximate an adiabatic condition on the back surface of the channel and on the narrow sides were machined into the bar. The approximately adiabatic condition on the back surface was implemented by circulating water at the mean temperature of the working fluid through a passage directly behind the back surface of the channel. Five type-K thermocouples were epoxy-sealed in wells drilled into the back surface such that the beads were 1.78 mm below the back surface of the (unshimmed) channel. The difference in the heat capacities of R-11 and water allowed the back surface of the channel to be maintained near the mean of the inlet and outlet temperatures of the working fluid. Figure 3 shows that a typical bulk temperature rise through the channel resulted in a temperature variation of ± 2.0°C about this mean, while the driving temperature difference was an order of magnitude larger.

The heated wall of the channel was a 76 μm thick Haynes 230 alloy foil that was clamped to the face of the aluminum bar. An

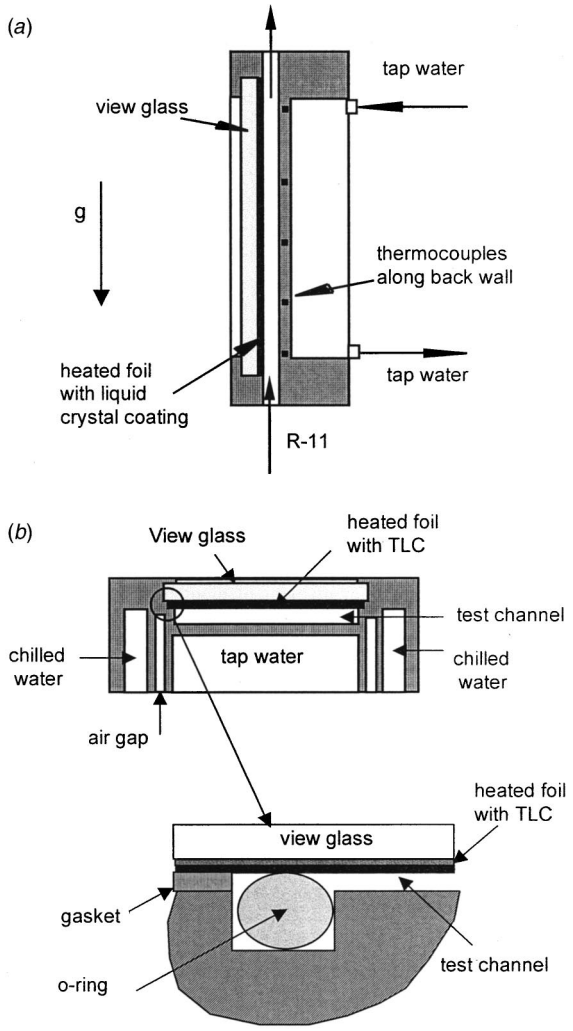

Fig. 1 Cross-section views of the channel: (*a*) longitudinal, and (*b*) transverse with construction detail. For (*b*) the gravity vector is pointing out of the page.

o-ring provided a pressure seal and a 0.25 mm thick gasket electrically isolated the foil from the channel. Thermochromic liquid crystal was painted on the dry side of the foil, and a clear glass sheet attached to the clamp held the foil flat so that the estimated variance in channel spacing was ± 0.1 mm. The heat flux was provided by electrically heating the foil with direct current from a pair of 200 ampere, 12 volt power supplies connected in series.

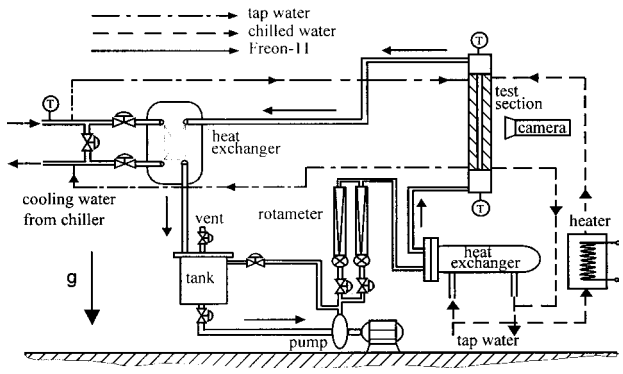

Fig. 2 Schematic of experiment apparatus

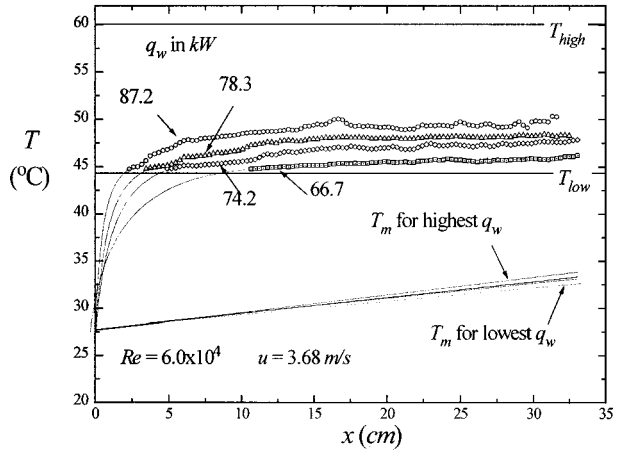

Fig. 3 Wall and bulk temperatures for Re=6.0×10⁴, H=2 mm

The voltage drop across the foil was measured at the connecting bus bars, and the current was measured from the voltage drop across a known resistor connected in series with the foil. The energy dissipated from the portion of the foil beneath the clamping frame was removed by chilled water flowing through passages in both the clamping frame and the edge of the aluminum bar. The sidewalls of the channel were isolated from this cooling flow by air gaps machined parallel to the channel walls into the aluminum bar.

The working fluid entered an inlet plenum chamber on the bottom of the channel, and exited through an identical chamber at the top of the channel. These chambers were circular in cross-section, and the test channel connected tangentially at the wall of each chamber. The foil was attached so that heating began at the start of the test channel with no unheated starting length. Rotameters were used to measure a volumetric flow rate controlled by a by-pass loop connected to a constant-speed pump. The fluid temperatures at the inlet and exit of the test section were measured by thermocouples and collected along with the foil voltage and current by a computer-controlled data acquisition system. No measurements of the inlet velocity profile could be made because of the size of the channel.

The visible surface of the foil was air-brushed with water-soluble black paint followed by several coats of a micro-encapsulated cholesteric liquid crystal formulation from Hallcrest, Inc. Thermochromic liquid crystals (TLC) display a color change across the spectrum from red at the lower end of the active temperature range through blue at the upper end. On either side of the active range the TLC surface appeared black. The surface was lighted by two 40 watt fluorescent tubes placed parallel to the flow direction. The image was captured by a charge-coupled-device color video camera. Real-time images were recorded on videotape, and single images were digitized directly by a 3×8 bit Matrox color frame-grabber in an Intel-type computer.

A general discussion of the application of quantitative TLC imaging to heat transfer research can be found in Hay and Hollingsworth [16]. The intensities of the red, green, and blue primaries (*R*, *G*, and *B* respectively) as recorded by the camera are cast as magnitudes of *hue*, *saturation*, and *monochromatic intensity*. The hue corresponds most closely to the wavelength of the light, and it provides a scalar against which temperature can be calibrated. Hue is defined in terms of the intensities of the three primaries as

$$\text{hue} \equiv \arctan\left(\frac{\sqrt{3}(G-B)}{2R-G-B}\right). \tag{1}$$

The hue-temperature relationship for this TLC is discussed at length in Hay and Hollingsworth [17]. The useful active range of the TLC as verified by six *in situ* calibrations in the present apparatus was 44.4 to 59.6°C. A fifth-order polynomial was fit to the calibration data and a computation of uncertainty using this calibration was done in accordance with Hay and Hollingsworth [16]. The typical single-pixel uncertainty was ±1.9°C, with the maximum of ±4.5°C occurring near the upper end of the range. The upper limit of the active band is set by this unacceptably high uncertainty. The lower end of the band is set by a loss of intensity as red fades to black. The image window was chosen to be a long, narrow slice (36 by 623 pixels) of the test surface centered on the centerline of the heated wall. The resulting spatial resolution was 0.56 mm×0.56 mm per pixel.

The hydraulic diameter used in the data reduction was $D_h = 2H$, as suggested by Shah and London [9]. The Reynolds number is defined as $\text{Re} \equiv \rho u D_h/\mu$. If the heat flux from the heated wall to the fluid is q_w, and $T_w(x) - T_m(x)$ is the local driving temperature difference, then the local heat transfer coefficient and the local Nusselt number can be defined as

$$\text{Nu}_x \equiv \frac{h_x D_h}{k} = \frac{q_w D_h}{k(T_w(x) - T_m(x))}, \tag{2}$$

where x is the axial coordinate. The heat flux and wall temperature were measured, and the local bulk fluid temperature, $T_m(x)$, was obtained by an enthalpy balance as

$$T_m(x) = T_i + \frac{4}{\rho u C_p D_{he}} \int_0^x [q_w - q_{\text{back}}(x)]dx, \tag{3}$$

where T_i is the inlet temperature of the liquid fed to the heated channel, u is the velocity, c_p is the liquid thermal capacity, and D_{he} is the equivalent heated diameter suggested by Katto [18] for handling asymmetrical heating situations. D_{he} is defined as

$$D_{he} = \frac{4 \times \text{flow area}}{\text{heated perimeter}}. \tag{4}$$

For a channel heated uniformly along its entire perimeter, $D_{he} = D_h$. For the present boundary condition, $D_{he} = 2D_h$. The local heat loss through the back surface of the channel is $q_{\text{back}}(x)$. The modified Grashof number is defined as $\text{Gr}^* \equiv \beta g \rho^2 D_{he}^4 q_w/\mu^2 k$, and the corresponding modified Rayleigh number is $\text{Ra}^* \equiv \text{Gr}^* \text{Pr}$.

The fluid properties were evaluated at $T_m(x)$. The temperature on the wetted side of the heated foil was estimated by a conduction analysis to be 0.06°C to 0.15°C higher than that measured by the imaging system, depending on the operating heat flux. The unwanted heat loss from the foil through the view glass was estimated by a one-dimensional conduction analysis to be less than 0.4 percent of the heat input. This correction was made to the values of $T_w(x)$. Values for $q_{\text{back}}(x)$ were determined form a one-dimensional heat loss analysis where the local fluid-to-surface resistance, $1/h(x)_{\text{back wall}}$ was approximated from Eqs. 2 and 3 with q_{back} set to zero. The maximum value of q_{back}/q_w was approximately 10 percent for the 2 mm channel, but fell to about 3 percent for the 1 mm and 0.5 mm channels due to inclusion of the thermal resistance of the stainless steel shim used to narrow the channel. Experimental uncertainties were calculated to first-order (stochastic contributions only) using the method of Kline and McClintock [19]. The typical single-sample relative uncertainty in Nu_x was less than ±6.0 percent for the H=2 mm channel, ±8.5 percent for the H=1 mm channel, and ±12 percent for the H=0.5 mm channel. These are based on single-pixel uncertainties of ±1.9°C for $T_w(x)$ and ±0.01 ampere for the electric current measurement. For $T_w(x)$ near the upper limit of the active band, the uncertainty in Nu_x increased; for example, for the H=2 mm channel it attained a maximum of approximately ±12 percent. The uncertainty in Re was less than ±5 percent and in Gr* was less than ±3.8 percent. The Nu_x data shown are based on data averaged over a sample window that is 5×5 pixels centered on the test surface centerline.

Table 1 Range of experimental variables for convection experiments

	$H = 2.0$ mm	$H = 1.0$ mm	$H = 0.5$ mm
$P_i(MPa)$	0.14 – 0.18	0.14 – 0.21	0.12 – 0.16
$G(kg/m^2s)$	60 – 5260	60 – 4856	166 – 3037
$q_w(kW/m^2)$	5.7 – 121.0	4.4 – 98.0	8.69 – 54.0
$u(m/s)$	0.04 – 3.68	0.04 – 3.31	0.11 – 2.03
$T_m(°C)$	15.7 – 34.9	17.4 – 37.0	12.6 – 30.7
Re	612 – 60,000	306 – 27,000	275 – 9340

Temperature Measurements and Repeatability of Nu_x. Table 1 shows a summary of the range of variables of the data obtained for the three spacings of the channels. The data span both laminar and turbulent flows. Typical axial distributions of wall temperatures are shown in Fig. 3 for $H=2.0$ mm, $Re=6.0\times10^5$ and for four values of q_w. Example images for laminar flow in the 1.0 mm and 0.5 mm channels along with the associated temperature distributions are shown in Fig. 4. These data are essentially an instantaneous ''snapshot'' of the temperature distribution because the entire field is acquired in the framing time of the camera (1/30 s), and no explicit temporal averaging is done. While the thermal mass of the foil/TLC/glass assembly does apply some degree of temporal filtering, fluctuations of substantially less than one second duration are clearly visible in the videotaped sequences from the experiments.

The image for $H=1.0$ mm illustrates the effect of an incorrectly balanced flow of chilled water through the passages in the edge of the aluminum bar. While the color (and thus temperature) gradient is reasonably perpendicular to the upper side of the image, a thin red/orange wedge can be seen approaching the lower side at a narrow angle. For this image, that side of the channel is overcooled, and the flow rate of chilled water to the frame passages in that side should be reduced. In this case, the incursion of this lateral gradient (associated with a temperature change of approximately 4°C) does not greatly affect the centerline temperature. The image of the $H=0.5$ mm illustrates properly balanced lateral boundary conditions.

The wall temperatures shown in Figs. 3 and 4 are the result of a spanwise-average across 36 pixels located along the center of a single TLC image. Only those temperatures that fell into the active range of the TLC can be measured. That range is indicated by the horizontal lines drawn at 44.4°C and at 59.6°C in Fig. 3. Dashed lines representing estimates of evolution of $T_w(x)$ near the inlet were placed on the graph to orient the reader. In Fig. 3, the $T_w(x)$ data were resampled to a coarser grid so that the data point symbols would be legible; a sense of the true spatial density of the data can be obtained from Fig. 4. The bulk fluid temperature, $T_m(x)$ was calculated from Eq. 3. The remainder of the results are computed from temperature information of this type. From inlet to exit, $T_m(x)$ varies by 4°C so that the driving temperature difference for $q_{\text{back}}(x)$ is no more than ±2°C.

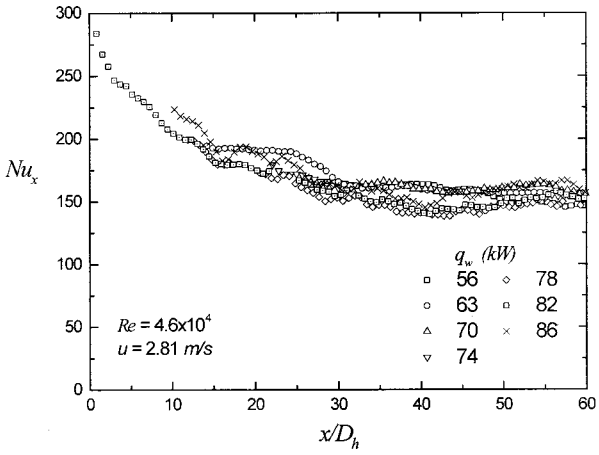

Fig. 5 Local Nu_x for simultaneously developing turbulent flow for $Re=4.6\times10^4$, $H=2$ mm

Figure 5 compares the Nu_x for $H=2.0$ mm, $Re=4.6\times10^4$ at seven different values of q_w. The data were obtained from different image frames in the same run as the power to the test surface was increased; and as such, are ''snapshots'' of the results of the heat transfer coefficient distribution for each q_w. In order to make the data point symbols visible, the data have been down-sampled by a factor of five. The Nu_x should not be a function of q_w; therefore, the differences between the curves are representative of moment-to-moment changes in the state of the system (such as small changes in flow rate or inlet temperature) and any system-

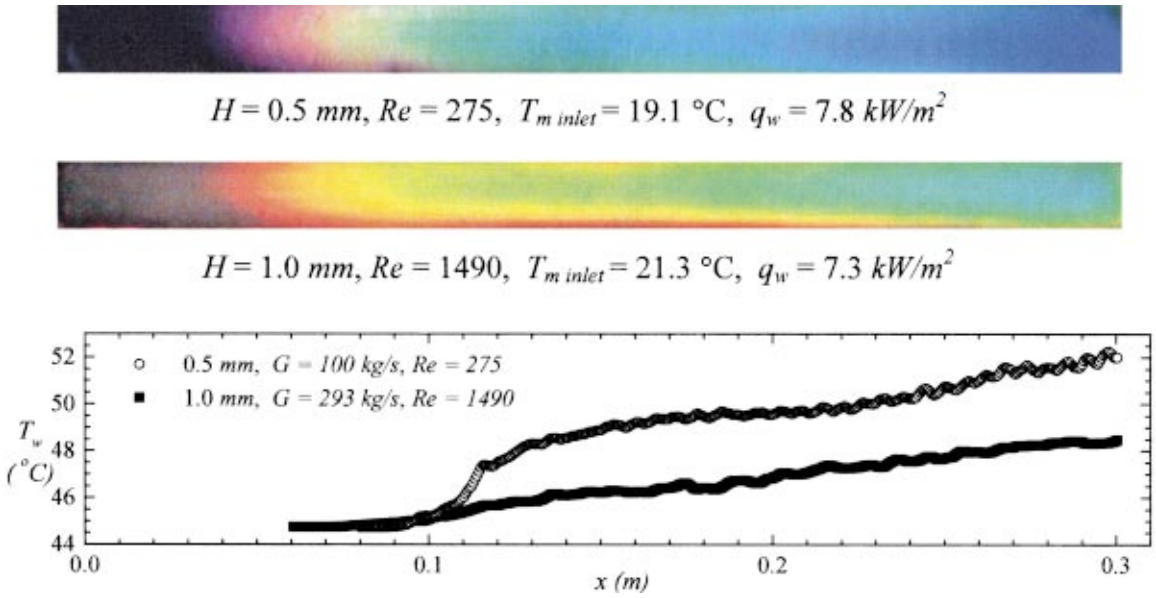

Fig. 4 Examples of liquid crystal images and associated temperature measurements along the centerline of the channel

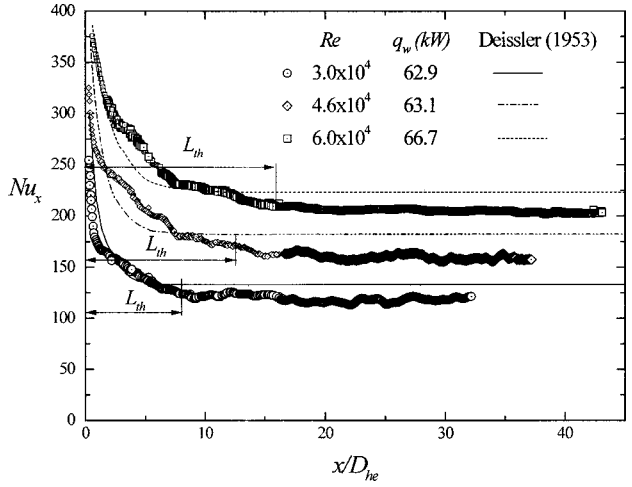

Fig. 6 Local Nu_x for three values of Re, $H=2$ mm

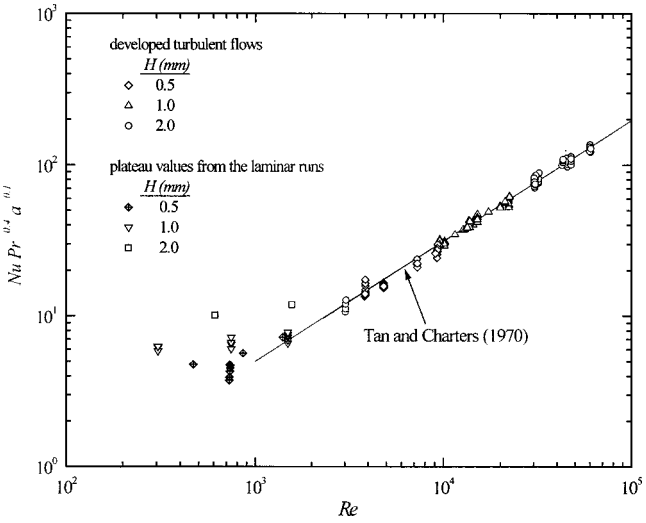

Fig. 8 Nusselt numbers compared to the correlation of Tan and Charters for fully developed turbulent flow

atic errors in the data reduction. The variation in the fully developed value of Nu_x is representative of the uncertainty in Nu_x determined by a root-sum-squares combination of the constituent quantities.

Results for the Turbulent Regime

The Evolution of Nu_x in the Developing Region. The streamwise evolution of Nu_x for three values of Re and $H=2$ mm at nearly the same q_w is plotted versus x/D_{he} in Fig. 6. For a magnitude reference, the theoretical solution for simultaneously developing turbulent flow inside a uniformly heated circular channel for a constant Pr of 4.14 (Deissler [20]) is included. For symmetric heating $D_{he}=D_h$. Measurements of Nu_x are shown from within one D_{he} of the channel entrance. An apparently linear decrease is observed in the vicinity of $3\leqslant x/D_{he}\leqslant 8$ followed by the asymptotic approach to a fully developed value that is 9–14 percent below the Deissler solution. If the thermal development entry length, L_{th}, is defined as x/D_{he} such that $Nu_x=1.05Nu_{\text{fully developed}}$, then L_{th} increases with Re, from $L_{th}\approx 8$ for $Re=3.0\times10^4$, to ≈ 15 for $Re=6.0\times10^4$. For the Deissler solution, $L_{th}\approx 5D_{he}$ (with $D_{he}=D_h$), and changes less with increasing Re.

Figure 7 compares the data for the developing Nu_x at $Re=4.6\times10^4$ for a 2 mm spacing to data from Sparrow and Cur [7] for an asymmetrically heated channel with an aspect ratio of 1:18 and an effective Pr through a mass-transfer analogy of 2.5. The boundary condition was an effectively uniform temperature on the ''heated'' wall, and adiabatic on the remaining surfaces. This comparison is attractive because of the close match in Re, the similarity in heated geometry, and both the differences in thermal boundary condition (uniform flux versus temperature) and in measurement technique. To account for the Pr difference, the data are plotted as Nu_xPr^n, with $n=-1/3$. Typical values quoted for n in the fully developed region are ≈ 0.33 and ≈ 0.40.

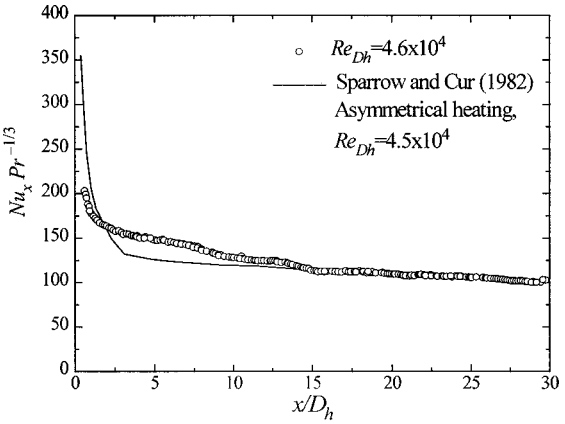

Fig. 7 Comparison of Nu_x for simultaneously developing turbulent flow in a rectangular channel, $H=2$ mm

The present data compare well with the results of Sparrow and Cur [7] downstream of the thermal development region. Disagreement in the developing region is to be expected due to the difference in Pr, but the primary difference seen is due to the approximately linear region identified above. The fully developed values differ little, certainly to within the estimate of n. We speculate that the linear-like portion of the Nu_x is caused by the geometry of the inlet plenum chamber.

Fully Developed Turbulent Flow. The Nu data collected for the fully developed turbulent flow region are plotted against Re in Fig. 8. This data set includes data for all three channel spacings, and is again displayed with spanwise-averaging, but without temporal averaging. Values of Re span both laminar and turbulent flow at inlet Pr from 4.0 to 4.4. The variation shown (typically ± 9 percent) at fixed Re is due to the issues discussed previously, plus additional repeatability issues resulting from system rebuilds, most particularly many different installations of the foil/TLC subsystem for different channel spacings as well as replacements for the same channel spacings due to operational mishaps.

Typical correlations for fully-developed heat transfer are of the form $Nu=C_0\,Re^{0.8}\,Pr^{0.4}$. The classical Dittus-Boelter correlation has $C_0=0.023$ and was obtained for a smooth, uniform-flux circular tube. Tan and Charters [6] reported that Nu for air in an asymmetrically heated rectangular channel (aspect ratio=1:3) with adiabatic conditions on the unheated walls were about 20 percent lower than given by Dittus-Boelter. They suggested a correlation for this geometry of the same form but with $C_0=0.018$. The present results show a trend with aspect ratio, $a\equiv H/W$, such that an excellent collapse is obtained for $C_0=0.02a^{0.1}$. In Fig. 8, data from all three channel-spacings is shown along with the Tan and Charters result. Data at laminar to transitional Re are shown to illustrate the Nu levels obtained for laminar flow with various amounts of mixed-convection augmentation as discussed later in the paper.

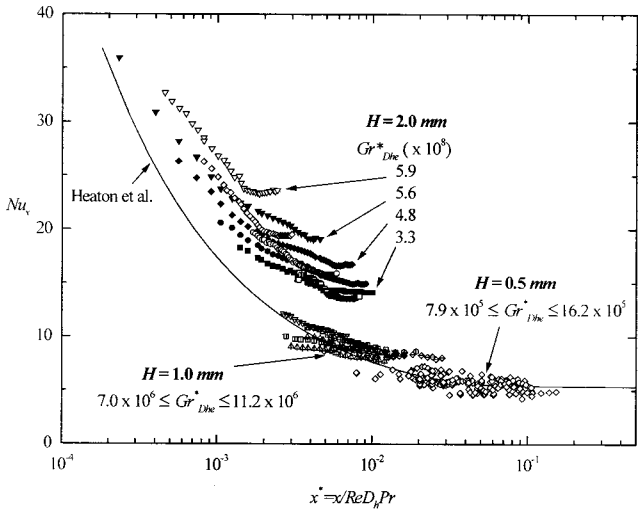

Fig. 9 Nusselt number evolution for $H=2.0$, 1.0, and 0.5 mm

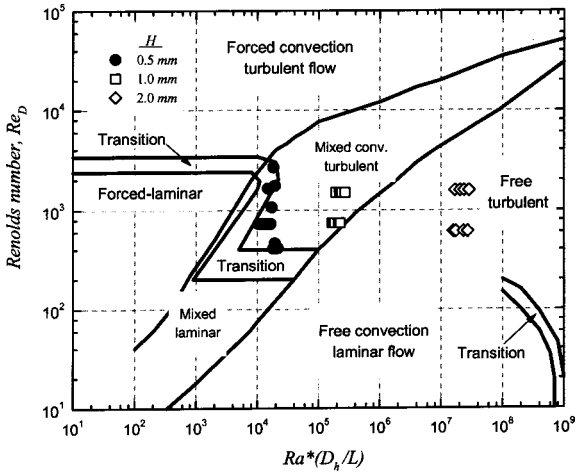

Fig. 10 Replica of Metais' figure showing the regimes for narrow channel data

Results for the Laminar Regime

Figure 9 presents Nu_x versus dimensionless axial distance, x^*, for the data for all three spacings. Also shown is the solution of Heaton et al. [12] for pure laminar forced convection for simultaneously developing flow in a flat duct with uniform heat flux at one wall and the other wall insulated. The data for the 2 mm channel have $Gr^* \approx 10^8$ and indicate an asymptotic value in the fully developed region. The value is roughly three times higher than the fully developed forced-convection value, and increases with increasing Gr*. Also, the apparent onset of this deviation occurs earlier with increasing Gr*. The data for the 1 mm channel have $Gr^* \approx 10^6$ and are better predicted by Heaton's result, but the data approach an asymptotic value slightly higher than Heaton's curve. The data for 0.5 mm have $Gr^* \approx 10^5$ and are predicted quite well by Heaton's result. For $H=2.0$ and 1.0 mm, the decay of Nu_x with axial distance (L_{th}) was foreshortened when compared to the forced convection solution. These data support the trend to lower L_{th} with increasing Gr* seen in the numerical solution of Aung and Worku [15].

The discussion of Fig. 9 does not directly reference Re or a mixed-convection grouping such as Gr^*/Re^2. Instead, the flow characterization given by Metais and Eckert [21] is applied. They provided a criterion for determining the ranges of non-negligible buoyancy effects in a vertical channel: mixed-convection flows for which Nu deviates by more than 10 percent from the pure forced or pure natural convection value. Figure 10 is a replica of the figure taken from Metais and Eckert where the ratio, D_h/L, is the hydraulic diameter to the channel length. Based on the measured values of Re and $Ra^*(D_h/L)$, the data for $H=2$ mm clearly fall into the range where buoyant forces drive a free-convection turbulent flow field. The data for $H=1$ mm fall into the range of turbulent mixed-convection flows, and the $H=0.5$ mm data fall in the range of mixed-convection transitional flows. These flow field characterizations supports the behavior seen in Fig. 9. It is interesting to note that while most of the data are at $Re<2000$, the presence of buoyancy forces drive flows that are classified as transitional to fully-turbulent. Real-time observations of the temperature patterns on the TLC surface reported in Chin et al. [22] at laminar Reynolds numbers showed a transient ''streakiness'' reminiscent of dye streak visualizations of the sublayer of a turbulent boundary layer. The classification of the flows from the 1 and 2 mm channels as buoyancy-driven turbulence explains this observation.

Conclusions

For turbulent flow, values for the fully developed Nu agree well with previous observations: they are approximately 10 percent below predictions for a uniformly heated circular channel of the same hydraulic diameter, and at matched Re, they agree well with results from the sublimation experiment by Sparrow and Cur [7]. In the developing region, the results were mixed. The behavior of the apparatus produced an unexplained linear trend in the developing Nu in the range of $1 \leqslant x/D_{he} \leqslant 8$. This behavior is most probably an entrance region effect stemming from the way in which the fluid entered the channel from the inlet plenum. While this is an interesting point, we do not claim any universality in this observation. It is perhaps best thought of as a testament to the difficulty of building channels of this dimension and to the capacity of liquid crystal thermography to illuminate the details of their performance.

For developed laminar flow in the 2 mm channel, the measured Nu is up to three times greater than expected from pure forced convection alone. This increase correlates with increasing buoyant force as given by the Grashof number. The departure is much less pronounced for the 1 mm channel, and the Nu_x for the 0.5 mm channel agree with theory to within the measurement uncertainty. These results indicate that mixed convection effects become pronounced at laminar Re for $Gr^* > 10^6$. Furthermore, the flow characterization provided by Metais and Eckert [21] works well for these flows. Visual observations of streamwise temperature streaks support a buoyancy-driven transition to turbulence at Re typical of laminar flows.

For the range of channel spacings investigated in this study, no evidence was found that the size of the spacing directly affected the heat transfer in the channel. Instead, we find that care must be taken to include the effects of buoyancy into the prediction of heat transfer rate at laminar-range Re, even though the channel spacing is small.

Liquid crystal thermography applied to this problem allowed measurements on a highly resolved spatial grid and with uncertainties in Nu_x of less than ± 6.0 percent. The technique does not create localized wall irregularities of the type that might be encountered with single-point devices. This advantage has a heightened importance given the present application to a thin channel. The main issues in the implementation, as always, are the requirement of a uniform flux boundary, sufficient optical access, and the selection of a proper active band such that the ''thermal window'' thus created is suitable to the problem at hand.

Acknowledgments

This work was supported by State of Texas Advanced Research Project 00365218 and by NSF Grant CTS-9701556.

Nomenclature

a = aspect ratio, H/W, dimensionless
A = area, m^2
C_p = specific heat, J/(kg°C)
D_h = hydraulic diameter, m
D_{he} = equivalent heated diameter, m
g = gravitational acceleration, m/s^2
Gr* = modified Grashof number, $=\beta g \rho^2 D_{he}^4 q_w / \mu^2 k$, dimensionless
h = heat transfer coefficient, $W/(m^2°C)$
H = channel height, m
k = thermal conductivity, W/(m°C)
L = channel length, m
L_h = hydraulic entry length, $\equiv x_{\text{developed}}/D_h$, dimensionless
L_{th} = thermal entry length, $\equiv x_{\text{developed}}/(D_h \,\text{Re}\,\text{Pr})$ or $x_{\text{developed}}/D_{he}$, dimensionless
Nu_x = local Nusselt number, $h_x D_h/k$, dimensionless
Pr = Prandtl number, $\mu c_p/k$, dimensionless
q_w = wall heat flux, W/m^2
q_{back} = heat flux into the back wall of the channel, W/m^2
Ra* = modified Rayleigh number, Ra*=Gr*Pr, dimensionless
Re = Reynolds number, $=\rho u D_h/\mu$, dimensionless
T_m = local bulk mean temperature of fluid, °C
T_w = local wall temperature, °C
u = velocity of fluid, m/s
W = test channel width (20 mm)
x = coordinate along the heated surface in axial direction, m
x^* = dimensionless distance along axial direction, $x/(D_{he}\,\text{Re}\,\text{Pr})$
β = volumetric coefficient of thermal expansion, dimensionless
μ = dynamic viscosity, kg/(ms)
ρ = density, kg/m^3

References

[1] Bhatti, M. S., and Shah, R. K., 1987, "Turbulent and Transition Flow Convective Heat Transfer in Ducts," *Handbook of Single-Phase Convective Heat Transfer*, Kakac, Shah, and Aung, eds., John Wiley & Son, New York, pp. 4.1–4.166.

[2] Shah, R. K., and Bhatti, M. S., 1987, "Laminar Convective Heat Transfer in Ducts," *Handbook of Single-Phase Convective Heat Transfer*, Kakac, Shah and Aung, eds., John Wiley & Son, New York, pp. 3.1–3.3

[3] Hartnett, J. P., and Kostic, M., 1989, "Heat Transfer to Newtonian and Non-Newtonian Fluids in Rectangular Ducts," *Advances in Heat Transfer*, **19**, Academic Press, San Diego, pp. 247–356.

[4] Kamidis, D. E., and Ravigururajan, T. S., 1999, "Single and Two-Phase Refrigerant Flow in Mini-Channels," *Proceedings of National Heat Transfer Conf.*, Albuquerque, August, 1999.

[5] Sparrow, E. M., Lloyd, J. R., and Hixon, C. W., 1966, "Experiments on Turbulent Heat Transfer in an Asymmetrically Heated Rectangular Duct," ASME J. Heat Transfer, **88**(2), pp. 170–174.

[6] Tan, H. M., and Charters, W. W. S., 1970, "An Experimental Investigation of Forced Convective Heat Transfer for Fully Developed Turbulent Flow in a Rectangular Duct With Asymmetric Heating," Sol. Energy, **13**, pp. 121–125.

[7] Sparrow, E. M., and Cur, N., 1982, "Turbulent Heat Transfer in a Asymmetrically or Asymmetrically Heated Flat Rectangular Duct With Flow Separation at Inlet," ASME J. Heat Transfer, **104**(2), pp. 82–89.

[8] Kostic, M., and Hartnett, J. P., 1986, "Heat Transfer to Water Flowing Turbulently Through a Rectangular Duct With Asymmetric Heating," Int. J. Heat Mass Transf., **8**, pp. 1283–1291.

[9] Shah, R. K., and London, A. L., 1978, "Laminar Flow Forced Convection in Ducts," Supplement 1 to *Advances in Heat Transfer*, Academic Press, New York.

[10] Maitra, D., and Raji, K. S., 1975, "Combined Free and Forced Convection Laminar Heat Transfer in a Vertical Annulus," ASME J. Heat Transfer, **97**, pp. 135–137.

[11] Yao, L. S., 1986, "Is a Fully-Developed and Non-Isothermal Flow Possible in a Vertical Pipe?." Int. J. Heat Mass Transf., **30**(4), pp. 707–715.

[12] Heaton, H. S., Reynolds, W. C., and Kays, W. M., 1964, "Heat Transfer in Annular Passages, Simultaneous Development of Velocity and Temperature Fields in Laminar Flow," Int. J. Heat Mass Transf., **7**, pp. 763–781.

[13] Mercer, W. E., Pearce, W. C., and Hitchcock, J. E., 1967, "Laminar Forced Convection in the Entrance Region Between Parallel Flat Plates," ASME J. Heat Transfer, **89**, pp. 251–257.

[14] Baek, B. J., Palaski, D. A., Armaly, B. F., and Chen, T. S., 1990, "Mixed Convection in an Asymmetrically Heated Vertical Parallel-Plated Duct Flow," *Proceedings of the 9th Intl. Heat Transfer Conference*, **4**, Jerusalem, Israel, pp. 369–374.

[15] Aung, W., and Worku, G., 1987, "Mixed Convection in Ducts With Asymmetric Wall Heat Fluxes," ASME J. Heat Transfer, **109**, pp. 947–951.

[16] Hay, J. L., and Hollingsworth, D. K., 1996, "A Comparison of Trichromic Systems for Use in the Calibration of Polymer-Dispersed Thermochromic Liquid Crystals," J. Exp. Thermal and Fluid Science, **12**, pp. 1–12.

[17] Hay, J. L., and Hollingsworth, D. K., 1998, "Calibration of Micro-Encapsulated Liquid Crystals Using Hue Angle and a Dimensionless Temperature," J. Exp. Thermal and Fluid Science, **18**, pp. 251–257.

[18] Katto, Y., 1986, "Forced Convection Boiling in Uniformly Heated Channels," *Handbook of Heat and Mass Transfer*, ed. by N. P. Cheremisinoff, Gulf Publishing Co., pp. 303–325.

[19] Kline, S. J., and McClintock, F. A., 1953, "Describing Uncertainties in Single Sample Experiments," Mech. Eng. (Am. Soc. Mech. Eng.), **75**, pp. 3–8.

[20] Deissler, R. G., 1953, "Analysis of Turbulent Heat Transfer and Flow in the Entrance Regions of Smooth Passages," *NACA*, TN 3016.

[21] Metais, B., and Eckert, E. R. G., 1964, "Forced, Mixed, and Free Convection Regimes," ASME J. Heat Transfer, **86**, pp. 295–296.

[22] Chin, Y., Hollingsworth, D. K., and Witte, L. C., 1998, "A Study of Convection in an Asymmetrically Heated Duct using Liquid Crystal Thermography," *Proceedings of the AIAA/ASME Thermophysics and Heat Transfer Conf.*, Albuquerque, HTD 375-3, pp. 71–78.

Thermal Optimization of a Circular-Sectored Finned Tube Using a Porous Medium Approach

Sung Jin Kim

Jae Wook Yoo

Seok Pil Jang

Department of Mechanical Engineering,
Korea Advanced Institute of Science and Technology,
Taejon, 305-701,
Korea

The present work investigates the heat transfer characteristics of a laminar fully developed forced convection in a circular-sectored finned tube with axially uniform heat flux and peripherally uniform wall temperature. The tubes with circular-sectored fins are modeled as a fluid-saturated porous medium. Using the Brinkman-extended Darcy model for fluid flow and the two-equation model for heat transfer, the analytical solutions for both velocity and temperature distributions are obtained and compared with the exact solution for fluid flow and the numerical solutions for conjugate heat transfer in order to validate the porous medium approach. The agreement between the solutions based on the porous medium approach and the conventional method is close within 5.3 percent. Based on the analytical solutions, parameters of engineering importance are identified to be the angle of the circular sector α and the effective conductivity ratio C, and their effects on fluid flow and heat transfer are studied. Also, the total thermal resistance is derived from the analytical solutions and minimized in order to optimize the thermal performance of a tube with circular-sectored fins. [DOI: 10.1115/1.1495517]

Keywords: Forced Convection, Heat Transfer, Porous Media, Tubes

Introduction

In order to enhance the rate of heat transfer, finned surfaces have been applied to cooling devices for electronic equipment and compact heat exchangers for many years [1,2]. The apparent advantage of fins is that they increase the heat transfer rate by providing additional surface area. However, fins placed in a tube make flow pattern complex and increase frictional resistance. As the number or the height of fins increases, flow friction increases and higher pumping power is required to supply the same rate of mass flow. Therefore, to design a compact heat exchanger with internally finned tubes, we should optimize the fin geometry, accounting for both fluid friction and heat transfer.

Many researchers have studied fully developed forced convection in internally finned tubes both numerically and experimentally [3–5]. Recently, for instance, Fabbri [6] proposed a polynomial lateral profile of the fins and optimized the geometry in the finned tube in order to make the heat transfer rate per unit of tube length as high as possible for a given weight and for a given hydraulic resistance. However, there are numerous parameters which affect the thermal performance of internally finned tubes such as radius, length, material of the tube, thermal properties of coolant, height, thickness, the number of fins, and so on. As a consequence, efforts in the previous numerical and experimental studies have involved tedious numerical calculations or extensive experiments in order to evaluate the effects of parameters on the thermal performance of finned tubes [7–10].

On the contrary, if analytic solutions can be obtained, the optimization of thermal performance and evaluation of parameters can be accomplished with ease. There are only a few works which present the analytical solutions for finned tubes. Shah and London [11] provided the analytical solutions for both axial velocity and temperature distributions in circular-sectored ducts for the case of an axially uniform heat input and a circumferentially uniform wall temperature at any cross section. When the wall heat flux was constant at any cross section, Hu and Chang [12] provided the Nusselt number of internally finned tubes with zero fin thickness analytically. Soliman and Feingold [13] investigated theoretically the fully developed laminar flow in internally finned tubes with fin shapes approximating real fin configurations as closely as possible. However, none of these investigators did either consider the conduction through the fins with an assumption that the temperature of the fin surface is constant, or present the optimal geometry of the fins based on the flow friction and heat transfer characteristics.

Due to the complex geometry of the finned tube and the conjugated heat transfer between the fluid and the fins, the conventional energy equation cannot be solved analytically. A so-called porous medium approach has been opted for modeling the fluid flow and heat transfer through a channel with a heat transfer augmentation device. Koh and Colony [14] modeled the microstructure as a porous medium. Later Tien and Kuo [15], and Kim and Kim [16,17] extended their work in order to analyze the heat transfer phenomenon in a microchannel heat sink. Using the porous medium approach, they evaluated the effects of geometric parameters and physical properties without tedious numerical computations. Similarly, Srinivasan et al. [18] studied fluid flow and heat transfer through spirally fluted tubes using a porous substrate approach. The model divided the flow domain into two regions, the flute region and the core region, with the flutes being modeled as a porous substrate.

In the present paper, heat transfer characteristics in the circular-sectored finned tube are studied using the porous medium approach. When the circular-sectored finned tube is modeled as a porous medium, analytical solutions for both velocity and temperature profiles within it can be obtained. The analytical solutions are based on the modified Darcy model for fluid flow and the two-equation model for heat transfer. To validate the porous medium model of the finned tube and the analytical solutions based on that model, the conjugate heat transfer problem is also solved numerically and the numerical results are compared with the analytical solutions. By using the analytical solutions, important variables in the engineering field are identified and their effects on fluid flow and heat transfer are studied. Finally, the analytical results made possible by the use of the porous medium model are applied to the thermal optimization of the finned tube. The total thermal resistance derived from the analytical solutions is mini-

Contributed by the Heat Transfer Division for publication in the JOURNAL OF HEAT TRANSFER. Manuscript received by the Heat Transfer Division November 30, 2001; revision received May 14, 2002. Associate Editor: V. K. Dhir.

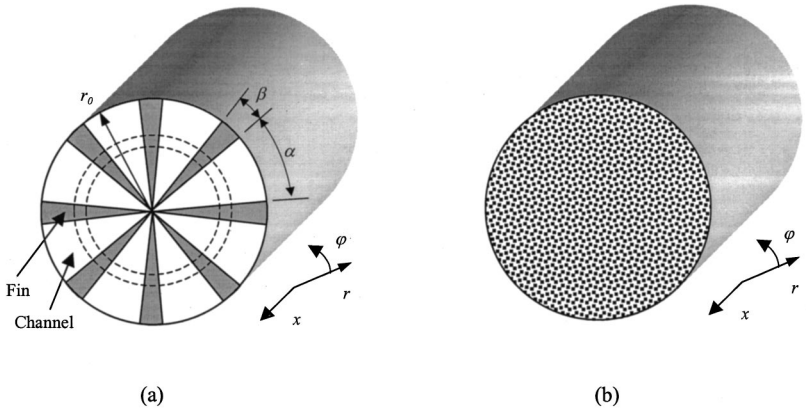

Fig. 1 Schematic view of the configurations of interest: (a) a tube with circular-sectored fins; (b) equivalent porous medium.

mized in order to optimize the thermal performance of finned tube. The point of this example is to demonstrate the cost and speed advantage of the new analytical solutions compared to more time consuming numerical procedures when used in design applications.

Mathematical Formulation and Theoretical Solutions

The problem under consideration in this paper is forced convective flow through a finned tube as shown in Fig. 1(*a*). The direction of fluid flow is parallel to the tube axis. The tube wall is uniformly heated and a coolant passes between the fins attached to the inside surface of the tube wall. In analyzing the problem, the flow is assumed to be steady, laminar, and both hydrodynamically and thermally fully developed. In addition, all thermo-physical properties are assumed to be constant.

The circular-sectored finned tube is modeled as a porous medium as shown in Fig. 1(*b*). The present analysis is based on the volume-averaging technique to establish the governing equations for the velocity and temperature fields in the finned tube. For the present system, the representative elementary volume for the volume-averaging can be visualized as a (dotted) ring aligned perpendicularly to the flow direction as shown in Fig. 1(*a*). The volume-averaging in the present analysis is equivalent to averaging in the φ direction because the geometry under consideration is uniform in the flow direction. The volume averaging technique is applied to the solid portion and the fluid portion, respectively, as follows:

$$\langle \phi \rangle_s = \frac{1}{V_s} \int_{V_s} \phi dV \tag{1}$$

$$\langle \phi \rangle_f = \frac{1}{V_f} \int_{V_f} \phi dV \tag{2}$$

where ϕ is a physical parameter, V is the averaging volume, and $\langle\ \rangle_f$ and $\langle\ \rangle_s$ denote a volume-averaged value over the fluid region and the solid region, respectively.

To analyze fluid flow and heat transfer, the volume-averaged momentum equation and volume-averaged energy equations for the solid and fluid phases are obtained and solved. As the volume-averaged momentum equation for the present system, the Brinkman-extended Darcy equation as proposed by Vafai and Tien [19] is used

$$\frac{1}{r}\frac{d}{dr}\left(r\mu_f \frac{d\langle u \rangle_f}{dr} \right) - \frac{\varepsilon \mu_f}{K}\langle u \rangle_f = \frac{d\langle p \rangle_f}{dx} \tag{3}$$

where p, μ, u, ε, K, and r are pressure, viscosity, velocity, porosity, permeability, and radial coordinate, respectively. This modified Darcy equation, which was developed to describe fluid flow in a porous medium, is used in place of the Darcy equation in order to account for the boundary effect. Due to the high solid-to-fluid conductivity ratio, the temperature difference between the solid and the fluid may not be small. Therefore, the two-equation model, which treats the solid and the fluid as separate entities, is used in the present analysis. The volume-averaged energy equations for the solid and fluid phase are expressed as

$$\frac{1}{r}\frac{d}{dr}\left(r(1-\varepsilon)k_s \frac{d\langle T \rangle_s}{dr} \right) = h_l a(\langle T \rangle_s - \langle T \rangle_f) \tag{4}$$

$$\varepsilon \rho_f c_f \langle u \rangle_f \frac{d\langle T \rangle_f}{dx} = h_l a(\langle T \rangle_s - \langle T \rangle_f) + \frac{1}{r}\frac{d}{dr}\left(r\varepsilon k_f \frac{d\langle T \rangle_f}{dr} \right) \tag{5}$$

where h_l, a, ρ_f, and c_f are the local heat transfer coefficient, wetted area per volume, density, and heat capacity, respectively. The boundary conditions necessary to complete the problem formulation are

$$\langle u \rangle_f = 0, \quad \langle T \rangle_s = \langle T \rangle_f = T_w \quad \text{at } r = r_0 \tag{6}$$

$$\frac{d\langle u \rangle_f}{dr} = 0, \quad \frac{d\langle T \rangle_f}{dr} = \frac{d\langle T \rangle_s}{dr} = 0 \quad \text{at } r = 0 \tag{7}$$

Now Eqs. (3)–(5) and B.C.s (6)–(7) can be nondimensionalized using the following dimensionless variables;

$$U = \frac{\langle u \rangle_f}{u_m}, \quad \eta = \frac{r}{r_o}, \quad \mathrm{Da} = \frac{\alpha^2}{12} \tag{8}$$

$$\theta_f = \frac{\langle T \rangle_f - T_w}{\dfrac{q''_w r_o}{(1-\varepsilon)k_s}}, \quad \theta_s = \frac{\langle T \rangle_s - T_w}{\dfrac{q''_w r_o}{(1-\varepsilon)k_s}}, \quad P = \frac{r_o^2}{\mu_f u_m}\frac{d\langle p \rangle_f}{dx} \tag{9}$$

For the fully developed flow subject to a constant heat flux,

$$\frac{d\langle T \rangle_f}{dx} = \frac{d\langle T \rangle_s}{dx} = \frac{dT_w}{dx} = \text{constant}, \tag{10}$$

and from the energy balance,

$$q''_w = \varepsilon \rho_f c_f u_m \frac{r_o}{2}\frac{\partial \langle T \rangle_f}{\partial x}. \tag{11}$$

The dimensionless governing equations and boundary conditions are expressed as follows:

$$\frac{1}{\eta}\frac{d}{d\eta}\left(\eta \frac{dU}{d\eta} \right) - \frac{1}{\mathrm{Da}}\frac{U}{\eta^2} = P \tag{12}$$

$$\frac{d^2\theta_s}{d\eta^2} + \frac{1}{\eta}\frac{d\theta_s}{d\eta} = \frac{h_l^*}{(1-\varepsilon)k_s}\frac{(\theta_s - \theta_f)}{\eta^2} \tag{13}$$

$$\frac{d^2\theta_f}{d\eta^2}+\frac{1}{\eta}\frac{d\theta_f}{d\eta}+\frac{h_l^*}{\varepsilon k_f}\frac{(\theta_s-\theta_f)}{\eta^2}=\frac{2(1-\varepsilon)k_s}{\varepsilon k_f}U \tag{14}$$

$$U=0,\quad \theta_s=\theta_f=0 \quad \text{at} \quad \eta=1 \tag{15}$$

$$\frac{dU}{d\eta}=0,\quad \frac{d\theta_f}{d\eta}=\frac{d\theta_s}{d\eta}=0,\quad \text{at} \quad \eta=0 \tag{16}$$

where $h_l^*=h_l a r^2=2rh_l/(\alpha+\beta)$.

The analytical solution to the momentum Eq. (12) with B.C.s (15) and (16) can be obtained as

$$U=2\left(\frac{1+2\sqrt{\mathrm{Da}}}{1-2\sqrt{\mathrm{Da}}}\right)(\eta^2-\eta^{1/\sqrt{\mathrm{Da}}}) \tag{17}$$

where the dimensionless pressure drop is determined by the relation $\int_0^1 U\eta d\eta=1/2$. Energy Eqs. (13) and (14) with B.C.s (15) and (16) can be solved by the following method:

(13) $+\frac{\varepsilon k_f}{(1-\varepsilon)k_s}$ (14):

$$\frac{d^2}{d\eta^2}\left(\theta_s+\frac{\varepsilon k_f}{(1-\varepsilon)k_s}\theta_f\right)+\frac{1}{\eta}\frac{d}{d\eta}\left(\theta_s+\frac{\varepsilon k_f}{(1-\varepsilon)k_s}\theta_f\right)=2U \tag{18}$$

(13)–(14):

$$\frac{d^2}{d\eta^2}(\theta_s-\theta_f)+\frac{1}{\eta}\frac{d}{d\eta}(\theta_s-\theta_f)-\frac{\lambda}{\eta^2}(\theta_s-\theta_f)=-\frac{2(1-\varepsilon)k_s}{\varepsilon k_f}U \tag{19}$$

where $\lambda=h_l^*(1/(1-\varepsilon)k_s+1/\varepsilon k_f)$.

After some algebraic manipulation, analytical solutions for the dimensionless temperature profiles of the fluid and solid phases are obtained as follows:

$$\theta_s=\frac{4}{(1+C)}\left(\frac{1+2\sqrt{\mathrm{Da}}}{1-2\sqrt{\mathrm{Da}}}\right)\left(\frac{\eta^{\sqrt{\lambda}}-\eta^4}{16-\lambda}+\frac{\eta^4-1}{16}-\frac{\eta^{\sqrt{\lambda}}-\eta^{2+(1/\sqrt{\mathrm{Da}})}}{\left(2+\frac{1}{\sqrt{\mathrm{Da}}}\right)^2-\lambda}-\frac{\eta^{2+(1/\sqrt{\mathrm{Da}})}-1}{\left(2+\frac{1}{\sqrt{\mathrm{Da}}}\right)^2}\right) \tag{20}$$

$$\theta_f=\frac{4}{(1+C)}\left(\frac{1+2\sqrt{\mathrm{Da}}}{1-2\sqrt{\mathrm{Da}}}\right)\left(\frac{\eta^4-1}{16}-\frac{\eta^{2+(1/\sqrt{\mathrm{Da}})}-1}{\left(2+\frac{1}{\sqrt{\mathrm{Da}}}\right)^2}-\frac{1}{C}\left(\frac{\eta^{\sqrt{\lambda}}-\eta^4}{16-\lambda}-\frac{\eta^{\sqrt{\lambda}}-\eta^{2+1/\sqrt{\mathrm{Da}}}}{\left(2+\frac{1}{\sqrt{\mathrm{Da}}}\right)^2-\lambda}\right)\right) \tag{21}$$

Results and Discussion

1 Velocity and Temperature Distributions. In order to obtain the velocity and temperature distributions from Eqs. (3)~(5), the permeability K and the local heat transfer coefficient h_l need to be determined. These parameters are related to the shear stress and the heat transfer rate at the solid/fluid interface along the fin. With any of volume-averaging techniques, we lose some information [20]: in the present case, the dependence of the velocity and temperature distributions in the circumferential direction. In porous medium studies, we typically replace the lost information with an empirical data for K and h_l. For the present configuration, however, these parameters can be determined analytically through an approximation. For this we assume that the pressure drop and heat transfer characteristics of the circular sector under consideration can be approximated as those found for the Poiseuille flow between two semi-infinite plates that meet with an angle of α and are subject to a constant heat flux. For small values of α an order of magnitude analysis shows that the diffusion of momentum and energy in the radial direction is negligible compared to that in the circumferential direction. Then the velocity and temperature distributions are obtained easily as

$$u=\frac{r^2}{2\mu}\frac{dp}{dx}\left(\varphi^2-\frac{\alpha^2}{4}\right) \tag{22}$$

$$T=\frac{q_w'' r\alpha}{k_f}\left(-4\frac{\varphi^4}{\alpha^4}+6\frac{\varphi^2}{\alpha^2}-\frac{5}{4}\right)+T_w \tag{23}$$

From this velocity distribution, the relation between the pressure drop in the flow direction and the mean velocity can be calculated. After comparing this relation with the Darcy equation, the permeability is obtained as follows:

$$K=\frac{\varepsilon r^2\alpha^2}{12} \tag{24}$$

Similarly, the local heat transfer coefficient is determined as follows:

$$h_l=\frac{-\frac{k_f}{r}\frac{\partial T}{\partial\varphi}\Big|_{\varphi=\alpha/2}}{T_w-\langle T\rangle_f}=\frac{5k_f}{r\alpha} \tag{25}$$

With these approximated values of K and h_l, the analytical solutions based on the porous medium approach are compared with the corresponding velocity and temperature distributions for the conjugate heat transfer problem comprising both the solid fin and the fluid. The formulation and the numerical method for the conjugate heat transfer problem are very similar to those in Patankar [21] and are not repeated here for the sake of brevity. Only the conventional energy equation is solved numerically because a closed-form solution exists for the fully-developed flow in the circular sector in the form of [11]

$$U=2\frac{\eta^2(\alpha-\tan\alpha)+\frac{32\alpha^3}{\pi^4}\Sigma_{n=1,3,\ldots}\eta^{n\pi/\alpha}\frac{1}{n^2\left(n+\frac{2\alpha}{\pi}\right)\left(n-\frac{2\alpha}{\pi}\right)}}{(\alpha-\tan\alpha)+\frac{128\alpha^4}{\pi^5}\Sigma_{n=1,3,\ldots}\frac{1}{n^2\left(n+\frac{2\alpha}{\pi}\right)^2\left(n-\frac{2\alpha}{\pi}\right)}} \tag{26}$$

Note that the velocity distribution given in Eq. (26) is the result of volume-averaging in the φ direction so that it may be compared with Eq. (17), which is the analytical solution of the present study. In Fig. 2, Eq. (17) is compared with the velocity profile of Eq. (26) for $\alpha=45$ deg. Similarly, in Fig. 3, Eqs. (20) and (21) are compared with the corresponding volume-averaged temperature distributions from the numerical solutions for $\alpha=45$ deg and $C=0.01$. As depicted in these figures, the analytical solutions based on the porous medium approach are found to be in close agreement with the corresponding results for the velocity and temperature profiles base on the conventional approach. In the range of 0 deg $\leqslant\alpha\leqslant$45 deg, the error between the two results is shown to increase with the angle of the circular sector α with a maximum error of 5.3 percent at $\alpha=45$ deg. This excellent agreement confirms that the permeability and local heat transfer coefficient are chosen appropriately enough to recover the lost information in averaging.

It is in order to determine when the porous medium model is applicable to the thermal analysis of the circular-sectored finned tube. For this purpose the Darcy number based on Eq. (24) and the local Nusselt number based on Eq. (25) are compared with that from the exact solution for fluid flow and that from the numerical

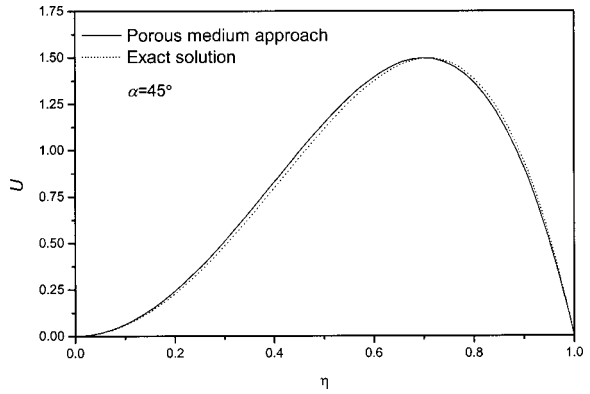

Fig. 2 Comparison of the velocity profile obtained from the porous medium approach with the exact solution

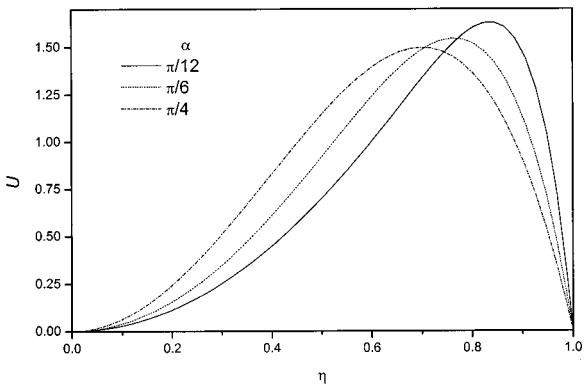

Fig. 5 Effect of α on velocity profiles

solution, respectively. In Fig. 4, the Darcy number based on Eq. (24) and the local Nusselt number based on Eq. (25) are shown to be in close agreement with exact results. Hence the porous medium approach introduced in the present paper is valid for $\alpha<45$ deg with a maximum error less than 5 percent.

It goes without saying that these analytical solutions from the porous medium model are helpful in identifying and studying the effects of variables of engineering importance. Thus, the extension to more practical research, such as optimization of the finned tube, is possible without tedious numerical computations. The analytical solutions, Eqs. (20) and (21), show that the dimensionless temperatures, θ_f and θ_s, are functions of α and C, since λ is expressed in terms of α and C. Figure 5 shows the effect of α (or Da) on the dimensionless velocity profiles. As shown in this figure, a decrease of α reduces the boundary effect on the velocity distribution and moves the position of the maximum velocity toward the tube wall. Also, the temperature difference between the fin and the fluid decreases with decreasing α because both the heat transfer coefficient and the wetted area per unit volume increase, as shown in Fig. 6. The influence of C on the fluid and solid temperatures is shown in Fig. 7. The solid temperature distributions are relatively insensitive to α and C. The solid temperature steadily drops from the tube wall temperature and exhibits a minimum at the center of the finned tube. In contrast, the fluid temperature distributions depend strongly on α and C. The fluid temperature decreases from its maximum at the tube wall to a

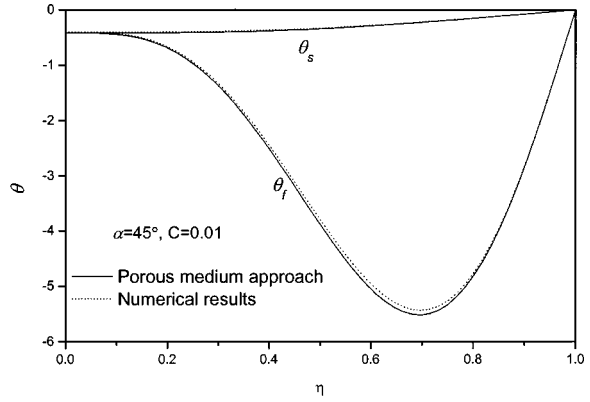

Fig. 3 Comparison of temperature profiles obtained from the porous medium approach with numerical solutions

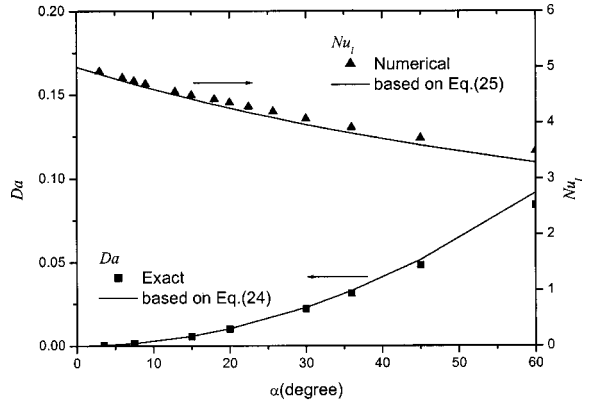

Fig. 4 Comparison of the approximated Da and Nu_l with the exact results

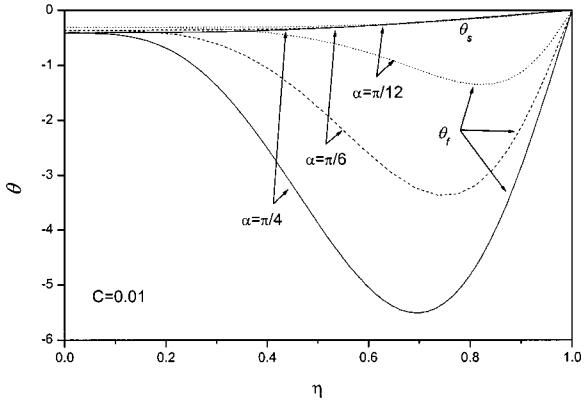

Fig. 6 Effect of α on temperature profiles

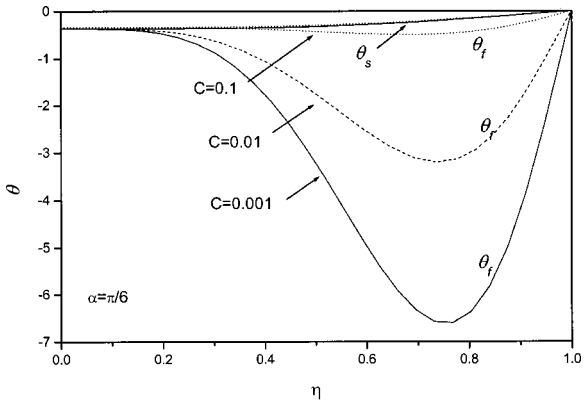

Fig. 7 Effect of *C* on temperature profiles

minimum at the position of the maximum velocity. It then increases to the centerline, but remains smaller than the fin temperature.

2 The Overall Nusselt Number. It is important in thermal design to enhance the heat transfer rate between the heated wall and the fluid, i.e., the convection heat transfer rate from the tube wall. As a measure of the convection heat transfer rate, the overall Nusselt number is typically used and defined as

$$\mathrm{Nu}_o = \frac{h_o D_h}{k_f} = \frac{q''_w}{T_w - T_{f,m}} \frac{D_h}{k_f} \tag{27}$$

where $T_{f,m}$ is the bulk mean temperature and expressed by averaging the product of the velocity and temperature distributions over the cross-sectional area, A_c:

$$T_{f,m} = \frac{1}{u_m A_c} \int_{A_c} u_f T_f dA \tag{28}$$

Since we adopted the porous medium approach, the velocity and temperature distributions in the φ direction are not available. Instead we have obtained averaged velocity and temperature profiles by applying the local volume-averaging technique. In previous works, the bulk mean temperature has been calculated using volume-averaged values in a fashion similar to as Eq. (28):

$$\langle T \rangle_{f,m} = \frac{1}{u_m A_c} \int_{A_c} \langle u \rangle_f \langle T \rangle_f dA \tag{29}$$

However, there may be an error in calculating the overall Nusselt number with the bulk mean temperature of Eq. (29). The bulk mean temperature of Eq. (29) is generally different from the bulk mean temperature of Eq. (28): Eq. (28) and Eq. (29) are same only when either u_f or T_f is independent of the volume-averaging direction, φ. Therefore, proper correction should be made if we calculate the overall Nusselt number based on the bulk mean temperature of Eq. (29). To obtain a general method of correction for Eq. (29), we consider a certain volume filled with solid and fluid phases. Inside this volume, u_f and T_f can be decomposed into two terms: volume-averaged value and spatial variation as follows:

$$u_f = \langle u \rangle_f + \tilde{u}_f \tag{30}$$

$$T_f = \langle T \rangle_f + \tilde{T}_f \tag{31}$$

where $\langle\ \rangle_f$ is designated as the mean value and $\sim$ is the variation from the mean value. By substituting Eqs. (30) and (31) into Eq. (28), a relation between Eq. (28) and Eq. (29) is expressed as

$$T_{f,m} = \langle T \rangle_{f,m} + \frac{1}{u_m A_c} \int_{A_c} \tilde{u}_f \tilde{T}_f dA \tag{32}$$

As shown in Eqs. (32), (28) and (29) differ by the second term on the right-hand side. To evaluate this term, we shall assume that the fluid flow and heat transfer characteristics in a pore are similar to those in a capillary tube. The flow is assumed to be fully-developed and laminar, and the tube wall subjected to a constant heat flux. Under these assumptions, spatial variations of the velocity and temperature profiles are obtained as follows:

$$\tilde{u}_f = 2u_m \left(1 - 4\frac{r^2}{d_p^2}\right) - u_m \tag{33}$$

$$\tilde{T}_f = -\frac{q'' d_p}{k_f} \left(0.208 - 2\frac{r^2}{d_p^2} + 2\frac{r^4}{d_p^4}\right) \tag{34}$$

where q'', k_f, and d_p are heat flux at the pore wall, conductivity of the fluid and pore diameter, respectively. Inserting Eqs. (33) and (34) into Eq. (32) and performing the integration over a single pore results in

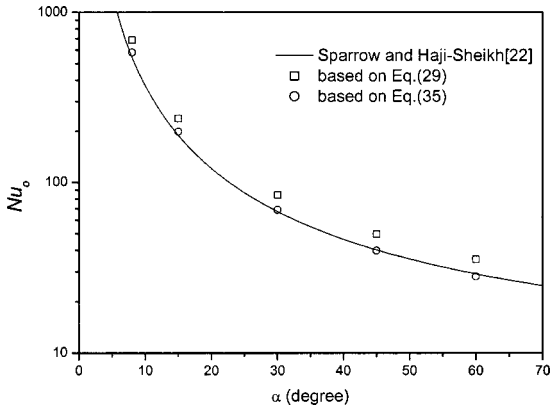

Fig. 8 Comparison of overall Nusselt number obtained from the porous medium approach with those presented by Sparrow and Haji-Sheikh

$$T_{f,m} = \langle T \rangle_{f,m} - 0.0625 \frac{q''}{k_f} d_p \tag{35}$$

Now, we apply this correction method to the problem of a circular-sectored finned tube. In a tube with noncircular cross sections, this correction method can still be applied by using the hydraulic diameter in place of the pore diameter. Thus we calculate the bulk mean temperature by substituting the hydraulic diameter of a circular sector for d_p in Eq. (35). In order to validate this correction method, we compare the overall Nusselt number based on Eq. (35) with those obtained for a special case where analytical solutions for the Nusselt numbers are available. In the limiting case when C approaches 0, the temperature of a fin becomes identical to the tube wall temperature. For this case, a closed-form solution for the temperature profile is presented in [22]. Figure 8 shows the overall Nusselt numbers based on Eq. (29), the overall Nusselt numbers based on Eq. (35), and those from the exact solution in [22]. Note that the overall Nusselt numbers based on Eq. (29) are about 18 percent larger than exact values, while the Nusselt number based on Eq. (35) agrees with the exact solution within 5 percent. Hence, it is evident that the correction method proposed here significantly reduces the error in evaluating the overall Nusselt number. Therefore, we calculate the overall Nusselt number using $T_{f,m}$ of Eq. (35), for thermal optimization of the circular-sectored finned tube, which will be presented in the next section.

Furthermore, we shall now show that the analytical solutions based on the porous medium approach are appropriate in predicting the thermal performance of the finned tube by examining two limiting values of Nu_o: $\mathrm{Da}\to\infty$ and $\mathrm{Da}\to 0$. In these cases, because u_f or T_f is independent of φ, Nu_o can be determined from Eq. (27) together with Eq. (28) or Eq. (29). For the first case, as Da approaches infinity, it can be easily shown that

$$\lim_{\mathrm{Da}\to\infty} \mathrm{Nu}_o = 4.364, \tag{36}$$

which is identical to the Nusselt number for a fully-developed convective flow through a plain circular tube with uniform heat flux on the tube wall. The condition of $\mathrm{Da}\to\infty$ is an imaginary case, which corresponds to the case where the angle between the two fins goes to infinity. In order to explain the limiting behaviors of the Nusselt number as $\alpha\to\infty$ we may imagine a case where $\alpha = n\pi$ where $n>2$. In this case the velocity and temperature profiles are a multivalued function on a so-called *Riemann* surface [23]. It is a sequence of superimposed planes cut and joined along the branch cuts in such a way that, if a point starts on a given plane, moves around a branch point, and approaches its original position after such a circuit, it moves across a cut from the initial plane onto another superposed plane corresponding to a second

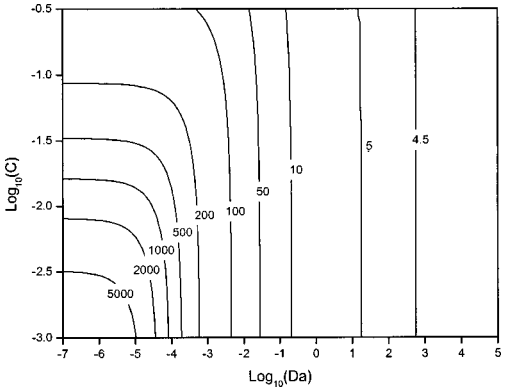

Fig. 9 Contour map of the overall Nusselt number

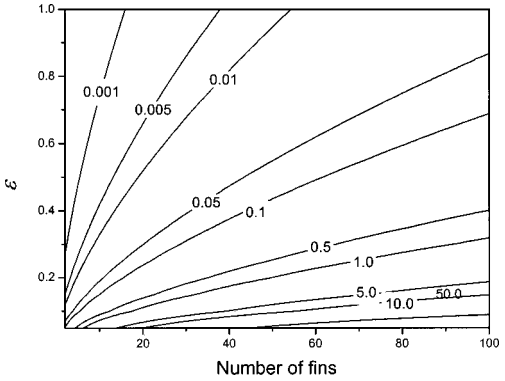

Fig. 10 Contour map of R_{flow}(°C/W)

branch of the function. As $\alpha\to\infty$, an infinite number of such planes would be required, and the resultant configuration would resemble an endless helicoidal surface. In this case, the effect of zero-thickness fins separated by an angle $\alpha=n\pi$ as $n\to\infty$ is negligible and the fluid flow approaches the internal flow in a circular tube with no fins. This is why the Nusselt number approaches 4.364 as Da$\to\infty$, which is identical to the Nusselt number for a fully developed convective flow through a plain circular tube with uniform heat flux on the tube wall.

On the other hand, as Da approaches 0 (or $\alpha\to0$), it can be shown that

$$\lim_{\mathrm{Da}\to0}\mathrm{Nu}_o=\frac{16(1+C)}{C} \tag{37}$$

The second limiting case of Da$\to$0 ($\alpha\to0$) does not mean that the circular tube is filled with fins only. As $\alpha\to0$, the angle between the fins gets very small and the radius becomes very large in order to maintain a flow under a fixed pressure drop. This makes the flow similar to that between semi-infinite plates separated with a very small angle. Then the boundary effect of a tube wall and the temperature difference between the fin and the solid phases are negligible. Hence it is not surprising to see that the Nusselt number given in Eq. (37) matches with the Nusselt number when the flow is assumed to be Darcian and the fluid is in local thermal equilibrium with the solid.

In order to show influences of Da and C on the thermal performance of the tube more clearly, the contour map of the overall Nusselt number with respect to Da and C is presented in Fig. 9. The overall Nusselt numbers are calculated with the corrected bulk mean temperature. In this figure, Nu increases as either Da or C decreases, which results from the increase in the local heat transfer coefficient or the decrease in the thermal resistance through the fin. More importantly, Nu is shown in Fig. 9 to approach an asymptotic value either as Da decreases while C is held constant or as C decreases while Da is held constant. The former is because the fins lose their efficiency as their length increases over a certain value, and the latter is because the ratio of the conduction resistance through the fins to the convection resistance gets smaller. This implies that there is a practical limit in the values of the Darcy number and the effective thermal conductivity ratio below which the heat transfer performance of the finned tube decreases.

Optimization of Thermal Performance

To optimize the thermal performance of the finned tube, the total thermal resistance should be minimized. The thermal resistance is the temperature difference of the two points of concern per unit heat flux. Minimizing the thermal resistance for the condition of constant wall heat flux means minimizing the temperature difference between the tube wall temperature at the exit and the coolant temperature at the inlet. The latter is a fixed value because a coolant at a normal temperature is continuously provided at the inlet during operation. Therefore, the minimization of the total thermal resistance can be realized by minimizing the tube wall temperature at the exit. The total thermal resistance is the sum of the thermal resistance for the flow of the coolant and that for the conduction through and convection between the fins.

$$R_{\mathrm{total}}=R_{\mathrm{flow}}+R_{\mathrm{fin}} \tag{38}$$

The thermal resistance for the flow of the coolant is responsible for the temperature rise of the coolant from the inlet to the exit. From the energy balance this resistance can be expressed as:

$$R_{\mathrm{flow}}=\frac{1}{\rho_f c_f Q}=\frac{\mu_f L}{\rho_f c_f \Delta p}\frac{2\left(2+\dfrac{1}{\sqrt{\mathrm{Da}}}\right)^2}{\varepsilon\pi r_o^4} \tag{39}$$

where Q, L, and Δp are volume flow rate, length of the tube and pressure difference between upstream and downstream, respectively. From the definition of the bulk mean temperature the thermal resistance for conduction through and convection between the fins can be represented by

$$R_{\mathrm{fin}}=\frac{1}{h_{fs}A_{fs}}=\frac{T_w-T_{f,m}}{q_w L(2\pi r_o)} \tag{40}$$

where h_{fs} and A_{fs} are the heat transfer coefficient between the fin and the fluid based on the bulk mean temperature and interfacial area between the fin and the fluid, respectively. Because R_{fin} includes the bulk mean temperature, the results are corrected as pointed out in the previous section.

In order to minimize the total thermal resistance, physical properties of the fluid, length and radius of the tube, and pressure drop are assumed to be given. Also, the maximum pressure difference across the tube is given a practical value. With these assumptions, Eqs. (39) and (40) show that the total thermal resistance is now a function of ε and Da. Because Da$=\alpha^2/12$ and the fins are equally distributed, we can find the optimum values of the number of fins and ε which minimize the total thermal resistance.

To demonstrate the cost and speed advantage of the new analytical solutions in optimizing the thermal performance of the circular-sectored finned tube, the thermal resistance of the finned tube is minimized in the following example case using the analytical solutions obtained from the porous medium model. The thermophysical and geometric details of the finned tube, for example, are listed as follows. The working fluid is water, the material of fins is aluminum, the length and radius of the tube are 2 m and 0.1 m, respectively; the pressure drop is 1 kPa. The thermal resistance for the flow of coolant is shown in Fig. 10, with respect to the porosity and the number of fins. It is clear that the thermal resistance for fluid flow increases as either the porosity decreases or the number of fins increases, due to reduction of flow rate

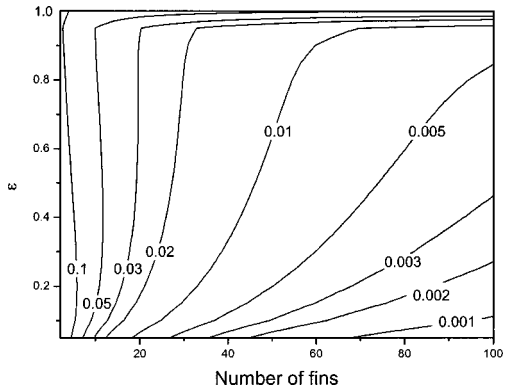

Fig. 11 Contour map of R_{fin}(°C/W)

through the tube. On the other hand, the trend of the thermal resistance through the fins is quite opposite to that for fluid flow as shown in Fig. 11. This plot shows that the thermal resistance through the fins decreases as either the porosity decreases or the number of the fins increases, since the local heat transfer coefficient between the fin and the fluid increases. Consequently, the opposing behavior of the two thermal resistances illustrates that the minimum of the total thermal resistance, which is the sum of the two thermal resistances, occurs as is shown in Fig. 12. The minimum value of the thermal resistance for the current example is 0.0229°C/W, when ε is 0.9 and the number of the fins is 41. One may think that the optimum value of the total thermal resistance is obtained when the porosity is 1, which is a tube with zero-thickness fins. The reason the thermal resistance has a minimum value when ε is smaller than 1 can be explained as follows: the smaller the thickness of the fin becomes (or as $\varepsilon \rightarrow 1$), the larger the conduction resistance through the fins becomes. This steep increase in the thermal resistance through the fins, as shown in Fig. 11, overshadows the decrease in the thermal resistance of fluid flow.

Conclusion

In the present paper, heat transfer characteristics in a tube with circular-sectored fins are studied by modeling the finned tube as a porous medium under a steady laminar forced convection condition. Analytical solutions of both the velocity and the temperature distributions are obtained and validated by comparing these with the exact solution for velocity distributions and the numerical solutions for temperature profiles. The analytical solutions made possible by the use of the porous medium model are shown to predict the volume-averaged velocity and temperature distributions in the circular-sectored finned tube quite well. The angle of the circular sector α and the effective thermal conductivity ratio C are revealed as parameters which affect the thermal performance of the finned tube. As either α decreases or C increases, the fluid temperature approaches the solid temperature. In addition, as either α or C decreases, the overall Nusselt number of the finned tube is shown to increase to an asymptotic value.

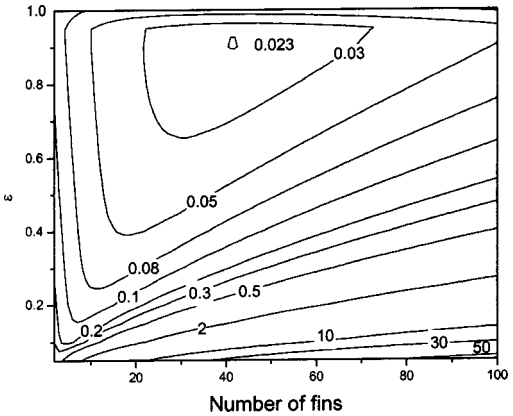

Fig. 12 Contour map of R_{total}(°C/W)

In order to optimize the thermal performance of the tube with circular-sectored fins, the total thermal resistance of the finned tube is expressed as the sum of the resistance for fluid flow and that for the conduction through and convection between the fins. Based on analytical solutions, the total thermal resistance is found to be a function of the porosity and the number of fins when working fluid, material of the fins, length, radius of the tube, and pressure drop are given. The thermal resistance for fluid flow increases while the resistance for conduction through and convection between the fins decreases, as either the porosity decreases or the number of fins increases. This opposing behavior suggests that there exists an optimum value for the total thermal resistance.

In the present paper, the thermal performance of a tube with circular-sectored fins is shown to be optimized with ease by modeling the finned tubes as a fluid-saturated porous medium. The porous medium approach used here could be utilized in analyzing and optimizing the thermal performance of compact heat exchangers with complex geometry and various heat sinks used for cooling electronic devices.

Acknowledgments

The authors would like to acknowledge Korea Research Foundation (Grant KRF-2000-042-E0004) for its support of the present work.

Nomenclature

A_c = cross-sectional area [m^2]
a = wetted area per volume [m^{-1}]
C = effective thermal conductivity ratio, $\varepsilon k_f/(1-\varepsilon)k_s$
c_f = heat capacity of the fluid [$J\,kg^{-1}\,K^{-1}$]
Da = Darcy number, $\alpha^2/12$
D_h = hydraulic diameter [m]
h_l = local heat transfer coefficient [$W\,m^{-2}\,K^{-1}$]
h_o = overall heat transfer coefficient [$W\,m^{-2}\,K^{-1}$]
K = permeability, $\varepsilon r^2\alpha^2/12$ [m^2]
k = thermal conductivity [$W\,m^{-1}\,K^{-1}$]
L = length of the tube [m]
Nu_l = local Nusselt number
Nu_o = overall Nusselt number
P = dimensionless pressure
p = pressure [$N\,m^{-2}$]
Q = volume flow rate
q''_w = wall heat flux
R = thermal resistance [°C/W]
r_o = radius of the tube [m]
T = temperature [K]
$\tilde{T}$ = spatial deviation of temperature
$T_{f,m}$ = bulk mean temperature, defined in Eq. (28)
$\langle T\rangle_{f,m}$ = bulk mean temperature, defined in Eq. (29)
U = dimensionless velocity
u = velocity [m/s]
$\tilde{u}$ = spatial deviation of velocity
V_f = averaging volume
x = axial coordinate
$\langle\ \rangle$ = volume averaged value

Greek symbols

α = angle of the circular sector [rad]
β = angle of the fin [rad]
ε = porosity, $\alpha/(\alpha+\beta)$
λ = dimensionless local heat transfer coefficient

φ = angular coordinate
η = dimensionless length, r/r_0
μ_f = viscosity [$\mathrm{kg\,m^{-1}\,s^{-1}}$]
ρ_f = density of the fluid [$\mathrm{kg\,m^{-3}}$]
θ = dimensionless temperature

Subscript

f = fluid
l = local
m = mean value
o = overall
s = solid
w = wall

References

[1] Bergles, A. E., 1997, ''Heat Transfer Enhancement—the Encouragement and Accommodation of High Heat Fluxes,'' ASME J. Heat Transfer, **119**, pp. 8–19.
[2] Webb, R. L., 1994, *Principles of Enhanced Heat Transfer*, John Wiley and Sons, New York, Chap. 8.
[3] Masliyah, J. M., and Nandakumar, K., 1976, ''Heat Transfer in Internally Finned Tubes,'' ASME J. Heat Transfer, **98**, pp. 257–261.
[4] Watkinson, A. P., Miletti, D. L., and Kubanek, G. R., 1975, ''Heat Transfer and Pressure Drop in Internally Finned Tubes in Laminar Oil Flow,'' ASME Paper No. 75-HT-41.
[5] Rustum, I. M., and Soliman, H. M., 1988, ''Numerical Analysis of Laminar Forced Convection in the Entrance Region of Tubes with Longitudinal Internal Fins,'' ASME J. Heat Transfer, **100**, pp. 310–313.
[6] Fabbri, G., 1998, ''Heat Transfer Optimization in Internally Finned Tubes Under Laminar Flow Conditions,'' Int. J. Heat Mass Transf., **41**, pp. 1243–1253.
[7] Rustum, I. M., and Soliman, H. M., 1988, ''Experimental Investigation of Laminar Mixed Convection in Tubes with Longitudinal Internal Fins,'' ASME J. Heat Transfer, **110**, pp. 366–372.
[8] Patankar, S. V., Ivanovic, M., and Sparrow, E. M., 1979, ''Analysis of Turbulent Flow and Heat Transfer in Internally Finned Tubes and Annuli,'' ASME J. Heat Transfer, **101**, pp. 29–37.
[9] Carnavos, T. C., 1980, ''Heat Transfer Performance of Internally Finned Tubes in Turbulent Flow,'' Heat Transfer Eng., **4**, pp. 32–37.
[10] Webb, R. L., and Scott, M. J., 1980, ''A Parametric Analysis of the Performance of Internally Finned Tubes for Heat Exchanger Application,'' ASME J. Heat Transfer, **120**, pp. 38–43.
[11] Shah, R. K., and London, A. L., 1978, *Laminar Flow Forced Convection in Ducts*, Academic Press, London.
[12] Hu, M. H., and Chang, Y. P., 1973, ''Optimization of Finned Tubes for Heat Transfer in Laminar Flow,'' ASME J. Heat Transfer, **95**, pp. 332–338.
[13] Soliman, H. M., and Feingold, A., 1977, ''Analysis of Fully Developed Laminar Flow in Longitudinal Internally Finned Tubes,'' Chem. Eng. J., **14**, pp. 119–128.
[14] Koh, J. C. Y., and Colony, R., 1986, ''Heat Transfer of Microstructures for Integrated Circuits,'' Int. Commun. Heat Mass Transfer, **13**, pp. 89–98.
[15] Tien, C. L., and Kuo, S. M., 1987, ''Analysis of Forced Convection in Microstructures for Electronic System Cooling,'' *Proc. Int. Symp. Cooling Technology for Electronic Equipment*, Honolulu, Hawaii, 1987, pp. 217–226.
[16] Kim, S. J., and Kim, D., 1999, ''Forced Convection in Microstructures for Electronic Equipment Cooling,'' ASME J. Heat Transfer, **121**, pp. 639–645.
[17] Kim, S. J., and Kim, D., 2000, ''On the Local Thermal Equilibrium in Microchannel Heat Sinks,'' Int. J. Heat Mass Transf., **43**, pp. 1735–1748.
[18] Srinivasan, V., Vafai, K., and Christensen, R. N., 1994, ''Analysis of Heat Transfer and Fluid Flow Through a Spirally Fluted Tube Using a Porous Substrate Approach,'' ASME J. Heat Transfer, **116**, pp. 543–551.
[19] Vafai, K., and Tien, C. L., 1981, ''Boundary and Inertia Effects on Flow and Heat Transfer in Porous Media,'' Int. J. Heat Mass Transf., **24**, pp. 195–203.
[20] Slattery, V. C., 1999, *Advanced Transport Phenomena*, Cambridge University Press, Cambridge, pp. 194–197.
[21] Patankar, S. V., 1980, *Numerical Heat Transfer and Fluid Flow*, Hemisphere Publishing Corp., New York.
[22] Sparrow, E. M., and Haji-Sheikh, A., 1965, ''Laminar Heat Transfer and Pressure Drop in Isosceles Triangular, Right Triangular and Circular Sector Ducts,'' ASME J. Heat Transfer, **87**, pp. 426–427.
[23] Hildebrand, F. B., 1976, *Advanced Calculus for Applications*, 2nd ed., Prentice Hall, New Jersey.

J. M. Crye

A. E. Ruggles
e-mail: aruggles@utk.edu

W. D. Pointer

University of Tennessee,
Department of Nuclear Engineering,
Knoxville, TN 37996-2300

D. K. Felde

P. A. Jallouk

M. T. McFee

M. W. Wendel

G. L. Yoder, Jr.

Oak Ridge National Laboratory,
P.O. Box 2008,
Oak Ridge, TN 37831

Measurement of the Heat Transfer Coefficient for Mercury Flowing in a Narrow Channel

The heat transfer coefficient is inferred from measurements for mercury flowing in a channel of cross-section 2 mm×40 mm with flow velocities from 1 m/s to 4 m/s and heat fluxes from 192 kW/m^2 to 1.14 MW/m^2. Mercury bulk temperatures vary from 67°C to 143°C. Inferred heat transfer coefficients agree with open literature tube data when compared on a Nusselt versus. Peclet number plot, with Nusselt numbers examined from 8 to 17 and Peclet numbers examined from 790 to 3070. [DOI: 10.1115/1.1518500]

Keywords: Forced Convection, Heat Transfer, Liquid Metals

Introduction

Mercury and other liquid metals offer high saturation temperatures relative to water at similar pressures. Liquid metals also provide higher heat transfer coefficients than water when comparable volumetric flow rates are considered. Therefore, mercury and other liquid metals are preferred heat transfer fluids for some applications. Some previous heat transfer studies noted degraded heat transfer with liquid metals attributed to incomplete wetting at the interface between the fluid and pressure boundary [1–3]. This concern along with generally wide scatter in the data in the literature motivated this study, which supported design of a liquid mercury target for a high energy proton beam [4–7]. A review of liquid metal heat transfer experiments was performed, and these data are presented herein as open literature data [8–20]. Much of these data were motivated by cooling applications in nuclear reactors. One previous heat transfer experiment was found employing mercury in narrow channels [8].

Several different techniques have been used in prior studies to infer the heat transfer coefficient for liquid metals flowing inside tubes. These techniques were reviewed to ascertain the most effective method for accurately inferring the heat transfer coefficient for a liquid metal flowing in a narrow channel. A common technique uses fluid flow in an annulus surrounding the tube to provide heating or cooling. In some cases, the fluid outside the tube is the same as the fluid inside the tube [9,10]. Wall temperature measurements are sometimes provided but uncertainties associated with position and bias due to the thermal balance on the measurement device make them of little use. Therefore, these experiments require that a model for the heat transfer coefficient in the annulus be used before the heat transfer in the tube can be inferred. Other experiments used forced convection of water, or condensation of water on the outside of the tube [11]. The inference of heat transfer coefficient inside the tube still requires use of a model for the heat transfer in the annulus. However, in most cases these models are better validated than those for annular flow of the liquid metal.

Direct electrical heating of the tube is employed for some data [12]. The liquid metal also conducts electricity and this complicates the energy balance for these experiments. In one case the exterior of the stainless steel tube is coated with copper to bias the electrical current distribution to the high electrical conductivity material [13]. This approach also allows the thermocouples placed on the outside of the tube to be embedded in a high thermal conductivity material, which lowers measurement uncertainty associated with the thermocouple placement.

Indirect electrical heating is also employed in some experiments [14–19]. Copper clad tubes are used for some data to facilitate thermal transport between the heaters and the tube, and to spread the heater energy uniformly over the tube surface. Thermocouples were embedded in the copper cladding where the temperature gradient is modest, which minimizes measurement uncertainty associated with the thermocouple placement.

There is one experiment where two narrow rectangular channels separated by a common wall are used to investigate the heat transfer coefficient in mercury [8]. The mercury in one channel absorbs the energy transferred from the other channel and the heat transfer coefficient for flow in a narrow channel is inferred from an energy balance on the two fluid flows. Problems in the design of the test section and continuous difficulty with contamination on the heat transfer surface make the quality of these data questionable.

The data from the investigations in the literature [8–19] were originally used to infer heat transfer coefficient using inconsistent assumptions, models, and thermo-physical property sets. These data were reviewed and presented in a consistent framework by Lubarsky and Kaufman [20]. The heat transfer data from the literature presented later in this paper use the methods from Lubarski and Kaufman and the combined data vary greatly about the mean value.

The experiment presented herein was designed to provide accurate heat transfer data for mercury flowing in narrow channels. The channel examined is heated indirectly, and the heater is separated from the channel by a layer of copper to spread the heater energy. The thermocouples that measure the wall temperature are positioned in the copper where the temperature gradients are modest. This approach appears to have produced data of good quality in tests involving tube flows.

Contributed by the Heat Transfer Division for publication in the JOURNAL OF HEAT TRANSFER. Manuscript received by the Heat Transfer Division June 14, 2001; revision received July 23, 2002. Associate Editor: K. S. Ball.

Data presented herein are collected from an electrically-heated straight test section with flow cross-section 2 by 40 mm. An unheated flow development length of 0.2 meters precedes the heated length of 0.2 meters. Flow velocities from 0.5 to 4.0 m/s were examined, and the heat flux ranged from 192 kW/m^2 to 1.14 MW/m^2. The fluid bulk temperature ranged from 67 to 143°C. Heat transfer coefficients inferred from this data lie within the open literature data taken in tubes. The data presented here extend previous measurements by testing heat flux values well above those of other tests with liquid metals.

The Experimental Facility

A thermal-fluid test facility was designed and constructed at the Oak Ridge National Laboratory to study the heat transfer characteristics of mercury flowing through a narrow rectangular channel. An electromagnetic circulating pump is used and is capable of providing 6 kg/s of mercury flow at a pump differential pressure of 0.25 MPa. The annular flow, linear induction pump was fabricated by the University of Latvia, Institute of Physics, and is equipped with proportional flow rate control. Primary circuit tubing is 316 stainless steel with a 31.8 mm inside diameter and 2.77 mm wall thickness. The facility has a design pressure of 1 MPa at 150°C. All of the tubing is inclined to allow mercury to drain into a storage tank. The circuit design includes a bypass around the test section that allows calibration of an electromagnetic flowmeter using a venturi meter. Two hand control valves, one located downstream of the test section and the other in the bypass leg, are used to control the flow between the test section and the bypass. A 152 mm 316 stainless steel API KETEMA heat exchanger with mercury flowing on the shell side, and water flowing on the tube side is used to remove pump power and the power added by the test section heaters. A 50 L storage tank located beneath the facility holds the mercury. Mercury used for these experiments is triple distilled and was sampled following addition to the facility to ensure that contaminants were not present.

The system is filled by applying helium overpressure to the mercury in the storage tank. A dip tube, internal to the tank, allows mercury to fill the circuit from bottom to top. Pressure is maintained by the helium overpressure. This design allows all mercury to drain into the storage tank if the system must be shut down quickly. A vent tank is attached at the highest elevation in the circuit, the top of the heat exchanger. The vent tank is designed to provide a mercury/helium interface that allows gas trapped to escape. The facility is enclosed by a Plexiglas splashguard, and a stainless steel catch pan is located beneath the facility to capture mercury leaks. An elevation drawing of the system is shown in Fig. 1. The entire facility is enclosed in a negative pressure room and vented from the building via a stack fan.

Instrumentation and Controls. Two flow measurement devices are used in the loop. A Venturi meter is located in the bypass leg of the loop, and an electromagnetic (EM) flowmeter is placed before the flow split. By shutting off flow to the test section, the EM flowmeter can be calibrated with the Venturi meter. This configuration also allows flow to be measured in the test section when the bypass is used. The range of the EM flowmeter is 0.06–0.5 L/s of mercury flow, while the Venturi meter has a range of 0.0-0.5 L/s.

Pump suction pressure, pump differential pressure, test section inlet pressure, test section outlet pressure, test section differential pressure, Venturi differential pressure, storage tank pressure, and vent tank pressure are measured on the mercury side of the facility. The heat exchanger outlet pressure is measured on the water side of the facility.

Liquid mercury temperatures are measured at the pump outlet, and the test section inlet and outlet using resistance temperature detectors. Pump inlet temperature is measured using a chromel-alumel thermocouple (type K).

Automatic controls are used to maintain mercury level and pressure during operation. Test section inlet temperature is controlled by altering the secondary side water flow rate, and mercury

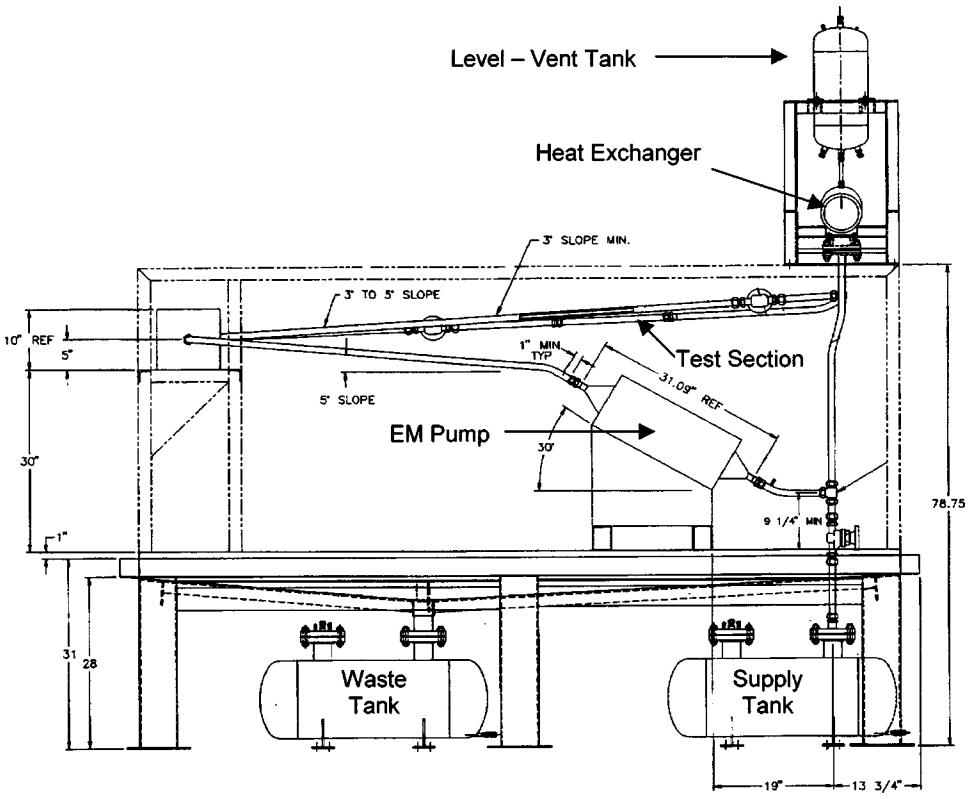

Fig. 1 Loop elevation (units in inches)

flow control is performed manually by adjusting EM pump voltage. The data acquisition and control system uses an Azonix μDCS Plus interface device along with Intellution FIX software to store the data.

Test Operations. Test operations are initiated by pressurizing the storage tank with the upper level tank vented. The system is filled to bring the mercury level to ~125 mm above the bottom of the upper tank. Pressure and level control systems are placed in automatic control mode once the mercury reaches the desired level and the EM pump is brought to the desired pumping rate over a period of a few minutes. Next, the test section flow line is isolated and the bypass line opened so that the EM flowmeter and Venturi flowmeter operate in series, allowing a calibration of the EM flow meter. The isolation valve on the test section line is opened, and the bypass line isolated to prepare the facility for testing. After this the system parameters are adjusted to obtain flow rates, temperatures, and pressures at the test section inlet, as specified in the test plan.

Test Section Description

The test section uses a copper heater block brazed to the back of a flat stainless steel channel wall. The heater is designed to produce up to 1.2 MW/m^2 at the mercury/stainless steel interface. A schematic drawing of the test section is shown in Fig. 2.

The flow channel is machined from 316 stainless steel, and has a rectangular mercury flow cross section of 2 mm gap by 40 mm wide that is 418 mm long. The mercury flow channel is formed by machining a slot 40.00 mm wide into a shim plate 2.00 mm thick. This shim plate is sandwiched between two stainless steel channel plates to form the flow channel and sealed using O-rings.

A 400 mm long by 40 mm wide pocket is machined in the back of the channel plates to reduce the thickness of the channel wall to 1.27 mm. Two heaters, each comprised of a copper block with miniature heater cables, are brazed to the two opposing stainless steel walls in the downstream 200 mm of the pocket. The heaters are located in the downstream half of the channel to allow the flow to fully develop in the channel prior to the heated zone.

The heater blocks were fabricated by the Delta M Corporation with 3.2 mm of copper between the heater cables and the stainless steel. The copper diffuses the thermal energy to produce a uniform heat flux at the copper/stainless steel interface. Thermocouples are installed in 0.89 mm grooves machined in the bottom of the copper plate. The copper heater block with thermocouples installed is brazed as a unit onto the stainless steel channel plate. A diagram of the heater dimensions and the locations of the thermocouples is shown in Fig. 3. The junctions of the inconel-sheathed 0.8 mm diameter type K thermocouples are located along the span-wise centerline.

Rigid ceramic plates are installed over the thin-walled region of the channel plates along with a supporting stainless steel backing plate. The plates provide support for the relatively thin wall regions of the channel and have low thermal conductivity. In addition to the rigid insulation, the entire test section region from the inlet mercury temperature measurement location to the outlet temperature location is insulated.

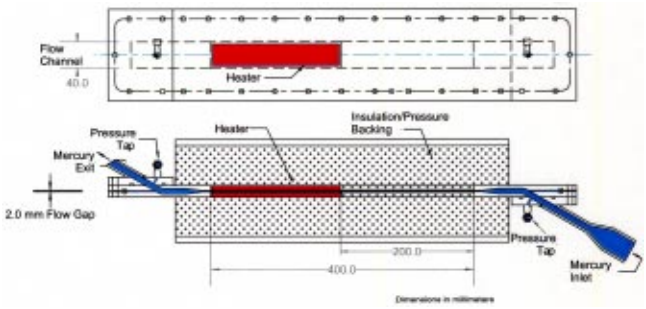

Fig. 2 Electrically heated test section design

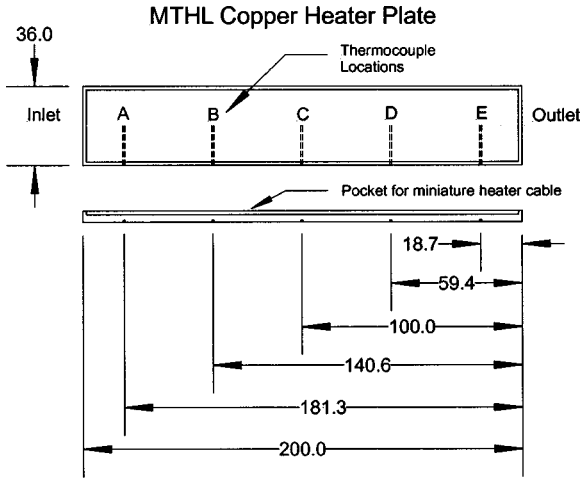

Fig. 3 Schematic of heater block showing thermocouple locations (dimensions in mm)

Heat Transfer Analysis and Results

The bulk temperature of the mercury is established at each of the five thermocouple locations in the test section via an energy balance on the portion of the test section exposed to the heaters. All the heater energy is delivered to the fluid, and the channel mean temperature for the heated section upstream of the thermocouple is used to establish the thermophysical properties of the mercury in the energy balance. The temperature at the mercury/stainless steel interface is determined using a one-dimensional heat conduction model with the measured temperature, T_{meas}, of the stainless steel outer surface. The stainless steel wall has thickness, $t_{ss}=1.27$ mm. The conductivity of the stainless steel, k_{ss}, is used at the local thickness averaged wall temperature value and a linear temperature profile is assumed in the stainless steel wall. The experimental value of the heat transfer coefficient is then established from,

$$h_{\text{experiment}}=\frac{1}{\dfrac{T_{\text{meas}}-T_{\text{bulk}}}{q''}-\dfrac{t_{ss}}{k_{ss}}} \tag{1}$$

The experimental Nusselt number is calculated using the local bulk conductivity. Heat transfer results are displayed in Fig. 4 with open literature data for several liquid metals in the background. Also shown is a correlation provided by Lubarski and Kaufman [20].

$$\text{Nu}=0.625*\text{Pe}^{0.4} \tag{2}$$

Variation in heat transfer coefficient with exposure time was reported after initial wetting in some previous mercury heat transfer studies [8]. Exposure time from less than one hour to more than 450 did not have any measurable effect on the inferred heat transfer coefficient obtained with the test section.

Uncertainty Analysis

The one-dimensional simulation of the thermal fluid performance of the test section used to infer the heat transfer coefficient from measured values was developed in a spreadsheet. All parameters affecting the inference of the heat transfer coefficient are resident in the simulation. The uncertainty in the inferred heat transfer coefficient attributable to the uncertainty in a single parameter is evaluated by propagating the uncertainty in the param-

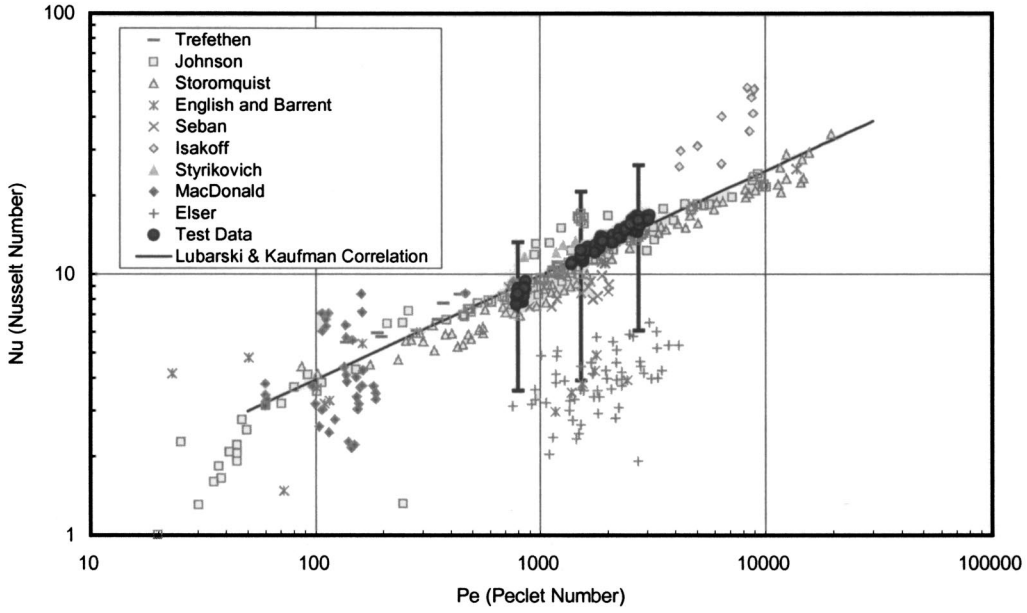

Fig. 4 Nusselt number versus Peclet number for various heat transfer studies in liquid metals

eter through the simulation. The change in heat transfer coefficient attributable to the uncertainty in each parameter is calculated by perturbing each parameter by its uncertainty and recording the corresponding change in the inferred heat transfer coefficient. The total uncertainty in the heat transfer coefficient is determined by summing absolute values of all these changes. The uncertainty in individual contributions to the inference of the heat transfer coefficient is established from the bias and precision of each parameter. Resistive temperature measurement devices (RTD's) were calibrated using an Omega RTD simulator, Model CL-301. The simulator was calibrated to NIST traceable standards. Thermocouples, pressure measurement devices, and the venturi flow meter were also calibrated to NIST standards. The magnetic flow meter was calibrated using the venturi flow meter. The bias for those instruments is determined from the calibration standards and data. The precision in these measurements is derived from examination of the temporal history of the measurement with the system at steady state. The variation in wall thickness between the flow channel and the thermocouples in the test section was determined by measurement. Bias associated with using a one dimensional analysis for a three dimensional geometry is evaluated computationally. Thermophysical property data for mercury were examined [21–25] to establish the possible bias for these parameters [7].

Seventeen factors contribute to the uncertainty in the inference of the heat transfer coefficient, and representative values are shown in Table 1. The terms labeled North Current and South Current refer to the current applied to the two sides of the test section. This representative case is for a heat transfer inference on the South side. For this case, the South Current affects the heat flux and bulk temperature while the North Current affects only the bulk temperature. This effect is seen in the uncertainty values in Table 1.

The variable labeled ''Heat Flux Multiple'' is a multiplication factor applied to the heat flux to account for three dimensional effects in the test section. Axial conduction and edge effects are estimated using a three dimensional CFD/conduction analysis. Several cases are examined using this computational model covering a velocity range of 1 to 4 m/s. The input for the analysis includes the velocity of the mercury, the inlet mercury temperature, and the power supplied to the heaters. The axial heat flux distribution along the span-wise centerline predicted by the CFD model for one set of conditions is shown in Fig. 5.

In all cases considered the heat flux predicted by the computational model in the relatively flat portions shown in Fig. 5 is

Table 1 Heat transfer uncertainty

Heat Transfer Variables	Units	Nominal Value	Precision Limit	Bias	Total Uncertainty in Variable	Change in Heat Transfer Coefficient
Volts	Volts	158.8	0.04%	0.1%	0.11%	0.53%
South Current	Amps	38.3	0.03%	0.2%	0.20%	0.94%
North Current	Amps	38.0	0.02%	0.1%	0.10%	0.03%
Inlet Temperature	C	62.8	0.52%	0.4%	0.66%	2.03%
Flow Rate	L/s	0.28	0.46%	2.5%	2.54%	1.38%
Wall Thickness	mm	1.27	0.0%	2.0%	2.00%	7.15%
Width of Heat Transfer	mm	36	0.0%	0.4%	0.35%	1.51%
Length of Heat Transfer	mm	200	0.0%	0.1%	0.06%	0.31%
Channel Width	mm	40	0.0%	0.3%	0.32%	0.00%
Small Gap	mm	2	0.0%	1.3%	1.27%	0.00%
Hg Density	kg/m^3	13419.9	0.01%	0.1%	0.11%	0.06%
Hg Cp	J/(C*kg)	137.7	0.01%	0.2%	0.22%	0.12%
Hg Thermal Conductivity	W/(m*C)	9.1	0.05%	17.1%	17.10%	0.00%
SS Thermal Conductivity	W/(m*C)	15.2	0.04%	1.0%	1.04%	3.20%
Distance to Thermocouple	mm	100	0.00%	1.0%	1.00%	0.57%
Thermocouple	C	161.4	0.21%	2.3%	2.30%	16.21%
Heat Flux Multiple	#	0.94	0.00%	2.7%	2.66%	12.66%

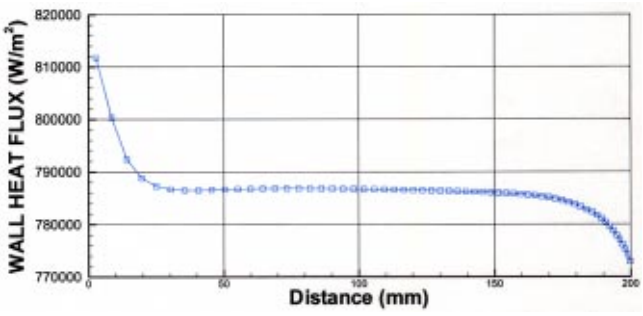

Fig. 5 Three-dimensional computational prediction of heat flux as a function of axial length in the heated part of the channel, velocity=3.5 m/s, average flux is 840 kW/m^2

approximately 94 percent of the heat flux calculated in the one dimensional model. Therefore, all the data shown in Figure 4 have a heat flux multiple of 0.94 applied. Furthermore, the local heat flux is higher than average at the entrance, and lower than the average at the exit of the heated region in the test section, as shown in Fig. 5. Data obtained from thermocouples located in the high or low heat flux regions are omitted from Fig. 4.

The most significant contributors to uncertainty in the inference of the heat transfer coefficient are the thermocouple measurement, heat flux reduction due to three dimensional effects, stainless steel wall thickness, and the stainless steel thermal conductivity. Uncertainty in each of these input values cause uncertainty in the heat transfer coefficient greater than 3 percent. For the case study in Table 1, the heat transfer coefficient is $38{,}483 \pm 17{,}965$ W/(m^2°C). This analysis is repeated for two other case studies, and three representative error bars are shown with all the data in Fig. 4. The total uncertainty is dominated by bias terms.

Conclusions

Inferred heat transfer coefficients are consistent with open literature tube data. The inferred heat transfer coefficient did not change from the initial loading of the facility with mercury to after several hundred hours of operation. This is the first mercury heat transfer data reported for narrow channels heated on both sides. This data was taken with attention to quantification of measurement precision with the expectation that the results would be used to develop models for use in the design of a liquid mercury target for a high energy proton beam. Much of the existing data for heat transfer in liquid metals was taken in the 1950s and 1960s, and the measurement precision for those data is not well characterized.

Acknowledgments

The authors wish to express their gratitude to Masanori Kaminaga. Mr. Kaminaga created a digital database of the open literature data that allowed the data to be displayed in the background of the Nusselt vs. Peclet number plots. Support for this research was derived from the Department of Energy, Oak Ridge National Laboratory through the Spallation Neutron Source target development effort.

References

[1] Smith, A. R., and Thompson, E. S., 1942, ''The Mercury-Vapor Process,'' Trans. ASME, **64**(2), pp. 625–646.
[2] Hackett, H. N., 1942, ''Mercury for the Generation of Light, Heat, and Power,'' Trans. ASME, **64**(2), pp. 647–656.
[3] Lyon, R. N., 1951, ''Liquid Metal Heat-Transfer Coefficients,'' Chem. Eng. Prog., **47**, pp. 75–79.
[4] Siman-Tov, M., et al., 1998, ''Thermal-Hydraulics of the Liquid Mercury Target for the Spallation Neutron Source (SNS),'' *Proc. 2nd Int. Topical Meeting on Nuclear Applications of Accelerator Technology (AccApp' 98)*, American Nuclear Society, La Grange Park, IL, pp. 417–427.
[5] Jallouk, P. A., et al., 2000, ''MTHL Water-Cooled Test Section Report,'' Spallation Neutron Source TSR-196, Oak Ridge, TN.
[6] Crye, J. M., et al., 2000, ''MTHL Electrically-Heated (Straight) Test Section Report,'' Spallation Neutron Source TSR-200, Oak Ridge, TN.
[7] Crye, J. M., et al., 2000, ''Mercury Thermal Hydraulic Loop (MTHL) Final Report'' Spallation Neutron Source TSR-209, Oak Ridge, TN.
[8] Sineath, H. H., 1949, ''Heat Transfer to Mercury—The Asymmetric Case,'' M.S. thesis, University of Tennessee, Knoxville, TN.
[9] Lyon, R. N., 1949, ''Forced Convection Heat Transfer Theory and Experiments with Liquid Metals,'' ORNL 361, Tech. Div., Eng. Res. Section, Oak Ridge National Laboratory; Oak Ridge, TN.
[10] Trefethen, L. M., 1950, ''Heat Transfer Properties of Liquid Metals,'' NP 1788, Tech. Info. Service, United States Atomic Energy Commission.
[11] Elser, D., 1949, ''Heat Transfer Measurements with Mercury,'' University of California, Institute of Engineering Research, Berkeley, CA.
[12] Stromquist, W. K., 1953, ''Effect of Wetting on Heat Transfer Characteristics of Liquid Metals,'' ORO-93, Tech. Info. Service, United States Atomic Energy Commission.
[13] English, D., and Barrett, T., 1950, ''Heat Transfer Properties of Mercury,'' E/R-547, Atomic Energy Research Establishment, Harwell, Berkshire, UK.
[14] Styrikovich, M. A., and Semenovker, I. E., 1940, ''Heat Exchange at Very Low Prandtl Numbers,'' J. Tech. Phys., **X**(16), pp. 1324–1330.
[15] Seban, R. A., 1950, ''Heat Transfer Measurements on Load Bismuth Eutectic in Turbulent Pipe Flow,'' University of California, Institute of Engineering Research, Berkeley, CA.
[16] Johnson, H. A., Hartnett, J. P., and Clabaugh, W. J., 1951, ''Heat Transfer to Molten Lead-Bismuth Eutectic in Turbulent Pipe Flow,'' final report, University of California, Institute of Engineering Research, Berkeley, CA.
[17] Johnson, H. A., Hartnett, J. P., and Clabaugh, W. J., 1953, ''Heat Transfer to Molten Lead-Bismuth Eutectic in Turbulent Pipe Flow,'' Trans. ASME, **75**(6), pp. 1191–1198.
[18] Isakoff, S. E., 1952, ''Heat and Momentum Transfer in Turbulent Flow of Mercury,'' Ph. D. thesis, Columbia University, New York.
[19] MacDonald, W. C., and Quittenton, R. C., 1954, ''A Critical Analysis of Metal 'Wetting' and Gas Entrainment in Heat Transfer to Molten Metals,'' Heat Transfer Research Studies for 1954, *Chemical Engineering Progress Symposium Series*, **50**(9), pp. 59–67.
[20] Lubarsky, B., and Kaufman, S., 1956, ''Review of Experimental Investigations of Liquid-Metal Heat Transfer,'' Report 1270, National Advisory Committee for Aeronautics, GPO, Washington D.C.
[21] Bauer, G. S., 1995, ''European Spallation Source (ESS)—Liquid Metal Target Studies,'' ESS95-33T.
[22] Cords, H., 1998, ''A Literature Survey of Fluid Flow Data for Mercury-Constitutive Equation,'' ESS98-81-T.
[23] Fleitman, A. H., and Weeks, J. R., 1971, ''Mercury as a Mercury Coolant,'' Nucl. Eng. Des., **16**, pp. 266–278.
[24] Lyon, R. N., 1952, *Liquid Metals Handbook*, Atomic Energy Commission, Washington, DC.
[25] Lide, D. R., and Kehiaian, H. V., 1994, *CRC Handbook of Thermophysical and Thermochemical Data*, CRC Press.

Unsteady Heat Transfer Analysis of an Impinging Jet

Yongmann M. Chung[1]
e-mail: Y.M.Chung@warwick.ac.uk

Kai H. Luo

Department of Engineering,
Queen Mary, University of London,
London E1 4NS, U.K.

Unsteady heat transfer caused by a confined impinging jet is studied using direct numerical simulation (DNS). The time-dependent compressible Navier-Stokes equations are solved using high-order numerical schemes together with high-fidelity numerical boundary conditions. A sixth-order compact finite difference scheme is employed for spatial discretization while a third-order explicit Runge-Kutta method is adopted for temporal integration. Extensive spatial and temporal resolution tests have been performed to ensure accurate numerical solutions. The simulations cover several Reynolds numbers and two nozzle-to-plate distances. The instantaneous flow fields and heat transfer distributions are found to be highly unsteady and oscillatory in nature, even at relatively low Reynolds numbers. The fluctuation of the stagnation or impingement Nusselt number, for example, can be as high as 20 percent of the time-mean value. The correlation between the vortex structures and the unsteady heat transfer is carefully examined. It is shown that the fluctuations in the stagnation heat transfer are mainly caused by impingement of the primary vortices originating from the jet nozzle exit. The quasi-periodic nature of the generation of the primary vortices due to the Kelvin-Helmholtz instability is behind the nearly periodic fluctuation in impingement heat transfer, although more chaotic and nonlinear fluctuations are observed with increasing Reynolds numbers. The Nusselt number distribution away from the impingement point, on the other hand, is influenced by the secondary vortices which arise due to the interaction between the primary vortices and the wall jets. The unsteady vortex separation from the wall in the higher Reynolds number cases leads to a local minimum and a secondary maximum in the Nusselt number distribution. These are due to the changes in the thermal layer thickness accompanying the unsteady flow structures. [DOI: 10.1115/1.1469522]

Keywords: Computational, Heat Transfer, Impingment, Laminar, Unsteady

1 Introduction

Impinging jets have been used in a variety of practical engineering applications to enhance heat transfer due to the high local heat transfer coefficient. Examples include quenching of metals and glass, cooling of turbine-blades, cooling and drying of paper and other materials, and more recently cooling of electronic equipment [1,2,3,4]. A survey of configurations used in jet impingement heat transfer studies is available in Viskanta [3]. A great number of studies have dealt with the heat transfer enhancement due to impinging jets and extensive reviews have been provided by Martin [1], Jambunathan et al. [2], and Viskanta [3]. The effects on the impingement heat transfer of several parameters such as the jet Reynolds number, nozzle-to-plate distance, nozzle geometry, roughness of the impinging wall have been investigated.

It is known from flow visualization studies [5] that impinging jet flows are very unsteady and complicated. The unsteadiness of the flow originates inherently from the primary vortices emanating from the nozzle of the jet caused by the shear layer instability of a Kelvin-Helmholtz type. These primary vortices dominate the impinging jet flow as they approach the wall. Large-scale coherent structures are found to play a dominant role in momentum transfer of the impinging jet [5,6,7,8]. After the primary vortices deflect from the wall, they convect along the impinging wall, and unsteady separation may occur. The time dependent separation of the wall jet part of an impinging jet was investigated experimentally by Didden and Ho [7].

Due to the highly unsteady flow characteristics, the impingement heat transfer is also strongly time dependent. However, most studies to date have focused on the time-mean heat transfer. The unsteady characteristics of the impingement heat transfer are not yet fully understood. Only a few studies are available in the literature [9,10]. The unsteady heat transfer in an excited circular impinging jet was investigated by Liu and Sullivan [10]. They found that enhancement and reduction of the local heat transfer were related to changes in the flow structure when an impinging jet was forced at different frequencies. It is important, therefore, to understand the unsteady heat transfer characteristics associated with the coherent flow structure.

In the present study, direct numerical simulations (DNS) of a confined impinging jet at low Reynolds numbers are performed to study the unsteady impingement heat transfer. The DNS approach is chosen because of its ability to capture unsteady vortex behavior and to resolve different time and length scales [11,12]. The unsteady compressible Navier-Stokes equations are solved in this study. A high-order finite difference method is used with accurate non-reflecting boundary conditions. The instantaneous flow fields of an impinging jet are examined to investigate the effect of the coherent vortical structures on the unsteady impingement heat transfer. Unlike previous studies [7,8,10] where the flow was forced at a particular frequency to obtain periodic flow structures, a natural unforced impinging jet flow is considered in this study.

2 Numerical Method

2.1 Governing Equations. For a compressible viscous flow, the governing equations (the unsteady continuity equation, Navier-Stokes equations, and energy equation) can be written in nondimensional form using the conservative variables $(\rho, \rho u_i, E_T, \rho f)$ [11,12]:

[1]Current address: Fluid Dynamics Research Center, Department of Engineering, University of Warwick, Coventry CV4 7AL, U.K.

Contributed by the Heat Transfer Division for publication in the JOURNAL OF HEAT TRANSFER. Manuscript received by the Heat Transfer Division January 16, 2001; revision received November 6, 2001. Associate Editor: K. S. Ball.

$$\frac{\partial \rho}{\partial t}+\frac{\partial \rho u_i}{\partial x_i}=0, \tag{1}$$

$$\frac{\partial \rho u_i}{\partial t}+\frac{\partial \rho u_i u_j}{\partial x_j}=-\frac{\partial p}{\partial x_j}\delta_{ij}+\frac{\partial \tau_{ij}}{\partial x_j}, \tag{2}$$

$$\frac{\partial E_T}{\partial t}+\frac{\partial E_T u_i}{\partial x_i}=-\frac{\partial p u_i}{\partial x_i}-\frac{\partial q_i}{\partial x_i}+\frac{\partial u_j \tau_{ij}}{\partial x_i}, \tag{3}$$

$$\frac{\partial \rho f}{\partial t}+\frac{\partial \rho f u_i}{\partial x_i}=\frac{1}{\mathrm{Re\,Sc}}\frac{\partial}{\partial x_i}\left(\mu\frac{\partial f}{\partial x_i}\right), \tag{4}$$

where ρ is the density, u_i are the velocity components in x_i directions, p is the thermodynamic pressure, τ_{ij} is the shear stress tensor, q_i is the heat flux vector, and f is the scalar variable. E_T is the total energy density (internal+kinetic):

$$E_T=\rho\left(e+\frac{1}{2}u_i u_i\right), \tag{5}$$

where e is the internal energy per unit mass ($\rho e=p/(\gamma-1)$), assuming the ideal-gas law.

In this study, all the flow variables are nondimensionalised with respect to values in the jet ($\rho_c^*, U_c^*, T_c^*, \mu_c^*$) and the jet width D^*.

$$\rho=\frac{\rho^*}{\rho_c^*},\quad u_i=\frac{u_i^*}{U_c^*},\quad e=\frac{e^*}{U_c^{*2}},\quad p=\frac{p^*}{\rho_c^* U_c^{*2}}.$$

The superscript * represents a dimensional quantity and the subscript c the jet centreline value.

Constitutive relations for the shear stress tensor τ_{ij} and the heat flux vector q_i are given by

$$\tau_{ij}=\frac{\mu}{\mathrm{Re}}\left(2S_{ij}-\frac{2}{3}\frac{\partial u_k}{\partial x_k}\delta_{ij}\right), \tag{6}$$

$$q_i=\frac{-\mu}{(\gamma-1)\mathrm{M}^2\mathrm{Pr\,Re}}\frac{\partial T}{\partial x_i}, \tag{7}$$

where, the viscosity μ is assumed to follow a power law, $\mu=T^{0.76}$ for air. The strain rate S_{ij} is defined by

$$S_{ij}=\frac{1}{2}\left(\frac{\partial u_i}{\partial x_j}+\frac{\partial u_j}{\partial x_i}\right). \tag{8}$$

Here, Re is the Reynolds number, M is the Mach number, Pr is the Prandtl number, Sc is the Schmidt number, and γ is the ratio of the specific heats. The Reynolds number is defined by $\mathrm{Re}=U_c^* D^*/\nu_c^*$, where U_c^* is the jet centerline velocity.

2.2 Boundary Conditions. The mean velocity profile at the inflow is a top-hat profile with smooth edges. A hyperbolic tangent profile is used [11,12,13]:

$$U=\frac{1}{2}\left[(U_c+U_a)+(U_c-U_a)\tanh\left(\frac{0.5-|x|}{2\theta}\right)\right], \tag{9}$$

where θ is the inflow momentum thickness and U_c is the jet center-line velocity. The co-flow velocity U_a is chosen to be zero in this study. At the impinging wall the no-slip conditions are imposed and the wall temperature is constant. Nonreflecting boundary conditions are used at the inflow and lateral exit boundaries [14,15].

Eqs. (1)–(4) can be written in a vector using the conservative variables $\mathbf{U}=(\rho,\rho u_i,E_T,\rho f)$.

$$\frac{\partial \mathbf{U}}{\partial t}+\frac{\partial \mathbf{F}^i}{\partial x_i}=\mathbf{D}, \tag{10}$$

where, $\partial \mathbf{F}^i/\partial x_i$ are the Euler derivatives in the x_i direction and no summation law is applied. Derivatives in other directions, including viscous terms are included in $\mathbf{D}$. At boundaries, $\partial \mathbf{F}^i/\partial x_i$ needs extrapolation while $\mathbf{D}$ can be evaluated directly. The conservative variables $\mathbf{U}$ are related to the primitive variables $\tilde{\mathbf{U}}=(\rho,u_i,p,f)$ as follows:

$$\frac{\partial \mathbf{U}}{\partial t}=\mathbf{P}\frac{\partial \tilde{\mathbf{U}}}{\partial t}, \tag{11}$$

$$\frac{\partial \mathbf{F}^i}{\partial x_i}=\mathbf{Q}^i\frac{\partial \tilde{\mathbf{U}}^i}{\partial x_i}. \tag{12}$$

Using the primitive variables $\mathbf{U}$, we transform Eq. (10) into primitive form,

$$\frac{\partial \tilde{\mathbf{U}}}{\partial t}+\mathbf{A}^i\frac{\partial \tilde{\mathbf{U}}}{\partial x_i}=\tilde{\mathbf{D}}. \tag{13}$$

where $\mathbf{A}^i=\mathbf{P}^{-1}\mathbf{Q}^i$, $\tilde{\mathbf{D}}=\mathbf{P}^{-1}\mathbf{D}$. Using a similarity transformation, $\mathbf{A}^i=\mathbf{S}^i\mathbf{\Lambda}\mathbf{S}^{i^{-1}}$, Eq. (13) gives

$$\frac{\partial \tilde{\mathbf{U}}}{\partial t}+\mathbf{S}^i\mathbf{\Lambda}\mathbf{S}^{i^{-1}}\frac{\partial \tilde{\mathbf{U}}}{\partial x_i}=\tilde{\mathbf{D}}. \tag{14}$$

If we define a vector $\mathcal{L}$ as

$$\mathcal{L}=\mathbf{\Lambda}\mathbf{S}^{i^{-1}}\frac{\partial \tilde{\mathbf{U}}}{\partial x_i}, \tag{15}$$

Eq. (15) may be written as

$$\frac{\partial \tilde{\mathbf{U}}}{\partial t}+\mathbf{S}^i\mathcal{L}=\tilde{\mathbf{D}}. \tag{16}$$

Finally, at boundaries Eq. (10) can be written as

$$\frac{\partial \mathbf{U}}{\partial t}+\mathbf{P}\mathbf{S}^i\mathcal{L}=\mathbf{D}. \tag{17}$$

$\mathbf{P}$, $\mathbf{S}^i$, and $\mathcal{L}$ are given in Appendix for x and y directions. At the inflow boundary, the nonreflecting boundary condition of Poinsot and Lele [15] is implemented, allowing the density to change in time. At the lateral exit, Thompson's [14] nonreflecting boundary condition is applied. For more details, refer to the papers by Thompson [14] and Poinsot and Lele [15].

2.3 Numerical Techniques. For spatial discretization, a sixth-order finite-difference compact scheme from Lele [16] is used in all directions. Third and fourth-order compact schemes are implemented at the boundary. The spatially discretized governing equations are advanced in time explicitly with a low storage third-order Runge-Kutta method [17]. Eq. (10) can be rewritten as

$$\frac{\partial \mathbf{U}}{\partial t}=\mathbf{E}. \tag{18}$$

At each sub-step, $\mathbf{U}$ is updated as follows:

$$\mathbf{U}^k=\alpha_k\Delta t\mathbf{E}^{k-1}+\mathbf{V}^{k-1}, \tag{19}$$

$$\mathbf{V}^k=\beta_k\Delta t\mathbf{E}^{k-1}+\mathbf{V}^{k-1}, \tag{20}$$

where,

$$\alpha_1=2/3,\quad \alpha_2=5/12,\quad \alpha_3=3/5,$$

$$\beta_1=1/4,\quad \beta_2=3/20,\quad \beta_3=3/5.$$

At the beginning of each time step, $\mathbf{U}^0=\mathbf{V}^0$. For more details, refer to Sandham and Reynolds [18], Luo and Sandham [11], and Jiang and Luo [12]. After both flow and thermal fields have reached a quasi-steady state, the averages over time were taken for several periods. For the definition of the period, refer to the next section.

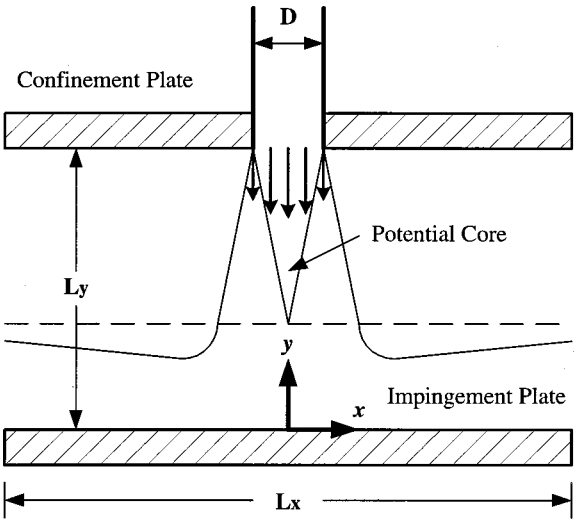

Fig. 1 Impinging slot jet configuration

3 Results and Discussion

Figure 1 shows an impinging slot jet configuration together with the definition of the relevant coordinates. The jet comes from the top and the impinging wall is located at $y=0$. A Cartesian coordinate system centred at the time-mean stagnation point on the impinging wall is used: x is the direction parallel to the impinging wall, and y is the negative jet direction. The corresponding lateral and axial velocities are u and v. The computational domain size of interest is $[-L_x/2, L_x/2]$, and $[0, L_y]$. Symmetry conditions are not used in the simulation. Simulations are performed at three Reynolds numbers Re=300, 500, and 1000. The physical constants used in this study are given in Table 1.

A grid refinement study was performed until more grid points do not cause any significant differences in the result. A hyperbolic sine function, sinh, is also used to give local grid refinement in the wall layer.

$$x(\xi)=L_x\frac{\sinh(b_x\xi)}{\sinh b_x},\quad -1\leqslant\xi\leqslant 1, \tag{21}$$

$$y(\eta)=L_y\frac{\sinh(b_y\eta)}{\sinh b_y},\quad 0\leqslant\eta\leqslant 1, \tag{22}$$

where b_x and b_y are grid control parameters. A computational grid up to 384×384 is used in the simulation. The spatial grid used in this study is very fine and the differences in mean quantities are less than 1 percent from the results using 50 percent more grid points in each direction. It is noted that the grid points used in this study are much larger than those used in previous numerical studies [19,20,21,22,23]. In those studies, symmetric boundary conditions were applied about the jet axis and the jet stagnation point was fixed.

Effects of the temporal resolutions are investigated by successively halving the time step. The time step is calculated by

$$\Delta t=\frac{CFL}{D_e+D_\mu}, \tag{23}$$

Table 1 Physical constants used in this study. Here, θ is the inflow momentum thickness of the jet.

Pr	M	Sc	γ	θ/D	T_c/T_w
1.0	0.3	1.0	1.4	0.05	1.25

Table 2 Test cases parameters of impinging jet simulations

Case	Re	L_x	L_y	mesh sizes
Case 1	300	10	10	256^2
Case 2	500	10	10	300^2
Case 3	1000	10	10	384^2
Case 4	300	8	4	256^2
Case 5	500	8	4	256^2
Case 6	1000	8	4	256^2

where

$$D_e=\pi c\left(\frac{1}{\Delta x}+\frac{1}{\Delta y}\right)+\pi\left(\frac{|u|}{\Delta x}+\frac{|v|}{\Delta y}\right), \tag{24}$$

$$D_\mu=\frac{\pi^2\mu}{(\gamma-1)\mathrm{M}^2\mathrm{Re}\,\mathrm{Pr}}\left(\frac{1}{\Delta x^2}+\frac{1}{\Delta y^2}\right), \tag{25}$$

based on numerical stability analysis. The theoretical value for stability is $CFL=\sqrt{3}$. But numerical tests indicate that the criterion can be relaxed and in practice, CFL numbers up to 4 have been used to give stable solutions. In this study, $CFL=3$ is used. The time steps used in the present study are very small. For example, Δt for Re=500 is about $1.0\times10^{-3}D/U_c$. With this time step, one period of the oscillating primary vortex is calculated by about 5000 time steps. The time histories of wall temperatures show identical results to those using half of the time steps.

Simulations with two values for the nozzle-to-plate distance ($L_y/D=4$ and 10) are performed. It is known that the extent of the potential core is 4–8 jet widths for slot nozzles [24,25]. $L_y/D=10$ is chosen to analyze the fully developed jet impingement case and $L_y/D=4$ is for the under-developed jet impingement case. The numerical parameters used in the present study are summarized in Table 2.

The numerical predictions (Case 2) are compared with the experimental data of Sparrow and Wong [26]. Sparrow and Wong (1975) used the naphthalene sublimation technique to measure the mass transfer. The mass transfer results were converted to heat transfer coefficients by employing a heat-mass transfer analogy. The Reynolds number of the experiment is Re=450. Figure 2 shows good agreement in the impingement region.

3.1 Heat Transfer Coefficient. Figure 3 shows an instantaneous scalar field of the impinging jet flow (Case 2). In this simulation, no forcing is imposed at the inflow and the jet develops in varicose (symmetric) mode near the jet nozzle. At Re=1000, the jet flow has a weak sinuous (asymmetric) mode as well as the varicose mode and the instantaneous jet stagnation point moves a little around the time-mean stagnation point ($x=0$). At higher Reynolds numbers, the jet flow becomes three-dimensional and turbulent before impinging on the wall. In this study, the Reynolds numbers are restricted to a low Reynolds number regime, where two dimensionality is valid. The primary vortices emanating from the jet shear layer are clearly seen, which is the characteristic of unsteady jet flow. As the flow is deflected from the impinging wall, a wall jet is developed. The wall jet separates due to the interaction with the primary vortices and the impinging wall, and as a result, secondary vortices are formed. The interaction of the primary vortices with the wall shear layer gives rise to unsteady vortical motions.

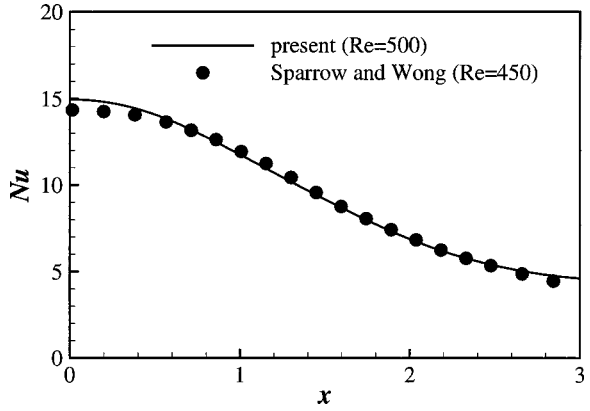

Fig. 2 Comparison with experimental data at Re=500. Symbols are the experimental data of Sparrow and Wong [26] at Re=450.

Temperatures very close to the impinging wall are monitored to understand the characteristics of the unsteady heat transfer of an impinging jet. Figure 4 shows the time history of the temperature at $y \approx 0.02$ at several locations along the impinging wall for $L_y/D=10$. As the first primary vortices emanating from the jet shear layer approach the wall, they cause a rapid change in temperature near the stagnation point. In Fig. 4, a sudden increase in temperature at $x=0$ is seen at about $t=16$ for all three Reynolds numbers. It does not appear that the propagation speed of the start-up vortex is a strong function of the Reynolds number. After the primary vortices impinge the wall, the jet flow changes the flow direction and the primary vortices progress downstream along the wall. The temperature increase caused by the moving primary vortices becomes smaller as the flow goes downstream further due to the continuous mixing with the surrounding fluid.

After an early transient period ($0<t<25$), the temperatures show unsteady and oscillating behavior. The fluctuations in the temperature increase with the Reynolds number and at Re=500 the oscillating behavior of the temperature is already clearly seen at all measuring locations. This is due to the direct influence of the coherent vortical structures of the impinging jet shown in Fig. 3. The unsteady temperature distributions show that the heat transfer characteristics at Re=500 are sufficiently coherent and repeatable although the behavior is not perfectly periodic. It is found that in the present study the dominant frequency corresponds to a Strouhal number of St≈0.2, based on U_c and D. This value falls within the range of other experimental [7,27] and numerical [8,28] results.

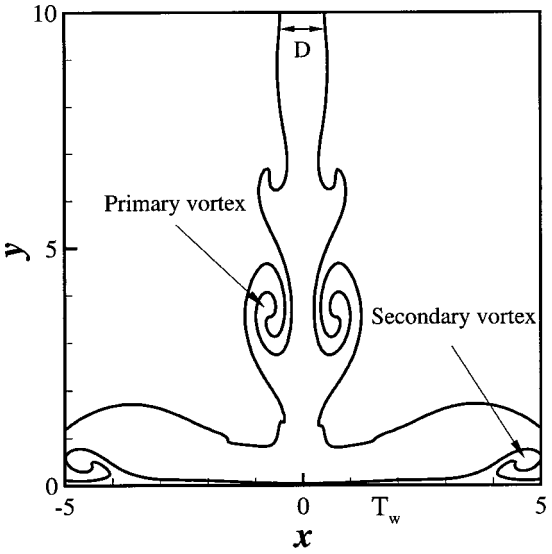

Fig. 3 Instantaneous scalar field of the impinging jet flow

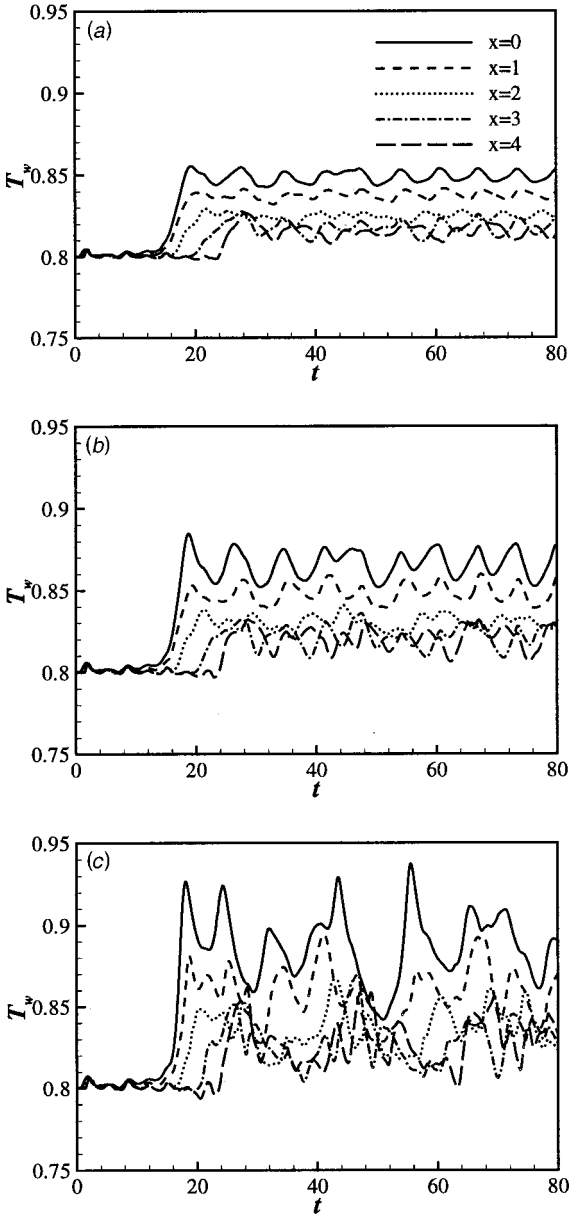

Fig. 4 Time history of temperature (at $y \approx 0.02$) at several locations on the impinging wall for $L_y/D=10$: (*a*) Re=300, (*b*) 500, and (*c*) 1000.

Some effects of the Reynolds number are found in Fig. 4. For a lower Reynolds number (Re=300), the unsteadiness of the temperature data is reduced substantially, mainly due to the weakness of the vortex formation in the jet shear layer. It is not surprising because at a low Reynolds number the viscous effects usually weaken the shear layer instability. The vortex formation is not completely suppressed but the weak vortices make the interaction with the impinging wall much weaker. As the Reynolds number increases, the temperature data become irregular at Re=1000 due to nonlinear effects, although the effects of large coherent structures are still discernible.

The time history of the temperature for $L_y/D=4$ is shown in Fig. 5. The overall features of the instantaneous temperatures in the $L_y/D=4$ case are quite similar to those in the $L_y/D=10$ case,

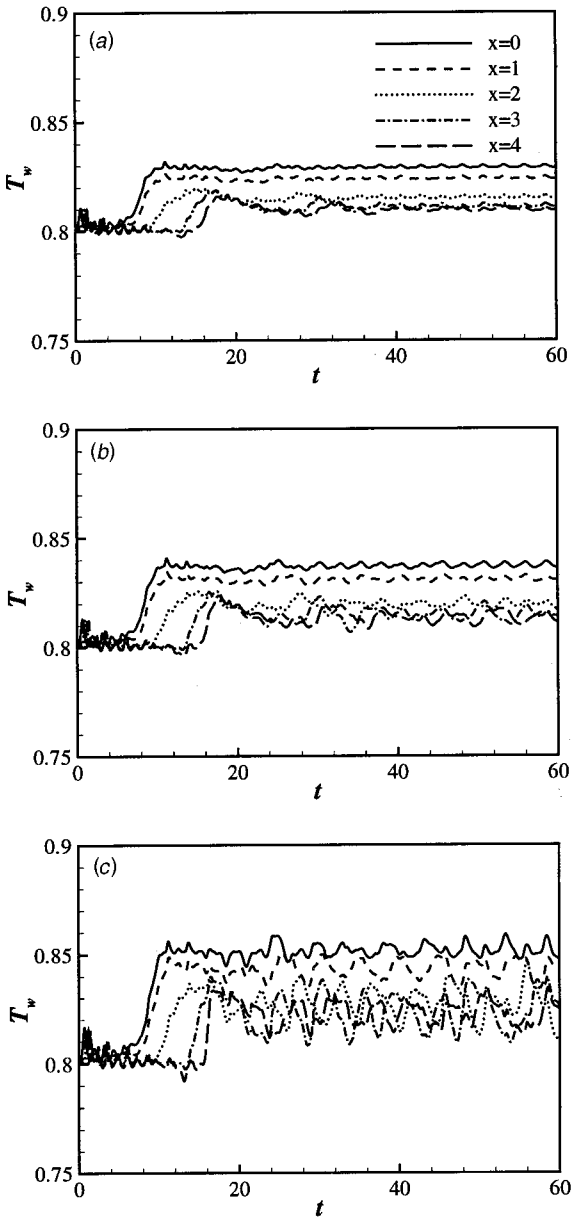

Fig. 5 Time history of temperature (at $y \approx 0.01$) at several locations on the impinging wall for $L_y/D=4$: (*a*) Re=300, (*b*) 500, and (*c*) 1000.

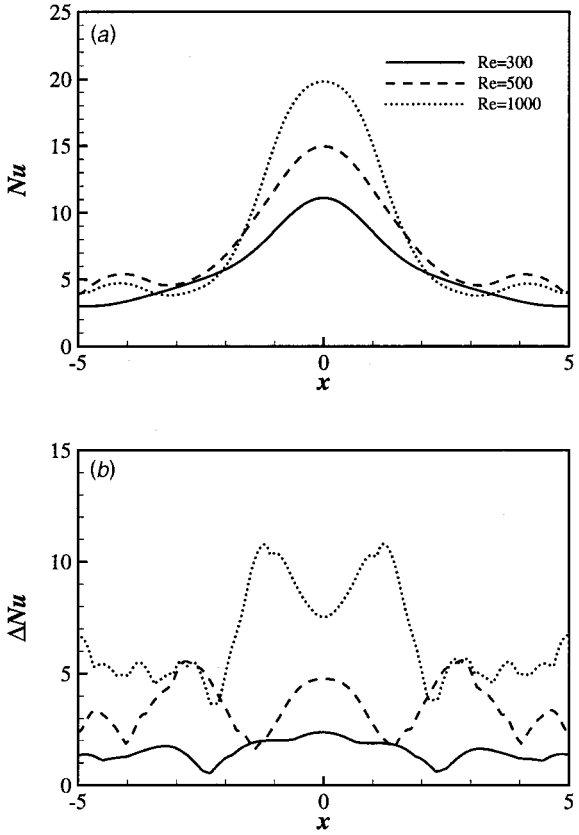

Fig. 6 Nusselt number distributions along the impinging wall for ($L_y/D=10$): (*a*) time-mean Nusselt number, and (*b*) fluctuating Nusselt number.

although unsteadiness is stronger in the latter case. Since $L_y=4$ is shorter than the extent of the potential core [24,25], the primary vortices cannot develop fully in this case. The weak primary vortices result in less vigorous unsteady heat transfer characteristics due to the weaker interaction with the wall shear layer. As far as the unsteady heat transfer characteristics are concerned, the results for the two values of the nozzle-to-plate distance are similar to each other. Here, most results are from the case with $L_y/D=10$.

The time-averaged Nusselt number distributions along the impinging wall are shown in Fig. 6 for $L_y/D=10$. Nusselt number is defined as

$$\mathrm{Nu}=\frac{D}{\Delta T}\frac{dT}{dy}, \tag{26}$$

where ΔT is the temperature difference (T_c-T_w). The fluctuating part of the instantaneous Nusselt number is also shown. The typical bell-shaped profiles are obtained near the stagnation point for all three Reynolds numbers. The stagnation Nusselt number increases as the Reynolds number and the present data can be well correlated by the relation $\mathrm{Nu}_{\mathrm{stag}} \sim \mathrm{Re}^{0.48}$. This is very close to the dependence of the stagnation Nusselt number predicted by a laminar boundary-layer theory, $\mathrm{Nu}_{\mathrm{stag}} \sim \mathrm{Re}^{0.5}$. Sparrow and Wong [26] found their data correlated with $\mathrm{Nu}_{\mathrm{stag}} \sim Re^{0.51}$ using the naphthalene sublimation technique. The quasi-laminar correlation $\mathrm{Nu}_{\mathrm{stag}} \sim \mathrm{Re}^{0.5}$ was also observed by Lytle and Webb [29], although the Reynolds numbers in their experiments were much higher.

For higher Reynolds numbers (Re=500 and 1000), the Nusselt number is maximal in the stagnation region. Away from the stagnation region it decreases to a local minimum and then goes through a secondary maximum peak. The secondary maximum in Nusselt number has been observed in many experiments. However, there is no consensus among researchers on what causes the secondary maximum. The disagreement concerning the formation of the secondary maximum is found in the review paper of Viskanta [3]. It has been attributed to either a transition from a laminar to turbulent boundary layer in the wall jet region [30,31] or a radial increase in turbulent kinetic energy [29,32]. In a visualization study, Popiel and Trass [5] suggested that the secondary vortices could be responsible for the local heat transfer enhancement and for the secondary maximum in local Nusselt number. Recently, Meola et al. [33] argued that the vortices emanating from the jet nozzle are responsible for the secondary Nusselt number maximum rather than a flow transition to turbulence. The Reynolds number of their experiments is from 10,000 to 173,000. In the present study, the Reynolds number is restricted to low values due to the relevant applications for electronics cooling, and the stagnation point is laminar, as revealed by the $\mathrm{Nu}_{\mathrm{stag}} \sim \mathrm{Re}^{0.5}$ proportionality. In such low-Reynolds number flows, where a flow transition to turbulence is not expected to play an important role,

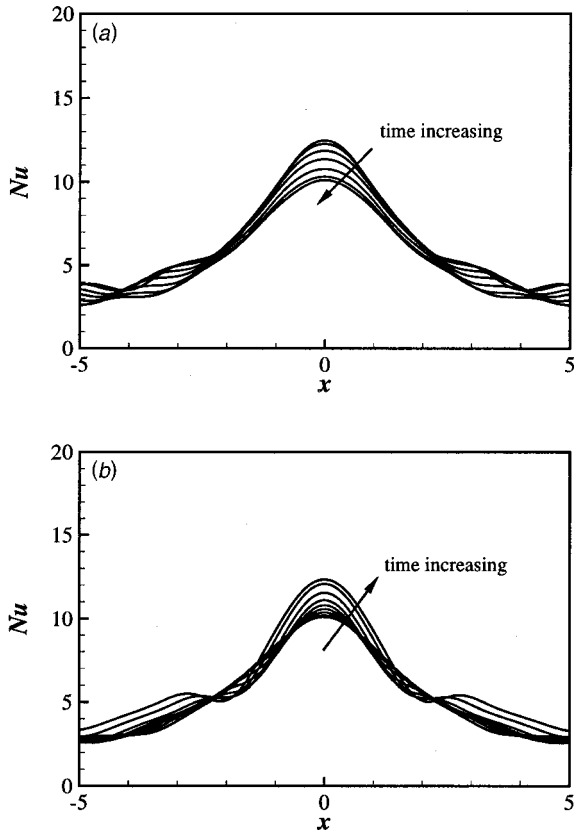

Fig. 7 Instantaneous Nusselt number along the impinging wall for Re=300 (Case 1): (*a*) temperature-decreasing phase (47.34 ≤*t*≤50.32), and (*b*) increasing phase (50.32≤*t*≤54.15). Time increment between each line is 0.467.

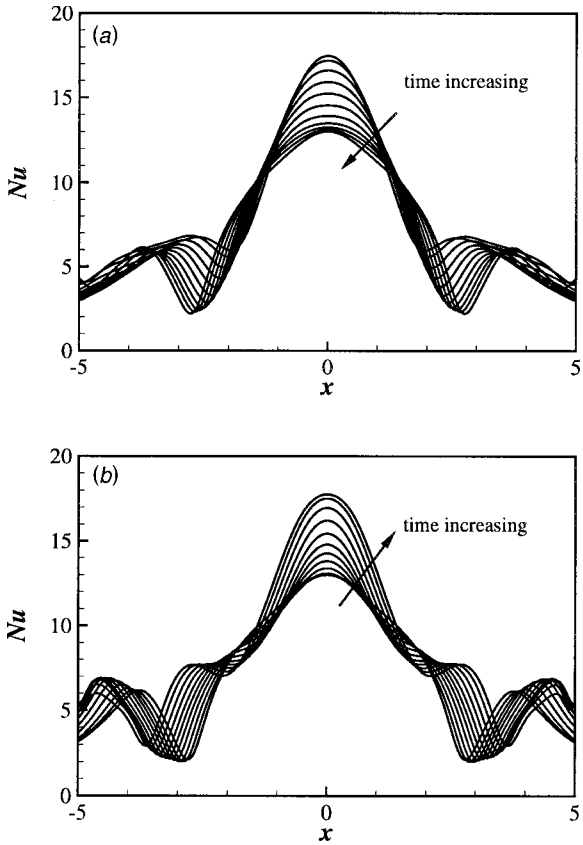

Fig. 8 Instantaneous Nusselt number along the impinging wall for Re=500 (Case 2): (*a*) temperature-decreasing phase (34.66 ≤*t*≤38.06), and (*b*) increasing phase (38.06≤*t*≤41.38). Time increment between each line is 0.326.

the secondary maximum in Nusselt number is considered as a results of the direct interaction of the wall with the unsteady primary vortices. We will revisit this point later in the next section.

The unsteadiness of the impingement heat transfer characteristics is clearly seen in Fig. 6(*b*), which shows the fluctuating part of the unsteady Nusselt number. Here, ΔNu is defined as the maximum difference in instantaneous Nusselt number at x, i.e., $\Delta \mathrm{Nu}(x)=\mathrm{Nu}_{\max}(x)-\mathrm{Nu}_{\min}(x)$. Interestingly, the fluctuating part of the instantaneous Nusselt number is very large. Even at the lowest Reynolds number (Re=300) the fluctuating part of the Nusselt number is substantial compared to the time-mean Nusselt number, which amounts to about 20 percent of the mean value. The unsteadiness is amplified as the Reynolds number increases. At Re =500, the fluctuating part becomes of the same order of magnitude as the time-mean value at $x=\pm 3$, where the time-mean Nusselt number has a local minimum.

To understand the unsteady heat transfer characteristics shown in Fig. 6, the instantaneous Nusselt number distributions during a typical *period* are analyzed. Since the temperature variation does not have a perfect periodicity as shown in Fig. 4, the time duration between two consecutive local maxima of the stagnation Nusselt number is considered as a *period* in this analysis. The half of the period between a local maximum to a local minimum is referred to as the temperature-decreasing phase and the other half between a local minimum to the next local maximum is referred to as the temperature-increasing phase. Figures 7, 8, and 9 show the instantaneous Nusselt number distributions along the impinging wall during one typical period for the three Reynolds numbers, respectively. The beginning and the end of the period is indicated in the caption of each figure.

The heat transfer coefficient generally decreases as the distance from the stagnation point increases. The maximum heat transfer is found at the stagnation point at all time instants as expected, although the absolute value is modulating substantially. It is interesting that the instantaneous Nusselt number distributions for Re =300 show a secondary local maximum during the temperature-increasing phase (Fig. 7(*a*)). Note that the time-mean Nusselt number for this Reynolds number decreases monotonically along the impinging wall without having a secondary maximum (see Fig. 6(*a*)). At Re=500, the strong unsteadiness of the heat transfer is clearly seen. During the temperature-decreasing phase shown in Fig. 8(*a*), the location for the local minimum moves downstream and the magnitude of the local minimum decreases in time. This is because the thermal boundary layer becomes thicker for $2\leqslant x\leqslant 3$ during this phase. During the temperature-increasing phase shown in Fig. 8(*b*), the magnitude of the local minimum is almost the same as the location itself moves downstream. As the Reynolds number increases (Re=1000), the instantaneous Nusselt number distributions become more irregular as shown in Fig. 9. The loss of symmetry is expected as Re is increased but it remains small at Re=1000. There is only a 0.5 percent of asymmetry for Re=500 and a 2 percent of asymmetry for Re=1000.

3.2 Unsteady Flow Field. To investigate the unsteady impingement heat transfer, the flow field of Re=500 is analyzed in more detail (Case 2). The Re=500 case is chosen since the instantaneous Nusselt number has a very strong periodicity as shown in Fig. 4(*b*). Figure 10 shows the time history of the instantaneous Nusselt number at the stagnation point, $\mathrm{Nu}_{\mathrm{stag}}$. The periodicity, which corresponds to St≈0.2, is discernible. The fluctuation part of Nu amounts to almost 40 percent of the time-mean value. The instantaneous Nusselt number has local maxima at $t=34.66$ and 41.38 and a local minimum at $t=38.06$.

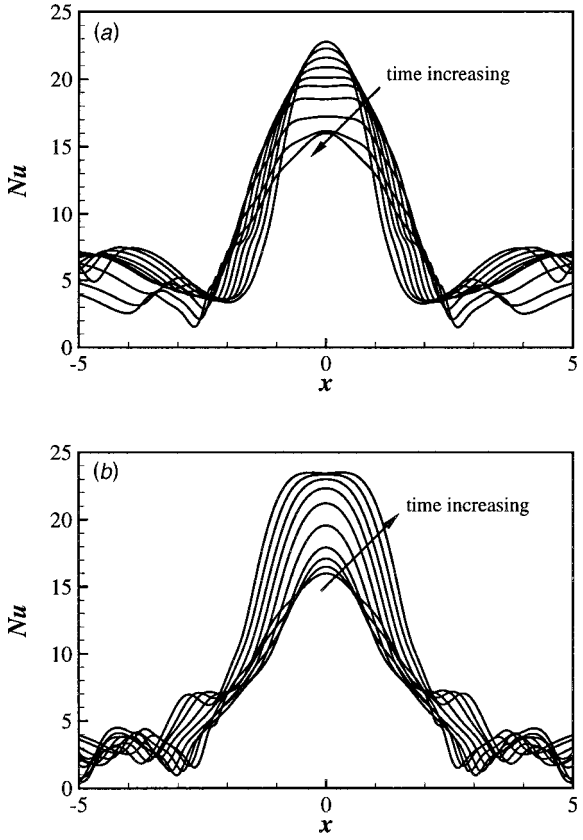

Fig. 9 Instantaneous Nusselt number along the impinging wall for Re=1000 (Case 3): (*a*) temperature-decreasing phase (32.00≤*t*≤36.32), and (*b*) increasing phase (36.32≤*t*≤40.65). Time increment between each line is 0.480.

To scrutinize the unsteady nature of the impingement heat transfer shown in Fig. 10, we examine the flow pattern and the temperature field together at several time instants. Time instants are marked as the open circle in Fig. 10 and summarized in Table 3. P1 represents the time instant when the instantaneous Nusselt number at the stagnation point has a local maximum, P2 and P3 correspond to the temperature-decreasing phase, P4 represents to the local minimum of the instantaneous stagnation Nusselt number, and P5 and P6 correspond to the temperature-increasing phase.

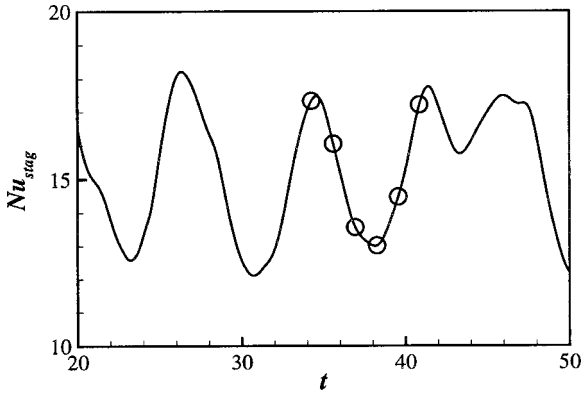

Fig. 10 Time history of the instantaneous stagnation Nusselt number for Re=500. Open circles indicate the time instants examined in Fig. 11.

Table 3 Data at several time instants marked in Fig. 10. x_v and y_v are the location of the primary vortex (PV), and ω_v is the strength of the primary vortex.

	t	Nu_{stag}	x_v	y_v	ω_v
P1	34.263	17.336	1.25	0.83	1.92
P2	35.596	16.055	1.78	0.79	1.90
P3	36.931	13.562	2.34	0.87	1.82
P4	38.254	13.010	2.82	0.98	1.78
P5	39.561	14.472	3.28	1.10	1.75
P6	40.857	17.220	3.67	1.15	1.73

Figure 11 shows the temperature and vorticity contour lines at four time instants marked in Fig. 10. Due to the strong symmetry (see Fig. 8), only one half of the flow field is shown without any loss of information or accuracy of comparison. The primary vortices close to the impinging wall are denoted by PV in the figure, where NV represents the next primary vortices emanating from the jet shear layer. The secondary vortices are indicated by SV in the lower part of Fig. 11. As can be seen in Fig. 11(*a*), the primary vortex PV locates very close to the wall at P1. The proximity of the strong primary vortex results in a thin shear layer and consequently a thin thermal boundary layer along the wall (note Pr=1.0).

As the primary vortex PV moves downstream, the temperature near the stagnation point decreases due to the thickening of the thermal boundary layer. The vorticity contour lines during the temperature-decreasing phase are displayed in Fig. 11(*b*). As the primary vortex PV progresses downstream, the location of the primary vortices, y_v, increases slightly indicating a thickening of the thermal boundary layer downstream along the impinging wall [7]. This feature is responsible for the decrease in the local minimum Nusselt number during the temperature-decreasing phase shown in Fig. 8(*a*). The passage of the primary vortex PV is associated with a vorticity maximum at the impinging wall. The interaction of the primary vortex PV with the shear layer results in a secondary vortex near the wall at the later stage of the temperature-decreasing phase at P3. The primary and secondary vortices are counter-rotating.

As the primary vortex PV moves further downstream while the new primary vortex NV is yet to affect the dynamics near the impinging wall directly, the stagnation Nusselt number keeps decreasing. Figure 11(*c*) shows the temperature and vorticity contour lines at P4 corresponding to a local minimum of the stagnation Nusselt number. The formation of the secondary vortex SV is clearly seen at $x=3$. The secondary vortex SV is detached from the wall and results in unsteady separation. The unsteady separation region moves downstream together with the primary vortex PV. Upstream of the unsteady separation region, the instantaneous Nusselt number has a local minimum, as seen in Fig. 8. A secondary maximum in instantaneous Nusselt number was observed in the separation region. The role played by the unsteady separation in the impingement heat transfer is examined in more detail in Fig. 12.

As the new primary vortex NV approaches the wall, the stagnation Nusselt number begins to increase again. The vorticity contour lines during the temperature-increasing phase are displayed in Fig. 11(*d*). The primary vortex PV is located far from the stagnation point and has little influence on the heat transfer near the

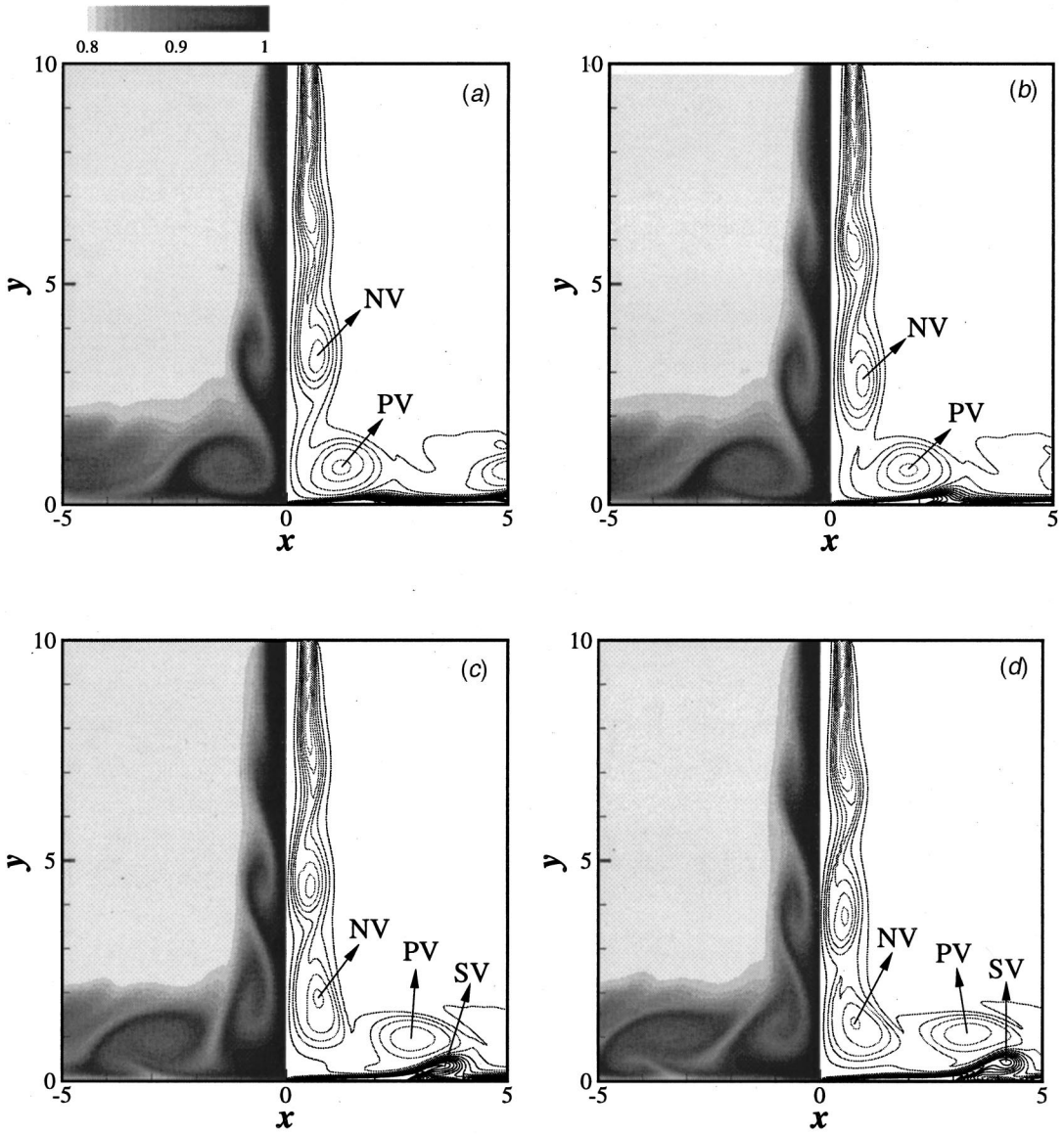

Fig. 11 Temperature (left) and vorticity (right) contour lines at several time instants for Re=500: at (*a*) P1, (*b*) P2, (*c*) P4, (*d*) P5.

stagnation region. The influence from the new primary vortex NV is, however, increasing as it approaches the wall.

The location and the strength of the primary vortex PV are summarized in Table 3. The location of the primary vortex shows a characteristic *V*-shape [7]. The strength of the vortex is weakened during the period due to the viscous effects but the decrease is only 10 percent of the strength. It is found that the modulation of the instantaneous Nusselt number is attributed to the dynamics of the primary vortices emanating from the jet shear layer as well as the strength of the vortices.

The enlarged picture of the temperature field and velocity vector plots at P5 are shown in Fig. 12. Beneath the primary vortex is clearly seen an unsteady separation region centred at $x=4.2$, $y=0.14$. The thermal boundary layer becomes thick upstream of the unsteady separation region and the instantaneous Nusselt number has a local minimum at $x=3.4$ as shown in Fig. 12(*a*). This is consistent with the instantaneous Nusselt number distributions shown in Fig. 8(*b*). It is found that the leg of the secondary vortex corresponds to the location for the local minimum Nusselt number (see Fig. 11(*d*)). Around the head of the secondary vortex, there is a strong engulfing motion, which causes an increase in the heat transfer. This engulfing motion is responsible for the secondary maximum in the Nusselt number distributions observed in Fig. 8.

4 Concluding Remarks

Unsteady heat transfer characteristics of an impinging jet flow have been studied numerically. The instantaneous Nusselt number has very strong fluctuations and this unsteadiness increases with increasing Reynolds number. Detailed analysis of the instantaneous flow field and heat transfer characteristics has been performed. It is found that the unsteady heat transfer characteristics are strongly correlated with the vortex dynamics of the jet flow. The oscillating behavior of the impingement heat transfer is caused directly by the primary vortices moving towards the impinging wall. Unsteady separation also plays an important role in the impingement heat transfer. Unsteady separation induces a secondary maximum and a local minimum of the instantaneous heat transfer along the impinging wall. The instantaneous Nusselt number has a local minimum upstream of the unsteady separation region due to the thickened thermal boundary layer. A secondary maximum in the instantaneous Nusselt number is observed in the

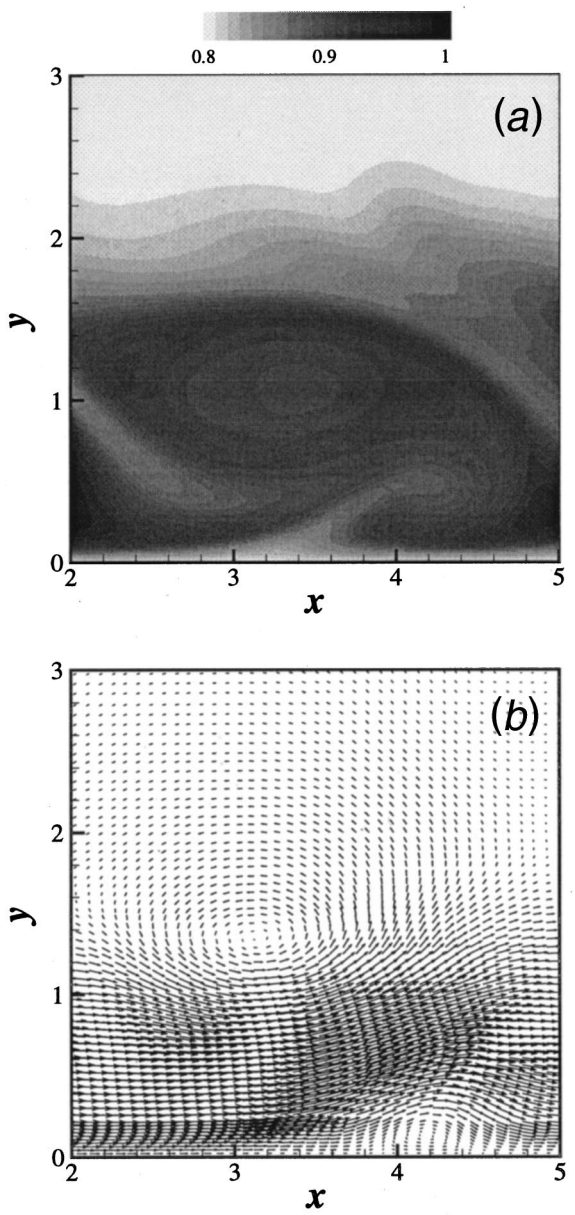

Fig. 12 Instantaneous flow and temperature field at P5: (*a*) temperature contour lines, and (*b*) vector plot.

separation region. The secondary maximum is attributed to the engulfing motion around the secondary vortex, which reduces the thickness of the thermal boundary layer.

Acknowledgments

The support of the Engineering and Physical Sciences Research Council (EPSRC) of the United Kingdom under grant number GR/L56237 is gratefully acknowledged. The research was conducted while the first author was employed by Queen Mary, University of London.

Nomenclature

Roman Symbols

c = sound speed
D = jet width
e = internal energy per unit mass
E_T = total energy per unit mass
h = heat transfer coefficient, $h=(k/\Delta T)(dT/dy)$
k = thermal conductivity
L_x = domain size in x direction
L_y = domain size in y direction
M = Mach number
Nu = Nusselt number, $\mathrm{Nu}=hD/k$
p = static pressure
Pr = Prandtl number
q_i = heat flux vector
Re = Reynolds number, $\mathrm{Re}=U_cD/\nu$
S_{ij} = strain rate, $S_{ij}=0.5(\partial u_i/\partial x_j+\partial u_j/\partial x_i)$
St = Strouhal number, $St=fD/U_c$
T = temperature
u_i = velocity components
U_a = co-flow velocity
U_c = jet centreline velocity
x = lateral coordinate
y = normal to the wall coordinate

Greek Symbols

γ = ratio of the specific heat
θ = inflow momentum thickness
μ = dynamic viscosity
ν = kinematic viscosity
ρ = density
τ_{ij} = shear stress tensor
ω = vorticity, $\omega=dv/dx-du/dy$

Subscripts

c = jet centreline value
stag = stagnation point
v = primary vortices
w = wall value

Appendix

A diagonalizing similarity transformation may be generated for $\mathbf{A}^i$ by forming the matrix $\mathbf{S}$ such that its columns are the right eigenvectors $\mathbf{r}_i$ of $\mathbf{A}^i$, and its inverse $\mathbf{S}^{-1}$, whose rows are the left eigenvectors $\mathbf{l}_i^T$. The similarity transformation is then

$$\mathbf{A}^i=\mathbf{S}^i\mathbf{\Lambda}\mathbf{S}^{i^{-1}}, \tag{27}$$

where $\mathbf{\Lambda}$ is the diagonal matrix of eigenvalues: $\mathbf{\Lambda}_{ij}=0$ for $i\neq j$, $\mathbf{\Lambda}_{ij}=\lambda_i$ for $i=j$.

$$\mathbf{P}=\begin{pmatrix} 1 & 0 & 0 & 0 & 0 & 0 \\ u & \rho & 0 & 0 & 0 & 0 \\ v & 0 & \rho & 0 & 0 & 0 \\ w & 0 & 0 & \rho & 0 & 0 \\ \frac{1}{2}(u^2+v^2+w^2) & \rho u & \rho v & \rho w & \frac{1}{\gamma-1} & 0 \\ f & 0 & 0 & 0 & 0 & \rho \end{pmatrix}.$$

A In the x-Direction. The $\mathcal{L}_i^x$'s are given by:

$$\mathcal{L}_1=\lambda_1\left(\frac{\partial p}{\partial x}-\rho c\frac{\partial u}{\partial x}\right), \tag{28}$$

$$\mathcal{L}_2=\lambda_2\left(c^2\frac{\partial \rho}{\partial x}-\frac{\partial p}{\partial x}\right), \tag{29}$$

$$\mathcal{L}_3=\lambda_3\frac{\partial v}{\partial x}, \tag{30}$$

$$\mathcal{L}_4=\lambda_4\frac{\partial w}{\partial x}, \tag{31}$$

$$\mathcal{L}_5=\lambda_5\left(\frac{\partial p}{\partial x}+\rho c\frac{\partial u}{\partial x}\right), \tag{32}$$

$$\mathcal{L}_6=\lambda_6\frac{\partial f}{\partial x}, \tag{33}$$

where λ_i^x, the eigenvalues of $\mathbf{A}^x$, are given by

$$\lambda_1=u-c,\quad \lambda_2=\lambda_3=\lambda_4=\lambda_6=u,\quad \lambda_5=u+c. \tag{34}$$

$$\mathbf{S}^x=\begin{pmatrix} \frac{1}{2c^2} & \frac{1}{c^2} & 0 & 0 & \frac{1}{2c^2} & 0 \\ -\frac{1}{2\rho c} & 0 & 0 & 0 & \frac{1}{2\rho c} & 0 \\ 0 & 0 & 1 & 0 & 0 & 0 \\ 0 & 0 & 0 & 1 & 0 & 0 \\ \frac{1}{2} & 0 & 0 & 0 & \frac{1}{2} & 0 \\ 0 & 0 & 0 & 0 & 0 & 1 \end{pmatrix}.$$

B In the *y*-Direction. The $\mathcal{L}_i^y$'s are given by:

$$\mathcal{L}_1=\lambda_1\left(\frac{\partial p}{\partial y}-\rho c\frac{\partial v}{\partial y}\right), \tag{35}$$

$$\mathcal{L}_2=\lambda_2\frac{\partial u}{\partial y}, \tag{36}$$

$$\mathcal{L}_3=\lambda_3\left(c^2\frac{\partial \rho}{\partial y}-\frac{\partial p}{\partial y}\right). \tag{37}$$

$$\mathcal{L}_4=\lambda_4\frac{\partial w}{\partial y}, \tag{38}$$

$$\mathcal{L}_5=\lambda_5\left(\frac{\partial p}{\partial y}+\rho c\frac{\partial v}{\partial y}\right). \tag{39}$$

$$\mathcal{L}_6=\lambda_6\frac{\partial f}{\partial y}, \tag{40}$$

where λ_i^y, the eigenvalues of $\mathbf{A}^y$, are given by

$$\lambda_1=v-c,\quad \lambda_2=\lambda_3=\lambda_4=\lambda_6=v,\quad \lambda_5=v+c. \tag{41}$$

$$\mathbf{S}^y=\begin{pmatrix} \frac{1}{2c^2} & 0 & \frac{1}{c^2} & 0 & \frac{1}{2c^2} & 0 \\ 0 & 1 & 0 & 0 & 0 & 0 \\ -\frac{1}{2\rho c} & 0 & 0 & 0 & \frac{1}{2\rho c} & 0 \\ 0 & 0 & 0 & 1 & 0 & 0 \\ \frac{1}{2} & 0 & 0 & 0 & \frac{1}{2} & 0 \\ 0 & 0 & 0 & 0 & 0 & 1 \end{pmatrix}.$$

References

[1] Martin, H., 1977, "Heat and Mass Transfer Between Impinging Gas Jets and Solid Surfaces," Adv. Heat Transfer, **13**, pp. 1–60.

[2] Jambunathan, K., Lai, E., Moss, M. A., and Button, B. L., 1992, "A Review of Heat Transfer Data for Single Circular Jet Impingement," Int. J. Heat Fluid Flow, **13**, pp. 106–115.

[3] Viskanta, R., 1993, "Heat Transfer to Impinging Isothermal Gas and Flame Jets," Exp. Therm. Fluid Sci., **6**, pp. 111–134.

[4] Beitelmal, A. H., Saad, M. A., and Patel, C. D., 2000, "The Effect of Inclination on the Heat Transfer Between a Flat Surface and an Impinging Two-Dimensional Air Jet," Int. J. Heat Fluid Flow, **21**, pp. 156–163.

[5] Popiel, C. O., and Trass, O., 1991, "Visualization of a Free and Impinging Round Jet," Exp. Therm. Fluid Sci., **4**, pp. 253–264.

[6] Ho, C. M., and Nosseir, N. S., 1981, "Dynamics of an Impinging Jet. Part 1. The feedback phenomenon," J. Fluid Mech., **105**, pp. 119–142.

[7] Didden, N., and Ho, C. M., 1985, "Unsteady Separation in a Boundary Layer Produced by an Impinging Jet," J. Fluid Mech., **160**, pp. 235–256.

[8] Olsson, M., and Fuchs, L., 1998, "Large Eddy Simulations of a Forced Semi-confined Circular Impinging Jet," Phys. Fluids, **10**(2), pp. 476–486.

[9] Özdemir, I. B., and Whitelay, J. H., 1992, "Impingement of an Axisymmetric Jet on Unheated and Heated Flat Plates," J. Fluid Mech., **240**, pp. 503–532.

[10] Liu, T., and Sullivan, J. P., 1996, "Heat Transfer and Flow Structure in a Excited Circular Impinging Jet," Int. J. Heat Mass Transf., **39**(17), pp. 3695–3706.

[11] Luo, K. H., and Sandham, N. D., 1997, "Direct Numerical Simulation of Supersonic Jet Flow," J. Eng. Math., **32**, pp. 121–142.

[12] Jiang, X., and Luo, K. H., 2000, "Direct Numerical Simulation of the Puffing Phenomenon of an Axisymmetric Thermal Plume," Theor. Comput. Fluid Dyn., **14**, pp. 55–74.

[13] Luo, K. H., and Sandham, N. D., 1997, "Instability of Vortical and Acoustic Models in Supersonic Round Jets," Phys. Fluids, **9**(4), pp. 1003–1013.

[14] Thompson, K. W., 1987, "Time Dependent Boundary Conditions for Hyperbolic Systems," J. Comput. Phys., **68**, pp. 1–24.

[15] Poinsot, T. J., and Lele, S. K., 1992, "Boundary Conditions for Direct Simulations of Compressible Viscous Flows," J. Comput. Phys., **101**, pp. 104–129.

[16] Lele, S. K., 1992, "Compact Finite Difference Schemes With Spectral-like Resolution," J. Comput. Phys., **103**, pp. 16–42.

[17] Williamson, J. H., 1980, "Low-Storage Runge-Kutta Schemes," J. Comput. Phys., **35**, pp. 48–56.

[18] Sandham, N. D., and Reynolds, W. C., 1991, "Three-Dimensional Simulations of Large Eddies in the Compressible Mixing Layer," J. Fluid Mech., **224**, pp. 133–158.

[19] Law, H.-S., and Masliyah, J. H., 1984, "Mass Transfer Due to a Confined Laminar Impinging Two-Dimensional Jet," Int. J. Heat Mass Transf., **27**(4), pp. 529–539.

[20] Al-Sanea, S., 1992, "A Numerical Study of the Flow and Heat-Transfer Characteristics of an Impinging Laminar Slot-Jet Including Crossflow Effects," Int. J. Heat Mass Transf., **35**(10), pp. 2501–2513.

[21] Chou, Y. J., and Hung, Y. H., 1994, "Impingement Cooling of an Isothermally Heated Surface With a Confined Slot Jet," ASME J. Heat Transfer, **116**, pp. 479–482.

[22] Lee, X. C., Ma, C. F., Xheng, Q., Zhuang, Y., and Tian, Y. Q., 1997, "Numerical Study of Recovery Effect and Impingement Heat Transfer With Submerged Circular Jets of Large Prandlt Number Liquid," Int. J. Heat Mass Transf., **40**(11), pp. 2647–2653.

[23] Chen, M., Chalupa, R., West, A. C., and Modi, V., 2000, "High Schmidt Mass Transfer in a Laminar Impinging Slot Jet Flow," Int. J. Heat Mass Transf., **43**, pp. 3907–3915.

[24] Gauntner, J., Livingood, N. B., and Hrycak, P., 1970, "Survey of Literature on Flow Characteristics of a Single Turbulent Jet Impinging on a Flat Plate," NASA TN D-5652, Lewis Research Center, USA.

[25] Livingood, N. B., and Hrycak, P., 1973, "Impingement Heat Transfer From Turbulent Air Stream Jets to Flat Plates—A Literature Survey," NASA TM X-2778, Lewis Research Center, USA.

[26] Sparrow, E. M., and Wong, T. C., 1975, "Impingement Transfer Coefficients Due to Initially Laminar Slot Jets," Int. J. Heat Mass Transf., **18**, pp. 597–605.

[27] Ho, C. M., and Huerre, P., 1984, "Perturbed Free Shear Layers," Annu. Rev. Fluid Mech., **16**, pp. 365–424.

[28] Hoffmann, G., and Benocci, C., 1994, "Numerical Simulation of Spatially-Developing Planar Jets," in *Application of Direct and Large Eddy Simulation to Transition and Turbulence*, AGARD-CP-551, pp. 26-1–26-6.

[29] Lytle, D., and Webb, B., 1994, "Air Jet Impingement Heat Transfer at Low Nozzle-Plate Spacings," Int. J. Heat Mass Transf., **37**, pp. 1687–1697.

[30] Garimella, S., and Rice, R., 1995, "Confined and Submerged Liquid Jet Impingement Heat Transfer," ASME J. Heat Transfer, **117**, pp. 871–877.

[31] Colucci, D., and Viskanta, R., 1996, "Effect of Nozzle Geometry on Local Convective Heat Transfer to a Confined Impinging Air Jet," Exp. Therm. Fluid Sci., **13**, pp. 71–80.

[32] Behnia, M., Parneix, S., Shabany, Y., and Durbin, P. A., 1999, "Numerical Study of Turbulent Heat Transfer in Confined and Unconfined Impinging Jets," Int. J. Heat Mass Transf., **20**, pp. 1–9.

[33] Meola, C., de Luca, L., Carlomagno, G. M., 1996, "Influence of Shear Layer Dynamics on Impingement Heat Transfer," Exp. Therm. Fluid Sci., **13**, 29–37.

Simulation of Laminar Slot Jets Impinging on a Moving Surface

Himadri Chattopadhyay
PEHT Group,
Central Mechanical Engineering Research Institute,
Durgapur-713 209, India
e-mail: chimadri@hotmail.com

Sujoy K. Saha
Dept. of Mechanical Engineering,
Bengal Engineering College,
Howrah-711 103, India
e-mail: sujoy_k_saha@hotmail.com

Laminar flow and heat transfer on a moving surface due to a bank of impinging slot jets have been numerically investigated. Two types of jet, namely axial and knife-jet with an exit angle of 60 deg were considered. The surface velocity up to two times the jet velocity at the nozzle exit was imposed on the impinging surface. It has been observed that while with increasing velocity of the impinging surface, the total heat transfer reduces; the distribution pattern becomes more uniform. For the same amount of mass and momentum flux at the nozzle exit, heat transfer from the axial jet is considerably higher than that from the vectored jets at all surface velocities considered. It was found that the local heat transfer over the surface for the case of the axial jet and the knife-jet scales with $Re^{0.5}$ *and* $Re^{0.55}$*, respectively.* [DOI: 10.1115/1.1501089]

Keywords: Forced Convection, Heat Transfer, Impingement, Jets, Laminar, Modeling

Introduction

Impinging jets are extensively employed in high heat flux application and thus widely investigated by researchers [1–4]. In [2] heat transfer to impinging isothermal gas and flame jets has been considered. Mass transfer in addition to heat transfer between impinging gas jets and solid surfaces has been considered in [3]. However, though in many situations, e.g., drying of papers and textiles, the impinging surface moves perpendicular to the jet direction, relatively fewer studies have incorporated the effect of surface motion over the transport process. Studies on a single jet impinging on a moving surface were reported by Subba Raju and Schlunder [5]. They have measured spatially averaged heat transfer coefficients due to a single impinging jet on a moving, constant temperature metal belt and found that the heat transfer coefficient increased with the surface speed till a maximum value of 1.5 to 2 times the value for stationary surface was obtained. Zumbrunnen [6] used a similarity solution to derive the velocity components, which were used to determine heat and mass transfer distributions. This study showed reduction in heat and mass transfer downstream of the direction of surface motion as comparatively warmer or higher concentration fluid was entrained by the surface motion.

Polat and Douglas [7] conducted experiment on heat transfer from multiple impinging jets on a permeable moving surface. Their study showed a decrease in heat transfer with increasing surface motion while the amount of throughflow increased heat transfer. Huang et al. [8] have reported that at higher plate speeds, Nusselt numbers were smaller at the locations where the surface motion opposed the dividing jet flow and Nusselt numbers were higher where the surface motion and dividing jet flow were in the same direction.

Chen et al. [9] performed a numerical analysis, in the laminar range, of an array of submerged two-dimensional jets impinging on a uniform heat flux or constant temperature moving surface. This study showed that neglecting surface motion effects could lead to significant overestimates of heat transfer. Recently, the effect of surface motion on the turbulent flow and heat transfer using axial slot jets was reported by Chattopadhyay et al. [10]. They have used a dynamic subgrid model of LES as the computational tool and predicted the heat transfer in a bank of axial slot jets with the impinging surface velocity varying up to two times the jet velocity. The reduction in heat transfer was as high as 30 percent when the surface velocity was two times the reference velocity.

In industrial practices, normally a bank of jet is used and the jets can emanate either from a round tube or orifice or a slot. The simplest form of a jet is the axial jet (from a circular hole or a rectangular slot) where the issuing fluid is directed perpendicular to the impinging surface. In case of the slot (or planar) jets, when the flow emanates horizontally at a particular angle, a horizontal knife-jet is formed. For round tubes, they are referred to as radial jets. In Fig. 1, distributions of heat transfer coefficients for axial slot jet and horizontal knife-jets are schematically compared. In the present work we have studied slot jets, which emanate (*a*) axially and hit the plate perpendicularly and (*b*) at an angle of 60 deg from the side of the slot (knife-jet). The knife-jet (from a slot) is equivalent to radial jets (from a circular hole) and it should not be confused with vectored round jets generally referred to as radial jets. The main advantage of a horizontal-knife-jet from a slot (or a radial jet in case of a round tube) is that the moderately high heat or mass transfer can be distributed on a larger area than that of the axial jet. Because of this, in recent years the radial jets are getting increased attention, Page et al. [11]. Laschefski et al. [12] have investigated the effect of the exit angle of circular radial jet on flow field and heat transfer in the laminar region. For the same amount of the mass and momentum flux at the nozzle exit, laminar radial jets produce lower average and peak heat transfer than the axial jet. On the other hand, with the vectoring of the impinging jet, the location of peak heat transfer could be controlled. Investigations on axial slot jets by this group [13] produced similar result. Cziesla et al. [14] have demonstrated that the knife-jets at an exit angle of 60 deg are superior to the axial jets in the turbulent range. Their study has shown that the flow field on the impinging plate due to the horizontal-knife-jets culminates in an oscillatory flow dominated by vortical motions. Such motions play a significant role in enhancing heat transfer. A recent numerical study of Chattopadhyay and Saha [15] could confirm that in the turbulent regime vectoring the jets produces better heat transfer even in the case of a moving plate, compared to the standard axial jet.

Though, generally such jets would be turbulent, laminar jets are often encountered in applications such as electronic cooling. Laminar jets are also employed when situations demand relatively lower stagnation pressure as in the case of fragile materials [16]. In a recent analysis of laminar rectangular jet by Sezai and Mohamad [17], it has been rightly pointed out that despite abundance of literature on jet impingement, even today laminar jets are far from being fully understood. While majorities of the studies as-

Contributed by the Heat Transfer Division for publication in the JOURNAL OF HEAT TRANSFER. Manuscript received by the Heat Transfer Division May 7, 2001; revision received June 3, 2002. Associate Editor: V. K. Dhir.

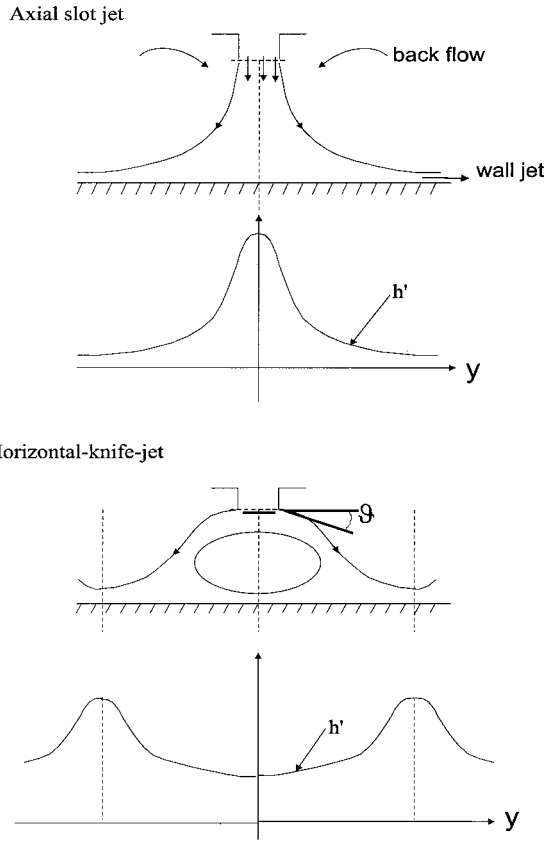

Fig. 1 Schematic comparison of axial jet and knife-jet

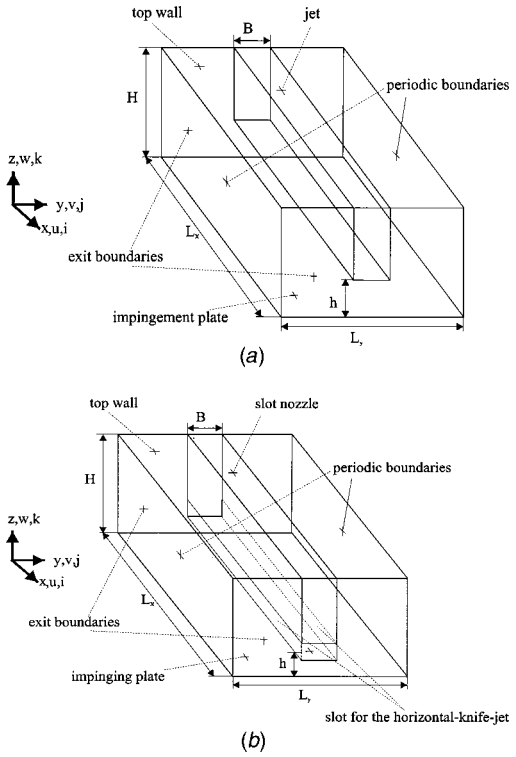

Fig. 2 Computational domain for (*a*) axial and (*b*) knife-jet

sume a two-dimensional jet structure, it has been demonstrated that three-dimensionality brings in additional complexity in the flow physics and hence alters the flow structure and heat transfer process. While some work on the jet impingement on a moving wall in the turbulent regime is already reported by the present authors [10,15], the three-dimensional simulation of the effect of surface motion on the laminar impinging jets is now undertaken in the present work. This can serve as a baseline for comparing the effect of turbulence. Moreover, to our knowledge, no literature on the effect of surface motion on laminar knife-jets exists. The present analyses were carried out within the Reynolds number range of 200 for both axial and knife-jets. The surface velocity of the impingement plate is varied up to two times the jet velocity at the nozzle exit. In the present study, the characteristic length for defining Re is twice the jet width, which is the hydraulic diameter for such a configuration [3]. For the purpose of comparison, the mass flux as well as the momentum flux at the jet exit have been considered same for the axial as well as knife-jet. We have used the transient formulation so that the evolution of the flow field could be studied in detail and the state of the flow, i.e., whether laminar or turbulent, need not be assumed but could be assured by analysing the velocity traces and their power spectra counterparts. It may be mentioned here that the flow field due to periodic jets become chaotic at Re of 415 and 250 for the axial and the knife-jet, respectively, as reported by Laschefski et al. [18].

A periodic element of a nozzle-bank serves as the computational domain as shown in Fig. 2. While the width of the computational domain is 10 times the jet width, the pitch of the jet bank was taken as 8B. The distance between the top plate and the impinging plate is assumed to be 6B. In this study, the nozzle height to jet width ratio is 2 and for the knife-jets exit angle was fixed at 60 deg following the recommendation of Cziesla et al. [14].

Mathematical Formulation

The jet fluid is assumed to be incompressible with constant properties and the jets are discharging in an ambience of the same fluid. The flow field is represented by the Navier-Stokes equations. For the present work, we have assumed that the effect of temperature variation on the properties of the fluid is negligible. The flow medium is air, which is a Newtonian fluid. We also assume negligible dissipation effect on temperature and negligible volume expansion. The non-steady Navier-Stokes and the energy equation are given by

$$\frac{\partial u_i}{\partial x_i} = 0 \tag{1}$$

$$\frac{\partial u_j}{\partial t} + \frac{\partial (u_i u_j)}{\partial x_j} = -\frac{\partial p}{\partial x_j} + \frac{1}{\mathrm{Re}} \nabla^2 u_j \tag{2}$$

$$\frac{\partial T}{\partial t} + \frac{\partial (u_i T)}{\partial x_i} = \frac{1}{\mathrm{Re\,Pr}} \nabla^2 \nabla^2 T \tag{3}$$

It may be mentioned here that though in the present range of computation, a steady state solution is expected, we have used the unsteady formulation and observed the time history of the flow till it achieved steady state. As such, time marching in such formulations is equivalent of successive under relaxation and is very popular in solving elliptic equations, Ferziger and Peric [19]. Studies on slot jets by Laschefski et al. [18] showed that the transition to turbulence follows the route through periodic doubling and chaos. The flow-field due to periodic slot jets and knife-jets became chaotic at Re of 415 and 250, respectively. Therefore, the other reason of using a transient formulation was to ensure the steadiness of the flow field. The issue of steadiness has to be assured from the time trace of velocity rather than assuming it.

Boundary Conditions. At the jet exit, a constant velocity profile is used. Since 2B is the characteristic length, the jet width

at the nozzle exit is 0.5. For the knife-jets, as the jet emanates at an angle ϑ with the horizontal direction, the velocity components at the inlet are given by:

$$w_{\text{in}} = -\sin(\vartheta) \tag{4}$$

$$v_{\text{in}} = \pm\cos(\vartheta) \tag{5}$$

The above distribution assures that the amount of mass and momentum flux for knife-jets are same as in the case of axial jet. The $\pm$ sign indicates that the horizontal components of the exit velocity at the left and right sides of the slot are in opposite direction. While for the axial jet, the jet emanates at $z=1.0$, for the knife jets there are two openings on the left and right side (each at 0.5 unit from the center-line at $z=1.0$).

Dirichlet type of boundary condition is applied on all the walls. While the velocity of the impinging surface v_s is directly prescribed, the velocities at the fixed walls were set at zero.

The present geometry allows the inflow from the ambient into the computational domain due to the entrainment effect by jet flows. The amount of backflow at the exit planes is unknown. Consequently, the exit boundary condition has to fulfill the condition of mass conservation. Laschefski et al. [18] have shown that for the given configuration of impinging jets, the vanishing gradient can not be used on the exit boundaries. In their numerical code based on SIMPLEC algorithm, they used vanishing gradient of pressure correction. In the present work, following [20–21] we have used

$$p_{\text{exit plane}} = 0.7\ \ p_{\text{interior}} + 0.3p_{\infty}\,. \tag{6}$$

Thus the pressure at the exit plane is an interpolated value of the ambient pressure and the adjacent cells. In earlier investigations in the turbulent regime [10,14,15], this boundary condition was successfully employed.

In the present work, while the jet is assumed to be at ambient temperature ($T_{\text{in}}=0.0$), the non-dimensional plate temperature T_s was fixed at unity.

Method of Solution

The conservation equations for momentum and energy were solved by a fractional step finite difference technique due to Kim and Moin [22]. The Adams–Bashforth scheme is used to get second order time discretization for the convective terms. The spatial discretization scheme uses central difference formulation which is of second order accuracy. Crank-Nicholson scheme is employed to discretize the diffusive terms.

The time discretization of the Navier-Stokes equations can be written as

$$\frac{u_i^{n+1}-u_i^n}{\Delta t} + \delta p^{n+1} = -\frac{3}{2}\text{conv}^n + \frac{1}{2}\text{conv}^{n-1} + \frac{1}{2\,\text{Re}}(\text{diff}^n + \text{diff}^{n+1}) \tag{7}$$

Replacement of the velocity of the following time step u_i^{n+1} by an intermediate velocity u_i^*

$$u_i^* = u_i^{n+1} + \Delta t \Delta p^{n+1} \tag{8}$$

yields the following term

$$\frac{u_i^*-u_i^n}{\Delta t} = -\frac{3}{2}\text{conv}^n + \frac{1}{2}\text{conv}^{n-1} + \frac{1}{2\,\text{Re}}(\text{diff}^n + \text{diff}^{n+1}). \tag{9}$$

Application of Eq. (1) to Eq. (9) gives finally the Poisson equation for the pressure field

$$\Delta^2 p^{n+1} = \frac{1}{\Delta t}\Delta u_i^*\,. \tag{10}$$

Once the pressure field is solved, Eq. (10) yields the final velocity field

$$u_i^{n+1} = u_i^* - \Delta t \nabla p^{n+1} \tag{11}$$

Results and Discussions

In the present work, a $152\times120\times102$ stretched grids with the finest grid of $\Delta Z=0.0025$ near the impinging surface have been employed. This enables the observation of flow structure in sufficient detail. The code has been validated by comparing the results with the studies of Chen et al. [9], as shown in Fig. 3(*a*). The discrepancies can be attributed to the fact that while they have studied the two-dimensional configuration, we simulated a three-dimensional situation with entrainment at the boundaries. From Fig. 3(*b*) it can be readily observed that the results for the stationary surface also agree well with the results of Laschefski et al. [13]. However, the values are slightly lower for the present computation. The stagnation Nusselt number from the present code was very close to that reported by Chou and Hung [23] and van Heiningen et al. [24].

Two-dimensional simulations with 152×102 grids and periodic boundary conditions were also performed for a stationary surface and also at $\text{Re}=200$ with $v_s=0.5$. The skin friction coefficient and Nusselt number distribution curves deviated by more than 10 percent except the boundaries. For example, in the two-dimensional simulation, the value of average Nusselt number at $\text{Re}=200$ and $v_s=2.0$ was 4.63 as against 5.34 from the three-dimensional simulation. However, the results from the two-dimensional simulation agree within 5 percent with that of Chen et al. [9]. It may be mentioned here that in realistic situations the slots will be of finite width with the entrainment effect at the boundaries and thus the results of three-dimensional simulation is more realistic. Grid independence of the present study was ascertained by comparing the Nu value at $132\times102\times82$, $152\times122\times102$ and $172\times142\times122$

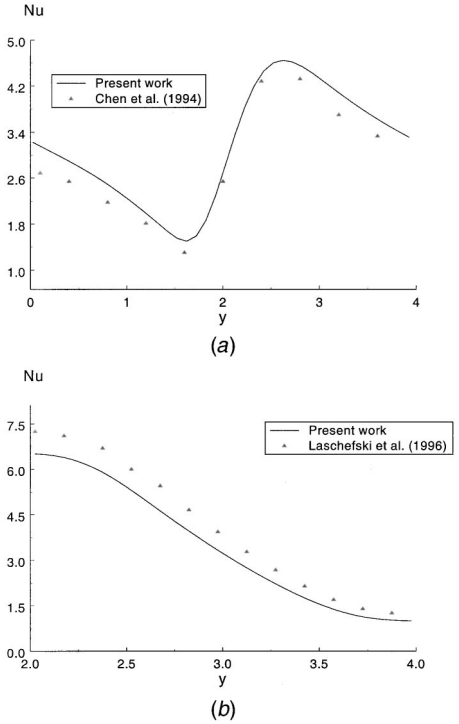

Fig. 3 Comparison of Nu distribution with the results of (*a*) Chen et al. [9] ($v_s=1.0$) and (*b*) Laschefski et al. [13] (Re =200, $v_s=0$, i.e., fixed surface)

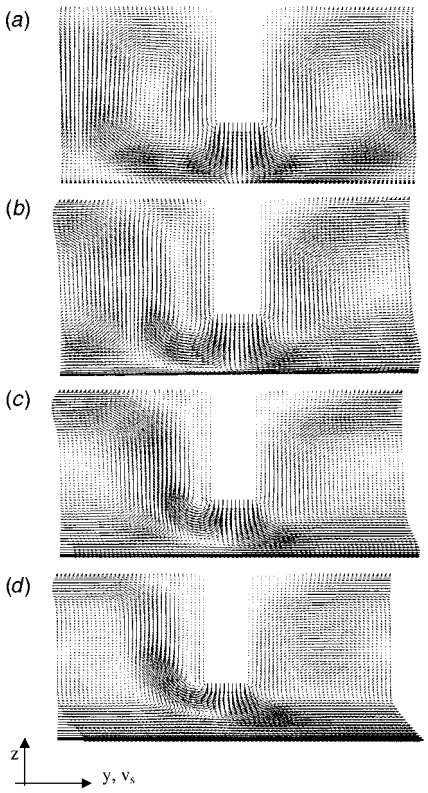

Fig. 4 Velocity vectors for axial jet at *y-z* midplane at Re =100 for (*a*) v_s=0.1, (*b*) 0.5, (*c*) 1.0, and (*d*) 2.0

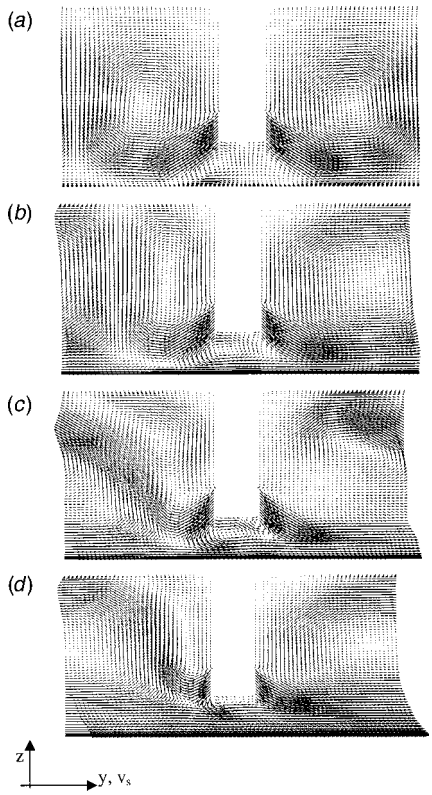

Fig. 5 Velocity vectors for knife-jet at *y-z* midplane at Re =100 for (*a*) v_s=0.1, (*b*) 0.5, (*c*) 1.0, and (*d*) 2.0

grids for Re=200 and $v_s=0.5$. The average Nusselt numbers were 5.31, 5.4, and 5.43, respectively in the increasing order of grid numbers. It was observed from these data that the value of Nu due to the present grid mesh differed from that of the extrapolated grid-insensitive situation by about 2 percent.

The heat transfer due to the jet can be represented by the Nusselt number distribution over the impingement plate. Under the present non-dimensionalization scheme, the Nusselt number is evaluated as the temperature gradient

$$\mathrm{Nu}=-\left.\frac{\partial T}{\partial z}\right|_S \tag{12}$$

The Nusselt number distribution can be averaged on the surface area A to obtain a global Nusselt number

$$\mathrm{Nu}=\frac{1}{A}\int\int \mathrm{Nu}(x,y)\,dx\,dy \tag{13}$$

It has been already mentioned that we have used the transient formulation. The velocity traces at three monitoring points were observed and analyzed using Fourier transformation. It was found that the flow is steady at all surface velocities for the axial jet. However, for the knife-jet the flow field is periodic at Re=200 and $v_s=2.0$. Thus at $v_s=2.0$, time-averaged value of Nu has been reported. To calculate the time-average 20 periodic cycles were used.

The velocity vectors at different plate velocities for the axial and the knife-jet in y-z mid-plane are shown in Figs. 4 and 5, respectively. The flow structure of knife-jet is significantly different from axial jets. However, for both types of jets, it can be envisaged that at higher range of plate velocity, the vortical flow structures are less dominant and the flow at the vicinity of the impinging plate strongly attaches itself with the plate surface. The vortex structure with a flow-separation zone at the lower-left corner shifts in the direction of surface motion as v_s increases. At very high values of v_s, i.e., $o(1)$, flow separation no longer takes place. At higher surface velocities, flow magnitudes in the interior of the domain become smaller indicating significant reduction in mixing and thus energy exchange.

Figures 6(*a*) and 6(*b*) show the variation of time and width-averaged (i.e., averaged in x-direction) Nusselt number at Re

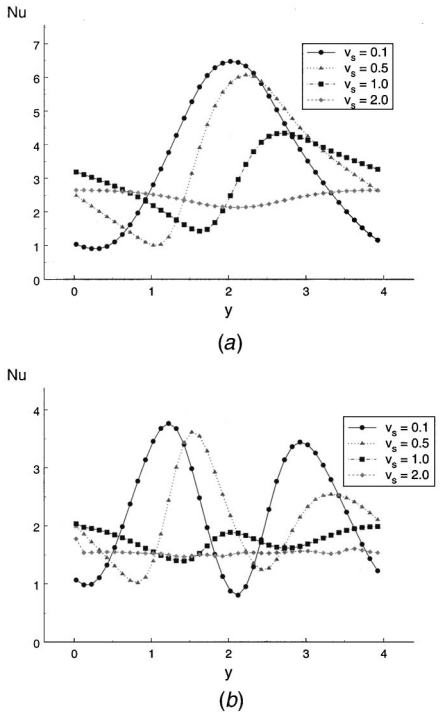

Fig. 6 Width-averaged Nusselt number distribution at Re =100 for (*a*) axial jet and (*b*) knife-jet (plate motion in *y*-direction)

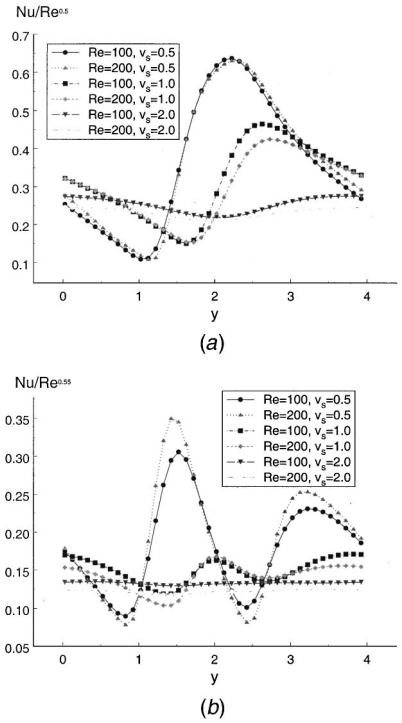

Fig. 7 Scaling of local heat transfer distribution with Re for (*a*) axial and (*b*) knife-jet (plate motion in *y*-direction)

$=100$ for axial and knife-jets respectively at different surface velocities. For the axial jet, as the point of flow separation moves in the y direction, the local minima in the Nu-distribution curve also shifts rightwards with increasing v_s. At $v_s=0.1$, the profile deviates slightly from the symmetric distribution observed in case of a stationary surface and heat transfer is maximum at about $y=1.9$,

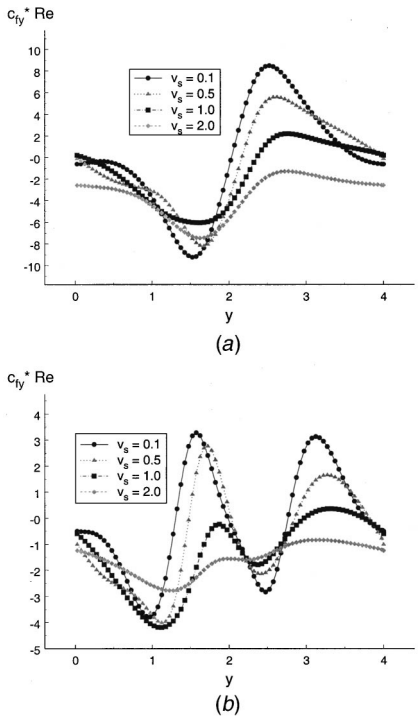

Fig. 8 Width-averaged friction factor distribution at Re=100 for (*a*) axial and (*b*) knife-jet (plate motion in *y*-direction)

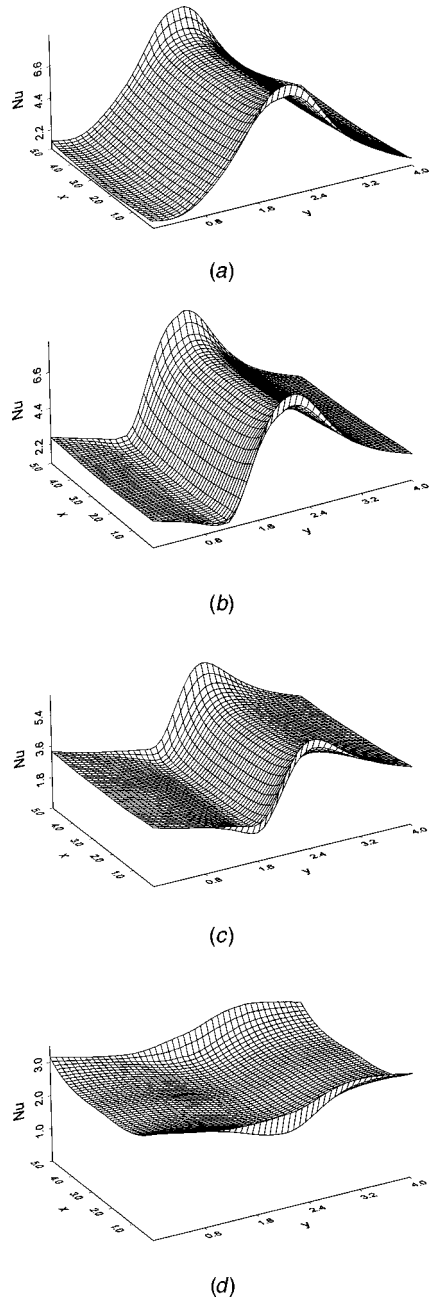

Fig. 9 2-D distribution of Nu for axial jet at Re=100 for (*a*) $v_s=0.1$, (*b*) 0.5, (*c*) 1.0, and (*d*) 2.0 (plate motion in *y*-direction)

i.e., somewhat left of the centerline of the jet. In other words, the maximum of heat transfer distribution moves upstream of the direction of the plate movement. At $v_s=0.5$, the magnitude of the peak value reduces and the peak-point shifts about half the value of B downstream, i.e., in the direction of the plate movement. When the plate velocity is equal the jet velocity ($v_s=1.0$), an inclined *s*-shaped distribution pattern is formed and while the peak value reduces, it also shifts further right by about the jet width from the center. At $v_s=2.0$, the profile becomes almost flat. It can also be observed that with increasing v_s heat transfer in the middle of the domain decreases but in the vicinities of the adjacent jet increases. For the vectored jets, two peaks corresponding to the two faces of the issuing jets are clearly discernible at relatively lower plate speed. The lower peak can be observed in the downstream of the jet centerline and the ratio of the two peak values are about 1.1 and 1.4 for $v_s=0.1$ and 0.5, respectively. At $v_s=1.0$, a single peak occurs. As in axial jet, the distribution

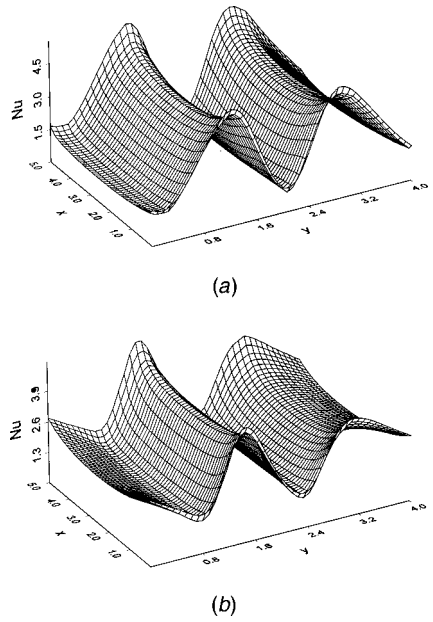

Fig. 10 Two-dimensional distribution of Nu for knife-jet at Re =100 for (*a*) v_s=0.1 and (*b*) 0.5 (plate motion in *y*-direction)

pattern flattens considerably with increasing v_s and the total heat transfer reduces. On their studies on laminar slot jets, van Heiningen et al. [24] reported that the distribution of heat transfer over the impinging plate scales with $Re^{0.5}$. In Fig. 7, heat transfer results are shown with the modified *y*-axis, scaled with an appropriate power of Re. It is interesting to note from Fig. 7(*a*) that even for a moving surface local heat transfer due to axial slot jet scales with $Re^{0.5}$. However, for the case of the knife-jet, the scaling is better at $Re^{0.55}$.

In Fig. 8, the distribution of *y*-component of friction coefficient for these two types of jets are presented. The heat transfer pattern is closely linked to the flow structure. It can be seen from Fig. 8 that c_{fy} is always negative at higher v_s, indicating that the plate motion is no longer aided by the flow and flow separation does not take place. Thus flow in the immediate plate vicinity is mostly influenced by the surface velocity and less affected by jet structure, thereby producing a more uniform heat transfer field. As evident from the flow structures, fluid transport in the vertical direction just adjacent to the plate reduces with increasing surface speed. This in turn reduces the energy convection from the plate and reduces the total amount of heat transfer.

Figure 9 shows the three-dimensional plots of time-averaged Nusselt number distributions on the impingement surface for the axial jet at surface velocities of 0.1, 0.5, 1.0, and 2.0. As the jets follow a swirling path after it emanates from the nozzle [14], the hydrodynamic and thermal boundary layers along the *x*-direction will vary. In turn, the Nusselt number has a strong spatial dependence in *x*-direction. At the entrainment boundaries (i.e., $x=0.0$ and 5.0), local enhancement can be clearly observed from these figures. With increasing plate velocity, the local peaks are shifted further from the center and the original saddle like distribution observed over a stationary plate transforms into a flatter surface, indicating reduction in heat transfer. The profiles of heat transfer and skin friction distribution for the axial jets follow the trend predicted by Chen et al. [9]. The quantitative difference can be attributed to three-dimensionality of the present investigation and use of a very fine grid. In Fig. 10, three-dimensional distribution for the knife-jet at $v_s=0.1$ and 0.5 is presented. At higher surface velocity ($v_s \sim 1.0$) the distribution pattern assumes a flat profile as observed for axial jets. However, the amount of heat transfer is relatively higher for the axial jets compared to the knife-jets as shown in Table 1.

Table 1 Global Nusselt number

Re		Surface velocity v_s				
		0.0	0.1	0.5	1.0	2.0
100	Axial jet	3.74	3.71 (1)	3.69 (1.3)	3.29 (12)	2.63 (30)
	Knife-jet	2.59	2.56 (1)	2.38 (4)	1.97 (24)	1.90 (26)
	% Difference	30	30	35	40	27
200	Axial jet	5.45	5.39 (1)	5.34 (2)	4.44 (20)	3.42 (37)
	Knife-jet	4.08	4.04 (1)	3.62 (11)	2.74 (32)	2.36 (42)
	% Difference	25	25	32	38	30

Bracketed term indicates % reduction in Nu compared to the stationary case

In Table 1, the results with the values of global Nusselt numbers for the calculated range of surface velocity are provided. The computed values of Nu in axial jets for the stationary surface are in agreement with Laschefski et al. [13]. For the case of a moving plate, the calculated values are higher by about 10 percent compared to the results of Chen et al. [9]. Comparisons could not be made for the case of the vectored jets due to unavailability of literature. The bracketed terms in the table indicate the percentage reduction in heat transfer with increasing plate speed. It can be observed that at higher Re, for both the axial jet and the knife-jet, the reduction in heat transfer is more. Finally, it can be concluded that in the laminar region, vectoring of the jet does not enhance heat transfer over a moving plate for the same amount of mass and momentum flux at the jet exit.

Concluding Remarks

Heat transfer due to impinging slot jets on a moving surface has been studied in the laminar range. While with increasing plate speed, Nusselt number distributions tend to be more uniform, the total heat transfer reduces. At higher velocities of the impinging surface, flow field on the plate mostly attaches itself with the plate and flow separation does not take place. Unlike the case of turbulent slot jets, the heat transfer from the axial jets in the laminar flow regime are found to be greater by about 30 percent than that from the knife-jets with an exit angle of 60 deg.

Nomenclature

A = area of the impingement plate
a = thermal diffusivity
B = slot nozzle width
C_{fy} = *y*-component of friction coefficient ($\partial v/\partial y$)
H = height of the computational domain
h = nozzle-to-plate spacing
h' = heat transfer coefficient
k' = thermal conductivity
L = nozzle length
Nu = Nusselt number ($h'2B/k'$)
p = pressure
Pr = Prandtl number
Re = Reynolds number ($w_{in}2B/\nu$)
T = temperature
t = time
u = velocity component in *x*-direction
v = velocity component in *y*-direction
w = velocity component in *z* direction
W = width of the computational domain
x, y, z = spatial coordinates

Greek Symbols

ν = kinematic viscosity
ϑ = exit-angle of the jet

Subscripts

∞ = ambience
av = average
in = at jet exit
s = impinging surface

Superscripts

n = current time step

References

[1] Downs, S. J., and James, E. H., 1987, ''Jet Impingement Heat Transfer—A Literature Survey,'' ASME Paper 87-H-35.
[2] Viskanta, R., 1993, ''Heat Transfer to Impinging Isothermal Gas and Flame Jets,'' Exp. Therm. Fluid Sci., **6**, pp. 111–134.
[3] Martin, H., 1977, ''Heat and Mass Transfer Between Impinging Gas Jets and Solid Surfaces,'' *Advances in Heat Transfer*, **13**, Academic Press, pp. 1–60.
[4] Martin, H., 1990, ''Impinging Jets,'' in *Handbook of Heat Exchanger Design*, G. F. Hewitt, ed., Hemisphere, pp. 2.5.6.1–2.5.6.10.
[5] Subba, Raju, K., and Schlunder, E. U., 1977, ''Heat Transfer Between an Impinging Jet and a Continuously Moving Surface,'' Waerme-Stoffuebertrag., **10**, pp. 131–136.
[6] Zumbrunnen, D. A., 1991, ''Convective Heat and Mass Transfer in the Stagnation Region of a Laminar Planar Jet Impinging on a Moving Surface,'' ASME J. Heat Transfer, **113**, pp. 563–570.
[7] Polat, S., and Douglas, W. J. M., 1990, ''Heat Transfer Under Multiple Slot Jets Impinging on a Permeable Moving Surface,'' AIChE J., **36**, pp. 1370–1378.
[8] Huang, P. G., Mujumdar, A. S., and Douglas, W. J. M., 1984, ''Numerical Prediction of Fluid Flow and Heat Transfer Under a Turbulent Impinging Slot Jet with Surface Motion and Crossflow,'' ASME Paper 84-WA/HT-33.
[9] Chen, J., Wang, T., and Zumbrunnen, D. A., 1994, ''Numerical Analysis of Convective Heat Transfer From a Moving Plate Cooled by an Array of Submerged Planar Jets,'' Numer. Heat Transfer, Part A, **26**, pp. 141–160.
[10] Chattopadhyay, H., Biswas, G., and Mitra, N. K., 1999, ''Heat Transfer From a Moving Surface Due to Impinging Jets,'' *Proc. ASME Heat Transfer Division*, Vol. HTD 364-1, pp. 261–270.
[11] Page, R. H., 1991, ''Heat and Mass Transfer as a Consequence on Radial Jet Reattachment,'' *Transport Phenomena and Mass Transfer*, **1**, Elsevier Co., Amsterdam, pp. 432–443.
[12] Laschefski, H., Cziesla, T., and Mitra, N. K., 1995, ''Influence of Exit Angle on Radial Jet Reattachment and Heat Transfer,'' AIAA J., **9**(1), pp. 169–174.
[13] Laschefski, H., Cziesla, T., Biswas, G., and Mitra, N. K., 1996, ''Numerical Investigation of Heat Transfer by Rows of Rectangular Impinging Jets,'' Numer. Heat Transfer, Part A, **30**, pp. 87–101.
[14] Cziesla, T., Chattopadhyay, H., and Mitra, N. K., 1998, ''Large Eddy Simulation of Flow and Heat Transfer of an Impinging Radial Jet,'' *Proc. 16 Intl. Conference on Numerical Methods in Fluid Dynamics*, Lecture Notes in Physics, **515**, Springer, pp. 141–146.
[15] Chattopadhyay, H., and Saha, S. K., 2001, ''Numerical Investigations of Heat Transfer Over a Moving Surface Due to Impinging Knife-Jets,'' Numer. Heat Transfer, Part A, **39**, pp. 531–549.
[16] Chen, M., Chalupa, R., West, A. C., and Modi, V., 2001, ''High Schmidt Mass Transfer in a Laminar Impinging Slot Jet Flow,'' Int. J. Heat Mass Transf., **43**, pp. 3907–3915.
[17] Sezai, I., and Mohamad, A. A., 1999, ''Three-Dimensional Simulation of Laminar Rectangular Impinging Jets Flow Structure, and Heat Transfer,'' ASME J. Heat Transfer, **121**, pp. 50–56.
[18] Laschefski, H., Cziesla, T., and Mitra, N. K., 1997, ''Evolution of Flow Structure in Impinging Three-dimensional Axial and Radial Jets,'' Int. J. Numer. Methods Fluids, **25**, pp. 1083–1103.
[19] Ferziger, J. H., and Peric, M., 1997, *Computational Methods for Fluid Dynamics*, Springer, New York.
[20] Childs, R. E., and Nixon, D., 1986, ''Unsteady Three-Dimensional Simulations of a VTOL Upwash Fountain,'' AIAA-Paper-86-0212.
[21] Grinstein, F. F., Oran, E. S., and Boris, J. P., 1987, ''Direct Numerical Simulation of Axisymmetric Jets,'' AIAA J., **25**, pp. 92–98.
[22] Kim, J., and Moin, P., 1985, ''Application of a Fractional-Step Method to Incompressible Navier-Stokes Equations,'' J. Comput. Phys., **59**, pp. 308–323.
[23] Chou, Y. J., and Hung, Y. H., 1994, ''Impingement Cooling of an Isothermally Heated Surface with a Confined Slot Jet,'' ASME J. Heat Transfer, **116**, pp. 479–482.
[24] van Heiningen, A. R. P., Mujumdar, A. S., and Douglas, W. J. M., 1976, ''Numerical Prediction of the Flow Field and Impingement Heat Transfer Caused by a Slot Jet,'' ASME J. Heat Transfer, **98**, pp. 654–658.

Laminar Fluid Flow and Heat Transfer in a Lid-Driven Cavity Due to a Thin Fin

Xundan Shi
Graduate Student

J. M. Khodadadi
Professor
e-mail: khodajm@auburn.edu.

Mechanical Engineering Department,
Auburn University, 201 Ross Hall,
Auburn, AL 36849-5341

A finite-volume-based computational study of steady laminar flow and heat transfer (neglecting natural convection) within a lid-driven square cavity due to a single thin fin is presented. The lid moves from left to right and a fixed thin fin can be positioned perpendicular to any of the three stationary walls. Three fins with lengths equal to 5, 10, and 15 percent of the side, positioned at 15 locations were examined for $Re=500$, 1000, 2000, and $Pr=1$ (total of 135 cases). Placing a fin on the right wall brings about multi-cell recirculating vortices compared to the case without a fin that exhibits a primary vortex and two small corner cells. A fin slows the flow near the anchoring wall and reduces the temperature gradients, thus degrading heat transfer capacity. A fin positioned near the top right corner of the cavity can reduce heat transfer most effectively in cases with all three different Reynolds numbers and lengths. Regardless of the Reynolds number, placing a fin on the right wall—compared to putting a fin on the left and bottom walls—can always enhance heat transfer on the left wall and at the same time, reduce heat transfer on the bottom, right and top walls. A long fin has the most marked effect on the system's heat transfer capabilities. Mean Nusselt number was successfully correlated to the Reynolds number, length of the fin and its position. [DOI: 10.1115/1.1517272]

Keywords: Cavities, Convection, Finned Surfaces, Heat Transfer, Vortex

Introduction

Knowledge of fluid flow and heat transfer in a rectangular cell modified by the presence of vertical or horizontal plate fins is of great interest because introduction of thin fins is one way to control heat transfer in various engineering applications. Laminar natural convection in differentially heated cavities with internal fins (partitions) has been studied extensively, for example [1,2] among others. The high packaging density and increasing heat flux from the electronic modules have necessitated the use of forced convection in electronic cooling practices. The existence of chips or boards in a rectangular cell could have significant effect on the resulting flow field and heat transfer. No attention has been given to investigation of shear-driven cavity with isothermal fins [3]. Such problems are, however, commonly encountered, e.g., estimation of heat loss of electronic packages in a closed cavity, design of various drying devices and decreasing the heat loss in various engineering applications. Besides being a simple benchmark geometry for study of complex flow phenomena, a cavity system can simulate a lubricating groove between sliding plates or approximate the separated flow in a surface cavity with an external stream flowing over it.

In spite of its simplicity, the lid-driven cavity flow is a classic benchmark problem for studying a number of interesting fluid flow phenomena. A great number of studies have focused on this problem and an excellent review paper was recently reported by Shankar and Deshpande [3]. In general, interest has focused on low Reynolds number laminar regime for square cavities ([4], among many others who assumed two-dimensional flow). Others have concentrated on studying deep slender cavities [5] and onset of instabilities limited to two-dimensional flows [6,7].

The objective of this study was to determine the effect of very thin fins at different positions on the two-dimensional flow field, heat transfer and drag force of the moving wall. Three different orientations of the fin are studied where the fin protrudes from one of the three stationary walls, namely the left, bottom or right walls. Numerical solutions are obtained over a range of the Reynolds number. The dependence of fluid flow and heat transfer on the length and location of the fin is studied in detail. It should be noted that real flows for the range of the Reynolds number studied for lid-driven cavities with no fins are expected to be three-dimensional [3] and it is not clear as of now if the presence of a fin will be a stabilizing effect to the flow system.

Problem Formulation

The proposed physical model for a two-dimensional lid-driven cavity with a fin is shown in Fig. 1. The top wall is moving at the speed of U_{lid} from left to right, whereas the remaining three walls are stationary. The moving wall is maintained at a temperature (T_h) different from the remaining walls of cavity (T_c), with $T_h > T_c$. A thin fin that is made of a highly-conductive material can attach to different positions on the left, bottom, or right walls. The temperature of the fin is maintained at the temperature of the wall to which it is attached, so the Biot number is much smaller than 1. The effect of natural convection is neglected, so the ratio Gr/Re^2 is taken to be much smaller than 1. A special coordinate system (s) along the walls is adopted with its origin at $x=0$ and $y=H$, as identified by the dashed lines in Fig. 1. The coordinate of the fin (s_p) indicates the position of the fin, i.e., $s_p=0$ to H (left wall), $s_p=H$ to $H+L$ (bottom wall), and $s_p=H+L$ to $2H+L$ (right wall). In order to investigate the effect of the fin's length 1_p, three values of 1_p equal to 5 percent, 10 percent, or 15 percent of enclosure's length L are studied. A dimensionless variable for the length of the fin is defined as $\ell=1_p/L$. The fin can be attached to five possible locations that are equally spaced on the left, bottom or right walls.

Dimensionless Form of the Governing Equations. The fluid within the enclosure is an incompressible fluid and the fluid properties are constant. The flow within the enclosure is assumed two-dimensional, steady and laminar. The gravity effect and viscous

Contributed by the Heat Transfer Division for publication in the JOURNAL OF HEAT TRANSFER. Manuscript received by the Heat Transfer Division March 21, 2002; revision received August 12, 2002. Associate Editor: A. F. Emery.

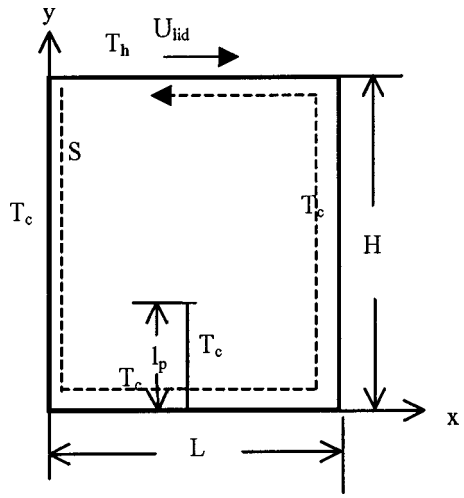

Fig. 1 Physical geometry and the coordinate system

dissipation are neglected. Dimensionless form of the governing equations can be obtained via introducing dimensionless variables:

$$X=\frac{x}{L},\quad Y=\frac{y}{L},\quad U=\frac{u}{U_{\text{lid}}},\quad V=\frac{v}{U_{\text{lid}}},$$

$$P=\frac{p}{\rho U_{\text{lid}}^2},\quad \theta=\frac{T-T_c}{T_h-T_c}. \tag{1}$$

The governing equations of continuity, momentum and thermal energy are then written in dimensionless form:

$$\frac{\partial U}{\partial X}+\frac{\partial V}{\partial Y}=0, \tag{2}$$

$$U\frac{\partial U}{\partial X}+V\frac{\partial U}{\partial Y}=-\frac{\partial P}{\partial X}+\frac{1}{\text{Re}}\left(\frac{\partial^2 U}{\partial X^2}+\frac{\partial^2 U}{\partial Y^2}\right), \tag{3}$$

$$U\frac{\partial V}{\partial X}+V\frac{\partial V}{\partial Y}=-\frac{\partial P}{\partial Y}+\frac{1}{\text{Re}}\left(\frac{\partial^2 V}{\partial X^2}+\frac{\partial^2 V}{\partial Y^2}\right), \tag{4}$$

$$U\frac{\partial \theta}{\partial X}+V\frac{\partial \theta}{\partial Y}=\frac{1}{\text{Pr Re}}\left(\frac{\partial^2 \theta}{\partial X^2}+\frac{\partial^2 \theta}{\partial Y^2}\right). \tag{5}$$

The Reynolds number is defined as $\text{Re}=U_{\text{lid}}L/\nu$ and the Prandtl number is $\text{Pr}=\nu/\alpha$. The dimensionless form of the boundary conditions can be expressed as follows

$$\begin{aligned}&\text{at } X=0,1 \text{ and } Y=0: \quad U=V=0,\theta=0,\\ &\text{at } Y=1: \quad U=1,V=0,\theta=1,\\ &\text{on the fin:} \quad U=V=0,\theta=0.\end{aligned} \tag{6}$$

Therefore, Re, Pr, $S_p=s_p/H$ and ℓ are the dimensionless variables that govern this problem. In this study, the Prandtl number of the fluid is fixed to 1.

Computational Details. The steady-state governing equations were solved by the finite-volume-method using Patankar's [8] SIMPLE algorithm. A two-dimensional uniformly-spaced staggered grid system was used. Hayase et al.'s [9] QUICK scheme was utilized for the convective terms, whereas the central difference scheme was used for the diffusive terms. In order to keep consistent accuracy over the entire computational domain, a third-order-accurate boundary condition treatment suggested by Hayase et al. [9] was adopted.

Grid Independence Study. In order to determine the proper grid size, a grid independence test was conducted for the Reynolds number of 1000 in a square cavity with a fin positioned at the middle of the bottom wall. The length of the fin was set to be 50 percent of L. Seven different grid densities (40×40, 60×60, 80×80, 100×100, 120×120, 150×150 and 240×240) were used.

The minimum value of the stream function of the primary vortex ($\psi_{\min}$) is commonly used as a sensitivity measure of the accuracy of the solution. Another monitored quantity, the dimensionless drag coefficient (C_d) of the moving lid is defined as:

$$C_d=\frac{F_d}{\rho U_{\text{lid}}^2 WL}, \tag{7}$$

where W is the width of cavity ($W=1$) and F_d is the drag force on the moving wall. Comparison of the $\psi_{\min}$ and C_d values among seven cases [10] revealed that 150×150 and 240×240 grid densities gave nearly identical results but 80×80 and coarser grid systems predicted substantially smaller values. Considering both the accuracy and the computational time, the following calculations were all performed with a 150×150 uniformly-spaced grid system.

Parameters for Numerical Simulations. Tolerance of the normalized residuals upon convergence is set to 10^{-6} for every calculation case. The under-relaxation parameters for u, v, and T are all set to 0.6, whereas under-relaxation parameter for pressure correction is set to 0.3. However, converged solutions can not be obtained for 4 cases ($\text{Re}=2000$, $\ell=0.15$, and $S_p=0.33$, 0.5, 0.67 and 0.83). To achieve converged solutions for these cases, it was necessary to retain the unsteady terms in the momentum and energy equations. The temporal derivatives were approximated using a second-order implicit difference scheme, namely the three-time-level scheme. The success of the time-dependent method over the stationary one suggests that for these parameters a turning point in the parameter space is being approached.

Results and Discussion

In order to understand the flow field and heat transfer characteristics of this problem, a total of 135 cases were calculated. This involved studying the effect of a fin attached at 5 evenly-spaced positions on the left, bottom or right walls. The Reynolds numbers are 500, 1000, and 2000, and the fin's length can be 5 percent, 10 percent, and 15 percent of the width of the cavity. All the calculations were performed on a Cray SV1 of the Alabama Supercomputer Network, located in Huntsville, Alabama.

Flow and Heat Transfer in the Lid-Driven Cavity Without Fins. It is necessary to look at the flow fields and temperature fields in a cavity without the fin before we analyze the actual cases for this study. Figure 2 shows the streamlines and temperature fields in a lid-driven cavity for $\text{Re}=500$, 1000, and 2000. With the increasing of the Reynolds number, a new vortex appears near the left wall's top corner and the dominance of the primary clockwise-rotating cell remains unchanged, whereas the two counter-clockwise-rotating cells at the corners of the bottom wall gain prominence. All the three streamline fields were plotted with the same contour level settings. So it is easy to notice that the streamlines are more skewed and packed on the right side with the increasing of the Reynolds number. Because of this, the gradient of temperature fields near every wall becomes higher that indicates the enhancement of heat convection near the wall with the increasing of the Reynolds number. As discussed in great detail by Shi [10], these computed flow fields agree with Ghia et al.'s [4] results very well, whereas the temperature fields agree with results of Torrance et al. [11]. The close agreement with benchmark literature indicates the efficacy of the numerical methodology that was utilized.

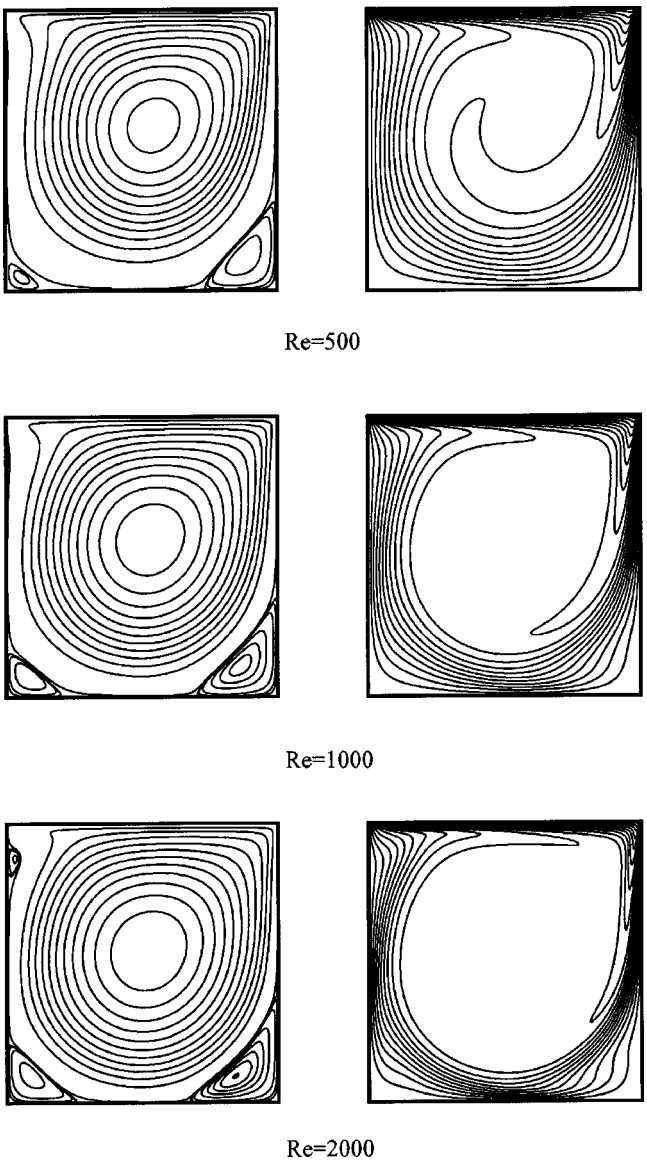

Fig. 2 Steamlines and temperature fields for the lid-driven cavity without fins for Re=500, 1000, and 2000 (contour level increments of the primary vortex and temperature are 0.1 and 0.05, respectively)

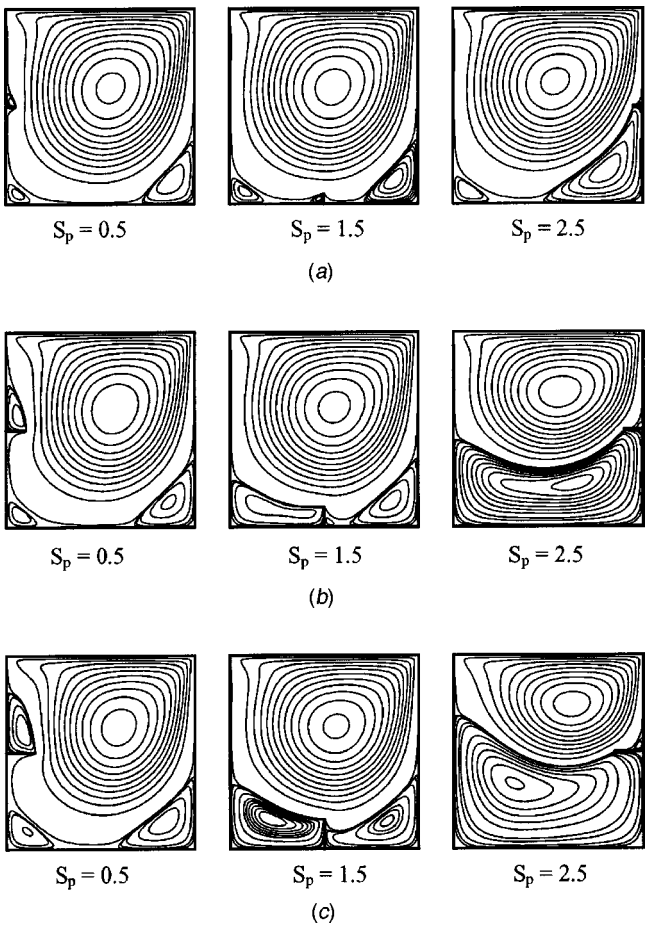

Fig. 3 Flow fields for fins at different positions with Re=500: (*a*) $\ell=0.05$, (*b*) $\ell=0.1$, and (*c*) $\ell=0.15$

Flow Fields in a Lid-Driven Cavity With a Thin Fin. Figures 3(*a–c*) show the flow fields for a lid-driven cavity (Re $=500$) with a fin at three representative positions for different lengths of the fin, $\ell=0.05$, 0.1, and 0.15, respectively. The plots in the left, middle, and right columns correspond to cases with the fins positioned on the left, bottom and right walls of the cavity, respectively. Examining the streamline patterns for Re=500 and $\ell=0.05$—three of which are shown in Fig. 3(*a*), one can conclude that placing a 0.05 thin fin at various positions only changes the flow fields near the fin except for the case of the fin placed at $S_p=2.67$. If the fin is positioned away from the two small counter-clockwise-rotating vortices at the corners of the bottom wall, weak counter-clockwise-rotating vortices form on both sides of the fin. The vortex with lower S coordinate value naturally is stronger due to the direction of the bulk spinning fluid. If the fin is placed within the two small vortices at the corners of the bottom wall, due to the short length of the fin, the effect is localized within these vortices. Overall, the character of the dominant clockwise-rotating vortex in the cavity remains unchanged as S_p increased. An interesting flow phenomenon occurred when $S_p=2.67$ (not shown in Fig. 3(*a*)), where the two small counter-clockwise-rotating vortices on the bottom wall merge to form a big counter-clockwise-rotating vortex. At the same time, the center of main clockwise-rotating vortex moved upward and the value of stream function at its center decreased. These flow field behaviors carry over to other cases with the increase of the length of the fin. From Figs. 3(*b*) and 3(*c*) one can observe that the above-mentioned merging of vortices occurs with a $0.1L$ fin placed at $S_p=2.5$, 2.67, and 2.83, and a $0.15L$ fin at $S_p=2.33$, 2.5, 2.67, and 2.83 (two of which are shown on the right column for $S_p=2.5$). In these cases, the newly-merged counter-clockwise-rotating vortex almost fills all the space in the cavity between the fin and the bottom wall. As for the flow in the vicinity of the longer fins in Figs. 3(*b*) and 3(*c*), these local disturbances are more pronounced compared to those observed in Fig. 3(*a*). In comparison with Fig. 2, the flow patterns in the cavity with a fin on the right wall look very different from that in the cavity without a fin. In general, a fin placed on the right wall brings about more changes to the flow field than fins on the left or bottom walls. The flow fields for Re=1000 for different lengths of the fin, $\ell=0.05$, 0.1, and 0.15, exhibit flow patterns similar to those for Re=500 and are not presented here, but can be found elsewhere [10]. With the increase of the Reynolds number, the vortices formed due to the presence of the fin are generally enhanced.

Figures 4(*a–c*) show the flow fields for Re=2000 with fins placed at five representative positions for different lengths of the fin, $\ell=0.05$, 0.1, and 0.15, respectively. Similar to the flow fields described above for Re=500 and 1000, all these cases exhibit identical trends. But it is also noticed that when a fin is positioned

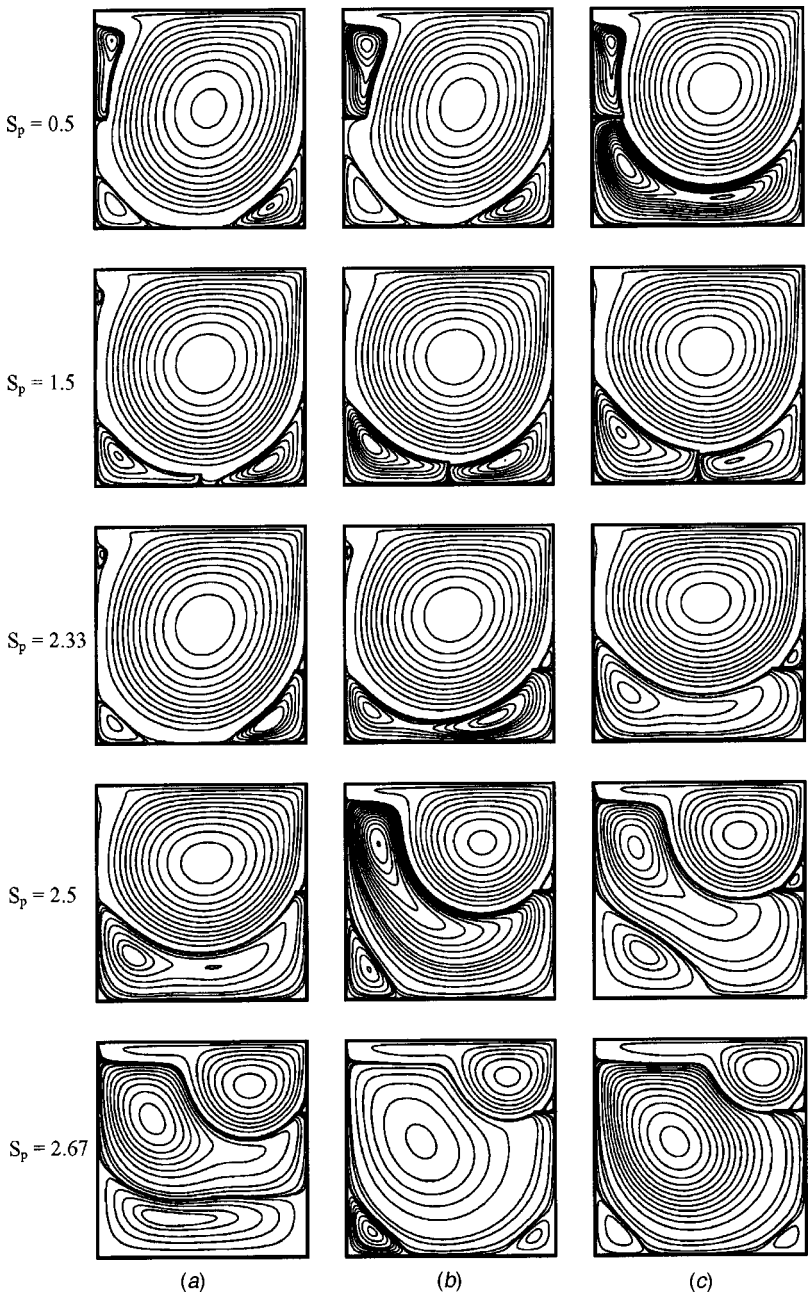

Fig. 4 Flow fields for fins at different positions with Re=2000: (*a*) $\ell = 0.05$, (*b*) $\ell = 0.1$, and (*c*) $\ell = 0.15$

at $S_p = 2.5$, the $0.1L$ or $0.15L$ fins (Figs. 4(*b*) and 4(*c*), respectively) can give rise to a second clockwise-rotating vortex, located at the left corner of the bottom wall. Cases with a $0.1L$ or $0.15L$ fin at $S_p = 2.67$ show two clockwise-rotating vortices at the corners of the bottom wall. But for the case with a $0.05L$ fin at the same position (Fig. 4(*a*)), a big counter-clockwise-rotating vortex between the bottom and top clockwise-rotating vortices was observed. In summary, the flow patterns not only depend on the position of fin but also depend on the length of fin. Cases with different lengths of the fin at the same position exhibit different flow pattern structures. Another interesting point from the observation of the Re=2000 cases is the merging of two clockwise-rotating vortices into a big clockwise-rotating vortex when a $0.15L$ fin is attached at $S_p = 0.5$ or 0.67. The variation of the drag coefficient (Eq. 7) with position of the fin, length of fin and the Reynolds number was studied in comparison to the cases with no fin ($C_d = 0.0588$, 0.0359, and 0.0229 for Re=500, 1000, and 2000, respectively). It was observed that the drag coefficient increases upon lowering Re. The drag coefficient also is bigger when the fin is attached at most positions on the left or right walls and it rises with the increase of the length of fin. Placing a fin at any position on the bottom wall changes the value of C_d only less than 2 percent.

Temperature Fields in a Lid-Driven Cavity With a Thin Fin. Figures 5(*a–c*) show the contours of dimensionless temperature (θ) for a lid-driven cavity (Re=2000) with a fin at five representative positions for $\ell = 0.05$, 0.1, and 0.15, respectively. The value of θ on the moving wall is 1, whereas the value of θ on the other three walls and the fin is zero, and the contour levels are incremented by 0.05. Since natural convection is neglected in this

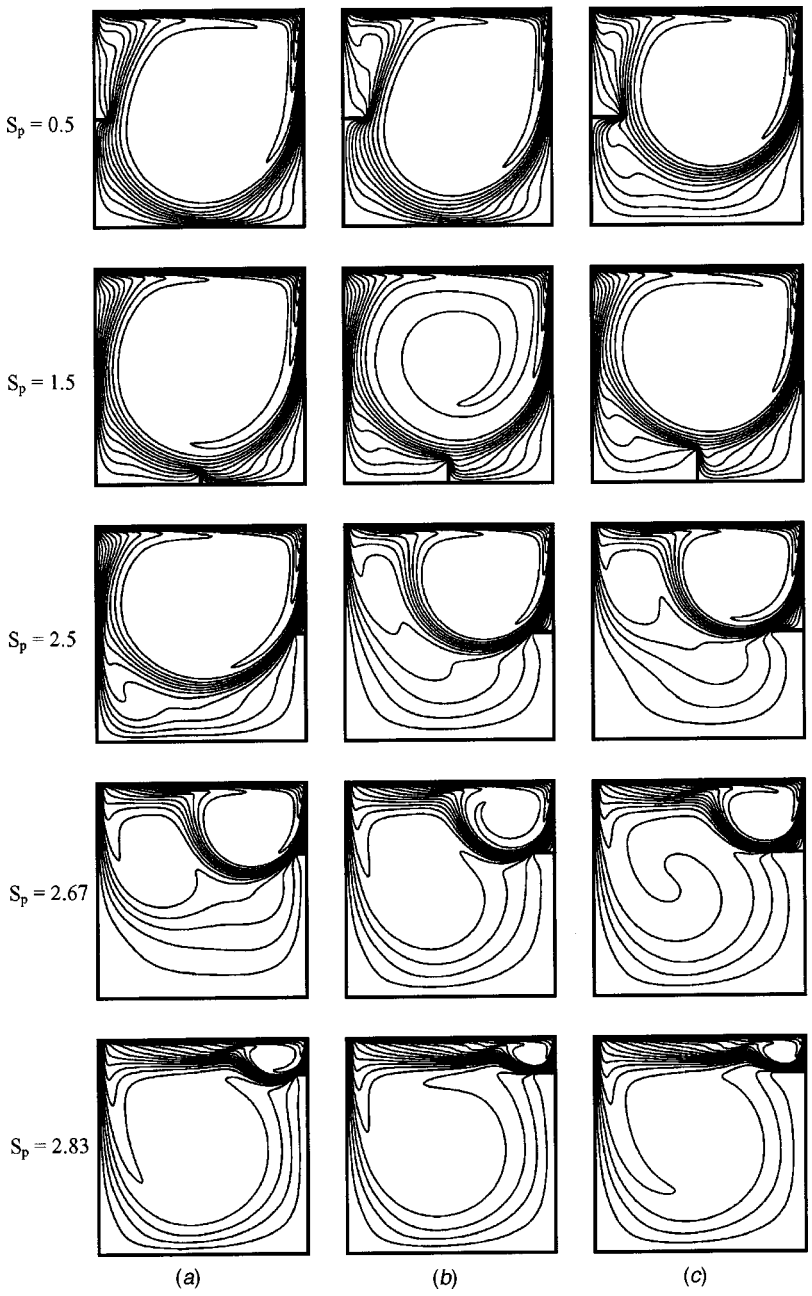

Fig. 5 Temperature fields for fins at different positions with Re=2000: (*a*) ℓ =0.05, (*b*) ℓ=0.1, and (*c*) ℓ=0.15 (contour level increment of 0.05)

study, the energy equation does not influence the momentum equation, however the temperature distribution is closely related to the flow field. Comparing Figs. 5(*a*) and 2, a 0.05*L* long fin at most positions only changes the temperature distribution locally and the rest of the cavity remains unaffected. This is because the main flow vortex has not changed upon introduction of a 0.05*L* long fin and the fin only changes the velocity distribution locally. As mentioned before, a 0.05*L* long fin at S_p=2.5, 2.67, and 2.83 (Fig. 4(*a*)), a 0.1*L* long fin at S_p=2.33, 2.5, 2.67, and 2.83 (Fig. 4(*b*)) or a 0.15*L* long fin at S_p=2.33, 2.5, 2.67, and 2.83 (Fig. 4(*c*)) can cause merging of two counter-clockwise-rotating vortices into a big counter-clockwise-rotating vortex and appearance of other vortices at the ends of the bottom wall. Since the stream function value at the center of these vortices are much smaller than that at the center of the clockwise-rotating vortex next to the moving lid, the flow moves slower within these vortices and thus decreased heat transfer capability is expected. As a result, the temperature gradients in the corresponding regions (Figs. 5(*b*) and 5(*c*)) have decreased in above cases evident from the parting of the contour levels from each other.

Temperature fields for Re=500 and 1000 for different lengths of the fin, ℓ=0.05, 0.1, and 0.15 are not shown here (see [10]). Among the three fins, the 0.15*L* fin has the most marked effect on the temperature distribution. Compared with temperature fields without a fin in Fig. 2, the existence of the fin generally slowed the flow moving near the wall with a fin and at the same time reduced the temperature gradients, thus degrading heat transfer capacity of that wall.

Variation of the Local Nusselt Number on the Walls of the Cavity. In order to evaluate how the presence of the fin affects

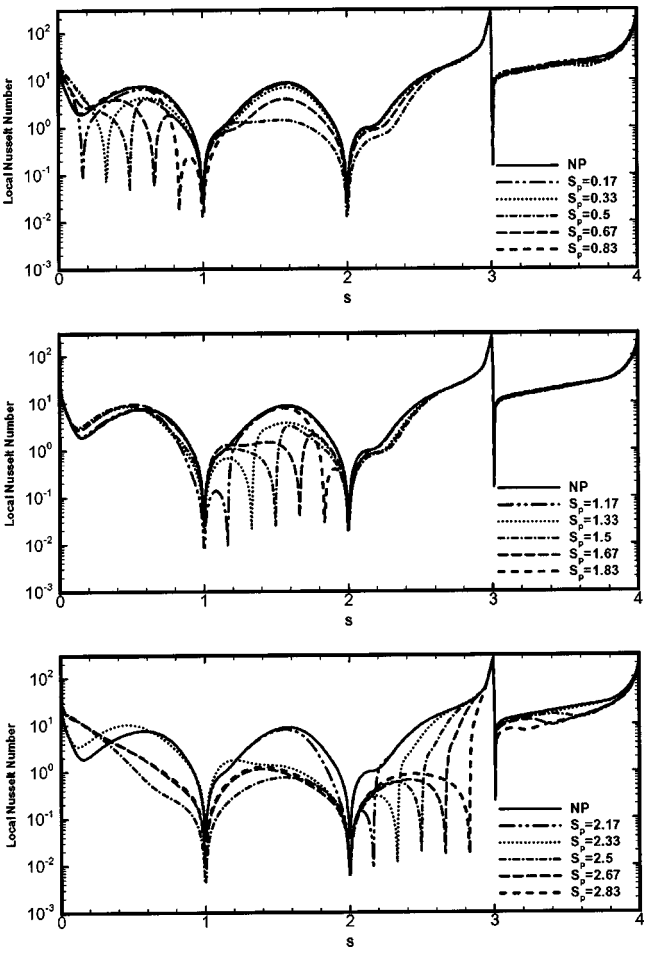

Fig. 6 Variation of the Nusselt number along four walls of the cavity with fins at different positions (Re=2000,$\ell=0.15$)

the heat transfer rate along the four walls, it is necessary to define the local Nusselt number on the left, bottom, right and top walls. These are defined as

$$\mathrm{Nu}_\ell = \left.\frac{\partial\theta}{\partial X}\right|_{X=0}, \quad \mathrm{Nu}_b = \left.\frac{\partial\theta}{\partial Y}\right|_{Y=0}, \quad \mathrm{Nu}_r = -\left.\frac{\partial\theta}{\partial X}\right|_{X=1},$$

$$\mathrm{Nu}_t = -\left.\frac{\partial\theta}{\partial Y}\right|_{Y=1}, \tag{8}$$

with the subscripts ℓ, b, r, and t referring to the left, bottom, right and top walls, respectively.

In order to present the local Nusselt number variation, the use of the S coordinate system was adopted. For example, variation of the Nu_ℓ with Y is plotted in graphical form as Nu_ℓ versus $S(0\sim1)$. The other three Nusselt numbers (Nu_b, Nu_r, and Nu_t) can be treated similarly and thus the variation of the local Nusselt number along the four walls can be presented in one graph with $S=0\sim4$. Figure 6 shows the variation of the local Nusselt number along the four walls of the cavity with a fin placed at 15 different positions (Re=2000) for fins with length 0.15. In each diagram, the variation of the local Nusselt number on the four walls for the cases of no fin is shown as solid lines and denoted by the symbol (*NP*, that stands for no partition). It was concluded that the presence of the fin on the left and bottom walls ($0<S<2$) only degrades heat transfer rate locally for shorter fins and heat transfer rates on all the other walls do not change appreciably, except for the case of the longest fin (Fig. 6). But a fin positioned on the right wall ($2<S<3$) not only degrades the heat transfer rate locally, but also has marked effect on the other walls. Specifically, a $0.05L$ fin positioned at $S_p=2.67$ and 2.83 brings about heat transfer enhancement on the top half of the left wall and heat transfer reduction on the bottom half of the left wall, and the entire right and top walls. Similar results were observed for Re=1000 cases. On the other hand, an $\ell=0.05$ fin at $S_p=2.5$ and 2.67 with Re =500 enhances the heat transfer on the left wall and decreases heat transfer rate on the bottom, right, and top walls. Comparing Fig. 6 with results for the low Reynolds number case of 500, it is concluded that the fin has marked effect on changing the local Nusselt number with increase of the Reynolds number and the length of the fin. A fin positioned near the top right corner of the cavity can reduce heat transfer most effectively in cases with all three different Reynolds numbers and lengths. Given a Reynolds number, a long fin has the most marked effect on changing heat transfer along the walls.

Table 1 Mean Nusselt number on every wall without a fin

Re	$\overline{Nu}$			
	Left Wall	Bottom Wall	Right Wall	Top Wall
500	3.61	1.72	10.90	16.23
1000	4.17	2.70	14.63	21.51
2000	5.10	4.04	19.97	29.16

Variation of the Average Nusselt Number on the Walls of the Cavity. The average (or mean) Nusselt number, $\overline{\mathrm{Nu}}$, for every wall can be obtained by integrating Eq. (8), as given below:

$$\overline{\mathrm{Nu}_\ell} = \int_0^1 \mathrm{Nu}_\ell dY, \quad \overline{\mathrm{Nu}_b} = \int_0^1 \mathrm{Nu}_b dX,$$

$$\overline{\mathrm{Nu}_r} = \int_0^1 \mathrm{Nu}_r dY, \quad \overline{\mathrm{Nu}_t} = \int_0^1 \mathrm{Nu}_t dX. \tag{9}$$

Table 1 gives the values of the mean Nusselt number for every wall for Re=500, 1000, and 2000 for a lid-driven cavity without a fin. From the table, one can see that the mean Nusselt number on every wall increases with the rise of the Reynolds number. The right wall has the best heat transfer rate, whereas the bottom wall offers the worst heat transfer rate among the left, bottom and right walls. Also note that the sum of the mean Nusselt numbers for the left, bottom and right walls equals the mean Nusselt number of the top wall.

In order to study the effect of the fin on the average heat transfer rate for every wall in a lid-driven cavity, we introduce a variable called the Nusselt Number Ratio (NNR), with its definition given as:

$$\mathrm{NNR} = \frac{\overline{\mathrm{Nu}}|_{\text{with a fin}}}{\overline{\mathrm{Nu}}|_{\text{without a fin}}}. \tag{10}$$

Values of NNR for every wall (NNR_ℓ, NNR_b, NNR_r, and NNR_t) can be obtained according to Eq. (10). Value of NNR bigger than 1 indicates the heat transfer rate is enhanced on that surface, whereas NNR less than 1 indicates the heat transfer rate is reduced. The mean Nusselt number for every wall can be obtained from the product of NNR and mean Nusselt number for that wall in Table 1.

Figure 7 shows the variations of NNR for every wall with fin's position for Re=2000 and $\ell=0.15$. It is observed that placing a fin on the right wall can always enhance heat transfer on the left wall and at the same time, reduce heat transfer on the bottom, right and top walls. This is true for all other Reynolds numbers, except for the Re=500 case with a fin at $S_p=2.83$ which causes heat transfer enhancement on the bottom wall instead of reducing it. Putting a fin on the right wall can bring about the greatest

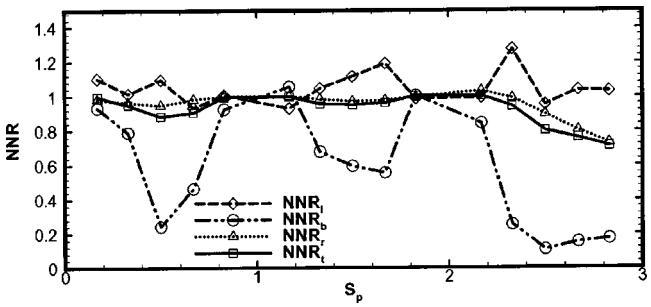

Fig. 7 Variation of NNR for every wall with fin's position (Re =2000,ℓ=0.15)

change of heat transfer rate on every wall compared to putting a fin on the left and bottom walls. As expected, a long fin has the most marked effect on the system compared to a short fin. Putting a fin at the middle of the left or right walls also causes the greatest effect compared to any other position on these two walls. Heat transfer on the bottom wall can be reduced more easily than left or right walls.

Variation of the Average Nusselt Number for the Cavity. In order to evaluate the overall heat transfer for the cavity, we should look at the average Nusselt number for the whole system. The average Nusselt number for a square lid-driven cavity with a fin is given as:

$$\overline{\mathrm{Nu}}=\frac{1}{3+2\ell}\times\left(\int_0^1 \mathrm{Nu}_\ell dY+\int_0^1 \mathrm{Nu}_b dX+\int_0^1 \mathrm{Nu}_t dY+\int_0^\ell \mathrm{Nu}_f|_{\text{side 1}} dX+\int_0^\ell \mathrm{Nu}_f|_{\text{side 2}} dX\right), \tag{11}$$

where Nu_f is the local Nusselt number on the two sides of the thin fin. These are defined:

$$\mathrm{Nu}_{f|\text{side 1}}=\left.\frac{\partial\theta}{\partial Y}\right|_{\text{side 1 of fin}}, \tag{12}$$

$$\mathrm{Nu}_{f|\text{side 2}}=-\left.\frac{\partial\theta}{\partial Y}\right|_{\text{side 2 of fin}}. \tag{13}$$

Equations 11 to 13 are applicable for a horizontal fin attached to either left or right walls. Similar equations can be obtained for a vertical fin that is attached to the bottom wall.

Figures 8(*a–c*) show the variations of the mean Nusselt number with the position of the fin. It can be seen that a fin placed on the right wall can reduce the mean Nusselt number of the system dramatically. A cavity with a fin placed at the middle of the left or bottom walls has the lowest mean Nusselt number compared to a fin placed at any other position on those walls. For a given position of the fin, the mean Nusselt number increases with the increase of the Reynolds number and decreases with the increase of the length of the fin. Comparing these three figures, the range of the variation of the mean Nusselt number is small for a short fin at different positions on the left and bottom walls, whereas longer fins give rise to greater variability of the heat transfer rate.

Availability of a correlation for the mean Nusselt number is necessary for the design of similar systems. A correlation in the form of the mean Nusselt number as a function of the Reynolds number, the length of the fin and the position of the fin was obtained. Based on the trends exhibited in Figs. 8(*a–c*), the general form of the correlation was assumed to be:

$$\overline{\mathrm{Nu}}=(a_1\xi^2+a_2\xi+a_3)\mathrm{Re}^b\ell^c, \tag{14}$$

with $\xi=S_p-\lfloor S_p\rfloor$ ($\lfloor\cdot\rfloor$ is the *floor function*). The values of the coefficients *a*'s, *b*, and *c* are summarized in Table 2. The general trends of these correlations are shown in Fig. 9 where the computed mean Nusselt numbers for every computed case and the curve fitting correlations are presented.

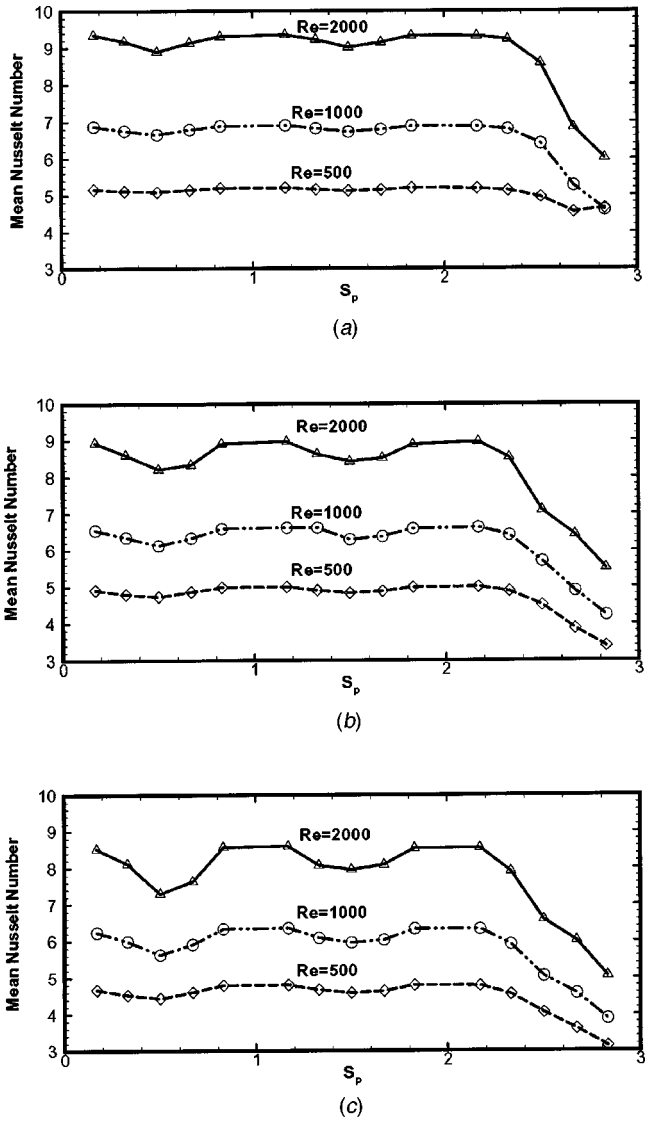

Fig. 8 Variation of the mean Nusselt number with positions of fins: (*a*) ℓ=0.05, (*b*) ℓ=0.1, and (*c*) ℓ=0.15

Table 2 Correlation coefficients, a_1, a_2, a_3, *b* and *c*

		Left Wall $\xi=S_p$ $0<S_p<1$	Bottom Wall $\xi=S_p-1$ $1<S_p<2$	Right Wall $\xi=S_p-2$ $2<S_p<3$
a's	a_1	0.1653	0.1161	-0.1112
	a_2	-0.1639	-0.1193	-0.0888
	a_3	0.3253	0.33	0.3896
b	Average Value	0.4093	0.4111	0.3647
	(Standard Deviation)	(0.023)	(0.0099)	(0.0631)
c	Average Value	-0.1086	-0.0922	-0.1566
	(Standard Deviation)	(0.013)	(0.0168)	(0.079)

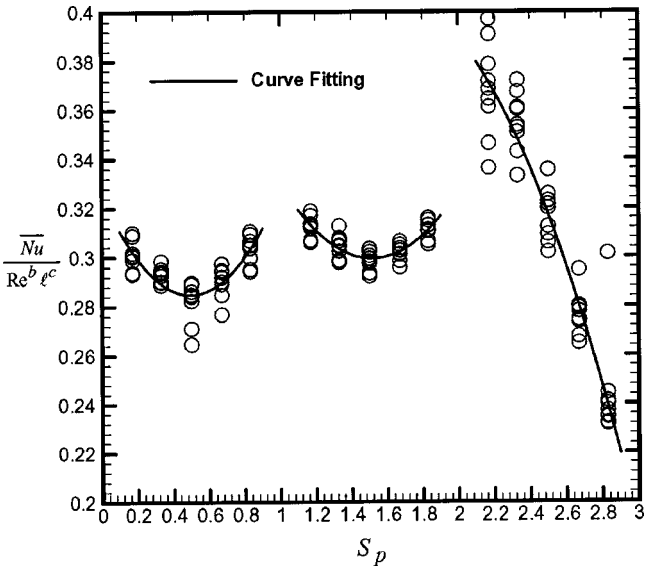

Fig. 9 Curve fittings for the mean Nusselt number

Conclusions

1. The flow patterns due to a fin placed on the right wall can bring about multi-cell recirculating vortices compared to the case without a fin that exhibits a primary vortex and two small corner cells. Placing a fin on the left or bottom walls modifies the flow slightly, whereas longer fins cause more marked changes to the flow field.
2. The presence of a fin slowed the flow near that wall and at the same time reduced the temperature gradients, thus degrading heat transfer capacity on that wall. Among the three fins studied, the longest fin ($0.15L$) has the most marked effect on the temperature distribution.
3. The local Nusselt number on the wall with the fin changes markedly with increase of the Reynolds number and the length of the fin. A fin positioned near the top right corner of the cavity can reduce heat transfer most effectively for all Reynolds numbers and fin lengths. A long fin has the most marked effect on changing heat transfer along the walls for a given Reynolds number.
4. Regardless of the Reynolds number, placing a fin on the right wall—compared to putting a fin on the left and bottom walls—can always enhance heat transfer on the left wall and at the same time, reduce heat transfer on the bottom, right and top walls. A long fin has the most marked effect on the system's heat transfer capabilities.
5. The mean Nusselt number of the cavity was successfully correlated to the Reynolds number, length of the fin and its position.

Nomenclature

C_d = drag coefficient, defined by Eq. (7)
l_p = length of the fin, m
ℓ = dimensionless length of the fin, i.e., $1_p/L$
L = length of the cavity, m
NNR = Nusselt number ratio, defined by Eq. (10)
Nu = local Nusselt number, defined by Eq. (8)
$\overline{\text{Nu}}$ = average or mean Nusselt number, defined by Eq. (9)
s = coordinate adopted for distance along the walls, m
S = dimensionless coordinate, i.e., $S=s/H$
T_c = temperature of the left, bottom and right walls, K
T_h = temperature of the moving lid, K
U_{lid} = velocity of the moving lid, m/s

Greek Symbols

θ = Dimensionless temperature, i.e., $(T-T_c)/(T_h-T_c)$

Subscripts

ℓ, b, r, t = related to the left, bottom, right and top walls
p = related to the fin (partition)

References

[1] Fu, W. S., Peng, J. C., and Shiel, W. J., 1989, "Transient Laminar Natural Convection in an Enclosure Partitioned by an Adiabatic Baffle," Numer. Heat Transfer, Part A, **16**, pp. 325–350.
[2] Yamaguchi, Y., and Asako, Y., 2001, "Effect of Partition Wall on Natural Convection Heat Transfer in a Vertical Air Layer," ASME J. Heat Transfer, **123**, pp. 441–449.
[3] Shankar, P. N., and Deshpande, M. D., 2000, "Fluid Mechanics in the Driven Cavity," Annu. Rev. Fluid Mech., **32**, pp. 93–136.
[4] Ghia, U., Ghia, K. N., and Shin, C. T., 1982, "High-Re Solutions for Incompressible Flow Using the Navier-Stokes Equations and a Multigrid Method," J. Comput. Phys., **48**, pp. 387–411.
[5] Prasad, A. K., and Koseff, J. R., 1996, "Combined Forced and Natural Convection Heat Transfer in a Deep Lid-Driven Cavity Flow," Int. J. Heat Fluid Flow, **17**, pp. 460–467.
[6] Goodrich, J. W., Gustafson, K., and Halasi, K., 1990, "Hopf Bifurcation in the Driven Cavity," J. Comput. Phys., **90**, pp. 219–261.
[7] Shen, J., 1991, "Hopf Bifurcation of the Unsteady Regularized Driven Cavity Flow," J. Comput. Phys., **95**, pp. 228–245.
[8] Patankar, S. V., 1980, *Numerical Heat Transfer and Fluid Flow*, Hemisphere Pub. Co., Washington, DC.
[9] Hayase, T., Humphrey, J. A. C., and Grief, R., 1992, "A Consistently Formulated QUICK Scheme for Fast and Stable Convergence Using Finite-Volume Iterative Calculation Procedures," J. Comput. Phys., **98**, pp. 108–118.
[10] Shi, X., 2002, "Fluid Flow and Heat Transfer within Enclosures with Fins and Partitions," Ph.D. thesis, Department of Mechanical Engineering, Auburn University.
[11] Torrance, K., Davis, R., Eike, K., Gill, P., Gutman, D., Hsui, A., Lyons, S., and Zien, H., 1972, "Cavity Flows Driven by Buoyancy and Shear," J. Fluid Mech., **51**, Part 2, pp. 221–231.

Mixed Convection From a Cylinder With Low Conductivity Baffles in Cross-Flow

Bassam A/K Abu-Hijleh
e-mail: bassam@just.edu.jo
Department of Mechanical Engineering
Jordan University of Science and Technology,
P.O. Box 3030 Irbid 22110,
Jordan

The problem of laminar mixed convection from an isothermal cylinder with low conductivity baffles in cross flow was solved numerically. The average Nusselt number was calculated at different combinations of number of baffles, baffle height, Reynolds number, and buoyancy parameter. The reduction in the Nusselt number is as much as 75 percent. When using a small number of baffles at low values of buoyancy parameter, an odd number of baffles reduced the Nusselt number more than an even number of baffles, especially at high values of Reynolds number. This is not the case at high values of buoyancy parameter. There is an optimal baffle height, Reynolds number dependent, for maximum heat transfer reduction beyond which an increase in baffle height does not result in further decrease in heat transfer. [DOI: 10.1115/1.1518494]

Keywords: Computational, Finite Difference, Finned Surfaces, Heat Transfer, Laminar, Mixed Convection

Introduction

Laminar convection from a heated cylinder is an important problem in heat transfer. It is used to simulate a wide range of engineering applications as well as provide a better insight into more complex systems of heat transfer. There are several situations where forced and natural convection occur with relatively comparable significance. This case is referred to as mixed convection heat transfer. Accurate knowledge of the overall convection heat transfer around circular cylinders is important in many fields, including heat exchangers, hot water and steam pipes, heaters, refrigerators and electrical conductors. Because of its industrial importance, this class of heat transfer has been the subject of many experimental and analytical studies. The problem received continuous attention since the early work of Morgan [1] and Churchill and Chu [2]. Work on mixed convection from a smooth cylinder, no baffles, include that of Badr [3], Ahmad [4], and Abu-Hijleh [5]. Recent economic and environmental concerns have raised the interest in methods of reducing or increasing the convection heat transfer, depending on the application, from a horizontal cylinder. Classical methods such as the use of insulation materials are becoming a cost as well as an environmental concern. Researchers continue to look for new methods of heat transfer control. The use of porous material to alter the heat transfer characteristics has been reported by several researchers including Vafai and Huang [6], Al-Nimr and Alkam [7], and Abu-Hijleh [8]. Common wisdom has it that baffles can be used to reduce the heat transfer in both natural and forced convection situations. To the best of the author's knowledge, there is no documented work that details the effect of baffle height and number of baffles used on the mixed convection heat transfer from an isothermal cylinder in cross-flow at different values of Reynolds number and buoyancy parameter. This paper presents the numerical results of using low conductivity baffles on the cylinder's outer surface in order to reduce the heat transfer from the cylinder to the surrounding fluid. The fluid under consideration is air. The elliptic momentum and energy equations were solved numerically using the stream function-vorticity method on a stretched grid. This detailed study included varying the Reynolds number ($\mathrm{Re}_D=10, 40, 100, 200$), buoyancy parameter ($\kappa=0,0.5,1,2,5$), number of baffles ($B=0, 2, 3, 4, 5, 7, 8, 11, 12, 17, 18$), and the nondimensional baffle height ($H=0, 0.25, 0.75, 1.5, 3$). The baffles were distributed equally around the cylinder perimeter with the first baffle located at $\theta=0$, Fig. 1.

Contributed by the Heat Transfer Division for publication in the JOURNAL OF HEAT TRANSFER. Manuscript received by the Heat Transfer Division October 16, 2000; revision received July 22, 2002. Associate Editor: D. A. Kaminski.

Mathematical Analysis

The steady-state equations for the two-dimensional laminar mixed convection over a cylinder, including the Boussinesq approximation, are given by:

$$\frac{1}{r}\frac{\partial(ru)}{\partial r}+\frac{1}{r}\frac{\partial v}{\partial\theta}=0 \tag{1}$$

$$u\frac{\partial u}{\partial r}+\frac{v}{r}\frac{\partial u}{\partial\theta}-\frac{v^2}{r}=\frac{1}{\rho}\left[\rho g\beta(T-T_\infty)\sin(\theta)-\frac{\partial p}{\partial r}\right]+\nu\left[\frac{\partial^2 u}{\partial r^2}+\frac{1}{r}\frac{\partial u}{\partial r}-\frac{u}{r^2}+\frac{1}{r^2}\frac{\partial^2 u}{\partial\theta^2}-\frac{2}{r^2}\frac{\partial v}{\partial\theta}\right] \tag{2}$$

$$u\frac{\partial v}{\partial r}+\frac{v}{r}\frac{\partial v}{\partial\theta}+\frac{uv}{r}=\frac{1}{\rho}\left[\rho g\beta(T-T_\infty)\cos(\theta)-\frac{1}{r}\frac{\partial p}{\partial\theta}\right]+\nu\left[\frac{\partial^2 v}{\partial r^2}+\frac{1}{r}\frac{\partial v}{\partial r}-\frac{v}{r^2}+\frac{1}{r^2}\frac{\partial^2 v}{\partial\theta^2}+\frac{2}{r^2}\frac{\partial u}{\partial\theta}\right] \tag{3}$$

$$u\frac{\partial T}{\partial r}+\frac{v}{r}\frac{\partial T}{\partial\theta}=\alpha\nabla^2 T \tag{4}$$

where,

$$\nabla^2\equiv\left[\frac{\partial^2}{\partial r^2}+\frac{1}{r}\frac{\partial}{\partial r}+\frac{1}{r^2}\frac{\partial^2}{\partial\theta^2}\right]$$

Equations (1)–(4) are subject to the following boundary conditions:

1. On the cylinder surface, i.e., $r=r_o$; $u=v=0$, and $T=T_o$.
2. Far-stream from the cylinder, i.e., $r\to\infty$; $u\to U_\infty\cos(\theta)$ and $v\to -U_\infty\sin(\theta)$. For the temperature, T, the far-stream boundary condition is divided into an inflow ($\pi/2\leqslant\theta\leqslant 3\pi/2$) and an outflow ($0\leqslant\theta<\pi/2$ and $3\pi/2<\theta\leqslant 2\pi$) regions, Fig. 1. The far-stream temperature boundary conditions are $T\to T_\infty$ and $\partial T/\partial r\to 0$ for the inflow and outflow regions, respectively.

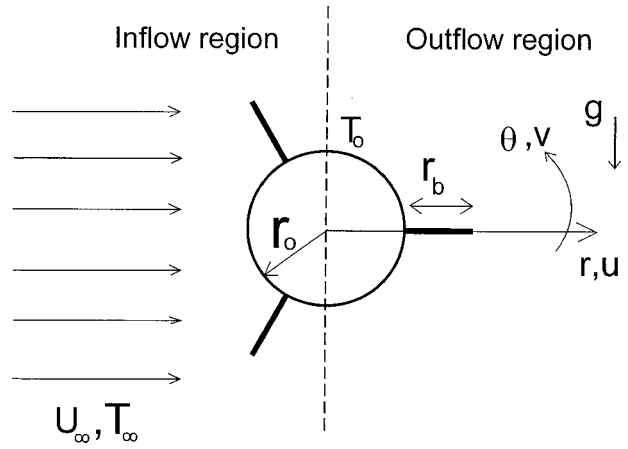

Fig. 1 Schematic of the flow field and physical parameters

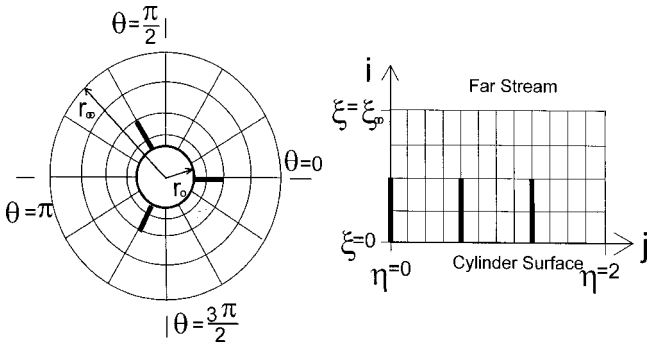

Fig. 2 Schematic of the finite difference grid in the physical (left) and the computational (right) domains

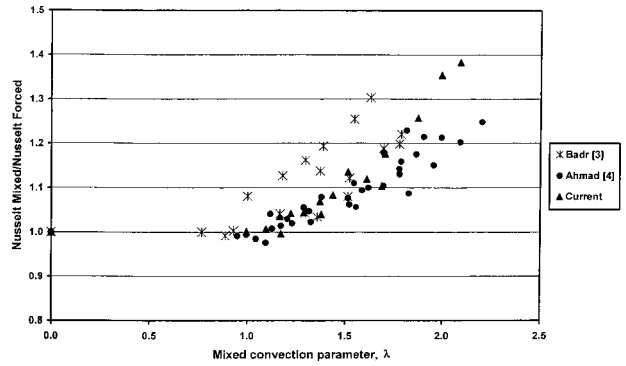

Fig. 3 Code verification for the case of a smooth cylinder

3. On the baffle surface; $u=v=0$. Since the baffles are assumed to be very thin and of very low conductivity, there will be no heat conduction along the baffles. Thus, the temperature at any point along the baffle will be the average temperature of the fluid just above and below the baffle, i.e., $T_{ij}=(T_{ij+1}+T_{ij-1})/2$, see Fig. 2. The baffles are equally spaced around the perimeter of the cylinder.

The average Nusselt number on the cylinder surface, based on diameter, is calculated as

$$\overline{\mathrm{Nu}_D}=\frac{1}{2\pi}\frac{D}{k}\int_0^{2\pi}h(\theta)d\theta=-\frac{D}{2\pi}\int_0^{2\pi}\frac{\partial T(r_o,\theta)/\partial r}{(T_o-T_\infty)}\partial\theta \quad (5)$$

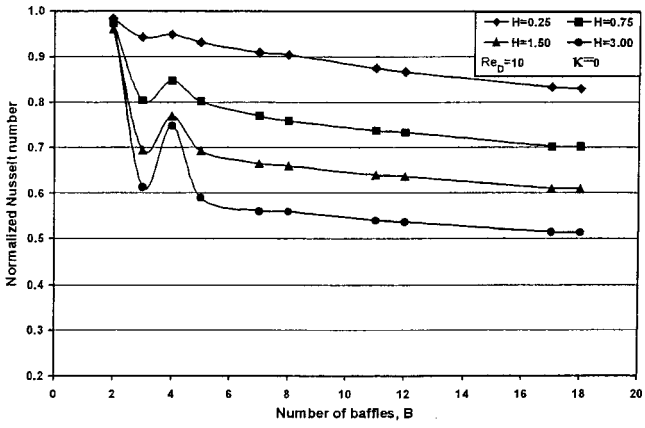

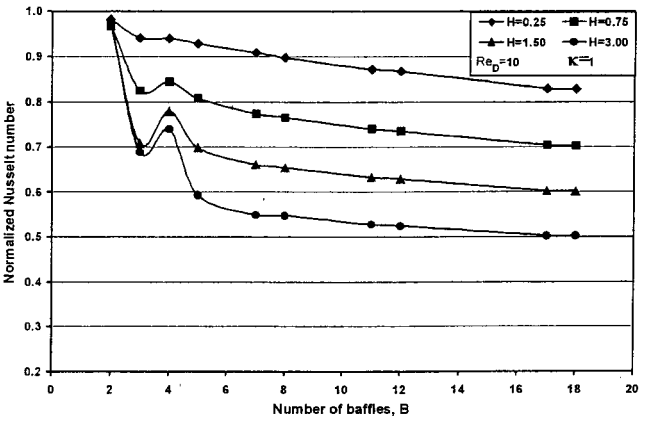

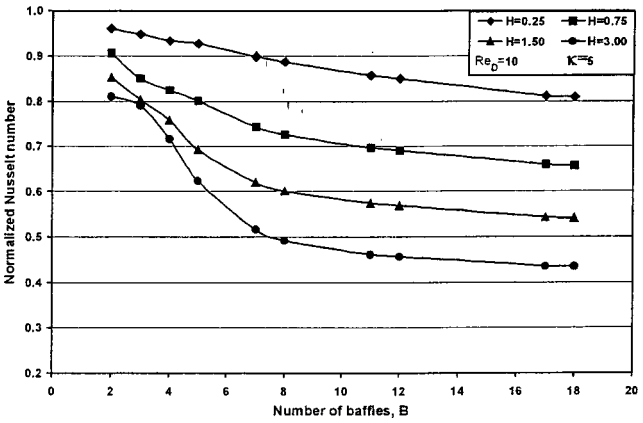

Fig. 4 Variation of the normalized Nusselt number with number of baffles at different values of baffle height and buoyancy parameter, case of $Re_D=10$

The following nondimensional groups are introduced:

$$R\equiv\frac{r}{r_o},\quad U\equiv\frac{u}{U_\infty},\quad V\equiv\frac{v}{U\infty}$$

$$\phi\equiv\frac{(T-T_\infty)}{(T_o-T_\infty)},\quad P\equiv\frac{(p-p_\infty)}{\frac{1}{2}\rho U_\infty^2} \quad (6)$$

Using the steam function-vorticity formulation, the nondimensional form of Eqs. (1)–(4) is given by

$$\omega=\nabla^2\psi \quad (7)$$

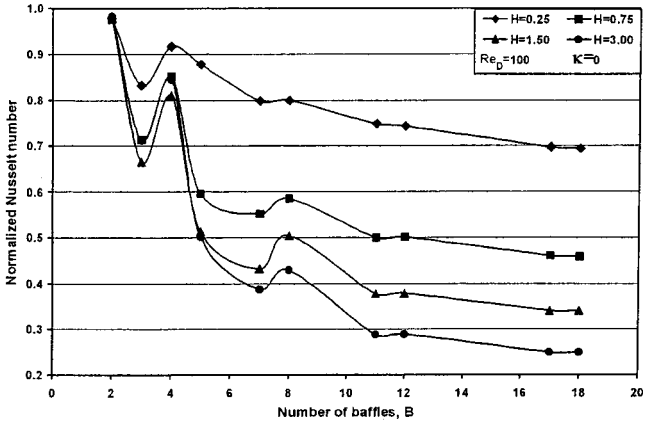

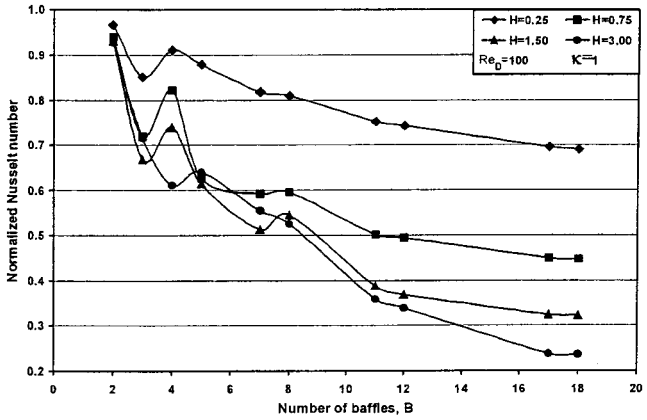

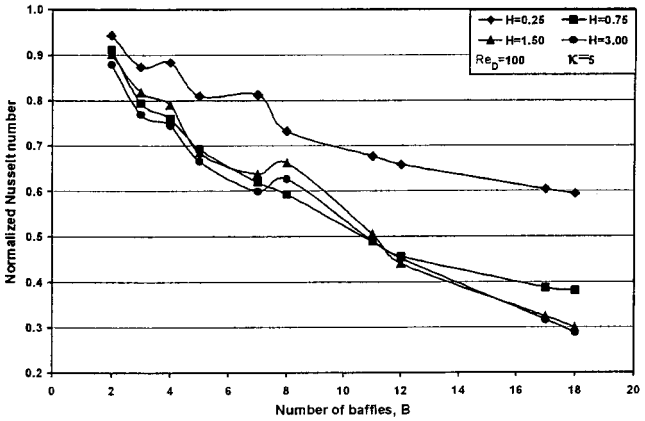

Fig. 5 Variation of the normalized Nusselt number with number of baffles at different values of baffle height and buoyancy parameter, case of $Re_D=100$

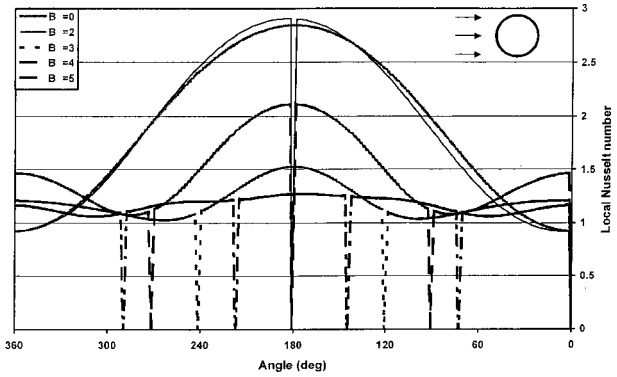

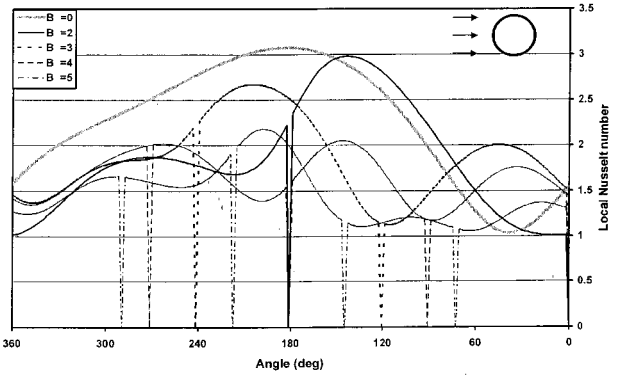

Fig. 6 Distribution of the local Nusselt around the cylinder for the case of $Re_D=10$ and $H=3$ at different number of baffles, at $\kappa=0$ (top) and $\kappa=5$ (bottom). Direction of x-axis reversed to reflect flow direction.

$$U\frac{\partial\omega}{\partial R}+\frac{V}{R}\frac{\partial\omega}{\partial\theta}=\frac{1}{\mathrm{Re}}\nabla^2\omega-\frac{Gr}{\mathrm{Re}^2}\left[\cos(\theta)\frac{\partial\phi}{\partial R}-\frac{1}{R}\sin(\theta)\frac{\partial\phi}{\partial\theta}\right] \tag{8}$$

$$U\frac{\partial\phi}{\partial R}+\frac{V}{R}\frac{\partial\phi}{\partial\theta}=\frac{1}{\mathrm{Re\,Pr}}\nabla^2\phi \tag{9}$$

where the nondimensional stream-function and vorticity are given by

$$U\equiv\frac{1}{R}\frac{\partial\psi}{\partial\theta},\quad V\equiv-\frac{\partial\psi}{\partial R} \tag{10}$$

The new nondimensional boundary conditions for Eqs. (7)–(9) are given by

1. On the cylinder surface, i.e., $R=1.0$; $\psi=\partial\psi/\partial R=0$, $\omega=\partial^2\psi/\partial R^2$, and $\phi=1.0$.
2. Far-stream form the cylinder, i.e., $R\to\infty$; $1/R\ (\partial\psi/\partial\theta)=\cos(\theta)$ and $(\partial\psi/\partial R)=\sin(\theta)$. For the nondimensional temperature, $\phi=0$ and $(\partial\phi)/(\partial R)=0$, for the inflow and outflow, respectively.
3. On the baffle surface; $\psi=0$, $\omega=-(1/R^2)(\partial^2\psi/\partial\theta^2)$, and $\phi_{ij}=(\phi_{ij+1}+\phi_{ij-1})/2$.

In order to accurately resolve the boundary layer around cylinder, a grid with small radial spacing is required. It is not practical to use this small spacing as we move to the far-stream boundary. Thus a stretched grid in the radial direction is needed [9]. This will result in unequally spaced nodes and would require the use of more complicated and/or less accurate finite difference formulas. To overcome this problem, the unequally spaced grid in the physical domain (R,θ) is transformed into an equally spaced grid in the computational domain (ξ,η) [9], Fig. 2. The two domains are related as follows:

$$R=e^{\pi\xi},\quad \theta=\pi\eta \tag{11}$$

Equations (7)–(9) along with the corresponding boundary conditions need to be transformed into the computational domain. In the new computational domain, Eqs. (7)–(9) are transformed to:

$$\omega=\frac{1}{E^2}\left[\frac{\partial^2\psi}{\partial\xi^2}+\frac{\partial^2\psi}{\partial\eta^2}\right] \tag{12}$$

$$\frac{\partial^2\omega}{\partial\xi^2}+\frac{\partial^2\omega}{\partial\eta^2}=\mathrm{Re}\left[\frac{\partial\psi}{\partial\eta}\frac{\partial\omega}{\partial\xi}-\frac{\partial\psi}{\partial\xi}\frac{\partial\omega}{\partial\eta}\right]+E\frac{\mathrm{Re}^2}{\mathrm{Gr}}\left[\cos(\pi\eta)\frac{\partial\phi}{\partial\xi}-\sin(\pi\eta)\frac{\partial\phi}{\partial\eta}\right] \tag{13}$$

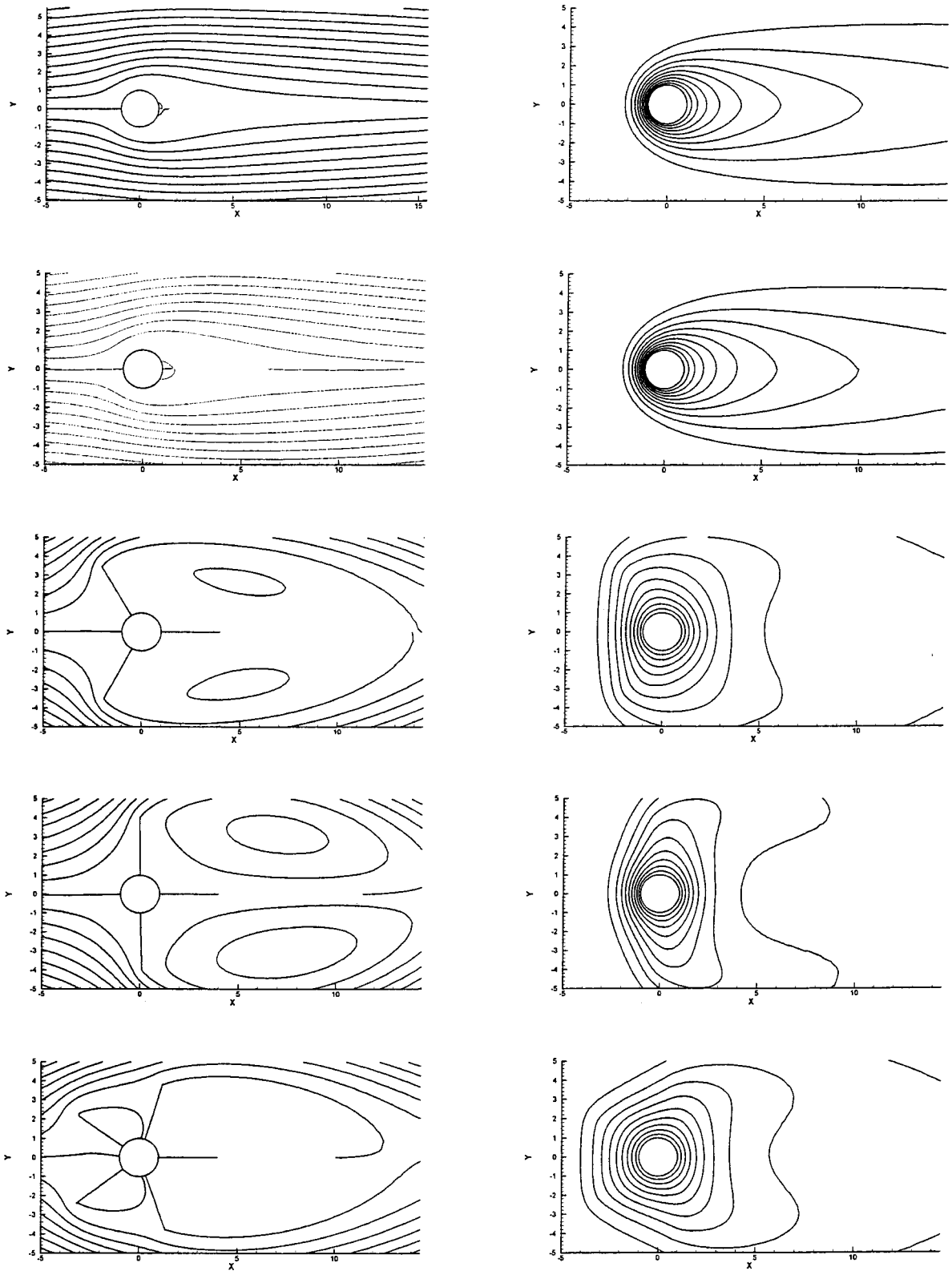

Fig. 7 Streamline and isothermal contours at different number of baffles (from top: $B=0$, 2, 3, 4, and 5) for the case of Reynolds number (Re_D)=10, buoyancy parameter (κ)=0, and baffle height (H)=3

$$\frac{\partial^2\phi}{\partial\xi^2}+\frac{\partial^2\phi}{\partial\eta^2}=\mathrm{Re}\,\mathrm{Pr}\left[\frac{\partial\psi}{\partial\eta}\frac{\partial\phi}{\partial\xi}-\frac{\partial\psi}{\partial\xi}\frac{\partial\phi}{\partial\eta}\right] \tag{14}$$

where,

$$E=\pi e^{\pi\xi} \tag{15}$$

The transformed boundary conditions are given by

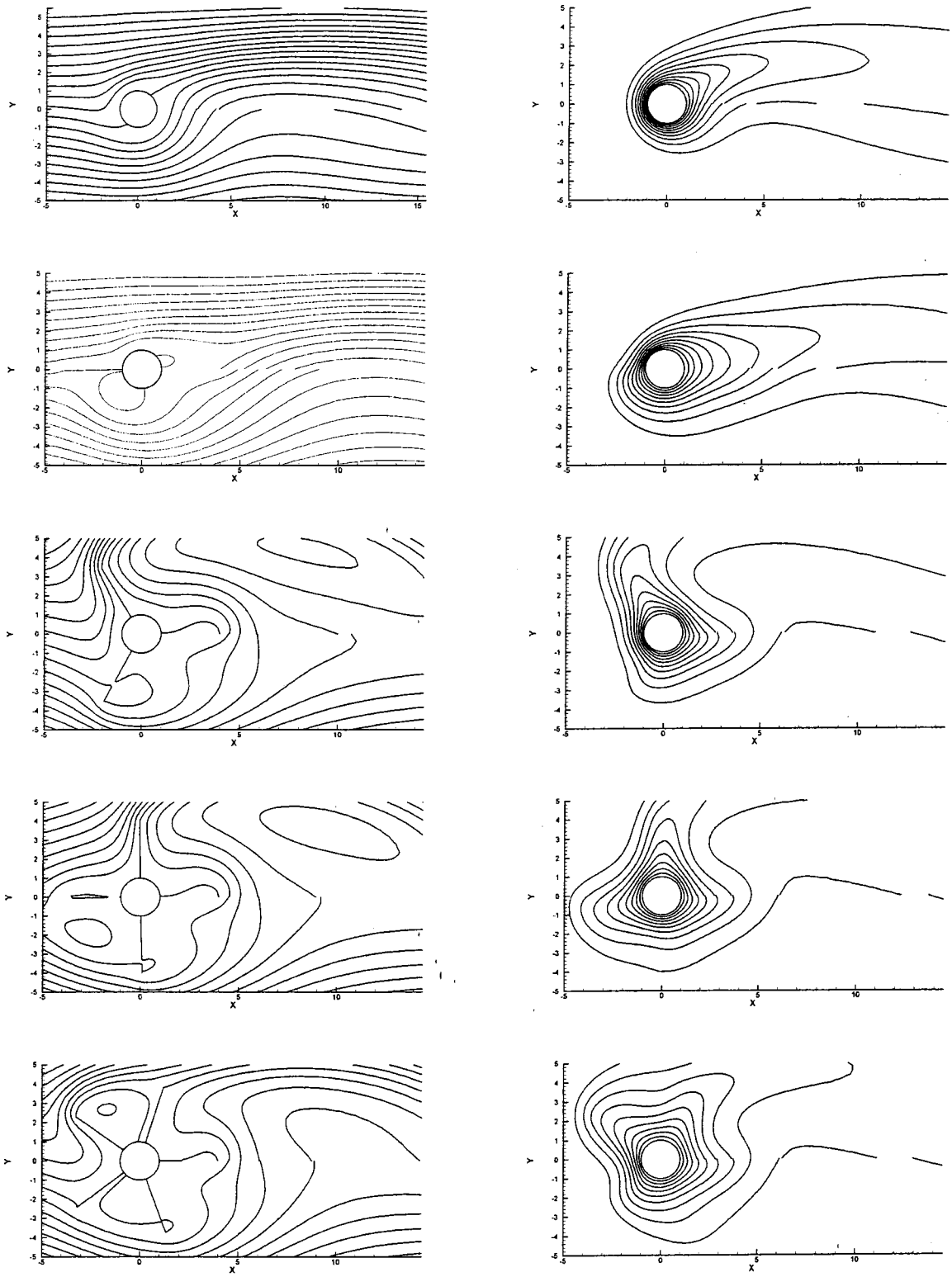

Fig. 8 Streamline and isothermal contours at different number of baffles (from top: $B=0$, 2, 3, 4, and 5) for the case of Reynolds number (Re_D)=10, buoyancy parameter (κ)=5, and baffle height (H)=3

1. On the cylinder surface, i.e., $\xi=0$; $\psi=\partial\psi/\partial\xi=0$, $\omega=(1/\pi^2)\partial^2\psi/\partial\xi^2$, and $\phi=1.0$.
2. Far-stream from the cylinder, i.e., $\xi\rightarrow\infty$; $\partial\psi/\partial\xi=E\sin(\theta)$. In the inflow region; $\omega\rightarrow 0$ and $\phi\rightarrow 0$. In the outflow region; $\partial\omega/\partial\xi\rightarrow 0$ and $\partial\phi/\partial\xi\rightarrow 0$.
3. On the baffle surface; $\psi=0$, $\omega=-(1/\pi^2)(\partial^2\psi/\partial\xi^2)$, and $\phi_{ij}=(\phi_{ij+1}+\phi_{ij-1})/2$.

The elliptic system of PDEs given by Eqs. (12)–(14) along with the corresponding boundary conditions was discretized using fi-

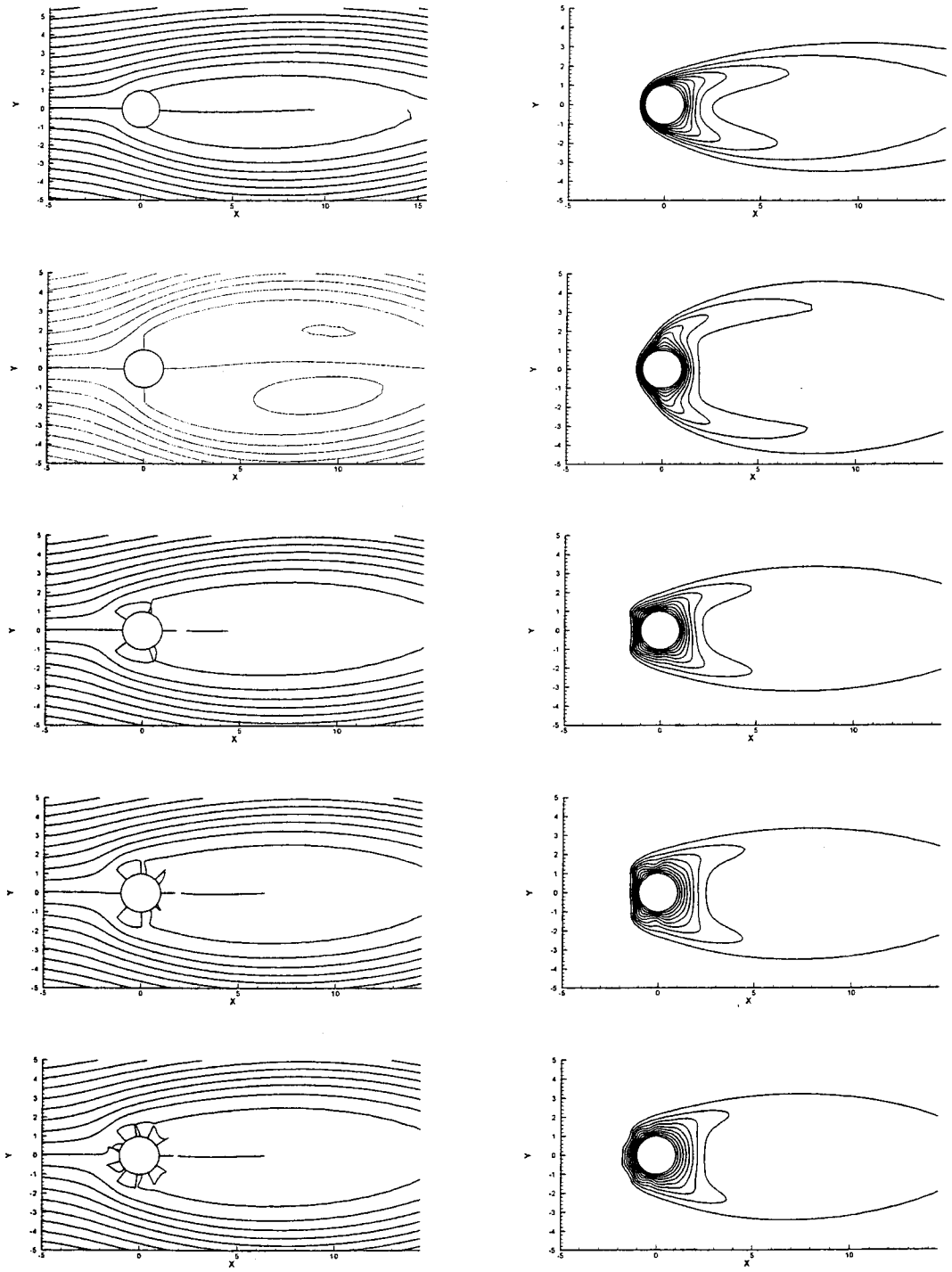

Fig. 9 Streamline and isothermal contours at different number of baffles (from top: $B=0$, 4, 5, 8, and 11) for the case of Reynolds number (Re_D)=100, buoyancy parameter (κ)=0, and baffle height (H)=0.75

nite difference method. The resulting system of algebraic equations was solved using the hybrid scheme [10]. Such a method proved to be numerically stable for convection-diffusion problems. The finite difference form of the equations was checked for consistency with the original PDEs [9]. The iterative solution procedure was carried out until the error in all solution variables (ψ, ω, ϕ) became less than a predefined error level (ϵ). Other predefined parameters needed for the solution method included the placement of the far-stream boundary condition (R_∞) and the number of grid points in both radial and tangential directions, N and M, respectively. Extensive testing was carried out in order to determine the effect of each of these parameters on the solution. This was done to insure that the solution obtained was independent of and not tainted by the predefined value of each of these parameters. The testing included varying the value of ϵ from 10^{-3} to 10^{-6}, R_∞ from 5 to 50, N from 100 to 200, and M from 100 to 200. The results reported herein are based on the following combination: $N=148-157$, $M=170-180$, $R_\infty=20$, and $\epsilon=10^{-5}$. The variation in the number of grids used in the radial and tangential direction was baffle number and baffle height dependent. The variation is required in order to insure that all baffles coincide

with one of the grid's radial lines and that the edge of the baffles coincide with one of the grid's tangential lines, Fig. 2. The resolution of the grid used is better than most grids used in published studies of forced convection from a heated cylinder [11]. Previous work by the author [5] showed that the mixed convection Nusselt number can be related to the forced convection Nusselt number via a mixed convection parameter ($\lambda \equiv \mathrm{Re}_D^{0.06793} \kappa^{0.2335}$). This parameter combines the effects of forced convection, represented by Reynolds number, and natural convection, represented by the buoyancy parameter. Figure 3 shows the ratio of mixed to forced Nusselt number versus the mixed convection parameter (λ) for the data of Badr [3], Ahmad [4], and the results of the current code for the case of a cylinder without baffles, reference case. The current results are well within the range of the published data.

Results

The presence of the baffles has an effect on both the hydrodynamic as well as the thermal characteristics of the flow. The baffles tend to obstruct both the natural and forced convection heat transfer currents from the cylinder surface, thus reducing the heat transfer from the cylinder to the surrounding fluid. The calculated Nusselt number of a cylinder with baffles, at a given combination of Reynolds number and buoyancy parameter, is normalized by the Nusselt number of a smooth cylinder, no baffles, at the same combination of Reynolds number and buoyancy parameter. This way the relative magnitude of the change in the heat transfer due to the baffles can easily be deduced using such representation.

Figures 4 and 5 show the change in the normalized Nusselt number at different combinations of number of baffles, baffle height, and buoyancy parameter, at Reynolds number values of 10 and 100, respectively. The study included the effect of all baffle and buoyancy parameters at four values of Reynolds number ($\mathrm{Re}_D = 10, 40, 100, 200$). The data analysis showed that the trend at $\mathrm{Re}_D = 40$ was similar to that at $\mathrm{Re}_D = 10$ while the trend at $\mathrm{Re}_D = 200$ was similar to that at $\mathrm{Re}_D = 100$. Thus for space considerations, only the results at $\mathrm{Re}_D = 10$ and 100 will be included in this paper. The general trend is that an increase in the number of baffles and/or the baffle height results in a reduction in the normalized Nusselt number. The reduction was as much as 75 percent, Fig. 5. At low Reynolds number and buoyancy parameter, Fig. 4, increasing the number of baffles beyond a certain value results in minimal reduction in the value of normalized Nusselt number. This indicates that there is an optimal number of baffles for maximum heat transfer reduction. This is not the case at high values of Reynolds number and/or buoyancy parameter. For such cases, the reduction in the normalized Nusselt number continues as the number of baffles increases. At high values of Reynolds number, there is an optimal baffle height, B, beyond which an increase in the baffle height does not result in further reduction in the normalized Nusselt number, Fig. 5. At high values of Reynolds number, the thermal boundary layer is thin. The reduction in the heat transfer from the cylinder is caused mainly by the baffle/thermal boundary layer interaction. The part of the baffle that is outside the thermal boundary layer has little effect on the thermal boundary layer and resulting heat transfer from the cylinder. Thus increasing the baffle height beyond a certain value, Reynolds number dependent, has minimal effect on the normalized Nusselt number.

Figures 4 and 5 show an interesting behavior in the change in the normalized Nusselt number at low buoyancy parameter. In Fig. 4, increasing the number of baffles from 3 to 4 results in an increase in the normalized Nusselt number. This was especially clear for the case $\kappa = 0$. The cause of this is the way the baffles are arranged around the cylinder perimeter. Recalling that the first baffle is always located at $\theta = 0$, an odd number of fins results in baffles located further up in the incoming stream, Fig. 1. The local Nusselt number is highest at the upstream side of the cylinder. Placing more baffles on the upstream side of the cylinder will result in more reduction in the local Nusselt number, and thus more significant reduction in the overall Nusselt number. As the buoyancy parameter increases, the flow direction changes and the advantage of the odd number of baffles over an even number of baffles starts to decrease. In Fig. 4, and at $\kappa = 5$, this advantage has vanished and increasing the number of baffles results in further reduction in the normalized Nusselt number, regardless of the number of baffles. Figure 6 shows the local Nusselt number distribution around the cylinder for the case of $\mathrm{Re}_D = 10$ and $H = 3$ at different number of baffles, at $\kappa = 0$ (top) and $\kappa = 5$ (bottom). The effectiveness of an odd number of baffles at low buoyancy parameter can be seen clearly in this figure. The same trend can be seen in Figs. 7 and 8 which show the streamline and isothermal contours for the same cases shown in Fig. 6. At higher values of Reynolds number, Fig. 5, the advantage of odd number of baffles continues at higher number of baffles in what resembles a ''harmonic'' behavior. Figure 9 shows the streamline and isothermal contours for the case of $\mathrm{Re}_D = 100$, $H = 0.75$, and $\kappa = 0$ at different number of baffles. The harmonic change in the heat transfer from the cylinder can be easily identified by the extent of the horseshoe isothermal contour downstream of the cylinder.

Conclusion

The changes in the mixed convection heat transfer from a cylinder in cross flow due to the addition of low conductivity baffles was studied numerically. The study covered a wide range of parameters: $10 \leq \mathrm{Re}_D \leq 200$, $0 \leq \kappa \leq 5.$, $0 \leq B \leq 18$, and $0 \leq H \leq 3$. The general trend is that an increase in the baffle number and/or height results in an reduction in the heat transfer from the cylinder, as much as 75 percent. The baffles are most effective at high values of Reynolds number. A low number of odd baffles is more effective than an even number of baffles at low values of buoyancy parameter. This advantage extends to higher number of baffles at higher values of Reynolds number. This advantage is not present at high values of buoyancy parameter. There is an optimal baffle height, Reynolds number dependent, for maximum heat transfer reduction beyond which an increase in baffle height does not result in further decrease in heat transfer.

Nomenclature

B = number of equally spaced baffles
D = cylinder diameter, $2\,r_o$
E = parameter in computational domain, $\pi e^{\pi\xi}$
g = gravity
Gr = Grashof number based on cylinder radius, $g\beta(T_o - T_\infty) r_o^3/\nu^2$
Gr_D = Grashof number based on cylinder diameter, $g\beta(T_o - T_\infty) D^3/\nu^2$
H = non-dimensional baffle height, r_b/r_o
h = local convection heat transfer coefficient
k = conduction heat transfer coefficient
M = number of grid points in the tangential direction
N = number of grid points in the radial direction
$\overline{\mathrm{Nu}}_D$ = average Nusselt number based on cylinder diameter
P = nondimensional pressure
p = pressure
Pr = Prandtl number
R = nondimensional radius
r = radius
r_b = radius of baffle
Re = Reynolds number based on radius, $U_\infty r_o/\nu$
Re_D = Reynolds number based on diameter, $U_\infty D/\nu$
T = temperature
U = nondimensional radial velocity
u = radial velocity
V = nondimensional tangential velocity
v = tangential velocity

Greek Symbols

α = thermal diffusivity
β = coefficient of thermal expansion
ϵ = measure of convergence of numerical results
η = independent parameter in computational domain representing tangential direction
θ = angle
κ = buoyancy parameter, $\mathrm{Gr}_D/\mathrm{Re}_D^2$
λ = mixed convection parameter, $\lambda \equiv \mathrm{Re}_D^{0.06793}\kappa^{0.02335}$
ν = kinematic viscosity
ξ = independent parameter in computational domain representing radial direction
ρ = density
ϕ = nondimensional temperature
ψ = nondimensional stream function
ω = nondimensional vorticity

Subscripts

D = value based on cylinder diameter
o = value at cylinder surface
∞ = free stream value

References

[1] Morgan, V. T., 1975, ''The Overall Convection Heat Transfer from Smooth Circular Cylinder,'' Adv. Heat Transfer, **11**, pp. 199–264.
[2] Churchill, S. W., and Chu, H. H. S., 1975, ''Correlating Equations for Laminar and Turbulent Free Convection from a Horizontal Cylinder,'' Int. J. Heat Mass Transf., **18**, pp. 1049–1053.
[3] Badr, H. M., 1983, ''A Theoretical Study of Laminar Mixed Convection from a horizontal Cylinder in a Cross Stream,'' Int. J. Heat Mass Transf., **26**, pp. 639–653.
[4] Ahmad, R. A., and Qureshi, Z. H., 1992, ''Laminar Mixed Convection from a Uniform Heat Flux Horizontal Cylinder in a Crossflow,'' J. Thermophys. Heat Transfer, **6**, pp. 277–287.
[5] Abu-Hijleh, B. A/K, 1999, ''Laminar Mixed Convection Correlations From an Isothermal Cylinder in Cross Flow at Different Angles of Attack,'' Int. J. Heat Mass Transf., **42**, pp. 1383–1388.
[6] Vafai, K., and Huang, P. C., 1994, ''Analysis of Heat Transfer Regulation and Modification Employing Intermittently Emplaced Porous Cavities,'' ASME J. Heat Transfer, **116**, pp. 604–613.
[7] Al-Nimr, M. A., and Alkam, M. K., 1998, ''A Modified Tubeless Solar Collector Partially Filled With Porous Substrate,'' Renewable Energy **13**, pp. 165–173.
[8] Abu-Hijleh, B. A/K, 2001, ''Natural Convection Heat Transfer from a Cylinder Covered with an Orthotropic Porous Layer,'' accepted for publication in the Numer. Heat Transfer, **40**(7), pp. 767–782.
[9] Anderson, J. D., 1994, *Computational Fluid Dynamics: The Basics with Applications*, McGraw Hill, New York.
[10] Patankar, S. V., 1980, *Numerical Heat Transfer of Fluid Flow*, McGraw Hill, New York.
[11] Ahmad, R. A., 1996, ''Steady-State Numerical Solution of the Navier-Stokes and Energy Equations around a Horizontal Cylinder at Moderate Reynolds Numbers from 100 to 500,'' Heat Transfer Eng., **17**, pp. 31–81.

M. Collins
e-mail: mcollins@uwaterloo.ca
Dept. of Mechanical Engineering,
University of Waterloo,
Waterloo, Ontario, Canada, N2L 3G1

S. J. Harrison
e-mail: harrison@me.queensu.ca
Dept. of Mechanical Engineering,
Queen's University,
Kingston, Ontario, Canada, K7L 3N6

D. Naylor
e-mail: dnaylor@acs.ryerson.ca
Dept. of Mechanical, Aerospace,
and Industrial Engineering,
Ryerson University,
Toronto, Ontario, Canada, M5B 2K3

P. H. Oosthuizen
e-mail: oosthuiz@me.queensu.ca
Dept. of Mechanical Engineering,
Queen's University,
Kingston, Ontario, Canada, K7L 3N6

Heat Transfer From an Isothermal Vertical Surface With Adjacent Heated Horizontal Louvers: Numerical Analysis

The present study examines the influence of heated, horizontal, and rotatable louvers on the convective and radiative heat transfer from a heated or cooled vertical isothermal surface. The system represents an irradiated Venetian blind adjacent to the indoor surface of a window. Detailed heat transfer results were obtained using a steady, laminar, two-dimensional, conjugate conduction/convection/radiation finite element model for two window temperatures (warm and cool compared to ambient) and irradiation levels, two louver to surface spacings, and three louver angles. The effect of the heated louvers on the heat transfer rate from the surface has been demonstrated. [DOI: 10.1115/1.1481357]

Keywords: Computational, Finite Element, Heat Transfer, Mixed Mode, Modeling

Introduction

It is common for a louvered shading device, such as a Venetian blind, to be mounted on the indoor surface of a window to provide privacy and to control day-lighting. In addition, the presence of these shading devices will affect natural convection and radiant heat exchange from the window. As a result, there will be a change in the heat transmission and solar heat gain, through the window.

At present, advances are being made that demonstrate the complex thermal interaction between a shade and a window, in the absence of solar irradiation. Several previous studies have examined the effect of a Venetian blind on the free convective heat transfer at an indoor glazing surface when there is no solar irradiance (i.e., for ''nighttime'' conditions). Machin et al. [1] performed interferometry and flow visualization. Their experiment used a Mach-Zehnder Interferometer to examine the local and overall convection coefficients from the surface of an isothermal surface at various blind to surface spacings and louver angles. They found that when an aluminum blind was placed close to the surface, the slats caused a strong periodic variation in the local Nusselt number distribution. Ye et al. [2] conducted a two-dimensional finite element study of this problem. In that study, the effects of thermal radiation were neglected and the blind slats were modeled as zero thickness, no-slip, impermeable surfaces. A similar numerical study has been done by Phillips et al. [3], which included the effect of heat conduction along the blind slats, and radiation heat exchange. Their improved model showed excellent correlation with interferometric data.

In the present investigation, a move from the previously mentioned ''nighttime'' models, to a ''daytime'' model that includes the effects of incident solar energy has been performed. Generally, such systems can be examined using solar-thermal separation [4], which assumes that the short wave solar radiation, and long wave radiative heat transfer can be examined separately for a given system. An optical analysis of the system will determine directly transmitted, reflected through, and absorbed components of solar irradiation. The absorbed component can then be used as input into a thermal analysis that is solved independently.

The present study examines the influence of heated horizontal louvers (representing irradiated blind slats) on the local and average convective and radiative heat transfer from a vertical isothermal surface (representing a window). The investigation was conducted using a finite element model of this same system.

Advancement in the analysis of shade and window systems will be of benefit to industry standard software such as Vision [5] and Window [6]. Both provide a one-dimensional analysis of the radiative and convective heat transfer through a window, where convection from the indoor surface is obtained using accepted correlations for an isothermal vertical flat surface. The effects of shading devices are neglected in the mentioned software due to their inability to analyze the complex geometry of these systems. This study has the ultimate intention of producing simplified correlations, to aid in adapting window analysis software to the examination of window and shade combinations.

Physical Model

In this study, the indoor glazing surface was idealized as an isothermal vertical flat surface of height (l) that was heated to temperature (T_p) above the ambient room temperature (T_∞). A Venetian blind consisting of seventeen horizontal louvers, was positioned a nominal distance (b) from the surface and the individual slats were inclined at an angle with respect to the horizontal (ϕ). A heat flux (q_b) was applied to one side of each slat to simulate the solar radiation absorbed by the blind. Figure 1 shows the system geometry and a photograph of the physical system on which the geometry was based.

The numerical model was an idealized approximation of a real fenestration. For an actual window, there will be frame effects and only the center-of-glass region will be nearly isothermal. Also, the actual indoor glazing temperature will increase with the solar irradiance, rather than being fixed. However, the idealized system was consistent with an experimental model, and these simplifications eliminate several secondary parameters, such as the frame geometry and the glazing external thermal boundary condition.

The slats were modeled after those from a commercially available aluminum Venetian blind. The slats had a width (w), thick-

Contributed by the Heat Transfer Division for publication in the JOURNAL OF HEAT TRANSFER. Manuscript received by the Heat Transfer Division June 18, 2001; revision received March 7, 2002. Associate Editor: C. Amon.

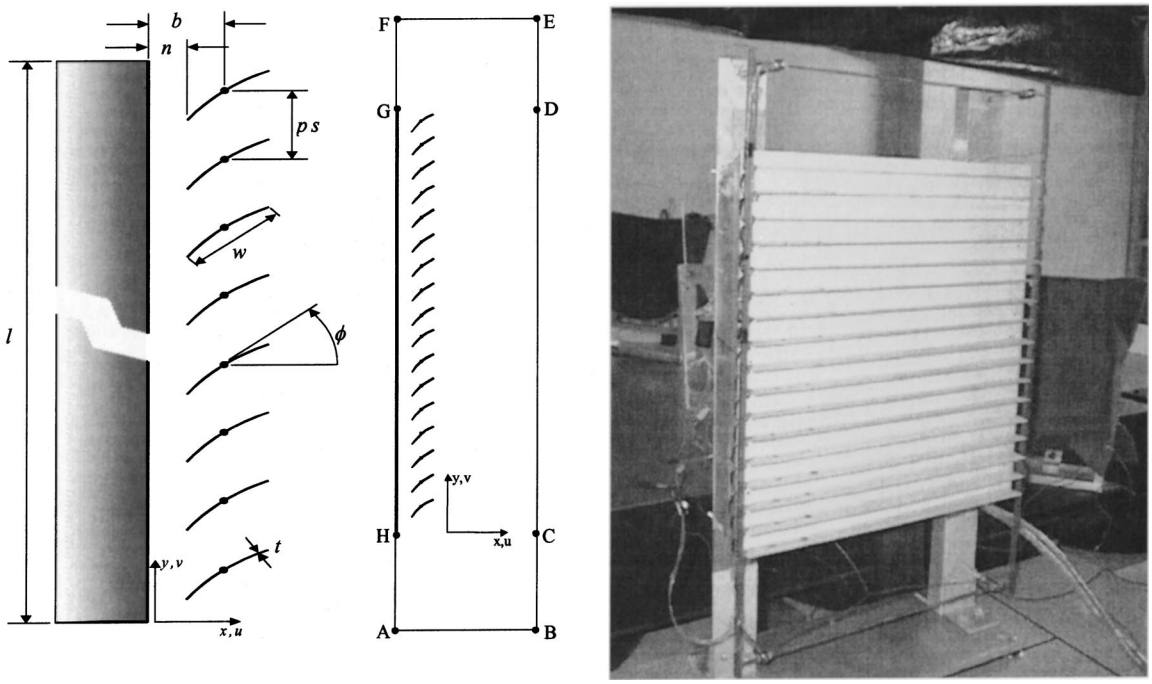

Fig. 1 System geometry (left), computational domain (mid) and photo (right)

ness (t), an arc length and a radius of curvature (rc) typical of many commercially available products. The slats were held at a pitch of $ps=22.2$ mm. This slat pitch ratio ($ps/w=7/8$) is typical of many commercially available Venetian blinds. The slats were assumed to have a uniform hemispherical emissivity ($\varepsilon_p=\varepsilon_b=0.81$) and thermal conductivity (k_b).

It was decided that two surface temperatures, one level of irradiation, one nominal blind spacing, and three blind angles would be examined. An additional set of test runs at 0 deg slat angle, with an increased nominal distance, allows for an examination of the effects of surface to blind leading edge, n (i.e., 7.3 mm tip-to-surface spacing can be examined despite the fact that the louver angle changes).

Numerical model parameters that remained constant for all experiments are given in Table 1. Table 2 shows the sequence of numerical conditions. Fluid properties were evaluated at an estimated film temperature of 300 K and were taken from Touloukian et al. [7–9]. Film temperatures predicted by the numerical model after the present analysis showed that the average fluid temperature was between 297 K and 302 K for all validation cases.

Governing Equations

In developing the numerical model, a number of assumptions have been made. These include

- The flow is steady, laminar, incompressible and two-dimensional.
- The thermo-physical properties are constant, except for fluid density, which is treated by means of the Boussinesq approximation.
- Gray diffuse radiation exchange between the window, blind and room has been considered, and the fluid is a nonparticipating medium.

For the purposes of model execution, the problem has been nondimensionalized. The dimensionless governing equations for the fluid are

$$\frac{\partial U}{\partial X}+\frac{\partial V}{\partial Y}=0 \tag{1}$$

Table 1 Constant input variables

l (mm)	ps (mm)	w (mm)	t (mm)	rc (mm,deg)	ε_p	ε_b	ε_∞	k_b (W/m-K)
379.6	22.2	25.4	0.17	52.3, 27.3	0.81	0.81	1.00	120

Table 2 Sequence of numerical conditions

Case	q_h (W/m^2)	T_∞ (K)	T_p (K)	ϕ (deg)	b (mm)	n (mm)
1	125	297	283	0	15.4	3.0
2	150	297	298	0	15.4	3.0
3	125	297	283	0	20.0	7.3
4	150	297	298	0	20.0	7.3
5	125	297	283	45	15.4	7.3
6	150	297	298	45	15.4	7.3
7	125	297	283	-45	15.4	7.3
8	150	297	298	-45	15.4	7.3

$$\frac{1}{\mathrm{Pr}}\left(U\frac{\partial U}{\partial X}+V\frac{\partial U}{\partial Y}\right)=-\frac{\partial P}{\partial X}+\left(\frac{\partial^2 U}{\partial X^2}+\frac{\partial^2 U}{\partial Y^2}\right) \tag{2}$$

$$\frac{1}{\mathrm{Pr}}\left(U\frac{\partial V}{\partial X}+V\frac{\partial V}{\partial Y}\right)=-\frac{\partial P}{\partial Y}+\left(\frac{\partial^2 V}{\partial X^2}+\frac{\partial^2 V}{\partial Y^2}\right)+\mathrm{Ra}_R(T^*-1) \tag{3}$$

$$U\frac{\partial T^*}{\partial X}+V\frac{\partial T^*}{\partial Y}=\left(\frac{\partial^2 T^*}{\partial X^2}+\frac{\partial^2 T^*}{\partial Y^2}\right) \tag{4}$$

The above equations have been cast in dimensionless form using the following dimensionless variables

$$X=\frac{x}{l}\quad Y=\frac{y}{l}\quad U=\frac{u}{\alpha_f/l} \tag{5}$$

$$V=\frac{v}{\alpha_f/l}\quad P=\frac{pl^2}{\mu_f\alpha_f}\quad T^*=\frac{T}{T_\infty}$$

Note that the temperature has been scaled using the absolute ambient temperature because of the coupled radiative heat transfer. As a result, in Eq. (3) the modified or ''Radiation'' Rayleigh number (Ra_R) has been defined as

$$\mathrm{Ra}_R=\frac{g\beta_f T_\infty l^3}{\alpha_f \upsilon_f} \tag{6}$$

However, the results will be presented in terms of the conventional Rayleigh number (Ra_l)

$$\mathrm{Ra}_l=\frac{g\beta_f(T_p-T_\infty)l^3}{\alpha_f \upsilon_f} \tag{7}$$

The relationship between Ra_R and Ra_l is

$$\mathrm{Ra}_l=\mathrm{Ra}_R(T_p^*-1) \tag{8}$$

Steady conduction in the solid blind is governed by Fourier's Equation in Laplacian form

$$\frac{\partial^2 T^*}{\partial X^2}+\frac{\partial^2 T^*}{\partial T^2}=0 \tag{9}$$

The dimensionless flux to the top of each slat surface is

$$q_b^*=\frac{q_b l}{k_f T_\infty} \tag{10}$$

The radiative heat transfer was calculated using the net radiation method [10], assuming all surfaces to be gray and diffuse. The dimensionless radiative heat flux from each sub-surface (q_j') was calculated as follows

$$\sum_{j=1}^{N}\left(\frac{\delta_{kj}}{\varepsilon_j}-F_{kj}\frac{1-\varepsilon_j}{\varepsilon_j}\right)q_j^*=N_{RC}\sum_{j=1}^{N}F_{kj}(T_k^{*4}-T_j^{*4}) \tag{11}$$

where

$$q_j^*=\frac{q_j l}{k_f T_\infty}\quad\text{and}\quad N_{RC}=\frac{\sigma T_\infty^3 l}{k_f}$$

In Eq. (11), N_{RC} the radiation-to-conduction interaction parameter.

A sketch of the dimensionless computational domain is shown in Fig. 1. Referring to Fig. 1, the dimensionless boundary conditions are

$$U=V=0,\quad T^*=T_p^*\quad \mathrm{GH}$$

$$U=V=0,\quad T^*=T_p^*\quad \mathrm{FG,\ HA}$$

$$\partial U/\partial X=V=0,\quad T^*=1\quad \mathrm{BCDE}$$

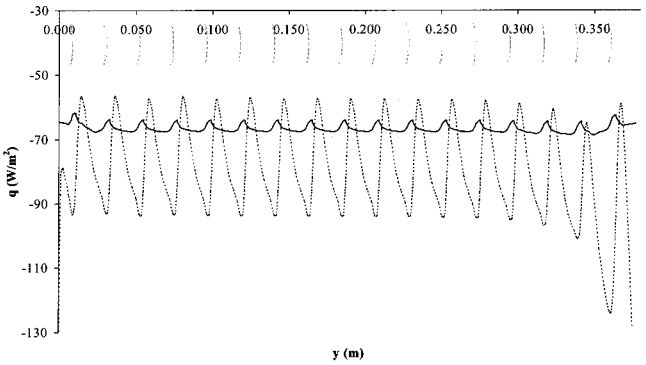

Fig. 2 Convective and radiative heat flux for validation case 1: $b=15.4$ mm, $\phi=0$ deg, $T_p=283$ K. The solid and dotted lines represent radiative and convective heat transfer respectively. Slat positions are superimposed on graphs for clarity.

At the surface of the slats, no-slip and impermeability conditions apply ($U=V=0$). Continuity conditions for temperature and heat flux also apply at this solid-fluid interface, which can best be expressed in dimensionless form as:

$$K_{bf}\left.\frac{\partial T^*}{\partial N}\right|_{\text{solid}}=\left.\frac{\partial T^*}{\partial N}\right|_{\text{fluid}}+\frac{q_b l}{k_j T_i}-\frac{q_j l}{k_f T_i} \tag{12}$$

where N is the normal vector and K_{bf} is the blind to fluid conductivity ratio.

Equations (1) through (11) have been solved subject to the specified boundary conditions using a finite element method. Nine-node quadratic elements with biquadratic interpolation functions were used for temperature and velocity. Pressure was eliminated from the momentum equations using the penelty formulation [11]. The discretized equations were solved using successive substitution, with incremental loading and under-relaxation to speed convergence.

Numerical accuracy was checked in a number of ways. Extensive grid density and far field boundary testing has been done [3]. Based on this testing, a graded mesh with approximately 27,000 nodes was used. Referring to Fig. 1, upper (FE) and lower (AB) entrance regions were set at a dimensionless height of 0.105, and the dimensionless domain width was set at 0.171. At these values, the average convective and radiative Nusselt number data were found to be grid and boundary independent. The ability of the model to model free convection from a vertical plate (with no slats) was also compared to Ostrach's [12] boundary layer solution. That analysis showed agreement 4.1 percent difference in the calculated Nusselt number at $\mathrm{Ra}_l=10^6$, and 0.8 percent difference at $\mathrm{Ra}_l=10^8$. Finally, numerical results have been verified experimentally in a companion paper [13].

Results and Discussion

For clarity in presenting the results, the dimensional flux is presented instead of the Nusselt number. Due to the fact that the isothermal surface can be hot or cold, negative and positive Nusselt numbers result, where the sign is not indicative of the direction of heat flow. For the present convention, positive flux is from the surface, while negative is into the surface. Local and average heat flux rates can be seen in Figs. 2 to 9 and Table 3 respectively. Slat positions are shown in gray in Figs. 2 to 9.

The convective and radiative flux for the cold surface was consistently larger in magnitude than that for the warm surface when considering cases involving identical geometry. For example, the convective flux for the cold surface was 52 percent larger in magnitude than that for the warm surface when considering cases 1 and 2. The remaining cases show an increase of 141 percent between the cold and hot surface results. The average radiative heat

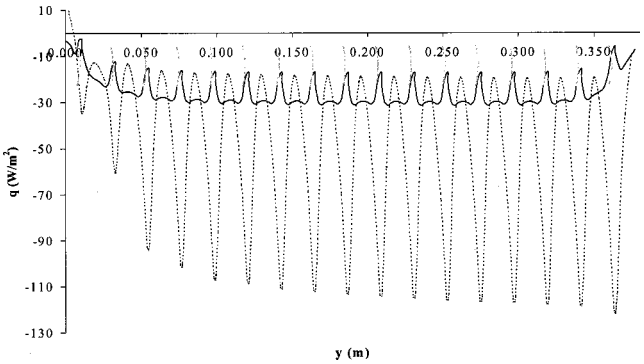

Fig. 3 Convective and radiative heat flux for validation case 2: $b=15.4$ mm, $\phi=0$ deg, $T_p=298$ K. The solid and dotted lines represent radiative and convective heat transfer respectively. Slat positions are superimposed on graphs for clarity.

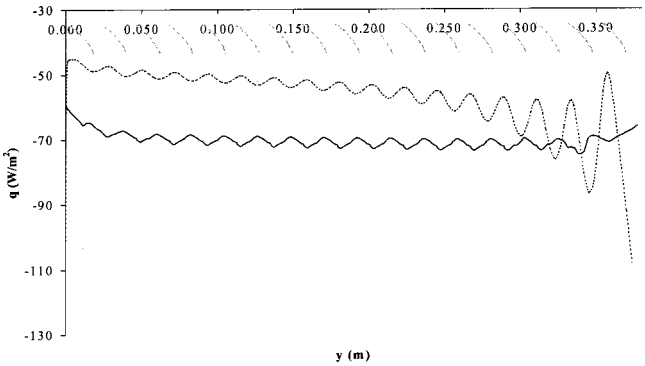

Fig. 6 Convective and radiative heat flux for validation case 5: $b=15.4$ mm, $\phi=45$ deg, $T_p=283$ K. The solid and dotted lines represent radiative and convective heat transfer respectively. Slat positions are superimposed on graphs for clarity.

flux for the cold surface was 162 percent larger than that for the warm surface when considering 0 deg slat tilt, i.e., cases 1 verses 2, and 3 verses 4. The +45 deg and −45 deg tilt angles show an increase of 108 percent between the cold and hot surface results, i.e., cases 5 verses 6, and 7 verses 8. In all cases, the average heat transfer occured in the direction of the surface. This is a significant point. Conceivably, heat transfer at the window surface may occur when no surface-to-air temperature difference exists due to heating of the shade layer. As such, a modified interior heat transfer coefficient may be indeterminate. It does not, however, prevent analysis of the heat transfer at the inner glass, or analysis of a fenestration from that perspective.

The radiative and convective heat transfer are of the same magnitude for the cases examined. Although the emissivities of the louvers and plate are representative of those found in many window and shade systems, it does present the possibility that thermal aspects of the system can be controlled to a significant degree by modifying emissivities. Decreasing the glass emissivity should result in less radiant exchange between the louvers and room, and

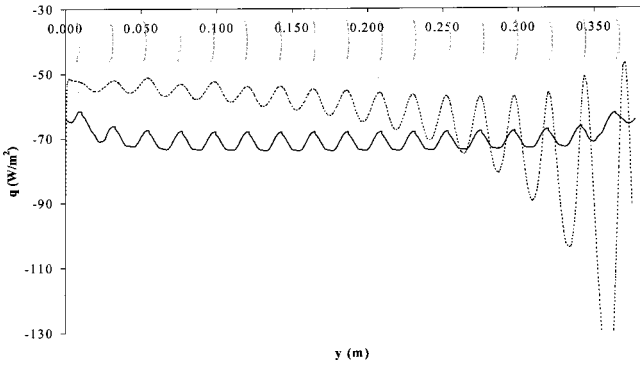

Fig. 4 Convective and radiative heat flux for validation case 3: $b=20.0$ mm, $\phi=0$ deg, $T_p=283$ K. The solid and dotted lines represent radiative and convective heat transfer respectively. Slat positions are superimposed on graphs for clarity.

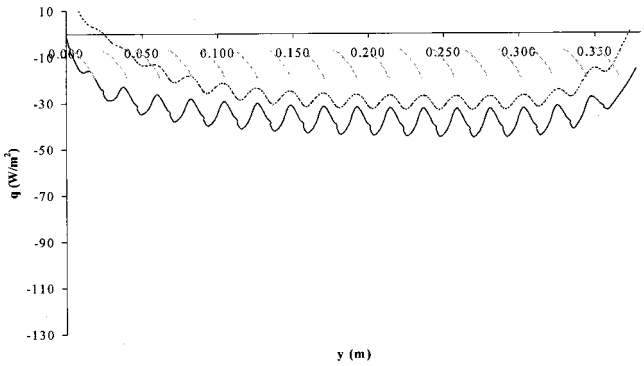

Fig. 7 Convective and radiative heat flux for validation case 6: $b=15.4$ mm, $\phi=45$ deg, $T_p=298$ K. The solid and dotted lines represent radiative and convective heat transfer respectively. Slat positions are superimposed on graphs for clarity.

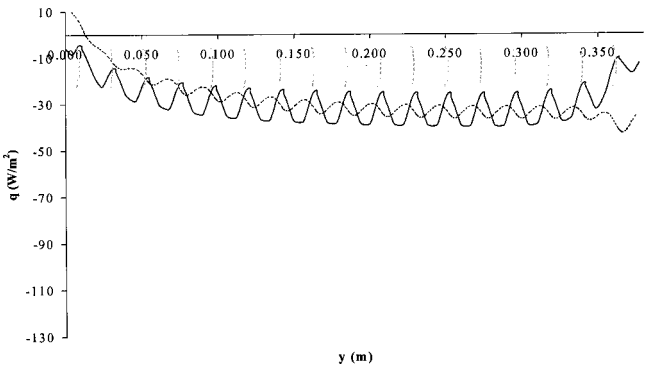

Fig. 5 Convective and radiative heat flux for validation case 4: $b=20.0$ mm, $\phi=0$ deg, $T_p=298$ K. The solid and dotted lines represent radiative and convective heat transfer respectively. Slat positions are superimposed on graphs for clarity.

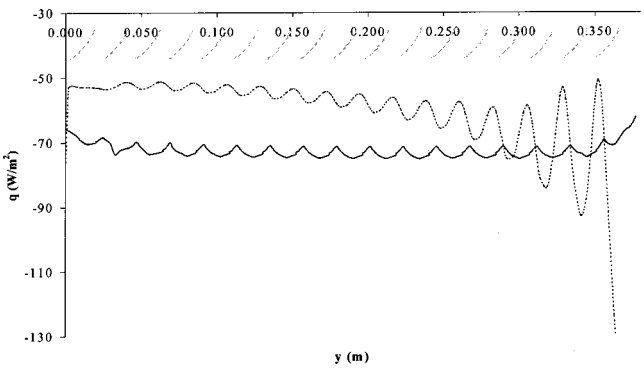

Fig. 8 Convective and radiative heat flux for validation case 7: $b=15.4$ mm, $\phi=-45$ deg, $T_p=283$ K. The solid and dotted lines represent radiative and convective heat transfer respectively. Slat positions are superimposed on graphs for clarity.

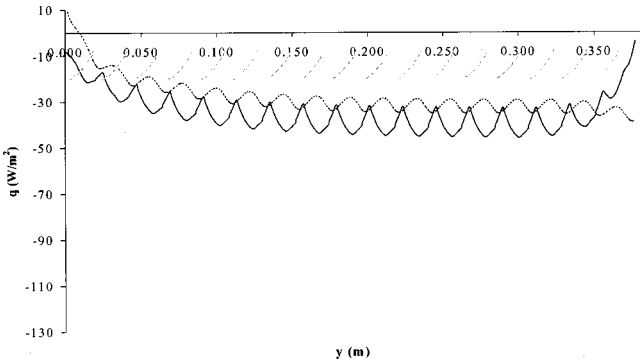

Fig. 9 Convective and radiative heat flux for validation case 8: $b=15.4$ mm, $\phi=-45$ deg, $T_p=298$ K. The solid and dotted lines represent radiative and convective heat transfer respectively. Slat positions are superimposed on graphs for clarity.

the window. This would result in an increase in the level of absorbed solar energy which stays within the room, and a decrease in the radiative heat transfer to and from the glass surface (i.e., the window would have a higher thermal resistance). Increasing the glass emissivity would have the opposite effect. Decreasing the blind emissivity would likely result in higher louver temperatures and greater convective heat transfer from the lovers, but would otherwise have little effect on heat transfer from the glass. Again, increasing the louver emissivity would have the opposite effect.

A more significant result is apparent when considering the effects of system geometry. In Figs. 2 and 3, for cases 1 and 2, the proximity of the slat leading edges and the surface produce a significant periodic effect on the convection from the surface, where an increase in the local convective flux occurs when the leading edge and surface are positioned close together. In Figs. 4 through 9, for cases 3 to 8, when the slat leading edge was furthest from the surface, the blind angle was observed to have little effect on the convective heat flux. Considering radiative heat flux, for cases 1 and 2, when the slat leading edge was closest to the surface, peaks in the local heat transfer rate were sharper and more distinct than in the other models. In this case, a decrease in the local radiative flux occured when the leading edge and surface were close together. As the blind was moved away from the surface, the ''view'' from the surface becomes largely independent of vertical location and slat angle. In cases 3 to 8, while some periodicity is evident in both the radiative and convective heat flux, the results of cases 3, 5, and 7 and cases 4, 6, and 8 are not significantly different. The physical significance of this result is apparent. Solar heat gain is more strongly influenced by the level of directly transmitted and reflected solar radiation, then the inward-flow of absorbed solar radiation. Changing the placement and angle of a blind louver has little effect on the thermal characteristics of the system, unless the blind is very close to the indoor glass surface.

Table 3 Numerically predicted convective and radiative heat flux from the surface. Results for the middle third of the surface are presented in brackets.

Case	$\overline{q}_C$ (W/m^2)	$\overline{q}_R$ (W/m^2)
1	-79.2 (-79.0)	-66.6 (-66.7)
2	-52.2 (-57.1)	-25.4 (-27.9)
3	-64.0 (-60.8)	-70.4 (-71.6)
4	-27.5 (-32.0)	-28.9 (-33.2)
5	-56.1 (-56.1)	-70.3 (-72.6)
6	-21.3 (-29.7)	-34.0 (-38.7)
7	-62.4 (-59.5)	-72.6 (-75.7)
8	-27.6 (-31.8)	-34.9 (-40.3)

The final trend evident from this data is the steady and periodic nature of the data. If the first five slats from the bottom and top of each model are disregarded, q_C and q_R do not change significantly with location. Previous investigations [1,3] have also suggested that the blind may suppress boundary layer growth. Together, these points give confidence in using the model to predict center-of-glass heat transfer for larger window and shade systems. Unfortunately, this did not hold true for all of the validation cases. In cases 4, 6, and 8, the viewfactor between the surface and the louvers was large, and the blind slat temperature continued to rise with increased distance up the surface, thereby producing a gradual increase in q_R. Likewise, an increase was noted in the level of convective flux from the surface when the blind was further away and counterflow existed (cases 3, 5, and 7). While some of this increase was due to boundary layer growth, the majority was undoubtedly a result of end effects. Even though the cases represented extreme conditions, the increase in radiative and convective flux was not significant, and should not prevent a center-of-glass analysis with the data.

Conclusions

Numerically determined radiative and convective heat transfer from an indoor window glazing with an adjacent horizontal Venetian blind has been obtained. The following conclusions were drawn from the results.

- For the cases examined, convective and radiative heat flux was found to be into the surface, despite the fact that for cases 2, 4, 6, and 8, the surface temperature was higher than the ambient room temperature. This prevents the determination of an equivalent air film coefficient for the inside glazing, i.e., the hot blind layer would result in negative and indeterminate heat transfer coefficients. Total heat flux at that boundary, however, may still be used to determine solar heat gain for the system.
- Radiative and convective heat transfer were of the same magnitude in all cases. Some control heat transfer from the system could therefore be accomplished by manipulating the emissive properties of the glass and blind.
- The effect of louver tip to surface spacing was clearly demonstrated. As the louver is moved away from the surface, the local convective and radiative heat flux were less affected by individual louvers. There was little difference between the results of cases 3, 5 and 7, and 4, 6, and 8, despite the fact that the louver angle changed. At a certain spacing, the dimension b was no longer needed to determine heat transfer from the system. Thermal gain in a window and shade combination cannot be effectively controlled by these parameters.
- For the majority of cases, in the middle section of the surface, the local convective and radiative heat flux results tended to be periodic with very little increase in magnitude. Slight increases in the radiative flux, however, could be seen under specific conditions. While this growth could conceivably become significant, it was unavoidable, and the validity of a traditional center-of-glass analysis was supported. Future analysis may be needed on a larger system to determine under what conditions this growth occurs.

Acknowledgments

The authors gratefully acknowledge the support of the Natural Sciences and Engineering Research Council of Canada. Jeff Phillips, Alan Machin, and Nuno Duarte are also thanked for their contributions.

Nomenclature

b = nominal louver spacing, mm
F = radiation shape factor, dimensionless

g = gravity, m/s^2
k = conductivity, W/m-K
K = conductivity, dimensionless
l = surface height, mm
n = louver tip to surface spacing, m
N = normal vector
N_{RC} = radiation-to-conduction interaction parameter, dimensionless
P = pressure, Pa
P = pressure, dimensionless
Pr = Prandtl number, dimensionless
ps = louver pitch, mm
q = heat flux, W/m^2
Ra = Raleigh number, dimensionless
rc = louver radius of curvature, mm
t = louver thickness, mm
T = temperature, K
u, v = velocity, m/s
U, V = velocity, dimensionless
w = louver width, mm
x, y = coordinate axis, mm
X, Y = coordinate axis, dimensionless

Symbols

α = thermal diffusivity, m^2/s
β = volume expansion coefficient, l/K
δ = Kronecker delta, dimensionless
ε = emissivity, dimensionless
ϕ = louver angle, deg.
μ = dynamic viscosity, kg/m-s
ν = kinematic viscosity, m^2/s
σ = Stefan-Boltzmann Constant, W/m^2-K^4

Subscripts

C = convective
b = blind
f = fluid
p = surface
R = radiative
∞ = ambient/room

Other

$*$ = alternative dimensionless notation
$\overline{\ }$ = average

References

[1] Machin, A. D., Naylor, D., Oosthuizen, P. H., and Harrison, S. J., 1998, ''Experimental Study of Free Convection at an Indoor Glazing Surface with a Venetian Blind,'' Journal of HVAC&R Research, **4**(2), pp. 153–166.

[2] Ye, P., Harrison, S. J., Oosthuizen, P. H., and Naylor, D., 1999, ''Convective Heat Transfer from a Window with Venetian Blind: Detailed Modeling,'' ASHRAE J., **105**(2), pp. 1031–1037.

[3] Phillips, J., Naylor, D., Oosthuizen, P. H., and Harrison, S. J., 2000, ''Modeling of the Conjugate Heat Transfer from a Window Adjacent to a Louvered Shade,'' *Sixth International Conference on Advanced Computational Methods in Heat Transfer*, Madrid, Spain, pp. 127–136.

[4] Klems, J. H., and Warner, J. L., 1992, ''A New Method for Predicting the Solar Heat Gain Coefficient of Complex Fenestration Systems,'' *Thermal Performance of the Exterior Envelope of Buildings Conference V*, Clearwater Beach, FL.

[5] Wright, J. L., 1992, ''Glazing System Thermal Analysis,'' CANMET, Advanced Glazing System Laboratory, VISION3, Minister of Supply and Services Canada, University of Waterloo, 1992.

[6] Finlayson, E. U., Arasteh, D. K., Huizenga, C., Rubin, M. D., and Reilly, M. S., 1993, ''WINDOW 4.0: Documentation of Calculation Procedures,'' Energy and Environmental Division, Lawrence Berkeley Laboratory.

[7] Touloukian, Y. S., Liley, P. E., and Saxena, S. C., 1970, ''Thermal Conductivity: Nonmetallic Liquids and Gases,'' *Thermophysical Properties of Matter*, **3**, Thermophysical Properties Research Center (TPRC), Purdue University, Plenum Publishing, New York.

[8] Touloukian, Y. S., and Makita, T., 1970, ''Specific Heat: Nonmetallic Liquids and Gases,'' *Thermophysical Properties of Matter*, **6**, Thermophysical Properties Research Center (TPRC), Purdue University, Plenum Publishing, New York.

[9] Touloukian, Y. S., Saxena, S. C., and Hestermans, P. 1975, ''Viscosity: Nonmetallic Liquids and Gases,'' *Thermophysical Properties of Matter*, **11**, Thermophysical Properties Research Center (TPRC), Purdue University, Plenum Publishing, New York.

[10] Siegel, R., and Howell, J. R., 1970, *Thermal Radiation Heat Transfer*, McGraw-Hill, Toronto.

[11] Fluent, 1999, ''FIDAP 8 Documentation Suite,'' Fluent Inc.

[12] Ostrach, S., 1953, ''An Analysis of Laminar Free-Convection Flow and Heat Transfer about a Flat Plate Parallel to the Direction of the Generating Body Force,'' NACA Technical Report 1111.

[13] Collins, M., Harrison, S. J., Oosthuizen, P. H., and Naylor, D., 2002, ''Heat Transfer from an Isothermal Vertical Surface with Adjacent Heated Horizontal Louvers: Validation,'' Submitted for publication to ASME Journal of Heat Transfer.

M. Collins
e-mail: mcollins@uwaterloo.ca
Dept. of Mechanical Engineering,
University of Waterloo,
Waterloo, Ontario N2L 3G1, Canada

S. J. Harrison
e-mail: harrison@me.queensu.ca
Dept. of Mechanical Engineering,
Queen's University,
Kingston, Ontario K7L 3N6, Canada

D. Naylor
e-mail: dnaylor@acs.ryerson.ca
Dept. of Mechanical, Aerospace, and Industrial Engineering,
Ryerson University,
Toronto, Ontario M5B 2K3, Canada

P. H. Oosthuizen
e-mail: oosthuiz@me.queensu.ca
Dept. of Mechanical Engineering,
Queen's University,
Kingston, Ontario K7L 3N6, Canada

Heat Transfer From an Isothermal Vertical Surface With Adjacent Heated Horizontal Louvers: Validation

The present study examines the influence of heated, horizontal, and rotateable louvers on the convective heat transfer from a heated or cooled vertical isothermal surface. The system represents an irradiated Venetian blind adjacent to the indoor surface of a window. Detailed temperature field and local surface flux data were obtained using a Mach-Zehnder Interferometer for two window temperatures (warm and cool compared to ambient) and irradiation levels, two louver to plate spacings, and three louver angles. The results have been compared to a steady, laminar, two-dimensional, conjugate conduction/convection/radiation finite element model of this problem. The effect of the heated louvers on the heat transfer rate from the plate surface has been demonstrated and the results of the numerical study have been validated. [DOI: 10.1115/1.1481358]

Keywords: Experimental, Heat Transfer, Interferometry, Mixed Mode, Modeling

Introduction

It is common for a louvered shading device, such as a Venetian blind, to be mounted on the indoor surface of a window to provide privacy and to control day-lighting. In addition, the presence of these shading devices will affect natural convection and radiant heat exchange from the window. As a result, there will be a change in the heat transmission and solar heat gain, through the window.

At present, advances are being made that demonstrate the complex thermal interaction between a shade and a window, in the absence of solar irradiation. Several previous studies have examined the effect of a Venetian blind on the free convective heat transfer at an indoor glazing surface when there is no solar irradiance (i.e., for ''nighttime'' conditions). Machin et al. [1] performed interferometry and flow visualization. Their experiment used a Mach-Zehnder Interferometer to examine the local and overall convection coefficients from the surface of an isothermal plate at various blind to plate spacings and louver angles. They found that when an aluminum blind was placed close to the plate surface, the slats caused a strong periodic variation in the local Nusselt number distribution. Ye et al. [2] conducted a two-dimensional finite element study of this problem. In that study, the effects of thermal radiation were neglected and the blind slats were modeled as zero thickness, no-slip, impermeable surfaces. A similar numerical study has been done by Phillips et al. [3], which included the effect of heat conduction along the blind slats and radiation heat exchange. Their improved model showed excellent correlation with interferometric data.

In Collins et al. [4] a move from the previously mentioned ''nighttime'' models, to a ''daytime'' model that included the effects of incident solar energy was performed. In the present study, convective heat transfer results, obtained using a Mach-Zehnder Interferometer, are used to validate that numerically model. Additionally, temperatures measured during the experiments will be compared to numerically predicted temperatures.

It should be stated that while radiation exchange was calculated in the numerical model, the experimental setup can only measure convective heat transfer. As such, only data resulting from the numerical and experimental analysis of free convection will be presented here. However, considering the strongly coupled nature of the radiative and convective heat transfer in this system, validation of the convective heat transfer provides excellent confidence in the radiative model.

Apparatus and Procedure

In the experimental study, the indoor glazing surface was idealized as an isothermal vertical flat plate of height (l) that was heated to temperature (T_p) above the ambient room temperature (T_∞). A Venetian blind consisting of seventeen horizontal louvers, was positioned a nominal distance (b) from the plate surface and the individual slats were inclined at an angle with respect to the horizontal (ϕ). A heat flux (q_b) was applied to one side of each slat to simulate the solar radiation absorbed by the blind. Figure 1 shows the system geometry and a photograph of the physical system.

The experimental setup is an idealized representation of a real fenestration. For an actual window, there will be frame effects and only the center-of-glass region will be nearly isothermal. Also, the actual indoor glazing temperature will increase with the solar irradiance, rather than being fixed. However, the idealized system is consistent with the numerical model, and these simplifications eliminate several secondary parameters, such as the frame geometry and the glazing external thermal boundary condition.

The flat plate used for this experiment was machined from two sheets of Aluminum. The main sheet had flow channels milled into the back surface, while the front surface of the plate (the experimental surface) was precision flat milled. Testing on a coordinate mapping machine showed it flat to within ± 0.046 mm of the average height. Pins placed in precisely located holes drilled into the front of the plate aided in leveling the experimental model and examination of the resulting interferograms. The second Aluminum sheet became the backing plate and served to close the flow channels with the aid of an O-ring and liquid gasketing. The assembled plate was backed with foam insulation and mounted on an Aluminum stand. An illustration of the plate is given in Fig. 2.

Contributed by the Heat Transfer Division for publication in the JOURNAL OF HEAT TRANSFER. Manuscript received by the Heat Transfer Division June 18, 2001; revision received March 7, 2002. Associate Editor: C. Amon.

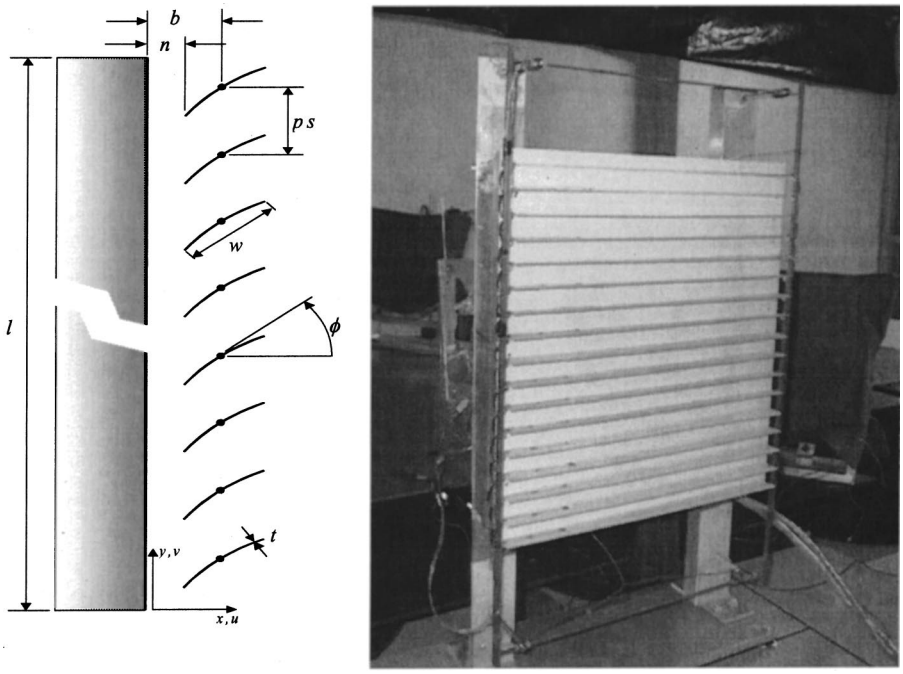

Fig. 1 System geometry (left) and photo (right)

The plate was heated and cooled using a precision temperature bath. It was intended that the flow channel configuration, in which the inlet and outlet coil inward side by side, would make the plate essentially isothermal. Ten precision drilled holes were made from the plate back so that thermocouples could be inserted to just below the test surface of the experimental setup. Testing showed that the plate remained isothermal to within ± 0.1°C from the average over the entire surface.

Slats from a commercially available aluminum Venetian blind were used for this experiment. The slats had a width (w), thickness (t), an arc length and a radius of curvature (rc) typical of many commercially available products. The slats were held at a pitch of ($ps = 22.2$ mm) by two precision machined steel posts. This slat pitch ratio ($ps/w = 7/8$) is typical of commercially available Venetian blinds. To simulate solar loading, two thin foil electric heaters (with dimensions 167 mm$\times$14 mm$\times$0.15 mm) were bonded to the concave side of each slat. After the heaters were bonded to the slats, they were sprayed with paint to give a uniform hemispherical emissivity ($\varepsilon_p = \varepsilon_b = 0.81$). The slat thermal conductivity (k_b) was also measured. Fine thermocouples (40 gauge) were bonded to the top surface of the slats using high conductivity epoxy. The thermocouple tips were placed one third the way along the length of the slat and in the center of the slat profile.

For each experiment, the blind slats were adjusted to the desired slat angle using a jig. The blind tip to plate spacing was subsequently adjusted using gauge blocks. Consequently, the inner slat tip to plate spacing was carefully controlled, and the slat angle varied slightly from slat to slat because of small dimen-

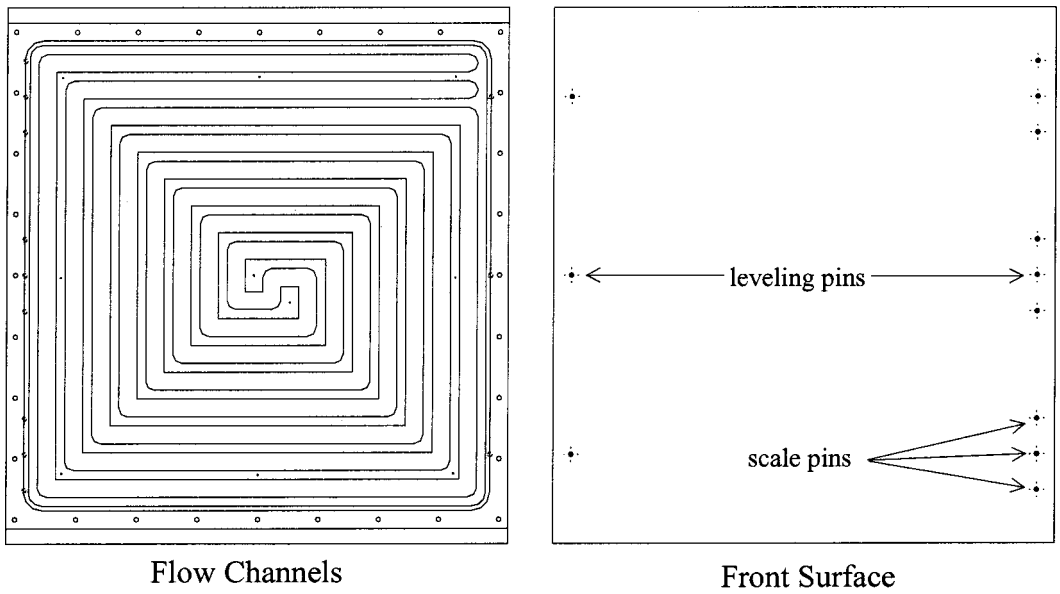

Fig. 2 Schematic of isothermal plate (back cover removed for clarity)

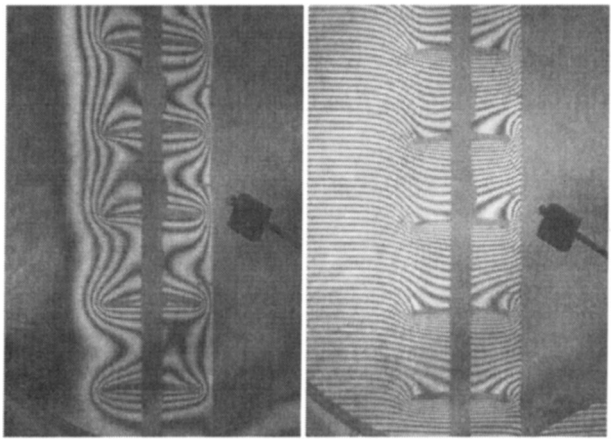

Fig. 3 Comparison of infinite fringe (left) and wedge fringe (right) interferograms

sional imperfections. This approach was taken because previous experimental and numerical studies with an unheated blind have shown that it is more important to control the slat tip to plate spacing [1,3]. The vertical position of the blind relative to the plate was such that the lower tip of the first slat was in line with the plate leading edge when the blind was fully closed.

Due to optical restrictions, the maximum interferogram size could only be 0.20 m in diameter, whereas the experimental model was 0.38 m high. As a result, accounting for some picture overlap, and the loss of some information at the top and bottom of the circular interferogram, it was decided to examine the plate as three distinct sections. The plate and blind were mounted on a table that allowed control of the experimental model's vertical position. Interferograms were then taken at the bottom, middle, and top of the experimental model.

An optical window mounted in a sheet of acrylic was placed on each end of the model. This assembly prevented entrainment of air into the sides of the model, promoting a more two dimensional flow and temperature field. To reduce the effect of air currents within the laboratory, the interferometer was located inside a large unventilated enclosure.

A 20 cm diameter beam Mach-Zehnder Interferometer was used to measure the heat transfer coefficients. In this instrument, light from a 10 mW He-Ne laser is split into two beams of approximately equal intensity. One beam passes through the uniform temperature ambient air, and the other beam passes by the experimental model. Because of changes in index of refraction in the heated air surrounding the model, the two light beams are no longer in phase when they are recombined. This phase shift produces an interference pattern in the optical output of the Mach-Zehnder Interferometer, which can be photographed. When the test beam and reference beam are parallel upon recombination (the infinite fringe mode), the constructive and destructive interference fringes are isotherms. For an ideal gas, the temperature T is related to the fringe shift η as follows

$$T = \frac{T_p}{\frac{2\eta R\lambda T_p}{3rZp} + 1} \tag{1}$$

where R is the gas constant for air (287.1 Pa m^3/kgK), λ is the wavelength of He-Ne laser light (6.328×10^{-7} m), r is the specific refractivity of air (1.504×10^{-4} m^3/kg), Z is the length of the model in the direction of beam travel (357.7 mm), and p is the absolute ambient pressure.

When the temperature gradient in the air at the plate surface was sufficiently high (approx. $dT/dx = 1500$ K/m), the gradient was calculated by linear extrapolation using the first two clearly visible destructive interference fringes on a scan perpendicular to the surface. Equating the convective heat transfer rate to the conductive heat transfer rate in the air at the surface gives the local heat transfer coefficient (h), as follows

$$h = \frac{-k_p \left.\frac{dT}{dx}\right|_{x=0}}{(T_p - T_\infty)} \tag{2}$$

where k_p is the thermal conductivity of the air evaluated at the plate surface temperature (T_p).

For some experiments the temperature gradient at the surface was very low and an accurate measurement of the gradient could not be obtained from the above extrapolation procedure. A new interferometric technique has been developed recently to overcome this problem. Naylor and Duarte [5] have shown that the temperature gradient can be measured directly from a wedge fringe interferogram. In the wedge fringe mode, the optics are adjusted to produce constant fringe gradient with a spacing (d) in the y-direction, which is superimposed on the fringe field caused be temperature variations. In the ambient, the wedge fringe shift intersects the plate surface at an angle α. It has been shown that the local convective heat transfer coefficient is related to this fringe angle by

$$h = \frac{2R\lambda T_p^2 k_p}{3rZp(T_p - T_\infty)d\tan\alpha} \tag{3}$$

Table 1 Constant input variables

l (mm)	ps (mm)	w (mm)	t (mm)	rc (mm,deg)	ε_p	ε_b	ε_∞	k_b (W/m-K)
379.6	22.2	25.4	0.17	52.3, 27.3	0.81	0.81	1.00	120

Table 2 Sequence of experimental/numerical conditions. Experimental target is in brackets.

Case	q_b (W/m^2)	T_∞ (K)	T_p (K)	ϕ (deg)	b (mm)	n (mm)
1	123.9 (125)	296.7 (297)	283.3 (283)	0	15.4	3.0
2	151.5 (150)	296.2 (297)	298.3 (298)	0	15.4	3.0
3	124.5 (125)	296.2 (297)	283.3 (283)	0	20.0	7.3
4	151.5 (150)	296.7 (297)	298.3 (298)	0	20.0	7.3
5	124.0 (125)	296.5 (297)	283.3 (283)	45	15.4	7.3
6	151.1 (150)	296.2 (297)	297.8 (298)	45	15.4	7.3
7	124.4 (125)	296.7 (297)	283.3 (283)	-45	15.4	7.3
8	151.3 (150)	296.7 (297)	298.3 (298)	-45	15.4	7.3

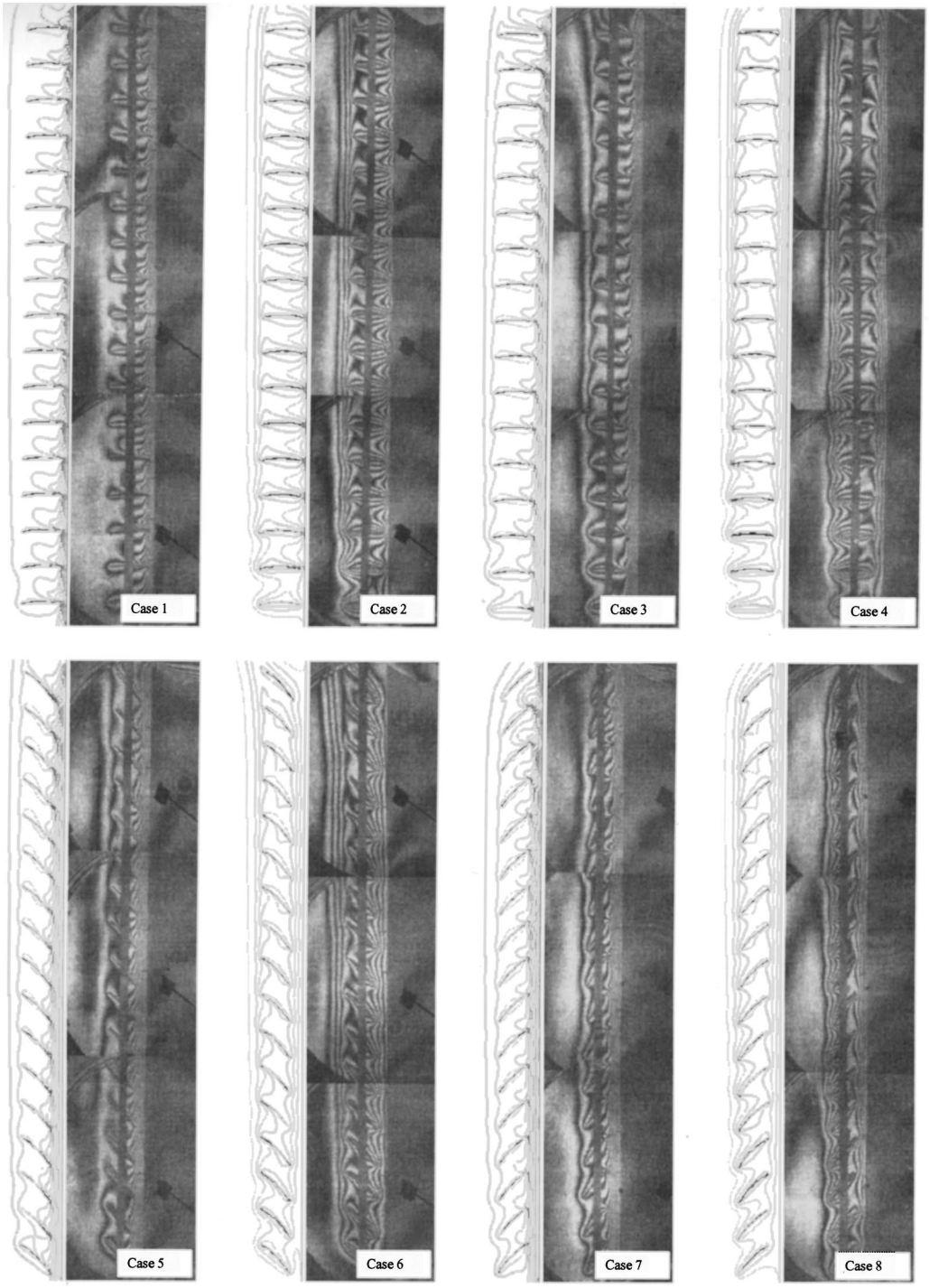

Fig. 4 Comparison of isotherms for all cases. Interferometric (left) and numerical (right).

The local convective heat transfer coefficient was obtained by measuring the angle of intersection of a line of constant fringe shift with the plate. An example of an infinite and a wedge fringe interferogram is given in Fig. 3.

Data was collected in conjunction with the numerical tests described in Collins et al. [4]. As such, two plate temperatures, one level of irradiation, one nominal blind spacing, and three blind angles would be examined. An additional set of test runs at 0 deg slat angle, with an increased nominal distance, allows for an examination of the effects of plate to blind leading edge, n (i.e., 7.3 mm tip-to-plate spacing can be examined despite the fact that the louver angle changes). Steady-state data was collected over a period of approximately 30 min for each experimental case.

Experimental parameters that remained constant for all experiments are given in Table 1. Table 2 shows the sequence of experimental and numerical model conditions. Fluid properties were evaluated at an estimated film temperature of 300 K and were taken from Touloukian et al. [6–8]. Film temperatures predicted by the numerical model after the present analysis showed that the average fluid temperature was between 297 K and 302 K for all validation cases.

With any experimental investigation there is always a certain

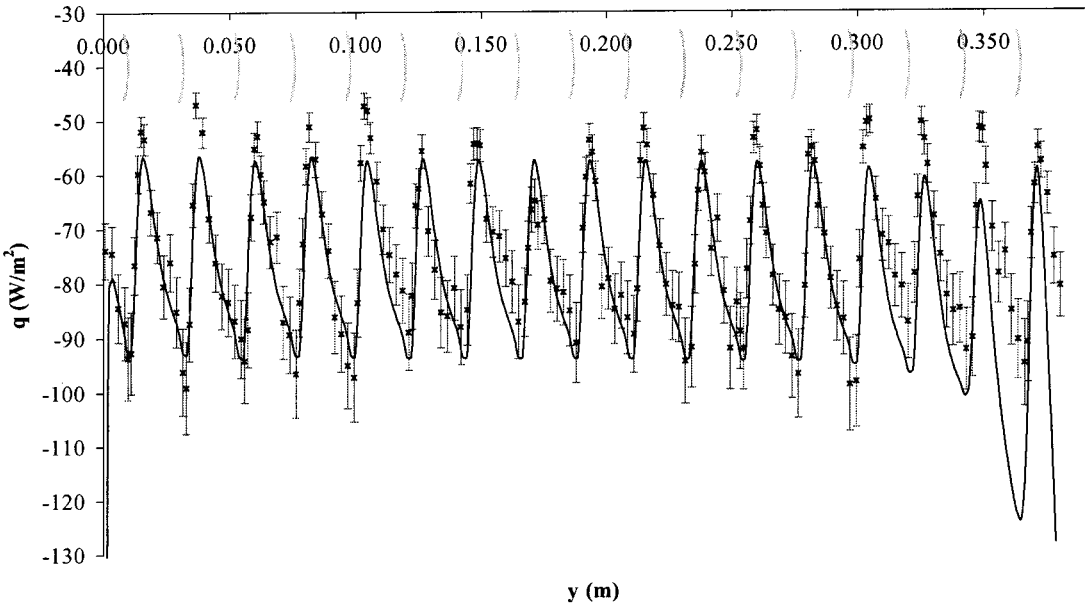

Fig. 5 Convective heat flux for validation case 1: $b=15.4$ mm, $\phi=0$ deg, $T_p=283$ K. Points represent interferometric results with associated experimental uncertainty. Solid line represents numerical results. Slat positions are superimposed on graphs for clarity.

degree of unavoidable uncertainty. Since Mach-Zehnder interferometry is a widely used technique for quantitative heat transfer (and other) measurements, a considerable amount of attention [9,10,11,12] has been directed towards the corrections that are recommended when deviation from when ideal two-dimensional conditions exist. A discussion of probable sources of error inherent in this type of study was done by Machin [13] in his Thesis. The errors discussed were end effects, refraction, diffraction, misalignment, beam convergence/divergence, fringe center location and scale factor.

An uncertainty analysis has been performed on the data using the method of Kline and McClintock [14]. This method uses the relative uncertainty in the various primary experimental measurements to estimate the uncertainty of the final result. If each independent variable was given the same odds, then the relation between the uncertainty for the variables δx_1, and the uncertainty for the result δR, would be

$$\delta R = \pm \sqrt{\left(\frac{\partial R}{\partial x_1}\delta x_1\right)^2 + \left(\frac{\partial R}{\partial x_2}\delta x_2\right)^2 + \cdots + \left(\frac{\partial R}{\partial x_n}\delta x_n\right)^2} \quad (4)$$

Attention should be drawn to relative magnitude of the uncertainties in this root-sum-squared technique. Very little would be accomplished in reducing the uncertainty of any of the smaller variables as the square of the larger variables dominate the total

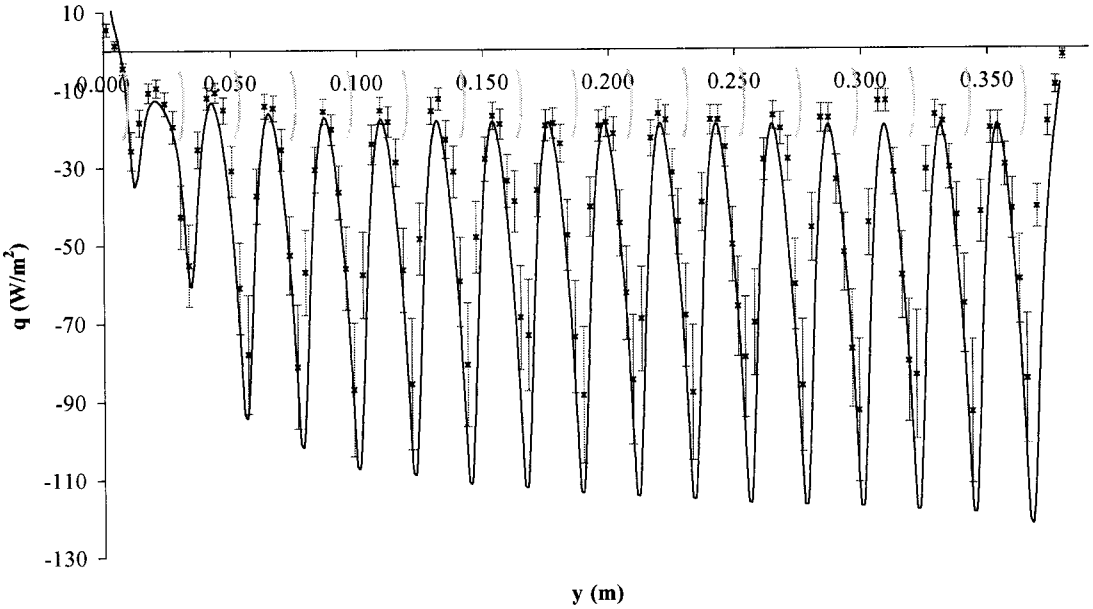

Fig. 6 Convective heat flux for validation case 2: $b=15.4$ mm, $\phi=0$ deg, $T_p=298$ K. Points represent interferometric results with associated experimental uncertainty. Solid line represents numerical results. Slat positions are superimposed on graphs for clarity.

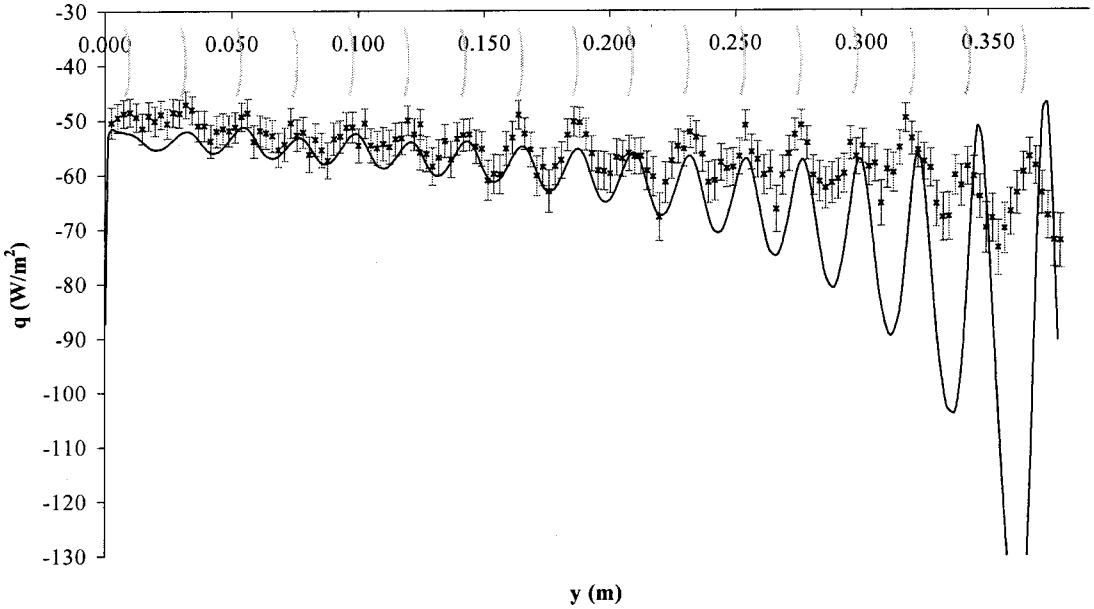

Fig. 7 Convective heat flux for validation case 3: $b=20.0$ mm, $\phi=0$ deg, $T_p=283$ K. Points represent interferometric results with associated experimental uncertainty. Solid line represents numerical results. Slat positions are superimposed on graphs for clarity.

uncertainty in the final result. In this experiment, the accuracy of temperature measurements dominated the uncertainty.

Results and Discussion

For clarity in presenting the results, the dimensional flux has been presented instead of the Nusselt number. Due to the fact that the isothermal plate can be hot or cold, negative and positive Nusselt numbers result, where the sign is not indicative of the direction of heat flow. For the present convention, positive flux is from the plate, while negative is into the plate. A comparison of numerically and experimentally obtained isotherms is given in Fig. 4. Local and average heat flux rates can be seen in Figs. 5–12 and Table 3 respectively. Slat positions and experimental uncertainty are shown in gray in Figs. 5–12.

The experimental data correlated well with numerical results. For the majority of cases, the error is within the uncertainty of the experimentally determined results. More importantly, the instantaneous convective flux, shown in Figs. 5–12, agree with numerically obtained data both in trend and magnitude. Visibly, the surrounding temperature field, as shown in Fig. 4, also shows excellent agreement.

While the quality of the experimental/numerical comparison is good, a number of discrepancies are evident in the experimental data. It is advantageous, at this point, to identify these problems

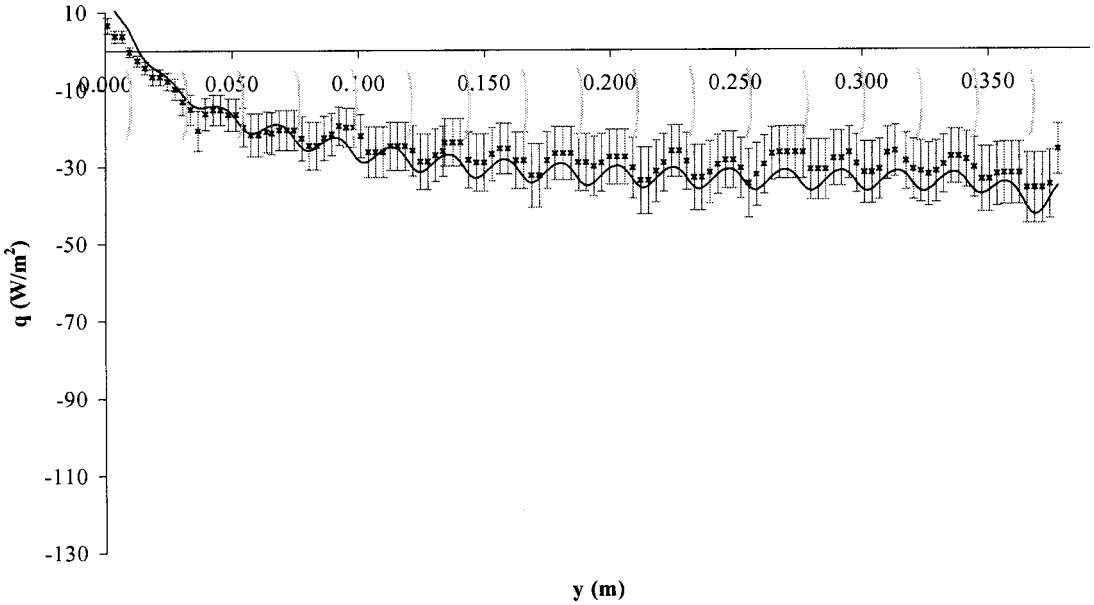

Fig. 8 Convective heat flux for validation case 4: $b=20.0$ mm, $\phi=0$ deg, $T_p=298$ K. Points represent interferometric results with associated experimental uncertainty. Solid line represents numerical results. Slat positions are superimposed on graphs for clarity.

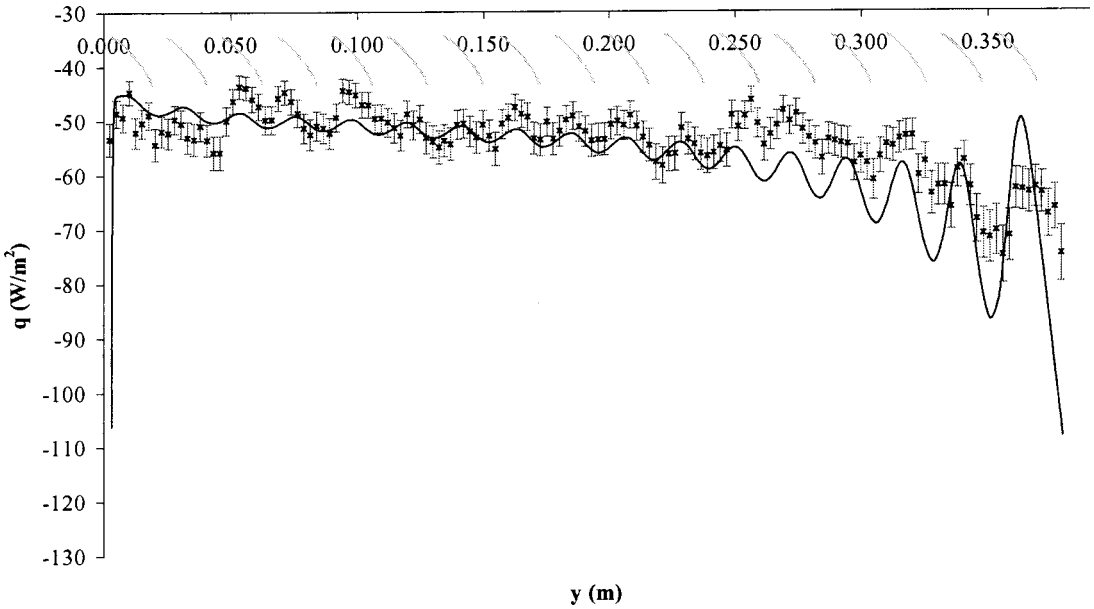

Fig. 9 Convective heat flux for validation case 5: $b=20.0$ mm, $\phi=45$ deg, $T_p=283$ K. Points represent interferometric results with associated experimental uncertainty. Solid line represents numerical results. Slat positions are superimposed on graphs for clarity.

and discuss their significance. They include aspects of modeled verses experimental inlet and outlet conditions, as well as deficiencies in the experimental method.

As indicated in Table 3, the experimentally measured average heat flux for case 2 was found to be 25 percent lower than the numerically predicted results, even though the results shown in Fig. 5 appear to be accurate. The discrepancy is a result of the wedge fringe method of analyzing interferometric data. In this particular case, the fringe angle can only be measured on the fringes themselves, which are spaced by a distance d. With this spacing, the extreme peaks demonstrated by the numerical results have been missed, resulting in an underprediction of the average heat flux.

It was expected that the top and bottom slats in each case would be affected by the radiative heat transfer conditions set in the numerical model. The temperature was not set as a boundary condition on the top and bottom sections of the numerical model because those could either be regions of inflow or outflow. The radiation model, however, must use the temperature of these sections to calculate radiant exchange between the slats and the room in the direction of the inlet and outlet. As a result, the bottom and top slats are largely radiating to the fluid temperature at the inlet and outlet, as opposed to the T_∞. It can be seen in Figs. 5 through 12 that this did not have any noticable effect on the end slats.

One significant difference between the numerical model and the experiment existed at the bottom and top edges of the plate. In the

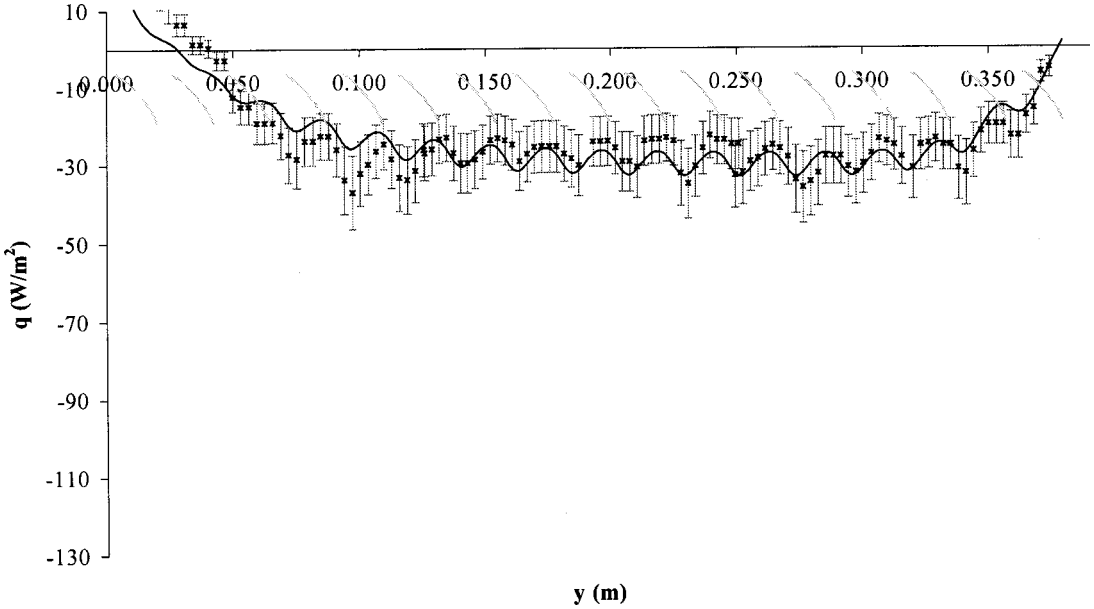

Fig. 10 Convective heat flux for validation case 6: $b=20.0$ mm, $\phi=45$ deg, $T_p=298$ K. Points represent interferometric results with associated experimental uncertainty. Solid line represents numerical results. Slat positions are superimposed on graphs for clarity.

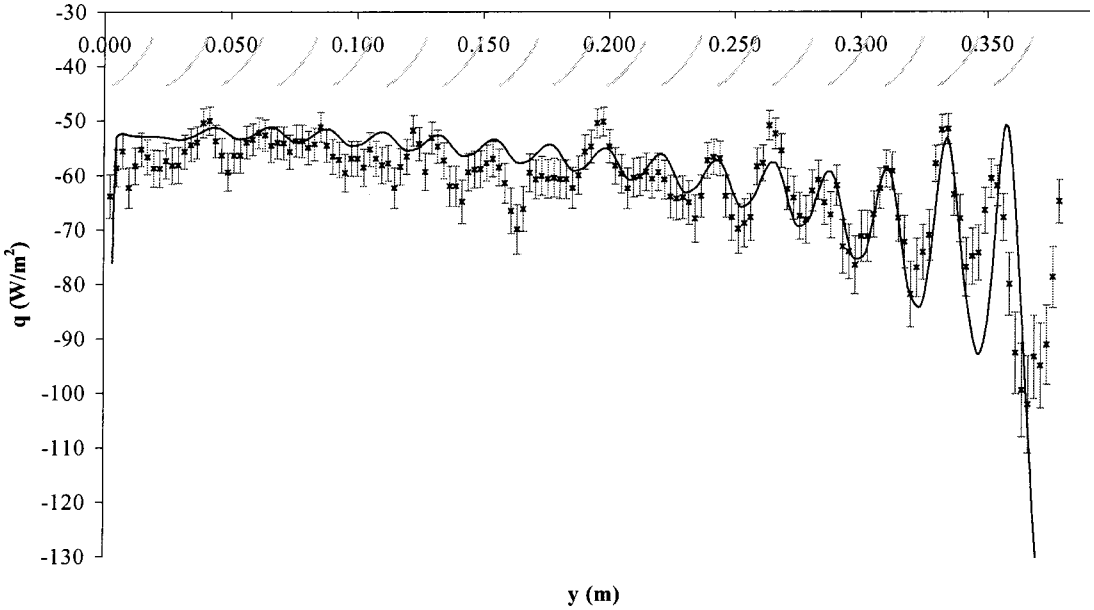

Fig. 11 Convective heat flux for validation case 7: $b=20.0$ mm, $\phi=-45$ deg, $T_p=283$ K. Points represent interferometric results with associated experimental uncertainty. Solid line represents numerical results. Slat positions are superimposed on graphs for clarity.

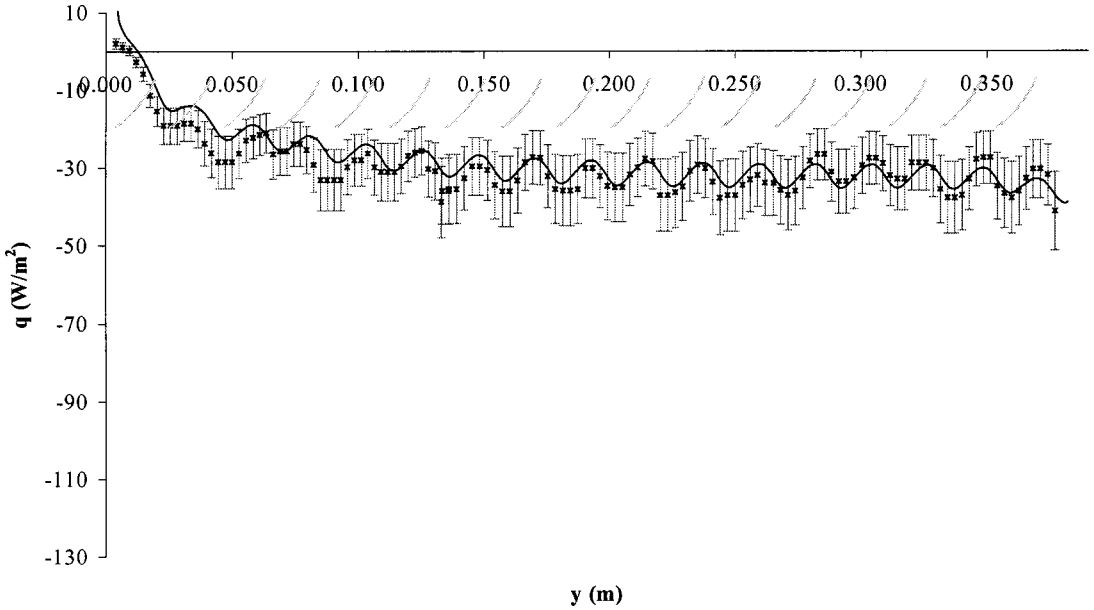

Fig. 12 Convective heat flux for validation case 8: $b=20.0$ mm, $\phi=-45$ deg, $T_p=298$ K. Points represent interferometric results with associated experimental uncertainty. Solid line represents numerical results. Slat positions are superimposed on graphs for clarity.

experiment, flow was entrained around the sharp edge of the plate. In the numerical model, an adiabatic wall continues above and below the plate. While this difference has no identifiable effect on cases where the plate was warmer than the ambient (i.e., cases 2, 4, 6, and 8), it did have an effect on the cases where the plate was cooler than ambient (i.e., cases 1, 3, 5, and 7). In particular, the top portion of data from case 3 does not follow the experimental results as well as any of the other cases. During the experiment, air flowing downward from the cold plate is entrained around the sharp lead edge of the plate, while hot air from the blind rises and is guided away from the plate by the momentum of the air flow which was developed on the room-side of the blind. This allows the boundary layer on the plate to grow unhindered to the topmost slat as if no blind was present. By contrast, because the numerical model assumes that the unheated wall continues above the heated

Table 3 Comparison of predicted and measured convective heat flux for the plate. Results for the middle third of the plate are presented in brackets.

Case	$\overline{q}_C$ Numerical (W/m^2)	$\overline{q}_C$ Experimental (W/m^2)
1	-79.2 (-79.0)	-75.1 (-76.1)
2	-52.2 (-57.1)	-39.2 (-43.4)
3	-64.0 (-60.8)	-55.8 (-56.7)
4	-27.5 (-32.0)	-25.1 (-28.9)
5	-56.1 (-56.1)	-53.1 (-53.4)
6	-21.3 (-29.7)	-20.6 (-27.0)
7	-62.4 (-59.5)	-61.3 (-60.5)
8	-27.6 (-31.8)	-28.9 (-33.4)

Table 4 Comparison of predicted and measured blind slat temperatures. *M* and *E* denote modeled and experimental results, respectively. Experimental measurement accuracy is ±0.2 K.

Case	T Slat 4 (K)		T Slat 6 (K)		T Slat 8 (K)		T Slat 10 (K)		T Slat 12 (K)		T Slat 14 (K)	
	M	E	M	E	M	E	M	E	M	E	M	E
1	299.9	301.0	300.0	301.1	300.0	301.2	300.0	301.5	300.0	301.7	300.1	301.0
2	309.4	309.3	309.6	309.2	309.7	309.2	309.8	309.7	309.8	309.8	309.8	309.6
3	303.1	303.3	303.1	303.2	303.1	303.2	303.1	303.8	303.1	303.7	303.0	303.8
4	309.8	309.7	310.7	310.0	311.1	310.2	311.4	311.0	311.6	311.1	311.7	310.9
5	302.3	301.5	302.4	301.9	302.6	302.0	302.6	302.5	302.8	302.7	302.8	303.1
6	308.7	308.7	309.3	308.7	309.8	308.4	310.0	309.3	310.2	309.4	310.3	308.7
7	302.5	302.4	302.6	302.3	302.7	302.2	302.7	302.7	302.7	302.5	302.8	302.5
8	308.9	308.6	309.9	308.8	310.4	308.6	310.7	309.4	310.8	309.7	311.0	309.5

plate, flow from the blind is pulled back towards the wall by downward flow entrained by the cold plate, thereby increasing the air temperature and heat flux in that area. This effect is less significant in the three other cold cases due to the proximity of the blind to the plate in case 1, and the slat angle in cases 5 and 7. These conditions provide added stability to the flow, which quickly removes the effect of a downward developing boundary layer. This problem was not apparent in the warm plate cases (2, 4, 6, and 8) because no counter flow is produced.

Due to optical restrictions, the experimental data in Figs. 5 through 12 were obtained from three individual photographs. As a result of environmental changes occuring between the times at which these photos were taken, some step discontinuities are evident in all of the data. The flux measured in the top 1/3rd of case 5 demonstrates the problem clearly. This reduction is due to a small change ($<$0.2 K) in the ambient temperature at the time that the final interferometer picture was taken. This was acknowledged as a limitation of the current experimental setup.

Although these discrepancies have been identified, they are not considered to be a weakness of the numerical model. In fact, the continuing unheated portion of wall present in the numerical analysis, is closer to a realistic window situation than the experimental setup. More importantly, if the blind can be shown to suppress the growth of convective heat transfer from the plate surface, the center portion of the model can then be used as a center of glass heat transfer rate for other window sizes. In this respect, the top and bottom portions of the model would be disregarded.

Although the experimental setup is unable to directly validate the radiative heat transfer calculated by the numerical model, blind temperatures measured during the experiments can confirm that predicted blind slat temperatures are correct. Table 4 shows a comparison of this data for selected louvers where the average difference between the modeled and experimental results is only 0.64 K.

As can be seen, the experimental results are in excellent agreement with the numerically obtained temperatures. In this way, additional confidence was gained in the numerical results, especially when considering the predicted radiation exchange.

Conclusions

Experimentally determined natural convective and radiative heat transfer from a horizontal Venetian blind adjacent to an indoor window glazing has been obtained and compared to the results produced with a conjugate heat transfer numerical model of the system. With the exception of some readily explained departures between the experimental and numerical results, the local and average convective heat transfer coefficients were found to agree closely both in magnitudes and trends. Furthermore, experimentally obtained blind temperatures and isotherms were in close agreement with those obtained from the numerical model. This provides additional confidence in the numerical results.

Acknowledgments

The authors gratefully acknowledge the support of the Natural Sciences and Engineering Research Council of Canada. Jeff Phillips, Alan Machin, and Nuno Duarte are also thanked for their contributions.

Nomenclature

b = nominal louver spacing, mm
d = fringe spacing, m
h = heat transfer coefficient, W/m^2-K
k = conductivity, W/m-K
l = plate height, mm
n = louver tip to plate spacing, m
p = pressure, Pa
ps = louver pitch, mm
q = heat flux, W/m^2
r = specific refractivity, m^3/kg
R = gas constant, Pa m^3/kgK
rc = louver radius of curvature, mm
t = louver thickness, mm
T = temperature, K
w = louver width, mm
x, y = coordinate axis, mm
Z = model width, m

Symbols

α = fringe angle, rad or
ε = emissivity, dimensionless
ϕ = louver angle, deg
η = fringe shift, dimensionless
λ = wavelength, m

Subscripts

C = convective
b = blind
f = fluid
p = plate
R = radiative
∞ = ambient/room

Other

$*$ = alternative dimensionless notation
$\overline{\ }$ = average

References

[1] Machin, A. D., Naylor, D., Oosthuizen, P. H., and Harrison, S. J., 1998, "Experimental Study of Free Convection at an Indoor Glazing Surface with a Venetian Blind," Journal of HVAC&R Research, **4**(2), pp. 153–166.

[2] Ye, P., Harrison, S. J., Oosthuizen, P. H., and Naylor, D., 1999, "Convective Heat Transfer from a Window with Venetian Blind: Detailed Modeling," ASHRAE J., **105**(2), pp. 1031–1037.

[3] Phillips, J., Naylor, D., Oosthuizen, P. H., and Harrison, S. J., 2000, "Modeling of the Conjugate Heat Transfer from a Window Adjacent to a Louvered

Shade,'' *Sixth International Conference on Advanced Computational Methods in Heat Transfer*, Madrid, Spain, pp. 127–136.
[4] Collins, M. R., Harrison, S. J., Oosthuizen, P. H., and Naylor, D., 2002, ''Heat Transfer from an Isothermal Vertical Flat Plate With Adjacent Heated Horizontal Louvers: Radiation Analysis,'' Submitted for publication to ASME Journal of Heat Transfer.
[5] Naylor, D., and Duarte, N., 1999, ''Direct Temperature Gradient Measurement Using Interferometry,'' Exp. Heat Transfer, **12**, pp. 279–294.
[6] Touloukian, Y. S., Liley, P. E., and Saxena, S. C., 1970, ''Thermal Conductivity: Nonmetallic Liquids and Gases,'' *Thermophysical Properties of Matter*, **3**, Thermophysical Properties Research Center (TPRC), Purdue University, Plenum Publishing, New York.
[7] Touloukian, Y. S., and Makita, T., 1970, ''Specific Heat: Nonmetallic Liquids and Gases,'' *Thermophysical Properties of Matter*, **6**, Thermophysical Properties Research Center (TPRC), Purdue University, Plenum Publishing, New York.
[8] Touloukian, Y. S., Saxena, S. C., and Hestermans, P., 1975, ''Viscosity: Nonmetallic Liquids and Gases,'' *Thermophysical Properties of Matter*, **11**, Thermophysical Properties Research Center (TPRC), Purdue University, Plenum Publishing, New York.
[9] Eckert, E. R. G., and Goldstein, R. J., *Measurements in Heat Transfer*, Hemisphere Publishing Corp, Bristol, PA.
[10] Hauf, W., and Grigull, U., 1970, ''Optical Methods in Heat Transfer,'' *Advances in Heat Transfer*, **6**, Academic Press, New York, pp. 133–366.
[11] Mehta, J. M., and Black, W. Z., 1977, ''Errors Associated with Interferometric Measurement of Convective Heat Transfer Coefficients,'' Appl. Opt., **16**(6), pp. 1720–1726.
[12] Flack, R. D., 1987, ''Mach-Zehnder Interferometer Errors Resulting from Test Section Misalignment,'' Appl. Opt., **17**(7), pp. 985–987.
[13] Machin, A. D., 1997, ''An Experimental Study of Free Convection Heat Transfer from a Vertical Flat Plate in the Presence of Louvers,'' MESc. thesis, The University of Western Ontario, London, Ontario, Canada.
[14] Kline, S. J., and McClintock, F. A., 1953, ''Describing Experimental Uncertainties in Single Sample Experiments,'' Mech. Eng. (Am. Soc. Mech. Eng.), **73**, pp. 3–8.

Apparent Radiative Properties and Radiation Scattering by a Semitransparent Hemispherical Shell

Tai-Hsi Fan

Andrei G. Fedorov
Asst. Prof.
Assoc. Mem. ASME
e-mail: andrei.fedorov@me.gatech.edu

Multiscale Integrated Thermofluidics Laboratory,
G. W. Woodruff School of Mechanical Engineering,
Georgia Institute of Technology,
Atlanta, GA 30332-0405

Knowledge of the apparent radiative properties of a semitransparent hemispherical shell placed on an opaque surface is of fundamental interest and is also important to a number of applications in materials processing and manufacturing, ranging from metallurgical slag foaming to batch foams in glass melting to hollow bead fabrication. This paper extends our recent work [7] using the analytical and numerical ray tracing techniques to study radiative transfer in the system described. Specifically, the local volumetric heating rate and the scattering phase function of a thin hemispherical shell exposed to incident collimated radiation are calculated both analytically and numerically, and the results are discussed in detail. To further elucidate the results, the comparison is made of the total apparent transmittance of the hemispherical shell to a plane parallel layer of semitransparent material. [DOI: 10.1115/1.1497357]

Keywords: Heat Transfer, Radiation, Scattering

Introduction

Knowledge of the apparent radiative properties of the semitransparent hemispherical shell placed on an opaque surface is of fundamental interest and is also important to a number of applications in materials processing and manufacturing. One particular example is glass manufacturing. During glass melting, the raw materials (also called batch) are fed into the glass melting furnace and float on the free surface of the melt as islands until they are completely melted. The chemical reactions and moisture evaporation take place in the batch during its heating, fusion, and melting, and it results in the large number of bubbles, many of which are trapped on the surface of the batch and produce batch foam. These foams scatter the incident thermal radiation from the combustion space and provide significant resistance to radiant heating and melting of the batch [1], thereby diminishing the energy efficiency of the glass melting process. Unlike the foams formed on the free surface of the molten glass that possess a structure of multiple layers of spherical or polyhedral bubbles separated by the liquid lamella, the batch foam is a collection of often non-overlapping individual gas bubbles that only partially emerge from the batch Fig. 1(*a*). Hence, a thin hemispherical shell placed on top of the opaque surface as shown in Fig. 1(*b*) can be considered as a fairly good simplified representation of the batch foam. Due to significant structural differences, the radiative transfer models developed for conventional glass foams [2,3] cannot be used for the batch foams, and thus prediction of the apparent radiative characteristics of batch foams is the subject of this paper.

In addition to glass manufacturing, understanding of the local radiant heating of a semitransparent hemispherical shell is needed for optimization of the novel process for fabrication of hollow perforated beads for acoustic and thermal insulation [4]. In this process, the gas is injected from a small orifice into the molten droplet placed on the substrate to form a bubble surrounded by the thin lamella of the liquid material, which is then solidified by rapid cooling through the substrate to form a solid hemispherical bead. The parameters (e.g., the shell thickness and structure) and quality of the final product are defined by the relative magnitude of the local heating rates due to collimated thermal radiation incident from the top and the local cooling rates needed for solidification.

The objective of this paper is to develop a complete fundamental understanding and analytical tools for predicting radiative characteristics and heat transfer in semitransparent hemispherical shell suspended in the radiatively non-participating environment. In our previous work [7], we developed approximate, closed-form analytical expressions for the total apparent reflectance, transmittance, and absorptance of such a shell and validated our analysis by using numerical ray tracing solution of the problem. The focus of this work is on the local, spatially resolved radiation characteristics of the semitransparent hemispherical shell, such as the scattering phase function and the local volumetric rate of radiant heating. These properties are critically important to optical, spectroscopic studies of the foam morphology (i.e., phase function) and mechanisms of the foam rapture due to the local thermally induced instabilities and stress (i.e., volumetric heating rate). To further elucidate the results, the comparison is made of the total apparent transmittance of the hemispherical shell to that for a plane parallel layer of the same semitransparent material [5,6].

Analysis

The schematic of the idealized physical arrangement and the coordinate system are shown in Fig. 1(*b*). Several simplifying assumptions are made to make the problem amenable to analytical solution.

Assumptions.

1. Incident radiation is normal to the substrate, collimated and its intensity is constant.
2. The surrounding medium is radiatively nonparticipating with the indices of refraction equal to unity.
3. The shell is made of a homogeneous, gray, and weakly absorbing material characterized by the constant complex index of refraction ($m_2 = n_2 - ik_2$).
4. The shell is treated as a ''cold'' medium, i.e., self-emission of radiation is neglected.

Contributed by the Heat Transfer Division for publication in the JOURNAL OF HEAT TRANSFER. Manuscript received by the Heat Transfer Division July 2, 2001; revision received May 28, 2002. Associate Editor: R. Skocypec.

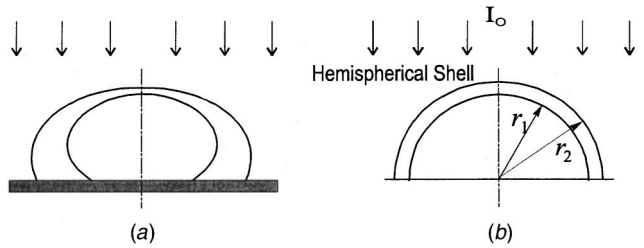

Fig. 1 Schematic of collimated radiation incident on the batch foam: (*a*) actual arrangement; and (*b*) idealized arrangement.

5. The diameter and the thickness of the shell are much greater then the wavelength of the incident radiation, i.e., diffraction and interference effects are not considered.
6. Polarization effects are not considered.
7. All interfaces are optically smooth and obey geometric optic principles.

Closed-Form Solution and Ray Tracing Algorithm. An analytical ray tracing procedure is used and results in the analytical expressions for the apparent radiative properties of the thin hemispherical shell, owing to an existence of a recursive pattern in the physical domain. The ray tracing method follows the optical path of a single energy bundle of incident radiation as it undergoes a repeating pattern of multiple reflections within the shell (Fig. 2). Here we only present the summary of formulas needed for performing the calculations, and an interested reader is referred to the paper by Fan and Fedorov [7] for the detailed discussion of the model development. Specifically, the total apparent reflectance (R), transmittance (T), and absorptance (A) for any energy bundle are given by the following expressions:

$$R=\frac{\rho'_{12}+(1-\rho'_{12}-\rho_{12})\rho_{23}\tau^2}{1-\rho_{12}\rho_{23}\tau^2} \tag{1}$$

$$T=\frac{(1-\rho'_{12})(1-\rho_{23})\tau}{1-\rho_{12}\rho_{23}\tau^2} \tag{2}$$

$$A=\frac{(1-\tau)(1-\rho'_{12})(1+\rho_{23}\tau)}{1-\rho_{12}\rho_{23}\tau^2} \tag{3}$$

respectively, where

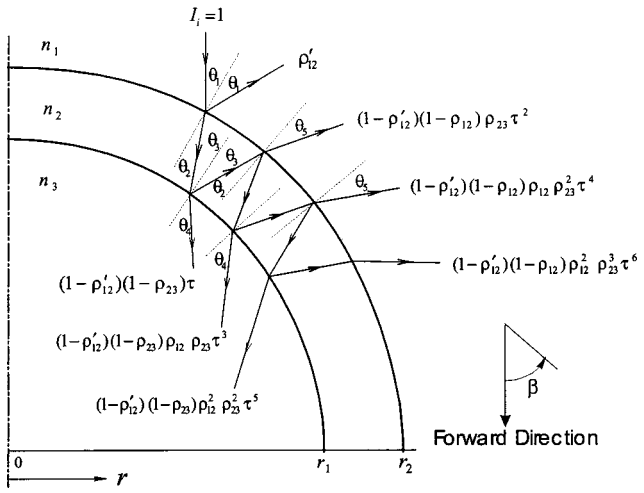

Fig. 2 Tracing an energy bundle in the hemispherical semi-transparent shell

$$\rho'_{12}=\frac{1}{2}\left[\frac{\tan^2(\theta_1-\theta_2)}{\tan^2(\theta_1+\theta_2)}+\frac{\sin^2(\theta_1-\theta_2)}{\sin^2(\theta_1+\theta_2)}\right],\quad 0\leqslant r\leqslant r_2 \tag{4}$$

$$\rho_{21}=\rho_{12}=\frac{1}{2}\left[\frac{\tan^2(\theta_2-\theta_5)}{\tan^2(\theta_2+\theta_5)}+\frac{\sin^2(\theta_2-\theta_5)}{\sin^2(\theta_2+\theta_5)}\right],\quad 0\leqslant r\leqslant r_2 \tag{5}$$

$$\begin{cases}\rho_{23}=\dfrac{1}{2}\left[\dfrac{\tan^2(\theta_3-\theta_4)}{\tan^2(\theta_3+\theta_4)}+\dfrac{\sin^2(\theta_3-\theta_4)}{\sin^2(\theta_3+\theta_4)}\right], & 0\leqslant r\leqslant r_1\\ \rho_{23}=1, \quad r_1\leqslant r\leqslant r_2\end{cases} \tag{6}$$

In Eqs. (1–6), ρ'_{12} is the reflectivity of the surrounding/shell interface at the point where a given energy bundle is incident on the top surface of the shell, $\rho_{12}=\rho_{21}$ is the reflectivity of shell/surrounding interface, ρ_{23} is the reflectivity of shell/inside gas interface, and τ is the transmissivity associated with a single pass of the energy bundle across the shell thickness and equal to exp $[-\kappa(r_2\cos\theta_2-r_1\cos\theta_3)]$. In the last expression, κ is an absorption coefficient of the shell material, which relates to its absorptive index k_2 through the relationship $\kappa=4\pi k_2/\lambda_0$.

In the case of the radially uniform irradiation, the discrete energy bundles possess the same energy and located equidistantly in the radial direction. Other kinds of energy distribution of incident radiation can also be investigated within the deterministic ray tracing algorithm we developed by simply adjusting the distance and/or energy content of the ray bundles. Application of the Snell's law and a simple geometric analysis [7] result in the following recursive relations for the angle of initial incidence ($\theta_1^{(i)}$) and for the angles of consecutive reflections within the shell ($\theta_2^{(i)}, \theta_3^{(i)}, \theta_4^{(i)}, \theta_5^{(i)}$) for the ith energy bundle (Fig. 2):

$$\theta_1^{(i)}=\sin^{-1}\left[\left(\frac{i-1}{N-1}\right)r_2\right],\quad \theta_2^{(i)}=\sin^{-1}\left(\frac{n_1}{n_2}\sin\theta_1^{(i)}\right),$$

$$\theta_3^{(i)}=\sin^{-1}\left(\frac{r_2}{r_1}\sin\theta_2^{(i)}\right),\quad \theta_4^{(i)}=\sin^{-1}\left(\frac{n_2}{n_3}\sin\theta_3^{(i)}\right),$$

$$\theta_5^{(i)}=\sin^{-1}\left(\frac{n_2}{n_1}\sin\theta_2^{(i)}\right) \tag{7}$$

where N is the total number of bundles considered, and i is the bundle index starting from 0 at the centerline of the hemisphere. Finally, in the case of radially uniform incidence, the total apparent absorptance, reflectance and transmittance are computed by summing up the contributions from all energy bundles, i.e.,

$$A_{\text{total}}=\frac{\Sigma_{i=1}^{N}A^{(i)}}{N},\quad R_{\text{total}}=\frac{\Sigma_{i=1}^{N}R^{(i)}}{N},\quad T_{\text{total}}=\frac{\Sigma_{i=1}^{N}T^{(i)}}{N} \tag{8}$$

respectively. To validate the analytical expressions for radiative properties given by Eq. (8), a numerical ray tracing algorithm [7] was developed and applied to the problem in hand. The comparison of the results [7] indicates that the approximate analytical results agree within 3.7 percent with the results of numerical simulations as long as the thickness of shell does not exceed 5 percent of the shell radius.

A general three-dimensional ray tracing technique [8] uses analytical representation of the geometry in a three-dimensional vector space to find the intersection points of the ray bundle with the discrete elements it crosses. This approach requires some additional modifications if the solution of the intersection equation is not unique. Our simplified approach considers two concentric hemispherical interfaces, defined by the inner and the outer radii r_1 and r_2, respectively. Because of the azimuthal independence, instead of solving the bundle-interface intersection equation in the vector form, the intersection points on the two-dimensional plane can be found analytically (using Eq. (13) from [7]), at least in the case of normal incidence of collimated radiation, thereby reducing the computational complexity associated with implementation of the ray-tracing algorithm. Also, if the angle of incidence for a given ray bundle is larger than the critical angle, the reflectivity is

assigned to a unit value. Furthermore, the substrate is assumed to be "cold" and black so that no energy is reflected back or emitted towards the shell by the substrate, thereby significantly reducing the complexity of the shell-substrate interactions and the computational procedure.

In the presented ray tracing algorithm, any discrete element inside the computational domain can have infinitely many possibilities of incoming bundle directions that result in crossing its boundaries, and the intensity of each such energy bundle decays along the traveled path according to the Beer's Law, $I(\mathbf{r},\mathbf{s}) = I_0 \exp(-\int_0^S \kappa\, ds)$. In order to compute the local volumetric heating rate at every point within the shell, an average intensity of radiation needs to be computed by using the local radiant energy conservation and calculating the energy fraction deposited on each element from every direction. That is [7]:

$$I_{\text{avg}}(\mathbf{r},\mathbf{s}) = \sum_{(i)} \frac{I(\mathbf{r},\mathbf{s})[1-\exp(-\int_0^{S'} \kappa\, ds')]dx}{\kappa\, dA\, d\Omega} \tag{9}$$

where $\mathbf{r}$ denotes the element location, $\mathbf{s}$ is the vector in the direction of propagation of the energy bundle, s' is the distance traveled by the energy bundle through a given discrete element (it is different for different bundle directions $\mathbf{s}$), dx is a spacing between the bundles of incident collimated radiation (it is inversely proportional to a total number of energy bundles N used in calculations), dA is the cross-sectional projection area of a given element in respect to the direction of propagation of a given energy bundle, and $d\Omega$ is the incremental solid angle for a given energy bundle. Using an averaged local intensity, the local volumetric heating rate due to thermal radiation absorbed by an element of the computational domain is given by

$$\dot{Q}_{\text{rad}}(\mathbf{r}) = -\nabla \cdot \mathbf{q}_{\text{rad}}(\mathbf{r},\mathbf{s}) = \kappa \int I\, d\Omega = \kappa \sum_{k=1}^{m} I_{\text{avg}}(k)\Delta\varphi(k) \tag{10}$$

where $\Delta\varphi$ is the increment angle in polar direction from a spherical symmetry plane. The total apparent absorptance of the hemispherical shell is expressed as a ratio of the energy absorbed by all elements in the computational domain and the incident energy [7], i.e.,

$$A_{\text{total}} = \frac{\Sigma_{i,j}\kappa(\Sigma_k I_{\text{avg},ij}(k)\Delta\varphi(k))\Delta A_{ij}}{r_2 I_0} \tag{11}$$

The three summations in Eq. (11) are needed to account for the fact that each element in the two-dimensional computational domain is defined by two independent indices (i and j) and an additional index (k) is used to trace directional dependence of the local average intensity field for each ijth element.

Scattering Phase Function. When the incident energy bundle hits the hemispherical shell, part of its energy is reflected immediately by the outer interface and the remaining part penetrates into the semitransparent shell. After that, a given energy bundle undergoes multiple internal reflections and during this process some of its energy is absorbed and some is leaked out (redirected to different scattering directions) through both inner and outer interfaces. In order to construct the scattering phase function, we consider the first reflection from the outer interface and the consecutive internal reflections accompanied by the radiation energy leakage through the shell interfaces as separate events. These events are characterized by the radiant energy redirection or scattering at an angle β (see Fig. 2) and by the fraction of the incident radiation energy leaving the shell due to the first reflection (Λ_1^R) or the radiant energy leakage after ith internal reflection through the outer (Λ_i^R) and inner (Λ_i^T) interfaces. In other words, we decompose the entire trajectory of any given energy bundle into the elements with well defined scattering characteristics (β,Λ), which can be readily computed analytically or numerically by tracing the bundle propagation. Eventually, we combine all contributions (Λ_1^R, Λ_i^R, and Λ_i^T) for any given scattering direction (β) and rescale them in order to obtain a normalized scattering phase function. The analytical developments and the results shown next decisively indicate that the scattering phase function of the semitransparent hemispherical shell is well approximated by the popular Henyey–Greenstein phase function [5,6].

As shown by Fan and Fedorov [7], the recursive pattern traced by the energy bundle as it travels within the shell (see Fig. 2) is defined by the angles θ_2 through θ_5 as well as by the reflectivities ρ'_{12}, ρ_{12}, ρ_{23} and transmissivity τ that all depend on the angle of incidence θ_1 only. Hence, using Eqs. (4) and (7), the fraction of the incident radiation energy scattered by the shell due to the first reflection (Λ_1^R) can be expressed by a function of the scattering angle β as follows:

$$\Lambda_1^R(\beta) = \frac{1}{2}\left\{ \frac{\tan^2\left[(\pi-\beta)/2 - \sin^{-1}\left(\frac{n_1}{n_2}\sin[(\pi-\beta)/2]\right)\right]}{\tan^2\left[(\pi-\beta)/2 + \sin^{-1}\left(\frac{n_1}{n_2}\sin[(\pi-\beta)/2]\right)\right]} + \frac{\sin^2\left[(\pi-\beta)/2 - \sin^{-1}\left(\frac{n_1}{n_2}\sin[(\pi-\beta)/2]\right)\right]}{\sin^2\left[(\pi-\beta)/2 + \sin^{-1}\left(\frac{n_1}{n_2}\sin[(\pi-\beta)/2]\right)\right]} \right\} \tag{12}$$

by noting that the angle of incidence of a given energy bundle θ_1 and the scattering angle β are related through

$$\theta_1 = (\pi-\beta)/2 \tag{13}$$

Analogously, due to repeating pattern of internal reflections created within the shell (Fig. 2), the fraction of the incident radiation energy leaving the shell by leakage after ith internal reflection through the outer interface is given by

$$\Lambda_i^R(\theta_{1i}) = (1-\rho'_{12}(\theta_{1i}))(1-\rho_{12}(\theta_{1i})) \times (\rho_{12}(\theta_{1i}))^{i-2}(\rho_{23}(\theta_{1i}))^{i-1}(\tau(\theta_{1i}))^{2i-2}, \quad i = 2\sim\infty \tag{14}$$

where the parameter θ_{1i} in Eq. (14) is a function of the scattering angle β,

$$\theta_{1i} = \frac{1}{2}\left\{ \pi - \beta - (2i-1)\left[\sin^{-1}\left(\frac{r_2}{r_1}\frac{n_1}{n_2}\sin\theta_{1i}\right) - \sin^{-1}\left(\frac{n_1}{n_2}\sin\theta_{1i}\right)\right]\right\}, \quad i = 2\sim\infty \tag{15}$$

Equation (15) is a nonlinear and implicit equation with respect to θ_{1i} and, thus, requires an iterative numerical solution with the careful selection of an initial guess to achieve fast convergence. In general, Eq. (15) may have infinitely many solutions, however, the physically plausible solution is unique: that is the parameter θ_{1i} must result in the scattering angle β that is between 0 and π. By combining the contribution from the radiation reflected upon the initial incidence on the shell and leaked through the outer interface, the scattering distribution function resulting from the radiation/outer interface interactions can be determined,

$$\Lambda^R(\beta) = \Lambda_1^R(\beta) + \sum_{i=2}^{\infty} \Lambda_i^R(\theta_{1i}(\beta)), \quad 0 \leqslant \beta \leqslant \pi \tag{16}$$

The same procedure can be also applied to the radiant energy escaping the shell through the inner interface, which results in the forward scattering only. Specifically, the fraction of the incident radiation energy leaving the shell due to leakage after i^{th} internal reflection through the inner interface is given by (Fig. 2),

$$\Lambda_i^T(\theta_{1i})=(1-\rho'_{12}(\theta_{1i}))(1-\rho_{23}(\theta_{1i}))\times(\rho_{12}(\theta_{1i}))^{i-1}(\rho_{23}(\theta_{1i}))^{i-1}(\tau(\theta_{1i}))^{2i-1},\quad i=1\sim\infty \tag{17}$$

where the parameter θ_{1i} depends on the scattering angle β and satisfies the following implicit nonlinear equation:

$$\theta_{1i}=-\beta+\sin^{-1}\left(\frac{n_1}{n_3}\frac{r_2}{r_1}\sin\theta_{1i}\right)-(2i-1)\left[\sin^{-1}\left(\frac{r_2}{r_1}\frac{n_1}{n_2}\sin\theta_{1i}\right)-\sin^{-1}\left(\frac{n_1}{n_2}\sin\theta_{1i}\right)\right],\quad i=1\sim\infty \tag{18}$$

The scattering distribution function resulting from the radiation/inner interface interactions is for the forward direction only, and it accounts for the radiant energy from all incident energy bundles leaving the shell through the inner interface at a given scattering angle β,

$$\Lambda^T(\beta)=\sum_{i=1}^{\infty}\Lambda_i^T(\theta_{1i}(\beta))+\sum_{i=1}^{\infty}\Lambda_i^T(\theta'_{1i}(-\beta)),\quad 0\leqslant\beta\leqslant\pi \tag{19}$$

Note that the negative scattering angles β are in principle possible, albeit hardly realized under practical conditions (see Fig. 2 for the coordinate system). However, for the sake of generality, this fact is elegantly incorporated into the scattering distribution function, Eq. (19), by invoking the symmetry of the problem in hand.

We now can combine both components of the total scattering distribution function, given by Eqs. (16) and (19), and, after normalization (i.e., $\int\Phi\, d\Omega=4\pi$), the scattering phase function for the semitransparent hemispherical shell is given by

$$\Phi(\beta)=\frac{4\pi(\Lambda^R(\beta)+\Lambda^T(\beta))}{\int_{4\pi}(\Lambda^R(\beta)+\Lambda^T(\beta))d\Omega},\quad 0\leqslant\beta\leqslant\pi \tag{20}$$

It is interesting to note that for an extremely thin hemispherical shell (i.e., relative to its radius), $\theta_1\approx\theta_4$, $\theta_2\approx\theta_3$, and $r_1\approx r_2$. Thus, Eqs. (16) and (19) can be reduced to Eqs. (1) and (2) with the following dependence on the scattering angle,

$$\Lambda^R(\beta)=\frac{\rho'_{12}+(1-\rho'_{12}-\rho_{12})\rho_{23}\tau^2}{1-\rho_{12}\rho_{23}\tau^2},\quad 0\leqslant\beta=\pi-2\theta_1\leqslant\pi \tag{21}$$

$$\Lambda^T(\beta)=\frac{(1-\rho'_{12})(1-\rho_{23})\tau}{1-\rho_{12}\rho_{23}\tau^2},\quad \beta=0 \tag{22}$$

Results and Discussion

The numerical simulations have been performed for different element sizes and number of energy bundles. The validity of the numerical ray-tracing algorithm has been carefully checked by ensuring that the results are independent of the number and the size of discrete elements in the computational domain and of the total number of energy bundles used in simulations. As it follows from Table 1(*a*), use of 1000 energy bundles produces fully converged results with the uncertainty in the total apparent reflectance and transmittance less than 0.1 percent as compared to much greater number (5000) of energy bundles. The sensitivity of the simulation results in respect to the number of discrete elements used is reported in Table 1(*b*). The dimensionless maximum local volumetric heating rate is chosen for the comparison of results because it has the greatest sensitivity to the number of elements used in simulations. It is clear that full convergence (with the uncertainty less than 0.5 percent) is achieved when 1000 energy bundles and 8×36 elements are employed. Further increase in the number of elements and energy bundles results in a very slightly improved accuracy and thus is not warranted. Thus, all simulation results reported hereafter have been obtained by using 1000 energy bundles and 8×36 elements. In addition, the overall energy conservation has always been achieved by ensuring that the sum of the total apparent absorptance, transmittance, and reflectance is equal to unity.

Table 1 (*a*) Convergence of the numerical ray tracing method as function of the number of energy bundles used in the simulations ($r_1/r_2=0.9$, $\tilde{\kappa}=0.1$, $n_2=1.5$); and (*b*) convergence of the numerical ray tracing method as function of the number of discrete elements used in simulations ($r_1/r_2=0.8$, $\tilde{\kappa}=0.1$, $n_2=1.5$).

Number of Bundles	10	50	100	500	1000	5000
R_{total}	0.2300	0.1913	0.1837	0.1764	0.1762	0.1759
A_{total}	0.0102	0.0119	0.0120	0.0121	0.0121	0.0121

(*a*)

	1000 energy bundles				5000 energy bundles	
Number of Elements	4x9	4x18	8x18	8x36	16x36	16x72
$\dot{Q}_{max}$ (dimensionless)	0.121	0.135	0.141	0.148	0.147	0.150

(*b*)

The focus of this work is on the local volumetric radiant heating and resolving angular dependence of radiation scattering by the hemispherical semitransparent shell. However, to provide a suitable introduction to the problem and facilitate the result interpretation, we first briefly summarize the results on the total apparent radiative properties of the shell and validation of the analytical model, which are discussed in detail in [7]. Figure 3 shows the comparison of the results of the total apparent absorptance (A_{total}) and reflectance (R_{total}) obtained using a closed-form, but approximate analytical solution of the problem and those representing an ''exact'' solution of the problem using the numerical ray-tracing technique. Clearly, the analytical and numerical models produce essentially the same results for the total apparent absorptance, whereas their predictions of the total apparent reflectance agree very well (i.e., within 1 percent) in the limit of the very thin shell (i.e., when $r_1/r_2\to1$). The main reasons for such a discrepancy are an approximation involved in using an infinite rather than a finite algebraic series representation for the total apparent reflectance as well as the trigonometric relationships [Eq. (7)] that are used for tracking the reflection angles, and this is discussed in greater detail in [7]. In short, the closed-form analytical solution of the problem presented here produces the results accurate within 3 percent only if the ratio of the shell inner and outer radii is

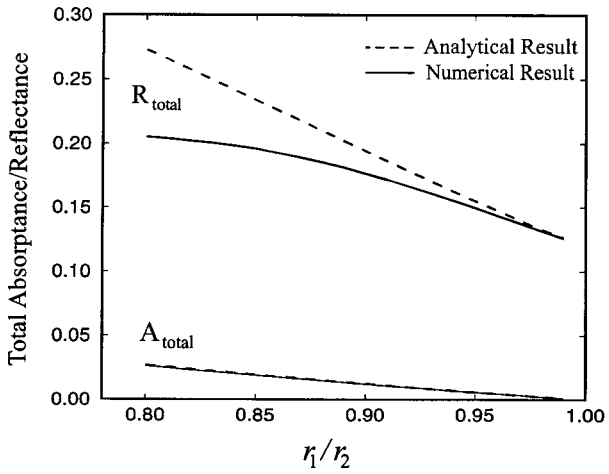

Fig. 3 Total apparent absorptance and reflectance as functions of the normalized shell thickness ($n_2=1.5$, $\tilde{\kappa}=0.1$)

$r_1/r_2 \geq 0.95$. Otherwise, one should resort to the numerical ray tracing method in order to obtain an accurate prediction of the reflectance by the hemispherical shell.

To evaluate the resistance to radiation propagation introduced by the hemispherical shell, we compare the total apparent transmittance of the hemispherical shell and that of a plane parallel layer of the same thickness and made of the same semitransparent material. The apparent radiative properties for the planar configuration is readily available from the radiation textbooks [5,6]. The results presented in Fig. 4 clearly indicate that the hemispherical shell impedes much more significantly the propagation of the radiation relative to the planar layer, and this difference increases sharply as the thickness of the shell/layer increases (i.e., r_1/r_2 decreases). This fundamental result has very important practical implications. For example, in glass melting it permits to quantify the resistance to radiant heating provided by the batch foams, thereby helping optimize the process and operating conditions.

In addition to the exact calculation of the total apparent radiative properties of the shell, the numerical ray tracing allows one to predict the local radiation intensity field at any point in the shell [Eq. (9)] and, thus, the local volumetric radiant heating rate [Eq. (10)]. The latter is illustrated in Fig. 5 by showing the isolines (contours) of the local heating rate normalized by the total irradiation $r_2 I_0$. As expected, the strongest heating spot $\dot{Q}_{\max}$ is predicted in the area within the shell, which is located near the point at the inner shell interface when the onset of the total internal reflection occurs. This is because the intensity of radiation concentrated in this region of the shell is the largest as it is not reduced anymore by the radiation leakage through the inner interface. It is also observed that the very top portion of the shell, where the incident radiation impinges essentially normal to the outer shell interface, is heated much more uniformly than the region near the shell circumference, where the local heating is defined by rather intricate superposition of radiation intensities resulting from multiple reflection within the shell. Once again, this fundamental result is of the great interest to a number of materials processing applications, where one is trying to heat the shell-like material by thermal radiation. In such a case, especially if the material properties are sensitive to the local temperature and have to be carefully controlled [4], one could use the fundamental understanding developed and the model as a tool to design the radiant heating system capable of producing uniform heating of all parts of the shell.

Figure 6 shows the normalized scattering phase function of the semitransparent hemispherical shell (solid line), and its components due to direct reflection of incident radiation from the outer

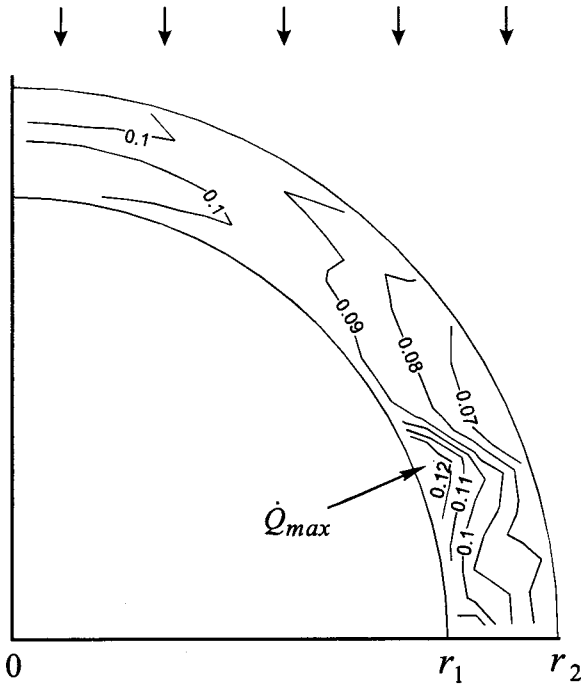

Fig. 5 Isolines of the normalized volumetric radiant heating rate within the shell ($\tilde{\kappa}=0.1$, $r_1/r_2=0.8$, $n_2=1.5$)

interface (dashed line) and interactions of the radiation trapped within the shell with the outer (dash-dotted line) and inner (dash-double-dotted line) shell interfaces as given by Eqs. (20), (12), (14), and (17), respectively. Note that the component of the scattering phase function due to direct reflection of radiation (dashed line) represents a typical scattering phase function for a large spherical particle, whose scattering characteristics depend on the specular reflectivity of interface only [6]. The second contribution shown as the dash-dotted line is due to radiation leakage through the outer interface, and it exhibits a strong increase beginning at the scattering angle that corresponds to an onset of the total internal reflection regime at the inner shell interface. After that, this component of the phase functions remains relatively constant, providing the major contribution to the forward scattering energy with the directional $\cos\beta$ larger than 0.5. Finally, as expected, the component of the scattering phase function due to radiation/inner interface interactions (dash-double-dotted line) has a single strong spike in forward direction characterized by the scattering angle

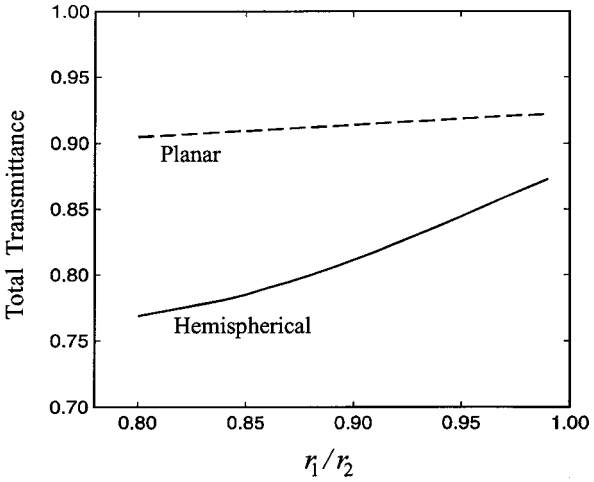

Fig. 4 Comparison of the total apparent transmittance of the planar layer and hemispherical shell ($n_2=1.5$, $\tilde{\kappa}=0.1$)

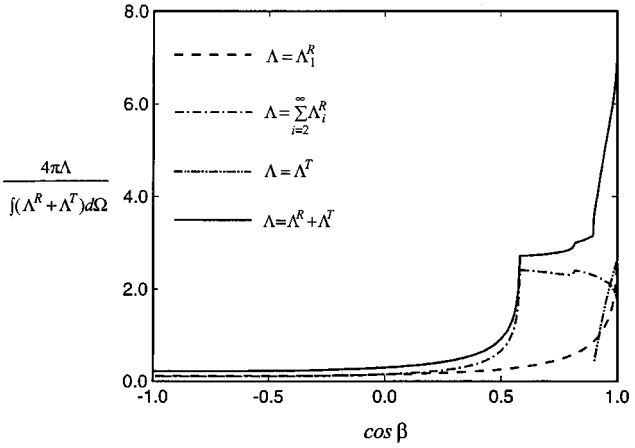

Fig. 6 Normalized scattering phase function and its three components ($\tilde{\kappa}=0.1$, $r_1/r_2=0.8$, $n_2=1.5$)

essentially equal to zero. As the shell thickness becomes thinner (i.e., r_1/r_2 decreases), the last two components of the scattering phase function shift more toward the forward direction. The total scattering phase function combines all three components and is depicted by the dashed line in Fig. 7.

Our calculations shown in Figs. 6 and 7 indicate that the scattering of normally incident collimated radiation by the hemispherical shell favors strongly the forward direction. Thus, in order to achieve some generality in presenting results and to permit comparison with other previously studied physical situations, we tried to express the scattering phase function in terms of the popular Henyey-Greenstein phase function [5,6].

$$\Phi(\beta)=\frac{1-g^2}{(1+g^2-2g\cdot\cos\beta)^{3/2}} \tag{23}$$

with the dimensionless asymmetry factor g given by

$$g=\frac{1}{4\pi}\int_{4\pi}\Phi(\beta)\cos\beta\, d\Omega \tag{24}$$

In Fig. 7, the Henyey-Greenstein (HG) phase function is used to approximate the predicted scattering phase function for the hemispherical shell, and the asymmetry factor g is calculated for three different shell thickness. In the case of intermediate shell thickness ($r_1/r_2=0.9$), the HG approximation is quite accurate across the entire range of the scattering angle, except for the strong peak at $\cos\beta\cong 0.75$, corresponding to an onset of the total internal reflection at the inner shell interface. In the case of a thicker shell ($r_1/r_2=0.8$), the HG function provides satisfactory approximation for $\cos\beta\leqslant 0.50$, but overpredicts the probability of scattering in the forward direction. On the contrary, for the very thin shell with $r_1/r_2=0.99$, the forward scattering is underpredicted by the HG approximation.

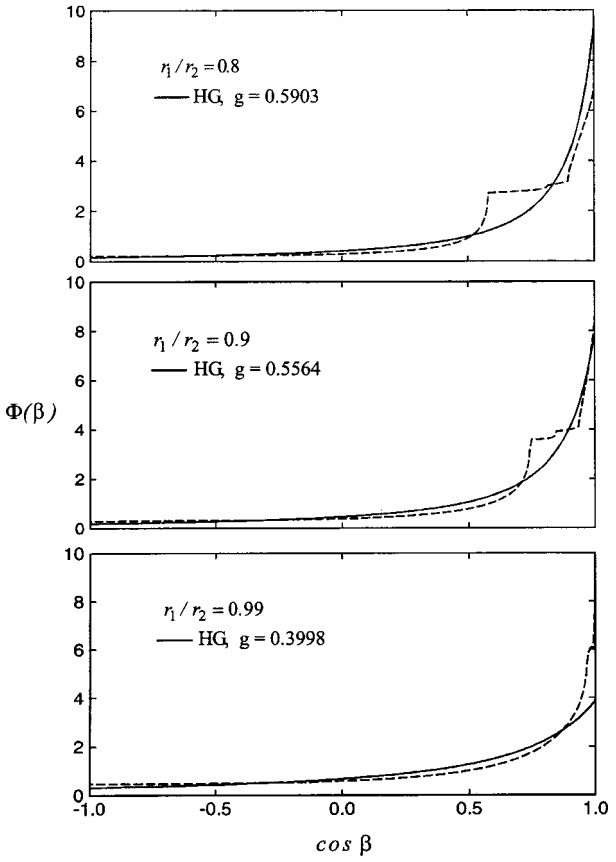

Fig. 7 Normalized scattering phase function and Henyey-Greenstein approximation ($\tilde{\kappa}=0.1$, $n_2=1.5$)

Conclusions

This paper presents a closed-form analytical solution of the problem involving thermal radiation interactions with a hemispherical, semitransparent shell placed on the cold black surface. It permits calculation of the total apparent radiative properties of the shell, its scattering phase function, and the local volumetric radiant heating of the shell under conditions of the normal incidence of collimated radiation. The predictions of the analytical model have been carefully validated by comparing with the ''exact'' solution for the benchmark case obtained by using the numerical ray tracing technique. The comparison of the results indicate that the approximate analytical results agree within 3.7 percent with the results of numerical simulations as long as the thickness of shell does not exceed 5 percent of the shell radius.

To elucidate the relative magnitude of the resistance to radiation propagation introduced by the shell, the comparison is made of the total apparent transmittance of the hemispherical shell to that of the plane parallel layer of semitransparent material. The results indicate that the hemispherical shell impedes significantly the propagation of the radiation as compared to the plane parallel layer of the same thickness, and this difference increases sharply with an increase in thickness of the shell/layer.

Analysis of the local volumetric radiant heating indicates a relatively uniform heating of the shell near its top, where radiation is incident almost normal to the shell surface. At the same time, a significant non-uniformity in local heating is observed near the circumference of the shell with the maximum in the part of shell located near the point of an onset of the total internal reflection at the inner shell interface.

Scattering of radiation by the shell has also been analyzed in great details, and the key components of the scattering phase function has been identified and quantified. The results of calculations indicate a strongly forward character of the radiation scattering by the shell, and the scattering phase function can be sufficiently well represented by the Henyey-Greenstein approximation.

The results of this study not only provide an insight into the fundamentals of radiation/shell interactions but also contribute to improving a number of important applications ranging from metallurgical slag foaming to batch foams in glass melting to hollow bead fabrication.

Nomenclature

A = absorptance
dA = cross-sectional projection area
I_0 = intensity of incident collimated radiation
k = absorptive index
N = total number of energy bundles
n = refractive index
$\dot{Q}_{\text{rad}}$ = volumetric heating rate
$\mathbf{q}_{\text{rad}}$ = radiation heat flux
R = reflectance
r = radius
r_1, r_2 = radii of the inner and outer hemispheres, respectively
$\mathbf{r}$ = spatial position vector
s = distance traveled by an energy bundle
$\mathbf{s}$ = direction of ray propagation
T = transmittance

Greek Symbols

β = scattering angle
Ω = solid angle
Λ_1^R = fraction of incident radiation scattered by first reflection of the energy bundle

Λ_i^R = fraction of incident radiation scattered (i.e., leaving the shell) through the outer shell surface after *i*th refractive pass of the energy bundle

Λ_i^T = fraction of incident radiation scattered (i.e., leaving the shell) through the inner shell surface after *i*th refractive pass of the energy bundle

Φ = scattering phase function

φ = polar angle

$\tilde{\kappa}$ = dimensionless absorption coefficient ($\tilde{\kappa}=\kappa r_2$)

ρ = reflectivity of the interface

τ = transmissivity

Superscript

(i) = refers to the bundle index

Subscripts

total = refers to total apparent properties

1 = refers to surrounding medium

2 = refers to shell material

3 = refers to medium inside the shell

References

[1] Laimbock, P. R., 1998, "Foaming of Glass Melts," Ph.D. dissertation, Technical University of Endhoven, Endhoven, The Netherlands, pp. 1–140.

[2] Fedorov, A., and Viskanta, R., 2000, "Radiative Transfer in a Semitransparent Glass Foam Blanket," Phys. Chem. Glasses, **41**, pp. 127–130.

[3] Fedorov, A., and Viskanta, R., 2000, "Radiation Characteristics of Glass Foams," J. Am. Ceram. Soc., **83**, pp. 2769–2800.

[4] Fedorov, A., Degertekin, F. L., and Hesketh, P., 2001, "Novel Method for Fabrication of Hollow Perforated Beads," U.S. patent application, pending.

[5] Modest, M. F., 1993, *Radiative Heat Transfer*, McGraw-Hill, New York.

[6] Siegel, R., and Howell J. R., 1992, *Thermal Radiation Heat Transfer*, Taylor & Francis, London.

[7] Fan, T. H., and Fedorov, A., 2002, "Radiative Transfer in a Semitransparent Hemispherical Shell," J. Quant. Spectrosc. Radiat. Transf., **73**, pp. 285–296.

[8] Chan, C. K., and Tien, C. L., 1974, "Radiative Transfer in Packed Spheres," ASME J. Heat Transfer, **96**, pp. 52–58.

The Application of an Inverse Formulation in the Design of Boundary Conditions for Transient Radiating Enclosures

Hakan Ertürk

Ofodike A. Ezekoye

John R. Howell

Department of Mechanical Engineering,
The University of Texas at Austin,
Austin, TX 78712-1063

This study considers the design of thermal systems that are built to radiatively heat objects from a specified initial condition to a specified steady state following a prescribed temperature history. The enclosure housing the object, the object itself, and the heaters all have thermal capacity. The necessary power input distributions for the heaters during the heating process are sought to satisfy the design specifications. The problem is thus a transient inverse boundary condition estimation problem, where the geometry and the properties of the surfaces are specified and the boundary condition on the heater wall is to be found by making use of the information provided at the design surface for each time step. The boundary condition estimation problem requires the solution of a set of Fredholm equations of the first kind. Such a problem is known to be ill-posed. The introduction of the transient nature makes the inverse problem nonlinear and even more interesting, challenging, and realistic. A solution algorithm is proposed and used to produce a solution for a sample problem. In order to model radiative heat transmission, the Monte Carlo method is used, which enables us to handle specularly reflecting surfaces and blockage effects. The inverse problem is solved by the conjugate gradient method, which provides smooth and accurate results after the first few steps. [DOI: 10.1115/1.1513574]

Keywords: Control, Furnaces, Heat Transfer, Inverse, Optimization, Radiation

Introduction

Design of thermal processing systems involves satisfying desired conditions in the part of the system where the thermal processing takes place. We call this part of the system the ''design environment''. The conditions desired in the design environment are dependent on the process for which the thermal system is built. The design conditions can be reached by controlling the conditions in other parts of the system through heaters, burners or coolers. Therefore, the ultimate goal in a thermal design problem is to build the required system with the correct geometry, materials, and to determine the necessary input from the engineering devices for the system to satisfy the needs of the process to be carried out in the design environment. The complete design process involves a number of design iterations of prototype building and testing. Reducing the total number of design iterations by one or two will result in significant savings. This can often be achieved through the use of available simplified models and numerical simulation techniques. Our study focuses on a part of the design problem: The design of a system, for which the design environment, geometry and the materials are specified and the required boundary conditions are to be calculated. The developed methodology can then be used as a tool for the complete design problem.

For a process furnace, such as the ones used for rapid thermal processing (RTP), chemical vapor deposition (CVD), drying, curing of paint, food processing, annealing, or curing of coated materials, the thermal problem is to heat the design object with a prescribed distribution of temperature and net radiant energy input throughout the heating period. These known distributions are usually spatially uniform, as uniform temperatures prevent thermal stresses, non-uniform chemical deposition, or uneven drying or cooking due to temperature gradients. Because each object has a finite heat capacitance, no steady state is available instantly. In order to reach a steady state, the design object must be heated from an initial state while the object follows a particular heating history, during which the design environment is to be kept at the desired spatial distribution at all times.

This study involves the design of thermal systems where high temperatures are present, and the dominant mode of heat transfer is thermal radiation. The exchange of thermal radiation depends on the fourth power of temperature. The physical problem considered here can be very complex with wavelength, direction and temperature dependent properties, involving non-linearity due to multimode heat transfer and the transient nature of the problem. Furthermore, the geometry of the systems can include other levels of complexities like blockage effects.

The traditional way to solve a design problem is to guess an input for the energy supply devices used in the system and then use mathematical models to check whether the desired conditions in the design environment are satisfied. The guessed value is modified based on the preceding results until the desired conditions are reached. Such trial-and-error methods are computationally expensive; moreover, it can be difficult to obtain smooth and physically reasonable or feasible solutions.

So called ''inverse design'', on the other hand, involves the solution of the design problem by using all available information prescribed for the design environment to provide a direct solution for the necessary input. As the required input for the system is determined from the output, this kind of formulation is called the ''inverse formulation'' and the method of design is called ''inverse design''. As a direct solution is considered, the computational expense of the inverse methods is considerably lower than trial-and-error methods, but the drawback is that the inverse problem is defined in terms of a set of Fredholm equations of the first kind, which is known to be ill-posed. The defining equation must be regularized in order to obtain an accurate, smooth, and physically reasonable solution. There exists a number of regularization techniques including truncated singular value decomposition (TSVD),

Contributed by the Heat Transfer Division for publication in the JOURNAL OF HEAT TRANSFER. Manuscript received by the Heat Transfer Division September 14, 2001; revision received June 10, 2002. Associate Editor: R. Skocypec.

modified TSVD (MTSVD), Tikhonov regularization, and the conjugate gradient method (CGM), which could be used for the regularization of the system.

Inverse heat transfer problems have been attracting interest since the late 1950s. There have been many studies in the field mostly on inverse conduction problems and the fundamental texts include references [1–4]. More recently, [5] presented a comprehensive overview covering inverse convection and radiation problems in addition to conduction problems. Most of these studies focus mainly on measurement problems. One of the first studies addressing the applicability of inverse formulation for thermal design is [6]. In [7], the application of the inverse design for steady radiating systems is considered, while [8] considers multimode heat transfer combining convection and radiation that introduces nonlinearity to the problem. A comprehensive summary about inverse thermal design, focusing mainly on steady-state radiating systems is presented in [9].

Formulation

The problem considered in this study involves transient, combined mode heat transfer. The differential form of the energy equation for a surface that can be considered lumped across the thickness δ inside an enclosure is:

$$q''_{cv}(x,t)+q''_r(x,t)-\nabla\cdot q''_{cd}(x,t)\,\delta+Q'''(x,t)\,\delta=\rho c_p\delta\frac{\partial T(x,t)}{\partial t} \tag{1}$$

where q''_{cv} is the convective heat flux, the heat flux due to conduction is

$$q''_{cd}(x,t)=-k\nabla T(x,t) \tag{2}$$

and the net radiative heat flux at a point on the surface is

$$q''_r(x,t)=\varepsilon(x)\sum_{k=1}^{N_S}\int\left[\left(\frac{1}{\varepsilon(x')}-1\right)q''_r(x',t)+\frac{1}{\varepsilon(x')}E(x',t)\right]K(x,x')dx'-E(x,t) \tag{3}$$

for a system with N_S surfaces and $K(x,x')dx'=dF_{dx-dx'}$.

The complete set of equations includes equations for all design, heater and reflector surfaces and the radiative term in Eq. (1) must be calculated from the radiative exchange equation given in Eq. (3). In its given form, the simultaneous solution of the coupled inverse and initial value problem requires the calculation of the radiative heat flux and emissive power values simultaneously for the complete set. An alternative approach uses the exchange factors ($\tilde{F}$) instead of configuration factors, and can be helpful especially for problems where specularly reflecting surfaces are present.

$$q''_r(x,t)=\sum_{k=1}^{N_S}\int E(x',t)d\tilde{F}_{dx-dx'}-E(x,t) \tag{4}$$

where the exchange factor between differential elements dx and dx' is defined as the rate of energy emitted from differential element dx that is absorbed by differential element dx', and it includes all the effects of intermediate reflections. Then the energy equation can be written for each point on the design surface as

$$\sum_{k=1}^{N_U}\int E(x',t)d\tilde{F}_{dx-dx'}=\rho c_p\delta\frac{\partial T(x,t)}{\partial t}-k\delta\nabla^2T(x,t)-q''_{cv}(x,t)-\sum_{k=1}^{N_T}\int E(x'',t)d\tilde{F}_{dx-dx''}+E(x,t) \tag{5}$$

where the summation over N_U denotes the surfaces with unknown temperature distributions, and N_T denotes the surfaces with known temperature distributions at time t. For a boundary condition estimation problem with a prescribed temperature history, the boundary and initial conditions are

$$T(x,0)=T_o \tag{6}$$

T_o being the initial temperature for every surface in the enclosure and

$$T(x,t)=T_d(x,t) \tag{7}$$

for the design surface, where T_d is the temperature history that is to be followed on that surface.

In the given form, all the terms in the right hand side of Eq. (5) are known. The unknown term, the emissive power distribution of the heater surfaces, is on the left hand side of the equation and is inside the integral. Equation (5) is recognized as a Fredholm equation of the first kind, which is ill-posed, with the exchange factors being the kernel for the system.

Numerical Discretization and Solution Procedure

When the integral form of Eq. (5) is discretized using an explicit Euler scheme in time, it becomes

$$\sum_{m=1}^{N_U}\sum_{j=1}^{N_{s,m}}E_j^n\tilde{F}_{i-j}=\rho_i c_{p,i}\delta_i\frac{T_d^{n+1}-T_i^n}{\Delta t}-q''^{\,n}_{cd,i}-q''^{\,n}_{cv,i}-\sum_{m=1}^{N_T}\sum_{k=1}^{N_{s,m}}E_k^n\tilde{F}_{i-k}+E_i^n \tag{8}$$

where $N_{s,m}$ is the number of sub-surface elements for surface m, the conduction heat flux is

$$q''^{\,n}_{cd,i}=k\nabla_d^2T_i^n \tag{9}$$

and ∇_d^2 is the discretized Lagrangian.

From the prescribed design temperature history $T_d(t)$, the desired temperature distribution at the time step $n+1$, T_d^{n+1}, is known. The designer's goal is to find the necessary heater temperature distribution, through solution of Eq. (8), at time step n to satisfy the net radiative heat flux at the same time step, so that the desired temperature distribution at the time step $n+1$ will be reached. Once the exchange factors for the enclosure are known, Eq. (8) can be reduced to a system of discretized linear Fredholm equations of the first kind written as

$$\tilde{F}_{i-j}E_j=b_i \tag{10}$$

where b_i is the net radiative heat flux absorbed by design subelement i that originates from the heater elements, the terms on the right hand side of Eq. (8).

The system characterized by Eq. (10) is then solved to find the necessary temperature distribution along the heater surfaces for the time step n. In order to obtain smooth, accurate, and physically reasonable solutions the linear system of equations must be regularized.

The necessary heat input for the heaters to satisfy the required heater distributions at each time step can be evaluated from the discretized energy and radiative transfer equations for the heaters after the heater temperatures are found. The relation is

$$Q_i''^{\,n-1}=\rho_i c_{p,i}\delta_i\frac{T_i^n-T_i^{n-1}}{\Delta t}-q''^{\,n-1}_{cd,i}-q''^{\,n-1}_{cv,i}-\sum_{m=1}^{N_S}\sum_{j=1}^{N_{s,m}}E_j^{n-1}\tilde{F}_{i-j}+E_i^{n-1} \tag{11}$$

Due to the ill-conditioned character of the systems solved at each time step and the nature of the design problem itself, satisfying the necessary temperature distribution while following the

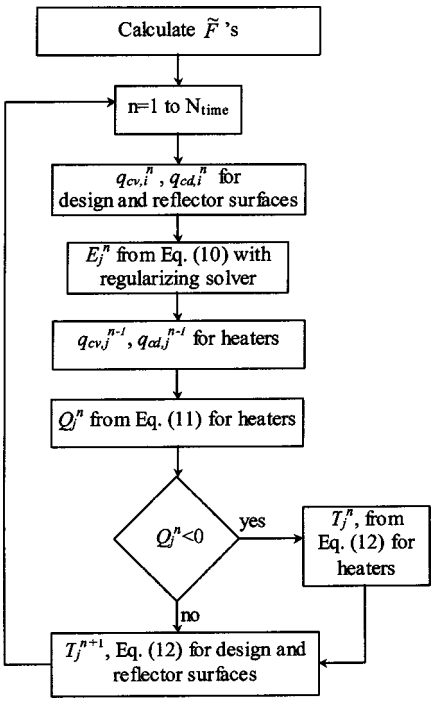

Fig. 1 The flowchart of the solution algorithm

desired heating profile may predict the removal of power from some heater elements at some time steps. Since adding and removing power from heater elements at the same time will not be desirable for practical purposes, the heaters with negative powers are just turned off and the power input is set to zero for those elements in such a situation. This introduces some difference between the predicted and desired design condition. The heater temperature for the step n in the corresponding elements is corrected according to

$$T_i^n = T_i^{n-1} + \frac{\Delta t}{\rho_i c_{p,i} \delta_i} \left(q''^{\,n-1}_{cd,i} + q''^{\,n-1}_{cv,i} + \sum_{m=1}^{N_S} \sum_{j=1}^{N_{s,m}} E_j^{n-1} \tilde{F}_{i-j} - E_i^{n-1} \right) \tag{12}$$

The constraint of no negative heater inputs, the regularization of the system and solution of the linear system all introduce some error, and the design surface will not receive exactly the same radiative flux as evaluated from Eq. (8). Therefore, the resulting temperature distribution on the design surface at the time step $n+1$ needs to be corrected according to the supplied radiative energy by Eq. (12), replacing n by $n+1$. Similarly, the temperature distributions of the reflector surfaces can be updated for the time step $n+1$ by utilizing Eq. (12), replacing n by $n+1$, once the necessary temperature distribution along the heaters is calculated for the time step n.

The procedure described is applied from the initial time step, where the design, reflector and the heater surfaces are all at a prescribed initial condition. An outline of the procedure is presented in the flowchart in Fig. 1.

Sample Problem

The problem considered in this study is a transient thermal boundary condition estimation problem, in which the designer aims at controlling the thermal conditions in the design environment by setting the necessary thermal conditions on the heater surfaces. The design surface is to be heated from an initial state to a final steady-state, while it is kept at a spatially uniform temperature, following a specified heating profile.

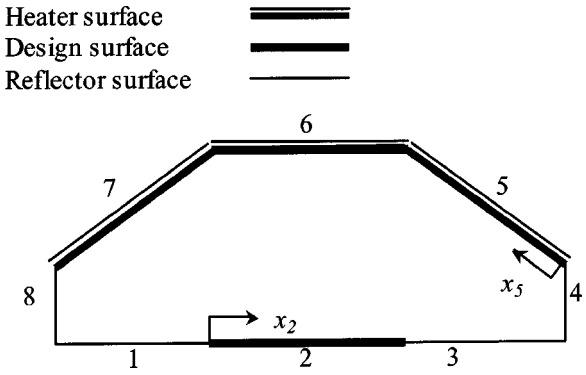

Fig. 2 The geometry of the furnace

The use of the proposed algorithm is demonstrated in a sample problem. A two-dimensional evacuated furnace with eight straight surfaces, which are all gray, with thin-strip resistance heater surfaces 5, 6, and 7, design surface 2 and reflector surfaces 1, 3, 4, and 8 as shown in Fig. 2 is considered. The heater surfaces are nichrome with an oxidized rough surface leading to diffusely reflecting surfaces. The reflector surfaces are polished aluminum, and are therefore specularly reflecting with a larger reflectivity than the heater and design surfaces. The design surface is silicon carbide, which is diffusely reflecting. The heater surfaces are made up of 30 nichrome strip heaters each of uniform temperature that are slightly separated from each other. There is no forced flow inside the enclosure and it is assumed that the effect of natural convection is negligible when compared with the thermal radiation and the conduction along the surfaces. The backside of the design surface is insulated and it does not touch the reflector surfaces at the edges; so thermal radiation is the only means of exchanging heat from the design surface to its surroundings. Furthermore, it is assumed that the conduction across the plate thickness is negligible when compared with the thermal radiation exchange on the inside of the enclosure and conduction along the plate so that the surface can be approximated as lumped across the plate thickness. Other assumptions are that all the thermal properties are constant and independent of the temperature variations in the system, and the system is in local thermodynamic equilibrium.

The required heating history is presented in Fig. 3 and is defined by a polynomial providing a smooth heating curve from an initial temperature of 300 K to a final temperature of 1000 K and $T_d(t)$ is uniform across surface 2. The geometric data and required thermal properties of the surfaces are presented in Table 1.

Results and Discussion

The problem of transient heating of the design object is solved to evaluate the necessary power input for the 30 individual strip heaters (10 on each surfaces 5, 6, and 7 of Fig. 2) to provide the necessary radiative flux for the design surface so that it will be heated spatially isothermal, following the specified temperature history presented in Fig. 3 in a total time of 60 sec. Certain considerations should be underlined regarding the solutions, so that the results can be discussed more clearly.

In this study, exchange factors are calculated once by the Monte Carlo method (MCM) before the rest of the calculations as the geometry and the radiative properties do not change. The MCM is a statistical solution technique that makes use of sampling of photon bundles that carry the radiative energy. The method produces very accurate solutions within limits of statistical accuracy, which can be estimated. It is also a very flexible method and has a simple

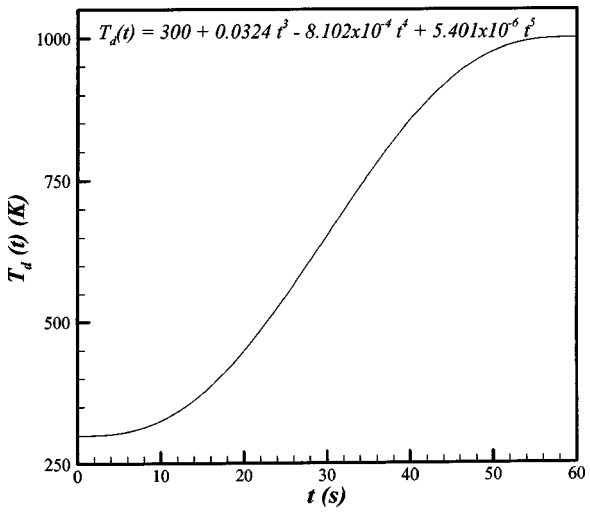

Fig. 3 Desired design surface temperature history

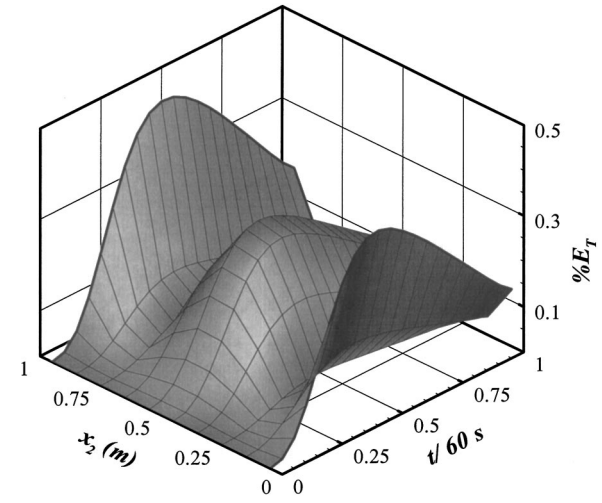

Fig. 4 The errors based on design surface temperature and the design specification

formulation that enables easier handling of additional complexities like specularly reflecting surfaces, complex geometries and effects of participating media and scattering. The method is explained in detail in [10–12] and it will not be discussed here. The verification of the MCM used in this study is available in [13] for similar irregularly shaped enclosure problems.

In order to produce regularized solutions the conjugate gradient method (CGM) is used in this study. The CGM is a solution algorithm that can be used to evaluate the exact solution vector $\mathbf{h}$ for any linear system that is defined in the form, $\mathbf{Cu}=\mathbf{b}$, in N-steps, where N is the number of unknowns.

For a linear system with a symmetric and positive definite coefficient matrix $\mathbf{C}$, the CGM can be interpreted as a way to minimize the function, $H(\mathbf{u})=[\mathbf{C}(\mathbf{h}-\mathbf{u})]\cdot(\mathbf{h}-\mathbf{u})$, which has a value of zero when $\mathbf{u}=\mathbf{h}$, at its minimum. The method can be generalized for any arbitrary system when the system defined by Eq. (10) is multiplied by $\mathbf{C}^T$. The function, $H(\mathbf{u})$, minimizes as $\nabla H(\mathbf{u})$ and the residual of the system reach zero, as it can be shown that the gradient of the functional is equivalent to the negative of twice the residual for the system $(\nabla H(\mathbf{u})=-2\mathbf{r})$, where the residual for the system is defined as

$$\mathbf{r}=\mathbf{b}-\mathbf{Cu} \tag{13}$$

In the CGM, the solution is defined as a linear combination of the C-conjugate vectors. At each step, a new C-conjugate vector is introduced that is used to modify the solution, leading to a monotonic decrease in the norm of the residual vector.

The derivation of the method to solve a linear system of equations such as Eq. (10) is presented in [14], and it will not be repeated here. The basic advantages of the CGM can be summarized as; the simplicity of computational procedures, the requirement of small memory for storing intermediate results and parameters and its robust convergence characteristics, i.e., the superiority of each approximation when compared with the previous ones. In addition, the original coefficient matrix is stored and used as is. Furthermore, the intermediate solution produced in each step can be considered as a different and unique solution; however, as more steps are included, the error is reduced, but oscillations in the solution increase. Therefore, the CGM can be considered to produce N-different solutions, which enable the user to choose one particular solution, based on the competing needs (accuracy versus smoothness) of the problem under consideration.

The use of the method as a tool in inverse and/or ill-conditioned problems is discussed in detail in [15]. Reference [5] presents an extensive discussion of the application of the method for various inverse heat transfer problems. In [16] its similarity with another regularized solution technique used in inverse problems, truncated singular value decomposition (TSVD) is presented, underlining its advantages in terms of memory requirement and computation time over TSVD. Based on the information presented in [16] CGM is preferred over TSVD as a regularized solver for this study.

For an ill-conditioned problem, it can be shown that there is a compromise between the accuracy and smoothness of the solution considered. The very first steps of the CGM produce fairly accurate but smooth results, while the further steps improve the accuracy at the expense of a loss of smoothness and physical meaning. As solutions that are not smooth are not desired for practical purposes in engineering problems, a solution that is both accurate and smooth with a physical meaning is selected among the N possible solutions. The problem of deciding on the solution which is to be considered as an optimal solution is usually tackled in inverse problems with the help of the so called "L-curve" that is a plot of the variation of the residual norm against the solution norm.

In a transient problem, it should be emphasized that it is not only desired to obtain spatially smooth distributions but also smoothly changing temporal distributions for each spatial location along time. If the optimal number of CGM steps is sought at each time step, significant fluctuations in the variables along time result, as the CG-step yielding the optimal solution may change at each time step. In order to get a smooth distribution along time, solutions must be produced using a fixed CG-step for each time step rather than using the optimal solution. This leads to a loss in accuracy in certain time steps where a more accurate and still smooth solution might be available from the use of more CGM steps.

The proposed solution procedure is applied for the sample problem and Fig. 4 displays the error of the achieved temperature distribution along the design surface throughout the process, which is defined as

Table 1 The geometric and thermal parameters that define surfaces

Surface	δ (m)	ρ(kg/m^3)	c_p (J/kgK)	L (m)	k (W/mK)	ε
1	0.001	2702	903	0.8	227	0.05
2	0.001	3160	675	1	454	0.9
3	0.001	2702	903	0.8	227	0.05
4	0.001	2702	903	0.4	227	0.05
5	0.0001	7870	447	1		0.95
6	0.0001	7870	447	1		0.95
7	0.0001	7870	447	1		0.95
8	0.001	2702	903	0.4	227	0.05

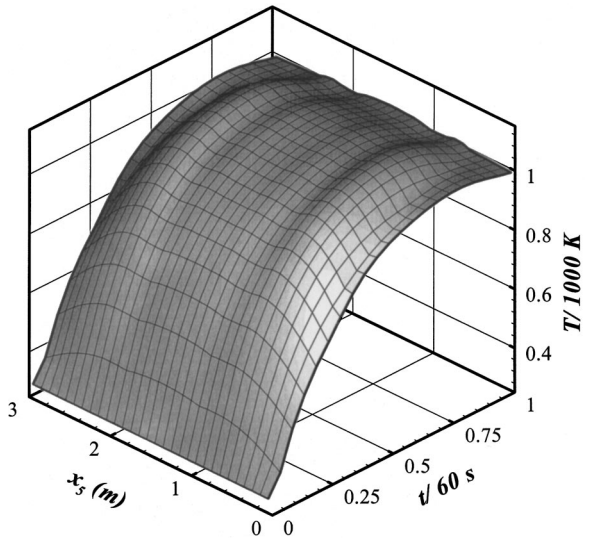

Fig. 5 The temperatures of thirty heater strips along the heating process

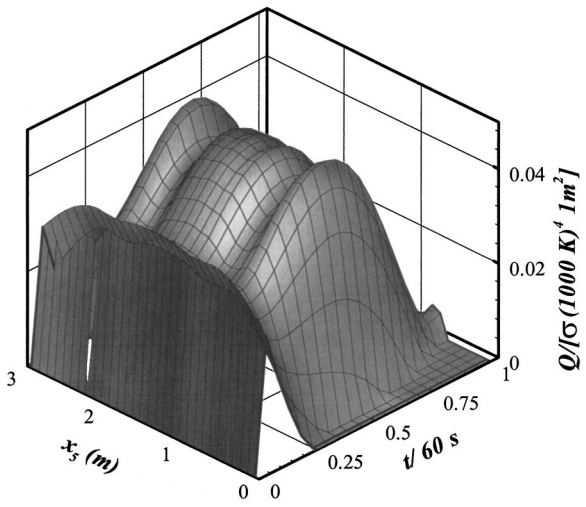

Fig. 6 The necessary power input for thirty heater strips

$$\%E_{T,i}^{n} = 100\,\frac{|T_i^n - T_d(t)|}{T_d(t)} \tag{14}$$

It may be observed from Fig. 4 that the accumulated errors affect the system the most when the non-dimensional time is about 27 sec. ($t/60\,s = 45$), reaching a maximum error of 0.45 percent, where the average error is 0.12 percent. The maximum and average errors decrease to 0.16 and 0.07 percent, respectively, as the system reaches steady state. The actual solution accuracy is limited by the assumptions considered for the formulation, property values and the radiation solver used. Observe that the locus of the maximum error is usually at the tips of the design surface. This information can be used by the designer to reconfigure the heater or enclosure geometry to achieve better agreement with the prescribed design environment.

The resulting error distribution on the design surface, demonstrated in Fig. 4, is achieved for the temperature history on the 30 heater strip surfaces displayed in Fig. 5. The temperature of the heater strips is slightly above the temperature of the design surface at all times, as the design surface follows the prescribed temperature history, $T_d(t)$. Furthermore, the distribution along the heater strips is such that when combined with the resulting design and reflector surface temperature distributions, the spatially uniform heat flux and temperature conditions are satisfied on the design surface. The temperature of the heater strips increases until it peaks at approximately around 39 sec. ($t/60\,s = 0.65$) at a value near 1100 K and then decreases to the steady state temperature of the design surface.

The 30 heater strips exchange energy by thermal radiation with other surfaces and each other, and receive energy as an input. In order to control the temperature distribution of the heater strip that in turn controls the temperature distribution on the design surface, the input power distribution is varied. The necessary power input is displayed in Fig. 6. In order to obtain the necessary power input distribution presented in Fig. 6 an additional constraint is used at the initial time step. For the problem under consideration, the required heat flux on the design surface is zero with all initial design and reflector surface temperatures being 300 K. It is apparent that a uniform distribution of 300 K along 30 heater strips will satisfy the design constraints exactly. However, the regularized inverse solution predicts a heater profile that has a slight gradient. The heater strips close to the edges tend to have values lower than 300 K and the ones close to the middle higher than 300 K so that the energy equation is satisfied at every location. When the design constraint that restricts the energy removal from the strips is applied, the values of the non-dimensional temperature below 300 K are corrected to 300 K leaving the ones above as they are. This sudden change from isothermal initial conditions at the end of the initial time step due to the regularization error necessitates a large amount of power input per time step to account for the heat capacity of the heaters, especially for simulations utilizing a very small time step ($\Delta t < 0.376$ sec.). Therefore, a second constraint is applied for the initial time step to remove the ''artificial'' need for the power input that has nothing to do with the physical needs of the system. This constraint limits the power input for all heater strip elements at the initial time step leading the heater strips not to change their temperature.

All the results presented in Figs. 4–6 are obtained using a time step size of $\Delta t = 0.0226$ sec. and 64 surface elements with a 26×10 grid resolution. The exchange factors are pre-calculated by MCM using 400 million sample photon bundles in 2682.3 seconds using a Pentium™ III 650 MHz platform. The result from the first CG-step was used in order to obtain physical solutions with smooth spatial and time profiles, during the entire heating for 2660 time steps using 5.6 sec. of computation time. Identical solutions result when the grid resolution is doubled, utilizing 128 surface elements with a 52×20 grid. Although the accuracy of the inverse solutions could have been improved by using the results of further CG-steps, this increases the norm of the solution as displayed in the *L*-curve. The *L*-curve represents the variation of the residual norm with the solution norm for a single time step and a sample *L*-curve from the solution presented is displayed for the 665th time step in Fig. 7. Every point in Fig. 7 represents a possible solution resulting at the end of each CG-step for the subsequent time step. While the decrease in the residual norm represents the increase in solution accuracy, the corresponding increase in the solution norm represents the decrease in the smoothness of the solution. Therefore, the solutions produced by the use of further CG-steps are more accurate but have a greater tendency to produce non-physical solutions than the earlier CG-steps.

In order to investigate the effect of the CG-step used in the solution of the sample design problem, the maximum percentage error of solutions produced using different CG-steps and time step sizes are compared in Fig. 8. It can be observed that the time step size is an important parameter that affects the level of accuracy in the solution. The time discretization error dominates the solution when a large time step is used. Therefore, for time step sizes larger than 3.76 sec. the system at some point overheats the design surface due to discretization errors in such an amount that satisfying the design goal becomes numerically impossible using posi-

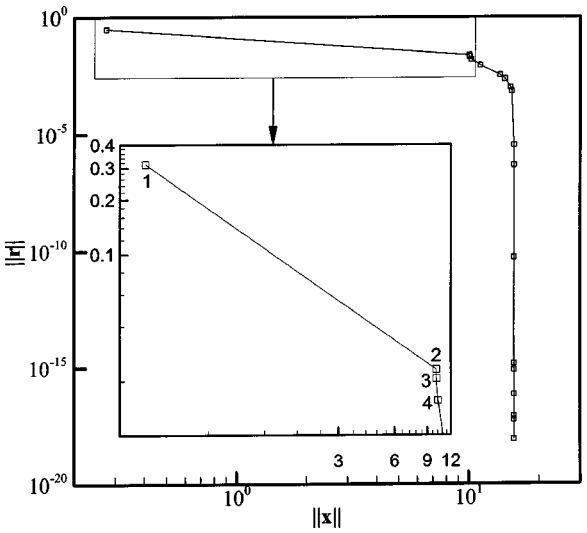

Fig. 7 The *L*-curve, variation of the solution norm with residual norm for time step 665

tive emissive power on the heater elements. As a result, no physical result is available. On the other hand, when the time step is decreased, the total number of time steps used for the solution increases. This simply results in increasing the cumulative effect of regularization errors, perhaps leading the system to a state where it is also impossible to maintain a physical solution as stated above. Therefore, the algorithm cannot produce any solution when the time step is reduced below some value.

The range of time steps where it is possible to produce a physically meaningful solution differs for solutions that use the results of a different number of CG-steps. This range is from 3.76 to 0.0226, 3.76 to 0.301 and 3.76 to 0.0188 sec. when the results of the first, second and third CG-step are used, respectively. The solutions that use the results of the first and the third CG-steps have a larger time step size range than the solution that uses the result of the second CG-step. This is because the solution evaluated using the result of the first CG-step is the smoothest; thus, even though it is affected most by the cumulative effect of the regularization error as the number of time steps used increases, it still can produce physically reasonable solutions up to some point.

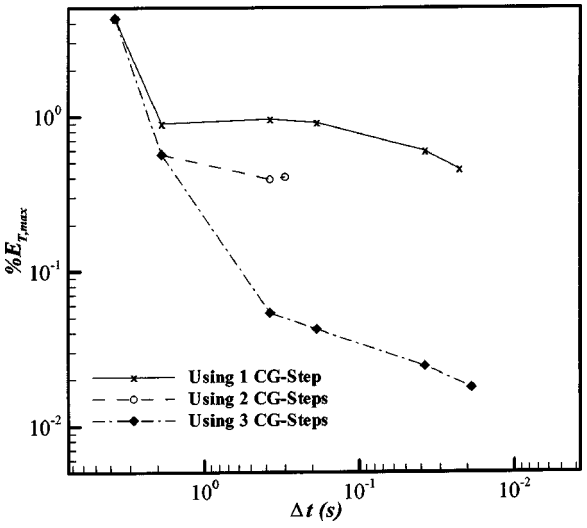

Fig. 8 The change in solution accuracy with the CG-step used and time step size

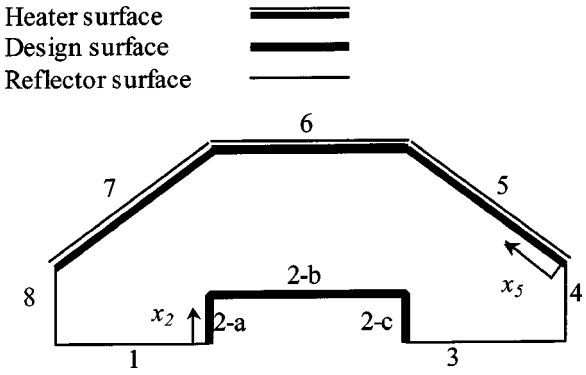

Fig. 9 The geometry of the furnace for the modified case

On the other hand, the solution evaluated using the result of the third CG-step is subject to the least regularization error among the three solutions and the cumulative effect of the regularization error starts affecting the system later than the other two although it produces the least smooth solutions. The solution using the results of the second CG-step satisfies neither of the conditions, and as a result has the smallest range of useful time step size.

One of the main characteristics of inverse problems is that the resulting solutions are very sensitive to perturbations in input. That is why it is customary to test the solution procedures developed to tackle inverse problems by introducing some perturbation to the problem considered [5]. In our case, inverse design, some changes in the designed system, analogous to the perturbations in the measured data, should be considered to test the versatility of the design technique developed. One should be very careful when introducing changes for a design problem as this can lead to a problem that has no solution within the acceptable level of accuracy. Two tests with modifications in the input data are considered in this study; the first is the use of reflector surfaces that have larger emissivity ($\varepsilon=0.5$) and the second is replacing the slab design surface with a two-dimensional surface so that the furnace geometry becomes as displayed in Fig. 9. The lengths of surfaces 2-a and 2-c in Fig. 9 is 0.3 m and the new design surface introduces blockage into the problem leading the spatially isothermal heating of the surface to be more difficult to achieve than it was in the previous case. The rest of the problem's conditions for the materials used, geometry, and the design objective are unchanged.

Figure 10 displays the required heater temperature distribution throughout the process, for the case with reflector surfaces having $\varepsilon=0.5$. The distribution is calculated using the results of the first CG-step and a time step size of of $\Delta t=0.0226$ sec. The maximum error of the design is less than 0.6 percent. When Figs. 5 and 10 are compared, it can be observed that the temperature gradient along the heater strips is greater in the case where reflector surfaces have $\varepsilon=0.5$ it can be concluded that the original case is more likely to be the preferred configuration, both in terms of achieving the design goal more accurately and in terms of efficiency considerations as in the original case the reflector surfaces absorb less energy. The results are in agreement with physical intuition, as highly reflecting sidewalls will make it easier to achieve spatially uniform distributions.

The second modification considered is the change in the design surface geometry as shown in Fig. 9. The required temperature distributions along the heater strips are displayed in Fig. 11. The maximum error in the design surface absolute temperature for the final case is less than 0.7 percent, which can be a significant error for applications like RTP or CVD but can be considered within acceptable limits when the governing assumptions are considered. The solution presented in Fig. 11 are produced using the results of a single CG-step with a time step size of $\Delta t=0.0376$ sec., which

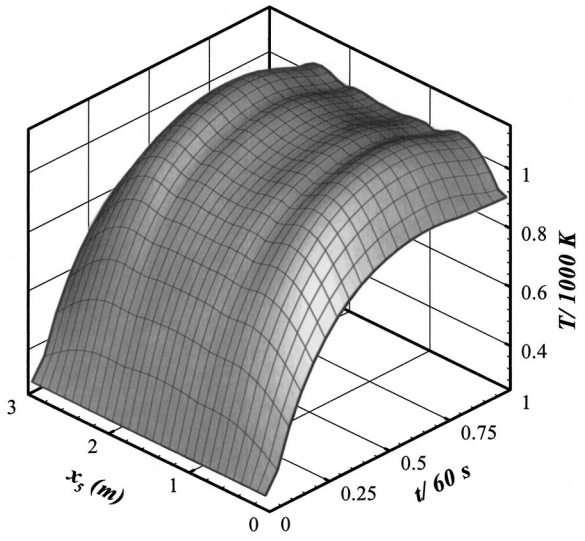

Fig. 10 The temperatures of thirty heater strips along the heating process for the problem with reflector surfaces having $\varepsilon=0.5$

is the limiting value for the case. In order to further improve the solutions, the designer should consider other changes, either in geometry or the materials used.

The main advantage of the proposed procedure is that it can produce a transient direct solution and it can be applied with any similar regularization technique instead of CGM or any other method to formulate the radiation transfer instead of MCM with the limitations outlined. When the temperature dependency of the thermal properties becomes important the solution technique could be modified by two different approaches. Both of these approaches require the calculation of configuration factors instead of the exchange factors at the beginning. One of the approaches is then to calculate the exchange factors at each time step based on the properties varying with changing temperature distributions and following the rest of the steps in the procedure as outlined in Fig. 1. The burden of the calculation with this approach is the calculation of exchange factors from configuration factors. The alternative approach to get rid of this burden is using the configurations factors in the formulation directly, i.e., using Eq. (3) instead of Eq. (4) leading to a larger number of simultaneous equations to solve at each time step.

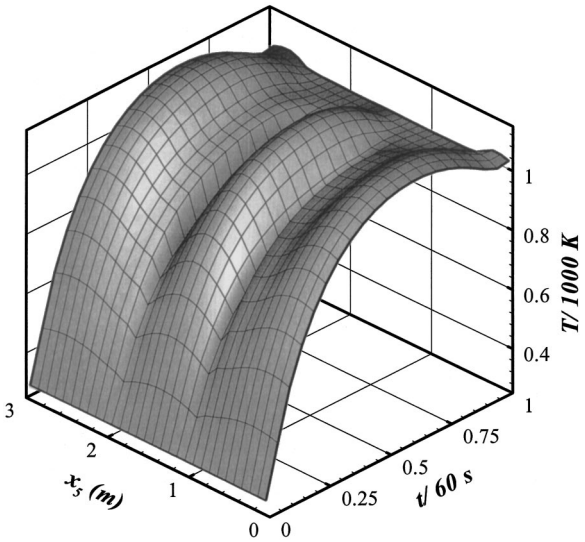

Fig. 11 The temperatures of thirty heater strips along the heating process for the furnace geometry displayed in Fig. 9.

Conclusions

A transient heating design problem is solved as a transient boundary condition estimation problem. Heating of a design surface is considered in an irregularly shaped radiating enclosure. It is desired that the temperature should be kept uniform over the surface while the surface is heated following a specified heating profile. A number of heater strips together with specularly reflecting, polished, reflector surfaces are used to reach the design goal, through varying the temperatures of the heaters by controlling the power input for each of the heater strips.

A design technique based on inverse formulation is used for solving for the necessary power input for the strip heaters. Exchange factors are used to simplify the formulation of the radiative transfer equation. The Monte Carlo method and the conjugate gradient method are used in the solution of the particular problem; but the same methodology can be applied using any method that is capable of providing the exchange factor information and regularized solutions.

The inverse boundary condition estimation problem, which is set by the conditions based on the previous time step, is solved for each time step by using the conjugate gradient method. In order to avoid changes in the resulting profiles the results of a fixed number of solution steps are used in all time steps. This yields smooth profiles at the expense of some loss in accuracy in terms of meeting the prescribed transient temperature distribution of the design environment. Even so, the difference between the specified design goal and the obtained results does not exceed 1 percent, at any place and any time, during the entire heating process.

The proposed solution technique extends the capabilities of inverse design from steady design problems to transient design problems, which are more realistic engineering problems in many cases. The problem can be extended to the case where the thermal properties vary by considering updating the thermal properties at the end of each time step. For the case where radiative properties such as emissivities vary, a formulation based on configuration factors rather than exchange factors will be preferable.

Acknowledgments

The authors thank the National Science Foundation for support under grant CTS-0070545.

Nomenclature

A = area (m^2)
$\mathbf{b}$ = right hand side vector
$\mathbf{C}$ = the coefficient matrix
$\tilde{F}$ = exchange factor
N = number of unknowns or the elements
Q = power input for heater strips (W)
$\mathbf{r}$ = residual vector of the system
$\mathbf{u}$ = vector of unknowns or solution
x = local coordinates along surfaces (m)
$\%E_T$ = the absolute percentage error based on the temperature achieved

Greek Symbols

δ = plate thickness (m)

Subscripts

cd = due to conduction
cv = due to convection
d = design specification
o = initial condition
r = due to thermal radiation
S = surfaces in the enclosure

s = sub-surfaces in a surface
T = surfaces with unknown temperature distributions in the corresponding time step
U = surfaces with unknown temperature distributions in the corresponding time step

Superscripts

n = n-th time step
$''$ = flux (per area)
$'''$ = volumetric rate (per volume)

References

[1] Tikhonov, A. N., Goncharsky, A. V., Stepanov, V. V., and Yagola, A. G., 1995, *Numerical Methods for Solving Ill-Posed Problems*, Kluwer Academic Publishers, Boston, MA.

[2] Beck, J. V., Blackwell, B., and St. Clair, Jr., C. R., 1985, *Inverse Heat Conduction*, John Wiley and Sons Inc., New York.

[3] Alifanov, O. M., 1994, *Inverse Heat Transfer Problems*, Springer-Verlag, Berlin.

[4] Alifanov, O. M., Artyukhin, E. A., and Rumyantsev, S. V., 1995, *Extreme Methods for Solving Ill-Posed Problems with Applications to Inverse Heat Transfer Problems*, Begell House, New York.

[5] Özişik, M. N., and Orlande, H. R. B., 2000, *Inverse Heat Transfer*, Taylor and Francis, New York.

[6] Kennon, S. R., and Dulikravich, G. S., 1985, ''The Inverse Design of Internally Cooled Turbine Blades,'' ASME J. Eng. Gas Turbines Power, **107**(1), pp. 123–126.

[7] Howell, J. R., Ezekoye, O. A., and Morales, J. C., 2000, ''Inverse Design Model for Radiative Heat Transfer,'' ASME J. Heat Transfer, **122**, pp. 492–502.

[8] França, F. R., Ezekoye, O. A., and Howell, J. R., 2001, ''Inverse Boundary Design, Combining Radiation and Convection Heat Transfer,'' ASME J. Heat Transfer, **123**(5), pp. 884–891.

[9] França, F. R., Howell, J. R., Ezekoye, O. A., and Morales, J. C., 2002, ''Inverse Design of Thermal Systems,'' *Advances in Heat Transfer*, J. P. Hartnett and T. F. Irvine, eds., **36**, Elsevier, pp. 1–110.

[10] Siegel, R., and Howell, J. R., 2002, *Thermal Radiation Heat Transfer*, 4th ed., Taylor and Francis, Washington DC.

[11] Farmer, J. T., and Howell, J. R., 1997, ''Comparison of Monte Carlo Strategies for Radiative Heat Transfer in Participating Media,'' *Advances in Heat Transfer*, Hartnett, J. P., Irvine, T. F., eds., **31**, Academic Press, New York, pp. 333–425.

[12] Modest, M. F., 1993, *Radiative Heat Transfer*, McGraw-Hill Book Co, Singapore.

[13] Ertürk, H., Ezekoye, O. A., and Howell, J. R., 2000, ''Inverse Solution of Radiative Transfer in Two-Dimensional Irregularly Shaped Enclosures,'' *Proc. 2000 ASME International Mechanical Engineering Congress and Exhibition*, ASME HTD-Vol. 366-1, Orlando, Florida, November 5–10, 2000, pp. 109–117.

[14] Beckman, F. S., 1960, ''The Solution of Linear Equations By the Conjugate Gradient Method,'' *Mathematical Methods For Digital Computers*, A. Ralston and H. S. Wilf, eds., John Wiley and Sons, New York, pp. 62–72.

[15] Hansen, P. C., 1998, *Rank-Deficient and Discrete Ill-Posed Problems: Numerical Aspects of Linear Inversion*, SIAM Publications, Philadelphia, PA.

[16] Ertürk, H., Ezekoye, O. A., and Howell, J. R., 2002, ''Comparison of Three Regularized Solution Techniques in a Three-Dimensional Inverse Radiation Problem,'' J. Quant. Spectrosc. Radiat. Transf., **73**, pp. 307–316.

Combined Radiation and Conduction in Glass Foams

Mark J. Varady
Grad. Res. Assistant

Andrei G. Fedorov
Asst. Prof.
e-mail: andrei.fedorov@me.gatech.edu

Multiscale Integrated Thermofluidics Laboratory,
G. W. Woodruff School of
Mechanical Engineering,
Georgia Institute of Technology,
Atlanta, GA 30332-0405

Understanding of heat transfer in glass foams and the development of theoretical tools for predicting heat transfer properties of glass foams is critical to improving the efficiency of glass manufacturing. In this paper, combined radiation and conduction heat transfer in a semitransparent glass foam layer is analyzed. The foam layer is thin and of the uniform thickness, bounded by hot combustion gases on top and glass melt on bottom, and exposed to isotropic radiation originating from hot refractories. Heat transfer is assumed to be one-dimensional perpendicular to the plane-parallel foam layer. A previously developed model is used to calculate effective extinction coefficients and scattering phase function of the foam layer using a void size distribution and assuming all voids to be spherical. These radiation properties are then used along with a Schuster-Schwarzchild two-flux approximation to solve the radiative transfer equation (RTE). A method for obtaining the effective thermal conductivity of the foam layer is also presented. The RTE and the energy conservation equations are simultaneously solved using a numerical iteration procedure. The effect of foam thickness and bubble size on the temperature distribution in the foam layer is studied. [DOI: 10.1115/1.1513579]

Keywords: Furnaces, Heat Transfer, High Temperature, Insulation, Manufacturing

Introduction

The bulk of the glass products ranging from glass containers and decorations to optical fibers and TV displays are produced from the glass that is melted in the large-scale glass melting furnaces. The raw materials are fed into the furnace through the inlet ports in the form of socalled batch logs. Multiple burners in the combustion space above the melt are used to heat up the refractory walls of the furnace to sufficiently high temperatures, and the hot refractories in turn supply radiant energy for melting the raw materials. During melting, chemical reactions in the batch produce gas bubbles, which rise toward the surface due to buoyancy forces and convective currents in the melt [1–3] to become trapped at the free surface of the glass melt, forming a thin layer of glass foam that covers between one to two thirds of the free surface of the glass pool. Being semitransparent, the glass foam layer attenuates thermal radiation emitted by the hot refractories and combustion gases through both absorption and scattering. This causes a significant decrease in the radiative heat flux that reaches the glass melt, leading to an increase in required melting time and a decrease in heating efficiency.

Although heat, mass, and radiation transports in the combustion space (reviewed by Webb [4]) and in the glass melt (reviewed by Viskanta [5]) have been studied quite extensively, only recently some progress was made in understanding heat and mass transfer in glass foams [6]. In particular, Fedorov and Viskanta [7,8] developed a methodology for predicting the effective radiative properties (absorption and scattering coefficients and scattering phase function) of the glass foams and radiative transfer in glass foam blanket. Both cases of collimated and diffuse radiation incidence have been considered, and analytical expressions for the total apparent reflectance, transmittance, and absorptance of the foam layer have been obtained by accounting for external and internal reflecting boundaries of the layer. The results of this work confirmed Trier's [9] indirect observations that the transmittance of thermal radiation even through a relatively thin (2 cm thick) foam layer never exceeds 20 percent or, in other words, the foam blanket provides significant resistance to radiative heat transfer from the hot refractories and combustion products to the batch and molten glass in the tank. Among different parameters of the foam layer, the thickness of the foam layer and the mean bubble size showed major impact on the radiative characteristics of the foam [7,8].

In this work, combined conduction and radiation heat transfer in glass foams is analyzed. The radiative transfer model developed by Fedorov and Viskanta [7] is used to obtain the effective radiative properties of the foam layer. These properties are then incorporated into a combined conduction and radiation heat transfer model of the foam layer. The resulting temperature distribution in the foam layer is analyzed to elucidate the degree to which the foam layer impedes heat transfer to the glass melt. Also, the effect of foam parameters, such as thickness and mean bubble size, that have been previously identified as most important [8] to radiative heat transfer in foams is studied and discussed in detail.

Analysis

Foam Layer Model. Consider a plane parallel layer of glass foam in a glass melting furnace as schematically shown in Fig. 1. This layer consists of many gas bubbles separated by thin glass melt films (lamellae) and is bounded by the slowly circulating glass melt at the bottom and moving hot combustion gases at the top. The origin of the coordinate system is at the top surface of the glass foam layer and the axis points toward the bottom of the layer. The glass foam layer is assumed to be of uniform thickness, l, and to extend indefinitely in the plane perpendicular to the x-axis. Visual observations and analysis of samples taken from the actual furnaces confirm the validity of such a one-dimensional representation of the foam layer.[1] The foam structure is very complex: it consists of the spherical (at the bottom) and polyhedral (at the top) bubbles and its porosity may vary across the thickness of the layer from 0.5 to 0.97. A detailed description of the structure and composition of glass foams is available [3,6]. There is a great deal of uncertainty and difficulty in experimental determination of the foam structure [3], and this demands development of a simplified, yet realistic representation of the foam structure. A para-

Contributed by the Heat Transfer Division for publication in the JOURNAL OF HEAT TRANSFER. Manuscript received by the Heat Transfer Division July 17, 2001; revision received June 26, 2002. Associate Editor: R. Skocypec.

[1]Typical foam layers observed in actual and laboratory furnaces (Owens Corning and Techneglas, USA and Schott Glas, Germany) are between 2 to 10 centimeters thick and extended over several meters over the surface of the molten glass mainly between the batch logs, thereby supporting the validity of the one-dimensional analysis.

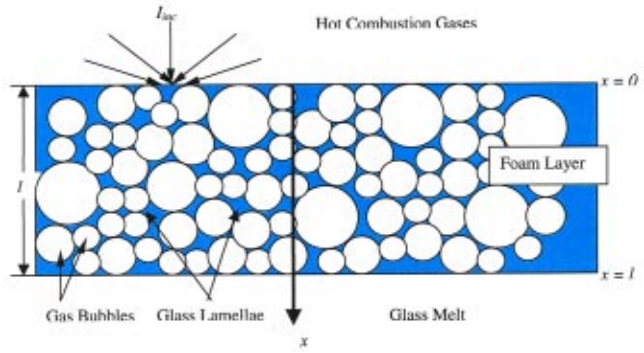

Fig. 1 Schematic of glass foam layer

metric representation of the bubble size distribution in the glass foam was proposed by Fedorov and Viskanta [7] based on the modified gamma function [10]. The extensive parametric studies [8] indicate that a uniform bubble (assumed to be spherical) size distribution across the foam layer with a carefully selected mean bubble diameter may be sufficiently accurate, considering significant uncertainties in determining other input parameters (e.g., spectral radiative properties of the glass and glass thermal conductivity as function of temperature). A balance between the surface tension and buoyant forces reveals the dominant bubble size to be between 3 and 5 mm, and the average porosity of the foam layer is about 0.7 for the operating conditions found in the actual furnaces [6,7].

Governing Equations. The general energy conservation equation for the foam layer is given by [11]

$$\rho\left(\frac{\partial u}{\partial t}+\mathbf{v}\cdot\nabla u\right)=-\nabla\cdot\mathbf{q}-p\nabla\cdot\mathbf{v}+\mu\Phi+\dot{Q} \tag{1}$$

For a typical glass foam layer, the motion of the bubbles is slow and convective terms in the energy conservation can be ignored. Thermal radiation that is incident on top of the foam layer originates primarily from the hot and rough refractory walls of the furnace, whose temperature remains essentially constant because of the large thermal capacity of the refractory bricks. These facts support a steady-state approach to treatment of heat transfer in the glass foam layer subjected to isotropic incident radiation. The flow and heat transfer in the combustion space and glass melt above and below the foam layer, respectively, are assumed steady and fully developed with uniform temperature. Thus, within one-dimensional representation of the foam layer and assuming the heat transfer within the foam layer is steady with no heat generation or viscous dissipation, the energy conservation equation becomes,

$$\frac{d}{dx}\left[-k\frac{dT}{dx}+q_r\right]=0 \tag{2}$$

where q_r is the total radiative heat flux, which is obtained by integrating the spectral radiative heat flux distribution over the entire spectrum.

The spectral radiative heat flux is related to the spectral intensity of radiation, I_λ, which for an absorbing, emitting, and scattering medium is given by the solution of the RTE, which is given by [10]

$$\nabla\cdot[I_\lambda(\mathbf{s},\hat{\mathbf{\Omega}})\hat{\mathbf{\Omega}}]=-\beta_\lambda(\mathbf{s})I_\lambda(\mathbf{s},\hat{\mathbf{\Omega}})+\kappa_\lambda(\mathbf{s})I_{b\lambda}(T(\mathbf{s}))+\frac{\sigma_\lambda}{4\pi}\int_{4\pi}I_\lambda(\mathbf{s},\hat{\mathbf{\Omega}}')\Phi_\lambda(\mathbf{s},\hat{\mathbf{\Omega}}'\rightarrow\hat{\mathbf{\Omega}})d\hat{\mathbf{\Omega}}' \tag{3}$$

where $\mathbf{s}$ is the position vector of a particular point in the medium with respect to a given coordinate frame, $\hat{\mathbf{\Omega}}$ is a line-of-sight direction unit vector, β_λ, κ_λ, and σ_λ are the spectral extinction, absorption, and scattering coefficients, respectively, and $I_{b\lambda}$ is Planck's blackbody emission function. The scattering phase function, Φ_λ, is the probability that a beam of radiation of a certain wavelength traveling in direction $\hat{\mathbf{\Omega}}'$ will be deflected into direction $\hat{\mathbf{\Omega}}$.

Expressing the RTE in terms of optical thickness, τ_λ, for the case of isotropic incident radiation gives [7]

$$\mu\frac{dI_\lambda}{d\tau_\lambda}=-I_\lambda(\mu)+[1-\omega_\lambda]I_{b\lambda}(T(\tau_\lambda))+\omega_\lambda\int_{-1}^{1}I_\lambda(\mu')F(\mu,\mu')d\mu' \tag{4}$$

where μ is the cosine of the angle between the given direction and the x-axis, ω_λ is the single scattering albedo, and $F(\mu,\mu')$ is the azimuth averaged scattering phase function. Introducing the Schuster-Schwarzchild two-flux approximation [7,10] and integrating over the forward and backward hemispheres yields two coupled ordinary differential equations for the intensity field,

$$\frac{1}{2}\frac{dI_\lambda^+}{d\tau_\lambda}=-[1-\omega_\lambda F_d]I_\lambda^++\omega_\lambda[1-F_d]I_\lambda^-+[1-\omega_\lambda]I_{b\lambda}(T(\tau_\lambda)) \tag{5a}$$

$$-\frac{1}{2}\frac{dI_\lambda^-}{d\tau_\lambda}=-[1-\omega_\lambda F_d]I_\lambda^-+\omega_\lambda[1-F_d]I_\lambda^++[1-\omega_\lambda]I_{b\lambda}(T(\tau_\lambda)) \tag{5b}$$

where F_d is the fraction of radiation scattered in the forward hemisphere and is given by Fedorov and Viskanta [7]. These equations can be transformed into a second order ordinary differential equation with spectral radiative heat flux as the dependent variable:

$$\frac{d^2q_{r\lambda}}{dx^2}=(A_\lambda^2-B_\lambda^2)q_{r\lambda}+2\pi E_\lambda\frac{dI_{b\lambda}}{dx} \tag{6}$$

with $A_\lambda=-2\beta_\lambda(1-\omega_\lambda F_d)$, $B_\lambda=2\beta_\lambda\omega_\lambda(1-F_d)$, and $E_\lambda=2\beta_\lambda(1-\omega_\lambda)$.

The total radiative heat flux is then given by

$$q_r=\int_0^\infty q_{r\lambda}d\lambda \tag{7}$$

Equations (6) and (7) combined with the energy conservation equation, Eq. (2), and proper boundary conditions allow for a solution of the temperature field in the foam layer.

Boundary Conditions. Equation (6) requires two boundary conditions and these are obtained assuming the boundaries of the foam layer are semitransparent, non-emitting, and diffusely reflecting [10]:

$$I_\lambda(\mathbf{s},\hat{\mathbf{\Omega}})=I_{\text{inc},\lambda}(\mathbf{s},\hat{\mathbf{\Omega}})+\frac{\rho_d(\mathbf{s})}{\pi}\int_{\hat{\mathbf{n}}\cdot\hat{\mathbf{\Omega}}'<0}I_\lambda(\mathbf{s},\hat{\mathbf{\Omega}}')|\hat{\mathbf{n}}\cdot\hat{\mathbf{\Omega}}'|d\hat{\mathbf{\Omega}}' \tag{8}$$

Equation (8) is simplified by invoking a two-flux approximation, and the resulting boundary conditions on the top and bottom bounding surfaces are:

$$I_\lambda^+(0)=(1-\rho_{12})\left(\frac{n_f}{n_g}\right)^2I_{b\lambda}(T_{\text{eff},t})+\rho_{21}I_\lambda^-(0) \tag{9}$$

$$I_\lambda^-(l)=(1-\rho_{32})\left(\frac{n_f}{n_l}\right)^2I_{b\lambda}(T_{\text{eff},b})+\rho_{23}I_\lambda^+(l) \tag{10}$$

where $T_{\text{eff},t}$ and $T_{\text{eff},b}$ are the effective ''emission'' temperatures of the bounding media at the top (refractory walls and combustion space) and bottom (glass melt) of the foam layer, respectively; n_f,

n_g, and n_l are the refractive indices of the foam, combustion gases, and the glass melt, respectively. These boundary conditions are then expressed in terms of spectral radiative heat flux using $q_{r\lambda}=\pi(I_\lambda^+-I_\lambda^-)$, giving

$$2(1+K_2)q_{r\lambda}(0)+\frac{2(1-K_2)}{A_\lambda+B_\lambda}\left.\frac{dq_{r\lambda}}{dx}\right|_{x=0}=\frac{4\pi E_\lambda(1-K_2)}{A_\lambda+B_\lambda}I_b(0)+4\pi K_1 \tag{11}$$

$$-2(1+K_4)q_{r\lambda}(l)+\frac{2(1-K_4)}{A_\lambda+B_\lambda}\left.\frac{dq_{r\lambda}}{dx}\right|_{x=l}=\frac{4\pi E_\lambda(1-K_4)}{A_\lambda+B_\lambda}I_b(l)+4\pi K_3 \tag{12}$$

where $K_1=(1-\rho_{12})(n_f/n_g)^2 I_{b\lambda}(T_{\text{eff},t})$, $K_2=\rho_{21}$, $K_3=(1-\rho_{32})\times(n_f/n_l)^2 I_{b\lambda}(T_{\text{eff},b})$, and $K_4=\rho_{23}$. The energy conservation equation, Eq. (2), requires two boundary conditions, which are obtained by performing energy balances at the interfaces. At the top interface, heat is transferred to the foam layer by convection from the circulating combustion gases and radiation that is absorbed at the interface. In addition, the top of the glass foam layer emits radiation in the wavelength region where glass is opaque. At the bottom interface, heat is transferred by convection from the slowly circulating glass melt. Thus,

$$-k_f\left(\frac{dT_f}{dx}\right)_{x=0}=h_g[T_g-T_f(0)]+\varepsilon_{op}\int_{\lambda_c}^{\infty}[E_{b\lambda}(T_{\text{eff},t})-E_{b\lambda}(T_f(0))]d\lambda \tag{13}$$

$$-k_f\left(\frac{dT_f}{dx}\right)_{x=l}=h_l[T_f(l)-T_l] \tag{14}$$

where λ_c is the critical wavelength beyond which the glass is opaque, and ε_{op} is the emissivity of the foam layer surface beyond the critical wavelength.

Solution Method

Numerical Approach. A band model is employed to perform spectral integration in computing the total radiative heat flux. Dividing the entire spectrum into N intervals (bands) and assuming the spectral radiative heat flux to be constant in each band, the overall energy conservation equation, Eq. (2), becomes

$$\sum_{i=1}^{N}\frac{dq_{ri}}{dx}\Delta\lambda_i-\frac{d}{dx}\left[k_f\frac{dT_f}{dx}\right]=0 \tag{15}$$

where q_{ri} is the spectral radiative heat flux for band (i) computed using Eq. (6) for each band ($i=1,2,\ldots N$). These $N+1$ equations, Eq. (6) for each band and Eq. (15) are solved iteratively according to the following procedure. (1) assume/update the temperature field, $T_f(x)$; (2) solve Eq. (6) to calculate the spectral radiative heat flux for each band ($i=1,2,\ldots N$) using boundary conditions Eqs. (11) and (12); (3) using spectral radiative heat fluxes, solve the overall energy conservation equation, Eq. (15), to obtain an updated temperature distribution in the foam; and (4) repeat the process by returning to step (1) until the error in predicting the temperature is less than 10^{-6} between successive iterations. It should be noted that the first term in Eq. (15) is a nonlinear function of the temperature. In order to obtain convergence in the iterative process, the fully implicit scheme is used to discretize Eq. (15) and the nonlinear dependence of the radiative heat flux on temperature is incorporated into the solution by introducing the following linearization of the spectral radiative heat flux:

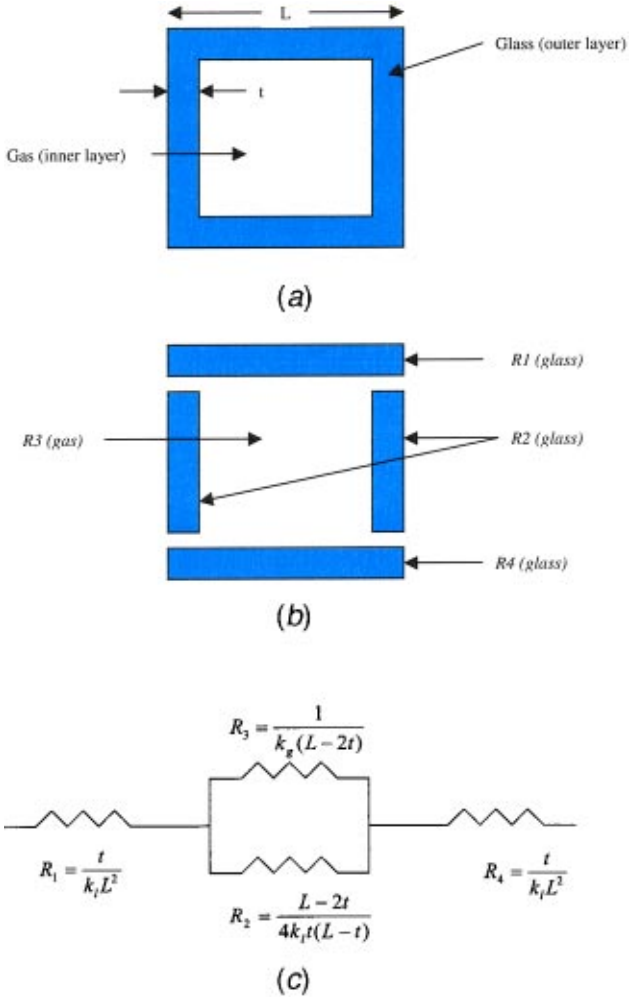

Fig. 2 (*a*) Typical cubic cell; (*b*) thermal resistance elements of the cubic cell; and (*c*) equivalent thermal resistance network for computing the effective thermal conductivity of the foam

$$\left.\frac{dq_{ri}}{dx}\right|_{T_f}\approx\left.\frac{dq_{ri}}{dx}\right|_{T_f^{\text{old}}}+\left.\frac{d}{dT}\left[\frac{dq_{ri}}{dx}\right]\right|_{T_f^{\text{old}}}[T_f-T_f^{\text{old}}] \tag{16}$$

where T_f^{old} is the temperature field in the previous iteration. The tridiagonal matrix inversion algorithm (TDMA) is used to solve the resulting set of linear algebraic equations.

Model Parameters

Effective Thermal Conductivity of Glass Foam. Equation (15) requires an effective conductivity of the foam (k_f) as one of the key parameters. The development of the effective thermal conductivity of the foam layer presented here parallels the development by Pilon et al. [12] for the gas diffusion coefficient in closed-cell foams. The foam layer is viewed as a collection of cubic cells, stacked directly on top of one another, so that they are aligned perfectly in the vertical direction. Each cubic cell has glass walls and a cubic, gas filled cavity. A cross section of the cubic cell is shown in Fig. 2(*a*). Conduction across the cubic cell can be modeled with an equivalent thermal resistance network. The cubic cell is broken into four separate resistance elements as shown in Fig. 2(*b*) with resistance values shown in Fig. 2(*c*). Combining these resistances yields an effective resistance, which can be used to express the thermal conductivity of the foam as

$$k_f = k_l L \frac{4k_l t(L-t) + k_g(L-2t)^2}{2t[k_g(L-2t)^2 + 4k_l t(L-t)] + k_l L^2(L-2t)} \quad (17)$$

Defining a dimensionless thickness, $\xi = t/L$, the effective thermal conductivity of the glass foam can be written as

$$k_f = k_l \left(\frac{4k_l \xi(1-\xi) + k_g(1-2\xi)^2}{2k_g \xi(1-2\xi)^2 + 4k_l \xi^2(1-\xi) + k_l(1-2\xi)} \right) \quad (18)$$

or it may be expressed in terms of the foam porosity, ϕ, which is linked to the dimensionless thickness, ξ, as follows:

$$\phi = \frac{(L-2t)^3}{L^3} = (1-2\xi)^3 \quad (19)$$

Thus, given thermal conductivities for the glass melt and gas, the effective thermal conductivity of the glass foam layer becomes only a function of the porosity. The conductivity of the glass melt is a function of the temperature and is given by [13]

$$k_l = 1 + \frac{T - 273.15}{600} \left[\frac{W}{m \cdot K} \right] \quad (20)$$

The thermal conductivity of the gas is assumed to be constant in the temperature range of the glass foam layer and is given by $k_g = 0.05$ W/m-K [14].

Glass Parameters. The band model presented by Viskanta and Wu [15] is used to describe the spectral behavior of the absorption coefficient of glass. This is a three-band model with the following parameters:

$$\kappa_\lambda = 25 \ \text{m}^{-1} \quad \text{for} \ 0 \leqslant \lambda < 2.7 \ \mu\text{m}$$

$$\kappa_\lambda = 250 \ \text{m}^{-1} \quad \text{for} \ 2.7 \leqslant \lambda < 4.7 \ \mu\text{m}$$

$$\kappa_\lambda = \infty \ \text{m}^{-1} \quad \text{for} \ \lambda > 4.7 \ \mu\text{m}$$

Thus, the glass foam layer is semitransparent to radiation with a wavelength below the critical value of 4.7 μm and is opaque to radiation that has a wavelength above this value. Following the work by Lee and Viskanta [16], the refractive index of the glass and its emissivity in the opaque region are $n_g = 1.5$ and $\varepsilon_{op} = 0.9$, respectively. The reflectivities of the combustion gas/foam interface are given by empirical correlations in ([17], p.21) based on data compiled by Orchard [18]. No such data exists for the foam/glass melt interface reflectivities, which for the purposes of this analysis are estimated using Snell's law for an optically smooth interface.

Environmental Parameters. The temperature of the combustion gases and refractories is expected to be around 1800 K, which is also taken as the effective ''emission'' temperature. Similarly, the glass melt temperature is assumed to be 1000 K and the effective ''emission'' temperature at the bottom of the layer is also assumed to be 1000 K. The convective heat transfer coefficient for the combustion gas/foam layer interface is expected to be about 100 W/m-K [16]. The convective heat transfer coefficient at the foam/glass melt interface is uncertain as it is locally dependent on the complex natural convection flow structure in the glass melt and transport of bubbles near the foam/glass melt interface, which are function of the specific furnace type and operating conditions. In the large scale furnaces, the case considered here, the glass melt velocity near the free surface is only a few centimeters per minute because of the slow circulation of the glass melt [19], and we assume a relatively low value of glass/foam heat transfer coefficient, 5 W/m-K, to reflect such a behavior. In general, the heat transfer coefficient should be calculated by performing detailed simulations of heat and fluid flow in the glass melt for the specific furnace design and specific operating conditions [5].

Model Validation

There are two major sources of uncertainties that must be assessed and controlled to have confidence in the validity of the simulations results. First comes from the accuracy of the model for predicting effective radiative and thermophysical properties of the foam, which was carefully assessed in [6–8], and also from the validity of the assumptions used in the model formulation, which is discussed in the previous section. The second source is due to the numerical methods used for solving the problem in hand, and the validation procedure is discussed next.

The convergence tests were performed on the baseline case of a 5 cm thick foam layer with a uniform bubble size distribution. Successive increase of the number of nodes led to convergence of the temperature field. The largest error was at the bottom boundary where increasing the number of nodes from 500 to 1000 gave a 0.5 K difference. The difference at all other corresponding nodes was on the order of 1×10^{-2}. To obtain a satisfactory combination of computational efficiency and accuracy, 500 nodes were used for all cases.

The effect of the number of bands used for spectral integration below the critical wavelength was also studied. Increasing the number of bands led to a convergent temperature field, and to obtain sufficiently accurate results, 20 bands were used below the critical wavelength. The number of bands used above the critical wavelength is not as crucial since the amount of radiant energy in this spectral region is relatively small.

The numerical algorithm developed in previous section was tested on the relatively simple case of a plane parallel, gray, absorbing-emitting medium between two isothermal plates at 1000 K and 500 K to verify that it produces accurate results. Figure 3 illustrates the temperature distribution across this layer for various values of the conduction to radiation parameter, N_{cr}, as defined by Modest [10]. Comparing these results to those given by Modest ([10], p. 719) shows excellent agreement, as our predictions and those by Modest on Fig. 3 lie on top of each other. It should be mentioned that the algorithm displays instabilities if $N_{cr} < 10^{-5}$ (i.e., when radiation is essentially the only mode of heat transfer) because the source linearization procedure [Eq. (16)] is not sufficiently robust (i.e., requires a good initial guess) to handle the problems with a overwhelming dominance of the nonlinear (radiation) phenomena. Fortunately, this does not present a problem, since N_{cr} in the typical glass foam layers is on the order of 10^{-2} or higher.

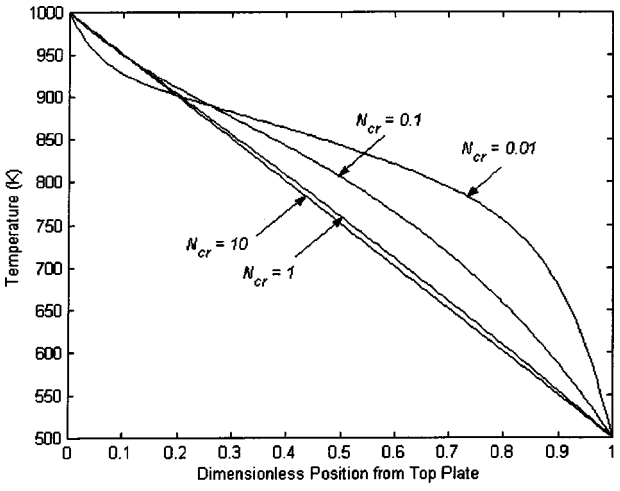

Fig. 3 Code validation results: comparison of the temperature profiles for different values of the conduction to radiation parameter [10]

Results and Discussion

In all simulations, the parameters were taken as those presented in the previous sections unless otherwise noted. Since the foam layer thickness is expected to range from 1 cm to 10 cm, the baseline case is taken as a 5 cm, isotropically scattering foam layer with a uniform bubble size of 5 mm as representative to the actual arrangement [7]. Figure 4 shows the temperature field for the baseline case along with the temperature field for a layer under the same conditions with zero resistance to radiation transport (i.e., the spectral extinction coefficient, β_λ, is zero across the entire spectrum). The case of zero-resistance to radiation is such when pure heat conduction equation is solved within the foam layer (i.e., foam is assumed not to scatter or absorb radiation in the spectral range where it is semitransparent), yet the convection +radiation boundary condition (Eq. (13)) is still used to account for fraction of radiation absorbed at the top surface of the foam within the spectral region where glass is opaque. Thus, the purpose of Fig. 4 is to emphasize the difference between the cases when one does and does not account for the radiation/foam interactions in the spectral region where glass is semitransparent. The foam layer shows a temperature drop from about 1745 K to 1113 K compared to the temperature decrease from 1770 K to 1592 K shown in the zero-radiation resistance foam layer. This confirms that the heat transfer to the glass melt is significantly impeded by the presence of the foam layer. This observation agrees with the result obtained by Fedorov and Viskanta in [7,8], which predicts a total apparent transmittance of zero for a 5 cm thick foam layer. The comparison between the results obtained when both radiation and conduction are considered (solid line) and when radiation is neglected (dashed line) provides also a good illustration to the relative magnitude of radiation to conduction heat transfer resistances. In the case of the optically thick foams (thickness greater than 5 cm for the soda-lime glass considered here), the radiation heat transfer resistance dominates and accounts for greater than 75 percent of the total resistance to heat transfer across the foam layer (see Fig. 4). On the other hand, for the optically thin foams (thickness below 3 cm) comparison of the results obtained for the cases when both conduction and radiation are considered and when radiation is neglected (not shown here) indicates that the radiative transfer becomes a less significant (less than 30 percent of the total resistance is due to radiative transfer), although still not a negligible factor in determining of the total resistance to heat transfer.

The impedance of heat transfer to the glass melt depends strongly on the thickness of the foam layer as shown in Fig. 5, which shows temperature profiles for a foam thickness ranging from 1 cm to 10 cm. Because the incident radiation can more easily penetrate a thinner foam layer (i.e., the amount of scattering and absorption experienced by the radiation is reduced), the temperature at the glass melt interface is greater. Examining Fig. 5, a 1 cm foam layer has a temperature of 1345 K at the glass melt interface, 232 K higher than that for the baseline 5 cm foam layer. Furthermore, the temperature at the glass melt interface tends toward the glass melting temperature for thicker foam layers because the thicker the foam layer, the smaller the fraction of radiation that reaches the interface between the foam and glass melt, thereby decreasing heat transfer to the glass melt. As the foam layer thickness grows, the temperature profiles approach the asymptotic limit set by the curve for 10 cm thick foam, provided all other parameters remain the same. Also, Fig. 5 shows that thicker foam layers exhibit a higher temperature at the foam/combustion gas interface because of an increased total resistance to heat transfer. If the furnace is considered to be a perfectly insulated box, as a first approximation, then an increase in the foam temperature stipulates an equivalent increase in the effective temperature of the refractories in order to maintain the required supply of energy for heating the glass melt. This leads to an increased generation of NO_x pollutants via thermal mechanisms in the combustion space and also promotes wear of the furnace crown, resulting in a significant decrease in the furnace longevity.

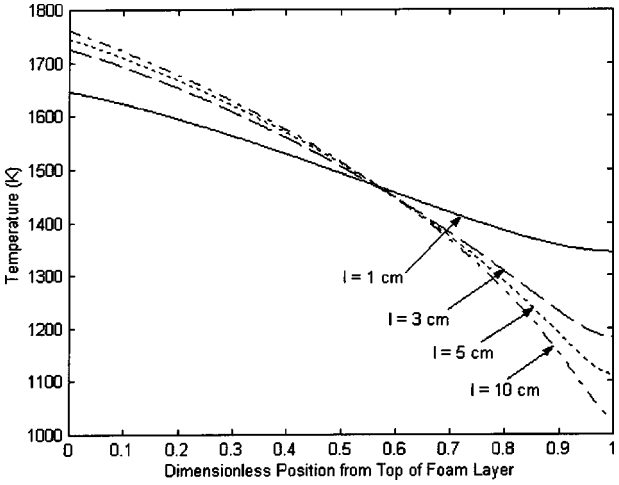

Fig. 5 Effect of foam layer thickness on temperature profile for the foam layer with average bubble diameter a=5 mm

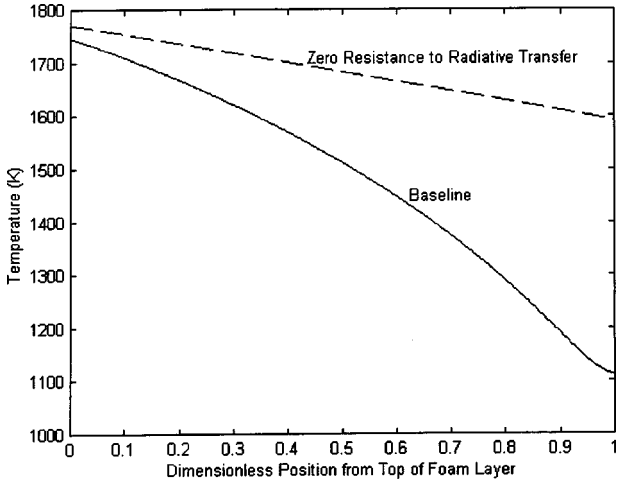

Fig. 4 Temperature field for baseline case and a zero-radiation resistance layer

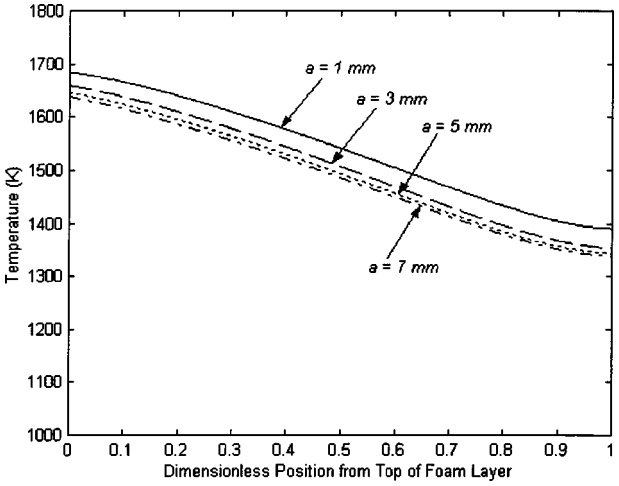

Fig. 6 Effect of bubble size on temperature distribution for a 1 cm foam layer

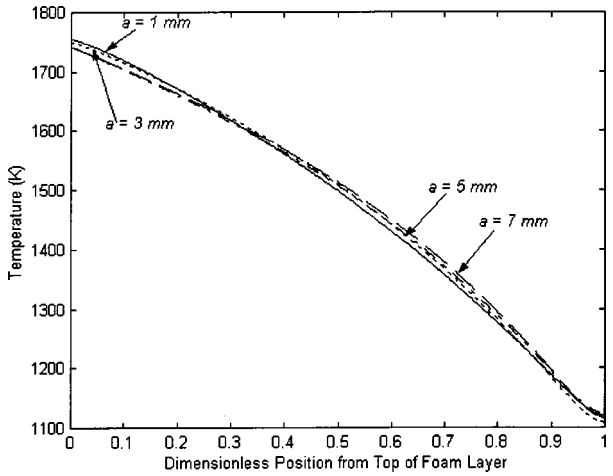

Fig. 7 Effect of bubble size on temperature field for a 5 cm foam layer

The effect of bubble size on the temperature field was also investigated. Temperature fields for foam layers containing bubbles of a uniform size from 1 to 7 mm are illustrated in Figs. 6 and 7, which correspond to a foam layer thickness of 1 cm and 5 cm, respectively. These figures show that bubble size has more influence on the temperature field for thinner foam layers. Essentially, foam layers thicker than about 4 cm become opaque for bubble sizes on the order of 5 mm [7], which is the prevalent bubble size expected for the glass melting process. Since the 5 cm foam layer is effectively opaque, the temperature field is almost independent of bubble size. For the 1 cm foam layer, radiation is only partially absorbed by the foam, and the temperature at each point in the foam layer decreases with increasing bubble size, with the difference becoming smaller as the bubble size increases. To explain this, consider Fig. 8, which plots the spectral extinction coefficient according to the model presented by Fedorov and Viskanta [7] for different bubble sizes. The trend observed for the spectral extinction coefficient is the same as for the temperature field. For a smaller bubble size, the extinction coefficient is larger, causing more of the radiation to be attenuated within the foam layer, which raises its temperature.

Finally, the effect of the heat transfer coefficient at the molten glass/foam interface has been also assessed. The results indicate that a change in the heat transfer coefficient by one order of magnitude from its baseline value of 5 W/m-K has very little effect on the temperature distribution across the foam layer, as long as it is optically thick (i.e., when the layer thickness is greater than 5 cm for soda-lime glass). The shape of the temperature profiles remains the same, and only the temperature of the foam/molten glass interface becomes slightly lower (i.e., closer to the glass melt temperature T_l) when the heat transfer coefficient is increased. This is because the dominant resistance to heat transfer lies in the foam itself, rather than at the top (foam/combustion space) and bottom (foam/glass melt) interfaces, as long the foam layer is optically thick. Only when the foam layer is optically thin (the actual thickness is less than 3 cm), an order-of-magnitude increase in the foam/molten glass heat transfer coefficient results in a significant decrease of the foam/molten glass interface temperature (by about 200°C to 300°C). However, such thin foams are unlikely to be stable in the actual furnace environment because of strong combustion-induced pressure fluctuations in the furnace environment above the foam [6].

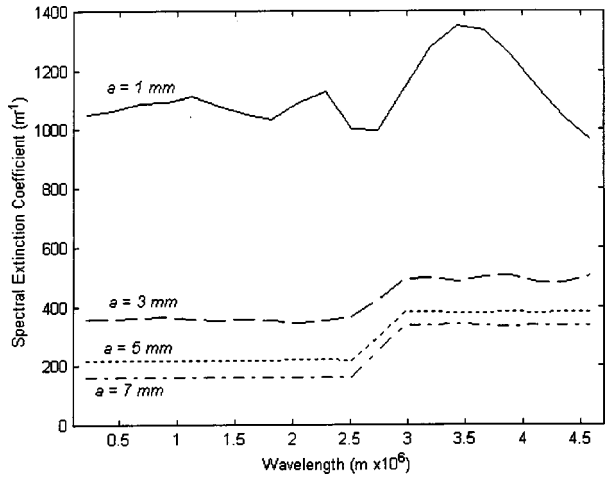

Fig. 8 Effect of bubble size on spectral extinction coefficient

Conclusions

Combined conduction and radiation heat transfer through a foam layer with application to a glass melting has been studied. The results show that the foam layer offers a significant resistance to radiative transport, which reduces the heat flux to the glass melt and the temperature at the interface with the glass melt. Thus, the amount of heat received by the glass melt is much less in areas of the glass melting furnace where thicker foam layers are present, which makes the melting process more costly and inefficient. Thicker foam layers also have a higher combustion gas/foam layer interface temperature because of an increased resistance to the heat transfer, which in turn leads to an overall higher temperatures of the furnace environment. This facilitates an increased generation of thermally actuated pollutants such as nitric oxides. The bubble size and heat transfer coefficient at the foam/molten glass interface are also important in determining the temperature distribution in the foam layer, but only for optically thin foam layers.

Finally, the theoretical model of the heat transfer in the foam developed here makes the first step in establishing a critical, and so-far missing link [6] that is required to couple heat and mass simulations of the combustion space [4] and of the glass melt [5] towards development of an integrated approach for the model-based optimal design of glass melting furnaces. In addition, knowledge of the local temperature distribution across the foam is critically important to understanding and controlling foam formation and stability as well as the chemical composition and quality of the molten glass [6]. This is because the mass transport properties of the foam regulates diffusion of chemical species from the combustion space to the glass melt and vice versa, and gas diffusion through the glass foams is a thermally activated processes, as the effective mass diffusion coefficient of major gas species (O_2, SO_2, CO_2, H_2O, and others) depends exponentially on the local temperature of the foam [12].

Nomenclature

Symbol

F_d = fraction of forward scattered radiation
h = convective heat transfer coefficient
I = intensity of radiation
k = thermal conductivity
l = foam layer thickness
L = size of the foam unit cell
n = refractive index
$\hat{\mathbf{n}}$ = unit vector normal to surface
p = pressure
$\dot{Q}$ = internal heat generation
$\mathbf{q}$, q = heat flux
T = temperature
t = time
u = internal energy

$\mathbf{v}$ = velocity
x = coordinate in direction perpendicular to foam layer

Greek Symbols

β = extinction coefficient
ε = emissivity
κ = absorption coefficient
σ = scattering coefficient
ρ = density
μ = viscosity
ϕ = porosity
Φ = scattering phase function or viscous dissipation function in Equation (1)
λ = wavelength (refers to a spectral quantity)
$\hat{\mathbf{\Omega}}$ = unit direction vector
ω = single scattering albedo
τ = optical thickness ($=\int_0^x \beta dx$)

Subscripts

b = refers to blackbody
c = refers to conduction
eff = refers to an effective value
f = refers to foam
g = refers to gas phase
inc = refers to incident radiation on the top of the foam
l = refers to liquid phase (glass melt and lamellae)
r = refers to radiation

Superscripts

$+$ = refers to forward hemisphere
$-$ = refers to backward hemisphere

References

[1] Kappel, J., Conradt, R., and Scholze, H., 1987, ''Foaming Behavior on Glass Melts,'' Glass Sci. Technol. (Amsterdam), **60**(6), pp. 189–201.
[2] Kim, D., and Hrma, P., 1991, ''Foaming in Glass Melts Produced by Sodium Sulfate Decomposition Under Isothermal Conditions,'' J. Am. Ceram. Soc., **74**(3), pp. 551–555.
[3] Laimbock, P. R., 1998, ''Foaming of Glass Melts,'' Ph.D. thesis, Technical University of Eindhoven, The Netherlands.
[4] Webb, B. W., 1997, ''Measuring and Modeling Combustion in Glass Melting Furnaces,'' Glass Researcher, **6**(2), pp. 16–18.
[5] Viskanta, R., 1994, ''Review of Three-Dimensional Mathematical Modeling of Glass Melting,'' J. Non-Cryst. Solids, **177**, pp. 347–362.
[6] Fedorov, A. G., and Pilon, L., 2002, ''Glass Foams: Formation, Transport Properties, and Heat, Mass, and Radiation Transfer,'' J. Non-Cryst. Solids, in press.
[7] Fedorov, A., and Viskanta, R., 2000, ''Radiative Transfer in a Semitransparent Glass Foam Layer,'' Phys. Chem. Glasses, **41**(3), pp. 127–135.
[8] Fedorov, A., and Viskanta, R., 2000, ''Radiation Characteristics of Glass Foams,'' J. Am. Ceram. Soc., **83**(11), pp. 2769–2776.
[9] Trier, W., 1963, ''Warmeubergangzwischen Flamme and Glasbad in Glasschmelzwannenofen,'' Glass Sci. Technol. (Amsterdam), **36**(3), pp. 73–86.
[10] Modest, M., 1993, *Radiative Heat Transfer*, Mc-Graw-Hill, New York, NY.
[11] Rohsenow, W. M., and Choi, H. Y., 1961, *Heat, Mass and Momentum Transfer*, Prentice Hall, Englewood Cliffs, NJ.
[12] Pilon, L., Fedorov, A., and Viskanta, R., 2000, ''Gas Diffusion in Closed Cell Foams,'' J. Cell. Plast., **36**(6), pp. 451–474.
[13] Ungan, A., and Viskanta, R., 1986, ''Melting Behavior of Continuously Charged Loose Batch Blankets in Glass Melting Furnaces,'' Glass Sci. Technol. (Amsterdam), **59**(10), pp. 279–291.
[14] Touloukian, Y. S., Liley, P. E., and Saxena, S. C., eds., 1973, ''Thermal Conductivity; Nonmetallic Liquids and Gases,'' Thermophysical Properties of Matter, **3**, Plenum Press, New York, NY.
[15] Viskanta, R., and Wu, X., 1983, ''Effect of Radiation on the Melting of Glass Batch,'' Glass Sci. Technol. (Amsterdam), **56**(6/7), pp. 138–147.
[16] Lee, K. H., and Viskanta, R., 1999, ''Comparison of the Diffusion Approximation and the Discrete Ordinates Method for the Investigation of Heat Transfer in Glass,'' Glass Sci. Technol. (Amsterdam), **72**(8), pp. 254–265.
[17] Egan, W. G., and Hilgeman, T. W., 1979, *Optical Properties of Inhomogeneous Materials: Applications to Geology, Astronomy, Chemistry, and Engineering*, Academic Press, New York, NY.
[18] Orchard, S. E., 1969, ''Reflection and Transmission of Light by Diffusing Suspensions,'' J. Opt. Soc. Am., **59**(12), pp. 1584–1597.
[19] Pilon, L., Zhao, G., and Viskanta, R., 2002, ''Three-Dimensional Flow and Thermal Structure in Glass Melting Furnaces,'' Glass Sci. Technol. (Amsterdam), **76**(2/3), pp. 55–68.

A Holistic Optimization of Convecting-Radiating Fin Systems

M. Sasikumar

C. Balaji
e-mail: balaji@acer.iitm.ernet.in

Heat Transfer and Thermal Power Laboratory,
Department of Mechanical Engineering,
Indian Institute of Technology Madras,
Chennai 600 036, India

A convecting-radiating fin array, which stands vertically outside of a horizontal rectangular duct, has been analyzed for various design constraints. Fully developed turbulent flow is considered inside the duct. This study takes into account the variation of fluid temperature along the duct, which has been ignored in most of the earlier studies. The one-dimensional governing equation for temperature distribution along the fin is solved for all the fins of the fin array and the total heat transfer rate per unit system mass, total entropy generation rate and optimum fin height based on maximum heat transfer rate per unit system mass are evaluated from the derived temperature profiles. These quantities are then correlated as functions of geometric and flow parameters for three types of fin profile. Optimum solutions are generated based on (i) maximum heat dissipation rate per unit system mass and (ii) minimum entropy generation rate. A procedure to combine these two optima in order to obtain a "holistic" optimum is also discussed.
[DOI: 10.1115/1.1497358]

Keywords: Convection, Optimization, Radiation

Introduction

The performance of heat exchanging devices can be improved by heat transfer augmentation techniques such as the use of extended surfaces. This improves the convective and radiative heat transfer rates, which result in decrease of system size and weight. Fins are especially attractive for these applications because they offer an economical, trouble free solution to the problem, when properly designed. In recent years, a great deal of research effort has been devoted to the analysis and optimization of extended surfaces. An experimental study on natural convection heat transfer from horizontal fin arrays has been performed by various researchers like Harahap and McManus [1], and Jones and Smith [2], and the same configuration with radiation and mutual irradiation between fins was analyzed by Donovan and Rohrer [3], Rammohan Rao and Venkateshan [4]. From these studies, it was observed that natural convection is a dominant process. Generally, heat transfer processes are accompanied by thermodynamic irreversibility such as entropy generation. The production of entropy may be due to fluid friction and heat transfer across a finite temperature difference. These irreversibilities can be minimized by keeping the entropy generation pertinent to the thermal system to the minimum. The coupling between entropy generated due to the above mentioned irreversibilities was examined using the concept of heat exchanger irreversibility by Bejan [5] and also discussed the origin of irreversibility production mechanism and its distribution through a fluid medium under convective heat transfer situation. Numerical thermodynamic optimization studies have been conducted by Nag and Mukherjee [6], and Balaji et al. [7] for various thermal situations.

The above review of literature shows that a lot of work has been done in the area of heat transfer optimization of fins and entropy generation minimization as well. However, optimization of thermal systems by holistically considering the above two competing criteria is an undeveloped area. Such an analysis would enable a much better understanding of the problem and make useful correlations available. This is the main objective of the present work. In the present study, turbulent flow inside a flat duct on which the convecting-radiating fins stand vertically, has been considered and one dimensional fin equation for a convecting-radiating fin array is solved using various numerical techniques.

Mathematical Formulation

The problem considers an array of equally spaced vertical fins standing on the top of a rectangular duct bathed by fully developed turbulent flow. This is shown in Fig. 1. The bottom side of the duct is truly adiabatic. The fin profile can be rectangular, triangular or trapezoidal in general. The following assumptions are made in the present work.

(i) The fin material is homogeneous and the material properties are constant.
(ii) Steady state conditions prevail in the fin system.
(iii) The flow inside the duct is considered to be fully developed and turbulent.
(iv) The temperature gradient across the fin thickness is very small as compared to the gradient along the fin height.
(v) The duct and fin width are unity.

Heat transfer takes place by convection from the fluid to the wall of the tube, whereas from the surface of the fin and the duct heat is lost by both convection and radiation to the environment. The mutual interaction between adjacent fins has also been considered. Aluminum has been chosen as the fin and duct material because of its high thermal conductivity and low density. Under steady state conditions, the application of energy conservation principle along a fin yields [8],

$$\frac{d^2\phi_1}{dY^2}-D_1H\frac{d\phi_1}{dY}-Nct_bD_2(\phi_1-\phi_\infty)-Nrt_bD_2\phi_1^4+\left(\frac{Nrt_bD_2}{2\sigma T_b^4}\right)\times[G_l+G_r]=0 \quad (1)$$

where, G_l and G_r are the irradiations from the left and right side of the fin respectively and D_1, D_2 are the fin constants, which are given by,

$$D_1=\frac{m}{(t_b-mYH)} \quad \text{and} \quad D_2=\frac{\sqrt{m^2+4}}{(t_b-mYH)}$$

Contributed by the Heat Transfer Division for publication in the JOURNAL OF HEAT TRANSFER. Manuscript received by the Heat Transfer Division January 31, 2001; revision received May 29, 2002. Associate Editor: G. S. Dulikravich.

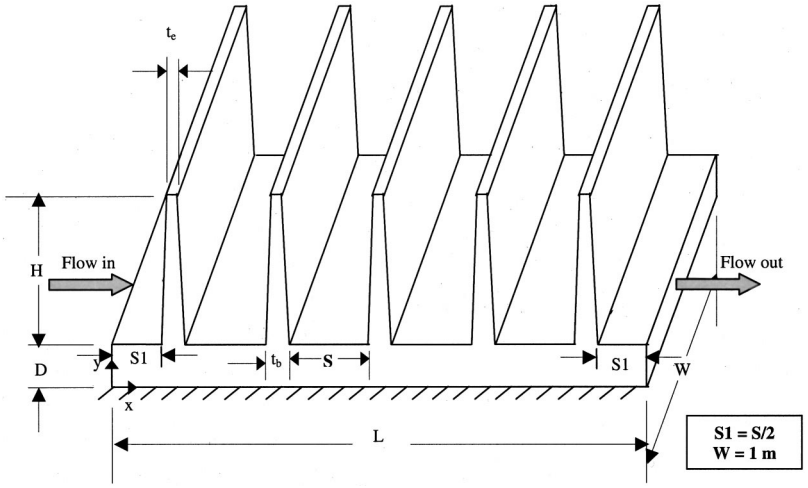

Fig. 1 Schematic of the physical system being investigated. The figure shows a general case of trapezoidal-profiled fins arranged on a horizontal duct

where, "*m*" is defined as the ratio of the difference between the fin base and end thickness to height of the fin, and is given by, $m=(t_b-t_e)/H$. The non-dimensional variables are defined by

$$Nc=\frac{H^2h_{1\infty}}{kt_b},\quad Nr=\frac{\varepsilon\sigma H^2T_b^3}{kt_b},\quad \text{and}\quad \phi_1=T/T_{b1},\quad Y=y/H \tag{2}$$

Equation (1) represents the dimensionless governing equation for a one-dimensional convecting-radiating fin. The boundary conditions are given by

$$Y=0,\quad \phi_1=1\quad \text{and}\quad Y=1,$$

$$\frac{d\phi_1}{dY}+\left(\frac{Hh_{1\infty}}{k}\right)(\phi_1-\phi_\infty)+\left(\frac{\varepsilon\sigma HT_b^3}{k}\right)(\phi_1^4-\phi_\infty^4)=0 \tag{3}$$

An energy balance needs to be carried out on the unfinned portion of the duct, because heat will be transferred from the unfinned portion too. The duct wall is considered to be very thin, so that conduction along the duct wall is neglected. So, heat convected from the fluid in this portion is directly transferred to the environment by convection and radiation. An energy balance [9] on a small element of the unfinned portion of the duct gives,

$$\frac{d\phi_{2f}}{dX}+\left(\frac{\varepsilon sw}{mCpT_{in}}\right)(\sigma\phi_{2s}^4T_{in}^4-G)+\left(\frac{h_{2\infty}sw}{mCp}\right)(\phi_{2s}-\phi_\infty)=0 \tag{4}$$

and

$$(\phi_{2f}-\phi_{2s})=\left(\frac{\varepsilon}{h_fT_{in}}\right)(\sigma\phi_{2s}^4T_{in}^4-G)+\left(\frac{h_{2\infty}}{h_f}\right)(\phi_{2s}-\phi_\infty) \tag{5}$$

The dimensionless variables are defined by,

$$\phi_{2s}=\frac{T_s}{T_{in}},\quad \phi_{2f}=\frac{T_f}{T_{in}},\quad \phi_\infty=\frac{T_\infty}{T_{in}}\quad \text{and}\quad X=\frac{x}{s}.$$

The initial condition is given by, at $x=0$, $T_f=T_{in2}$, where T_{in2} is the local fluid entry temperature in the unfinned portion ($T_f=T_{in}$ for the first unfinned portion). In this study, the heat transfer coefficients $h_{1\infty}$, $h_{2\infty}$, and h_f are computed based on the correlations available in literature [10]. As regards radiation, two types of shape factors need to be used in the present analysis, (i) shape factor between the fin elements, and (ii) shape factor between the fin and duct elements. Hottel's Crossed String method [11] has been used to obtain the shape factors between these elements. After obtaining N^2 view factors for N elements, the radiosity formulation is used for calculating the radiosities and irradiation on the fin and the duct surfaces. Radiosity is assumed uniform over the area of any element. The dimensionless radiosity of *i*th element is given by,

$$\phi_{ri}=\varepsilon_iR_i+(1-\varepsilon_i)\sum_{j=1}^{N+1}F_{ij}\phi_{rj}$$

$$\text{where}\quad \phi_{ri}=\frac{J_i}{\sigma T_a^4}\quad \text{and}\quad R_i=\frac{T_i^4}{T_a^4} \tag{6}$$

The irradiation on the *i*th element can be obtained by

$$G_i=\sum_{j=1}^{N}F_{ij}\phi_{rj}.$$

Because of the variation of fluid temperatures along the duct, the temperature profile of one fin is different from the adjacent fin. So, the irradiation on a fin from a fin on right side is different from that from a fin on the left side.

Solution Procedure

The geometry of the system is fixed by the input data of fin height, fin thickness, number of fins, mass flow rate, duct spacing and emissivity of the surface. With the assumed values of nodal temperature of all the fin and the duct elements, the radiosity Eq. (6) is evaluated using a Gauss-seidel iterative procedure in order to obtain the updates for the radiosities and the convection heat transfer coefficients are calculated using the available correlations. With these updated values, the one-dimensional fin equations are solved using a finite difference scheme with a second order Lagrangian polynomial, whereas the energy balance equations of the unfinned portion are solved by Euler's implicit method to obtain the new set of nodal temperature values. The convective heat transfer coefficients in the inside of the duct are computed using Dittus-Bolter equation with an equivalent hydraulic diameter of the duct. The above procedure is repeated until the error on the temperature updates is less than the required convergence criterion (10^{-5}) and upon convergence, the temperature distribution along the duct is obtained. The properties of the coolant fluid have been evaluated at the average temperature of the fluid at inlet and outlet, whereas the outside air properties are taken as functions of the film temperature of the surface. One-dimensional semi-cosine grid pattern with 30 elements along the fin height has been used. The convergence criterion used throughout this analysis is as given:

Table 1 Range of parameters considered in the present study

Parameters	Range	Units
H	0.01 – 0.10	m
n	4 – 25	-
t_b	0.003	m
t_p	0.001 – 0.003	m
D	0.01 – 0.10	m
L	1.0 – 2.5	m
m_f	0.125 – 0.325	kg/s
ε	0.05 – 0.95	-
T_∞	303	K
T_{in}	373	K
Fluid inside the duct	Air	-
Pr	0.7	-
Fin material	Aluminum	-

$$\left|\frac{\phi_{new}-\phi_{old}}{\phi_{old}}\right|<10^{-5}$$

Since steep gradients will be encountered near the wall, the semi-cosine grid pattern gives a finer grid near the fin base and progressively lesser grids towards fin the tip. After obtaining the fluid temperature distribution, the heat transfer rate per unit mass of the system and the total entropy generation rate due to heat transfer are calculated by summing all the elemental quantities.

Then the total entropy generation rate is given by

$$S_{gen,total}=S_{gen,heat}+S_{gen,fluid}. \quad (7)$$

Entropy generation due to heat transfer is defined as the irreversibility produced on the fin and the duct because of conductive, convective and radiative resistances. The entropy generation rate due to the fluid friction is calculated by using the following relation,

$$S_{gen,fluid}=m_f\Delta P/\rho_f T_\infty \quad (8)$$

where, the pressure difference is given by $\Delta P=(4fL/D)(\rho_f V^2/2)$ and friction coefficient f is given by $f=0.046/\mathrm{Re}^{0.2}$ for turbulent flow [12].

Results and Discussion

A coolant like air with inlet temperature of 373 K has been considered for the present study. The geometric and flow parameters which characterize the present problem are duct spacing (D), duct length (L), fin height (H), number of fins (n), mass flow rate (m_f) of the fluid and the surface emissivity (ε). The range of above-mentioned parameters can be seen from Table 1. Before undertaking the parametric study, a detailed grid independence has been performed for various combinations of parameters and it is found that the variation of total heat transfer per unit mass with number of elements is almost negligible after 20 elements. Hence, a grid pattern of 20 elements in each finned and unfinned portion is used in all the calculations. Within this range, results such as optimum fin height, fin and fluid temperature distribution, total heat transfer rate per unit mass and total entropy generation rate are obtained. An asymptotic validation has been performed for a typical case to compare the numerical results with analytical values for a particular fin system configuration and the excellent agreement of results can be seen from Fig. 2. Figure 3 shows the

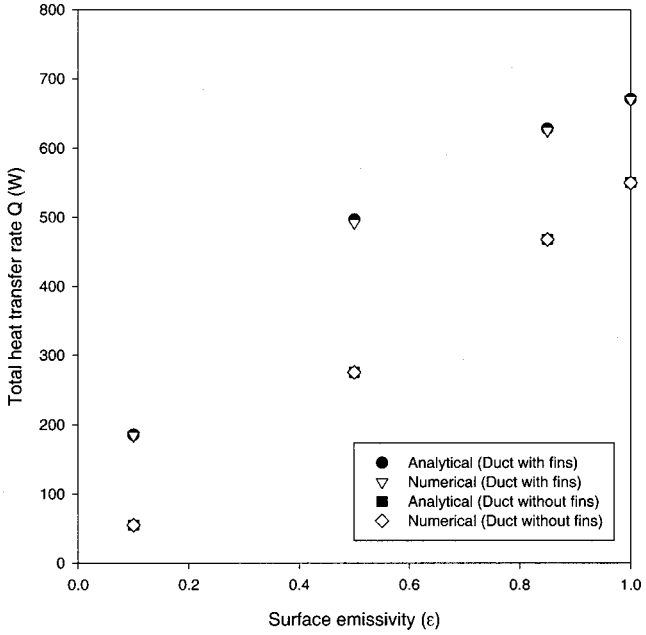

Fig. 2 Asymptotic validation plot shows the agreement of numerical values of total heat dissipation rate with analytical solution ($H=0.10$ m, $s=0.05$ m, $t_b=0.0015$ m, $T_{in}=400$ K, and $n=10$)

fluid temperature distribution along the duct for a particular set of geometric parameters. From the figure, it is observed that the temperature drop is linear in the unfinned portion of the duct, while a steep drop is observed in the finned portion of the duct, as expected. This variation of fluid temperature along the duct for a particular combination of parameters has been compared with the numerical data of Sunilkumar [13], who considered the problem of a purely radiating fin system and the good agreement can also

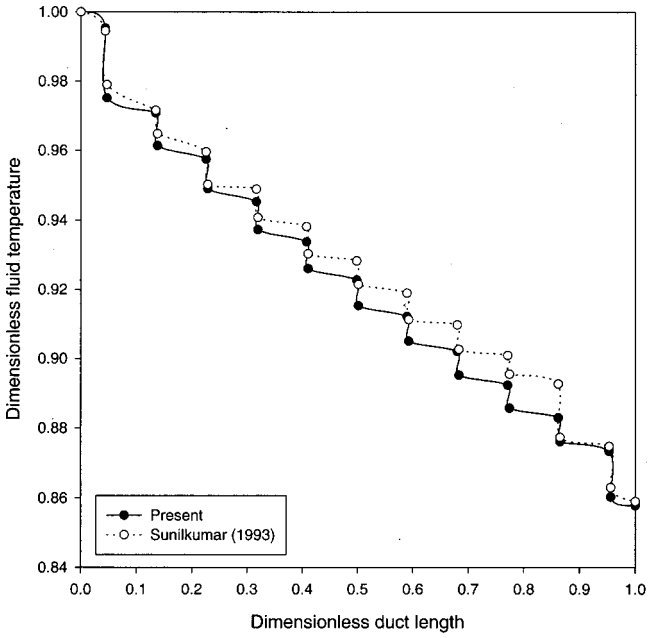

Fig. 3 Comparison of dimensionless fluid temperature values of the present analysis with data of numerical analysis of Sunilkumar [13] for a particular combination of parameters ($mC_p=14$ W/m·K, $k=114$ W/m·K, $L=0.50$ m, $T_{in}=450$ K, $H=0.08$ m, $n=12$, and $\varepsilon=0.50$)

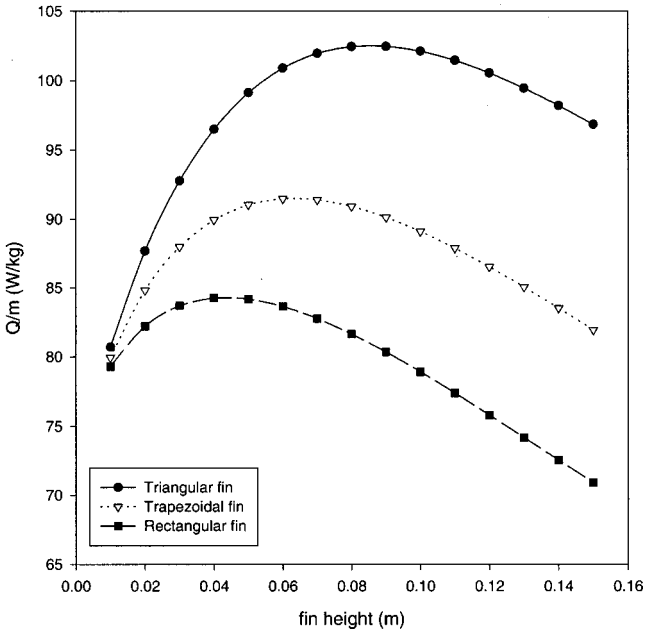

Fig. 4 Variation of total heat transfer rate per unit mass with various fin heights for three fin profiles. The following parameters are considered: ($n=10$, $L=1.0$ m, $D=0.03$ m, $m_f=0.25$ kg/s, and $\varepsilon=0.50$)

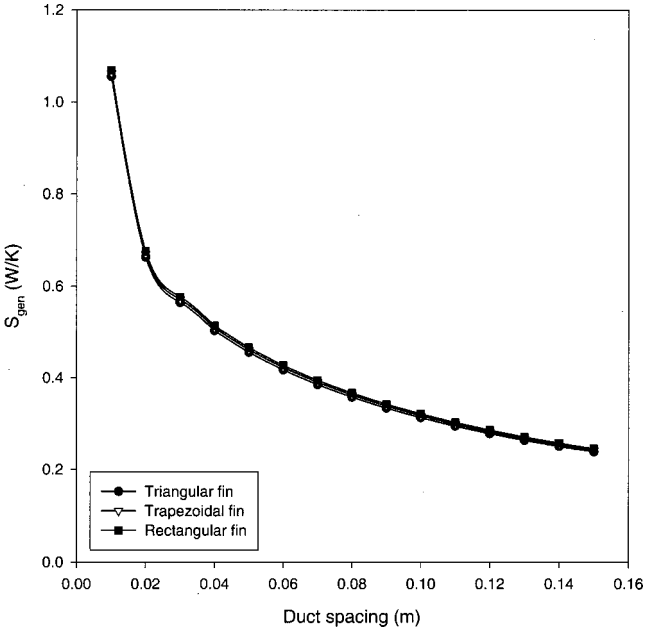

Fig. 5 Variation of total entropy generation rate with duct spacing for three fin profiles. The graph is plotted for the following of parameters ($n=10$, $L=1.0$ m, $H=0.05$ m, $m_f=0.25$ kg/s, and $\varepsilon=0.50$)

be seen in this figure. The results of total heat dissipation from a rectangular cavity open at the top end with constant base temperature and variable wall temperature has also been compared with results available in the literature [14] for various aspect ratios. A reasonably good agreement has been found with the results of this study.

Effect of Various Parameters on the Performance of Fin System

The quantity of utmost importance in the design of a fin system is the heat transfer rate per unit mass of the system. In order to improve the performance of a thermal system, this quantity should be improved. But from the viewpoint of second law, an increase in total heat transfer rate from the system will increase the entropy generation rate. The system's departure from the reversible limit may be characterized by its second law efficiency, which will be higher if the entropy generation rate can be reduced to lower values. Hence, the total entropy generation from the system is also incorporated as a design criterion in this optimization analysis and an effort is made to consider both criteria in order to obtain ''holistic'' optima. Figure 3 shows the variation of total heat transfer rate per unit mass with respect to fin height for three fin profiles. From this figure, it can be observed that the triangular fins have higher heat dissipation rate per unit system mass as compared to other fins. Besides, from the viewpoint of entropy generation also triangular fins are more effective than other configurations. This study emphasizes the advantages of triangular fins over the other fin profiles. If rectangular or trapezoidal fins are employed instead of triangular fins, the increase of system mass is much severe and this is inadequately compensated by the increase in total heat dissipation. Hence, triangular profiled fins show the best performance. But from the view point of ease of manufacturing, rectangular fins offer some advantage over the other two fin profiles.

Meanwhile, as the fin height increases, the total heat transfer rate per unit mass attains a peak value and then starts decreasing. The height at which the peak occurs is called the optimum fin height and these points are marked in Fig. 4. This is because, up to this maximum height, the heat transfer rate increases more rapidly than does the mass of the system and beyond that, the increase in height only adds mass without a commensurate increase in the heat transfer rate. But there is a linear variation with respect to fin height as far as the total entropy generation rate is concerned. The variation of total entropy generation rate with respect to duct spacing for three fin profiles has been illustrated in Fig. 5. Up to some value of duct spacing, the total entropy generation rate increases abruptly; beyond that point, the variation becomes almost constant. For lower values of duct spacing, the effect of fluid friction and heat transfer on entropy generation is very severe. This is mainly due to high friction factors at lower values of duct spacing.

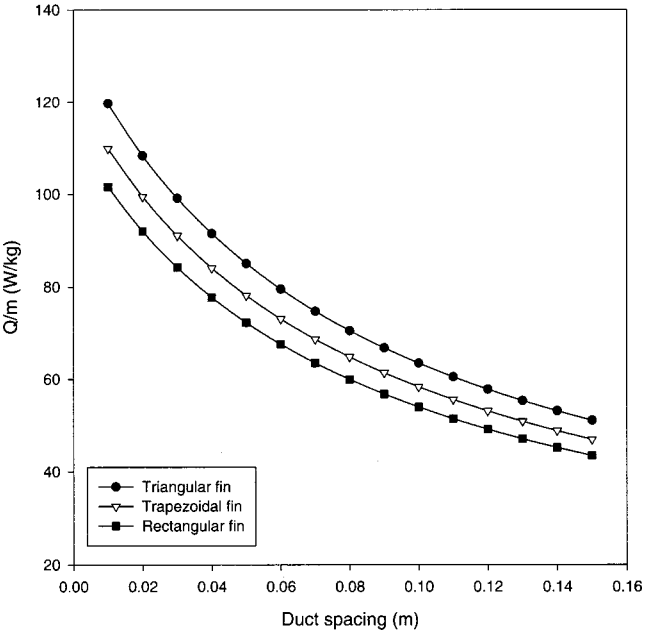

Fig. 6 Variation of total heat transfer rate per unit mass with duct spacing for three fin profiles and the following combination of parameters ($n=10$, $L=1.0$ m, $H=0.05$ m, $m_f=0.25$ kg/s, and $\varepsilon=0.50$)

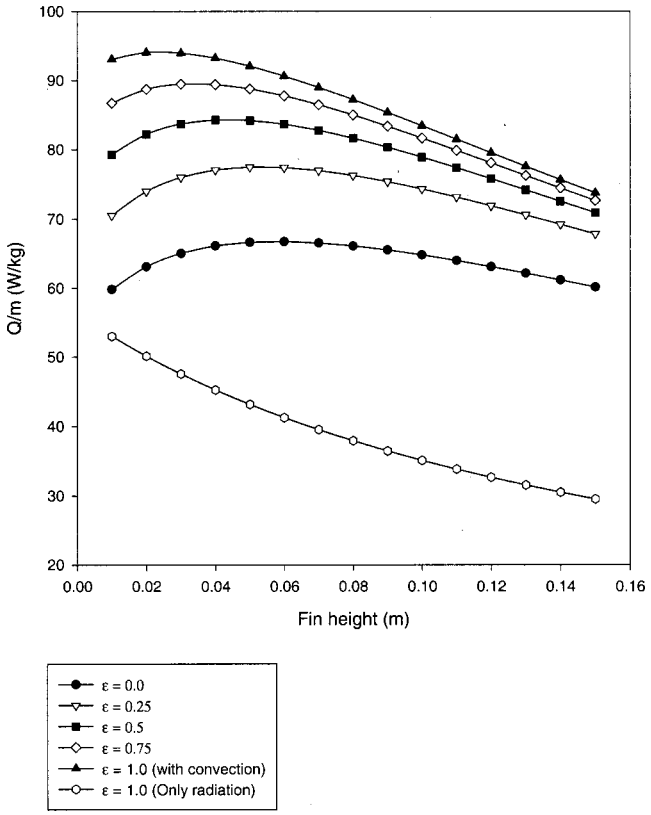

Fig. 7 Comparison of convection and radiation mode of heat transfer. The figure shows the variation of total heat transfer rate per unit mass with fin height for various emissivities and the following parameter values ($L=1.0$ m, $D=0.03$ m, and $m_f=0.25$ kg/s)

Figure 6 depicts that the variation of total heat transfer rate per unit mass with various duct lengths. As the duct length increases, the mass of the system increases much more rapidly than does the total heat transfer rate and hence the total heat transfer rate per unit system mass decreases. However the variation of total entropy generation rate with duct length is linear. From these, it is clear that a fin system with a lower duct length is more effective from both heat transfer and entropy points of view. However, the spacing between two fins is based on the duct length and number of fins. For better convective heat transfer rates, this spacing should not fall below the 2δ limit, where δ is the thermal boundary layer thickness along the fin for these conditions and is obtained by using standard correlations [10] for a vertical heated wall. So, for a typical case, the duct length and number of fins are selected in such away that the 2δ limit should be satisfied.

Figure 7 has been drawn to compare the convective and radiative heat transfer rates for a typical case of design parameters and the variation of total heat transfer rate per unit mass is shown against fin height. From the figure, it is clear that the short fins give better performance than long fins in the viewpoint of total heat dissipation rate per unit system mass for the case of both convection and radiation. The shorter fins are mainly more effective in the case of radiation, because short fins have smaller temperature variation along the fin height with favorable shape factors to the ambient. The same trend had been obtained in the experimental analysis of Rammohan Rao [4].

Optimum Fin Height

A detailed study was carried out to obtain the value of optimum fin height, choosing various combinations of parameters normally encountered in the design of thermal systems. Typically for a particular value of duct spacing, duct length, number of fins, mass flow rate and emissivity; the fin height is increased gradually from a low value [say 0.01 m] to a high value [say 0.1 m] in suitable steps, until an optimum is reached. This optimum corresponds to maximum heat transfer rate per unit system mass. This procedure is repeated for the possible combinations of parameters in the given range that are shown in Table 1, and adequate number of points near the peak of the curve are chosen for the calculation of optimum fin height. A large number of such curves have been analyzed in the present study. Figure 7 shows the variation of the total heat transfer rate per unit system mass with fin height for different values of emissivity. The existence of optimum fin height is shown in the figure and is observed that the optimum value decreases as emissivity increases. This is due to the fact that for short fins, the temperature distribution along the fin becomes uniform when emissivity increases; hence the optimum shifts to lower values of fin height.

Table 2 Values of constant and exponents for correlations: (*a*) correlations for optimum fin height ($H_{opt}=C_1 e^{(m_f^{*a})} n^b L^c D^d e^{(e^{*e})}$); (*b*) correlations for total heat transfer rate per unit system mass ($\gamma=C_2(1+H)^a m_f^b e^{(n_1^{*c})} L^d e^{(e^{*D_1})} e^{(f^{*}\varepsilon_1)}$); and (*c*) correlations for total entropy generation rate ($S_{gen}=C_3 H^a m_f^b (1+n)^c L^d D^e (1+\varepsilon)^f$).

(*a*) Correlations for Optimum fin height

$$H_{opt} = C_1 e^{(m_f{}^{*a})} n^b L^c D^d e^{(e^{*e})}$$

Fin profile	C_1	a	b	c	d	e
Trinagular fin	0.168	-0.143	-0.137	0.140	0.064	-0.194
Trapezoidal fin	0.325	-0.388	-0.358	0.289	0.141	-0.408
Rectangular fin	0.357	-0.543	-0.419	0.315	0.179	-0.642

(*b*) Correlations for total heat transfer rate per unit system mass

$$\gamma = C_2 (1+H)^a m_f{}^b e^{(n_1{}^{*c})} L^d e^{(e^{*D_1})} e^{(f^{*}\varepsilon_1)}$$

Fin Profile	C_2	a	b	c	d	e	f
Triangular fin	13.00	3.07	0.296	2.83	-0.281	-7.72	-0.325
Trapezoidal fin	22.72	1.92	0.293	2.28	-0.234	-7.76	-0.348
Rectangular fin	39.76	0.940	0.331	1.68	-0.173	-7.71	-0.349

(*c*) Correlations for total entropy generation rate

$$S_{gen} = C_3 H^a m_f{}^b (1+n)^c L^d D^e (1+\varepsilon)^f$$

Fin Profile	C_3	a	b	c	d	e	f
Triangular fin	0.196	0.165	0.983	0.301	0.677	-0.597	0.294
Trapezoidal fin	0.218	0.198	0.897	0.355	0.595	-0.548	0.232
Rectangular fin	0.148	0.347	0.507	0.527	0.458	-0.513	0.179

Correlations

Based on the detailed numerical study, in order to present results in a directly usable form in the given range of parameters, correlations are proposed. A multiple nonlinear regression procedure is used to evolve these correlations and the constants and exponents that are involved in these correlations are given in Table 2 for three kinds of fin profiles. These correlations and discussion there on are presented below.

Correlation for Optimum Fin Height

The correlation for optimum fin height is given by,

$$H_{\text{opt}} = C_1 e^{(m_f^{*a})} n^b L^c D^d e^{(\varepsilon^* e)} \tag{9}$$

The correlation coefficient is 0.98 with an RMS error of ±5.8 percent. From this study, the variation of optimum fin height with mass flow rate and emissivity has been found to be exponential, where as the optimum fin height varies monotonically with the other parameters.

Correlation for Total Heat Transfer Rate per Unit System Mass

The correlation for total heat transfer rate per unit mass is given by,

$$\gamma = C_2 (1+H)^a m_f^b e^{(n_1^{*c})} L^d e^{(e^* D_1)} e^{(f^* \varepsilon_1)} \tag{10}$$

where, $n_1 = n/(1+n)$, $D_1 = D/(1+D)$, and $\varepsilon_1 = (1-\varepsilon)/(1+\varepsilon)$.

Equation (10) has a correlation coefficient of 0.98 and the RMS error is ±6.7 percent on the estimated values. The form of the correlation is in line with the effects of various parameters that influence the total heat transfer rate and this been discussed earlier. The above correlation is applicable only for fin height upto the optimum fin height, as beyond this value, the total heat transfer rate per unit system mass decreases as fin height increases. Hence, the analysis of the fin system beyond this limit has not been carried out in the present study and the optimum fin height is the maximum limit for fin height, for further optimization studies.

Correlation for Total Entropy Generation Rate

The values of total entropy generation rate for all possible set of parameters are correlated by the following way.

$$S_{\text{gen}} = C_3 H^a m_f^b (1+n)^c L^d D^e (1+\varepsilon)^f \tag{11}$$

The estimated entropy generation has a RMS error of ±7 percent and the correlation coefficient is found to be 0.995. The strong influence of duct spacing, duct length and mass flow rate on the total entropy generation rate can be inferred from the correlation.

Optimization Study

The variation of two basic criteria were explained in the earlier sections and data obtained by numerical analysis were used to synthesize useful correlations. Now, it would be interesting to incorporate these two criteria together in order to obtain a ''truly holistic'' optimum solution for the fin system. This optimization could be done in two ways. One is to find an optimum solution for a thermal system that dissipates a fixed quantity of heat duty. The second one is to rate a thermal system, i.e., to obtain an optimum value of a crucial parameter with other parameters being held fixed. The latter is the prime objective of the present study.

The optimization proceeds with the assumption that all the parameters except mass flow rate are known. The objective is to have a fin system with an optimum flow rate at which the two competing criteria total heat transfer rate per unit system mass and total entropy generation rate which when considered together would result in a minimum total penalty. The optimization procedure starts with the calculation of the maximum and minimum values of total heat dissipation per unit system mass and total entropy generation rate respectively within the given range of mass flow rates for a particular set of parameters that are chosen randomly. Then the two correlations that are given in the above section are non-dimensionalized by the calculated maximum and minimum values by the following way. The values of the parameters are given by,

$$H = 0.03 \text{ m}, \quad n = 10 \text{ fins}, \quad L = 1.5 \text{ m}, \quad D = 0.03 \text{ m},$$

$$\varepsilon = 0.80$$

Range of mass flow rate is $m_f = 0.125$ kg/sec to 0.325 kg/sec. For Rectangular fins:

From Eq. (10). At $m_f = 0.325$ kg/sec, $\gamma_{\max} = 97.443$ W/kg

From Eq. (11). At $m_f = 0.125$ kg/sec, $S_{\text{gen,min}} = 0.532$ W/K

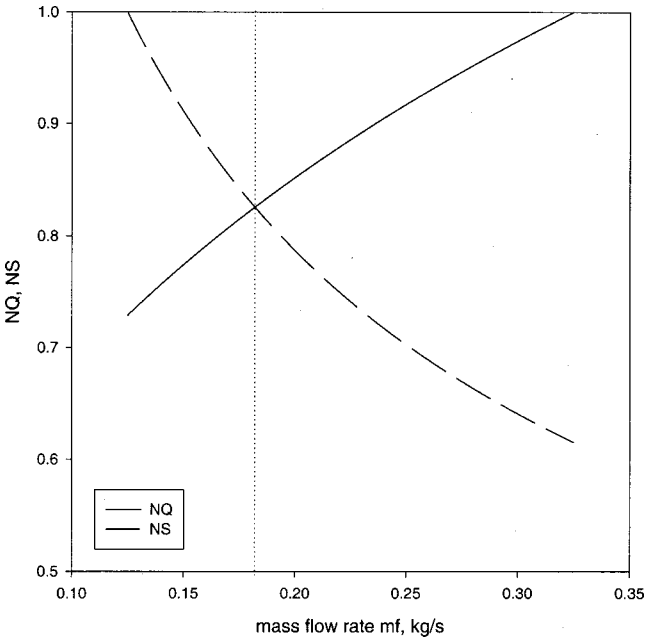

Fig. 8 Plot showing the variation of dimensional heat dissipation rate per unit system mass and dimensionless entropy generation rate with various mass flow rates and the following set of parameters ($n=15$, $L=1.5$ m, $D=0.03$ m, $H=0.03$ m, and $\varepsilon=0.80$)

The dimensionless form of the above two quantities are given by

$$NQ = \frac{\gamma}{\gamma_{\max}} = 1.451 * m_f^{0.331} \tag{12}$$

$$NS = \frac{S_{\text{gen,min}}}{S_{\text{gen}}} = 0.348 * m_f^{-0.507} \tag{13}$$

The variation of NQ and NS are plotted against mass flow rate in Fig. 8. The point at which the two curves cross each other may be deemed to be the holistic optimum and is noted to be 0.182 kg/sec. From this simple analysis it can be seen that the penalty on total heat transfer rate per unit mass is only 15 percent, while the total entropy generation has been reduced by 26 percent for particular set of parameters. The same procedure could be applied to all the possible combinations of parameters and an optimum solution for all other parameters can also be found by this simple way. One could also explore the possibility of considering other competing criteria in order to arrive at ''holistic'' optima.

Conclusions

A convecting-radiating fin array which stands vertically on a horizontal duct through turbulent flow is considered, has been analyzed and the following conclusions have been arrived at.

1 For the range of parameters considered in this study, it is observed that the convection is the dominant mode of heat transfer compared to radiation.
2 Arrays having shorter fin lengths showed better performance for convection as well as radiation.
3 The existence of an optimum fin height based on maximum heat transfer rate per unit system mass and its dependence on other parameters has been presented.
4 Some correlations are suggested which allow generalization of the available data within the range of parameters considered.

Optimization study that incorporates the two competing criteria of heat transfer optimization and entropy minimization together has been done for a specific example of ''rating'' of a convecting radiating fin array.

Nomenclature

D = duct spacing, m
F = shape factor between two elemental surfaces
G = irradiation parameter, W/m^2
h = convective heat transfer coefficient, $W \cdot m^2 \cdot K$
H = fin height, m
L = length of the duct, m
m_f = mass flow rate, kg/s
n = number of fins
Nc = conduction-convection interaction parameter, Eq. (2)
Nr = conduction-radiation interaction parameter, Eq. (2)
NQ = dimensionless parameter, defined in Eq. (12)
NS = dimensionless parameter, defined in Eq. (13)
Q = total heat transfer rate, W
Re = Reynolds number
s = fin spacing, m
S = entropy generation rate, W/K
t = fin thickness, m
V = fluid velocity inside the duct, m/s
w = fin and the duct width, assumed to be unity

Greek Symbols

ρ = fin density, kg/m^3
ϕ = dimensionless temperature, Eqs. (2) and (5)
γ = total heat transfer rate per unit mass of the fin system, W/kg

Subscript

1 = pertaining to the fin
2 = pertaining to the unfinned portion
b = pertaining to the fin base
f = pertaining to the fluid
s = pertaining to the duct surface
∞ = ambient

References

[1] Harahap, F., and McManus, H. N., 1967, ''Natural Convection Heat Transfer From Horizontal Rectangular Fin Arrays,'' ASME J. Heat Transfer, **89**, pp. 32–38.
[2] Jones, C. D., and Smith, L. F., 1970, ''Optimum Arrangement of Rectangular Fins on Horizontal Surfaces for Free Convection Heat Transfer,'' ASME J. Heat Transfer, **92**, pp. 6–10.
[3] Donovan, R. C., and Rohrer, W. M., 1971, ''Radiative and Convective Conducting Fins on a Plane Wall, Including Mutual Irradiation,'' ASME J. Heat Transfer, **93**, pp. 41–46.
[4] Rammohan Rao, V., and Venkateshan, S. P., 1996, ''Experimental Study of Free Convection and Radiation in Horizontal Fin Arrays,'' Int. J. Heat Mass Transf., **39**(4), pp. 779–789.
[5] Bejan, A., 1980, ''Second Law Analysis in Heat Transfer,'' Energy, **5**, pp. 721–732.
[6] Nag, P. K., and Mukherjee, P., 1987, ''Thermodynamic Optimization of Convective Heat Transfer Through a Duct with Constant Wall Temperature,'' Int. J. Heat Mass Transf., **30**(2), pp. 401–405.
[7] Balaji, C., Sri Jayaram, K., and Venkateshan, S. P., 1996, ''Thermodynamic Optimization of Tubular Space Radiators,'' J. Thermophys. Heat Transfer, **10**(4), pp. 705–707.
[8] Kern, D. Q., and Kraus, A. D., 1972, *Extended Surface Heat Transfer*, McGraw-Hill, New York.
[9] Mackay, D. B., 1963, *Design of Space Powerplants*, Prentice-Hall Inc., NJ.
[10] Churchill, S. W., and Chu, H. H. S., 1975, ''Correlating Equations for Laminar and Turbulent Free Convection from a Vertical Plate,'' Int. J. Heat Mass Transf., **18**, pp. 1323–1328.
[11] Siegel, R., and Howell, J. R., 1972, *Thermal Radiation Heat Transfer*, McGraw-Hill, New York.
[12] Bejan, A., 1982, *Entropy Generation Through Heat and Fluid Flow*, Wiley-Interscience Publication, New York.
[13] Sunilkumar, S., 1993, ''A Numerical Study of Optimized Space Radiators,'' PhD thesis, Department of Mechanical Engineering, Indian Institute of Technology, Madras.
[14] Balaji, C., and Venkateshan, S. P., 1995, ''Combined Conduction, Convection and Radiation in a Slot,'' Int. J. Heat Fluid Flow, **16**, pp. 139–144.

A Fractal Model for Nucleate Pool Boiling Heat Transfer

Boming Yu[1]

Ping Cheng
Fellow ASME

Department of Mechanical Engineering,
Hong Kong University of Science and Technology,
Clear Water Bay, Kowloon, Hong Kong, P.R. China

In this paper, a fractal model for nucleate pool boiling heat transfer is developed based on the fractal distribution of sites (areas) of nucleation sites on boiling surfaces. Algebraic expressions for the fractal dimension and area fraction of nucleation sites are derived, which are shown to be a strong function of wall superheat. The predicted fractal dimension is shown in good agreement with those determined by the box-counting method. The fractal model for nucleate boiling heat transfer is found to be a function of wall superheat, the contact angle of the fluid and the heater material, and physical properties of the fluid with a minimum number of empirical constants. The predicted total heat flux from a boiling surface based on the present fractal model is compared with existing experimental data. An excellent agreement between the model predictions and experimental data is found, which verifies the validity of the present fractal model. [DOI: 10.1115/1.1513580]

Keywords: Boiling, Heat Transfer, Phase Change

1 Introduction

Nucleate boiling occurs frequently in many industrial applications such as in energy conversion systems and in the cooling of high-energy-density electronic components. Over the past several decades, a great deal of effort has been devoted to the understanding and modeling of the boiling heat transfer process. Because boiling is a very complex and elusive process, one generally relies upon dimensionless groups and empirical constants for correlating data. The general procedures for correlating the boiling heat transfer data are: first calculate the heat flux from the surface by a bubble departing from a single nucleate site; then find the averaged nucleate boiling heat transfer from the product of heat flux q, the bubble number density N, and the bubble departure frequency f. In general, the parameters affecting the active nucleation site density include the procedure used in preparing the heater surface, surface finish, surface wettability, contact angle between heater and the fluid, as well as heater thickness. There are numerous correlations in the literature using the cumulative number of nucleation sites and/or cavities present on the surface to predict boiling heat transfer as a function of wall superheat. A comprehensive review on these correlations was given by Dhir [1].

It is generally recognized that there are three main mechanisms contributing to nucleate boiling heat transfer: the bubble generation and departure from nucleation sites on the superheated surface, natural convection on inactive nucleation areas of the heated surface, and micro-layer evaporation underneath the bubbles. Thus, the total average heat flux of the partial nucleate pool-boiling heat flux can be expressed as

$$q_{\text{tot}} = q_b + q_{nc} + q_{me} \tag{1}$$

Assuming that the area of influence is πD_b^2 and that areas of influence of neighboring bubbles do not overlap, Mikic and Rohsenow [2] obtained the average heat flux q_b (average over the whole boiling surface) due to the boiling as

$$q_b = K\sqrt{\pi(k\rho c_p)_l f} D_b^2 N_a \Delta T_w \tag{2}$$

where N_a is the number of active sites per unit area of heated surface, f is the bubble release frequency, D_b is the bubble diameter at departure, and K is the proportional constant for bubble diameter of influence which is taken to be 2 by Dhir [1] and by Mikic and Rohsenow [2] or 1.8 by Judd and Hwang [3]. In the literature, N_a is related to the *active* cavity diameter D_c by a variety of correlations with several empirical constants while $D_b f$, $D_b^{1/2} f$ and $D_b^2 f$ are correlated as different constants or as different empirical functions of material properties, see Dhir [1], Mikic and Rohsenow [2], and Ivery [4].

Natural convection from inactive nucleation areas of the heated surface as given by Mikic and Rohsenow [2] is

$$q_{nc} = (1 - KN_a \pi D_b^2) h_{nc} (T_w - T_\infty) \tag{3}$$

where h_{nc} is the average heat transfer coefficient for natural convection which is given by Han and Griffith [5]:

$$h_{nc} = 0.54 \rho c_p \left[\frac{\eta g (T_w - T_\infty) \alpha^3}{\sqrt{A} v} \right]^{1/4} \tag{4a}$$

for laminar natural convection where $10^5 < Ra < 2 \times 10^7$. For turbulent natural convection where $2 \times 10^7 < Ra < 3 \times 10^{10}$, h_{nc} is given by

$$h_{nc} = 0.14 \rho c_p \left[\frac{\eta g (T_w - T_\infty) \alpha^2}{v} \right]^{1/3} \tag{4b}$$

The heat flux due to the evaporating microlayer is given by Dhir [1] as

$$q_{me} = \rho_l h_{fg} N_a f V_{me} \tag{5}$$

where V_{me} is the volume of the microlayer evaporation which was derived by Benjamin and Balakrishnan [6] as

$$V_{me} = \frac{\gamma \xi \sqrt{\pi}}{10} B^2 \text{Ar}^{0.27} (\alpha_l t_g)^{3/2} \text{Ja}^* \tag{6}$$

where B is a constant (which is equal to 1.55 for water, CCl_4 and n-hexane, and 1/1.55 for n-pentane and acetone); t_g is the bubble growth time, which has several different forms as given by Ivery [4] as well as by Han and Griffith [5]. Ar and Ja* are the Archimedes number and the Jakob number given, respectively, by

$$\text{Ar} = g v_l (\sigma/\rho_l g)^{3/2}, \tag{7a}$$

$$\text{Ja}^* = \rho_{lC_{pl}} T_{\text{sat}} / (\rho_v h_{fg}), \tag{7b}$$

and ξ is given by

$$\xi = 1 - D_d^2 / D_i^2 \tag{7c}$$

[1]Permanent address: Department of Physics, Huazhong University of Science and Technology, Wuhan, 430074, P.R. China. e-mail: yu3838@public.wh.hb.cn

Contributed by the Heat Transfer Division for publication in the JOURNAL OF HEAT TRANSFER. Manuscript received by the Heat Transfer Division September 26, 2001; revision received June 14, 2002. Associate Editor: T. Y. Chu.

The experimental data of Torikai et al. [7] indicated that the ratio of D_d/D_i reaches a constant value soon after the bubble starts to grow. Mikic and Rohsenow [2] proposed that $D_b/D_{\inf}=0.5$ where $D_{\inf}$ is the diameter of area on heating surface affected by bubble departure. We now make a further approximation that $D_d/D_i=0.5$ in Eq. (7*c*).

As discussed by Dhir [1], a quantitative prediction of nucleate boiling heat flux from a superheated wall based on Eqs. (1)–(7) requires the knowledge of several additional empirical constants, because each of the quantities $D_b f$, $D_b^{1/2} f$, $D_b^2 f$ and N_a contains several empirical constants. Since different authors used different correlation equations, the calculation of nuclear boiling heat transfer so far lacks the consensus as to which set of empirical constants is to be used.

In this paper, we attempt to develop a mechanistic model for nucleate pool boiling heat transfer, based on the consideration that the fractal characteristics of sizes of active cavities on surfaces and the bubble release frequency are a function of *active* cavity sizes. Algebraic expressions for the fractal dimension and area fraction of nucleation sites are obtained, which are shown to be a strong function of wall superheat especially for $\Delta T_w<4°C$. The nucleate pool boiling heat flux is found to be a function of wall superheat, physical properties of the fluid, and the contact angle of the fluid and the heater material. The major advantage of the present model is that empirical constants are kept to a minimum number, and no new/additional empirical constant is introduced into the model by the fractal theory and technique. The predicted heat flux based on the present model is shown in excellent agreement with experimental data of Wang and Dhir [8]

2 Fractal Characteristics of Sizes of Cavities and Nucleation Sites on Surfaces

In the following, we consider that the *active* cavities formed on the heated surfaces are analogous to pores in porous media. Based on this concept, we can take advantages of recent developments on fractal theory of porous media. In particular, Yu and Cheng [9] found that the cumulative number of pores in porous media with the diameter larger than and equal to a particular value, D_s, obeys the following fractal scaling law [10–12]:

$$N(D_L \geqslant D_s)=(D_{s,\max}/D_s)^{d_f} \quad \text{with} \quad D_{s,\min} \leqslant D_s \leqslant D_{s,\max} \tag{8a}$$

where $D_{s,\max}$ is the maximum diameter of pores in porous media, D_s is the diameter of a pore, and d_f is the area fractal dimension (with $1<d_f<2$ in a two-dimensional space). If *active* cavities formed on surfaces are considered as pores in porous media, the cumulative number of *active* cavities with diameters greater than and equal to D_c is also described by Eq. (8*a*) with N and D_s replaced by N_a and D_c, respectively, i.e.,

$$N_a(D_L \geqslant D_c)=(D_{c,\max}/D_c)^{d_f} \quad \text{with} \quad D_{c,\min} \leqslant D_c \leqslant D_{c,\max} \tag{8b}$$

The total number of nucleation sites from the minimum active cavity to the maximum active cavity can be obtained from Eq. (8*b*) as

$$N_{a,\text{tot}}=N_a(D_L \geqslant D_{c,\min})=(D_{c,\max}/D_{c,\min})^{d_f} \tag{8c}$$

In fact, Majumdar [13] discussed such a possibility, and pointed out that the *active* cavities on a surface should also follow the power law by Eq. (8*a*). Equation (8*b*) shows that: (i) an increase of fractal dimension leads to an increase of cumulative number of sites, and (ii) $N_a \to \infty$ as $D_c \to 0$. Majumdar [13] also pointed out that the minimum active cavity diameter $D_{c,\min}$ and the maximum active cavity diameter $D_{c,\max}$ in Eq. (8*b*) could be predicted by Hsu's model [14] for nucleation site distribution, i.e.,

$$D_{c,\max}=\frac{\delta}{C_1}\left[1-\frac{\theta_{\text{sat}}}{\theta_w}+\sqrt{\left(1-\frac{\theta_{\text{sat}}}{\theta_w}\right)^2-\frac{4\zeta C_3}{\delta\theta_w}}\right] \tag{9a}$$

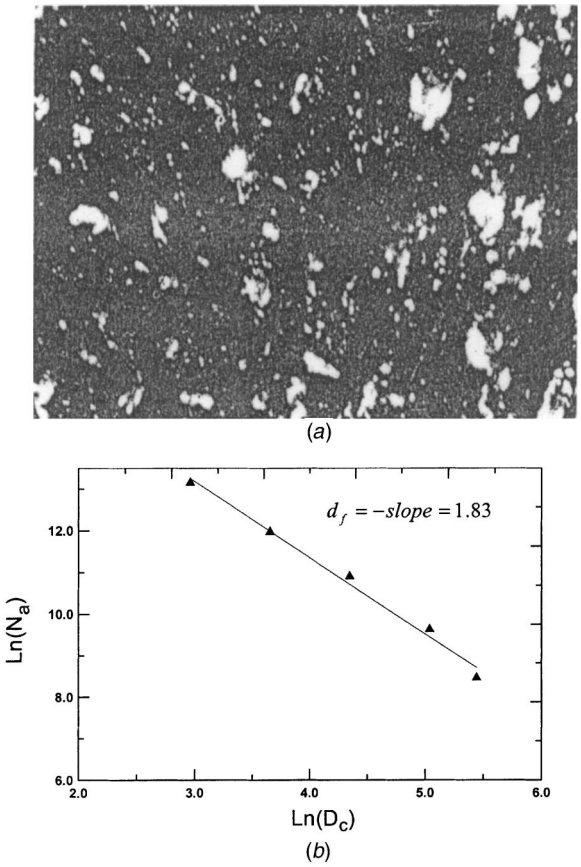

Fig. 1 (*a*) A photograph [8] of active nucleation sites for $\phi=90$ deg, $q=5.7\times10^5$ W/m^2, and $\Delta T_w=18°C$; and (*b*) determination of fractal dimension of nucleation sites from (*a*).

$$D_{c,\min}=\frac{\delta}{C_1}\left[1-\frac{\theta_{\text{sat}}}{\theta_w}\sqrt{\left(1-\frac{\theta_{\text{sat}}}{\theta_w}\right)^2-\frac{4\zeta C_3}{\delta\theta_w}}\right] \tag{9b}$$

where $\zeta=2\sigma T_{\text{sat}}/\rho_v h_{fg}$, $C_1=(1+\cos\phi)/\sin\phi$ and $C_3=1+\cos\phi$, with ϕ being the contact angle of the fluid and the heater material and with the angle of tangent to cavity mouth with respect to horizontal being zero. δ is the thermal boundary layer thickness of natural convection which can be obtained from Han and Griffith [5] to give

$$\delta=\frac{\rho c\alpha}{q_{NC}}(T_w-T_\infty) \tag{10}$$

where q_{NC} is the heat transferred by natural convection on a nonboiling surface:

$$q_{NC}=h_{nc}(T_w-T_\infty) \tag{11}$$

It follows from Eq. (3) that

$$q_{nc}=(1-KN_a\pi D_b^2)q_{NC} \tag{12}$$

Figure 1(*a*) is a photo image of nucleation sites for the contact angle $\phi=90$ deg, $q=5.7\times10^5$ W/m^2 at the wall superheat of 18 °C with a heating area of 2.5 cm^2, which was taken from Wang and Dhir's experimental data [8]. If the box-counting method [9] is applied to the photo image, a linear relationship on the logarithmic scale exists as shown in Fig. 1(*b*). The fractal dimension d_f of sizes (areas) of the nucleation sites can be determined from the slope to be 1.83. This confirms that the nucleation sites indeed follow the fractal scaling law given by Eq. (8*b*). In the next sec-

tion, a fractal model for nucleate pool heat transfer is derived based on the fractal distribution of nucleation sites on boiling surfaces.

3 Fractal Analysis of Nucleate Pool Boiling Heat Transfer

It has well been established that vapor or gas trapped in cavities and scratches on the heated surface serve as nuclei for bubbles. However, not all cavities or scratches present on heating surfaces can become active nucleation sites for nucleate boiling heat transfer. As pointed out by Bankoff [15], only those active cavities with diameters greater than $D_{c,\min}$ and with cone angle $\beta \leqslant \phi/2$ (with ϕ being the contact angle) can become active nucleation sites.

In the following, a fractal model for nucleate pool boiling heat transfer is derived based on the fact that the nucleation site size distributions on boiling surfaces follow the fractal power law given by Eq. (8*b*). The number of active cavities of sizes lying between D_c and D_c+dD_c can be obtained from Eq. (8*b*) as

$$dN_a = -d_f D_{c,\max}^{d_f} D_c^{-(d_f+1)} dD_c \tag{13a}$$

where $dD_c > 0$. Eq. (13*a*) can be written as

$$-dN_a = d_f D_{c,\max}^{d_f} D_c^{-(d_f+1)} dD_c \tag{13b}$$

Eq. (13*b*) shows that $-dN_a > 0$, which means that the nucleation site number decreases with the increase of the diameter of the active cavity.

Since the size distribution of nucleation sites is found to be fractal and bubble release frequency is related to the active cavity sizes (as will be discussed later), a fractal model for nucleating boiling heat flux can be obtained by modifying Eq. (2) as

$$\begin{aligned} q_b &= \int dq_b = \int K\sqrt{\pi(k\rho c_p)_l f} D_b^2 \Delta T_w (-dN_a) \\ &= \int_{D_{c,\min}}^{D_{c,\max}} C_b \sqrt{f}(-dN_a) \end{aligned} \tag{14}$$

where $C_b = K\sqrt{\pi(k\rho c_p)_l} D_b^2 \Delta T_w$ with the bubble diameter D_b at departure being correlated by (see Han and Griffith [5], Mikic and Rohsenow [2]:

$$D_b = C\left[\frac{\sigma}{g(\rho_l-\rho_v)}\right]^{1/2} \mathrm{Ja}^{*5/4} \tag{15}$$

with $C = 1.5\times 10^{-4}$ for water, and 4.65×10^{-4} for other liquids. If Eq. (15) is substituted into Eq. (14), it can be integrated and if the bubble departure frequency f is expressed in terms of D_c. To this end, we note that the bubbles release frequency, f, is usually defined by

$$f = 1/(t_w + t_g) \tag{16}$$

Van Stralen et al. [16] assumed that the waiting time is three times of the growth time, i.e.,

$$t_w = 3t_g \tag{17}$$

Han and Griffith [5] derived an analytical expression for the waiting time, t_w,

$$t_w = \frac{9}{4\pi\alpha}\left[\frac{(T_w-T_\infty)R_c}{T_w - T_{\mathrm{sat}}[1+(2\sigma/R_c\rho_v h_{fg})]}\right]^2 \tag{18}$$

Measurements by Wang and Dhir's [8] on a copper surface gave $R_c = 1.1\sim 27.7$ μm. For $R_c = 1$ μm and 10 μm, a rough estimation of the term $2\sigma/(R_c\rho_v h_{fg})$ in Eq. (18) give 0.1 and 0.01, respectively. Therefore, the term $2\sigma(R_c\rho_v h_{fg})$ in Eq. (18) can be neglected for the simplicity of integration, and Eq. (18) is thus reduced to

$$t_w = \frac{9}{4\pi\alpha}\left[\frac{(T_w-T_\infty)R_c}{T_w-T_{\mathrm{sat}}}\right]^2 = \frac{9}{4\pi\alpha}\left[\frac{(T_w-T_\infty)R_c}{\Delta T_w}\right]^2 \tag{19}$$

However, for a super smooth surface with a cavity radius $R_c < 1$ μm, the term $2\sigma/(R_c\rho_v h_{fg})$ in Eq. (18) cannot be neglected. Equation (19) indicates that the larger the *active* cavity, the longer the waiting time, which is consistent with the physical phenomena. Substituting Eqs. (17) and (19) into Eq. (16), it can be seen that the bubble release frequency, f, is related to the sizes of active cavities. With this expression, Eq. (14) can now be integrated to give

$$\begin{aligned} q_b &= \int_{D_{c,\min}}^{D_{c,\max}} C_b\sqrt{f}(-dN_a) \\ &= C_b \frac{2d_f}{d_f+1}\sqrt{\frac{\pi\alpha}{3}}\frac{\Delta T_w}{T_w-T_\infty} D_{c,\max}^{-1}\left[\left(\frac{D_{c,\max}}{D_{c,\min}}\right)^{d_f+1} - 1\right] \end{aligned} \tag{20a}$$

where C_b is independent of cavity size. Equation (20*a*) denotes that boiling heat transfer is a function of wall superheat, fractal dimension, physical properties of fluid and bubble diameter at departure. With the aid of Eq. (8*c*), Eq. (20*a*) can be rewritten as

$$q_b = C_b \frac{2d_f}{d_f+1}\sqrt{\frac{\pi\alpha}{3}}\frac{\Delta T_w}{T_w-T_\infty} D_{c,\max}^{-1}[(N_{a,\mathrm{tot}})^{1+1/d_f} - 1] \tag{20b}$$

which indicates that the boiling heat transfer is proportional to the total number of nucleation sites and inversely proportional to the maximum diameter of the bubbles. Similarly, a fractal model for heat flux from micro layer evaporation can be obtained by modifying Eq. (5) as

$$\begin{aligned} q_{me} &= \int dq_{me} = -\int \frac{\gamma\xi\sqrt{\pi}}{10} B^2 \mathrm{Ar}^{0.27}\mathrm{Ja}(\alpha_l)^{3/2}\rho_l h_{fg} t_g^{3/2} f dN_a \\ &= \int_{D_{c,\min}}^{D_{c,\max}} C_{me} t_g^{3/2} f(-dN_a) \\ &= C_{me}\frac{\sqrt{3}D_{c,\max}}{16\sqrt{\pi\alpha}}\frac{T_w-T_\infty}{\Delta T_w}\frac{d_f}{d_f-1}\left[\left(\frac{D_{c,\max}}{D_{c,\min}}\right)^{d_f-1} - 1\right] \end{aligned} \tag{21}$$

where $C_{me} = \frac{\gamma\xi\sqrt{\pi}}{10} B^2 \mathrm{Ar}^{0.27}\mathrm{Ja}(\alpha_l)^{3/2}\rho_l h_{fg}$ is independent of cavity sizes.

Based on characteristics of fractal media, Yu and Li [17] derived the following expression, which relates the pore volume fraction to fractal dimension, minimum and maximum pore size (analogous to the sizes of nucleation sites) in porous media:

$$\psi = \left(\frac{D_{c,\min}}{D_{c,\max}}\right)^{d-d_f} \tag{22}$$

where $d = 2$ in a two-dimensional space. If the volume (area) fraction of nucleation sites (see the white area in Fig. (1*a*)] is considered as pore volume (area) fraction in porous media, Eq. (22) can also be applied to describe the volume (area) fraction of nucleation sites. Thus, a fractal model for the natural convection component can be obtained by modifying Eq. (3) to give

$$q_{nc} = (1-K\psi)h_{nc}(T_w-T_\infty) \tag{23a}$$

$$= \left[1 - K\left(\frac{D_{c,\min}}{D_{c,\max}}\right)^{2-d_f}\right] h_{nc}(T_w-T_\infty) \tag{23b}$$

where the minimum and maximum active cavity size, $D_{c,\min}$ and $D_{c,\max}$, are given by Eq. (9).

4 Relationship Between Fractal Dimension and Wall Superheat

In this section, we will derive a relationship between fractal dimension and wall superheat. To this end, we seek the help in the porous medium literature. Recently, Yu and Cheng [9] derived a model for fractal dimension d_f, which is related to the microstructures and solid fraction V_s in a porous medium as

$$d_f = 2 + \ln(V_s)/\ln(d^+\sqrt{1/2V_s}) \tag{24}$$

where d^+ is the ratio of averaged particle diameter to the minimum particle diameter in the porous medium. If the particle in a porous medium are considered as nucleation sites in Fig. 1(*a*), the solid fraction V_s in Eq. (24) is analogous to the fraction of nucleation sites on a superheated surface. This implies that particles of different sizes are analogous to the cavities of different sizes. Thus, V_s and d_f in Eq. (24) will have the same meaning as ψ and d_f in Eq. (22). It follows from Eq. (22) that

$$d_f = 2 - \frac{\ln\psi}{\ln\dfrac{D_{c,\min}}{D_{c,\max}}} \tag{25}$$

Setting $\psi = V_s$ and eliminating d_f from Eqs. (24) and (25) leads to

$$V_s = \frac{(d^+)^2}{2}\left(\frac{D_{c,\min}}{D_{c,\max}}\right)^2 \tag{26}$$

Setting Eq. (22) equal to Eq. (26) yields

$$\psi = V_s = \left(\frac{D_{c,\min}}{D_{c,\max}}\right)^{2-d_f} = \frac{(d^+)^2}{2}\left(\frac{D_{c,\min}}{D_{c,\max}}\right)^2 \tag{27}$$

From Equation (27), we obtain

$$d_f = \frac{\ln\dfrac{(d^+)^2}{2}}{\ln\dfrac{D_{c,\max}}{D_{c,\min}}} \tag{28}$$

In nucleate pool boiling, we can replace d^+ by $\overline{D}_{c,\max}/D_{c,\min}$ where $\overline{D}_{c,\max}$ is the averaged value over all the maximum active cavities. Thus, Eqs. (26) and (28) become

$$V_s = \frac{1}{2}\left(\frac{\overline{D}_{c,\max}}{D_{c,\max}}\right)^2 \tag{29}$$

and

$$d_f = \frac{\ln\left[\dfrac{1}{2}\left(\dfrac{\overline{D}_{c,\max}}{D_{c,\min}}\right)^2\right]}{\ln\dfrac{D_{c,\max}}{D_{c,\min}}} \tag{30}$$

respectively. Note that $\overline{D}_{c,\max}$ can be evaluated from:

$$\overline{D}_{c,\max} = \frac{1}{(T_w - T_{\text{sat}})}\int_{T_{\text{sat}}}^{T_w} D_{c,\max}(T_w)\,dT_w$$

$$= \frac{1}{\Delta T_w}\sum_{j=1}^{m} D_{c,\max}(T_{w_j})\,\delta T_w = \frac{1}{m}\sum_{j=1}^{m} D_{c,\max}(T_{w_j}) \tag{31}$$

where $m = \Delta T_w/\delta T_w$ and we have assumed that δT_w is a constant. In the above equation, $T_{w_j} = T_{\text{sat}} + j(\delta T_w)$ with $j = 1,2,..m$. For example, if we choose $\delta T_w = 0.2°\text{C}$ then $m = 5$ for $\Delta T_w = 1°\text{C}$, and $m = 50$ for $\Delta T_w = 10°\text{C}$.

With the help of Eq. (27), Eq. (23*a*) can be expressed in terms of V_s to give

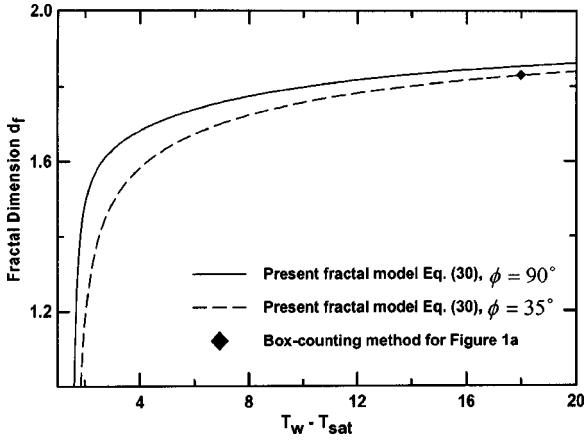

Fig. 2 Fractal dimension versus wall superheat for ϕ=35 deg, 90 deg

$$q_{nc} = (1 - kV_s)h_{nc}(T_w - T_\infty) \tag{32}$$

where V_s is determined by Eq. (29), and the factor $(1 - KV_s)$ is the area fraction for natural convection. Equation (32) is used for computation of the natural convection heat flux in this paper.

Equations (29) and (30) denote that the area fraction and fractal dimension d_f of nucleation sites are dependent upon $D_{c,\max}$ and $D_{c,\min}$ given by Eq. (9), which is a function of wall superheat and contact angle. The fractal dimension and the area fraction at ϕ=35 deg and 90 deg for the wall superheat in the range of $\Delta T_w < 20°\text{C}$ are plotted as dashed and solid lines respectively in Figs. 2 and 3. Figure 2 is a plot of the fractal dimension versus wall superheat for both ϕ=35 deg and ϕ=90 deg. According to the fractal geometry theory, the fractal dimension d_f should be in the range of $1 < d_f < 2$, in a two dimensional space. For a water/copper system with a contact angle ϕ=90 deg , it was found from Eq. (30) that $d_f > 1$ when the wall superheat $\Delta T_w > 1.62°\text{C}$. Similarly, for a water/copper system with a contact angle ϕ = 35 deg, $d_f > 1$ when $\Delta T_w > 1.85$ deg. This means that the number of active nucleate sites versus sizes is fractal if they are in the wall superheat as specified above. This shows that the contact angle affects the initiation of nucleate sites exhibiting the fractal behaviors. This initiation of fractal behavior of active nucleate sites is at a lower wall superheat for a contact angle ϕ=90 deg than that for contact angle ϕ=35 deg. Therefore, all figures in this paper are given in the ranges of $\Delta T_w \geqslant 1.62°\text{C}$ for contact angle ϕ=90 deg and $\Delta T_w \geqslant 1.85°\text{C}$ for contact angle ϕ=35 deg. Figure 2 shows that the fractal dimension increases rapidly from $d_f = 1$ and approaches a value of $d_f = 2$ as wall superheat is increases from very low wall superheat to infinity. However, the wall superheat in reality would not reach infinity and can only reach a finite value during nucleate pool boiling experiments. It is shown that a higher value of the contact angle results in a higher value of d_f. The effect of contact angle becomes smaller at higher values of wall superheat. For example, at $\Delta T_w = 18°\text{C}$, Eq. (30) gives d_f = 1.85 for ϕ=90 deg and $d_f = 1.83$ for ϕ=35 deg. The datum point of $d_f = 1.83$ at $\Delta T_w = 18°\text{C}$ for ϕ=90 deg, obtained based on the box-counting method from the image photo of Fig. 1(*a*) is also included in Fig. 2 for comparison purposes. However, the experimental datum point is closer to the theoretical prediction for ϕ=35 deg than for ϕ=90 deg although the difference between the values of 1.83 and 1.85 is small.

Figure 3 shows that the value of V_s, area fraction of nucleation sites, increases drastically with wall superheat for $\Delta T_w < 2°\text{C}$. Since the active nucleate sites are non-fractal when ΔT_w $< 1.62°\text{C}$ for a contact angle of 90 deg and when $\Delta T_w < 1.85°\text{C}$ for a contact angle of 35 deg, Fig. 3 only gives the result for $\Delta T_w \geqslant 1.62°\text{C}$ at the contact angle 90 deg and for $\Delta T_w \geqslant 1.85°\text{C}$ at the contact angle 35 deg. At very small wall superheat (ΔT_w

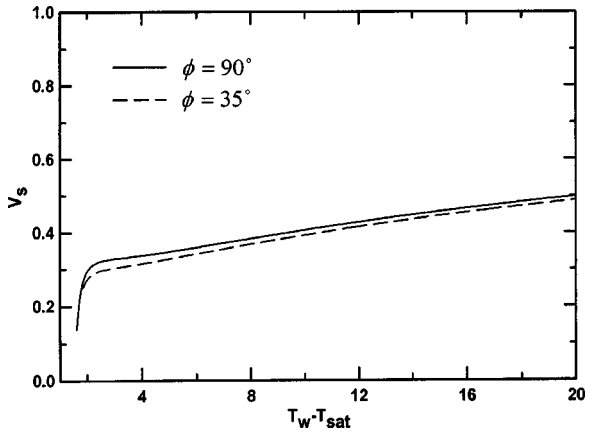

Fig. 3 Area fraction V_s of nucleation sites versus wall superheat for ϕ=35 deg, 90 deg

≪2°C), the effect of contact angle is small. At $\Delta T_w = 2°C$, the value of V_s are 0.27 and 0.30, respectively for ϕ=35 deg and 90 deg. Since the proportionality constant K=1.8 for the bubble diameter of influence is applied in this model, therefore $KV_s = 0.49 \sim 0.54$, i.e., 49 percent–54 percent of the boiling area is covered by the areas of influence of neighboring bubbles at $\Delta T_w = 2°C$. The value of V_s increases slowly as $\Delta T_w > 2°C$ and it approaches a value of 0.48 and 0.50 for ϕ=35 deg and 90 deg, respectively, when $\Delta T_w = 20°C$. Thus, $KV_s = 0.86 - 0.90$, i.e., about 86 percent to 90 percent of the boiling surface at these contact angles is covered by the areas of influence of neighboring bubbles at $\Delta T_w = 20°C$. It may be recalled that Eq. (2) was obtained by assuming that the areas of influence of neighboring bubbles do not overlap in partial nucleate boiling or in the isolated bubble regime. It can be seen that Eq. (32) is valid if $K \leqslant 2$ because the maximum value of V_s is approaching the values of 0.48 and 0.50 at ϕ=35 deg and ϕ=90 deg, respectively as seen from Fig. 3. Thus, this fractal model also indirectly confirms that the value of K=1.8 or 2.0 given by Dhir [1], Mikic and Rohsenow [2], Judd and Hwang [3], is a reasonable one. Wang and Dhir's [8] experiments on contact angle ϕ=90 deg for water/copper showed that when the wall superheat exceeded 20 °C, it was no longer in nucleate boiling state. Therefore, the wall superheat is not allowed to exceed 20 °C to keep it in nucleate boiling state. It appears that our model is valid only when $V_s \leqslant 0.5$ (or $\Delta T_w \leqslant 20°C$ for contact angle ϕ=90 deg) if K=1.8–2.0 is applied, because $1 - KV_s$ in Eq. (32) must be positive so that Eq. (32) is meaningful.

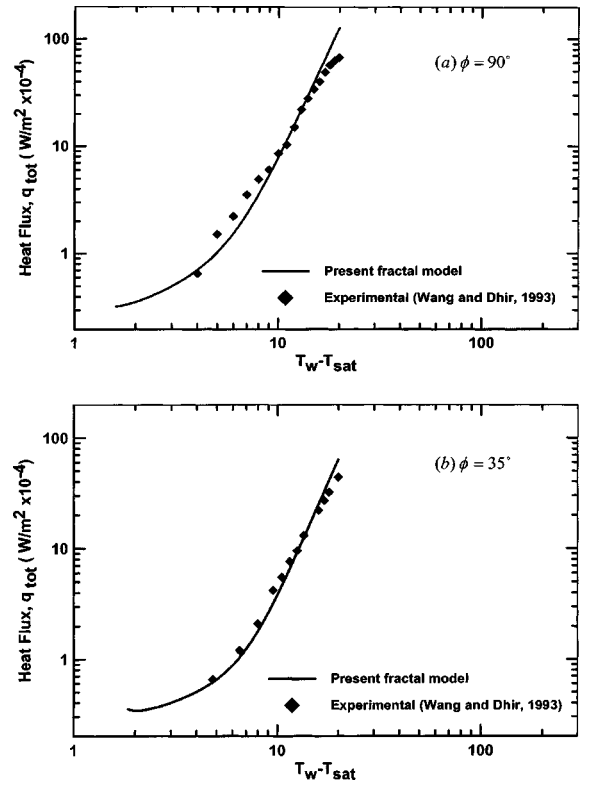

Fig. 4 A comparison between the fractal model prediction and experimental data of nuclear pool-boiling heat flux: (*a*) ϕ=90 deg, (*b*) ϕ=35 deg.

Table 1 Contributions of different mechanisms to nucleate boiling heat transfer of water at ϕ=90 deg

ΔT_w(°C)	q_{tot} W/m^2	q_b W/m^2	q_{me} W/m^2	q_{nc} W/m^2
1.62	3.25E+03	2.25E 00	1.19E+02	3.13E+03
2	3.57E+03	1.10E+01	2.72E+02	3.29E+03
3	4.97E+03	1.30E+02	8.58E+02	3.99E+03
4	7.02E+03	6.33E+02	1.74E+03	4.65E+03
5	1.02E+04	2.03E+03	2.92E+03	5.23E+03
6	1.52E+04	5.10E+03	4.38E+03	5.73E+03
7	2.31E+04	1.09E+04	6.11E+03	6.17E+03
8	3.52E+04	2.06E+04	8.11E+03	6.53E+03
9	5.30E+04	3.58E+04	1.04E+04	6.82E+03
10	7.82E+04	5.83E+04	1.29E+04	7.05E+03
11	1.13E+05	9.00E+04	1.56E+04	7.22E+03
12	1.59E+05	1.33E+05	1.85E+04	7.33E+03
13	2.19E+05	1.90E+05	2.17E+04	7.38E+03
14	2.96E+05	2.63E+05	2.51E+04	7.37E+03
15	3.91E+05	3.55E+05	2.87E+04	7.30E+03
16	5.09E+05	4.70E+05	3.25E+04	7.18E+03
17	6.53E+05	6.09E+05	3.64E+04	7.01E+03
18	8.24E+05	7.77E+05	4.06E+04	6.78E+03
19	1.03E+06	9.76E+05	4.50E+04	6.51E+03
20	1.27E+06	1.21E+06	4.95E+04	6.19E+03

4 Comparison With Heat Flux Data

Equations (1), (20), (21), and (29)–(32) form the present fractal model for the total nucleate pool boiling heat flux. It can be seen that the proposed fractal model is only a function of wall superheat, physical properties of the fluid, and the contact angle between the fluid and the heater material. The empirical constants in this model are: B=1.55, K=1.8, D_d/D_i=0.5, and $C = 1.5 \times 10^{-4}$, which were given by Benjamin and Balakrishnan [6], Judd and Hwang [3], Torikai et al. [7], Mikic and Rohsenow [2], Han and Griffith [5], respectively. Unlike the conventional correlation method, the present fractal model does not introduce any additional empirical constant. The procedures for calculating nucleate pool-boiling heat flux, based on the present fractal model, are summarized as follows:

1) Given T_w, T_{sat}, T_∞, and ϕ, find the physical properties of the fluid, ρ, c_p, h_{fg}, k, α, υ, and compute C_1 and C_3 in Eq. (9).

2) Calculate Ar, J_a^*, h_{nc}, and D_b, then find q_{NC} from Eq. (11), δ from Eq. (10), $D_{c,\max}$ and $D_{c,\min}$ from Eq. (9), $D_{c,\max}$ from Eq. (31), and V_s from Eq. (29).

3) Compute the value of d_f from Eq. (30).

4) Find C_b and C_{me}, and then find q_b, q_{me}, q_{nc}, and q_{tot} from Eqs. (20), (21), (32), and (1), respectively.

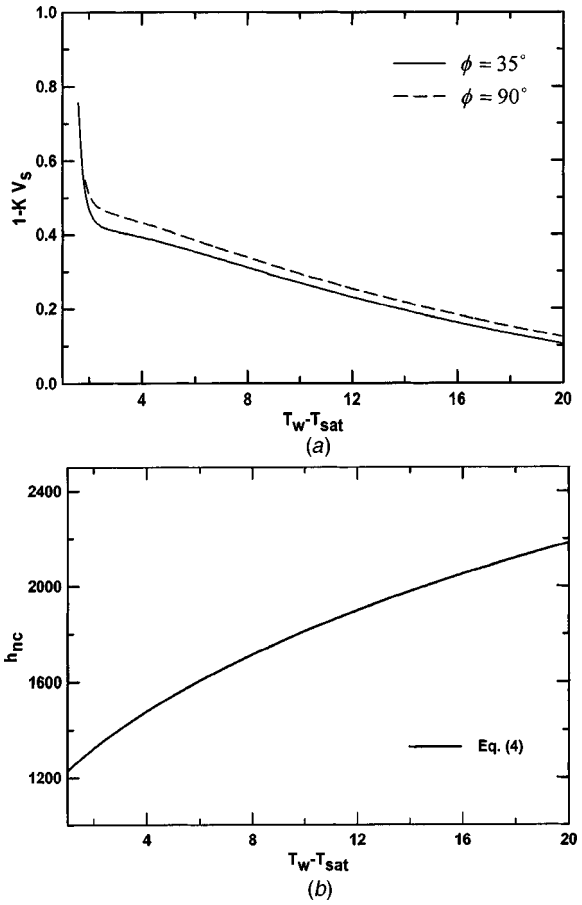

Fig. 5 (*a*) Area fraction for natural convection versus wall superheat for ϕ=35 deg, 90 deg; and (*b*) Natural convection coefficient versus wall superheat.

We now compare the heat flux obtained from the above procedures with the experimental results by Wang and Dhir [8] for nucleate pool boiling heat flux of water in the range of $\Delta T_w = 2-20$°C at 1 atm. Their heat flux data for contact angles of ϕ=90 deg and ϕ=35 deg are presented in Figs. 4(*a*) and 4(*b*), respectively. The solid line in Figs. 4(*a*) and 4(*b*) represent the predictions of the total nucleate boiling heat flux versus wall superheat according to the present fractal model, with the value of d_f computed from Eq. (30) for ϕ=90 deg and ϕ=35 deg, respectively. The results show that the total heat flux from the present fractal model is in excellent agreement with Wang and Dhir's data [8].

Table 1 lists the contributions from different heat transfer mechanisms calculated from the present fractal model for contact angles of ϕ=90 deg. It is seen from this table that at low wall superheat ($\Delta T_w \leqslant 6$°C), the natural convection is the dominant mode of heat transfer because of the low number density of nucleation sites on heats surface. This is in agreement with the other investigator's observation [Paul and Abdel-Khalik [18]]. From Table 1 it can also be seen that the natural convection heat flux first increases with wall superheat in the range of $1.62°C < \Delta T_w < 13°C$, and then decreases with the wall superheat for $\Delta T_w \geqslant 13$°C. This can be seen from Eq. (32), where the values of $(1-KV_s)$ and h_{nc} versus ΔT_w are presented in Fig. 5(*a*) and Fig. 5(*b*), respectively. Figure 5(*a*) shows that the value of $(1-KV_s)$, the fraction of available area for convection, decreases from 0.7 (at $\Delta T_w = 1.62$°C) for ϕ=90 deg and from 0.54 (at $\Delta T_w = 1.85$) for ϕ=35 deg drastically in the range of $\Delta T_w < 2$°C. It is shown that the available area for natural convection is reduced to 49 percent (for ϕ=90 deg) to 52 percent (for ϕ=35 deg), respectively, within the first 2 °C of wall superheat. For the wall superheat at $\Delta T_w > 2$°C, the available area for natural convection then decreases slowly and almost linearly. At $\Delta T_w = 20$°C, only 10 percent to 12 percent of the area is available for natural convection. On the other hand, Fig. 5(*b*) shows that the natural convection heat transfer coefficient h_{nc} (which is independent of the contact angle) increases with the wall superheat with different slopes: the rate is faster at low wall superheats than at higher wall superheats. Thus, the effects of $(1-KV_s)$ and h_{nc} are opposite with each other. In the wall superheat range of $\Delta T_w < 13$°C, the increase in h_{nc} is faster than the decrease in the available area for natural convection, leading to an increase of natural convection heat flux in this range of wall superheat. On the other hand, when $\Delta T_w \geqslant 13$°C, the decrease in area is faster than the increase of the convection heat transfer coefficient, leading to a decrease of heat flux by natural convection. As the wall superheat is increased to $\Delta T_w > 7$°C, both the number of nucleation sites and bubble release frequency increase, leading to a rapid increase of nucleate boiling heat flux, q_b, which becomes the dominant mechanism of heat transfer hereafter. This can be also explained from Eq. (20*b*), which shows that q_b is very sensitive to the total number of nucleation sites on a boiling surface. Table 1 also shows that the contribution from micro layer evaporation is not important for $\Delta T_w \geqslant 10$°C, which is also in agreement with other investigator's observation [Mikic and Rohsenow [2]]. A similar trend can also be observed from the numerical results obtained for the contact angle 35 deg, which is not presented because of page limitation.

5 Effects of Contact Angles

Figure 6 shows the effects of contact angle on the total nucleate pool boiling heat flux of water at 1 atm and at a specific wall superheat of 10 °C. It is shown that there is a large reduction in the total heat flux as the contact angle is decreased from ϕ=90 deg to ϕ=35 deg. This is consistent with Wang and Dhir [8] experimental results, which show a corresponding reduction in total heat flux as the contact angle was decreased as shown in Figs. 4(*a*) and 4(*b*).

To understand the effect of the contact angle on the boiling heat transfer, we now present the effects of the contact angle on the values of $D_{c,\max}$, $D_{c,\min}$ and $N_{a,\text{tot}}$ as shown in Figs. 7 and 8, respectively. It is shown that the values of $D_{c,\max}$, $D_{c,\min}$, and $N_{a,\text{tot}}$ decrease as the contact angle is decreased from 90 deg to 35 deg. It is seen that the value of $D_{c,\max}$ increases slowly at low wall superheats and then keeps approximately constant, while the value of $D_{c,\min}$ decreases monotonously with the increase of wall superheat. Because $N_{a,\text{tot}}$ is raised to the power of $(1+1/d_f)$ in Eq. (20*b*), a decrease in the value of $N_{a,\text{tot}}$ will lead to a drastic reduction in heat flux.

However, when contact angle is reduced from ϕ=90 deg to ϕ=35 deg, the large reduction in the total number of nucleation

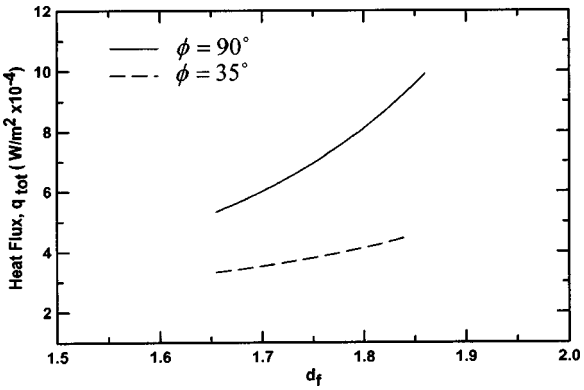

Fig. 6 Effects of contact angle and fractal dimension on boiling heat flux at ΔT_w=10°C

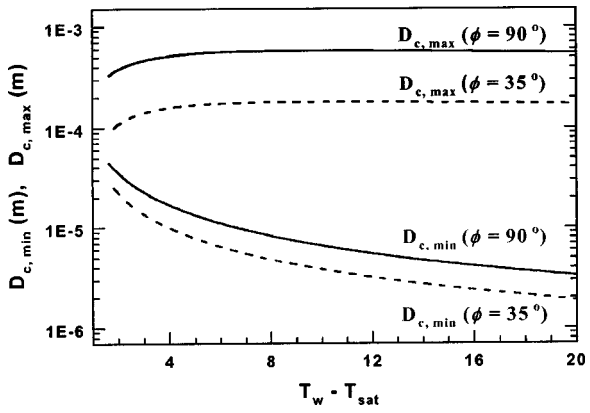

Fig. 7 Effects of contact angle on maximum and minimum diameters of nucleation sites

sites causes only a 2 percent reduction in area fraction V_s as shown in Fig. 3. This can be explained by examining the ratio of the area fraction V_s at ϕ=90 deg and ϕ=35 deg. According to Eqs. (8*c*) and (22), we have the ratio

$$\frac{V_{s,90}}{V_{s,35}} = \frac{\left(\frac{D_{c,\min,90}}{D_{c,\max,90}}\right)^{2-d_f,90}}{\left(\frac{D_{c,\min,35}}{D_{c,\max,35}}\right)^{2-d_{f,35}}} = \left(\frac{D_{c,\min,90}}{D_{c,\max,90}}\right)^2 \left(\frac{D_{c,\max,35}}{D_{c,\min,35}}\right)^2 \left(\frac{N_{a,\text{tot},90}}{N_{a,\text{tot},35}}\right) \tag{33}$$

which depends not only on the ratio of the total number of nucleation sites but also the combined factors on the size of nucleation sites, which are given by Eq. (9). Therefore although the reduction of the total number of nucleation sites is large (for about 4 times at ΔT_w=18°C), the ratio of $V_{s,90}/V_{s,35}$ may not be large and depends on the combination of effects of maximum and minimum diameters of nucleation sites. This combined effect causes the value of V_s to be insensitive to the contact angle.

6 Effects of Surface Conditions

It was shown in Fig. 2 that the fractal dimension, determined by the box-counting method from the photo image of nucleation sites, agrees well with theoretical prediction given by Eq. (30). For this reason, the total boiling heat flux based on this fractal model is also in excellent agreement with the same set of experimental data as shown in Fig. 4. It should be noted that the fractal theory given in Sections 2–4 has not taken into consideration the roughness and cleanness of the surfaces. These factors will undoubtedly affect the fractal dimension of the nucleation sites, and consequently the heat transfer rate. For such surfaces, the total boiling heat flux can also be determined from Eqs. (1), (20), (21), and (32) with the value of d_f determined by the box-counting method. However, since we define the fractal dimension d_f through Eq. (8*b*), i.e., the cumulative number of active cavities with diameter greater than and equal to D_c follows Eq. (8*b*). This means that the surface conditions such as roughness, cleanness etc., are comprehensively reflected by active sites and thus by the fractal dimension. How to relate the surface conditions such as roughness and cleanness to the active nucleation sites and thus to the fractal dimension is a challenging task that remains to be done.

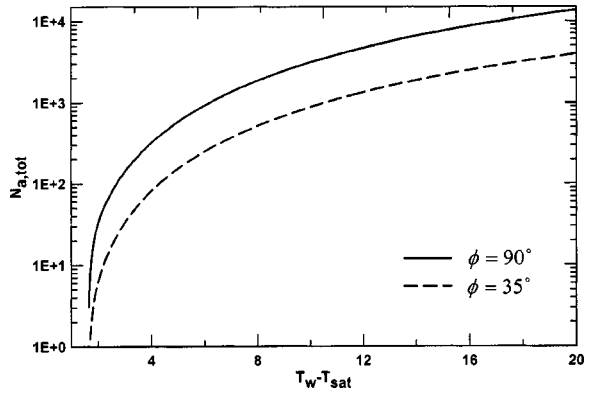

Fig. 8 Effects of contact angle on total number of nucleation sites

Figure 6 also shows the effects of fractal dimension (which reflects the surface condition) on the total nucleate pool boiling heat flux of water at 1 atm and at a specific wall superheat of 10°C. It is seen that the total boiling heat flux increases with fractal dimension. This is as expected because the increase of fractal dimension implies the increase of number of nucleation sites, leading to an increase on the boiling heat flux. Thus, the effects of roughness and cleanness on boiling heat flux can also be taken into consideration based on the present model.

7 Concluding Remarks

A fractal model for nucleate pool boiling heat transfer is derived based on the fractal characteristics of nucleation sites on superheated surfaces and the fractal theory. The predicted heat flux based on the proposed fractal model is shown in excellent agreement with experimental data. The validity of the present fractal model is thus verified.

The proposed model is a function of area (size) fractal dimension of nucleation sites, maximum and minimum active cavity, wall superheat, the contact angle between the fluid and the heater material, and physical properties of the fluid with empirical constants $K=1.8$, $B=1.55$, $D_d/D_i=0.5$, and $C=1.5\times10^{-4}$ which are associated with Eqs. (2), (6), (7*c*), and (15), respectively. Since no additional empirical constants are introduced, this fractal model contains less empirical constants than the conventional correlation equations. It should be noted that the values of K and D_d/D_i are true constants with definite physical meanings and are independent of the contact angle and other physical properties of the fluid. As discussed earlier, the value of B depends on the type of fluid while the value of C (which is associated with the bubble departure diameter) may depend also on the contact angle. Dhir [1] reviewed several models for bubble diameter at departure, and all of these models contain one or more empirical constants depending on the contact angle. Although several researchers such as Han and Griffith [5] have derived analytical expressions for bubble departure diameters, they did not subsequently apply these models to compute nucleate boiling heat transfer. Instead, they applied empirical formula of bubble departure diameters for the calculation of boiling heat transfer. Therefore, it is uncertain whether these analytical models are reliable. If an analytical expression can be derived for the bubble departure diameter based on the fractal characteristics of cavities, the empirical constant C may be eliminated from this model. This will be another aspect of our future work.

Acknowledgments

The authors gratefully acknowledge the support of this work through the RGC grant #HKUST6044/97E.

A = area of heating surface
Ar = Archimedes number, $(gv_1^2)(\sigma/\rho_l g)^{3/2}$
B = 1.55 given by Eq. (6)
C = 1.5×10^{-4} given by Eq. (15)
C_p = specific heat at constant pressure
D_c = cavity diameter
D_b = bubble diameter at departure
$D_{c,\max}$ = maximum cavity diameter
$D_{c,\min}$ = minimum cavity diameter

D_d = diameter of dry area under the bubble
D_i = instantaneous bubble diameter
D_{inf} = diameter of area on heating surface affected by bubble departure
D_s = spot diameter on surface
d_f = fractal dimension
f = frequency of bubble departure
g = gravity acceleration
h_{fg} = latent heat of evaporation
k = thermal conductivity
K = proportional constant for bubble diameter of influence
Ja = Jacob number, $(\rho C_p)_l \Delta T_w/(\rho_v h_{fg})$
Ja* = Jacob number, $(\rho C_p)_l T_{\text{sat}}/(\rho_v h_{fg})$
N_a = cumulative number of active cavities with diameter greater than or equal to D_c
N = cumulative number of spots
q = heat flux
R_c = cavity radius
Ra = Rayleigh number, $\eta g(T_w - T_\infty)D^3/(\alpha v)$
T_{sat} = saturation temperature
T_∞ = bulk temperature
ΔT_w = $T_w - T_{\text{sat}}$
t_w = waiting time
t_g = bubble growth time
V = volume

Greek Symbols

σ = surface tension of fluid
ρ = density
β = cone half angle
ϕ = contact angle
η = volumetric thermal expansion coefficient of liquid
α = thermal diffusivity of fluid
ν = kinematic viscosity
θ_{sat} = $T_{\text{sat}} - T_\infty$
θ_w = $TT_w - T_\infty$
δ = thermal layer thickness
ψ = volumetric (or area) fraction
γ = $\sqrt{\frac{k_w \rho_w c_{pw}}{k_l \rho_l c_{pl}}}$

Subscripts

b = aboling
l = liquid
max = maximum
me = microlayer evaporation
min = minimum
nc = natural convection
tot = total
v = vapor
w = wall
90 = contact angle ϕ=90 deg
35 = contact angle ϕ=35 deg

References

[1] Dhir, V. K., 1991, "Review, Nucleate and Transition Boiling Heat Transfer Under Pool and External Flow Conditions," Int. J. Heat Fluid Flow, **12**(4), pp 290–313.
[2] Mikic, B. B., and Rohsenow, W. M., 1969, "A New Correlation of Pool Boiling Data Including the Effect of Heating Surface Characteristics," J. Heat Transfer, **91**, pp. 245–250.
[3] Judd, R. L., and Hwang, K. S., 1976, "A Comprehensive Model for Nucleate Pool Boiling Heat Transfer Including Microlayer Evaporation," Int. J. Heat Mass Transf., **98**, pp. 623–629.
[4] Ivery, H. J., 1967, "Relationship Between Bubble Frequency, Departure Diameter, and Rise Velocity in Nucleate Boiling," Int. J. Heat Mass Transf., **10**, pp. 1023–1040.
[5] Han, C. Y., and Griffith, P., 1965, "The Mechanism of Heat Transfer in Nucleate Pool Boiling—Part I and II," Int. J. Heat Mass Transf., **8**, pp. 887–913.
[6] Benjamin, R., and Balakrishnan, A. R., 1996, "Nucleate Pool Boiling Heat Transfer of Pure Liquids at Low to Moderate Heat Fluxes," Int. J. Heat Mass Transf., **39**, pp. 2495–2504.
[7] Torikai, K., Hori, M., Akiyama, M., Kobori, T., and Adachi, H., 1964, "Boiling Heat Transfer and Burn Out Mechanism in Boiling Water Cooled Reactor," Third United Nations International Conference on the Peaceful Uses of Atomic Energy," Paper No. 28/P580.
[8] Wang, C. H., and Dhir, V. K., 1993, "Effect of Surface Wettability on Active Nucleation Site Density During Pool Boiling of Saturation Water," J. Heat Transfer, **115**, pp. 659–669.
[9] Yu, B. M., and Cheng, P., 2002, "Fractal Models for the Effective Thermal Conductivity of Bidispersed Porous Media," AIAA J. Thermophysics and Heat Transfer, **16**(1), pp. 22–29.
[10] Mandelbrot, B. B., 1982, *The Fractal Geometry of Nature*, W. H. Freeman, New York.
[11] Feder, J., 1988, *Fractals*, Plenum Press, New York.
[12] Majumdar, A. A., and Bhushan, B., 1990, "Role of Fractal Geometry in Roughness Characterization and Contact Mechanics of Surfaces," ASME J. Tribol., **112**, pp. 205–216.
[13] Majumdar, A., 1992, "Role of Fractal Geometry in the Study of Thermal Phenomena," Annu. Rev. Heat Transfer, **IV**, pp. 51–110.
[14] Hsu, Y. Y., 1962, "On the Size Range of Active Nucleation Cavities on a Heating Surface," J. Heat Transfer, **84**, pp. 207–215.
[15] Bankoff, S. B., 1958, "Entrapment of Gas in the Spreading of a Liquid over a Rough Surface," AIChE J., **4**, pp. 24–26.
[16] Van Stralen, S. J. D., Sohal, M. S., Cole, R., and Sluyter, W. M., 1975, "Bubble Growth Rates in Pure and Binary Systems: Combined Effect of Relaxation and Evaporation Microlayers," Int. J. Heat Mass Transf., **18**, pp. 453–467.
[17] Yu, B. M., and Li, J. H., 2001, "Some Fractal Characters of Porous Media," Fractals, **9**(3), pp. 365–372.
[18] Paul, D. D., and Abdel-Khalik, S. I,., 1983, "A Statistical Analysis of Saturated Nucleate Boiling Along a Heater Wire," Int. J. Heat Mass Transf., **26**, pp. 509–519.

Prediction of Critical Heat Flux for Convective Boiling of Saturated Water Jet Impinging on the Stagnation Zone

Zhen-Hua Liu
e-mail: liuzhenh@guomai.sh.cn

Qun-Zhi Zhu

School of Power and Energy Engineering,
Shanghai Jiaotong University,
Shanghai, 200030, P.R. China

A theoretical analysis and an experimental investigation were carried out for predicting the critical heat flux (CHF) of convective boiling for a round saturated water jet impinging on the jet stagnation zone. The model of the maximum liquid subfilm thickness based on the Helmholtz instability is used to derive a semi-theoretical equation and the correlation factor was determined from the experimental data. Finally, a semi-theoretical correlation was proposed for predicting CHF of convective boiling for saturated water jet impinging on the jet stagnation zone. [DOI: 10.1115/1.1518497]

Keywords: Boiling, Evaporation, Forced Convection, Heat Transfer, Jets

1 Introduction

Water jet impinging cooling of hot plate, as a highly effective cooling method, has been widely used in iron and steel industry, nuclear power process and some microelectronic devices making and thermal management processes. According to the ranges of plate temperatures, the heat transfer modes may be divided into forced convection, nucleate boiling, transition boiling and film boiling. For water jet impinging boiling on the hot plate, the assessment of the critical heat flux (CFH) is very important. The geometries of a water jet impinging on a horizontal hot plate can be divided into two modes as shown in Fig. 1. One mode is the free film flow was shown in Fig. 1(*a*) named as the mode *A* in this paper, in which a great heated disk or rectangular plate is cooled by a small liquid jet and the ratio of the heated disk diameter to the nozzle diameter is much larger than unity. In general, for this geometry condition, the jet impinging cooling experiments can be only carried out for the forced convection and nucleate boiling heat transfer regimes. After the burnout occurred, the heat-transfer surface would be divided into two zones of the jet stagnation zone (black zone) and the dry-out zone, and hence the temperatures and heat fluxes on the heat-transfer surface would be very inconsistent. The second mode is the stagnation jet flow as shown in Fig. 1(*b*) named as the mode *B* in this paper, in which the diameter of the heat-transfer surface is the same or smaller than the diameter of the jet nozzle. For this geometry condition, the jet impinging cooling experiments can be extensively carried out in the total boiling regimes including transition and film boiling with uniform wall temperatures and wall heat fluxes.

In the past two decades, for the mode *A*, the studies associated with CFH of saturated and subcooled liquids on the disk or rectangular plate have been performed extensively. A variety of the experimental results have been reported and various semi-theoretical correlations and empirical correlations have been proposed for predicting CHF for different parameters ranges such as compact velocities, ratios of liquid density to vapor density, heater geometries and multiple jet systems. [1–12]

In many boiling systems, CHF has often been attributed to the hydrodynamic instabilities associated with the liquid-vapor interface. In his analysis of CHF in pool boiling, Zuber [13] pointed out that as the bubble population increases at the heat-transfer surface, bubbles coalesce and form intermittent vapor blankets. The Taylor instability of blanket interface results in the effusion of equally-spaced vapor columns. As the heat flux increases, the velocity of vapor jets also increase with respect to the counter current flow of liquid moving towards the surface. Zuber postulated that CHF takes place as a result of the Helmholtz instability, which interrupts the counter current flow and prevents further contact of liquid with the heat-transfer surface. Haramura and Katto [14] proposed a concept of the maximum liquid subfilm-thickness on the high heat flux nucleate boiling surface. This modeling technique have been successfully applied to the jet impinging boiling for the mode of *A* [6,8,9,11], the falling film boiling [15–17], and the cross flow boiling [18,19]. This modeling concept postulated that a liquid subfilm have existed underneath each vapor bubble growing on the heat-transfer surface. The vapor bubble hovered a number of small jets that applied the bubble with vapor mass, leading to a timely growth of the bubble until it was pulled upward away from the surface by buoyancy. The bubbles were arranged in a rectangular array with a spacing equal to the most dangerous Taylor wavelength whereas the liquid subfilm thickness was one-fourth of the Helmholz wavelength. Burnout was assumed to take place when the liquid subfilm layer underneath the vapor bubble evaporated completely before the departure of the bubble.

For the mode *A*, the mechanism of the burnout is evidenced to be the dry-out at the outer edge of the free film flow zone. The thickness of the liquid subfilm layer is assumed to be equal or proportional to the maximum liquid subfilm thickness proposed by Haramura and Katto [14]. The dry-out phenomenon takes place firstly at the outer edge of the free film flow zone and expends rapidly to the whole free film flow zone. After burnout phenomenon occurred, only the stagnation zone could be impinged directly by current flow, liquid flow would be splashed completely off the heated surface at the edge of the stagnation zone along the radial direction. The following equation has been derived theoretically using the model of the maximum liquid subfilm thickness [6] for the mode *A*.

$$\frac{q_{c,0}}{Gh_{fg}} = 0.278\left(\frac{\rho_v}{\rho_l}\right)^{0.467}\left(1+\frac{\rho_v}{\rho_l}\right)^{1/3}\left(\frac{\sigma\rho_l}{G^2(D-d)}\right)^{1/3}\left(1+\frac{D}{d}\right)^{-1/3} \tag{1}$$

Monde and Kitajima [11] proposed an empirical correlation as follows:

Contributed by the Heat Transfer Division for publication in the JOURNAL OF HEAT TRANSFER. Manuscript received by the Heat Transfer Division February 14, 2001; revision received July 15, 2002. Associate Editor: V. P. Carey.

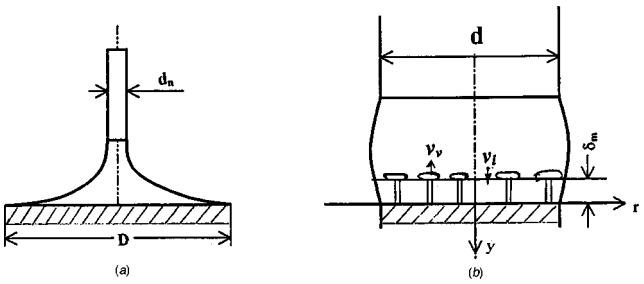

Fig. 1 The schematic diagrams of the physical model and coordinate: (*a*) the mode *A*; and (*b*) the mode *B*

$$\frac{q_{c,0}}{Gh_{fg}} = 0.278\left(\frac{\rho_v}{\rho_l}\right)^{0.645}\left(\frac{\sigma\rho_l}{G^2(D-d)}\right)^{0.343}\left(1+\frac{D}{d}\right)^{-0.343} \quad (2)$$

where, D and d denote the heated disk diameter and the nozzle diameter, respectively. G denotes the mass flux of jet flow. The applicable range of D/d has been not defined clearly for the above-mentioned two correlations. It is evident that the above-mentioned correlations can be not used for the mode *B*, in which D/d is equal to or less than unity and jet boiling heat transfer is limited in the stagnated zone.

Up still now, although many experimental studies for the mode *B* have been carried out for the boiling heat transfer of jet impinging at the stagnation zone, these studies focused mainly on the boiling heat transfer [20–23]. There are not systematically experimental and theoretical studies were reported for CHF for the mode *B*. Only a few data of CHF were included in the experimental results for the nucleate boiling heat transfer, and, a most of these experiments employed subcooled liquids as coolants [21,24–26]. The fundamental understanding of CHF of convective boiling for saturated liquid jet impinging on the stagnation zone is too poor.

In the present study, as first objective of this study on CHF of jet boiling for the mode *B*, a simplified theoretical analysis and an experimental investigation were carried out for predicting CHF of convective boiling for a round saturated water jet impinging on the jet stagnation zone which has the same size as that of the jet nozzle as shown in Fig. 1(*b*). The concept of the maximum liquid subfilm thickness based on the Helmholtz instability is used to derive semi-theoretical equation, and the correlation factor was determined from the present experimental data. Finally, a semi-theoretical correlation was proposed for predicting CHF of convective boiling of saturated water jet impinging on the stagnation zone.

2 Simplified Theoretical Analysis

The CHF model is based on two sub-models. First, an interfacial instability analysis proposed by Haramura and Katto [14] is used to describe the maximum liquid subfilm thickness. Second, a flow model is used to describe the local velocity of liquid in the stagnation zone. Then, an energy balance is written for the heated surface to obtain the average heat flux at CHF point. Figure 1(*b*) shows the schematic diagram of the analytical model for the model *B*. Here, a round water jet of diameter, *d*, impinges vertically on a circular flat plate having the same diameter as that of the nozzle with the compact velocity *V*, and the saturation temperature, T_0. After the burnout phenomenon occurred, the water jet flow zone has been limited in the stagnation zone (splashed liquid flow has not been drawn in this figure). As various forced convection boiling systems including the mode A of jet boiling, the Mode B of jet boiling can also use the concept of the maximum liquid subfilm thickness for predicating CHF. For the mode B, the burnout of nucleate boiling takes place when the incoming liquid, which comes from current flow and passes through the liquid subfilm layer along the radial direction, is evaporated just completely at the edge of the stagnation zone, i.e., the position of $d/2$. It must be noted that CHF corresponds to such a critical state when dry-out only takes place at the edge of the stagnation zone, but not in the whole stagnation zone. Leidenfrost point (the minimum heat flux point) would correspond to such a state when dry-out takes place in the whole stagnation zone.

Before the onset of the Helmholtz instability, the vapor jets leave the heated surface at velocity v, in counter current flow with respect to the liquid, which approaches the surface at velocity v_1. Mass conservation between the two phases gives;

$$v_v\rho_v A_v = \rho_l(A-A_v) \quad (3)$$

where, A_v and A denote the total cross-sectional area of the vapor jets and the total heat-transfer surface area, respectively. Assuming that all the heat transfer from the heat-transfer surface is converted into latent energy by evaporation of the incoming liquid, the velocity of the vapor jets can be obtained from the energy balance,

$$qA = v_v\rho_v A_v h_{fg}. \quad (4)$$

The Helmholtz instability occurs when relative velocity between the two phases satisfies the criterion,

$$|v_v-(-v_l)|^2 \geqslant \frac{2\pi\sigma(\rho_v+\rho_l)}{\rho_1\rho_v\lambda_H} \quad (5)$$

where, λ_H denotes the critical wavelength for Helmholtz instability. The maximum thickness δ_m of the liquid subfilm layer formed by the collapse of vapor jets is proportional to the order of λ_H. Combining Eqs. (3) to (5) yields the following relationship for δ_m.

$$\delta_m = C_1\left(1+\frac{\rho_v}{\rho_I}\right)\left[\frac{\sigma}{\rho_v(q|\rho_v h_{f_g})^2}\right] \quad (6)$$

where

$$C_1 = 2\pi c_\lambda\left[\frac{A_v/A}{1+(\rho_v/\rho_l)(A_v/A)/(1-A_v/A)}\right] \quad (7)$$

where, c_λ is a constant of the order of unity.

Equation (6) is the well-known expression of the maximum thickness of liquid subfilm layer proposed by Haramura and Katto [14]. It was proposed firstly for predicting the CHF in pool boiling system. It has been also successful in correlating CHF data for various forced convection boiling systems with the film flow such as falling film, wall jet, impinging jet of the mode *A*.

The ratio of A_v/A is assumed to be a constant or, at least, a weak function of pressure Haramura and Katto [14] obtained the expression, $A_v/A = 0.0584(\rho_v/\rho_l)^{0.2}$ by equating their relationship for CHF in pool boiling to Zuber's original equation. However, this assumption cannot be generalized to all boiling systems. In any case, such variations of A_v/A would not have a significant effect on CHF. in the present study, we employed the exponent relation in expression of Haramura and Katto, i.e.,

$$A_v/A = C_2(\rho_v/\rho_l)^{0.2} \quad (8)$$

where, C_2 is an unknown constant smaller than unity. Since under normal operating conditions $\rho_v/\rho_1 \ll 1$, Eq. (7) is simplified as,

$$C_1 = C_3(\rho_v/\rho_l)^{0.4} \quad (9)$$

CHF is postulated to occur when the latent energy of the incoming liquid, which incomes the subfilm layer through vapor blankets layer and penetrates the thin subfilm layer in the radial direction, is just equal to the total heat supplied in the heated stagnation zone. Namely, the incoming liquid is evaporated just completely at the edge of the stagnation zone. Hence, the following equation can be obtained.

$$M = (\pi d^2/4)q_{c,0}/h_{fg} = \pi d\,\delta_m\rho_l U(R) \quad (10)$$

where M denotes the total mass rate of the incoming liquid $U(R)$ denotes the assumed mean velocity of liquid flowing out the sub-

film layer at the edge of the stagnation zone along the radial direction when the liquid has been not evaporated, i.e., the jet flow is the single-phase flow. For this case, the following equations can be obtained

$$U(R)=\frac{1}{\delta_m}\int_0^{\delta_m} u_l(y,R)dy \tag{11}$$

Inside the velocity boundary layer of liquid, the distributions of velocity can be taken as exponential forms along the radial direction,

$$\frac{u_1}{u_\delta}=1-\frac{3}{2}\left(\frac{y}{\delta_l}\right)+\frac{1}{2}\left(\frac{y}{\delta_l}\right)^3 \tag{12}$$

where, δ_l denote the thickness of the velocity boundary of liquid, u_δ the velocity at the interface of the boundary layer, respectively. For the single-phase jet flow inside the stagnation zone, δ_l and u_δ can be expressed as follows [27]

$$u_\delta(r)/V=2r/d \tag{13}$$

$$\delta_1/d=211/\mathrm{Re}^{0.5} \tag{14}$$

Combining Eqs. (11) to (14) yields

$$U(R)=C_4V \tag{15}$$

Here, C_4 is generally a weak function of δ_m. In a special case of $\delta_l=\delta_m$, C_4 would is a constant and independent of $\delta_m(\delta_l$ and δ_m have the same order by a trial calculation). For the actual boiling flow, the total incoming mass rate is rather less than that in the single-phase flow due to interruption of the vapor blankets layer. But, it can be reasonably assumed that the proportional relationship between $U(R)$ and V in Eq. (15) is still available and only the correlation factor C_4 has a variation due to the effect of turbulent transport in the subfilm layer

Combining Eqs. (6), (9), and (10), yields,

$$q_{c,0}=C\left(1+\frac{\rho_v}{\rho_l}\right)\left[\frac{\sigma}{\rho_v(q_{c,0}/\rho_v h_{f_g})^2}\right]\left(\frac{\rho_v}{\rho_l}\right)^{0.4}\left[\frac{\rho_l h_{fg} V}{d}\right]. \tag{16}$$

Finally, a dimensionless form of Eq. (16) can be obtained as follows:

$$\frac{q_{c,0}}{Gh_{fg}}=C\left(1+\frac{\rho_v}{\rho_l}\right)^{\frac{1}{3}}\left(\frac{\sigma\rho_l}{G^2d}\right)^{\frac{1}{3}}\left(\frac{\rho_v}{\rho_l}\right)^{\frac{1.4}{3}} \tag{17}$$

where, C is a correlation factor and it can be determined from the experimental data.

For the case of the heated disk diameter less than the jet nozzle diameter, Eqs. (16) and (17) can still be employed. Hence, CHF is a constant, independent of the heated disk diameter in the jet stagnation zone.

3 Experimental Apparatus

In this study, steady heat transfer experiments were conducted for nucleate boiling regime to obtain boiling curves and determine critical heat fluxes. Figure 2 shows the schematic diagram of the experimental set up. It mainly consisted of the test specimen, the circulation system of water, the measuring devices and electric power supply.

Ion-exchanged water with the electric conductivity of about 3 ($\mu\Omega\ \mathrm{cm}^{-1}$) was used as the coolant (the maximum electric conductivity was less than 10 ($\mu\Omega\ \mathrm{cm}^{-1}$) in the experiments). Water was heated to the saturation temperature at atmospheric pressure in the high-level water tank, which was fitted with two immersion heaters and a reflux condenser mounted directly above the tank. Then, the saturated water was drained from the high-level water tank by a water pump, passed through a regulating valve and a flow meter into the jet nozzle made of a quartz glass tube, in which the temperature of water was measured finally by a thermocouple. Water jet impinged onto the test specimen, i.e., the heat-transfer surface, then was drained into a drain tank to be recycled. The distance between the nozzle exit and the specimen was fixed at 10 mm.

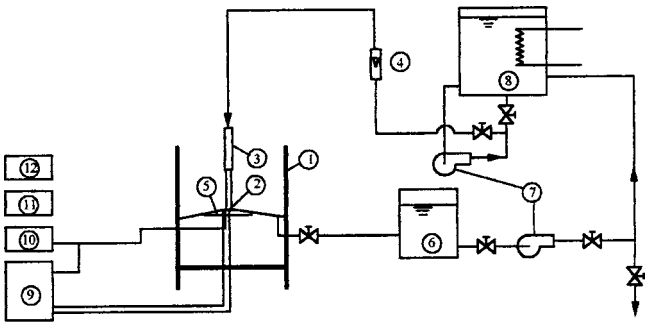

Fig. 2 The schematic diagram of the experimental setup

Figure 3 shows the schematic diagram of a test specimen. The test specimen was very thin Nickel Chromium alloy foil, 0.1 mm or 0.05 mm in thickness, and was directly linked with direct current (supplied by a silicon rectifier) to produce Joule heat. Two copper plates were spot welded at the two sides of the specimen as electric power lead lines. The specimen was closely fixed on a Teflon disk by using silicone glue and the welded parts were covered by silicone glue for insulation. Upward heat-transfer surface was cleared by acetone. A sheathed thermocouple of Φ 0.3 mm was spot welded at the center of the bottom of the specimen. The thermocouple was linked to a digital multimeter that fed the measured signals into a computer to get the wall temperatures making use of one-dimensional thermal conductive equation

$$\frac{d}{dy}\left(\lambda_s\frac{dT}{dy}\right)=Q' \tag{18}$$

where, $\lambda_s=17.4W/mK$, at 20 °C. Q' is the internal heat calculated by the electric power applied and the volume of the specimen.

Because the thermophysics properties of the specimen could be considered to be constant inside the specimen, and the bottom of the specimen is insulated,

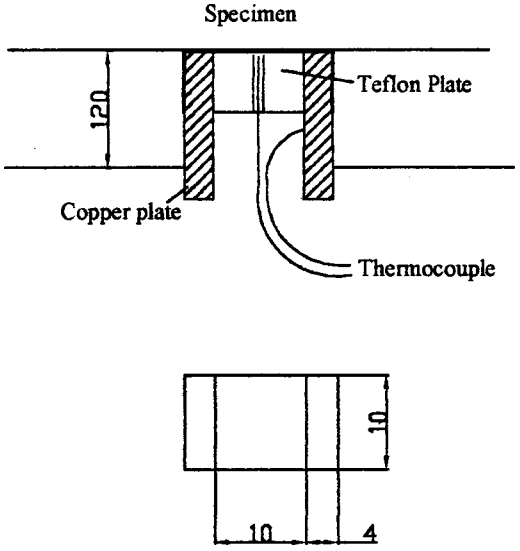

Fig. 3 The schematic diagram of a test specimen

$$T_w = T_b - \frac{|Q'|}{2\lambda_s}\Delta y^2 \tag{19}$$

where, Δy is the thickness of the specimen, T_w and T_b denote the temperatures of the heat-transfer surface and the measured bottom surface, respectively.

Three different specimens with the cross-section sizes of 10×10 mm, 6×6 mm, and 2×4 mm were used in this experiment and they corresponded to three round jet nozzle diameters, 10 mm, 6 mm, and 2 mm, respectively. The mass flux of water flowing out the nozzle is determined by means of a flow meter. Calibrations made at temperatures ranging from 20 °C to 70 °C show that the error is less than a few percent if the thermal variation of water density is taken into account. In the tests, the wave of the mass flux was limited within ±4 percent. The CHF value was determined by increasing the power input with a small step near the CHF point. When the heated surface temperature could not have a steady state and increased very quickly, the power input was cut automatically

In this experiment, the impact velocity of water ranged 0.5 m/s to 6 m/s and had the same uncertainty as that of the mass flux. By trial numerical simulations for the temperature contributions inside the specimen, the heat losses resulted from the thermal conduction in the copper plates and the bottom surface of the specimen have almost not effects on the temperatures and heat fluxes at the center of the specimen. Namely, the measured temperatures by the thermocouple were not affected by the heat losses. The calibration errors of the thermocouples were less than 0.2 K and the maximum uncertainty of the wall temperature was within 1.5 K near the CHF point. Hence, the maximum uncertainty of the wall superheat was within 5 percent near the CHF point. The power input was measured with a power meter with ±0.2 percent relative accuracy. The heat flux was calculated by dividing the measured power input (after it was corrected for the electric power losses in the copper plates) by the specimen area. The maximum uncertainty of the heat flux was about within 5 percent.

4 Results and Discussion

Figure 4(*a*)–(*c*) shows the experimental results of fully developed nucleate boiling heat transfer at the stagnation zone for saturated water jet using respectively three nozzle diameters. Heat transfer data are plotted in the form of boiling curves (wall heat flux against wall superheat) for different jet diameters and impact velocities. Prior to fully developed nucleate boiling higher velocities increase the heat transfer coefficients and delay the boiling incipience. Because the objective of this study is investigation of CHF, hence, the experimental data for the range of the superheat less than 10 K have not been presented in Fig. 4.

The Stephan-Abdelsalam's empirical correlation [28] is shown in Fig. 1 in form of solid lines. For nucleate pool boiling of water at atmospheric pressure, the correlation is as follows:

$$q = 52.4\Delta T_{\text{sat}}^{3.058}\ [\text{W/m}^2\text{K}], \quad 6 \leqslant \Delta T_{\text{sat}} \leqslant 22K \tag{20}$$

In fully developed nucleate boiling regime, the data resulted from different impact velocities and jet diameters generally converged into essentially the same boiling curve. The data agree qualitatively with the Eq. (20) and are rather higher than the calculation curve. These deviations may result from the different surface configurations such as surface roughness. The insensitivity of the boiling curve to changes in compact velocity indicates that heat transfer in the fully developed nucleate boiling regime is dominated by bubble activity on the surface, regardless of the contribution of single-phase turbulent transport in the bulk flow. However, the effect of the compact velocity becomes quite significant on CHF, which is increased with increasing the compact velocity. This trend is attributed to the increased liquid-solid contact on the heated surface and the decreased void fraction in the liquid flow. On the other hand, CHF is also increased with decreasing the jet diameter. This trend is attributed to the decreased

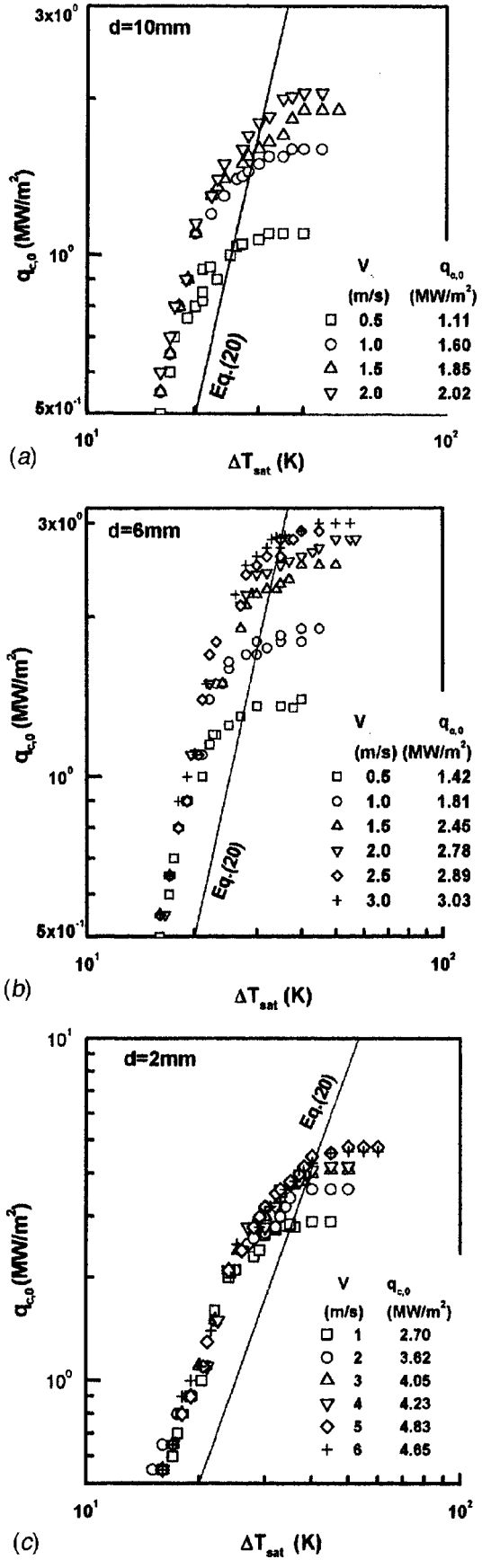

Fig. 4 Experimental results of boiling heat transfer for jet boiling: (*a*) the nozzle diameter of 10 mm (*b*) the nozzle diameter of 6 mm; and (*c*) the nozzle diameter of 2 mm.

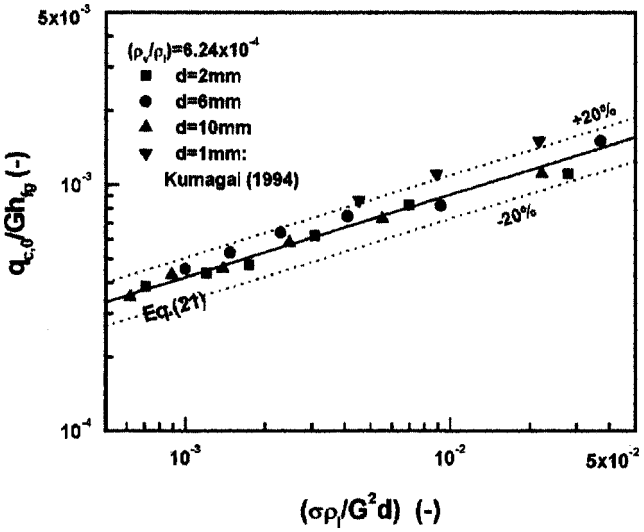

Fig. 5 Comparison between Eq. (21) and the CHF data

flow distance of the incoming liquid though the liquid subfilm layer, i.e., the decreased average evaporation distance of the incoming liquid.

Equation (17) is tested in Fig. 5 against experimental data of CHF obtained in the present study and Kumagai et al. (1994). Good agreement between the CHF data and the predictions is obtained for C=0.132.

$$\frac{q_{c,0}}{Gh_{fg}} = 0.132\left(1+\frac{\rho_v}{\rho_l}\right)^{1/3}\left(\frac{\sigma\rho_l}{G^2 d}\right)^{1/3}\left(\frac{\rho_v}{\rho_l}\right)^{1.4/3} \tag{21}$$

Equation (21) correlates CHF data with the maximum relative error less than ±20 percent, and can be recommended for predicting the CHF of saturated water jet boiling at the stagnation zone.

Because the thermophysics properties are constant for saturated water under the atmospheric pressure condition, the relation between $q_{c,0}$ and V as well as d can be simply expressed as

$$q_{c,0} = 0.36\times 10^6\left(\frac{V}{d}\right)^{1/3} \quad [\mathrm{W/m^2K}] \tag{22}$$

where, the unit of V and d are [m/s] and [m], respectively. Figure 6 shows the compared results between the CHF data and Eq. (22).

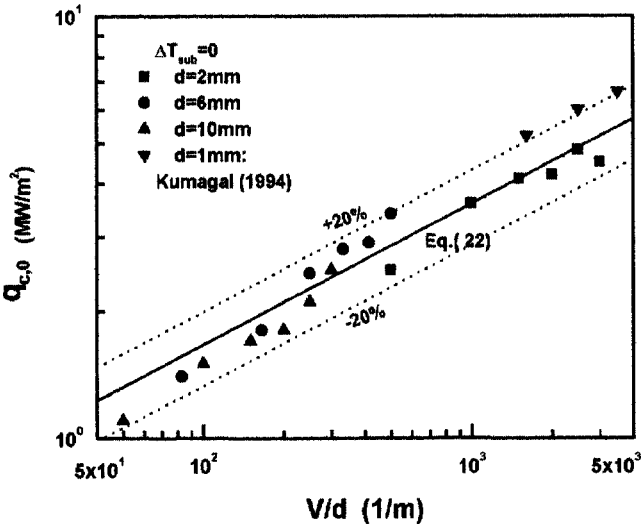

Fig. 6 Comparisons between Eq. (22) and CHF data

The CHF data proposed by Kumagai et al. [24] are rather higher than that of the present experiment. The reason may be due to that those data resulted from an unsteady cooling experiment, but the present data resulted from the steady experiment.

In general, for pool boiling of saturated water on the upward heat-transfer surface under atmospheric pressure, CHF is about 1.16 MW/m^2 [13]. This value can be taken as a lower limit of CHF for the convective boiling of water jet impinging on the stagnation zone, hence, the applicable range of Eqs. (21) and (22) can be estimated to be $(V/d)\geqslant 34.5$. Here, the unit of V and d are [m/s] and [m], respectively. For the range of $(V/d)<34.5$, CHF should be equal to that in pool boiling.

Since the present experiment was carried out at atmospheric pressure and only saturated water was used as a coolant, the ρ_v/ρ_l is fixed ($\rho_v/\rho_l=0.000624$) and the data cannot present the effects of thermophysics properties in wide range. In general, the exponents of the dimensionless numbers in the theoretical equation may be somewhat different from those in the experimental correlation due to some secondary effects, such as effects of correlation factors in Eqs. (7), (8), and (15), which have been assumed as constants in this study. But, they should be weak functions of the thermophysics properties and the jet conditions. Therefore, further work would be still needed to check and improve the applicability of the suggested correlating equation (21) in more wide range.

Conclusions

1 The model of the maximum liquid subfilm layer based on the Helmholtz instability was employed for predicting critical heat flux (CHF) of convective boiling of a round saturated water jet impinging on the stagnation zone. The steady boiling heat transfer experiment was conducted to determine the correlation factor.

2 Both the impact velocity and the nozzle diameter provide strong effect on CHF. Higher CHF was achieved with higher impact velocities and less nozzle diameters. The relationship of $q_{c,0}\propto(V/d)^{1/3}$ is available for saturated water jet under the atmospheric pressure condition.

3 Dimensionless Eq. (21) correlates the CHF data with the maximum relative error less than ±20 percent. Equation (21) can be recommended for predicting CHF of water jet boiling at the stagnation zone.

4 Further work would be still needed to check and improve the applicability of Eq. (21) in more wide range.

Acknowledgments

This work was supported by the National Natural Science Foundation of China under Grant No. 50176029.

Nomenclature

A = total heat-transfer surface area (m^2)
C = correlatin factor (−)
d = diameter of jet nozzle (m)
G = mass flux of liquid jet (kg m^{-2}s^{-1})
h_{fg} = latent heat of evaporation (Jkg^{-1})
M = total mass rate of liquid incoming into the subfilm layer (ms^{-1})
Re = Reynolds number of jet flow, $Re=Vd/v_1$(−)
q = wall heat flux (Jm$^{-2}\langle$s$^{-1}\rangle$)
$q_{c,0}$ = criticalheat flux for saturated liquid (Jm^{-2}s^{-1})
r = distance in the radial direction (m)
u = velocity of the radial direction (ms^{-1})
U = mean velocity of the radial direction (ms^{-1})
v = velocity of the vertical direction (ms^{-1})
V = compact velocity of liquid jet (ms^{-1})
y = distance in the vertical direction (m)

Greek Symbol

δ = thickness of boundary layer (m)
λ_H = critical wavelength for Helmholtz instability (m)
λ = thermal conductivity ($Jm^{-1}K^{-1}s^{-1}$)
T = temperature (K)
ΛT = superheat (K)
ν = kinematics viscosity (m^2s^{-1})
σ = surface tension ($N\ m^{-1}$)
ρ = density ($kg\ m^{-3}$)

Subscripts

0 = saturation
l = liquid
v = vapor
s = specimen
w = wall
δ = interface of velocity boundary layer

References

[1] Monde, M., and Kotto, Y., 1978, ''Burnout in a High Heat-Flux Boiling System with an Impinging Jet,'' Int. J. Heat Mass Transf., **21**, pp. 295–305.
[2] Katto, Y., and Shimizu, M., 1979, ''Upper Limit of CHF in the Saturated Forced Convection Boiling on a Heated Disk with a Small Impinging Jet,'' ASME Heat Transfer , **101**, pp. 265–269.
[3] Monde, M., 1980, ''Burnout Heat Flux in Saturated Forced Convection Boiling with an Impinging Jet,'' Heat Transfer-Jpn. Res., **9**, pp. 31–41.
[4] Monde, M., and Okuma, Y., 1985, ''Critical Heat Flux of Saturated Forced Convection Boiling on a Heated Disk with an Impinging Jet-CHF in L-regime,'' Int. J. Heat Mass Transf., **28**, pp. 547–552.
[5] Monde, M., 1987, ''Critical Heat Flux of Saturated Forced Convection Boiling on a Heated Disk with an Impinging Jet,'' ASME J. Heat Transfer , **109**, pp. 991–996.
[6] Katto, Y. 1985, ''Critical Heat Flux,'' *Advances in Heat Transfer,* J. P. Harnett and T. F. Irvine, Jr., eds., **17**, Orland, pp. 20–35.
[7] Sharan, A., and Lienhard, J. H., 1985, ''On Predicting Boiling Burnout in the Jet-Disk Configuration,'' ASME J. Heat Transfer , **107**, pp. 398–401.
[8] Katto, Y., and Yokoya, S., 1988, ''Critical Heat Flux on a Disk Heater Cooling by a Circular Jet of Saturated Liquid Impinging at the Center,'' Int. J. Heat Mass Transf. **31**, pp. 219–227.
[9] Monde, M., and Inoue, T., 1991, ''Critical Heat Flux in Saturated Forced Convection Boiling on a Heated Disk with Multiple Impinging Jets,'' ASME J. Heat Transfer , **113**, pp. 722–727.
[10] Monde, M., 1991, ''Critical Heat Flux in Saturated Forced Convection Boiling on a Heated Disk with One or Multiple Impinging Jets,'' Trends in Heat Mass and Momentum Transfer, **1**, pp. 33–44.
[11] Monde, M., Kitajima, K., Inoue, T., and Mitsutaka, Y., 1994, ''Critical Heat Flux in a Convection Subcooled Boiling with an Impinging Jet,'' ASME J. Heat Transfer , **7**, pp. 512–518.
[12] Monde, M., and Mitsutake, Y., 1996, ''Critical Heat Flux in a Convection Subcooled Boiling with Multiple Impinging Jets,'' ASME J. Heat Transfer , **117**, pp. 241–243.
[13] Zuber, N., 1959, ''Hydrodynamic Aspects of Boiling Heat Transfer,'' AEC Report No. AECU-4439.
[14] Haramura, Y., and Katto, Y., 1983, ''A New Hydrodynamic Model of Critical Heat Flux, Applicable Widely to Both Pool and Forced Convection Boiling on Submerged Bodies in Saturated Liquids,'' Int. J. Heat Mass Transf., **26**, pp. 389–399.
[15] Mudawar, I. A., Incroea, T. A., and Incropera, F. P., 1987, ''Boiling Heat Transfer and Critical Heat Flux in Liquid Films Falling on Vertically-Mounted Heat Sources,'' Int. J. Heat Mass Transf., **30**, pp. 2083–2095.
[16] Ueda, T., Inoue, M., and Nagatome, S., 1981, ''Critical Heat Flux and Droplet Entrapment Rate in Boiling of Falling Liquid Films,'' Int. J. Heat Mass Transf., **24**, pp. 1257–1266.
[17] Baines, R. P., El-Masri, M. A., and Rohsenow, W. M., 1984, ''Critical Heat Flux in Flowing Liquid Films,'' Int. J. Heat Mass Transf., **27**, pp. 1623–1629.
[18] Katto, Y., Yokoya, S., Miake, S., and Taniguchi, M., 1987, ''Critical Heat Flux on a Uniformly Heated Cylinder in a Cross Flow of Saturated Liquid Over a Very Wide Range of Vapor to Liquid Density Ratio,'' Int. J. Heat Mass Transf., **30**, pp. 1971–1977.
[19] Liu, W., Nariai, H., and Inasaka, F., 2000, ''Prediction of Critical Heat Flux for Subcooling Boiling,'' Int. J. Heat Mass Transf., **43**, pp. 3371–3390.
[20] Ishigami, S. K., Nakamishi, J. K., and Hikoshichi, T. A., 1978, ''Boiling Heat Transfer for a Plane Water Jet Impinging on a Hot Surface,'' *Proceedings of the 6th International Heat Transfer Conference*, Hemisphere Publishing Corp., Washington, DC, **1**, pp. 445–450.
[21] Nakamishi, J. K., Ishigami, S. K., Ochi, T., and Morita, I., 1980, ''Two-Dimensional Water Jet Impinging for Cooling of High Temperature Plate,'' Bull. JSME, **46**, pp. 714–724.
[22] Zhe, J., Sun, H., Ma, C. F., Lei, D., He, C., and Tian, Y., 1997, ''Experimental Study on Heat Transfer of Water Jet and Spraying Cooling High Temperature Wall,'' Chinese Journal of Engineering Thermophsics, **18**, pp. 629–633.
[23] Liu, H., and Wang, J., 2001, ''Study on Film Boiling Heat Transfer for Water Jet Impinging on a High Temperature Flat Plate,'' Int. J. Heat Mass Transf., **44**, pp. 2475–2481.
[24] Kumagai, S., Sano, T., Kamata, T., Suzuki, S., and Kubo, R., 1994, ''Boiling Heat Transfer to an Impinging Jet in Cooling a Hot Metal Slab,'' Bulletin of JASM (B), **60**, pp. 259–263.
[25] Kumagai, S., Sano, T., Kamata, T., Suzuki, S., and Kubo, R., 1995, ''Transient Cooling of Hot Plate with Impinging Water Jet,'' Bulletin of JASM (B), **61**, pp. 351–356.
[26] Ma, C. F., and Bergles, A. E., 1986, ''Jet Impinging Nucleate Boiling,'' Int. J. Heat Mass Transf., **29**, pp. 1095–1101.
[27] Miyazaki, H., and Siberman, E., 1972, ''Flow and Heat Transfer on a Flat Plate with a Two-Dimensional Laminar Jet Issuing from a Nozzle of Finite Height,'' Int. J. Heat Mass Transf., **15**, pp. 2097–2107.
[28] Stephan, K., and Abdelsalam, M., 1980. ''Heat Transfer Correlations for Natural Convection Boiling,'' Int. J. Heat Mass Transfer, **23**, pp. 73–81.

Heat Transfer Model for Evaporation of Elongated Bubble Flows in Microchannels

Anthony M. Jacobi
Professor of Mechanical Engineering,
Department of Mechanical Engineering,
University of Illinois,
Urbana, IL, USA

John R. Thome
Professor,
Laboratory of Heat and Mass Transfer (LTCM),
Swiss Federal Institute of Technology (EPFL),
Lausanne, Switzerland

Recent experimental studies of evaporation in microchannels have shown that local flow-boiling coefficients are almost independent of vapor quality, weakly dependent on mass flux, moderately dependent on evaporating pressure, and strongly dependent on heat flux. In a conventional (macrochannel) geometry, such trends suggest nucleate boiling as the dominant heat transfer mechanism. In this paper, we put forward a simple new heat transfer model based on the hypothesis that thin-film evaporation into elongated bubbles is the important heat transfer mechanism in these flows. The new model predicts the above trends and quantitatively predicts flow-boiling coefficients for experimental data with several fluids. The success of this new model supports the idea that thin-film evaporation into elongated bubbles is the important heat transfer mechanism in microchannel evaporation. The model provides a new tool for the study of such flows, assists in understanding the heat transfer behavior, and provides a framework for predicting heat transfer.
[DOI: 10.1115/1.1517274]

Keywords: Evaporation, Heat Transfer, Phase Change, Two-Phase

Introduction

There has been significant recent interest in microchannel heat transfer and, in particular, evaporation and condensation in highly compact microchannel heat exchangers has become important. Phase-change processes are key to the development of many micro-thermal machines, such as micro-refrigeration systems (see Shannon et al., [1]). The present study deals with evaporation in microchannels. The purpose of this work is to present a new model of two-phase heat transfer for this channel scale, and to use this model to explain recent data and observations reported in the literature.

The threshold from macro- to micro-behavior in two-phase flow is not yet well defined, and it depends on a number of factors, such as the heat transfer process, channel geometry, and flow properties. Kew and Cornwall [2] report that scale effects become evident when the hydraulic diameter is less than $2\sqrt{\sigma/(g(\rho_l-\rho_v))}$. For typical halocarbons in refrigeration or air-conditioning applications, this criterion implies that channel-size effects become important for diameters less than a couple of millimeters (1.9 mm for R134a, R12, and R22 at 0 C). For the present purpose, a macrochannel will be considered as one in which the bubbles are much smaller than the channel diameter, and a microchannel will be loosely identified as one in which the bubbles are constrained by the channel size. Consequently, for the present microchannel heat transfer modeling, it will be assumed that only one bubble can occupy the cross-section at any one time. We will not define the particular length scale necessary to achieve these conditions, but will assume they exist.

In macrochannels, evaporation is considered as controlled by two main mechanisms: nucleate boiling and two-phase convection. Most research in conventional macrochannels has focused on turbulent two-phase convection. In contrast, flows in microchannels span the laminar and turbulent regimes and hence laminar convection and thin-film evaporation may also be relevant. Some two-phase flow patterns existing in macrochannels may not be possible in microchannels. For example, capillary forces can prohibit stratified flows from occurring and, if one bubble spans the cross-section, the macroscale bubbly flow is not obtained. Furthermore, with capillary forces dominating, the film thickness in annular flow will not be strongly affected by gravity, and tube orientation will become unimportant—a potential advantage for application in micro-thermal machines. In order to properly interpret heat transfer data, and to understand the thermophysics of microchannels, the flow regime must be carefully considered as has been done in macrochannels by Kattan et al. [3–5].

Several recent studies have pointed to the dependence of microchannel heat transfer coefficients on heat flux as an indication of nucleate-boiling dominance. This hypothesis appears to be buttressed by a weak dependence on local quality and mass flux, as well as an increase in the coefficients with evaporating pressure. The purpose of this paper is to bring the consideration of flow regime into the interpretation of microchannel evaporation data, and to put forward an alternate hypothesis explaining these observations solely through thin-film evaporation as a much more plausible mechanism.

Literature Review

Mehendale et al. [6] recently provided an extensive review of single-phase and two-phase microchannel heat transfer, and other reviews are available [7]. We will not repeat an exhaustive review of flow in microchannels but will note that relatively few experimental studies have reported local flow boiling heat transfer coefficients in small channels. Our main purpose will be accomplished by discussing several recent studies that have reported such data, and studies that have sustained the growing notion that microchannel evaporation behavior can be explained in terms of macroscale nucleate boiling.

Tran and co-workers [8] investigated heat transfer for evaporation of R-12 inside a circular channel with a 2.46 mm diameter, and in a rectangular channel of 1.70×4.06 mm ($d_h=2.40$ mm). Previously, Wambsganss et al. [9] reported results for R-113 in a 2.92 mm diameter circular channel. In these studies, it was observed that for wall superheats larger than 2.75 K the local heat transfer coefficients did not change with mass velocity (50 to 695 kg/m^{2}s) nor with vapor quality (20 percent to 75 percent) but instead depended only on heat flux (7.5 to 59.4 kW/m^2). An attempt to fit their data to a typical nucleate boiling curve (of the form $q=a\Delta T^n$) yielded an exponent of $n=2.7$. This value of n is

Contributed by the Heat Transfer Division for publication in the JOURNAL OF HEAT TRANSFER. Manuscript received by the Heat Transfer Division July 31, 2001; revision received August 13, 2002. Associate Editor: V. P. Carey.

typical to that obtained in nucleate boiling correlations and commonly reported in the literature for macrochannels, and on that basis Tran and co-workers asserted that heat transfer was nucleate-boiling dominated in microchannel evaporation. At low superheats, below 2.75 K, they observed a significant change in the slope of their data plotted as a nucleate boiling curve (q versus ΔT), and they designated the low-superheat regime as convection-dominant. Heat-flux dependence still existed in this regime; however, it was much less than at higher wall superheats.

Zhao et al. [10] reported flow-boiling coefficients for CO_2 and R-134a in a microchannel of unspecified dimensions. They measured local heat transfer coefficients from inlet vapor qualities of 5 percent to outlet qualities of 30 percent but did not present the data as a function of quality. For mass fluxes from 250 to 700 kg/m^2 s at fixed heat fluxes, they did not observe mass-flux dependence for either CO_2 or R-134a for pressures ranging from 3970 to 5090 kPa and 350 to 490 kPa, respectively. In their heat flux range (8 to 25 kW/m^2), their results did not show a heat flux dependence. It may be important to note that all the tests of Zhao and co-workers were for wall superheats less than 2.75 K (from about 1 to 2 K). Hence, their data would have fallen in the lower heat-flux dependence zone observed by Tran and co-workers. Zhao et al. reported that for the same saturation temperature (283 K), CO_2 had heat transfer coefficients about 3 times those for R-134a.

Mehendale and Jacobi [11] provided a limited number of quasi-local data for evaporating flows of R-134a in horizontal, square passages, 0.8 by 0.8 mm. Their data were obtained as an average over the quality range from inlet to outlet and for most experiments the quality change was between 7 percent and 15 percent. A relatively low heat flux was used ($q < 3400$ W/m^2), and the mass flux ranged from about 1.8 to 15 kg/m^2 s. They did not report the wall superheat for these tests, but from their heat transfer coefficient data it is clear the wall superheat was less than 1 K. Nevertheless, Mehendale and Jacobi observed the heat transfer coefficient to be virtually independent of quality and dependent on heat flux. They observed mass flux dependence only at the highest flow rates. They explained these results in terms of nucleate boiling dominance at low mass-flow rates.

Bao et al. [12] reported local flow boiling coefficients for R-11 and R-123 inside a circular channel with a diameter of 1.95 mm. Their work reflects careful attention to experimental method and procedure; for example, consider their companion paper [13], in which they demonstrated their test facility provides energy balances within a few percent and yields single-phase results in agreement with accepted data. In their experiments, they used a single piece of tubing, 870 mm long. The first 400 mm of the tube was unheated, providing an entrance region; that section was followed by a 270 mm long test zone and then by a 200 mm unheated exit zone. For tests over a wide range of conditions (mass velocities from 50 to 1800 kg/m^2 s, vapor qualities from 0 to 90 percent, heat fluxes from 5 to 200 kW/m^2 and saturation pressures from 290 to 510 kPa), they observed that heat transfer coefficients were a strong function of heat flux and depended on saturation pressure; however, the effects of vapor quality and mass flux were very small. Hence, similar to the previous studies, they concluded that nucleate boiling dominated the heat transfer process—in fact, they demonstrated that the Cooper correlation [14] gave an approximate representation of their data (although it under-predicted their results by 20–50 percent). Using the same type of setup, Baird et al. [15] have also reported local heat transfer data for R-123 in a 0.92 mm diameter tube and CO_2 in the previous 1.95 mm tube, observing the same trends as in their earlier work.

Many of the studies cited above focus on the challenges of obtaining reliable data in the microchannel geometry, and data interpretation has been based on ideas and trends extrapolated from earlier experiences with macrochannels. As a demonstration of this approach for data interpretation, we calculated the recent flow pattern map of Kattan et al. [3–5] for macrochannels and found the flow regime in channels of less than 3 mm diameter is predicted as intermittent (i.e., slug flow) and then annular prior to reaching dry-out qualities. This prediction is congruent with the direct observations of Wambsganss et al. [9]. The heat transfer model of Kattan et al. is asymptotic for intermittent and annular flows, with a Cooper-based nucleate boiling contribution and a turbulent-film contribution. For small channels, the model predicts evaporative convection coefficients to depend on heat flux because the coefficient becomes nucleate-boiling dominated. While direct observations support the predicted flow pattern (an elongated bubble flow), nucleate-boiling dominance is only inferred from extrapolation of macrochannel heat transfer behavior.

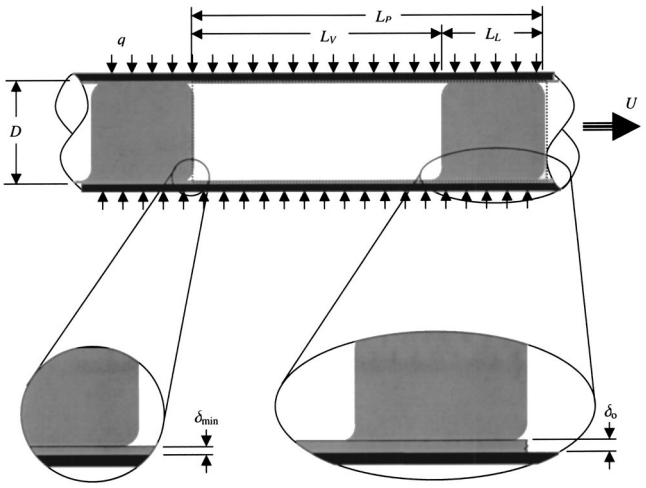

Fig. 1 Physical model of the elongated bubble flow regime expected in microchannel evaporating flows. A liquid-slug/vapor-bubble pair is identified for analysis, and the geometric description of the pair is provided.

This survey of the literature clearly shows evaporative convection coefficients in microchannels exhibit heat-flux dependence. Although the low-heat-flux cases exhibit less dependence (as in work by Tran and co-workers [8], Mehendale and Jacobi [11] and Zhao et al. [10]), many investigators have reported the heat flux dependence. The careful experiments of Bao et al. [12,13] provide compelling evidence that it exists. This heat-flux dependence of the convection coefficient, along with the relative independence from quality and mass flux, has been widely ascribed to the nucleate-boiling mechanism, well known from macrochannel studies. We will put forward an alternate explanation of this behavior, an explanation we believe is superior to the assertion that nucleate boiling is important in these flows. We will undertake to describe and support this alternate hypothesis through a simple thermal model of microchannel heat transfer.

Heat Transfer Model

We hypothesize that thin-film evaporation is the governing process in microchannel evaporation, and we will use that mechanism in a model to explore the expected heat transfer behavior for such a situation. We will demonstrate that this heat transfer mechanism can explain the trends reported above. Consider an elongated bubble/liquid-slug pair in a circular channel of diameter, D, as shown in Fig. 1. We shall refer to this system as the *pair*, and assign it a length of L_P. The length of the vapor bubble is L_V, and the liquid slug is given a length L_L. After inception, this pair moves down the channel with a velocity U. Due to the applied uniform heat flux, q, as the pair progresses down the channel, L_L decreases, and L_V increases. Because the vapor density is smaller than the liquid density, L_P increases and the local quality and void fraction (volume averaged over a pair) thus increase as the pair is propelled down the channel.

Central to this model is the idea that during elongated bubble flow a thin liquid film of uniform thickness is "laid down" by the passing liquid slug. The initial film thickness provided by the passing slug, δ_o, is governed by complex fluid dynamics within the slug and the film; we are not able to predict its thickness in a simple way, but we will simply assume its presence. It should be noted that after a liquid slug passes, the film begins to thin as evaporation proceeds. The thinning process continues until the next liquid slug passes. We will consider the effect of this thinning on the heat transfer coefficient later.

In order to estimate the period of time between generation of successive pairs, we assume that this period scales as if bubble growth follows the conduction-limited model of Plesset and Zwick [16] in a uniformly superheated liquid,

$$r(t)=\mathrm{Ja}\left(\frac{12\alpha_L\tau}{\pi}\right)^{1/2} \tag{1}$$

At $t=0$, growth of the bubble from a pre-existing vapor nucleus occurs. Using the definition of the Jakob number, and assuming the bubble will depart downstream the instant it spans the channel (neglecting the thin film, δ_o), the period of pair generation is estimated to be

$$\tau=\left(\frac{R\rho_V\lambda}{\rho_L c_{pL}\Delta T_{\mathrm{eff}}}\right)^2\frac{\pi}{12\alpha_L} \tag{2}$$

Equation (2) can be regarded simply as a scaling relation; it recognizes that a nucleation superheat is required to generate a bubble, and once the bubble forms it will grow in a conduction-limited fashion until the channel is bridged. The bubble will then be swept away and a new one will begin to grow, repeating the cycle at a frequency $1/\tau$. This simplified view of pair initiation neglects flow forces on the growing bubble and allows for no "waiting time" between bubbles. The effective superheat, ΔT_{eff}, can be adjusted to make the equality to hold in Eq. (2) for some unknown real nucleation superheat. Later, we can relate this effective superheat to a critical radius to demonstrate that physically reasonable radii are obtained.

In a simplification consistent with the view that a pair is formed at a $1/\tau$ frequency neglecting local flow effects on the growing nucleus, we will neglect (just at the point of pair formation) local density and velocity changes, and assume that up to the instant of detachment, the flow passes the nucleation site at the liquid velocity and density, thus over each period of bubble generation a pair length is swept out:

$$L_P(t=0)=L_{po}=\tau m/\rho_L \tag{3}$$

According to the idea that the pair forms the instant the bubble bridges the channel, we take the initial vapor length to be

$$L_V(t=0)=L_{Vo}=D \tag{4}$$

and from Fig. 1 we see that for all time,

$$L_P(t)=L_V(t)+L_L(t) \tag{5}$$

After pair formation, void fraction, velocity, and vapor quality can be calculated using basic definitions for a known fluid at a known mass flux m, and for an assumed film thickness δ_o. The basic definition of the void fraction gives:

$$\varepsilon(t)=\frac{L_V(t)(R-\delta_o)^2}{L_P(t)R^2}. \tag{6}$$

Recognizing that mass is carried through a flow area of $\pi(R-\delta_o)^2$, but that the mass flux, m, is defined by convention in terms of the total cross-sectional area, πR^2, the pair velocity $U(t)$ can be obtained by re-arranging the definition of mass flux:

$$U(t)=m\left(\frac{R^2}{(R-\delta_o)^2}\right)\left(\rho_L\frac{L_L(t)}{L_P(t)}+\rho_V\frac{L_V(t)}{L_P(t)}\right)^{-1}. \tag{7}$$

Finally, from the definition of quality, we can have

$$x(t)=U(t)\left(\frac{L_V(t)}{L_P(t)}\right)\frac{\rho_V}{m}\left(\frac{(R-\delta_o)^2}{R^2}\right). \tag{8}$$

Equations (2)–(5) are applied at $t=0$ and used to calculate the initial pair geometry (L_{Lo}, L_{Vo}, and L_{Po}). At any instant in time, the pair geometry can be used in Eqs. (6)–(8) to calculate the local void fraction, pair velocity, and vapor quality. Using an energy balance on the pair and mass conservation, coupled differential equations for the vapor and liquid length result as follows for a prescribed heat flux:

$$\frac{dL_V}{dt}=\frac{qD(L_V(t)+L_L(t))}{\rho_V(R-\delta)^2\lambda} \tag{9}$$

and

$$\frac{dL_L}{dt}=-\frac{qD(L_V(t)+L_L(t))}{\rho_L(R-\delta)^2\lambda} \tag{10}$$

Thus, with the initial conditions on L_V and L_L calculated, Eqs. (9) and (10) can be integrated forward in time, subject to the nonlinear constraint of Eqs. (5) through (8). At each time step, the pair geometry and velocity are calculated, and local void fraction and quality are found. We add a differential equation for position, and thereby calculate the position of the pair at each time step; i.e., we simultaneously integrate

$$\frac{ds}{dt}=U(t) \tag{11}$$

The equation set developed above thus provides two-phase flow characteristics as a function of position in the tube. If microchannel evaporation is thin-film dominated, then pair geometry and local velocity are key factors in modeling the heat transfer. These factors determine the fraction of tube area occupied by the film and the periodicity with which it is refreshed.

The current heat transfer model is based on the assumption that conduction through the thin liquid film dominates the heat transfer behavior. As a liquid slug passes, it lays down a film of thickness δ_o. Once the slug passes, transient thin-film evaporation begins and the film thickness decreases. Hence, the film is thinnest at the trailing edge of the elongated bubble. With the local value of pair passing frequency, τ, given by $L_p(t)/U(t)$, and accounting for conduction through a fictitious film into the passing liquid, the minimum film thickness is modeled with

$$\delta_{\min}=\delta_o-\frac{q}{\lambda\rho_L}\frac{L_p(t)}{U(t)} \tag{12}$$

Averaging over the period and length of the pair, the heat transfer coefficient is determined from an average film thickness, using a quasi-steady approach. Spatial and temporal averaging with Eq. (12) yields the following expression for local heat transfer coefficient

$$h(s;t)=k_L\left(\delta_o-\frac{qL_p(t)}{4\lambda\rho_L U(t)}\right)^{-1} \tag{13}$$

With Eq. (13), the local heat transfer coefficient can be determined as the flow equations are solved for local quality, void fraction, and location. An average heat transfer coefficient could then be determined by integrating Eq. (13) over position, s. However, we are interested in local behavior to compare to data reported in the literature. In particular, we are interested in whether this simplified thin-film model will provide predictions congruent with the data, offering support for the hypothesis that microchannel evaporation is thin-film dominated.

Recognizing it provides only an estimate for large superheats, we also calculate the critical radius suggested by the effective superheat from Eq. (2) using the following expression [17],

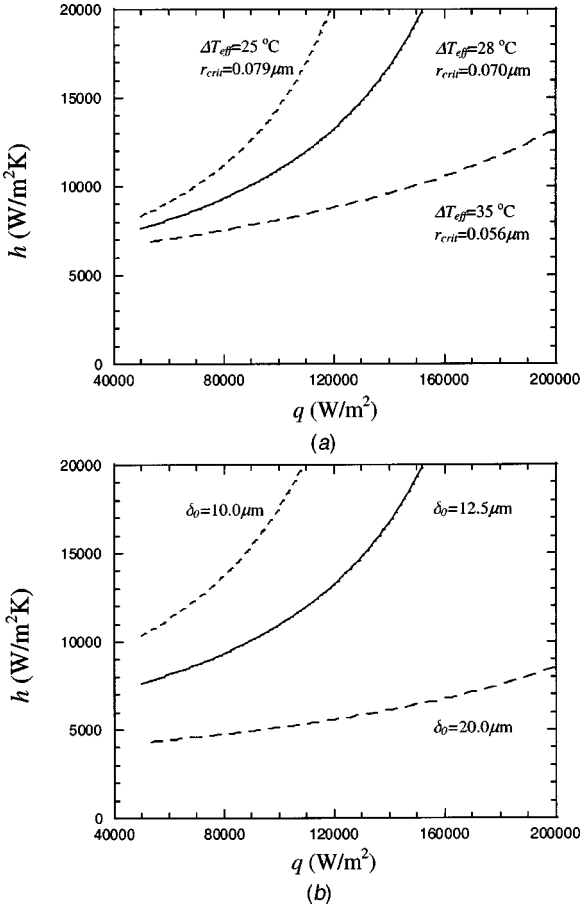

Fig. 2 Heat transfer behavior for R-11 at P_{sat}=460 kPa, D=2 mm, and m=446 kg/m^2 s, showing (*a*) h for varying ΔT_{eff} (r_{crit}) at a fixed initial thin-film thickness of δ_o=12.5 μm, and (*b*) h for varying δ_o at a fixed ΔT_{eff}=28 K (r_{crit}=0.070 μm).

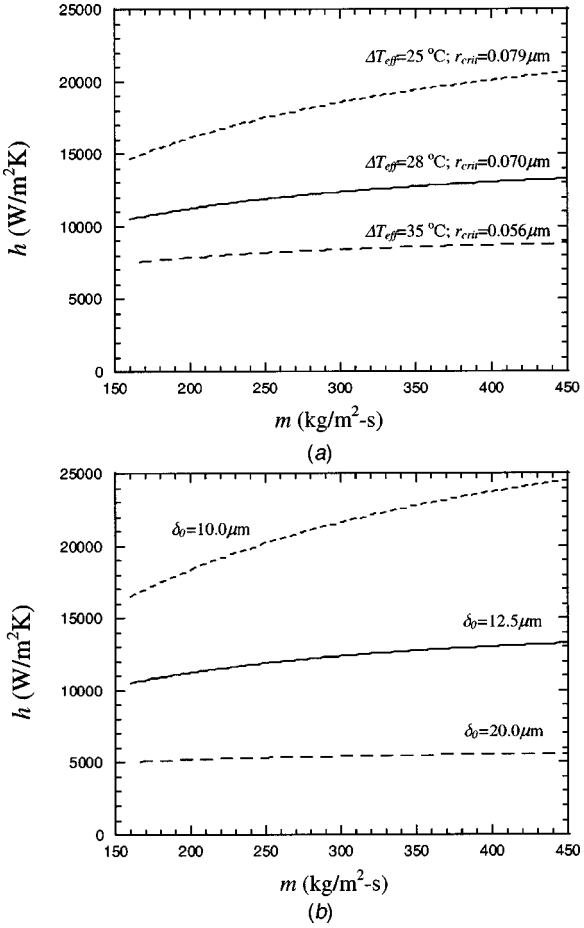

Fig. 3 Heat transfer behavior for R-11 at P_{sat}=460 kPa, D=2 mm, and q=120 kW/m^2, showing (*a*) h for varying ΔT_{eff} (r_{crit}) at a fixed initial thin-film thickness of δ_o=12.5 μm, and (*b*) h for varying δ_o at a fixed ΔT_{eff}=28 K (r_{crit}=0.700 μm).

$$\Delta T_{\text{eff}} = \frac{2\sigma}{r_{\text{crit}}(dp/dT)_{\text{sat}}}, \tag{14}$$

where r_{crit} is the critical radius of the pre-existing vapor nucleus, whose value is unknown and depends on the microgeometry and roughness of the surface. Our purpose in using Eq. (14) is not to obtain an accurate estimate of the critical radius; we simply wish to demonstrate that the suggested size of the critical radius is reasonable for a microchannel tube. We recognize that in our model—due to the nature of nucleation—we will ultimately assume a value of r_{crit} (or ΔT_{eff}), which then sets of the value of ΔT_{eff} (or r_{crit} based on Eq. (14)).

Discussion and Comparison to Experimental Results

The differential-algebraic equation (*DAE*) set developed above was solved using a Newton-Raphson method for the algebraic set, with simultaneous integration of the differential equations using a fifth-order Runge-Kutta-Verner. For all cases reported, the relative residual in the solution was less than 10^{-6}. Solutions to the model show that the period of sweeping, τ, is independent of location in the tube for all cases; that is, L_P/U is independent of quality. This finding is an obvious result, and with some manipulation of the DAE set, it can be shown that $d\tau/dt$ is always zero. Physically, this result is due to the fact that as the quality increases, $U(t)$ increases because of the increase in $L_P(t)$ and U increases at exactly the rate of increase in L_P. Although the result is obvious after consideration, it is reassuring to obtain it with the numerical procedure, and it emphasizes the important fact that sweeping frequency is a constant, set by pair-formation frequency.

We conducted a series of simulations designed to explore the trends predicted by the model and representative results are provided in Figs. 2 through 4 for R-11 at a saturation pressure of 460 kPa in a channel of 1.95 mm diameter. The parametric values used in these figures were selected to allow a comparison of the model results to the experimental data of Bao et al. [12] and to demonstrate the trends with a range of ΔT_{eff} and δ_o (the ''free'' parameters in the model). As demonstrated in Fig. 2, the heat transfer coefficient is predicted to increase with heat flux. This finding is in agreement with the behavior reported in the literature. It may be especially noteworthy that the dependence of h on q is low at small heat fluxes and higher at large heat fluxes. This result seems to explain why data obtained at a low heat flux show little heat-flux dependence (as in [8]), but high-heat-flux data exhibit strong heat flux dependence (as in [12]).

In Fig. 3 it is shown that the model predicts the heat transfer coefficient to be insensitive to mass flux for reasonable values of ΔT_{eff} and δ_o; again, the results are congruent with the extant literature. The values of Re_L range from about 1000 to 2500; so, the expectation is that the flow is laminar or just entering the transitional regime even at the highest mass fluxes. In the top graph, ΔT_{eff} (or r_{crit}) is shown to have a substantial effect on heat transfer but that heat transfer is still nearly independent of m, which agrees with the studies cited earlier. The variation in h versus m is minor relative to that for h versus q shown in Fig. 2, which also follows the trends observed experimentally.

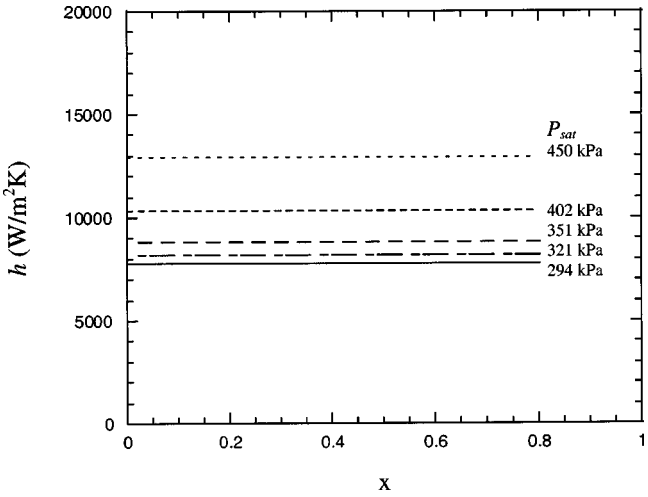

Fig. 4 The predicted heat transfer coefficient for R-11 as a function of vapor quality, with $\Delta T_{eff}=28$ K ($0.12<r_{crit}<0.06$ μm), for P_{sat} ranging from 294 to 450 kPa, with $\delta_o=12.5$ μm, $q=125$ kW/m^2, and $m=560$ kg/m^2 s to cover the conditions reported by Bao et al. [12]

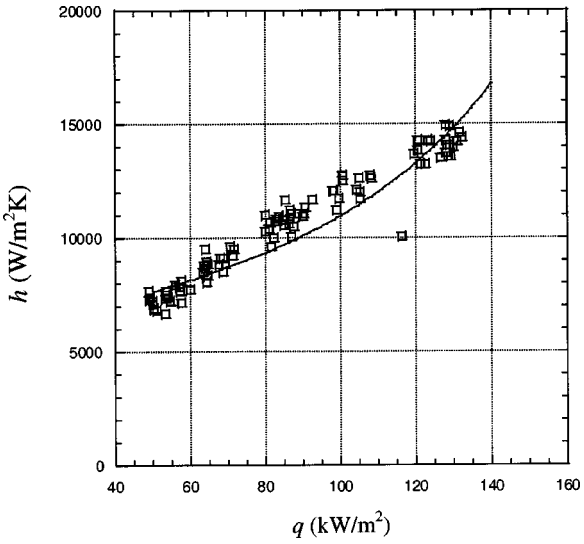

Fig. 5 Comparison of the new model to the data of Bao et al. [12] for R-11 at $P_{sat}=460$ kPa with the model parameters set to $\Delta T_{eff}=28$ K ($r_{crit}=0.070$ μm) and $\delta_o=12.5$ μm

In Fig. 4, the heat transfer coefficient is shown to be independent of vapor quality and to increase with saturation pressure. This set of simulations was conducted under conditions typical to those presented by Bao and co-workers [12] (in their Fig. 8), and a direct comparison to that earlier work shows remarkable agreement: the model properly predicts the behavior with quality and saturation pressure. All these trends are consistent with data reported by others; of course, these trends are also consistent with nucleate-boiling dominance. However, the predictions now presented are obtained using a heat transfer model based solely on evaporation of a thin liquid film trapped between a moving elongated bubble and the channel wall. Hence, based on the present analysis the dominant heat transfer mechanism in microchannel evaporation under these conditions is transient thin film evaporation with growth of elongated bubbles flowing down the channel and not conventional macrochannel nucleate pool boiling.

In order to make a compelling comparison of the new model to existing data, we considered the experiments of Bao et al. [12] in more depth. Using their test conditions, we adjusted the unknown effective nucleation superheat and the initial film thickness to minimize the least-square error between their data and the new model.[1] For parametric values of $\Delta T_{eff}=28$ K (equivalent to $r_{crit}=0.070$ μm) and $\delta_o=12.5$ μm, the average squared relative error between the experiments and the model was less than 10 percent, with the trends predicted as shown in the comparison of the model to the theory in Fig. 5. These results are for R-11 at a saturation pressure of 460 kPa in a 1.95 mm diameter tube. We have shown all data they obtained at this saturation pressure because the results are insensitive to quality and mass flux (as demonstrated earlier). It is necessary to point out that an error in the printing of [12] provides an erroneous curve for the data (in their Fig. 2); however, we have used the correct data for these conditions, as provided by Prof. Haynes. It is interesting to note the data of Bao et al. suggest h as almost linear with q, but the best values of ΔT_{eff} and δ_o predict nonlinear behavior. The model predictions would become more linear; i.e., show less curvature, for relatively larger film thickness and effective superheat; however, the model would under-predict heat transfer coefficients for such linear behavior. Viewing the data of Bao et al. through the framework of the new model, suggests thicker films and smaller critical radii than predicted by the model.

[1]We are indebted to Prof. B. S. Haynes for providing his data through private communication with JRT.

In our model, h depends on q because an increase in heat flux imposes more thinning during the period τ, and a thinner layer implies a higher heat transfer coefficient due to the reduced conductive resistance of the film. Likewise, as the saturation pressure is increased, the heat of vaporization decreases, and the film thins more rapidly during the sweep period τ, and thus h increases with saturation pressure.

We have also been able to conduct a general comparison to earlier heat transfer data of Wambsganss and co-workers for R-12 (see [8]). Their data show the same trends as noted for other fluids: h is almost independent of x and m, and depends strongly on q. By reading the heat transfer coefficient data from their Fig. 4, and fitting $h(q)$ for R-12 at a saturation pressure of $P_{sat}\sim 825$ kPa in a 2.46 mm diameter tube, we find that values of $\Delta T_{eff}=32$ K, and $\delta_o=20$ μm predict their measurements with an average deviation less than 13 percent (within their 15 percent uncertainty). Furthermore, the new model again predicts little dependence on x and m, in agreement with the experiments.

Unfortunately, a direct comparison to the data of Zhao et al. [10] is impossible because the microchannel dimensions are not provided. However, they show heat transfer data and note that h values for CO_2 are roughly three times those of R-134a under identical test conditions. Assuming a diameter of 2 mm and their operating conditions, the new model predicts heat transfer coefficients for CO_2 to be roughly twice those of R-134a (using $\Delta T_{eff}=28$ K, and $\delta_o=12.5$ μm). If the tube diameter is taken as 3 mm, the ratio is about four. Hence, our model correctly predicts the physical property dependence on thin film evaporation for their conditions for these two diverse fluids but no exact quantitative prediction is possible without the channel dimensions.

Hence, by judicious selection of the nucleation radius r_{crit} and the initial thin film thickness δ_o, the new model is able to describe all the experimental trends in the heat transfer coefficient versus m, x, q, and P_{sat} for four different fluids, both qualitatively and to some extent quantitatively for evaporation in the elongated bubble flow regime. As the nucleation radius is a function of the microgeometry of the surface, and its prediction is still an unresolved problem in nucleation theory, its value cannot be predicted analytically and must be assumed to determine ΔT_{eff} (or visa versa).

Conclusion

A new heat transfer model for evaporation in the elongated-bubble flow regime in microchannels has been proposed. The model is based on a simplified view of the fluid mechanics, with the hypothesis that thin-film evaporation is the dominant heat transfer mechanism. The new model requires a numerical solution to a nonlinear algebraic-differential-equation set. It also requires knowledge of two parameters: namely the effective nucleation superheat (or the critical nucleation radius), and the initial film thickness (ΔT_{eff} and δ_o). It may be possible to make estimates of ΔT_{eff} through r_{crit}, using microscopy to characterize the microchannel surface. This approach might then be extended to account for contact-angle and cavity size distribution effects on microchannel heat transfer. The work of Moriyama and Inoue [18] suggests estimation of δ_o might also be possible; however, further work on flow, thermal, and geometrical effects on the film thickness is needed for complete closure of the model. Some data suggest the model underestimates δ_o and ΔT_{eff}, but simply treating them as free parameters allows the model to serve as a predictive tool as herein demonstrated.

At this point, the importance of this model rests in its ability to demonstrate that recent data for two-phase heat transfer in microchannels can be explained with a thin-film evaporation mechanism as opposed to prior interpretations that conventional macroscale nucleate boiling is important. In its current form, this model of evaporation in the elongated-bubble flow regime predicts all trends in the microchannel heat transfer coefficient, both—to some extent—qualitatively and quantitatively; however, the model requires the judicious selection of the nucleation radius r_{crit} and the initial thin film thickness δ_o.

Acknowledgments

This work was initiated while A. M. Jacobi was an ERCOFTAC Scientific Visitor to the Laboratory of Heat and Mass Transfer at the EPFL in Lausanne. The authors are indebted to Dr. Vincent Dupont for a careful review of our work during manuscript preparation.

Nomenclature

c_{pL} = specific heat of the liquid
D = tube diameter
d_h = hydraulic diameter
h = flow boiling heat transfer coefficient
Ja = Jakob number, $\rho_L c_{pL} \Delta T_{\text{eff}} / (\rho_V \lambda)$
k_L = thermal conductivity of the liquid
L = length
m = mass flux
P_{sat} = saturation pressure
q = heat flux
R = tube radius
Re_L = liquid Reynolds number, mD/μ_L
r = bubble radius during initial growth phase
s = distance down tube axis
t = time
T = temperature
U = liquid-slug/vapor-bubble pair velocity
x = vapor quality

Greek Symbols

α = thermal diffusivity
ΔT = temperature difference
δ = film thickness
ε = void fraction
λ = latent heat of evaporation
μ = dynamic viscosity
ρ = mass density
σ = surface tension
τ = sweeping period

Subscripts

crit = critical radius at nucleation
eff = effective
L = liquid
P = pair
V = vapor
min = minimum
sat = saturation

References

[1] Shannon, M. A., Philpott, M. L., Miller, N. R., Bullard, C. W., Beebe, D. J., Jacobi, A. M., Hrnjak, P. S., Saif, T., Aluru, N., Sehitoglu, H., Rockett, A., and Economy, J., 1999, "Integrated Mesoscopic Cooler Circuits (IMCCs)," in *Proceedings of the ASME Advanced Energy Systems Division*, S. M. Aceves, S. Garimella, and R. B. Peterson, eds., ASME AES-Vol. 39, ASME, New York, pp. 75–82.

[2] Kew, P., and Conrwell, K., 1997, "Correlations for the Prediction of Boiling Heat Transfer in Small Diameter Channels," Appl. Therm. Eng., **17**, pp. 705–715.

[3] Kattan, N., Thome, J. R., and Favrat, D., 1998, "Flow Boiling in Horizontal Tubes. Part 1: Development of a Diabatic Two-Phase Flow Pattern Map," J. Heat Transfer, **120**, pp. 140–147.

[4] Kattan, N., Thome, J. R., and Favrat, D., 1998, "Flow Boiling in Horizontal Tubes. Part 2: New Heat Transfer Data for Five Refrigerants," J. Heat Transfer, **120**, pp. 148–155.

[5] Kattan, N., Thome, J. R., and Favrat, D., 1998, "Flow Boiling in Horizontal Tubes. Part 3: Development of a New Heat Transfer Model Based on Flow Patterns," J. Heat Transfer , **120**, pp. 156–165.

[6] Mehendale, S. S., Jacobi, A. M., and Shah, R. K., 2000, "Fluid Flow and Heat Transfer at Micro- and Meso-Scales with Application to Heat Exchanger Design," Appl. Mech. Rev., **53**(7), pp. 175–193.

[7] Gad-el-Hak, M., 1999, "The Fluid Mechanics of Microdevices—The Freeman Scholar Lecture," J. Fluid Mech., **121**, pp. 5–33.

[8] Tran, T. N., Wambsganss, M. W., and France, D. M., 1996, "Small Circular and Rectangular Channel Boiling with Two Refrigerants," Int. J. Multiphase Flow, **22**, pp. 485–498.

[9] Wambsganss, M. W., France, D. M., Jendrzejczyk, J. A., and Tran, T. N., 1993, "Boiling Heat Transfer in a Horizontal Small-Diameter Tube," J. Heat Transfer, **115**, pp. 963–972.

[10] Zhao, Y., Molki, M., Ohadi, M. M., and Dessiatoun, S. V., 2000, "Flow Boiling of CO_2 in Microchannels," ASHRAE Trans., **106**(1), pp. 437–445.

[11] Mehendale, S. S., and Jacobi, A. M., 2000, "Evaporative Heat Transfer in Mesoscale Heat Exchangers," ASHRAE Trans., **106**(1), pp. 446–452.

[12] Bao, Z. Y., Fletcher, D. F., and Haynes, B. S., 2000, "Flow Boiling Heat Transfer of Freon R11 and HCFC123 in Narrow Passages," Int. J. Heat Mass Transf., **43**, pp. 3347–3358.

[13] Bao, Z. Y., Fletcher, D. F., and Haynes, B. S., 2000, "Experimental Study of Gas-Liquid Flow in Narrow Conduit," Int. J. Heat Mass Transf., **43**, pp. 2313–2324.

[14] Cooper, M. G., 1984, "Heat Flow Rates in Saturated Nucleate Pool Boiling—A Wide-Ranging Examination Using Reduced Properties," Adv. Heat Transfer, **16**, pp. 157–239.

[15] Baird, J. R., Bao, Z. Y., Fletcher, D. F., and Haynes, B. S., 2000, "Local Flow Boiling Heat Transfer Coefficients in Narrow Conduits," *Boiling 2000: Phenomena and Engineering Applications*, A. Bar-Cohen, ed., Anchorage, Alaska, Apr 30–May 5, **2**, pp. 447–466.

[16] Plesset, M., and Zwick, S. A., 1954, "The Growth of Vapor Bubbles in Superheated Liquids," J. Appl. Phys., **25**, pp. 493–500.

[17] Collier, J. G., and Thome, J. R., 1994, *Convective Boiling and Condensation*, Third edition, Oxford Science Publications, Oxford, p. 543.

[18] Moriyama, K., and Inoue, A., 1996, "Thickness of the Liquid Film Formed by a Growing Bubble in a Narrow Gap Between Two Horizontal Plates," J. Heat Transfer, **118**, pp. 132–139.

Heat Transfer Coefficients During Condensation of the Zeotropic Refrigerant Mixture HCFC-22/HCFC-142b

F. J. Smit
Ph.D. student
Rand Afrikaans University,
Mechanical Engineering,
PO Box 524
Auckland Park,
2006, Johannesburg, South Africa
e-mail: jpm@ingl.rau.ac.za

J. R. Thome
Mem. ASME, Professor
Swiss Federal Institute of Technology Lausanne,
Laboratory of Heat and Mass Transfer,
CH-1015 Lausanne, Switzerland
e-mail: john.thome@epfl.ch

J. P. Meyer
Mem. ASME, Professor
University of Pretoria,
Mechanical and Aeronautical Engineering,
Pretoria, 0002, South Africa
e-mail: jmeyer@up.ac.za

Heat transfer coefficients during condensation of zeotropic refrigerant mixtures were obtained at mass fractions of 90 percent/10 percent, 80 percent/20 percent, 70 percent/30 percent, 60 percent/40 percent, and 50 percent/50 percent for HCFC-22/HCFC-142b and for pure HCFC-22 in a horizontal smooth tube at a high saturation pressure of 2.43 MPa. The measurements were taken in a series of eight 8.11 mm inner diameter smooth tubes with lengths of 1 603 mm. At low mass fluxes, from 40 kg/m^{2}s to 350 kg/m^{2}s where the flow regime is predominately stratified wavy, the refrigerant mass fraction influenced the heat transfer coefficient by up to a factor of two, decreasing as the mass fraction of HCFC-142b is increased. At high mass fluxes of 350 kg/m^{2}s and more, the flow regime was predominately annular and the heat transfer coefficients were not strongly influenced by the refrigerant mass fraction, decreasing only by 7 percent as the refrigerant mass fraction changed from 100 percent HCFC-22 to 50 percent/50 percent HCFC-22/HCFC-142b. The results also indicated that of three methods tested to predict heat transfer coefficients, the flow pattern correlation of Dobson and Chato (1998) gave the best results for pure HCFC-22 and for the mixtures utilizing the Silver-Bell-Ghaly method (1964).
[DOI: 10.1115/1.1484108]

Keywords: Condensation, Convection, Experimental, Heat Transfer, Two-Phase

Introduction

Hot-water heat pumps are especially used in countries with a mild climate in winter, that have no natural gas and where electrical heating is usually used for the heating of water. Heating of water with heat pumps is extremely energy-efficient. Savings of approximately 67 percent can be realized, compared to heating with direct electrical resistance heaters [3,4]. Hot-water heat pumps are vapor compression cycles, which use water-cooled condensers for the heating of hot water. The most widely used refrigerant for hot-water heat pumps is HCFC-22 ($CHClF_2$) with which a maximum hot-water temperature of 60°C to 65°C is possible with approximately the same condensing temperatures. This is possible by making use of the refrigerant's superheat, which can be 60°C because the compressor discharge temperature is approximately 120°C. The maximum condensation temperature of approximately 60°C is limited by the maximum safe operating pressure of available compressors. The compressors in winter have to run with evaporating temperatures of approximately 0°C and less. Under these conditions, the pressure ratio over the compressor will be approximately 4.9. This is approximately the maximum safe limit for small hermetically sealed compressors used in hot water heat pumps that will guarantee acceptable loads on the bearings. In addition, at too high condensing temperatures the compressor discharge temperature will be too high, which will lead to decomposition of the lubricating oil.

Although hot-water temperatures of 60°C to 65°C are adequate for domestic use, they are low when compared to temperatures that can be delivered by fossil fuel and direct electric resistance systems. This limits the potential applications of hot-water heat pumps. Smit and Meyer [5] as well as Johannsen [6] showed analytically that a zeotropic mixture of HCFC-22 and HCFC-142b ($CClF_2CH_3$) could be used to obtain higher temperatures. A hot-water outlet temperature of 120°C is possible if only HCFC-142b is used. The disadvantage of using only HCFC-142b is that its heating capacity is 15 percent lower and its heating COP (coefficient of performance) is 7 percent lower when compared to HCFC-22. Furthermore, it is flammable, but the flammability is decreased by adding HCFC-22. A mixture of 60 percent HCFC-22 with 40 percent HCFC-142b to 80 percent HCFC-22 with 20 percent HCFC-142b by mass, is recommended. With these mixtures the heating capacities are about the same as just HCFC-22, but its COP is increased while hot-water temperatures of 80°C (80 percent/20 percent HCFC-22/HCFC-142b) to 90°C (60 percent/40 percent HCFC-22/HCFC-142b) can be achieved. Mixtures of HCFC-22 with HCFC-142b form zeotropic mixtures with glides of 7°C and 5°C for 60 percent and 80 percent HCFC-22 respectively.

Literature searches by Smit [7], Kebonte [8] and Bukasa [9] showed that apparently no literature on detailed heat transfer coefficients for the recommended mass fractions of HCFC-22 with HCFC-142b at a condensing temperatures of 60°C or more (condensing pressure of 2.43 MPa) has been published yet. In addition, it seems as if no detailed condensation data exist for the mixture of HCFC-22/HCFC-142b. Meyer et al. [10] published an article on average condensation coefficients at this high condensing temperature but in the annulus of coiled tube-in-tube heat exchangers. Shizuya et al. [11] published an article on heat transfer coefficients but only for a mixture of HCFC-22 with HCFC-142b at a mass fraction of 50 percent HCFC-22 and 50 percent HCFC-142b.

For other refrigerant mixtures, several studies have been performed for condensation inside horizontal plain tubes to obtain quasi-local heat transfer coefficients, i.e., sectional average values over vapor quality changes of about 0.1 like those obtained here. Mochizuki et al. [12] obtained experimental results for three R-113/R-11 mixtures plus those of the two pure components. Dobson et al. [13] reported condensing data for a mixture of 60 percent R-32/40 percent R-125, which is a near azeotropic mix-

Contributed by the Heat Transfer Division for publication in the JOURNAL OF HEAT TRANSFER. Manuscript received by the Heat Transfer Division January 25, 2000; revision April 3, 2002. Associate Editor: S. S. Sadhal.

Table 1 Thermodynamic properties at different mass fractions of HCFC-22/HCFC-142b mixtures at a saturation pressure of 2.43 MPa

Mass fraction HCFC-22 [%]	100	90	80	70	60	50
T_f [°C]	60	63.23	66.64	70.53	74.64	79.10
T_g [°C]	60	65.72	71.07	76.13	80.97	85.64
Temperature glide [°C]	0	2.49	4.43	5.60	6.33	6.54
T_c [°C]	96.15	100.95	105.75	110.35	114.75	119.05
P_c [MPa]	4.990	5.0	4.988	4.954	4.899	4.822
ρ_f [kg/m^3]	1030	1013	995.6	977.7	959.5	940.8
ρ_g [kg/m^3]	111.6	110.8	110.7	111.0	111.8	112.9
μ_f [μPa.s]	107.6	107.2	106.5	105.5	104.2	102.6
μ_g [μPa.s]	14.97	14.94	14.88	14.81	14.73	14.65
i_{fg} [kJ/kg]	139.9	141.3	142.0	141.9	141.2	139.7
c_{Pf} [kJ/kg.K]	1.539	1.548	1.561	1.578	1.598	1.624
c_{Pg} [kJ/kg.K]	1.287	1.287	1.302	1.327	1.358	1.399
k_f [W/m.K]	0.06763	0.06641	0.06516	0.06389	0.06258	0.06125
k_g [W/m.K]	0.01636	0.01708	0.01767	0.01833	0.01904	0.01982
σ [N/m]	0.00351	0.00367	0.00377	0.00382	0.00380	0.00372

ture. Shao and Granryd [14,15] measured condensing heat transfer data for the three-component mixture R-407C and the near azeotropic mixture R-404A and made comparison tests with HCFC-22 and R-502, respectively, for a test facility with 10 consecutive subsections attached in series. For the R-407C comparison with HCFC-22, they found only a minor effect of the mixture at high mass velocities but a significant decrease with respect to HCFC-22 at mass velocities lower than 250 kg/m^{2}s. Uchida et al. [16] measured condensing coefficients for a 30 percent R-32/10 percent R-125/60 percent R-134a mixture. Chitti and Anand [17] reported results for R-32 and R-32/R-125 mixtures. None of these studies compared their data to a prediction method that accounted for mass transfer effects of the mixture. More recently, Thome [18] has presented a state-of-the-art review on the subject of condensation, including condensation of refrigerant mixtures.

The first objective of this work was to determine the heat transfer coefficients of the zeotropic mixture HCFC-22 with HCFC-142b at the following mass fractions: 90 percent/10 percent, 80 percent/20 percent, 70 percent/30 percent, 60 percent/40 percent and 50 percent/50 percent. The heat transfer coefficients are determined at a condensing saturation pressure of 2.43 MPa in smooth straight tubes. At this pressure the dew point temperature for condensation will vary between 60°C (100 percent HCFC-22) and 86°C (50 percent HCFC-22). The second objective was to use the measured heat transfer coefficients in this study to evaluate some of the commonly used local heat transfer methods for intube condensation.

The characteristics of HCFC-22 and the HCFC-22/HCFC-142b mixtures considered are calculated using REFPROP [19] and are given in Table 1.

Test Facility

A test facility was specifically constructed to measure in-tube condensation of pure refrigerants and refrigerant mixtures. The overall test facility is shown in Fig. 1. It was a vapor compression refrigeration and/or heat pump system. The compressor was a hermetically sealed, reciprocating type with a nominal power rating of 10 kW. An oil separator was connected parallel to the compressor with a by-pass line. By manually controlling the flow through the by-pass line and through the oil separator the oil mass fraction in the refrigerant could be controlled. Refrigerant liquid samples were taken downstream of the after-condenser and analyzed for oil mass fraction according to the ANSI/ASHRAE 41.4 [20] standard. For this study, full use was made of the oil separator and only results of oil mass fractions less than 0.01 percent were used.

The test-condenser consisted of eight separate coaxial double-tube condensers in series labeled *A*, *B*, *C*, up to *N*, where $N=8$, as shown in Fig. 1. The inner tube of each test section was a hard-drawn refrigeration copper tube with an inner diameter of 8.11 mm and an outer diameter of 9.53 mm (3/8 inch). The thermal conductivity of the tubes was 339 W/m.K. Spacers were used halfway in each test section to keep the inner tubes from sagging. The heat transfer length of each section was 1603 mm and the distance between pressure drop measuring points 1400 mm. The outer tube was also a hard-drawn copper tube with an inner diameter of 17.27 mm and an outer diameter of 19.05 mm (3/4 in.). Sight-glasses were installed between all the test sections to visually observe the refrigerant flow pattern. All test sections were well insulated with 13 mm of armoflex inside a 50 mm glass wool box to minimize heat leakage. A by-pass line was connected parallel to the test-condenser to control the refrigerant mass flow through the test sections. A water-cooled after-condenser was used to ensure that only liquid refrigerant enters a coriolis mass flow meter, whose accuracy is ±0.1 percent of the reading. The sight-glasses before and after the coriolis flow meter were to ensure that only liquid flows through it. A filter drier followed and then a hand-controlled expansion valve for controlling the evaporating temperature. A water-heated evaporator and a suction accumulator on the low-pressure side complete the refrigerant loop.

Two main water loops were used, one flowing through the condensing side and one flowing through the evaporating side. On the condensing side the water was kept constant at a temperature of 55°C to 85°C (depending on the experiments conducted) in a 1,000 liter insulated storage tank connected to a 15 kW chiller. The water flow rate through the test sections could be controlled with a hand-controlled valve. The flow rate of the water through the test sections was measured with a coriolis mass flowmeter with an error of ±0.2 percent of the reading. A similar flow loop was used on the evaporating side, also with an insulated 1,000 liter storage tank but connected to a 20 kW electric resistance heater. This water was also kept constant at a temperature of 8°C to 30°C, depending on the experiments conducted. By increasing or decreasing the temperature of the water through the evaporator, the refrigerant density at the compressor inlet and thus refrigerant mass flow could also be changed. The water temperatures in both loops could be thermostatically controlled at a constant temperature with an error of ±1°C. As the storage capacities of the two tanks were relatively large, the source and sink temperatures were very stable which helped in quickly obtaining steady state conditions during experiments.

Temperatures were measured with resistance temperature de-

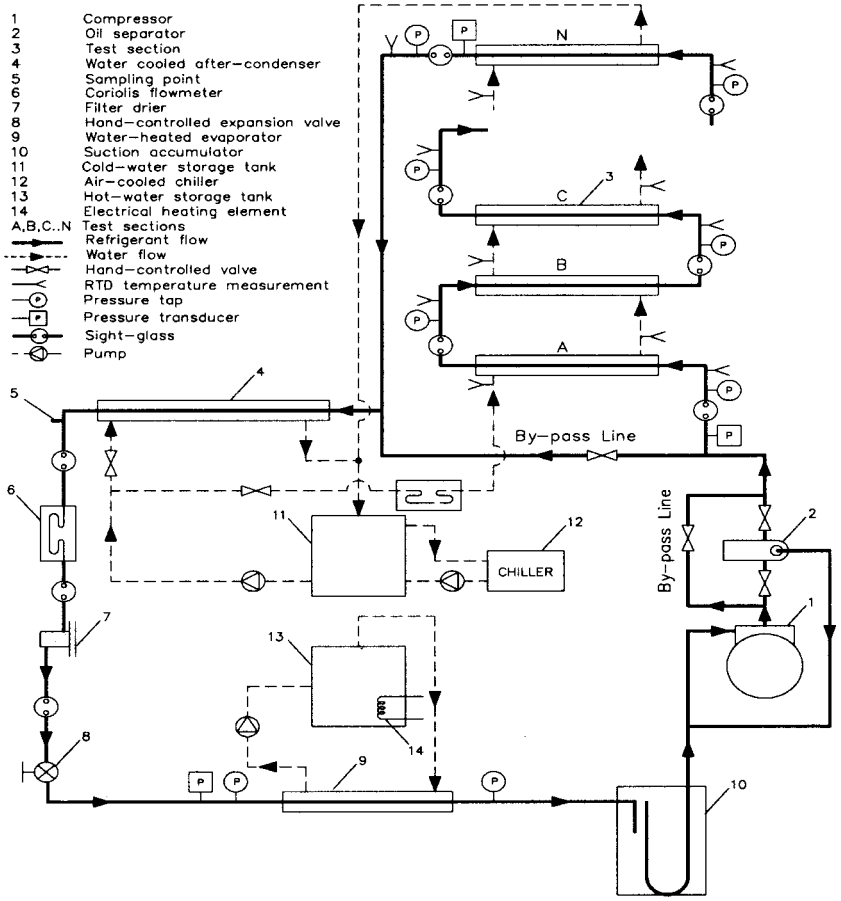

Fig. 1 Schematic of test facility

vices (RTDs) calibrated to measure temperature differences with errors less than ± 0.1°C. Temperatures were measured at the locations shown in Fig. 1. At each of these locations, three RTDs were located at the top, sides and bottom of the tube to take care of any circumferential temperature variation. The average temperature of the three values was used; with the side RTD weighted double, as the average temperature measurement. Absolute pressures on the high-pressure side were measured with a 160 mm dial pressure gauge with a range of 0 to 2,500 kPa. The gauge was calibrated to an error of ± 5 kPa. Pressure drops were measured with a differential pressure transducer with a range of 0 to 60 kPa, calibrated to an error of ± 0.05 percent of the reading. For smaller pressure drops, another differential pressure transducer, connected parallel to the first, was used with a range of 0 to 10 kPa. It was also calibrated to an error ± 0.05 percent of the reading.

Data Reduction

Annulus Heat Transfer Coefficient. Before the test condenser was connected to the experimental set-up shown in Fig. 1, the annulus heat transfer coefficient of each section was determined individually in a water-to-water configuration. The annulus heat transfer coefficient was determined by using the modified Wilson plot technique [21]. For each test section at least 20 data points were used, all with an energy balance error of less than ± 2 percent (the average heat duty between the inside heat duty and outside heat duty was used as the reference). Before the test condenser was connected into the experimental set-up it was dried with high flows of nitrogen and evacuated several times to a pressure of less than 6 Pa. Once connected and charged with HCFC-22, it was operated for 14 days during which time the refrigerant charge and filter drier were changed twice, to eliminate any remaining water moisture in the inner tube from the Wilson plot experiments before the experiments in this study were conducted. The modified Wilson plots gave the leading constants and Reynolds number exponents for the Dittus-Boelter correlation for the test channel annuli allowing the waterside coefficients to be calculated during the condensation tests.

Heat Transfer Coefficient. In each of the eight test sections, the mean sectional condensing heat transfer coefficient is determined for a change in vapor quality of about 0.1, based on the inlet and outlet conditions of the particular section. Assuming no fouling, the heat transfer coefficient for a section is obtained from the definition of the overall heat transfer coefficient:

$$h_i = \frac{1}{\left(\frac{1}{U_o} - \frac{A_o \ln(R_0/R_i)}{2\pi kL} - \frac{1}{h_o}\right)\frac{A_i}{A_o}} \tag{1}$$

where h_o is the waterside coefficient determined from the modified Wilson plot method. The conduction resistance term was taken into consideration in Eq. (1), although the term is very small in comparison with the two convective resistance terms. The overall heat transfer coefficient was calculated from the sensible heat gain of the water and the logarithmic mean temperature difference as follows

$$U_o = \frac{\dot{Q}_w}{A_o \Delta T_{\mathrm{LMTD}}} \tag{2}$$

where

$$\dot{Q}_w = \dot{M}_w c_{pw}(T_{w,\mathrm{out}} - T_{w,\mathrm{in}}) \tag{3}$$

The logarithmic temperature difference from the four terminal temperatures was calculated for the section as

$$\Delta T_{\mathrm{LMTD}}=\frac{(T_{r,\mathrm{in}}-T_{w,\mathrm{out}})-(T_{r,\mathrm{out}}-T_{w,\mathrm{in}})}{\ln[(T_{r,\mathrm{in}}-T_{w,\mathrm{out}})/(T_{r,\mathrm{out}}-T_{w,\mathrm{in}})]} \tag{4}$$

Quality. In the first test section, Q_w was equated to the refrigerant enthalpy change to obtain the outlet enthalpy (which is also the inlet enthalpy for the next test section as it is assumed that no heat losses occur through the insulation, so that

$$h_{\mathrm{out}}=\frac{\dot{Q}_w}{\dot{M}_r}+h_{\mathrm{in}} \tag{5}$$

where h_{in} is the refrigerant inlet enthalpy for the first or second test-section obtained from a refrigerant database [19] using its inlet pressure and temperature as the inlet enthalpy was usually in the superheat region. Usually the outlet of the second test section was in the two-phase region. Then the outlet enthalpy of the second test section was used in Eq. (5) in the place of h_{in}. The inlet and outlet enthalpies of each test section as well as the enthalpies of saturated vapor and liquid were used to determine the inlet and outlet qualities. Hence, the local vapor quality is

$$x=\frac{h-h_f}{h_g-h_f} \tag{6}$$

The average between the inlet and outlet qualities of each test section was used to determine the average refrigerant quality of the test section. For the mixtures, REFPROP [19] was used to calculate the enthalpy change of the particular mixture along the dewpoint temperature curve in the above calculations.

Experimental Uncertainty. A propagation of error analysis [22] was performed to determine the uncertainty in the measured heat transfer coefficients. Using this method, the uncertainty for the heat transfer coefficients was found to range from a low of ± 4 percent at the highest heat flux to a high of ± 20 percent at the lowest heat flux. Uncertainties in the average heat transfer coefficients obtained from the sectional heat transfer coefficients ranged from ± 7 percent to ± 13 percent over the mass flux range investigated.

Experimental Results

Verification of the Experimental Procedure and HCFC-22 Results. To verify the experimental procedure, comparisons were drawn from the literature as shown in Figs. 2 and 3. Figure 2 shows the average heat transfer coefficient (HTC) for HCFC-22. The heat transfer coefficients were integrated along the total length of the condenser using the trapezoidal rule to obtain the integrated average heat transfer coefficient.

Results were obtained over a mass flux range of 58 to 400 kg/m^{2}s at saturation temperatures of 35°C and 40°C. The average inlet quality was 85 percent and the average exiting quality was 10 percent. Over this small increase in saturation temperature from 35°C to 40°C a negligible difference in heat transfer coefficients was found. Also shown are the results obtained by Muzzio et al. [23] at a saturation temperature of 35°C with a similar tube. The average heat transfer coefficients of Muzzio et al. were determined by averaging the subsections of their test section. Results obtained in an 8.0 mm test tube (similar to the 8.11 mm used here) by Eckels and Unruh [24] are also shown at 40°C. They have used a single tube-in-tube test section with a length of 3.66 m and determined the average heat transfer coefficients with Eq. (1). The overall heat transfer coefficient was determined from measurements of the logarithmic mean temperature difference and the heat transfer from the refrigerant to the water in the annulus. The agreement between the average heat transfer coefficients measured by Muzzio et al. [23] and Eckels and Unruh [24] to those recorded during this study is within 7 percent for mass fluxes higher than approximately 150 kg/m^{2}s. At the lowest mass fluxes, the differences are as high as 18 percent. Under the test conditions, the mass flux increased by about 6.9 times, while the heat transfer coefficient only increased by about 2.1 times. Since prediction methods typically utilize $\mathrm{Nu}=f(\mathrm{Re}^{0.8})$, this shows the additional importance of flow regime transition over the mass flux range.

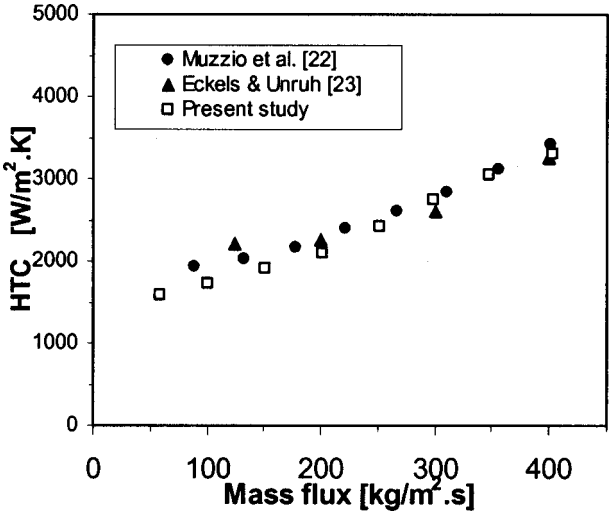

Fig. 2 Comparison to other literature of measured average heat transfer coefficients of HCFC-22 at condensing temperatures of 35°C and 40°C

Figure 3 shows the heat transfer coefficients for condensation at a mass flux of 300 kg/m^{2}s. The results obtained at condensation temperatures of 40°C and 60°C are shown. The results at 40°C were compared to those of Eckels and Unruh [24] (also shown in the plot), which were also obtained at 40°C. The uncertainty for the heat transfer coefficients of Eckels and Unruh ranged between ± 4 percent at the highest heat flux to ± 27 percent at the lowest heat flux. The heat transfer coefficients of the present study were larger than those of Eckels and Unruh [24] by 7 percent on average, with a maximum error of 20 percent at a quality of 80 percent.

It can also be concluded that the heat transfer coefficients are temperature dependent, as the heat transfer coefficients decrease with an increase in temperature from 40°C to 60°C. On average,

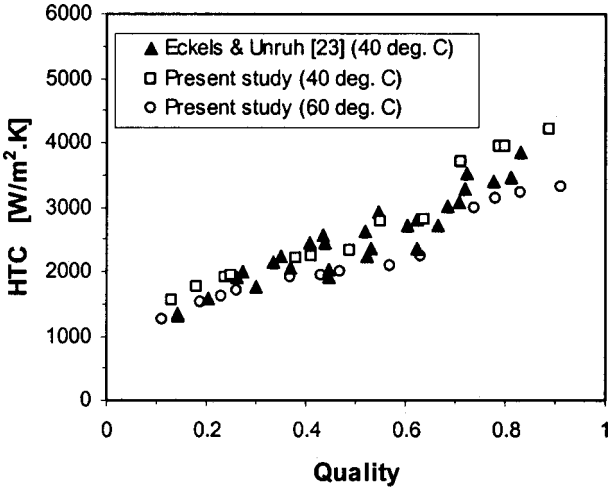

Fig. 3 Comparison of sectional heat transfer coefficients of HCFC-22 at temperatures of 40°C and 60°C at a mass flux of 300 kg/m^{2}s

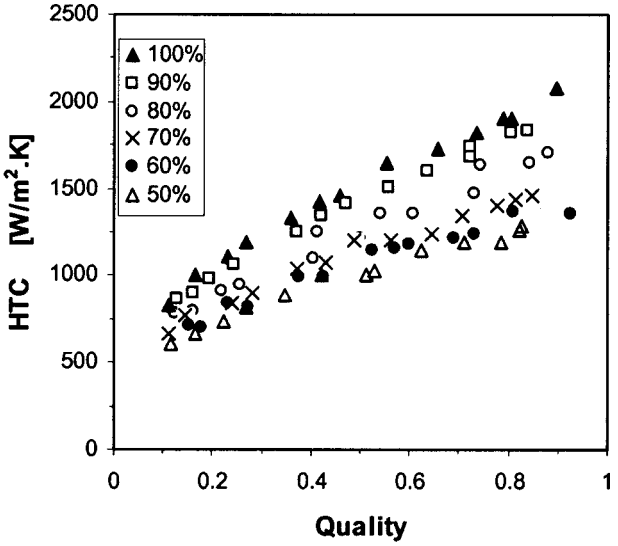

Fig. 4 Heat transfer coefficients at a mass flux of 100 kg/m²s (stratified-wavy flow) at different mass fractions of HCFC-22/HCFC-142b

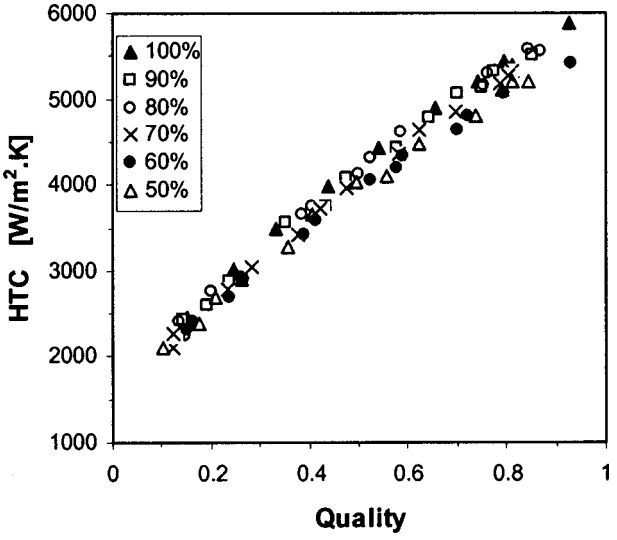

Fig. 6 Heat transfer coefficients at a mass flux of 600 kg/m²s (annular flow) at different mass fractions of HCFC-22/HCFC-142b

the heat transfer coefficients at 60°C are 16 percent lower than those at 40°C. The maximum difference is 25 percent and occurs where the flow regime changes from annular to stratified-wavy. The transition in the flow regime was between quality values of 0.63 and 0.71, based on observations in the sight glasses.

By calculating the Nusselt numbers of the heat transfer coefficients in Fig. 3, the effect of the temperature influence on the liquid thermal conductivity can be taken into consideration, which decreases by 12 percent from 40°C to 60°C. An excellent agreement was found between the Nusselt numbers with an average error of less than 3 percent, and a maximum error of 10 percent. Again, the maximum error occurs where the flow regime changes from annular to stratified-wavy.

Results for HCFC-22/HCFC-142b Mixtures. The results obtained for different mixtures of HCFC-22 with HCFC-142b are shown in Figs. 4 to 7. All the results are for a saturation pressure of 2.43 MPa. The dew and bubble point temperatures at this pressure are given in Table 1. In Figs. 4 to 6, the heat transfer coefficients are given as function of quality and in Fig. 7 the average heat transfer coefficients are given as function of mass flux. In Figs. 4 to 6 the mass fluxes were 100, 300, and 600 kg/m²s. These mass fluxes correspond to the flow regimes observed in the sight glasses between test sections, namely stratified wavy, mixed and annular flow regimes. The results were obtained for different mass fluxes from 100 percent HCFC-22, decreasing in steps of 10 percent to 50 percent/50 percent HCFC-22/HCFC-142b. The general conclusion drawn from Figs. 4 to 6, is that at low mass fluxes (Fig. 4) the heat transfer coefficients are more dependent on the mass fraction of HCFC-22/HCFC-142b, than at higher mass fluxes (Fig. 6).

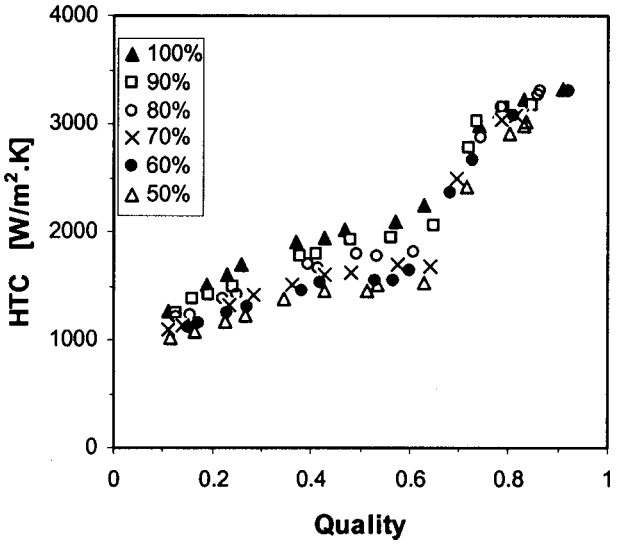

Fig. 5 Heat transfer coefficients at a mass flux of 300 kg/m²s (mixed flow) at different mass fractions of HCFC-22/HCFC-142b

In Fig. 4 the heat transfer coefficients for stratified-wavy flow decreased by 33 percent on average from pure HCFC-22 to 50 percent/50 percent HCFC-22/HCFC-142b. In Fig. 5, the flow regime changes from wavy annular to wavy in the direction of flow. While the flow is annular (quality >0.7), the heat transfer coefficients are not strongly dependent on the refrigerant composition. The decrease in heat transfer coefficients from 100 percent HCFC-22 to 50 percent/50 percent HCFC-22/HCFC-142b is on average approximately 7 percent. However, while in the process of changing from annular to wavy, and while in the wavy flow regime (quality <0.5) the heat transfer coefficients are more dependent on the refrigerant composition. In the wavy regime the heat transfer coefficients decrease on average by approximately 25 percent with respect to pure HCFC-22 for 50 percent/50 percent HCFC-22/HCFC-142b. The estimated change in flow regime from an annular regime to a wavy regime is at qualities between 0.58 to 0.64 for 100 percent HCFC-22 and decreases to between 0.63 and 0.73 for 50 percent/50 percent HCFC-22/HCFC-142b. The general trend is that if HCFC-142b is added to HCFC-22, transition from the annular regime to wavy regime happens sooner as the mass fraction of HCFC-142b increases. The larger adverse effect on heat transfer observed for the mixtures as the lower mass velocities is in line with that expected from the Silver-Bell-Ghaly method (presented in the next section) since the vapor heat transfer coefficient h_g decreases with decreasing flow rate.

At higher mass fluxes (i.e., 500 kg/m²s and more) the flow was visually observed to be predominately annular. The heat transfer coefficients were also not strongly influenced by the refrigerant mass fraction, as can be observed for the mass flux of 600 kg/m²s, shown in Fig. 6. The average decrease in heat transfer coefficients was only 7 percent with respect to pure HCFC-22 for 50 percent/50 percent HCFC-22/HCFC-142b.

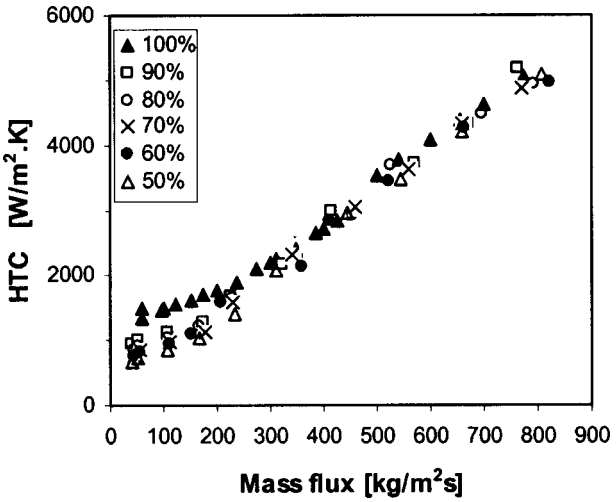

Fig. 7 Average heat transfer coefficients at a condensing temperature of 60°C at different mass fractions of HCFC-22/HCFC-142b

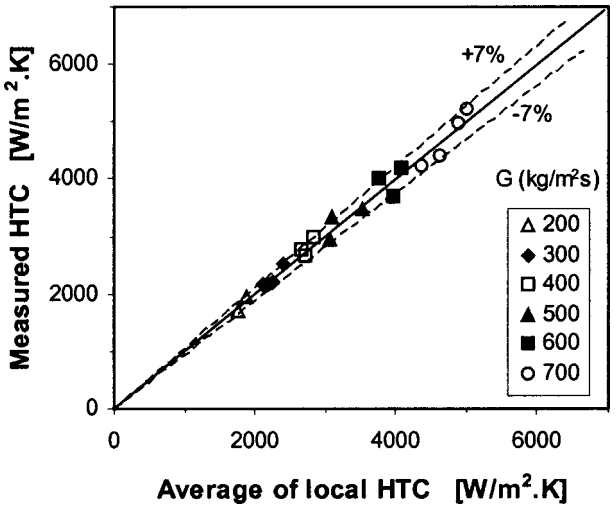

Fig. 8 Comparison of average heat transfer coefficients (measured from LMTD method) with average of heat transfer coefficients for HCFC-22

In Fig. 7 the average heat transfer coefficients are given as a function of mass flux. For each refrigerant mass fraction, heat transfer coefficients were measured at mass fluxes of 40 to 775 kg/m^{2}s at an average saturation pressure of 2.43 MPa. The average inlet quality was 85 percent and the average exiting quality was 10 percent. At mass fluxes from 40 to 350 kg/m^{2}s, the refrigerant mass fraction influences the average heat transfer coefficient by up to 100 percent. The heat transfer coefficients decrease if the mass fraction of HCFC-22 is decreased. At mass fluxes higher than 350 kg/m^{2}s, the heat transfer coefficients are not strongly influenced by mass fraction. Again, as with HCFC-22 at a saturation temperature of 40°C, the results indicate that the average heat transfer coefficients were slightly influenced by mass flux. Under the test conditions, the mass flux increased by about 1,300 percent, while the heat transfer coefficient only increased by about 380 percent. This illustrates the adverse effect of mass transfer on the condensation process together with the influence of flow pattern transition mentioned earlier.

As a final check on the accuracy of the measurement technique, a comparison was made of the average of the heat transfer coefficients for each data set and the measured average heat transfer coefficient determined from Eq. (1). The average of the heat transfer coefficients for the tests are determined with an area weighted average. Figure 8 compares the measured average heat transfer coefficient and the average of the sectional heat transfer coefficients for HCFC-22. The agreement is good as the average error is 4 percent and the maximum error is 7 percent.

Comparison With Correlations

The average and sectional heat transfer coefficients were compared to several leading correlations for in-tube condensation. Comparisons were drawn for both HCFC-22 as well as the mixtures, although the original correlations were developed for only single component refrigerants such as HCFC-22. For the mixtures, the Silver-Bell-Ghaly method [2] was used for the mass transfer correction.

Comparisons for HCFC-22. Figure 9 shows the deviation from the experimental data for average and sectional two-phase heat transfer coefficients that was predicted using the Shah [25] correlation with the experimental data. The Shah correlation is described as

$$\mathrm{Nu} = 0.023\,\mathrm{Re}_L^{0.8}\,\mathrm{Pr}_l^{0.4}\left[(1-x)^{0.8} + \frac{3.8x^{0.76}(1-x)^{0.04}}{p_r^{0.38}}\right] \quad (7)$$

The percentage deviations were calculated as follows:

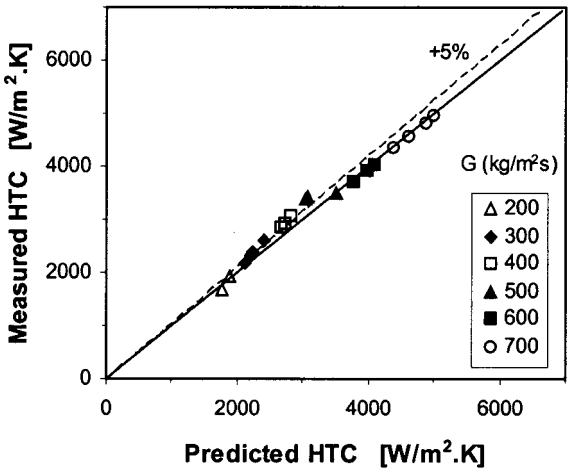

(*a*)

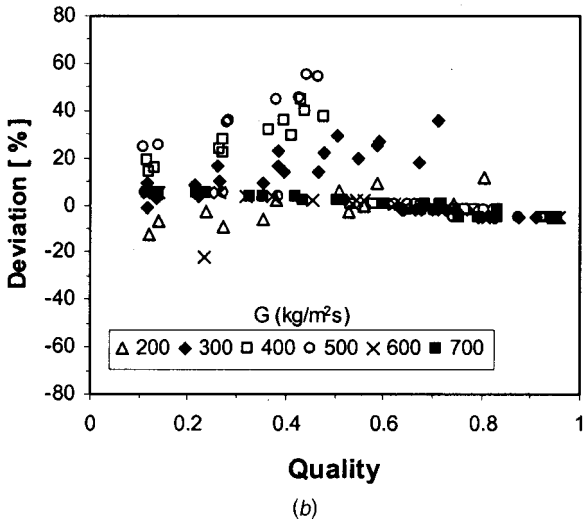

(*b*)

Fig. 9 Deviations for (*a*) average and (*b*) sectional HCFC-22 heat transfer coefficients between measurements and the Shah [25] correlation

$$\text{Deviation} = 100\frac{h_{\text{pred}} - h_{\text{exp}}}{h_{\text{exp}}} \tag{8}$$

and the average deviation was

$$\text{Average deviation} = \frac{\Sigma \text{abs (deviations)}}{\text{number of measurements}} \tag{9}$$

Figure 9(*a*) shows that a good agreement exists between the measurements and the correlation of Shah. The average deviation is 5 percent and the maximum deviation is 11 percent. At the lower mass fluxes, the average heat transfer coefficients are over predicted by the Shah correlation. When the flow regime is predominantly annular, at the higher mass fluxes, the agreement between measurements and the Shah correlation improves.

In Fig. 9(*b*) the deviations between the sectional heat transfer coefficients and the Shah [25] correlation are shown. In general, the deviations increase as the mass flux increase, up to a mass flux of 500 kg/^{2}s. In addition, the heat transfer coefficients show an autocorrelation with quality at these mass fluxes. At higher mass fluxes the deviations are very small. The Shah correlation, over predicts for qualities less than 55 percent and under predicts for the larger qualities. The largest deviations occur at refrigerant qualities less than 70 percent. At higher qualities, the deviations are less than 10 percent. It can therefore be concluded that for a predominantly annular flow regime, the Shah correlation predicts the heat transfer coefficients very well. As the flow regime changes to more wavy in nature, the predictions are less accurate.

In Fig. 10(*a*) the average measured heat transfer coefficients are compared to predictions by Cavallini and Zecchin [26] for their annular flow method, given by

$$\text{Nu} = 0.05\,\text{Re}_{eq}^{0.8}\,\text{Pr}_l^{0.33} \tag{10}$$

The average deviation from the measurements is 10 percent, and the maximum error is 18 percent. In general, all the values are overpredicted, especially at mass fluxes from 300 to 500 kg/m^{2}s.

The sectional deviations from the Cavallini and Zecchin [26] correlation are shown in Fig. 10(*b*). The same tendencies exist as with the Shah correlation, except that the errors are generally larger and the predictions of the heat transfer coefficients are usually higher. In addition, as with the Shah correlation, the predictions are very good at high refrigerant qualities where the flow regime is predominantly annular. Similar comparisons were drawn by Eckels and Unruh [24], except that larger deviations were found at high refrigeration qualities.

The Dobson and Chato [1] equation for annular flow is

$$\text{Nu} = 0.023\,\text{Re}_l^{0.8}\,\text{Pr}_l^{0.4}\left[1 + \frac{2.22}{X_{tt}^{0.89}}\right] \tag{11}$$

and for stratified-wavy flow it is

$$\text{Nu} = \frac{0.23\,\text{Re}_{vo}^{0.12}}{1 + 1.11X_{tt}^{0.58}}\left[\frac{\text{Ga}\,\text{Pr}_l}{\text{Ja}_l}\right]^{0.25} + 0.0195\left(1 - \frac{\theta_l}{\pi}\right)\text{Re}_l^{0.8}\,\text{Pr}_l^{0.4}\left(1.376 + \frac{c_1}{X_{tt}^{c_2}}\right)^{0.5} \tag{12}$$

where for $0 < \text{Fr}_1 \leq 0.7$,

$$c_1 = 4.172 + 5.38\,\text{Fr}_l - 1.564\,\text{Fr}_l^2$$

$$c_2 = 1.773 - 0.169\,\text{Fr}_l$$

For $\text{Fr}_1 > 0.7$,

$$c_1 = 7.242$$

$$c_2 = 1.655$$

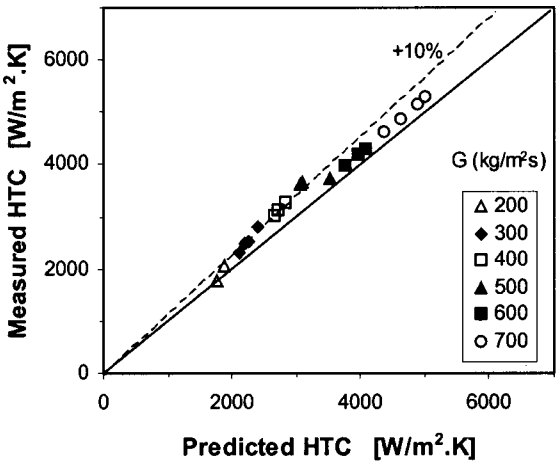

(*a*)

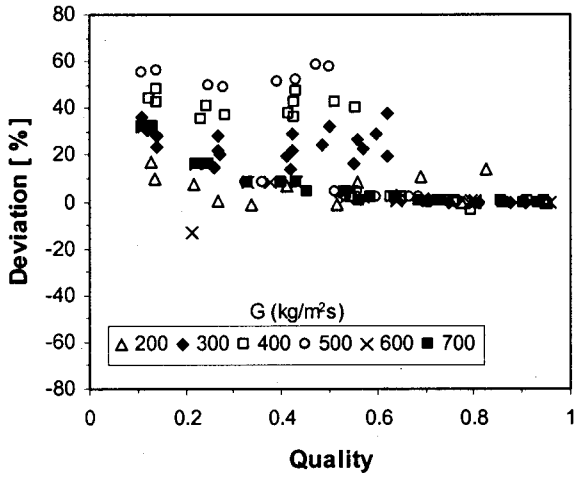

(*b*)

Fig. 10 Deviations for (*a*) average and (*b*) sectional HCFC-22 heat transfer coefficients between measurements and the Cavallini and Zecchin [26] correlation

The angle subtended from the top of the tube to the stratified liquid in stratified-weavy flow, θ_l, is determined from the following simplified equation of Jaster and Kosky [27], using the Zivi [28] void fraction equation for α:

$$\theta_l = \pi\left(1 - \frac{\arccos(2\alpha - 1)}{\pi}\right) \tag{13}$$

Due to the 1.376 inside the radical of Eq. (12), the correlation above matches the Dittus-Boelter single-phase correlation when $x = 0$.

The comparison of average measurements with predictions made by the correlation of Dobson and Chato [1] is shown in Fig. 11(*a*). The average deviation is 5 percent, and the maximum deviation is 8 percent. In general the correlation of Dobson and Chato predicted the average heat transfer coefficients better than the correlations of Shah [25] and Cavallini and Zecchin [26].

Figure 11(*b*) shows that the Dobson and Chato [1] correlation predicts the heat transfer coefficients better than the Shah [25] correlation and the Cavallini and Zecchin [26] correlation. All the deviations are within ±20 percent. Approximately the same number of coefficients is overpredicted as underpredicted. In addition, the deviations are not influenced by quality or mass flux. Hence, the method seems to rightly capture the effect of flow pattern transition.

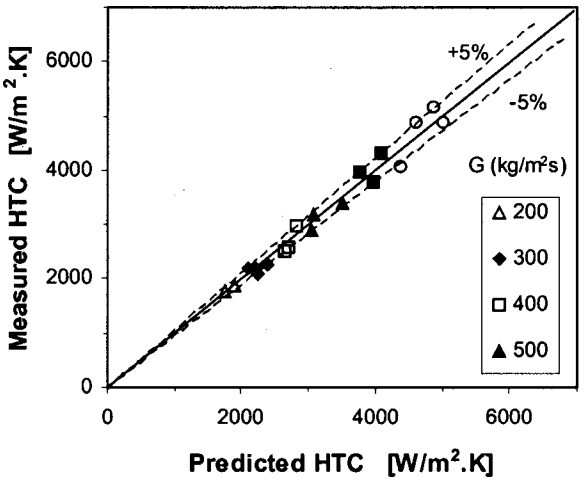

(*a*)

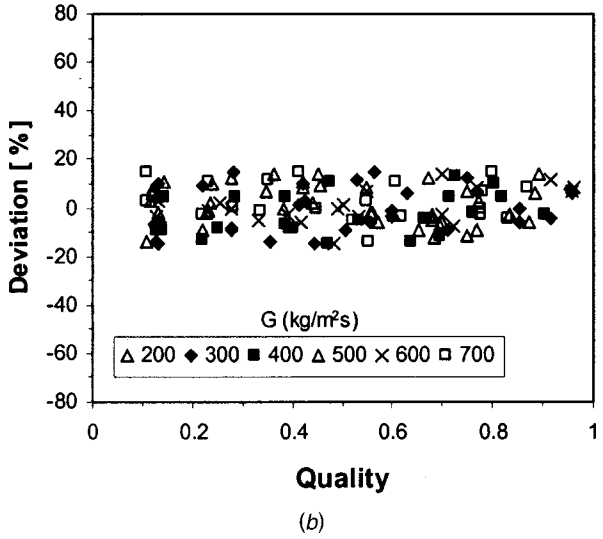

(*b*)

Fig. 11 Deviations for (*a*) average and (*b*) sectional HCFC-22 heat transfer coefficients between measurements and the Dobson and Chato [1] correlation

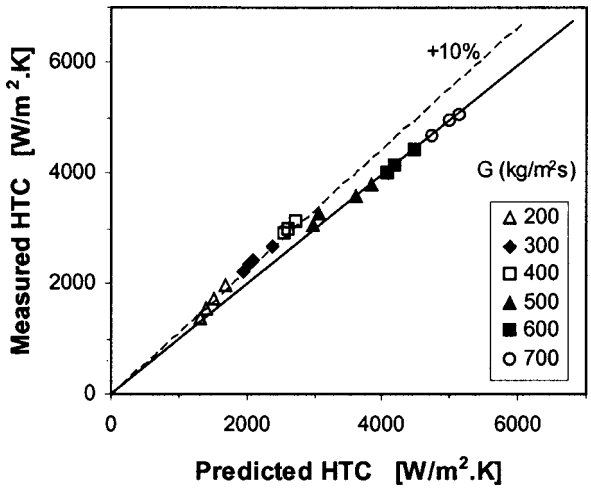

(*a*)

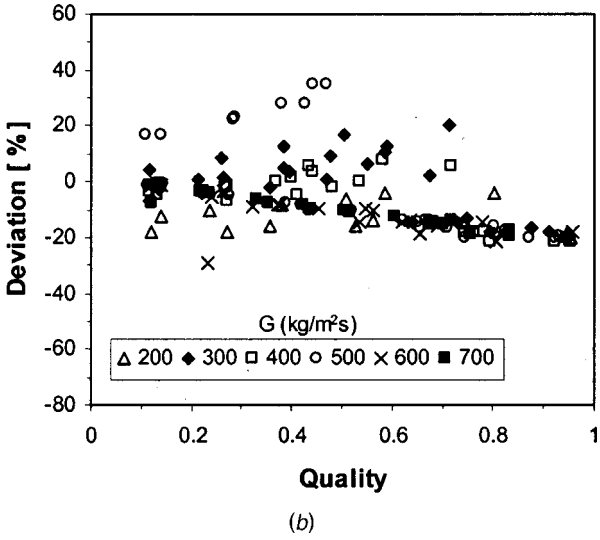

(*b*)

Fig. 12 Deviations for (*a*) average and (*b*) sectional HCFC-22/HCFC-142b (70 percent/30 percent by wt.) heat transfer coefficients and the Shah [25] correlation with Silver-Bell-Ghaly correction [2]

Comparisons for HCFC-22/HCFC-142b Mixtures. Only the results at a mass fraction of 70 percent/30 percent are shown in Figs. 12 to 14 as it is representative of all the mixtures considered. The Silver-Bell-Ghaly correction method [2] used is as follows:

$$\frac{1}{h_{\text{eff}}} = \frac{1}{h} + \frac{Z_g}{h_g} \tag{14}$$

The condensation heat transfer coefficient h was obtained from the relevant correlations in Equations (7), (10), (11), or (12) and h_g is the vapor heat transfer coefficient calculated from the Dittus-Boelter turbulent flow correlation using the vapor fraction of the flow in calculating the vapor Reynolds number. The parameter Z_g is the ratio of the sensible cooling of the vapor to the total cooling rate, which can be written as

$$Z_g = x c_{pg} \frac{dT_{\text{dew}}}{dh} \tag{15}$$

dT_{dew}/dh is the slope of the dew point temperature curve with respect to the enthalpy of the mixture as it condenses as obtained from REFPROP [19].

From the average heat transfer coefficients considered in Figs. 12(*a*), 13(*a*), and 14(*a*), it can be observed that the tendencies are the same as those of pure HCFC-22. The only difference is that the errors for the mixture between measurements and predictions increased by approximately 5 percent from those for pure HCFC-22. Most of the predictions are higher than the measurements. In addition, the correlation of Dobson and Chato [1] gave the best results, followed by the correlation of Shah [25] and then the correlation of Cavallini and Zecchin [26].

The same conclusion can also be drawn for the sectional heat transfer coefficients (Figs. 12(*b*), 13(*b*), and 14(*b*)). There is thus a good agreement between the tendencies of pure HCFC-22 (Figs. 9(*a*), 10(*a*), and 12(*a*)) and the mixtures of HCFC-22/HCFC-142b (Figs. 12(*b*), 13(*b*), and 14(*b*)). Where all the deviations for pure HCFC-22 were in a −20 percent to +60 percent band, the deviation band just shifted by +40 percent for the Shah [25] correlation (Fig. 12(*b*)) and by +60 percent for the Cavallini and Zecchin [26] correlation (Fig. 13(*b*)). The deviations from the Dobson and Chato correlation in Fig. 14(*b*) show that all the deviations are scattered within −30 percent to +20 percent. For pure HCFC-22 these were within ±20 percent.

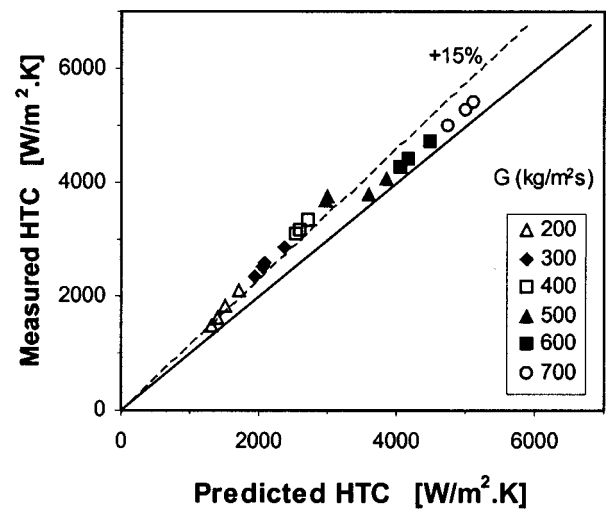

(*a*)

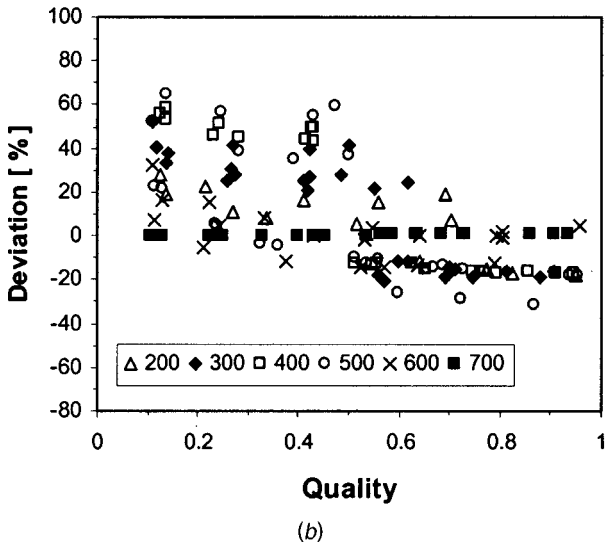

(*b*)

Fig. 13 Deviations for (*a*) average and (*b*) sectional HCFC-22/HCFC-142b (70 percent/30 percent by wt.) heat transfer coefficients and the Cavallini and Zecchin [26] correlation with Silver-Bell-Ghaly correction [2]

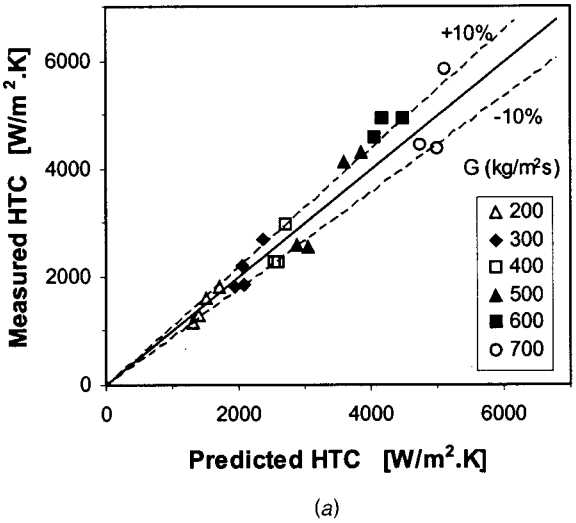

(*a*)

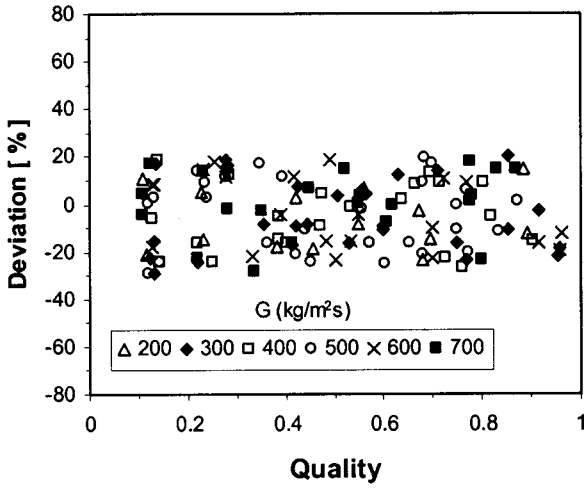

(*b*)

Fig. 14 Deviations for (*a*) average and (*b*) sectional HCFC-22/HCFC-142b (70 percent/30 percent by wt.) heat transfer coefficients and the Dobson and Chato [1] correlation with Silver-Bell-Ghaly correction [2]

It can therefore be concluded that correlations developed for pure refrigerants can also be used for the zeotropic refrigerant mixtures considered in this study taking into account the mass transfer effect with the Silver-Bell-Ghaly method. As with HCFC-22, the average heat transfer coefficients of the HCFC-22/HCFC-142b mixtures can be predicted better than the sectional heat transfer coefficients as function of quality. In addition, the deviations between measurements and predictions for HCFC-22 are smaller than those for the zeotropic refrigerant mixtures considered, as can be expected since the Silver-Bell-Ghaly method ignores the effect of interfacial roughness on the value of h_g.

Conclusion

This paper presents two-phase heat transfer coefficients for condensation of HCFC-22 and five mixtures of HCFC-22/HCFC-142b from 90 percent/10 percent to 50 percent/50 percent. Heat transfer coefficients were determined in an 8.11 mm inner diameter, horizontal smooth tube.

Heat transfer coefficients for HCFC-22 and the different mass fractions of HCFC-22/HCFC-142b as functions of quality were measured over a mass flux range of 40 kg/m^{2}s to 800 kg/m^{2}s. At each mass flux, heat transfer coefficients were determined over the full range of qualities. It was found in general that the heat transfer coefficients decreased as the mass fraction of HCFC-142b was increased. At low mass fluxes, between 40 kg/m^{2}s and 350 kg/m^{2}s, the flow regime was observed to be predominately wavy. In this regime the average heat transfer coefficient decreased by up to a third from pure HCFC-22 to 50 percent/50 percent HCFC-22/HCFC-142b. At high mass fluxes, of 350 kg/m^{2}s and more, the flow regime was predominately annular and the heat transfer coefficients decreased only by approximately 7 percent when the HCFC-142b mass fraction was increased to 50 percent.

Three correlations were compared to the heat transfer coefficients measured. It was found that the average heat transfer coefficients could be predicted better than the heat transfer coefficients as a function of quality. For all heat transfer coefficients, it was found that the Dobson and Chato [1] correlation gave the best agreement between measurements and predictions. This correlation was followed by the Shah [25] correlation and then by the Cavallini and Zecchin [26] correlation.

It has also been demonstrated that the Silver-Bell-Ghaly [2] correction method works well over a broad range of mass veloci-

ties from 200 kg/m^2·s to 700 kg/m^2·s, which covers the annular and stratified wavy flow regimes based on sight glass observations.

Nomenclature

Fr_l = liquid Froude number, $G^2/\rho_l^2 gD$
G = mass flux
Ga = Galileo number, $g\rho_1(\rho_l-\rho_g)D^3/\mu_l^2$
Ja_l = liquid Jacob number, $c_{pl}(T_{\mathrm{sat}}-T_s)/h_{fg}$
p_r = reduced pressure
Pr_l = liquid Prandtl number, $c_{pl}\mu_l/k_l$
Re_{eq} = equivalent Reynolds number, $\mathrm{Re}_v(\mu_v/\mu_l)(\rho_l/\rho_v)^{0.5}+GD(1-x)/\mu_l$
Re_L = Reynolds number assuming all mass flowing as liquid, GD/μ_l
Re_l = superficial liquid Reynolds number, $GD(1-x)/\mu_l$
Re_v = superficial vapor Reynolds number, GDx/μ_v
Re_{vo} = vapor only Reynolds number, GD/μ_g
T_f = bubble point temperature
T_g = dew point temperature
U = overall heat transfer coefficient
X_{tt} = Lockhart Martinelli parameter, $(\rho_g/\rho_l)^{0.5}(\mu_l/\mu_g)^{0.1}((1-x)/x)^{0.9}$
α = void fraction
θ_1 = angle subtended from the top of the tube to the liquid level

Subscripts

c = critical
exp = experimental
i = inner or in-tube
LMTD = logarithmic mean temperature difference
o = outer or annulus side
out = outlet of test section
pred = predicted
r = refrigerant
s = surface
sat = saturation
w = water

References

[1] Dobson, M. K., and Chato, J. C., 1998, "Condensation in Smooth Horizontal Tubes," ASME J. Heat Transfer, **120**, pp. 193–213.
[2] Silver, R. S., 1964, "An Approach to a General Theory of Surface Condensers," Proc. Inst. Mech. Eng., Part 1, **179**(14), pp. 339–376.
[3] Meyer, J. P., and Greyvenstein, G. P., 1991, "Hot Water for Homes in South Africa," Energy—The International Journal, **16**(7), pp. 1039–1044.
[4] Meyer, J. P., and Greyvenstein, G. P., 1992, "Hot Water for Large Residential Units, Hospitals and Laundries with Heat Pumps in South Africa: A Techno-economic Analysis," Energy Convers. Manage., **33**(2), pp. 135–143.
[5] Smit, F. J., and Meyer, J. P., 1998, "Investigation of the Potential Effect of Zeotropic Refrigerant Mixture on Performance of a Hot-Water Heat Pump," ASHRAE Trans., **104**, (Part 1A), pp. 387–394.
[6] Johannsen, A. F. B., 1992, "Potential of Non-Azeotropic Refrigerant Mixtures for Water-Heating Heat Pumps in South Africa," Department of Mineral and Energy Affairs, Report no. ED 8807, Pretoria, South Africa.
[7] Smit, F. J., 1996, "The Influence of a Non-Azeotropic Refrigerant Mixture on the Performance of a Hot-Water Heat Pump," M.Eng dissertation, Rand Afrikaans University, Johannesburg, South Africa.
[8] Kebonte, S. A., 1999, "Condensation Heat Transfer and Pressure Drop Coefficients of R22/R142b in a Water Cooled Helically Coiled Tube-in-Tube Heat Exchanger," M.Eng. dissertation, Rand Afrikaans University, Johannesburg, South Africa.
[9] Bukasa, J. M., 1999, "Average Boiling Heat Transfer and Pressure Drop Coefficients of R22/R142b in a Helically Coiled Water Heated Tube-in-Tube Heat Exchanger," M.Eng. dissertation, Rand Afrikaans University, Johannesburg, South Africa.
[10] Meyer, J. P., Bukasa, J. M., and Kebonte, S. A., 2000, "Average Boiling and Condensation Heat Transfer Coefficients of the Zeotropic Refrigerant Mixture R22/R142b in a Coaxial Tube-in-Tube Heat Exchanger," ASME J. Heat Transfer, **122**(1), pp. 186–188.
[11] Shizuya, M., Itoh, M., and Hijikata, K., 1995, "Condensation of Nonazeotropic Binary Refrigerant Mixtures Including HCFC-22 as a More Volatile Component Inside a Horizontal Tube," ASME J. Heat Transfer, **117**, pp. 538–543.
[12] Mochizuki, S., Inoue, T., and Tominaga, M., 1990, "Condensation Heat Transfer of Nonazeotropic Binary Mixtures (R113+R11) in a Horizontal Tube," Heat Transfer-Jpn. Res., **19**(2), pp. 13–24.
[13] Dobson, M. K., et al., 1994, "Heat Transfer and Flow Regimes During Condensation in Horizontal Tubes," ACRC Report TR-57, University of Illinois, Champaign-Urbana.
[14] Shao, W., and Granryd, E., 1995, "An Investigation of Flow Condensation of R22 and R407C in a Horizontal Smooth Tube," *Proc. 19th Int. Congr. of Refrig.*, The Hague, **4a**, pp. 527–534.
[15] Shao, W., and Granryd, E., 1995, "An Experimental Comparison of R502 and R404A in a Condensing Tube," *Heat Transfer in Condensation*, Eurotherm Seminar 47, Paris, Oct. 4–5, pp. 125–131.
[16] Uchida, M., Itoh, M., Shikazano, N., and Kudoh, M., 1996, "Experimental Study of the Heat Transfer Performance of a Zeotropic Refrigerant Mixture in Horizontal Tubes," *Proc. 1996 Int. Refrig Conf. at Purdue*, July 23–26, West Lafayette, IN, pp. 133–138.
[17] Chitti, M. S., and Anand, N. K., 1996, "Condensation Heat Transfer Inside Smooth Horizontal Tubes for R-22 and R-32/R-125 Mixtures," International Journal of HVAC&R Research, **2**, pp. 79–101.
[18] Thome, J. R., 1998, "Condensation of Fluorocarbon and Other Refrigerants: A State-of-the-Art Review," Air-Conditioning and Refrigeration Institute (ARI) Report, Arlington, VA, October, Chap. 8.
[19] NIST, 1998, NIST Thermodynamic and Transport Properties of Refrigerants and Refrigerant Mixtures Database, (REFPROP Ver. 6.01), National Institute of Standards and Technology, Gaithersburg, MD.
[20] ANSI/ASHRAE 1996, "Standard Method for Measurement of Proportion of Lubricant in Liquid Refrigerant," ASHRAE STANDARD 41.4, American Society of Heating, Refrigerating and Air-Conditioning Engineers, Atlanta, GA.
[21] Briggs, D., and Young, E., 1969, "Modified Wilson Plot Technique for Obtaining Heat Transfer Correlations for Shell and Tube Heat Exchangers," Chem. Eng. Prog., Symp. Ser., **65**(2), pp. 35–45.
[22] Kline, S., and McClintock, F., 1953, "Describing Uncertainties in Single-Sample Experiments," Mech. Eng. (Am. Soc. Mech. Eng.), **75**, pp. 3–8.
[23] Muzzio, A., Niro, A., and Arosio, S., 1998, "Heat Transfer and Pressure Drop during Evaporation and Condensation of HCFC-22 inside 9.52-mm O.D. Microfin Tubes at Different Geometries," Enhanced Heat Transfer, **5**, pp. 39–52.
[24] Eckels, S. J., and Unruh, B. J., 1999, "Local Heat Transfer Coefficients During Condensation of HCFC-22 and R-32/R-125 Mixtures," HVAC&R Research, **5**(1), pp. 59–76.
[25] Shah, M. M., 1979, "A General Correlation for Heat Transfer During Film Condensation Inside Tubes," Int. J. Heat Mass Transf., **22**, pp. 547–556.
[26] Cavallini, A., and Zecchin, R., 1974, "A Dimensionless Correlation for Heat Transfer in Forced Convection Condensation," *5th International Heat Transfer Conference*, Tokyo, **2**, pp. 309–313.
[27] Jaster, H., and Kosky, P. G., 1976, "Condensation in a Mixed Flow Regime," Int. J. Heat Mass Transf., **19**, pp. 95–99.
[28] Zivi, S. M., 1964, "Estimation of Steady-State Steam Void-Fraction by Means of the Principle of Minimum Entropy Production," ASME J. Heat Transfer, **86**, pp. 247–252.

Ice Block Melting Into a Binary Solution: Coupling of the Interfacial Equilibrium and the Flow Structures

Sophie Mergui
e-mail: mergui@fast.u-psud.fr

Sandrine Geoffroy

Christine Bénard

FAST-UMR CNRS 7608
(Universities Paris VI and Paris XI),
Campus Universitaire-Bâtiment 502,
91405 Orsay Cedex, France

Melting of a vertical ice block in a cavity filled with an aqueous solution is studied experimentally. Local interfacial temperatures and front velocities are measured allowing for a quantitative study of the coupling of the fluid motion, thermal equilibrium and the local heat transfers at the melting front. It is found that the front equilibrium shift is correlated to the classical parameter of the phase change process, that is the Stefan number, while the local heat transfer at the interface is correlated to the parameters characterizing thermosolutal natural convection. Quantitative results about the time evolution of the double-diffusive multi-layers structure in the fluid phase are obtained. The formation of the first thermosolutal layer is analyzed with the help of numerical simulations. It is found that the mechanism responsible for the onset of this layer is due to a well known double-diffusive instability. [DOI: 10.1115/1.1513572]

Keywords: Double Diffusion, Experimental, Heat Transfer, Melting, Natural Convection

1 Introduction

Thermosolutal natural convection plays an important role in controlling the kinetics of solid-liquid phase-change in mixtures [1–2]. Indeed the velocity and the local equilibrium of the solid-liquid interface are strongly coupled to the interface heat and mass transfer due to thermosolutal convection, through the interface balance equations. In solidification processes, the time evolution of this coupling is a main issue which governs the front velocity and the macro and micro segregation effects and then the homogeneity of the solid [3–8].

A large number of experimental or numerical studies has been devoted to double-diffusive convection associated with melting or solidification. In the case of solidification, the existence of a mushy zone at the solid/liquid interface is a specific problem that will not be considered here. In the context of melting, a series of fundamental experimental and theoretical studies is concerned with the buoyancy-induced flows driven by combined thermal and solute transport near a vertical melting ice surface in saline water [9–12]. For melting in cavity [13–21], an analytical and experimental study has been performed [13] focused upon the different modes of double-diffusive convection arising from a horizontal melting interface. In that configuration, a quantitative model and scaling analyses of melting or dissolving driven by compositional convection has been developed [14–16]. When the phase change interface is vertical, multicellular flow structures arise in the cavity, that strongly affect the melting rate [17–21]. In this configuration, the experimental studies are mainly qualitative. No quantitative measurements are available concerning the transport processes at the interface, except in [20] where the average heat transfer along the melting front is evaluated.

In the previous works, the coupling of double diffusive convection and the local interface equilibrium shift has not been analyzed. Neither has the time evolution of the flow structure been investigated.

In the configuration under study a block of pure ice is melted into an aqueous solution of sodium carbonate (Fig. 1). The initial state is out of equilibrium: the vertical block of pure ice is in thermal equilibrium with the aqueous solution (just a few hundredth of a degree below zero Celsius), but mass transfer is impeded by a thin metal sheet located at the interface. At the beginning of the experiment, the metal sheet is removed and the temperature of the opposite wall is raised. A thermal cell is very quickly generated in the solution which produces a downward thermal buoyancy force in the neighborhood of the front. Heat is transferred to the interface, which starts melting (Fig. 1(*b*)). An upward solutal buoyancy force, due to the melt of pure ice, is created along the front. The thermal and solutal forces are opposing (negative buoyancy number N) giving birth to an important shear close to the front. The upward solutal force being stronger than the thermal downward force ($8 \leqslant |N| \leqslant 172$ in our experiments), it removes part of the liquid from the thermal cell, and fills up an upper zone on top of the thermal cell, with a weak concentration mixture (Fig. 1(*c*)). For this reason, the thermal cell height would decrease regularly while a quiet upper zone would grow, until destabilization of this zone. In all our experiments, destabilization takes place at the bottom of the upper stagnant zone where a first vortex appears, closely followed by several others, at the same horizontal level; those vortices will finally merge to create a wide rotating cell (Fig. 1(*d*) and (*e*)). Depending on the parameters, this destabilization sequence would happen several times, beginning always at the bottom of the quiet zone on top of the cells.

The purpose of this study is to understand the phenomena ruling these flow structures and their time behavior. Three phenomena play a leading role: shift of the local temperature and concentration equilibrium at the front (Part 3); growth of the upper mixing zone (Part 4); destabilization of the upper mixing zone (Part 5). Preliminary results about the front average heat exchange and velocity have been obtained in a previous work [20], based on a first set of experiments with the same aqueous solution and a similar geometrical configuration. The interpretation of the experimental results in [20] relies on the boundary layer analysis for thermosolutal natural convection along a fixed vertical plate performed by A. Bejan [22], where *known* temperature and concentration are imposed on the *fixed* vertical wall. In the absence of

Contributed by the Heat Transfer Division for publication in the JOURNAL OF HEAT TRANSFER. Manuscript received by the Heat Transfer Division July 10, 2001; revision received May 6, 2002. Associate Editor: B. T. F. Chung.

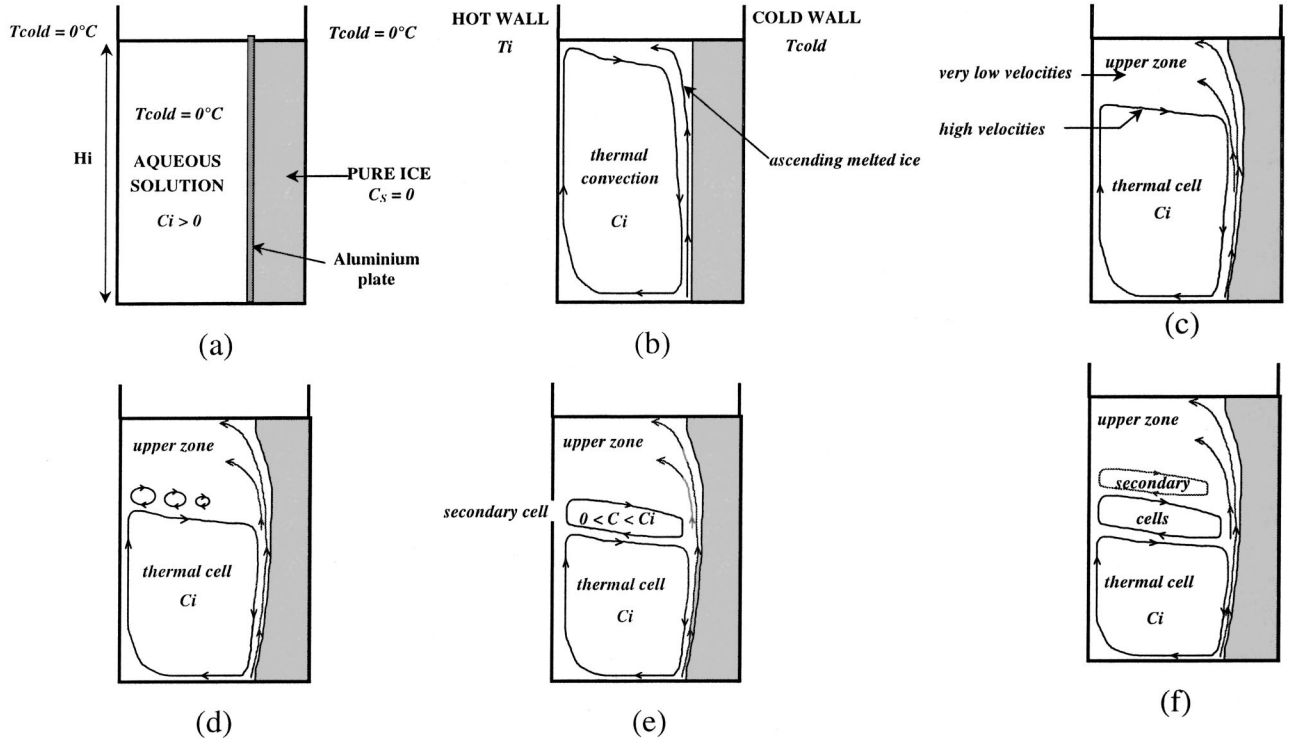

Fig. 1 Development of the structure of the fluid phase: (*a*) initial state; (*b*) build up of the thermal cell and development of an ascending solutal layer along the ice front; (*c*) growth of the upper low velocity and low concentration zone filled up by the ascending flow along the ice front. The thermal cell remains at the initial concentration and its temperature field is vertically stratified; (*d*) destabilization of the bottom part of the upper zone through a succession of corotating vortices; (*e*) the growing vortices merge into a wide horizontal rotating layer; and (*f*) the same destabilization process is reproduced several times.

measurements of the interface temperatures, it was admitted in [20] that the equilibrium temperature and concentration at the phase-change interface were such that $T_L \approx 0°C$ and $C_L \approx 0$, an hypothesis that corresponds to the limit of high velocity melting. Thus in the liquid, the thickness of the strongly varying temperature, concentration and velocity layers close to the melting interface were supposed scale by the dimensionless parameters given by the *fixed* wall boundary layer analysis, for dominant solutal force. Moreover, the specific problem set by the negative buoyancy ratio N, which creates a local zone of very strong shear stress, was not considered in [20].

In the present paper, accurate local temperature measurements at the melting front allow to estimate the local shift of the front equilibrium ($T_L \neq 0$, $C_L \neq 0$), at different heights of the convective cell and in the top stagnant mixing zone. It is shown in Part 3, that this local shift of the front equilibrium can be related to the dimensionless local heat and mass exchanges. The latter are shown to be proportional and to both depend on the solutal Rayleigh number Ra_S, confirming the partial result already found for the average Nusselt in [20], and putting forward a dimensionless characteristic melting time t_m. The study of the growth of the upper zone (Part 4) shows that, in the range of parameters scanned in our experiments, the flow structure and the kinetics of a melting process governed by double diffusive convection are globally controlled by two groups of dimensionless parameters: the melting time t_m and the filling time t_C. At a given dimensionless time t_m, the relative melted volumes are about the same for all experiments but the advancement of the upper zone filling process is not the same because t_C is not the same (Fig. 2). Finally, in Part 5, we show that the destabilization of the upper mixing zone is due to a known double diffusive instability [23], with no observable role of the shear stress imposed by the thermal cell to the lower part of the mixing zone. The localization of the destabilizing vortices at the bottom of the upper zone is explained by the weakness of the local concentration gradient, the dimensionless expression of which is analyzed in relation with the results of [23]. The double time scaling established in Part 4 and the role of N on the stability

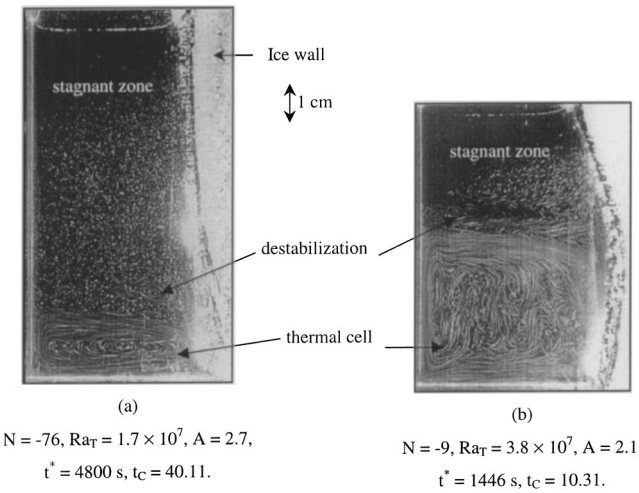

Fig. 2 Position and shape of the ice front are shown for two experiments at a same melting characteristic time, $t_m = 0.63$. The measured relative melted volumes are the same in both cases. These photographs show the weak velocity upper zone and the high velocity thermal cell (exposure time ≈20 s). The relative volumes of the upper zone are very different in both cases because the filling characteristic times t_C are very different. Destabilization takes place at the cold side (case (*a*)) or at the hot side (case (*b*)).

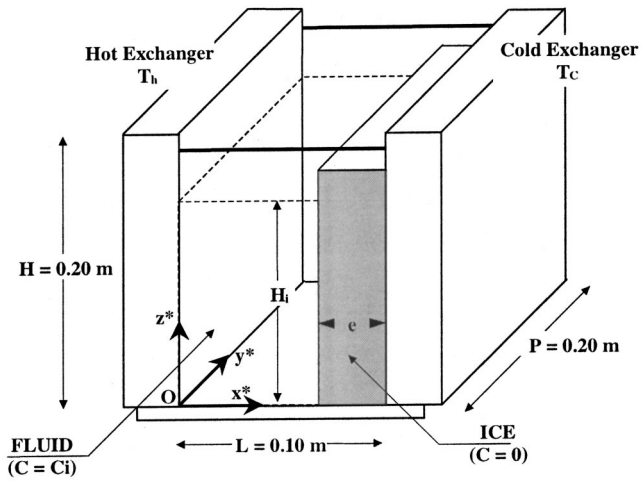

Fig. 3 Sketch of the experimental cell

of the mixing zone (Part 5) are the clues for understanding the different flow structures that can be observed according to the parameter values.

2 Presentation of the Experiments

2.1 Experimental Setup. The experimental setup is similar to the device presented in [20]. Nevertheless, important improvements have been made to closely control initial and boundary conditions and to avoid disturbances during destabilization of the upper zone. Moreover, the flow visualizations technique has been improved to allow for an accurate observation of the melting front position and of the destabilization process.

The new experimental cell (Fig. 3) consists of a rectangular cavity (height $H=0.20$ m, width $L=0.10$ m, depth $P=0.20$ m) designed to generate a two-dimensional flow. The two facing vertical walls are copper heat exchangers differentially heated at constant and uniform temperatures controlled by two independent thermal loops where a water-glycol mixture is circulated. Temperature measurements are performed using NiCr-NiAl thermocouples embedded at the inlets and outlets of each exchanger and at six locations in the exchanger walls. In all experiments, the wall temperatures of each exchanger are uniform to within 0.2 C. The vertical front and back walls as well as the horizontal bottom wall are made of 1 cm thick transparent glass sheets for flow observation. Due to volume variations, a free surface condition must be allowed at the insulated top of the cell. In order to reduce the heat losses through the passive walls and to approach adiabatic conditions on those walls, the cell is inside a temperature-controlled enclosure maintained at about 0°C.

According to previous works concerning the study of high Lewis number double diffusive convection and phase change in binary mixtures, a hypoeutectic aqueous solution of sodium carbonate (Na_2CO_3-H_2O) is used in our experiments. This liquid mixture is easy to handle and the dependence of its thermophysical parameters upon temperature and concentration is well known ([20]). The eutectic temperature, T_E, is -2.1°C and the eutectic concentration, C_E, is 5.93 wt percent [24]. The liquidus curve of the equilibrium phase diagram is well approximated by a linear relationship with a slope of -0.357°C/wt percent and the segregation coefficient is equal to zero (C_s, the concentration in the solid phase is zero). The pure ice block is carefully prepared from degasified distilled water.

Visualizations are performed by laser tomography with a thin vertical light sheet located at about 0.06 m from the front wall of the enclosure and perpendicular to the active walls. The flow structure is visualized either by fluorescein streaks that originate from fluorescein spots in the ice when reached by the melting front or by polycrystalline particles (diameter ≈ 30 μm, density ≈ 1 kg/m^3) added to the solution. For all the experiments, the development of the flow structure in the liquid phase is carefully observed as well as the time evolution of the front position, allowing for the determination of the average and local melting rate. Ice temperature measurements are performed with thin NiCr-NiAl thermocouples (accuracy ± 0.1°C) that have been embedded in several spots in the ice block during its preparation. Those measurements, coupled with local accurate observations of the moving interface (accuracy ± 0.2 mm), allow for the determination of instantaneous values of the local interface temperature.

The experimental procedure, illustrated in Fig. 1, has already been described in the introduction. Three stages are observed during the time evolution of the melting process. First, a short transient regime allows for the thermal cell and the boundary layers to build up. Then, a quasi-permanent regime is characterized by a constant average front velocity [20]. A final stage starts when the average front velocity weakens, fusion slowly decaying to the advantage of dissolution. The present analysis is mainly concerned with the quasi-permanent regime, presented in Parts 3 and 4 for the corresponding lapse of time in each experiment.

2.2 Characteristic Dimensionless Parameters. In the liquid bulk, the flow is assumed to be laminar, incompressible, two-dimensional and the Boussinesq approximation is used. Thus, the governing equations can be written in dimensionless form as:

$$\nabla \cdot \vec{v} = 0 \tag{2.1}$$

$$\frac{\partial \vec{v}}{\partial \tau} + (\vec{v}\cdot\nabla)\vec{v} = \mathrm{Pr}\ \nabla^2\vec{v} - \nabla\ \mathrm{P} + \mathrm{Ra_T}\ \mathrm{Pr}(\theta + N\phi)\vec{k} \tag{2.2}$$

$$\frac{\partial \theta}{\partial \tau} + \vec{v}\cdot\nabla\theta = \Delta\theta \tag{2.3}$$

$$\frac{\partial \phi}{\partial \tau} + \vec{v}\cdot\nabla\phi = \mathrm{Le}^{-1}\Delta\phi \tag{2.4}$$

where $\tau = t^*\alpha/H_i^2 = \mathrm{Fo}$, $\vec{v} = \vec{v}^* H_i/\alpha$, $\theta = (T - 0°\mathrm{C})/\Delta T$, $\phi = (C - C_i)/\Delta C$.

$\Delta T = T_i - 0$°C and $\Delta C = C_i - 0$ wt percent are the chosen reference temperature and concentration differences in the liquid.

Thermosolutal convection is characterized by five dimensionless parameters: the Prandtl number Pr, the Lewis number Le, the thermal Rayleigh number Ra_T, the buoyancy ratio N (or the solutal Rayleigh number $\mathrm{Ra}_S = |N|\,\mathrm{Le}\,\mathrm{Ra}_T$) and the aspect ratio A.

The dimensional energy and solute conservation equations at the interface are:

$$-k\left.\frac{\partial T(t^*,x^*)}{\partial x^*}\right|_{\mathrm{int}} = -k_S\left.\frac{\partial T_S(t^*,x^*)}{\partial x^*}\right|_{\mathrm{int}} + \rho L_f V^*(t^*) \tag{2.5}$$

$$-D\left.\frac{\partial C(t^*,x^*)}{\partial x^*}\right|_{\mathrm{int}} = C_L(t^*)V^*(t^*). \tag{2.6}$$

In a first approximation, the heat flux in the solid phase may be neglected as shown by our temperature measurements in the ice. If we consider the quasi-permanent regime only, we may introduce δ_T and δ_C, the characteristic thickness of the strong temperature and concentration variation layers along the interface, and write:

$$k\frac{T_i - T_L}{\delta_T} = \rho L_f V^* \quad \text{or} \quad \frac{V^*}{\alpha/\delta_T} = \mathrm{Ste} \tag{2.7}$$

$$D\frac{C_i - C_L}{\delta_C} = C_L V^* \quad \text{or} \quad \frac{V^*}{D/\delta_C} = \frac{C_i - C_L}{C_L}. \tag{2.8}$$

The Stefan number, $\mathrm{Ste} = C_p(T_i - T_L)/L_f$, is the sixth dimensionless parameter which characterizes this problem.

Combining Eqs. (2.7) and (2.8), to eliminate of the local front velocity V^*, we get:

$$\frac{\delta_T}{\delta_C} = \mathrm{Le}\ \mathrm{Ste}\frac{C_L}{C_i - C_L} \quad \text{or} \quad \frac{C_L}{C_i - C_L} = \mathrm{Le}^{-1}\ \mathrm{Ste}^{-1}\frac{\mathrm{Sh}}{\mathrm{Nu}}. \tag{2.9}$$

Finally, local thermodynamic equilibrium at the interface being assumed, the interface temperature and concentration are related by the linearized liquidus equation for Na_2CO_3–H_2O: $T_L = T_0 - 0.357\,C_L$ with $T_0 = 0°C$.

2.3 Set of Experiments. For the temperature and concentration ranges scanned by our experiments, the Lewis and Prandtl numbers of the Na_2CO_3 aqueous solution can be considered to be constant: Le≈190 and Pr≈11. Moreover we may admit that the diffusion coefficients do not significantly change with solute concentration and that their values for pure water can be used. All fluid properties are evaluated at the mean temperature, $T_m = (T_i + 0°C)/2$, and at the initial concentration C_i.

The variation range of the experimental control parameters are: the initial height of the fluid cavity (5 cm$\leqslant H_i \leqslant$18 cm), the initial ice thickness (1.5 cm$\leqslant e \leqslant$6 cm), the temperature of the hot wall (6°C$\leqslant T_i \leqslant$22°C), the initial concentration of the solution (2 wt percent$\leqslant C_i \leqslant$5.5 wt percent). The lower limit of C_i is imposed to prevent a density maximum in the liquid part [20]. The corresponding ranges of the dimensionless parameters are $2 \leqslant A \leqslant 4.8$, $1.5\times10^7 \leqslant \mathrm{Ra}_T \leqslant 2.3\times10^8$, $-172 \leqslant N \leqslant -8$ (leading to $3\times10^{10} \leqslant \mathrm{Ra}_S \leqslant 2.6\times10^{12}$) and $0.047 \leqslant \mathrm{Ste}^{\clubsuit} \leqslant 0.275$, where $\mathrm{Ste}^{\clubsuit} = C_p\Delta T/L_f$. Each experiment is referenced with a code name $R\alpha$-$N\beta$-$A\epsilon$, where α, β, and ϵ are the value of the solutal Rayleigh number, the buoyancy ratio and the aspect ratio, respectively.

A first group of experiments corresponds to the same $N = (\beta_C C_i)/(\beta_T \Delta T)$. They are also characterized by the same ΔT and the same C_i. Changing the Rayleigh numbers at a fixed N is performed by modifying H_i only. As a consequence, a given N corresponds to a given Ste (Ste$\propto\Delta T$). Thus, those experiments do not allow to discriminate between N and Ste.

To separate the N and Ste influence, another set of experiments has been performed: we scanned the largest possible range of the Stefan number by changing ΔT, all the other characteristic parameters (N, Ra_T, A) being fixed. To keep $N = (\beta_C C_i)/(\beta_T \Delta T)$ constant, we must change $\beta_C C_i/\beta_T$ proportionally to ΔT (with 2 wt percent$\leqslant C_i \leqslant$5.5 wt percent). Since β_C is roughly a constant and β_T nearly proportional to C_i, the largest variations obtained for Ste, with a fixed N, are of the order of 30 percent.

3 Local Equilibrium and Exchanges at the Moving Front

3.1 Interface Equilibrium Shift. Fusion of a pure material into a binary liquid mixture does not a priori impose known temperature and concentration at the melting front. The latter are determined by the local thermodynamic equilibrium resulting from the heat and mass exchanges at the front. The slower is the fusion process, the larger is the equilibrium shift from the high front velocity limit case $T_L = 0°C$, $C_L = 0$. More precisely (Eq. (2.7)) the lower the average Stefan number, the farther are the temperature and concentration from zero, and the closer to the dissolution thermodynamic equilibrium $C_L = C_i$.

Considering the liquidus curve, the local front temperature measurements that have been performed provide experimental values for the local front concentration C_L, that is, for the ratio $C_L/(C_i - C_L)$ at different levels of the melting front for the whole set of characteristic parameters (Fig. 4). As could be expected, the smaller is the Stefan number, the closer to C_i is C_L and thus the higher is $C_L/(C_i - C_L)$. But Fig. 4 also shows that two zones are to be considered: the lower zone where thermal convection is active, melting is quicker and C_L closer to zero, and the upper zone where there is no convective cell, melting is slower, and C_L farther from zero. Moreover we notice that the increase in $C_L/(C_i - C_L)$ is roughly a linear function of 1/Ste, for each zone, and that the linear relation is better verified for the convective zone than for the upper zone. The experimental accuracy is sufficient to establish that the approximate slope is higher for the upper mixing zone than for the convective zone. It should also be underlined that, in the convective zone, measurement uncertainties are too high to provide good estimates of C_L when it gets close to zero, which happens when the Stefan number increases to reach the order of magnitude of 0.25.

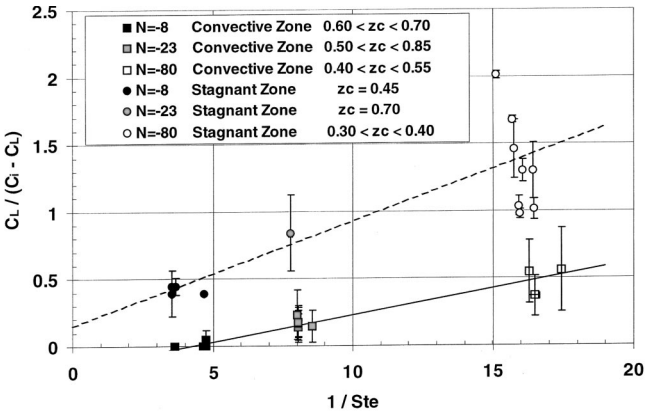

Fig. 4 $C_L/(C_i - C_L)$ as a function of 1/Ste. Local values of the front concentration C_L are obtained from local interface temperature measurements, local thermodynamic equilibrium being assumed (Eq. (2.10)). zc is the corresponding height range of the convective cell (valid for Fig. 5 and Fig. 6).

To get a deeper understanding of the linear correlation between $C_L/(C_i - C_L)$ and 1/Ste observed in the convective zone, let us use the simple scaling law given by Eq. (2.9). It shows that $C_L/(C_i - C_L)$ is indeed linear with Ste^{-1} and does not depend on other parameters if Sh/Nu does not depend on either Ste or Ra_S or N (Le is nearly constant in our experiments). It also points out that, if $C_L/(C_i - C_L)$ is smaller in the convective zone than in the mixing zone, Sh/Nu too must be smaller in the convective zone than in the mixing zone. Thus the study of the Sh/Nu ratio allows us to cross-check the experimental results for $C_L/(C_i - C_L)$ given in Fig. 4. Indeed, while $C_L/(C_i - C_L)$ is estimated through temperature measurements, the Nusselt number is obtained experimentally from front velocity measurements that provide an additional information on the system behavior.

As will be seen in paragraph 3.2, the experimental estimations of Nu_c, the Nusselt number in the convective zone, show that $\mathrm{Nu}_c \propto \mathrm{Ra}_s^{1/4}$. The experimental results for $C_L/(C_i - C_L)$ and Nu_c, together with Eq. (2.9), entail that $\mathrm{Sh} \propto \mathrm{Ra}_s^{1/4}$, a result that is commented upon in paragraph 3.3.

3.2 Nusselt Number and Front Velocity in the Convective and Mixing Zones. In [20], one of the main results is the independence of the average Nusselt number at the melting front, $\langle \mathrm{Nu} \rangle_{\mathrm{Hi}}$ with respect to the Stefan number and its correlation with $\mathrm{Ra}_s^{1/4}$ during the quasi-steady regime: $\langle \mathrm{Nu} \rangle_{\mathrm{Hi}} = \mathrm{H_i}/\delta_T = 0.2\,\mathrm{Le}^{-1/2}\,\mathrm{Ra}_s^{1/4}$.

The local measurements performed in the present work allow to go further and tell between the convective zone Nusselt number Nu_C and the stagnant mixing zone Nusselt number Nu_{ST}. This is done by sorting out two groups of local measurements of the time evolutions of the front positions during the quasi-steady regime: the first one corresponding to measurements performed at the level of the convective zone and the second one to measurements performed at the level of the mixing zone, with no secondary thermosolutal cell present. Figure 5 shows that independence from

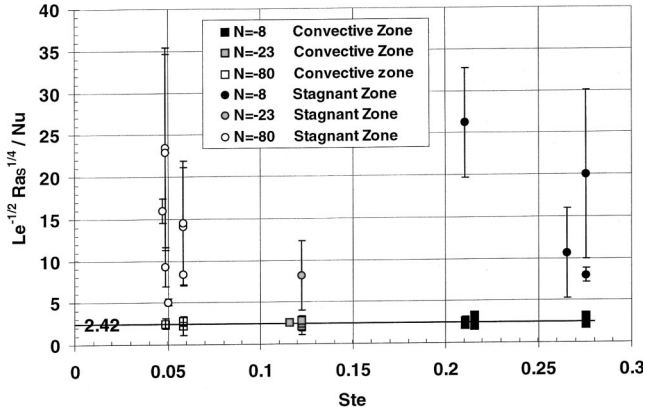

Fig. 5 $Le^{-1/2}Ra_s^{1/4}/Nu$ as a function of Ste, where Nu is the local Nusselt number obtained from local front velocity measurements in the upper stagnant zone or in the convective zone. This figure shows the correlation between the local Nusselt number in the convective zone with $Ra_s^{1/4}$ and its independence from Ste.

Ste and correlation with $Ra_s^{1/4}$ are strictly checked by Nu_C. Introducing the Lewis number as in [20], we can write:

$$Nu_C = 1/2.42 \ Le^{-1/2} \ Ra_s^{1/4} = 0.41 \ Le^{-1/2} \ Ra_s^{1/4}. \quad (3.1)$$

But, for the weaker and less precise Nu_{ST}, no correlation can be put forward.

As a consequence of Eqs. (2.7) and Eq. (3.1), the average dimensionless front velocity for the convective zone $V_C = H_i V_C^*/\alpha$ should be such that

$$V_C = H_i V_C^*/\alpha = Ste \ Nu_C = 0.41 \ Ste \ Le^{-1/2} \ Ra_S^{1/4}. \quad (3.2)$$

This is shown to be true in Fig. 6. In spite of the absence of observed correlation between Nu_{ST} and $Ra_S^{1/4}$, a rough correlation of the dimensionless front velocity in the mixing zone $V_{ST} = H_i V_{ST}^*/\alpha$ with Ste does exist, a result that can be explained by the strong relationship between V_{ST} and Ste.

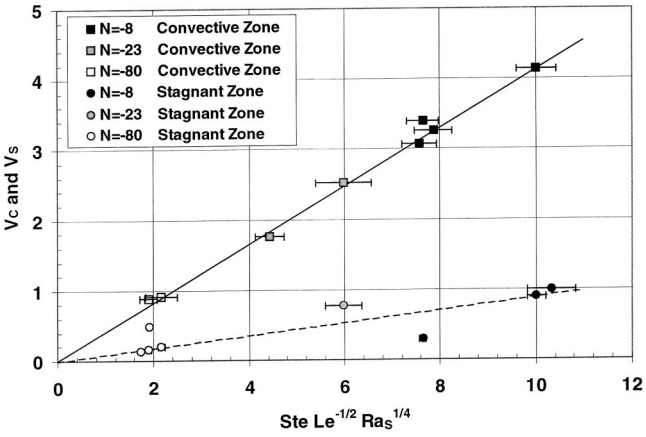

Fig. 6 Dimensionless front velocity in the upper stagnant zone, V_S, and in the convective zone, V_C, as a function of Ste $Le^{-1/2}Ra_S^{1/4}$. For the convective zone, a straight line of slope 0.41±0.01 is obtained by linear regression (correlation coefficient $J=0.99$). For the upper zone, the straight line obtained by linear regression leads to a slope of 0.09±0.01 (correlation coefficient $J=0.6$).

Let us underline that it may be useful to introduce an average dimensionless velocity V of the melting front, defined as the ratio to H_i of the total volume melted per unit time. V is a weighted average of V_C and V_{ST}:

$$V = H_i V^*/\alpha = 0.27 \ Ste \ Le^{-1/2} \ Ra_S^{1/4}. \quad (3.3)$$

A corresponding dimensionless melting time t_m can then be defined as:

$$t_m = t^* V^* H_i / L_i H_i = 0.27 \ A \ Ste \ Le^{-1/2} \ Ra_S^{1/4} \ Fo = A \ V \ Fo, \quad (3.4)$$

where $V^* H_i / L_i H_i$ is the relative increase of the melted volume per unit time.

At the precision of this experimental correlation which neglects the initial transient regime, Eq. (3.4) assesses that, at a given dimensionless time t_m, the relative melted volumes are the same for all the experiments (Fig. 2).

3.3 Comments on the Experimental Scalings of the Nusselt and Sherwood Numbers. The fact that Nu and Sh are not experimentally correlated to Ste, which characterizes the phase change kinetics, shows that the front exchanges depend primarily on the flow structures. This observation opens the possibility of using a *fixed* wall dimensional analysis of the convective exchanges as a reference. Such an analysis, for thermosolutal convection [22], allows the introduction of classical laminar boundary layer thickness $\delta_{F\nu}$, δ_{FT}, δ_{FS} at the three scales of the dynamical, thermal and solutal boundary phenomena:

$$\delta_{F\nu} \gg \delta_{FT} \gg \delta_{FS} \quad \text{since} \quad \nu \gg \alpha \gg D. \quad (3.5)$$

The reliability of the fixed wall reference is confirmed for the heat exchange by checking that the heat diffusion velocity $v^*_{THERM} = \alpha/\delta_{FT}$ is larger than the front velocity V^*: $4 \leqslant v^*_{THERM}/V^* = Ste^{-1} \leqslant 20$.

For the mass exchange, the relative orders of magnitude of the solute diffusion velocity v^*_{SOL} and of the front velocity are less convincing: in the convective zone, $v^*_{SOL}/V^* \approx 0.5$, and, in the upper zone, $0.5 \leqslant v^*_{SOL}/V^* \leqslant 2$. Nevertheless, let us admit that such orders of magnitude do not forbid the use of the fixed front approximation.

We are still left with the fact that, in our experiments, the scaling of Nu and Sh is by $Ra_s^{1/4}$, a result that Bejan obtains in his fixed wall analysis by assuming that the solutal forces are dominant at all scales or, in other terms, that $|N| \gg Le$. But our experiments all fit in the range $Le^{1/3} \leqslant |N| \leqslant Le$ which means that solutal forces control the solutal scale only and that thermal forces control the thermal scale only [25]. In such a case, it is still easy to show that, at the smallest scale that is at the solutal one, Sh, the dimensionless wall solute exchange, is scaled by $Ra_S^{1/4}$ (for a fixed wall). But no straightforward scaling parameter can be found for the wall heat exchange nor for the liquid flow along the wall, that is for the larger scales. Indeed at the solutal scale, close to the wall, the strong solutal force disturbs both the velocity gradient and the temperature gradient and prevent the theoretical boundary layers δ_{Fv} and δ_{FT} of the reference analysis from building up. The fact that $N<0$ still strengthens the perturbation. Indeed, at the level of the thermal cell, we observe, in all our experiments, a very strong shear between the downward thermal flow and the upward solutal flow close to the front. This suggests to choose, as the only meaningful scale related to the dynamic behavior of the boundary region, the thickness $\delta_I (\delta_I \gg \delta_{FS})$ of the upward flow; for distances to the front of the order of δ_I, the solutal forces, scaled by Ra_S, are balanced by the thermal forces, scaled by Ra_T. Thus the scaling of δ_I becomes a main issue to understand the scaling of the exchanges taking place at a larger scale than the solutal one. The thickness δ_I is directly connected to the upward flow $dW_F(t^*)/dt^*$ along the wall:

$$dW_F(t^*)/dt^* \propto \delta_I \mathbf{v}_I, \quad (3.6)$$

where $\mathbf{v}_I$ is the average fluid velocity in the layer of thickness δ_I. The scaling of $dW_F(t^*)/dt^*$, the flux extracted from the thermal cell (defined per unit length of depth in the third dimension), on the basis of our experiments is obviously of great interest since it gives an insight on the scaling of $\delta_I \mathbf{v}_I$. This is what is done in the next section with the analysis of the upper zone filling process.

4 Growth of the Upper Mixing Zone

Due to the lighter liquid released by the melting solid and to the resulting buoyancy effect, the upper zone (Figs. 1 and 2) is filled by a quick and narrow upward flow along the melting front formed from the bottom of the enclosure and going up to its top. No additional fluid escapes from the thermal cell to the upper zone, at their interface or along the hot wall. Indeed, a mixture of the binary solution and of a weak mass fraction of fluorescein ($\sim 0.5\times 10^{-5}$) can be injected at thermal equilibrium, through a needle, into the hot wall boundary layer of the thermal cell. Observation by laser tomography shows that no colored streak rises along the hot wall from the thermal cell into the upper zone, or at their interface. Another feature of the filling process of the upper zone is that all the melt goes to the upper zone. Indeed by adding small fluorescein spots in the ice, at several vertical levels and, in particular, close to the bottom of the experiment, we could observe that no fluorescein enters the thermal cell. Finally, a last aspect of the growth of the upper zone is that its volume $W_{up}(t^*)$ at a given time t^* is much larger than the melted volume $W_L(t^*)$ at the same time [20]. Indeed, at the level of the thermal cell, most of the liquid that is carried up to the mixing zone along the ice front is pulled out of the cell.

4.1 Simplified Scaling Analysis. The previous observations suggest to consider $W_{up}(t^*)$, the volume of the upper zone observed by laser tomography (Fig. 2), as the result of two contributions: an unknown volume $W(t^*)$ due to the shear stress extraction from the thermal cell, to be compared to the fixed wall approximation $W_F(t^*)$, and the melted volume $W_m(t^*)$, which is measured through the front position observation: $W_{up}(t^*) = W(t^*) + W_m(t^*)$.

Since we are not interested in the initial transition regime and we consider only the lapse of time while the convective movement in the lower cell can be considered permanent, the comparison between $W(t^*)$ and $W_F(t^*)$ is for $dW_F(t^*)/dt^*$, δ_I and $\mathbf{v}_I$ constant (Eq. (3.6)). The fixed wall analysis of the foregoing paragraph allows to scale $\mathbf{v}_I$ as $D\,\mathrm{Ra}_S^{1/2}/H_i$. Thus $dW_F(t^*)/dt^*$, the flux extracted from the thermal cell in the fixed wall approximation, can be written as:

$$dW_F(t^*)/dt^* = \gamma \delta_I D \;\; \mathrm{Ra}_s^{1/2}/H_i\,, \tag{4.1}$$

where γ is an unknown constant dimensionless coefficient. If indeed $W(t^*) \cong W_F(t^*)$, $dW(t^*)/dt^*$ will be time independent for every experiment. This is a first property suggested by our simple scaling approach that we will investigate experimentally.

But Eq. (4.1) opens another question: can this linear growth of the reduced upper zone volume $W(t^*)$ be expressed in dimensionless terms as a function of the characteristic parameters of the experiment only? Indeed Eq. (4.1) is dimensional ($\mathrm{m^2 s^{-1}}$), and, to put it into a dimensionless form, we must choose a dimensionless volume per unit depth and a dimensionless time. If we introduce as a dimensionless expression for W, $z = W/H_i L_i$, in the same way as we did for the melted volume (Eq. (3.4)), Eq. 4.1 becomes

$$dz(t^*)/dt^* = \gamma (D/H_i^2)\mathrm{Ra}_S^{1/2} A \;\; \delta_I/H_i\,. \tag{4.2}$$

Equation (4.2) suggests to set

$$t = t^*(D/H_i^2)\mathrm{Ra}_S^{1/2} A \;\; \delta_I/H_i = \mathrm{Fo}\;\; \mathrm{Le}^{-1} \;\; \mathrm{Ra}_S^{1/2} A \;\; \delta_I/H_i\,, \tag{4.3}$$

as a dimensionless time, so that

$$dz(t)/dt = \gamma. \tag{4.4}$$

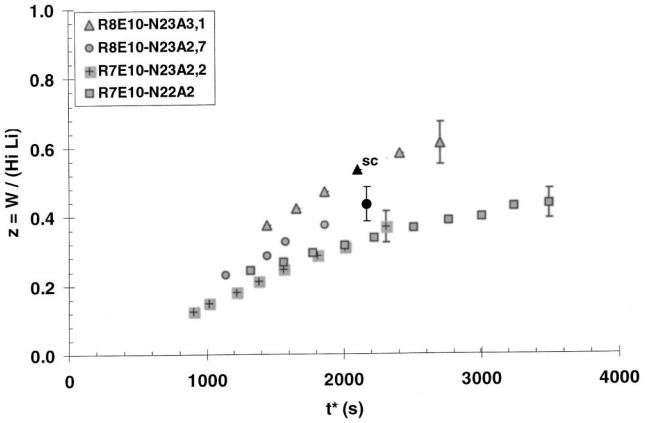

Fig. 7 Time evolution of the dimensionless experimental height of the upper zone: $N=-23$, $\mathrm{Ra}_S \approx 7.5\times 10^{10}$, $2 \leqslant A \leqslant 3.1$. For Δ and for ○, a secondary cell (sc) appears around $t^* = 2100$ s and $t^* = 2164$ s respectively. For □ and ⊞ no time is reached that corresponds to a secondary cell.

For t to be a unique dimensionless time describing the behavior of all our experiments, δ_I/H_i must depend on the dimensionless parameters of the experiments only. This will be examined here, on the basis of our experimental results. The problems at stake are whether, within our experimental precision, the linearity of Eq. (4.1) is confirmed by our experiments during the quasi-permanent regime and whether Eq. (4.2) can be written in a general dimensionless form (Eq. (4.4)).

4.2 Influence of the Aspect Ratio. Before analyzing the influence of Ra_S and N, let us first check whether A, the aspect ratio of the liquid part of the experiment, plays a role in the growth of the *volume* of the upper mixing zone. If, for given Ra_S and N, W does not depend on the aspect ratio, then the dimensionless volume $z = W/L_i H_i$ will depend on A. Thus, according to Eq. (4.1), δ_I/H_i should not depend on A but, according to Eqs. (4.3) and (4.4), any dimensionless time t characterizing the growth of z should be proportional to A. This is what is confirmed by Figs. 4.1 and 4.2, where the time evolutions of z, for four experiments with approximately the same solutal Rayleigh number ($\mathrm{Ra}_S \approx 7.5 \times 10^{10}$) and the same buoyancy number ($N=-23$), differing by their aspect ratio only ($2 \leqslant A \leqslant 3.1$), are compared. Time is dimensional for Fig. 7 and a dimensionless time proportional to A is used in Fig. 8. Those figures show that, if the dimensionless time

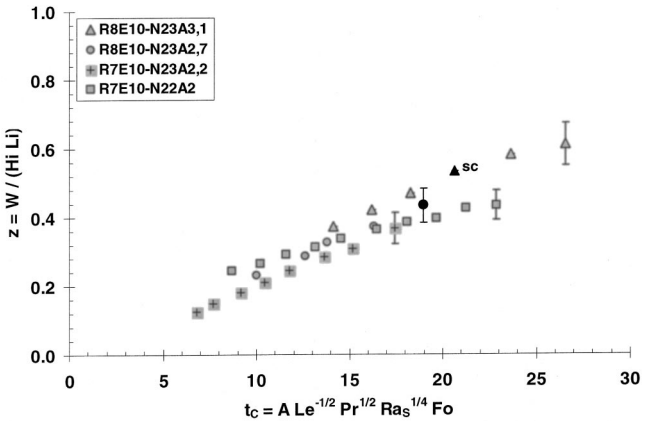

Fig. 8 Dimensionless time evolution of the dimensionless experimental height of the upper zone: $N=-23$, $\mathrm{Ra}_S \approx 7.5\times 10^{10}$, $2 \leqslant A \leqslant 3.1$.

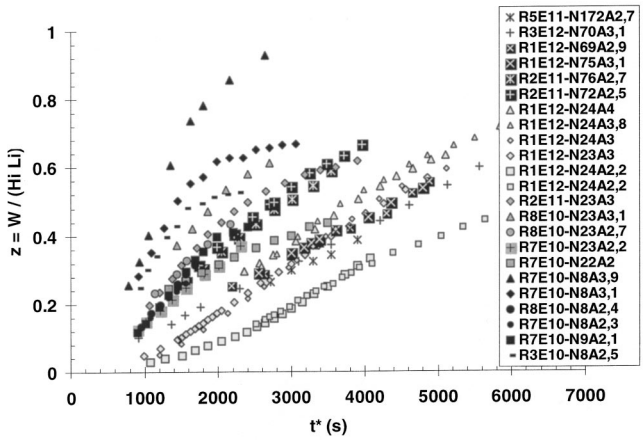

Fig. 9 Time evolution of the dimensionless experimental height of the upper zone: $1.5\times10^7 \leqslant Ra_T \leqslant 2.3\times10^8$, $-172 \leqslant N \leqslant -8$ ($3\times10^{10} \leqslant Ra_S \leqslant 3\times10^{12}$).

is scaled by A, the kinetics of the four experiments, which are different in Fig. 7, become very similar in Fig. 8.

Let us notice that, to be able to write t as

$$t_C = A\ \mathrm{Le}^{-1/2}\ \mathrm{Pr}^{+1/2}\ \mathrm{Ra}_S^{+1/4}\ \mathrm{Fo}, \tag{4.5}$$

the dimensionless time which is used in Fig. 8, we must express δ_I/H_i as

$$\delta_I/H_i \propto \mathrm{Ra}_S^{-1/4}\ \mathrm{Pr}^{+1/2}\ \mathrm{Le}^{+1/2}. \tag{4.6}$$

In this expression, δ_I/H_i is scaled by $\mathrm{Ra}_S^{-1/4}$, an hypothesis that plays no role in the comparison performed here for constant Ra_S and N, but that will become the major issue in the next paragraph.

4.3 Role of N and Ra_S. Let us first plot $z(t^*)$ (Fig. 9) and $z(t)$ (Fig. 10) for a wide range of parameters: $76 \leqslant N \leqslant -8$, $3\times10^{10} \leqslant \mathrm{Ra}_S \leqslant 3\times10^{12}$, $1.5\times10^7 \leqslant \mathrm{Ra}_T \leqslant 2.3\times10^8$.

The dimensionless time used in Fig. 10 is t_C, defined by Eq. (4.5). The comparison between Figs. 9 and 10 shows that this dimensionless formulation brings the curves together. But it can be noticed too that all the curves with high Ra_S ($\mathrm{Ra}_S \geqslant 10^{12}$) and high Ra_T ($\mathrm{Ra}_T \approx 2\times10^8$) tend to gather around a straight line (thin dashed line) of larger slope $\gamma \approx 0.039 \pm 0.001$ (correlation coefficient $J=0.98$), while the lower Ra_T ($\mathrm{Ra}_T \approx 10^7$) experiments correspond to smaller slopes (large dashed line). The main difference between those two categories of experiments is the formation kinetics of the secondary cells in the upper zone, the effect of which our simple correlation (Eq. (4.6)) cannot account for. For the large Ra_S and Ra_T experiments, secondary cells in the upper zone begin to be visible at times ranging from $t_1^* \approx 1500$ s to $t_2^* \approx 2500$ s, depending on the experiment. They correspond to $t_{C1} \approx 5.6$ and $t_{C2} \approx 9.4$, which belong to the time interval used to analyze the growth of the upper zone, in Fig. 10. For the lower Ra_S and Ra_T experiments, the secondary cells come later and are less active, so that their influence is negligible until $t_C \approx 15$. As a consequence, a linear growth of weaker slope is observed for those experiments. For $t_C \leqslant 15$, a straight line of slope $\gamma_1 = 0.025 \pm 0.003$ is obtained by linear regression with a good precision (correlation coefficient $J=0.91$). For further time instants, the slope tends to weaken slightly, probably due to the reduction of the thermal cell height analyzed in part 3. On the contrary, the strong activity of the secondary cells in the large Ra_S and Ra_T experiments compensate for this phenomenon and maintains the higher slope.

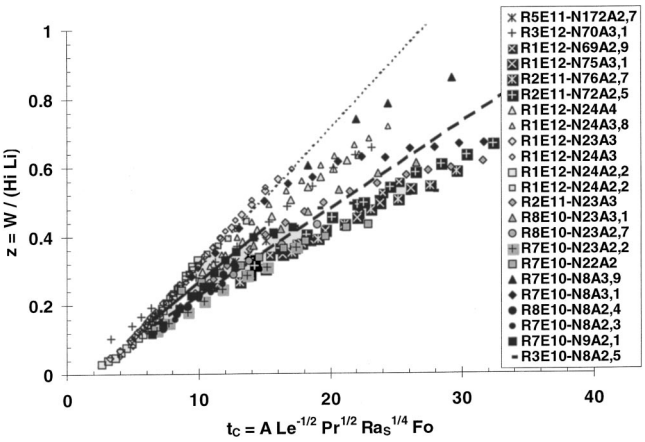

Fig. 10 Dimensionless time evolution of the dimensionless experimental height of the upper zone: $1.5\times10^7 \leqslant \mathrm{Ra}_T \leqslant 2.3\times10^8$, $-172 \leqslant N \leqslant -8$ ($3\times10^{10} \leqslant \mathrm{Ra}_S \leqslant 3\times10^{12}$).

Finaly, let us underline that more sophisticated hypotheses, introducing $N^x\,\mathrm{Ra}_S^y$ in the expression of δ_I/H_i, have also been checked. Their comparison with the basic dimensionless formulation of Eq. (4.6) demonstrates that, within the precision of both our experiments and the linear quadratic regression, the optimization of two exponents—a small x and a larger y—instead of one exponent y only with x fixed to zero, is meaningless. Thus, the only significant scaling of δ_I/H_i that can be proposed is by $\mathrm{Ra}_S^{1/4}$.

As a conclusion, for the entire range of parameters and $t_C \leqslant 15$, we propose a general correlation for the growth of the upper zone volume (solid line on Fig. 10):

$$dz/dt = \gamma = 0.03 \pm 0.004, \quad \text{with a correlation coefficient } J = 0.90.$$

5 Destabilization of the Upper Zone

A fluid with a stabilizing vertical solute gradient can be destabilized by lateral heating. The case of a step side wall heating was the first to be investigated in [26] and is still a subject of interest [27–29]. Another important case, which is close to our experimental situation, corresponds to a zero horizontal density gradient across the fluid and a slow side heating rate, that builds up a uniform horizontal temperature gradient. To study this configuration, linear and/or weakly nonlinear stability analyses of the onset of diffusive instabilities in a narrow slot have been performed, for the full range of thermal and solutal Rayleigh numbers [30–32]. They show that, when the salinity gradient is increased from very weak values to moderate values, the stationary shear-induced instability is replaced by a stationary double-diffusive cellular convection, after going through a transitional regime of oscillatory shear instabilities. In [32], four limit cases are analyzed: (1) the very weak salinity gradient regime mentioned above; (2) a very large temperature difference regime where the onset of instabilities is essentially independent of the temperature difference; (3) a regime with moderate gradients where the vertical wavelength of instabilities tends to infinity; and (4) the strong salinity gradient regime. The latest region has first been investigated by Thorpe et al. [23] and later revised by Hart [33] who considered more realistic boundary conditions and mean fields than Thorpe et al. The neutral curve given in [33] agrees exactly with the solution obtained by Thorpe et al. meaning that, in the strong salinity gradient regime, the boundaries and the mean flow do not play an important role in the destabilization process.

The present work is focused on the onset of the first vortices responsible for the formation of the first thermosolutal cell at the bottom of the upper stagnant zone. The development of the vortices takes place far enough from the free surface of the experimental cell to consider that the surface tension has no influence on the destabilization process. The upper zone concentration and temperature gradients that will trigger this destabilization process

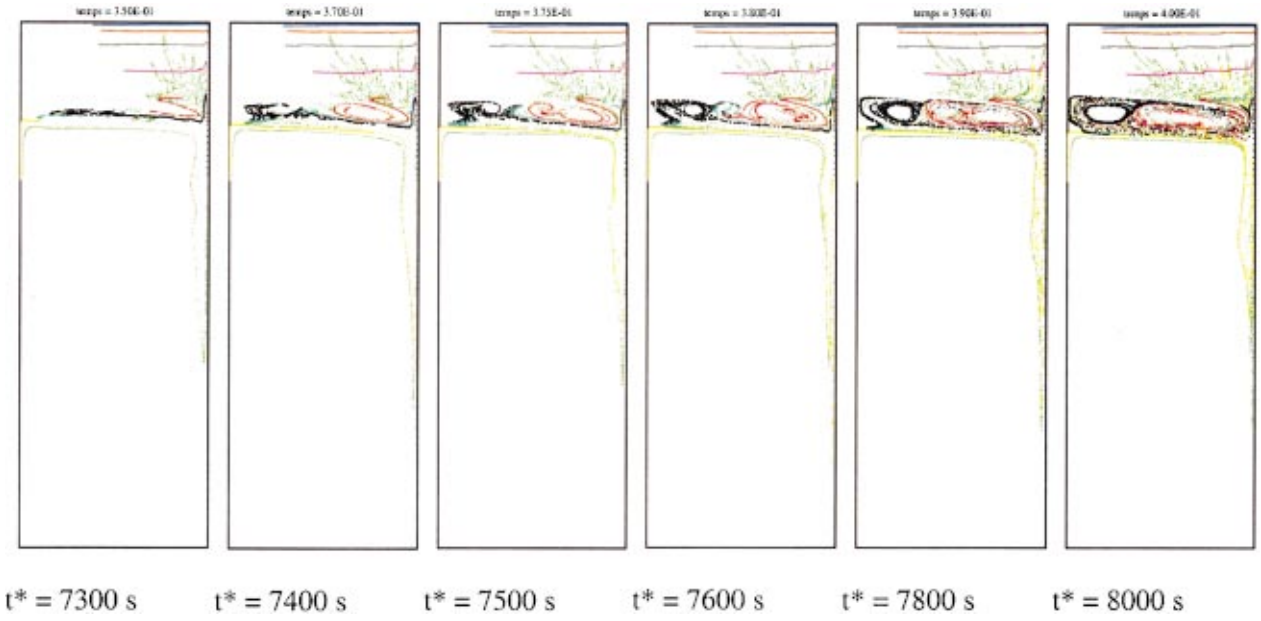

Fig. 11 Numerical simulation of the onset and the development of the first thermosolutal cell. Streaklines. Particles are released in the cavity at 9 locations specified by the coordinates $(x^*/H_i, z^*/H_i)$: in the hot boundary layer – – – $(9.6\,10^{-5}, 0.70)$, — — —$(4.7\,10^{-3}, 0.70)$; in the cold boundary layer — — —(0.3296, 0.80), — — —(0.3291, 0.80), — — —(0.3285, 0.80), — — —(0.3276, 0.80), — — —(0.3265, 0.70), — — —(0.3265, 0.80); near the cold wall: — — —(0.2817, 0.85). $Ra_T = 2.3\times10^8$; $N=-24$; $A=3$; Pr=11.2; Le=189.

gradually build up with the filling process. This zone is characterized by a strong vertical salinity gradient, as will be shown by the numerical simulations presented in the next paragraphs. Those features attempt to produce the asymptotic theoretical conditions considered in Thorpe's analysis.

Our experiments provide accurate measurements of the height of the stagnant zone at the onset of the destabilization thanks to meticulous observations of the time evolution of the flow. The results are investigated with the help of numerical simulations. The simplified model and the numerical method used are described in detail in [20,34]. Let us briefly recall that the model consists in a fixed rectangular cavity which is differentially heated and filled with a binary fluid initially at rest. A uniform zero concentration applied at the cold wall approximates the experimental ice wall. The opposing vertical hot wall is impermeable. The horizontal walls are adiabatic and impermeable. The set of coupled equations and boundary conditions is solved using a classical finite volume technique. A centered scheme is used for spatial discretization and time integration is based on a first order implicit scheme. The purpose of the simulations being to compute the height of the upper zone and the concentration and temperature distributions in the region of destabilization, the requirements in term of space and time resolution are important. The two-dimensional computational grid used is sinusoidal in the horizontal direction and regular in the vertical one, with a mesh size ranging from 93×281 to 291×501 and dimensionless time steps ranging from 10^{-6} to 5×10^{-6} ([34]).

5.1 Experimental Observations. The first vortex responsible for the formation of a secondary cell always appears at the bottom of the upper zone above the shear layer that is observed between the high velocity thermal cell and the weak velocity upper zone (Fig. 2). Its lateral position with regards to the walls depends on the experiment but is perfectly reproducible for given experimental conditions. A close observation of three experiments characterized by $N=-23$, $Ra_S=1\times10^{12}$, and an aspect ratio of 2.2, 3, and 4, shows that the distance of the first vortex to the cold wall does not depend on A. The first vortex is followed by other vortices that will finally occupy all the space on a horizontal layer between the hot wall and the ice wall. The number of such vortices giving rise to a thermosolutal cell varies from 3 to 6 according to experiments. It is reproducible for a given experiment.

5.2 Numerical Simulations. Figure 11 displays numerical streaklines, for a simulation at $Ra_T=2.2\times10^8$, $N=-22$ that corresponds to the experimental case R1E12-N23A3. The particles are released in the ascending boundary layers at the hot wall and the cold wall. The numerical result confirms the experimental one: the upper zone is fed by the cold side only. The particles released at the cold wall are accelerated upward by the solutal buoyancy force and then slowly heat up in the upper zone. Their very slow horizontal movement along the isodensity lines may be seen on the figure: in dimensional terms, the total duration of the evolution shown in the figure is about 15 minutes. Moreover, according to experimental observations, this numerical streakline representation confirms that destabilization appears as a succession of corotative vortices that merge to form a horizontal layer at the bottom of the stagnant zone.

5.3 Critical Height of Destabilization. For the numerical simulations, the dimensionless height of the upper zone, $z^*_{up}(t^*)/H_i = W_{up}(t^*)/H_i L_i$, is taken in the vertical mid-plane of the cavity, between the top horizontal wall and the vertical position where the sign of the streamfunction changes.

Table 1 reports the experimental and numerical values of the dimensionless height of the upper zone at destabilization. For given A and Ra_T, the dimensionless critical height increases when $|N|$ increases. For given A and N, the critical height decreases when the Rayleigh numbers increase. $|N|$ has a stabilizing effect and Ra_T a destabilizing one.

In spite of the simplifications of our numerical model, the computed critical heights agree well with the corresponding experimental measurements. Hence, in absence of measurements, it seems reasonable to rely on our numerical simulations to get information on the upper zone concentration and temperature field when destabilization occurs.

Figure 12 shows the concentration, temperature and density fields in the upper zone before the formation of a thermosolutal

Table 1 Experimental and numerical values of the dimensionless critical height of the upper zone at the onset of the destabilization

	Ra_T	Ra_S	A	Name	Experimental measurements	Numerical Simulations
N = -8	2×10^7	3×10^{10}	2.5	R3E10-N8-A2,5	0.41	0.38-0.42
	3.1×10^7	5×10^{10}	2.1	R5E10-N9-A2,1	0.38-0.42	
	4.5×10^7	6.6×10^{10}	2.2	R7E10-N9-A2,1	0.36-0.37	
			3.1	R7E10-N8-A3,1	0.25-0.32	0.29-0.33
			3.9	R7E10-N8-A3,9	0.28	0.28-0.30
N = -23	1.5×10^7	6.6×10^{10}	2.2	R7E10-N23-A2,2	0.59-0.63	0.52-0.56
			4	R7E10-N23-A4	0.49	
	1.8×10^7	7.2×10^{10}	2	R7E10-N22-A2	0.58-0.61	
		7.8×10^{10}	2.7	R8E10-N23-A2,7	0.48-0.55	0.535-0.55
			3.1	R7E10-N23-A3,1	0.50-0.55	0.46-0.52
	4.2×10^7	1.8×10^{11}	3	R2E11-N23-A3	0.42-0.47	
	2.3×10^8	1×10^{12}	2.2	R1E12-N24-A2,2	0.36-0.37	
			3	R1E12-N23-A3	0.27-0.30	
			3.8	R1E12-N23-A4	0.28-0.29	0.25
N = -75	5.2×10^6	7.3×10^{10}	2.4	STE*-R7E10-N76	0.77-0.83	0.77-0.83
	1.7×10^7	2.4×10^{11}	2.7	R2E11-N76-A2,7	0.61-0.64	
	7.0×10^7	9.8×10^{11}	3.1	R1E12-N75-A3,1	0.42-0.44	

cell. The isodensity lines are horizontal except in a thin layer near the cold wall and the density field is stably stratified. The heat transfer from the hot wall and the lower thermal cell is diffusive while the concentration field is vertically stratified. Hence, the basic state before destabilization is similar to the one encountered in Thorpe's et al. analysis.

According to the analysis presented in [23], destabilization occurs if:

$$|R_x| \geqslant 2{,}76(-R_z)^{+5/6}, \tag{5.1}$$

knowing that:

$$R_x = \frac{\mathrm{Ra}_T}{\pi^4 A^4}\frac{H_i}{\beta_T \Delta T}\left[\mathrm{Le}\ \beta_S\frac{\partial C}{\partial x^*} - \beta_T\frac{\partial T}{\partial x^*}\right] \tag{5.2}$$

$$R_z = \frac{\mathrm{Ra}_T}{\pi^4 A^4}\frac{H_i}{\beta_T \Delta T}\left[\mathrm{Le}\ \beta_S\frac{\partial C}{\partial z^*} - \beta_T\frac{\partial T}{\partial z^*}\right]. \tag{5.3}$$

For the simulations performed here, $R_x > 4.6\times10^5$ and $(-R_z) > 1.9\times10^6$ in the region of destabilization, confirming that we are in the case of very strong salinity gradients. Moreover, we do check that Eq. (5.1) is locally satisfied at destabilization. Since the numerical and experimental critical heights of destabilization are identical, we can conclude that the destabilization mechanism of the stagnant zone is well described by the theory developed by Thorpe's and al.

In our situation, the local quantities R_x and $(-R_z)$ given by Eqs. (5.2) and (5.3) can be related to the global characteristic parameters as follows [20]:

$$R_x \approx \frac{\mathrm{Ra}_T}{\pi^4 A^3}\mathrm{Le} \tag{5.4}$$

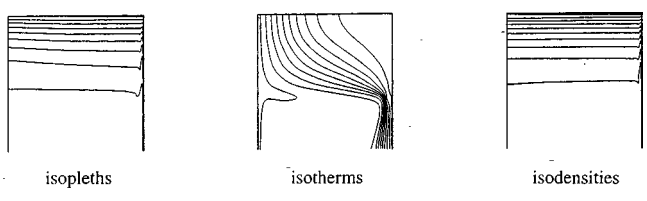

Fig. 12 Concentration, temperature and density fields in the upper zone before the destabilization ($t^*=6050$ s). $Ra_T=2.3\times10^8$; $N=-24$; $A=3$; Pr=11.2; Le=189.

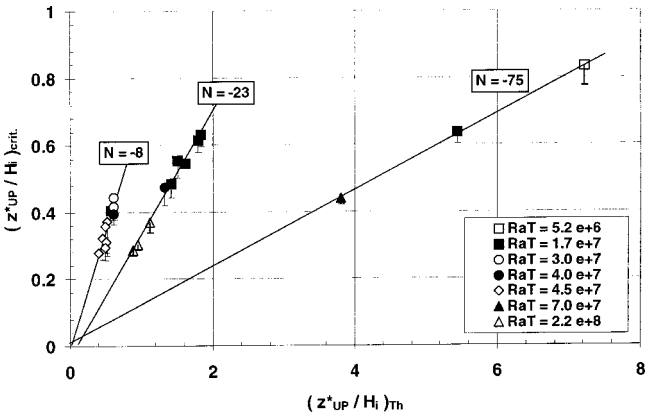

Fig. 13 Experimental dimensionless height of the stagnant zone at the onset of the destabilization as a function of the theoretical one

$$(-R_z) \approx \frac{\mathrm{Ra}_T}{\pi^4 A^4}|N|\mathrm{Le}\left(-\frac{\partial C}{\partial z^*}\right)\frac{H_i}{\Delta C} = R_x\frac{|N|}{A}\left(-\frac{\partial C}{\partial z^*}\right)\frac{H_i}{\Delta C}. \tag{5.5}$$

In the theoretical approach of Thorpe et al., the basic state is characterized by a uniform vertical salinity gradient $(-\partial C/\partial z^*) = \Delta C/z^*_{\mathrm{up}}$. In our configuration the uniformity of the salinity gradient that builds up in the upper zone is not controlled. Fig. 12 shows that the vertical salinity gradient, and thus $(-R_z)$, is weaker in the bottom part of the upper zone, which consequently appears as the most unstable region.

If we write the local salinity gradient at the bottom of the stagnant zone as $(-\partial C/\partial z^*) = \varphi(t^*, N, \mathrm{Ra}_T, A)\Delta C/z^*_{\mathrm{up}}(t^*)$, and combining Eqs. (5.1), (5.4), and (5.5), the height of the stagnant zone at destabilization can be written as:

$$\left(\frac{z^*_{\mathrm{up}}}{H_i}\right)_{\mathrm{crit}} = \varphi(t^*_{\mathrm{crit}}, N, \mathrm{Ra}_T, A)\,2.76^{6/5}\pi^{4/5}\frac{|N|}{(\mathrm{Le}\ \mathrm{Ra}_T A^2)^{1/5}}$$

$$= \varphi(t^*_{\mathrm{crit}}, N, \mathrm{Ra}_T, A)\left(\frac{z^*_{\mathrm{up}}}{H_i}\right)_{\mathrm{Th}} \tag{5.6}$$

where $(z^*_{\mathrm{up}}/H_i)_{\mathrm{Th}}$ is the critical height given by Thorpe et al. (it corresponds to $\varphi(t^*_{\mathrm{crit}}, N, \mathrm{Ra}_T, A) = 1$).

Figure 13 gives the experimental values of the critical height as a function of the theoretical one. It shows that our experimental situation is more unstable than the uniform gradient one, a result that we already knew ([20]): $(z^*_{\mathrm{up}}/H_i)_{\mathrm{crit}} < (z^*_{\mathrm{up}}/H_i)_{\mathrm{Th}}$ $(0 < \varphi(t^*_{\mathrm{crit}}, N, \mathrm{Ra}_T, A) < 1)$.

The striking new result is that, for a given N, the points are located on a straight line. This feature shows that, in the range of parameters under study, the coefficient φ depends neither on A nor Ra_T but depends strongly on N: $\varphi(t^*_{\mathrm{crit}}, N, \mathrm{Ra}_T, A) = \varphi(t^*_{\mathrm{crit}}, N)$.

$\varphi(t^*_{\mathrm{crit}}, N)$ decreases as $|N|$ increases. Indeed, the solute gradients created in the upper zone are closely related to the structure of the boundary layers along the cold wall. For high $|N|$, the ascending dynamic layer along the cold wall is thicker than the solutal boundary layer. Consequently, the external part of the upward flow which feeds the lower region of the stagnant zone is at the bulk concentration, the same as the thermal cell. This feature entails weak solute gradients at the bottom of the stagnant zone and thus small values of $\varphi(t^*_{\mathrm{crit}}, N)$. On the contrary, for small values of $|N|$, the ascending dynamic layer is developed at the scale of the solutal boundary layer leading to values of $\varphi(t^*_{\mathrm{crit}}, N)$ close to unity.

By linear regression for each $|N|$ (Fig. 13), we obtain: $\varphi(t^*_{\mathrm{crit}}, N = -8) = 0.70 \pm 0.02$ (correlation coefficient $J = 0.90$),

$\varphi(t^*_{\text{crit}}, N=-23)=0.37\pm0.02$ (correlation coefficient $J=0.991$), $\varphi(t^*_{\text{crit}}, N=-75)=0.114\pm0.003$ (correlation coefficient $J=0.999$).

This behavior does not prevent $(z^*_{\text{up}}/H_i)_{\text{crit}}$, which depends on N as $\varphi(t^*_{\text{crit}}, N)\times|N|$ (Eq. 5.6), from increasing with $|N|$, as already put forward by Table 2.

6 Conclusion

The results on thermosolutal melting presented in this paper focuses on particularly interesting zones of the characteristic parameters, where no easy simplification can be made. Indeed, considering the phase change itself, dissolution is not completely overcome by melting. As for thermosolutal convection, neither solutal nor thermal forces are dominant at all scales. Concerning the melting front behavior, the most striking feature is the dependence of the front equilibrium only on the Stefan number, and, accordingly the dependence of both the mass and heat fluxes at the front on $\text{Ra}_S^{1/4}$. As for the flow structures, we could give a quantitative explanation of the build up and destabilization of the stagnant upper zone. It is interesting to notice that, even though the numerical model greatly simplifies the front behavior, destabilization of the flow structure could be very well accounted for by the simulations.

The main limitation of the present work is due to using one given mixture only. Experimenting several mixtures would have allowed us to better decorrelate Ste and N. The role of Le or Pr could also have been checked. In particular, the extension of these results to metallurgy, that would be of special interest, cannot be proposed. This study could also be extended using different mixtures to other values of N, in particular to small values that we could not reach with a satisfying precision.

But for all those extensions of our results, the best strategy would be to use numerical simulation, on the whole set of our experiments, of a more complete numerical model.

Nomenclature

A = H_i/L_i aspect ratio of the initial liquid area
C = local dimensional concentration in the liquid phase (wt percent)
C_i = initial concentration of the aqueous solution (wt percent)
C_L = liquid concentration at the interface (wt percent)
C_p = heat capacity, (J/kg °C)
D = mass diffusivity in the liquid (m^2/s)
Fo = $t^*\alpha/H_i^2$ Fourier number
g = gravitational acceleration (m/s^2)
H_i = initial height of the liquid area (m)
k = thermal conductivity in the liquid (W/m °C)
k_{Solid} = thermal conductivity in the solid (W/m °C)
Le = α/D Lewis number
L_f = latent heat of the ice (J/kg)
L_i = initial width of the liquid area
N = $\beta_C\Delta C/\beta_T\Delta T$ buoyancy ratio
Nu_C = local Nusselt number in the thermal cell
Nu_{ST} = local Nusselt number in the upper stagnant zone
Pr = ν/α Prandtl number
Ra_S = $N\,\text{Le}\,\text{Ra}_T$ solutal Rayleigh number
Ra_T = $g\beta_T\Delta TH^3/\alpha\nu$ thermal Rayleigh number
Sh = local Sherwood number
Ste = $c_p(T_i-T_L)/L_f$ Stefan number
$\text{Ste}^{\clubsuit}$ = $c_p\Delta T/L_f$ Stefan number
t^* = dimensional time (s)
t_C = dimensionless filling characteristic time
t_m = dimensionless melting characteristic time
T = local dimensional temperature in the liquid phase (°C)
T_i = temperature of the hot wall (°C)
T_L = liquid temperature at the interface (°C)
T_{Solid} = temperature in the solid phase (°C)
V^* = dimensional interface velocity (m/s)
V_C = $H_iV_C^*/\alpha$ dimensionless interface velocity in the convective zone
V_{ST} = $H_iV_{ST}^*/\alpha$ dimensionless interface velocity in the upper stagnant zone
$W_{\text{UP}}(t^*)$ = volume of the upper zone per unit depth (m^2)
$W_m(t^*)$ = melted volume per unit depth (m^2)
$W(t^*)$ = volume due to the shear stress extraction from the thermal cell per unit depth (m^2)
x^* = dimensional horizontal coordinate
z = W/H_iL_i dimensionless expression of W
z^*_{up} = dimensional height of the upper zone
$(z^*_{\text{up}}/H_i)_{\text{crit}}$ = experimental dimensionless height of the upper zone at the onset of destabilization
$(z^*_{\text{up}}/H_i)_{\text{Th}}$ = theoretical dimensionless height of the upper zone at the onset of destabilization

Greek Symbols

ν = kinematic viscosity of the fluid (m^2/s)
α = thermal diffusivity of the fluid (m^2/s)
ρ = density of the fluid (kg/m^3)
δ_S = characteristic thickness of the solutal boundary layer along the interface
δ_T = characteristic thickness of the thermal boundary layer along the interface
δ_I = thickness of the upward flow along the interface (m)
β_S = solutal expansion coefficient (wt percent^{-1})
β_T = thermal expansion coefficient ($°C^{-1}$)
ΔC = C_i-0 wt percent reference concentration difference in the liquid
ΔT = T_i-0°C reference temperature difference in the liquid

References

[1] Huppert, H. E., and Turner, J. S., 1980, "Ice Blocks Melting Into a Salinity Gradient," J. Fluid Mech., **100**, pp. 367–384.
[2] Huppert, H. E., 1990, "The Fluid Mechanics of Solidification," J. Fluid Mech., **280**, pp. 287–302.
[3] Prescott, P. J., and Incropera, F. P., 1994, "Convective Transport Phenomena and Macrosegregation During Solidification of a Binary Metal Alloy: I—Numerical Predictions," ASME J. Heat Transfer, **116**, pp. 735–741.
[4] Prescott, P. J., and Incropera, F. P., 1994, "Convective Transport Phenomena and Macrosegregation During Solidification of a Binary Metal Alloy: II—Experiments and Comparisons With Numerical Predictions," ASME J. Heat Transfer, **116**, pp. 742–749.
[5] Campbell, T. A., and Koster, J. N., 1994, "Visualizations of Liquid-Solid Interface Morphologies in Gallium Subject to Natural Convection," J. Cryst. Growth, **140**, pp. 414–425.
[6] Yin, H., and Koster, J. N., 2000, "Double Diffusive Convective Flow and Interface Morphology During Transient Ga-5 percent In Alloy Melting," J. Cryst. Growth, **217**, pp. 170–182.
[7] Tanny, J., 1995, "Experimental Study on the Crystallization of a Binary Melt at the Vertical Boundary of an Enclosure," Int. J. Heat Mass Transf., **38**, pp. 1141–1150.
[8] Wettlaufer, J. S., and Worster, M. G., 1997, "Natural Convection During Solidification of an Alloy From Above With Application to the Evolution of Sea Ice," J. Fluid Mech., **344**, pp. 291–316.
[9] Josberger, E. G., and Martin, S., 1981, "A Laboratory and Theoretical Study of the Boundary Layer Adjacent to a Vertical Melting Ice Wall in Salt Water," J. Fluid Mech., **111**, pp. 439–473.
[10] Carey, V. P., and Gebhart, B., 1982, "Transport Near a Vertical Ice Surface Melting in Saline Water: Some Numerical Calculations," J. Fluid Mech., **117**, pp. 379–402.
[11] Carey, V. P., and Gebhart, B., 1982, "Transport Near a Vertical Ice Surface Melting in Saline Water: Experiments at Low Salinities," J. Fluid Mech., **117**, pp. 403–423.
[12] Sammakia, B., and Gebhart, B., 1983, "Transport Near a Vertical Ice Surface Melting in Water of Various Salinity Levels," Int. J. Heat Mass Transf., **26**, pp. 1439–1452.
[13] Woods, A. W., 1991, "Fluid Mixing During Melting," Phys. Fluids A, **3**, pp. 1393–1404.
[14] Woods, A. W., 1992, "Melting and Dissolving," J. Fluid Mech., **239**, pp. 429–448.

[15] Kerr, R. C., 1994, ''Melting Driven by Vigorous Compositional Convection,'' J. Fluid Mech., **280**, pp. 255–285.
[16] Kerr, R. C., 1994, ''Dissolving Driven by Vigorous Compositional Convection,'' J. Fluid Mech., **280**, pp. 287–302.
[17] Sugawara, M., and Irvine, T. F., 2000, ''The Effect of Concentration Gradient on the Melting of a Horizontal Ice Plate From Above,'' Int. J. Heat Mass Transf., **43**, pp. 1591–1601.
[18] Beckerman, C., and Viskanta, R., 1988, ''Double-Diffusive Convection Due to Melting,'' Int. J. Heat Mass Transf., **31**, pp. 2077–2089.
[19] Beckerman, C., and Viskanta, R., 1989, ''An Experimental Study of Melting of Binary Mixtures With Double-Diffusive Convection in the Liquid,'' Exp. Therm. Fluid Sci., **2**, pp. 17–26.
[20] Bénard, C., Bénard, R., Bennacer, R., and Gobin, D., 1996, ''Melting Driven Thermohaline Convection,'' Phys. Fluids, **8**, pp. 112–130.
[21] Joly, D., 1998, ''Evolution de la structure des écoulements de convection thermosolutale, induite par fusion: Etude expérimentale,'' (in French) Thèse de l'Université Pierre et Marie Curie, Paris, France.
[22] Bejan, A., 1984, *Convection Heat Transfer*, John Wiley & Sons, New York.
[23] Thorpe, S. A., Hutt, P. K., and Soulsby, R., 1969, ''The Effect of Horizontal Gradients on Thermohaline Convection,'' J. Fluid Mech., **38**, pp. 375–400.
[24] Washburn E. W., ed., 1926, *International Critical Tables of Numerical Data, Physics, Chemistry and Technology*, National Academic Press.
[25] Bennacer, R., and Gobin, D., 1996, ''Cooperating Thermosolutal Convection in Enclosures: I—Scale Analysis and Mass Transfer,'' Int. J. Heat Mass Transf., **39**, pp. 671–681.
[26] Chen, C. F., Briggs, D. G., and Wirtz, R. A., 1971, ''Stability of Thermal Convection in a Salinity Gradient Due to Lateral Heating,'' Int. J. Heat Mass Transf., **14**, pp. 57–65.
[27] Chen, C. F., and Chen, F., 1997, ''Salt-Finger Convection Generated by Lateral Heating of a Solute Gradient,'' J. Fluid Mech., **342**, pp. 161–176.
[28] Kranenborg, E. J., and Dijkstra, H. A., 1998, ''On the Evolution of Double-Diffusive Intrusions Into a Stably Stratified Liquid: A Study of the Layer Merging Process,'' Int. J. Heat Mass Transf., **41**, pp. 2743–2756.
[29] Dijkstra, H. A., and Kranenborg, E. J., 1998, ''On the Evolution of Double-Diffusive Intrusions Into a Stably Stratified Liquid: The Physics of Self-Propagation,'' Int. J. Heat Mass Transf., **41**, pp. 2113–2124.
[30] Thangam, S., Zebib, A., and Chen, C. F., 1981, ''Transition From Shear to Sideways Diffusive Instability in a Vertical Slot,'' J. Fluid Mech., **112**, pp. 151–160.
[31] Young, Y., and Rosner, R., 1998, ''Linear and Weakly Nonlinear Analysis of Doubly Diffusive Vertical Slot Convection,'' Phys. Rev. E, **57**, pp. 5554–5563.
[32] Kerr, O. S., and Tang, K. L., 1999, ''Double-Diffusive Instabilities in a Vertical Slot,'' J. Fluid Mech., **392**, pp. 213–232.
[33] Hart, J. E., 1971, ''On Sideways Diffusive Instability,'' J. Fluid Mech., **49**, pp. 279–288.
[34] Mergui, S., and Gobin, D., 2000, ''Transient Double Diffusive Convection in a Vertical Enclosure With Asymmetrical Boundary Conditions,'' ASME J. Heat Transfer, **122**, pp. 598–602.

Heat Transfer Enhancement by Delta-Wing-Generated Tip Vortices in Flat-Plate and Developing Channel Flows

M. C. Gentry[1]
Graduate Research Assistant

A. M. Jacobi
Professor of Mechanical Engineering

Department of Mechanical and Industrial Engineering,
University of Illinois at Urbana-Champaign,
Urbana, IL 61801

Using delta wings placed at the leading edge of a flat plate, streamwise vortices are generated that modify the flow; the same wings are also used to modify a developing channel flow. Local and average measurements of convection coefficients are obtained using naphthalene sublimation, and the structure of the vortices is studied using flow visualization and vortex strength measurements. The pressure drop penalty associated with the heat transfer enhancement of the channel flow is also investigated. In regions where a vortex induces a surface-normal inflow, the local heat transfer coefficients are found to increase by as much as 300 percent over the baseline flow, depending on vortex strength and location relative to the boundary layer. Vortex strength increases with Reynolds number, wing aspect ratio, and wing attack angle, and the vortex strength decays as the vortex is carried downstream. Considering the complete channel surface, the largest spatially averaged heat average heat transfer enhancement is 55 percent; it is accompanied by a 100 percent increase in the pressure drop relative to the same channel flow with no delta-wing vortex generator. [DOI: 10.1115/1.1513578]

Keywords: Convection, Enhancement, Heat Transfer, Vortex

Introduction

The performance of liquid-to-air and two-phase-to-air heat exchangers is important in many applications, including thermal management and processing systems found in the air-conditioning, automotive, refrigeration, chemical, and petroleum industries. Improving the performance of these heat exchangers can lead to a smaller surface-area requirement, reduced material cost, and a lower heat exchanger mass. Furthermore, improving heat exchanger performance can have a significant impact of the environment through improvements in energy efficiency. The total thermal resistance in these heat exchangers can be considered as the sum of three contributions: the liquid or two-phase convective resistance, the wall conductive resistance, and the air-side convective resistance. The air-side convective resistance is typically the dominant resistance to heat transfer [1] and efforts to improve these heat exchangers should focus on the air-side heat-transfer behavior.

Vortex generation is a technique that holds promise in air-side heat transfer enhancement. In this method, streamwise vortices (longitudinal vortices) are passively generated using surface modifications such as those shown in Fig. 1; such a flow manipulator is called a vortex generator (VG). Considerable research has been directed at VG-enhanced heat transfer; however, the complexity of the VG-heat-exchanger design space has made a complete understanding of the vortex flow and heat transfer interactions difficult to develop. The overall goal of this research is to provide experimental data and an interpretive framework that add to our understanding of VG-enhanced heat exchanger performance.

Literature Review

Extensive reviews of progress in heat transfer enhancement using streamwise vortices have been provided by Jacobi and Shah [2] and Fiebig [3,4][2]. The review presented below will focus on work directly related to this research, with a focus on establishing a clear context for the research objectives articulated later in the paper.

VG-Enhanced Flat-Plate Flows. Turk and Junkhan [5] evaluated the heat transfer impact of multiple rectangular-winglet VGs with various aspect ratios and attack angles mounted at the leading edge of a flat plate. They considered flows with a zero and favorable pressure gradient and reported that heat transfer enhancement generally increased with a favorable pressure gradient. They reported spanwise-averaged, local enhancements as high as 250 percent in a laminar flow. Turk and Junkhan provided no flow measurements or data on vortex location or strength, and it is thus difficult to explain the heat transfer results in terms of vortex interactions with neighboring vortices and the surface. In a closely related study, Torii et al.[6] investigated the local heat transfer downstream of a single delta-winglet VG on a flat plate. They used single-component, hot-wire anemometry to measure the streamwise velocity and conducted flow visualization to study the flow field. Heat transfer was studied using surface thermocouples with an imposed heat flux, and naphthalene sublimation in a small region (2.5 wing chords) downstream from the VG. Local heat transfer enhancements of over 200 percent were reported in the downwash region of the vortex flow. The experiments were all performed at a constant freestream velocity of 4 m/s, and the pressure-drop penalty associated with the enhancement was not reported. Since a delta-winglet VG was used, only a single tip vortex was generated, and consequently vortex-vortex interactions and their effect on surface heat transfer were not evaluated. Fur-

[1]Currently, Senior Research Engineer, ExxonMobil Upstream Research Company, Houston, TX 77252.

Contributed by the Heat Transfer Division for publication in the JOURNAL OF HEAT TRANSFER. Manuscript received by the Heat Transfer Division August 24, 2001; revision received June 26, 2002. Associated Editor: Kenneth S. Ball.

[2]A monograph collecting papers from a 1996 meeting on this topic is available as *Vortices and Heat Transfer. Results of a DFG-Supported Research Group (Notes on Numerical Fluid Mechanics Vol. 63)*, by M. Fiebig and N. K. Mitra, Springer-Verlag, Berlin, 2001. ISBN 3540415580.

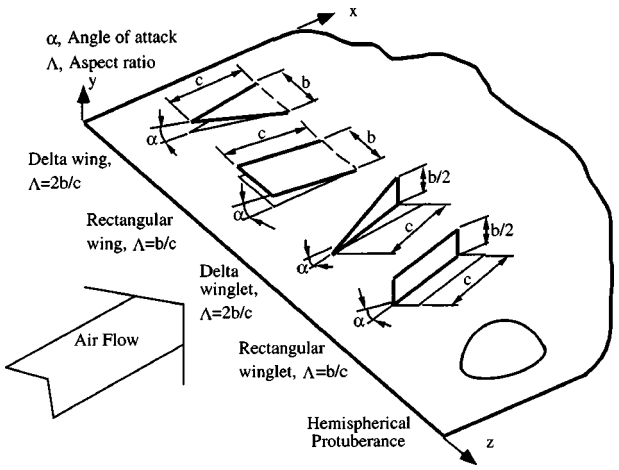

Fig. 1 Flow manipulators used as vortex generators to enhance heat transfer, along with the relevant geometrical definitions (adapted from Ref. [2])

thermore, due to the highly three-dimensional nature of the flow the streamwise velocity data are of limited value; they provide information on vortex location but not strength. Yanagihara and Torii [7] extended their earlier work by investigating multiple delta-winglet vortex generators. They concluded that arrays producing counter-rotating pairs of streamwise vortices are best for heat transfer. Again all measurements were performed at the same freestream velocity, and no pressure-drop data were presented. Even though multiple vortices were being generated, the interactions between neighboring vortices and the resulting effects on surface heat transfer were not discussed.

Gentry and Jacobi [8] studied the interactions between streamwise vortices induced by a delta-wing VG and the laminar boundary layer on a flat plate. They used quantitative flow visualization and naphthalene sublimation to study flow and heat transfer interactions. Using scaling arguments they asserted that a strong vortex located near the edge of the thermal boundary layer would produce maximum heat transfer enhancement. Then, with a potential flow model of vortex-vortex and vortex-surface interactions, they identified promising VG designs for this simple flat-plate flow. The sublimation data were used to prove the predictive ability of their approach. Because only surface-averaged sublimation data were obtained, no measurements of vortex strength were reported, and pressure drop was estimated from theory, the study provided a limited understanding of VG enhancement for a simple geometry.

There have been a number of studies of VG-enhanced heat transfer to a turbulent boundary layer. Eibeck and Eaton [9] studied a single vortex and, using a Rankine vortex model and velocity data, they interpreted their data in terms of vortex circulation and boundary-layer thickness. Pauley and Eaton [10] extended this work to consider vortex pairs. For common-inflow pairs, the vortices spread and lifted from the surface; whereas, common-outflow pairs moved together and lifted from the surface more rapidly than the common-inflow vortex pair. Corotating pairs moved together and coalesced into a single vortex as they were advected downstream. This research on streamwise vortices in turbulent boundary layers provides useful insights into vortex-vortex and vortex-surface interactions and their impact on heat transfer; however, because of the dramatic differences between laminar and turbulent flows, these results cannot be trivially extended to the low-Reynolds-number laminar flow conditions typical to compact heat exchangers.

VG-Enhanced Channel Flows. Fiebig et al. [11] studied heat transfer enhancement using delta and rectangular wings and winglets in flat-plate channels for Reynolds numbers between 1360 and 2270 based on plate spacing. Wings with an aspect ratio of 1.25 and winglets with an aspect ratio of 1.00 were evaluated, and the channel height was constant at 40 mm. They reported that the delta-wing VG provided local enhancements as high as 200 percent and was more promising than the winglets. Overall Colburn j factors were increased by 20 to 60 percent at a Reynolds number of 1360 for delta wings with attack angles from 10 deg to 50 deg. The VG-induced pressure drop was reported to be independent of VG type and proportional to projected wing area. In 1991, Fiebig et al.[12] extended this work by considering a broader range of VG designs. They used delta and rectangular wings and winglets with aspect ratios from 0.8 to 2.0, angles of attack from 10 deg to 60 deg, for Reynolds numbers from 1000 to 2000. They again reported local heat transfer enhancements greater than 200 percent immediately behind a delta-wing vortex generator and a 60 percent increase in drag. In all of this work, however, no measurements of vortex strength were reported, and heat transfer data were only presented for one side of the channel (the side with the vortex generator)—the effect of the vortices on the facing surface was neglected. Local heat transfer data were presented along the centerline of the fin extending from the center of the wing span to the end of the plate. Since the VGs create two tip vortices, a single measurement along the centerline does not capture the local effect of these vortices on surface heat transfer. Detailed local measurements of surface heat transfer are required to accurately evaluate the interaction between these vortices and the surface

A numerical study was performed by Brockmeier et al. [13] to evaluate the impact of delta-wing and delta-winglet VG in flat-plate channels. A delta wing with an aspect ratio of one was considered, with attack angles from 10 deg to 50 deg and Reynolds numbers from 1000 to 4000. With delta winglets at a 30 deg angle of attack, an average increase of 84 percent in the Nusselt number was predicted at a Reynolds number of 4000. No pressure drop predictions were presented. The results of this paper are very limited because of the small size of the computational domain. The channel length extended only 1.31 wing chord lengths downstream from the wing. Although detailed distributions of velocity, vorticity, and temperature were presented, these results are valid only for a distance downstream slightly larger than the wing chord itself. The incoming flow used in the computation was a fully developed, laminar channel flow, while the temperature field was modeled as developing. Biswas et al. [14] presented a comparison of numerical to experimental data for vortex-enhanced, fully developed, laminar channel flow. The vortices were generated with a delta winglet. The experiments and simulations were conducted at a single Reynolds number of 1580 based on channel height, with winglet attack angles of 15 deg, 30 deg, and 45 deg. Since a delta winglet was used, only one strong tip vortex was generated, so interactions between neighboring vortices were not investigated. Comparisons of the computed and measured streamwise velocity fields showed relatively good agreement between the simulations and the experiments. The experiments and the computations showed the same flow structures, but the magnitude of the velocities differed by as much as 20 percent. No local heat transfer results were presented; instead, the computed, spanwise-average Nusselt number for the side of the channel with the vortex generator was presented as a function of streamwise distance in the channel. A peak in the spanwise-averaged heat transfer was reported immediately downstream of the generator, and the enhancement decayed downstream. Fanning friction factors were computed to predict pressure drop performance of the channel flow. All the computations were confined to a channel extending less than 4 winglet chords downstream from the trailing edge of the winglet. The effect of streamwise vortices extends much farther downstream.

Closure. For laminar, flat-plate flow and channel flows, no measurements of vortex strength have been presented in the literature; this lack of data has limited our understanding of vortex-vortex and vortex-surface interactions, and without detailed local

heat transfer and flow measurements relating the flow structures to the surface heat transfer behavior, the understanding of vortex generation on flat-plate and channel flows remains incomplete. Although some numerical work has helped to fill this experimental gap, the numerical results are limited by the small computational domains and unrealistic flow assumptions (e.g., fully developed approach flow). Furthermore, it is a significant shortcoming that no local or average heat transfer measurements have been presented for the channel wall opposite to that upon which the VG is mounted. The vortex flow interacts with both sides of the channel, so investigating the surface heat transfer from both sides of the channel is important.

The primary objective of this research is to obtain an increased understanding of the flow structures, heat transfer enhancement, and pressure drop penalty encountered in wing-based vortex generation. This understanding will be obtained by focusing on the interactions between neighboring vortices and between vortices and the surface for both laminar flat-plate and developing channel flows. This study was pursued through an experimental approach. Local and average mass transfer measurements were obtained using the naphthalene sublimation technique. The flow structures were measured with quantitative flow visualization and a vane-type vortex meter. The pressure drop penalty associated with the heat transfer enhancement was also quantified. Experiments were performed for a variety of fin and vortex generator configurations over a range of flow conditions for laminar, flat-plate and laminar, developing channel flows. Since a primary application of this research is improving air-side heat transfer performance in compact heat exchangers, the experimental parameter space was designed so that the study spanned conditions typical to those applications.

Experimental Apparatus and Methods

Apparatus. Mass transfer and pressure drop experiments were performed in the wind tunnel shown schematically in Fig. 2. The wind tunnel had an elliptical inlet contraction with a 9:1 area ratio, and the flow was conditioned with a hexagonal cell, aluminum honeycomb and stainless steel screens. The flow area in the test section was 15.2×15.2 cm. Using a 20 μm hot-wire anemometer, the freestream velocity profile in the test section was determined to be flat to within 3 percent over the entire range of the experiments, and the freestream turbulence intensity ranged from approximately 1.1 percent to 2.3 percent, with an average value of approximately 1.6 percent over the freestream velocities used in these experiments. During experiments, the velocity was measured using an ASME Standard orifice plate (see Gentry and Jacobi [15]).

The naphthalene sublimation technique has been used extensively to study convection, and others have presented extensive reviews of the method [16,17]. Specimens are constructed of naphthalene, and direct measurements of sublimation from the specimens yield local and average mass transfer coefficients. In the current work, local sublimation depths were measured using a non-contact, optical technique known as laser triangulation. Our use of laser triangulation to determine sublimation depths is described in detail elsewhere [18], and on the basis of our earlier work, a 2-σ sublimation-depth uncertainty of ±6 μm is attained. As a redundant check, average mass transfer data were also obtained using an electronic balance ($\pm10^{-4}$ g) to measure specimen mass change during the wind-tunnel exposure. If the integrated local data and mass change measurements agreed to within 10 percent the data were deemed satisfactory. Agreement to within 5 percent was typical, and very few experiments were rejected. The cause for rejected data was usually easy to identify (e.g., the naphthalene specimen was accidentally chipped during placement, etc.).

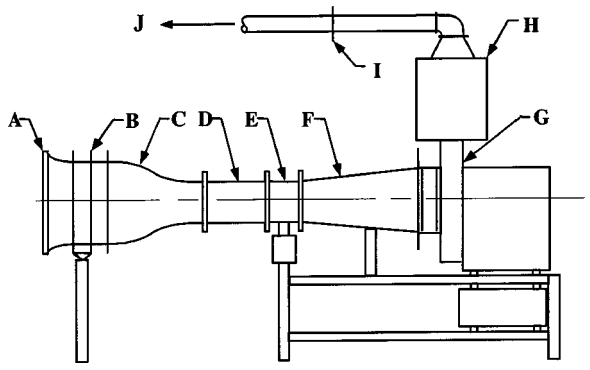

Fig. 2 Wind tunnel, with the following components: (A) inlet, (B) honeycomb and screens, (C) contraction, (D) test section, (E) instrumentation access, (F) transition, (G) blower, (H) acoustic plenum, (I) flow measurement section, and (J) discharge to outside laboratory

Aluminum plates were used for the experiments; they spanned the test section, were 11.4 cm long and 3.2 mm thick. For flat-plate experiments, one plate was fixed in the center of the test section; for developing channel-flow experiments, 17 identical plates were installed, yielding 16 parallel channels with a channel height of 5.4 mm. For sublimation experiments, naphthalene was cast into a cavity in the plates. The leading edge had a very thin (0.5 mm) lip to protect the leading-edge naphthalene from excessive sublimation. This lip introduced a very small ''unheated starting length'' because the velocity boundary layer started upstream of the concentration boundary layer; however, the magnitude of the error associated with the unheated starting length was determined to be negligible over the entire range of the experiments [15].

Flow visualization and vortex measurements were made in the closed-loop water tunnel typical to the wind tunnel and described in detail by Gentry and Jacobi [15]. Water was pumped from a return plenum to a flow conditioning section where screens and a honeycomb were used to shape the flow before it entered the contraction and test section. The water tunnel test section was typical to that used in the wind tunnel. The velocity in the water tunnel was measured by recording the time required for a dye marker to traverse a known distance. The water tunnel was equipped with gravity-feed dye reservoirs and a needle valve to control the dye injection rate. Images were recorded using a 35 mm camera and later digitized for analysis.

Measuring Vortex Strength. Vortex strength was determined using two different techniques. The first method was a direct measurement using the vane-type vortex meter shown schematically in Fig. 3. This vortex meter was constructed using a hollow stainless steel tube with 0.36 mm ID and 0.61 mm OD; the tube was configured with a 90 deg bend, as shown in the figure. A wire was inserted into the hollow tube, so that a blind hole 0.36 mm in diameter and about 3 mm in depth was formed in the end of the tube. Two vanes were formed by fixing aluminum foil ($2\times2\times0.07$ mm) to a small shaft (6 mm long, with a 0.2 mm diameter); thus, the shaft protruded 4 mm beyond the edge of the foil vanes, and its free end was inserted into the blind hole in the end of the hollow tube. This arrangement prevented the vanes from contacting the end of the hollow tube. In order to minimize friction between the shaft and the blind hole, a non-water-soluble based lubricant was applied. The vanes of the vortex meter were marked so an unambiguous measure of rotational speed was obtained using a stroboscopic lighting system.

The strength of the vortices was determined by measuring the rotation rate of the vortex meter while it was in the vortex tube. In order to know the location of the vortices, data were obtained while the flow structures were being visualized with ink. Measurements were conducted for the same flow conditions with and without the ink and the results differed by less than the experimental

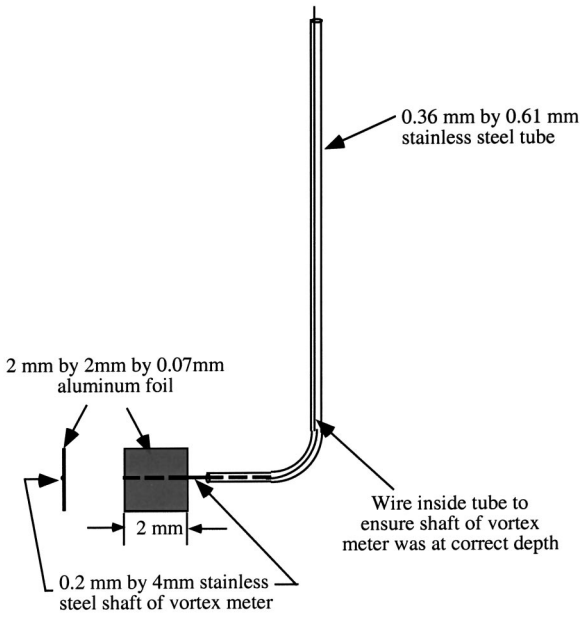

Fig. 3 This vane-type vortex meter was constructed using a small steel shaft, wire, a hypodermic needle, and small pieces of foil, sized to fit within the Thomson–Rankine vortex core

uncertainty (discussed later). The velocity distribution within a vortex can be modeled using the Thomson-Rankine vortex model [19]. In the forced region

$$V_\theta = \frac{\Gamma r}{2\pi a^2} \quad \text{for } r < a. \tag{1}$$

In the free vortex region

$$V_\theta = \frac{\Gamma}{2\pi r} \quad \text{for } r \geqslant a. \tag{2}$$

The radius, a—where V_θ is a maximum—was estimated using flow visualization and local mass transfer data[3], and it was found to be 1 to 1.2 mm ($\pm$0.2mm) over the entire parameter space. Thus, with the axis of the vortex meter is placed at the center of the vortex tube, the vanes of the meter are just inside the forced region, and the vortex meter can be used to estimate the circulation by re-arranging Eq. (1) or Eq. (2), with the radius of the vortex meter $r_{vm} = r \approx a$

$$\Gamma \approx 4\pi^2 r_{vm}^2 N \tag{3}$$

where N is the rotation rate of the vortex meter. Values of circulation obtained with the vortex meter and Eq. (3) will be compared to values estimated from the technical literature on delta wings and to the second method used in this study.

The second method for determining vortex strength relies on a potential-flow model and flow visualization to infer vortex strength from the observed trajectories of the vortices. In the flat-plate flow, the core-to-core and core-to-plate distances were determined from flow visualization images at streamwise locations of 1, 3, 5, 7, 9, and 11 cm from the leading edge. The core velocity in the y direction for a vortex is due to its interaction with the other vortices and the surface. With reference to Fig. 4, using the method of images and superposition, the y-velocity of vortex a can be written as follows:

[3]This evaluation was made by locating the center of the vortex using flow visualization and measuring the distance from the center of the vortex to the region of maximum heat transfer found from the local mass transfer data presented later in the paper. It was assumed the maximum local heat transfer coincided with the maximum surface-normal velocity.

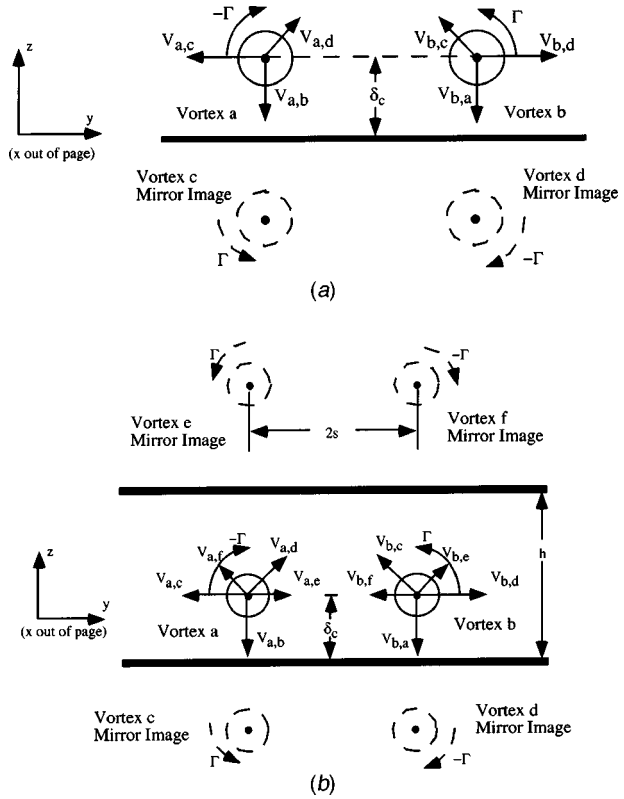

Fig. 4 A schematic showing tip vortices and their images, with induced velocities denoted as V_{ij} for the velocity of vortex i induced by vortex j: (*a*) vortices over a flat plate, and (*b*) vortices in a channel flow, where only the first-order image vortices are shown (images of images are neglected)

$$V_{a,y} = \frac{\Gamma}{4\pi\delta_c}\left(\frac{\gamma^2}{\gamma^2+1} - 1\right) \tag{4}$$

where $\gamma = \delta_c / s$. The y-velocity can be approximated as $V_{a,y} \approx \Delta y / \Delta t$, and assuming the vortex tube to move with the fluid (see Batchelor [20]) at a convective velocity equal to the freestream velocity, the transit time is approximated as $\Delta t \approx \Delta x / U_\infty$. Then, Eq. (4) may be re-written as

$$\Gamma \approx \frac{4\pi\delta_c U_\infty \cdot \dfrac{\Delta y}{\Delta x}}{\dfrac{\gamma^2}{\gamma^2+1} - 1} \tag{5}$$

Using the flow visualization to determine vortex trajectory, and thus Δy and Δx, an estimate of the vortex circulation is obtained from Eq. (5) for the flat-plate flow.

For a channel flow, the same idea can be invoked; however, the geometry and algebra are somewhat more complex, as shown in Fig. 4, and an infinite number of mirror vortices results. A first-order approximation can be obtained by considering only the first set of mirror-image vortices and neglecting the interactions between the image vortices (see Gentry and Jacobi [15] for further detail)

$$\Gamma \approx \frac{4\pi\delta_c U_c \cdot \dfrac{\Delta y}{\Delta x}}{\dfrac{\gamma^2}{\gamma^2+1} - 1 + \dfrac{1}{\sigma - 1} - \dfrac{\gamma^2(\sigma-1)}{(\sigma-1)^2\gamma^2 + 1}} \tag{6}$$

where U_c is the velocity in the channel, δ_c is the distance from the vortex core to the surface to which the vortex generator was at-

tached, and σ is the ratio of channel height to δ_c. Equation (6) is valid only for the region of the flow before the vortex reaches its equilibrium location along the channel centerline.

The uncertainty in circulation measurements obtained using the vortex meter is mainly due to uncertainty in core size, the assumed Thomson-Rankine model, the assumption that $r_{vm}=a$, and friction on the vane shaft. It is extremely difficult to assess this uncertainty. An insufficient number of data prohibits statistical analysis, and we did not construct meters of varying vane sizes to explore sensitivity to instrument design. Nevertheless, from our experience with the meter we believe a conservative estimate of the circulation uncertainty is +30 percent, −15 percent, due to geometrical-friction and geometrical effects, respectively. It is important to note that data obtained with the vortex meter mainly served as an independent check of circulation obtained from vortex trajectory data. Uncertainty in circulation data obtained using the vortex-trajectory method can be determined in a straightforward manner, using length-scale and velocity uncertainties and standard propagation of error methods with Eqs. (5) and (6). For the experiments to be reported later, this method has an uncertainty of less than 10 percent in Γ.

Interpreting Mass Transfer Data. Naphthalene sublimation experiments were performed, and local and average Sherwood numbers were obtained from sublimation data in the standard way (see [16] and [17]). However, in these experiments the specimen had a constant naphthalene test area, and VGs of varying size were tested. Larger VGs produced flow structures the affected a greater portion of the test area, giving an apparent advantage to larger vortex generators in surface-averaged results. A similar situation arises when the pressure drop experiments are conducted with a fixed number of vortex generators per channel. In order to compare the impact of different-sized VGs on an equal basis, the results are scaled to the affected span of the VG. That is, heat transfer enhancement and pressure-drop data are based on the ''repeatable'' span affected by each VG. In this way, the results are general. The results in heat transfer enhancement and pressure-drop penalty will represent the maximum that could be obtained, were many VGs placed at the repeatable span along the leading edge of a fin (typical to application). The results can also be used to predict other VG arrangements by partitioning the fin into a VG-enhanced and an unenhanced area. Therefore, this presentation based on a repeatable span is the most general approach and overcomes VG-size and area ambiguity. This approach requires that the repeatable span be measured.

The area affected by the vortices generated by a particular VG was determined from the flow visualization measurements, local naphthalene data, and experiments with multiple vortex generators. Then, the data are interpreted in an area-weighting scheme as

$$\overline{\mathrm{Sh}}A_T=\overline{\mathrm{Sh}}_eA_e+\overline{\mathrm{Sh}}_oA_o \tag{7}$$

and

$$\Delta PA_T=\Delta P_eA_e+\Delta P_oA_o\,. \tag{8}$$

$\overline{\mathrm{Sh}}_e$ is the Sherwood number for the area influenced by the vortices, A_e is the area of the naphthalene affected by the vortex, $\overline{\mathrm{Sh}}_o$ is the Sherwood number for the area unaffected by the vortices and A_o is the area of the naphthalene section not affected by the vortices. For the experiments to be reported now, the affected areas ranged from 15 to 25 cm^2 with an uncertainty of ±4 percent as reported by Gentry and Jacobi [15][4]. The total Sherwood number, $\overline{\mathrm{Sh}}$, and the baseline $\overline{\mathrm{Sh}}_o$, were measured directly. The total area was the naphthalene-test area of $A_T=34.8\,\mathrm{cm}^2$. With A_e known from the experiments, and with $A_o=A_T-A_e$, the only unknown remaining in Eq. (7) is $\overline{\mathrm{Sh}}_e$. The average mass transfer data are presented as $R_{\mathrm{Sh}}=\overline{\mathrm{Sh}}_e/\overline{\mathrm{Sh}}_o$, and this ratio is the enhancement factor for the area affected by the vortex. It should be noted that changing A_e by 10 percent leads to a maximum 6 percent change in the R_{Sh} values reported later. The pressure drop results can be analyzed in an analogous way; the results are presented as a pressure drop ratio, $R_p=\Delta P_e/\Delta P_o$.

Mass-averaged and local mass transfer, flow visualization, vortex strength, and pressure drop experiments were conducted for flat-plate and developing channel flows using delta-wing vortex generators with aspect ratios ranging from 0.5 to 2.0 and attack angles from 15 deg to 55 deg. The Reynolds numbers were chosen to represent conditions typically encountered in compact heat exchangers, and the inverse Graetz number was monitored to ensure that developing conditions existed throughout the channel flow experiments. Uncertainty in vortex circulation was discussed earlier. Uncertainty in local Sherwood numbers depends on the local sublimation depths and ranged from about 20 percent in regions of low Sh to 5 percent in regions of high Sh. The Sh uncertainty at a typical sublimation depth of 60 μm was approximately 10 percent. The highest local uncertainties occur on the periphery of the test specimen, and the lowest uncertainties occur in the vicinity of the vortices; thus, the best resolution is obtained in the region of interest.

Results and Discussion

Laminar Flat-Plate Flow. The flow visualization experiments revealed that under certain conditions a wavy, periodic character was manifest by the tip vortices, as shown in Fig. 5. The onset of this waviness in the vortex occurred when the core-to-plate distance was approximately equal to the laminar boundary layer thickness. Vortices that remained outside the boundary layer did not exhibit waviness. To our knowledge, there has been no prior report of this behavior in VG-enhanced flat-plate flows. We hypothesize that it is caused by a ''fluid buckling'' instability. It is well established that the axial core velocity in the delta-wing-generated vortex is slightly less than the freestream velocity. Thus, outside the boundary layer the core is in a state of ''tension''; however, as the boundary layer develops and the vortex flows into a region of slow-moving fluid, it enters a state of ''compression''. Using the approach of Bejan [21], the characteristic wavelength of the buckling instability is found to be about twice the diameter of the vortex streamtube, which we take to be twice the core-to-plate distance. The observed wavelengths and relative location of the vortex with respect to the boundary layer are presented in Table 1 in dimensionless form, and these results support the buckling-instability hypothesis. Alternate explanations for this waviness ex-

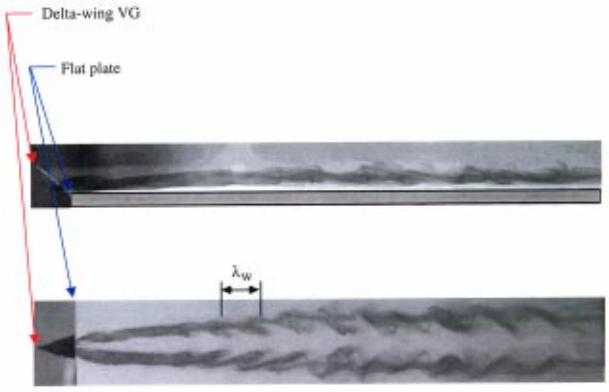

Fig. 5 Two views of an image recorded using dye-in-water visualization, showing instability in vortices generated by a delta-wing VG at the leading edge of a flat plate, with $\Lambda=1.25$, $\alpha=35$ deg, and $\mathrm{Re}_c=1300$. The λ_w periodicity corresponds roughly to that predicted using the buckling instability theory of Bejan [21].

[4]Note that the delta wings all had a chord of $c=1$ cm, and for $0.25<\Lambda<2$, the wing span was set to $0.25<b<1$ cm. The planform area of the delta wing varied from 0.8 percent to 3 percent of the affected area, and it was always less than 0.5 percent of the naphthalene test area, A_T.

Table 1 Observed characteristic wavelengths in vortex tube waviness and core height-to-boundary layer thickness ratio at onset of waviness for tip vortices above a flat plate The estimated uncertainties in λ_w/d_ν and δ_c/δ are 14 percent and 10 percent, respectively.

Flow Conditions	λ_w/d_ν, Data [-]	δ_c/δ at onset of waviness [-]
Re_c=300, Λ=1.25, α=35°	2.14	0.84
Re_c=300, Λ=2.00, α=35°	2.28	0.83
Re_c=300, Λ=1.25, α=15°	2.30	0.87
Re_c=800, Λ=0.5, α=35°	2.6	0.88
Re_c=800, Λ=1.25, α=35°	2.5	0.90
Re_c=800, Λ=2.0, α=15°	2.28	0.88
Re_c=800, Λ=0.5, α=35°	2.83	0.93
Re_c=1300, Λ=0.5, α=35°	2.5	0.83
Re_c=1300, Λ=1.25, α=15°	2.2	0.93
Re_c=1300, Λ=1.25, α=35°	2.5	0.92

ist: it may be due to a shear-layer instability caused by the velocity field distortion of the vortex. However, because it is clearly linked with the vortex entering the boundary layer, the instability is not due to conventional vortex breakdown (see Panton [22]) or direct inviscid interaction of the vortex with the surface (the well-known Crow instability [22]).

All the tip vortices traveled down the plate with the same general trajectory. Initially, the vortices are close together and interact strongly with each other, and in this counter-rotating configuration they induce each other to move toward the flat plate. As the vortices get closer to the surface, interaction with the surface becomes important and causes the vortices to spread apart (this interaction may be visualized using the method of images). The induced velocity toward the plate becomes weaker as the vortices spread apart, and they are slowly advected away from the plate by the small vertical velocity of boundary layer growth. Peace and Riley predicted this vortex trajectory in their computations [23].

Vortex strength and location are both important to the heat transfer effects of the VG enhancement. The dimensionless vortex circulation is shown as a function of Re_x for various wing aspect ratios, attack angles, and Re_c in Fig. 6. Data from both methods of measuring vortex strength are shown in the figure. Apparently, the strength of the vortices increases significantly with wing aspect ratio and decreases as the vortices flow downstream. Clearly, stronger vortices are generated at higher Re_c and higher attack angles. The increase in vortex strength with attack angle is not as pronounced as the increase observed with increasing Re_c and Λ. Data could not be obtained for flow conditions leading to vortex breakdown, and at the lowest attack angles it was impossible to obtain data with the vortex meter. The difference between the vortex meter and the vortex-trajectory measurement was 11 percent at Re_c=1300 and 2.5 percent at Re_c=800; this agreement supports the reliability of the vortex strength data. Further support for these data can be drawn from comparisons to the literature. Peace and Riley [23] provide numerical predictions for circulation as a function of time for a vortex pair approaching a flat surface. By assuming a convective velocity equal to the freestream, these predictions can be interpreted as the decay in circulation while vortices are carried the length of the test plate. For Λ=1.25, α=35 deg, and Re_c=1300, the numerical prediction gives a 64 percent

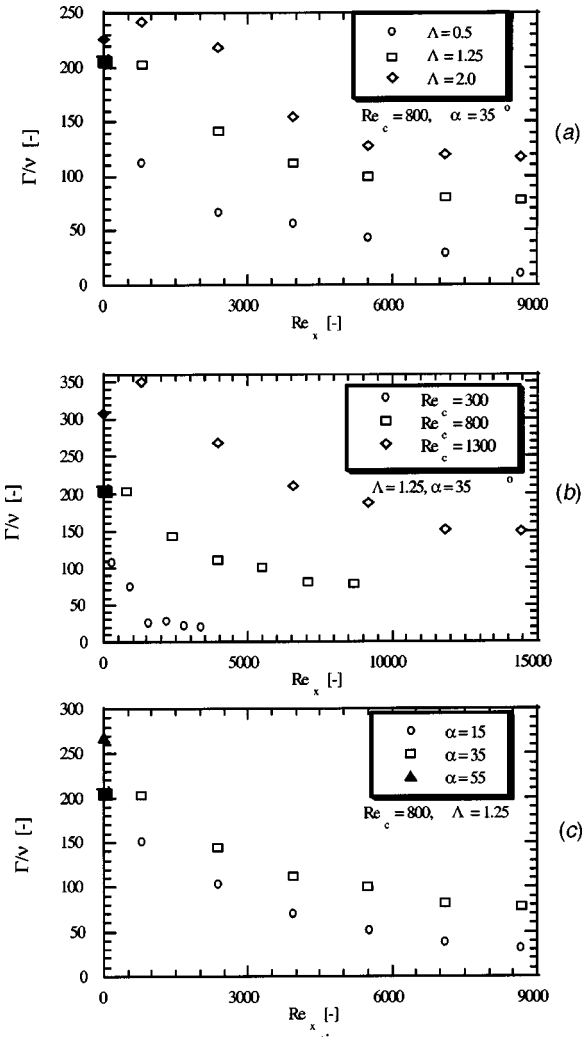

Fig. 6 Measured vortex circulation as a function of position downstream from the leading edge of a flat plate, over a range of (*a*) VG aspect ratio, (*b*) Re_c, and (*c*) VG attack angle. Closed symbols were obtained with the vane-type vortex meter, and open symbols were obtained from the flow visualization data.

decay in circulation, and our experiments show a 57 percent decay. At Re_c=800 and 300, the numerical and experimental results give decays of 65 percent compared to 60 percent, and 71 percent compared to 81 percent, respectively. General support is also provided by comparisons to the free delta-wing data of Pohlhamus [24], which give circulations 10 percent higher than the vortex-trajectory data of Fig. 6 (at the first measurement location). For other conditions, the free-wing data were an average of almost 20 percent higher than the current vortex-trajectory data. These comparisons provide further support to the validity of the new data, and although this support is indirect, it is consistent.

Surface plots of R_{Sh} are presented in Fig. 7, where the black points are measurements, and the surface was constructed using a bi-quadratic, least-squares regression to the data. The enhancement effect of the vortices generally increases with aspect ratio, attack angle, and Reynolds number, with R_{Sh}=1.4, 1.6, and 1.8 at Re_c=300, 800, and 1300, respectively. The surface plots presented in Fig. 7 are all for the same ratio of plate length to wing chord; however, it may be of interest to consider the enhancement as a function of L/c, especially if such a consideration suggests an optimal VG size or fin length. Although L and c were held constant in the experiments, R_{Sh} can be determined as a function of $x_L=L/c$ by integrating the local data over varying streamwise

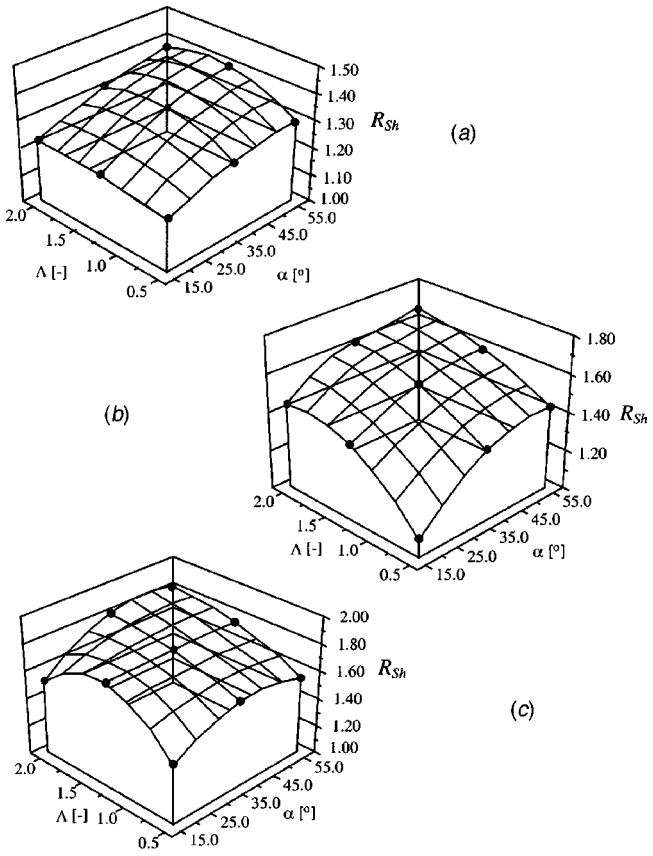

Fig. 7 Sherwood number enhancement for a flat-plate flow as a function of VG aspect ratio and attack angle at (*a*) Re_c=300, (*b*) Re_c=800, (*c*) Re_c=1300

distances. The results are shown in Fig. 8 for α=35 deg, Λ=1.25, Re_c=1300; the local data were integrated over the affected area, and the baseline data were obtained by integrating local data that were unaffected by the vortices. For very short integration lengths, the impact of the vortices is small because the thin boundary layers give rise to high mass transfer rates. As the plates length increases, the effect of the vortices on average mass transfer is more significant with a maximum of R_{Sh}=2.1 at Re_{x_L}=5000, and x_L=3.8 cm. The value of R_{Sh} decreases at downstream locations because the vortices weaken as they are advected downstream.

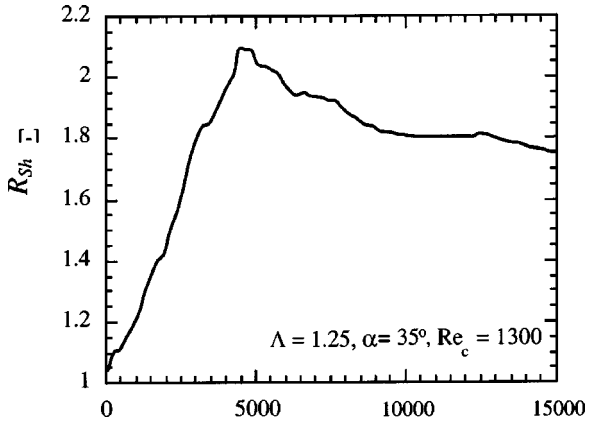

Fig. 8 Spatially averaged enhancement ratio for the flat-plate flow as a function Reynolds number based on integration length, with Λ=1.25, α=35 deg, and for Re_c=1300

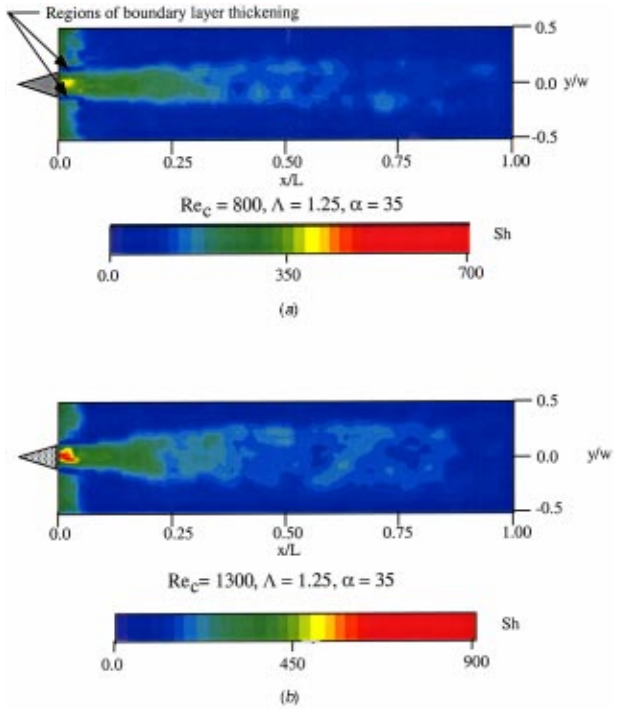

Fig. 9 Local Sherwood number distribution for a delta wing attached to a flat plate, with Λ=1.25, α=35 deg, and (*a*) Re_c=800, (*b*) Re_c=1300. Note that in regions of surface-normal inflow associated with the vortex pair an enhancement is realized, and in surface-normal outflow regions the boundary-layer thickens and a reduction in the convection coefficient is manifest. Note also that different scales are used for the two plots.

Local Sherwood number data for Λ=1.25, α=35 deg, and Re_c=800 and 1300 are given in Fig. 9. Comparison to flow visualization images reveals that the region of the largest enhancement corresponds to the location where the vortex flow is toward the surface. This flow normal to the surface thins the concentration boundary layer and enhances the convective transport. From the local data one can see that the effect of the vortices with larger circulation is more prominent. These data show that the vortices have an influence on the surface heat transfer over a streamwise distance of many wing chord lengths.

The impact of vortex strength and location relative to the boundary layer can be evaluated by considering the data for Re_c=800. The flow visualization data and calculated boundary-layer thickness show that the cores of these vortices are nearer to edge of the concentration boundary layer than at Re_c=1300. Despite the promising vortex location, the local mass transfer enhancement for Re_c=800 is significantly less than for Re_c=1300 at a given Re_x over most of the range of Re_x. The reason for this behavior is vortex strength. At Re_c=800, the vortices have an initial circulation a little over half that of Re_c=1300. This result indicates that vortex strength plays a more important role than vortex location in local mass transfer enhancement.

Developing Laminar Channel Flow. Vortex trajectories in the developing channel flow differ from those of the flat-plate flow. For the flat plate, the vortices spread and then continually rise away from the surface as they are carried downstream; however, when a second surface is introduced, the flow is bounded. Vortices are generated closer to the side of the channel with the vortex generator, and as in the flat-plate flow, they interact strongly with that surface and spread. As they spread, they move toward the channel centerline, carried by the vertical velocity of the developing flow. Once at the centerline, the symmetry of the channel causes the vortices to travel in parallel paths down the

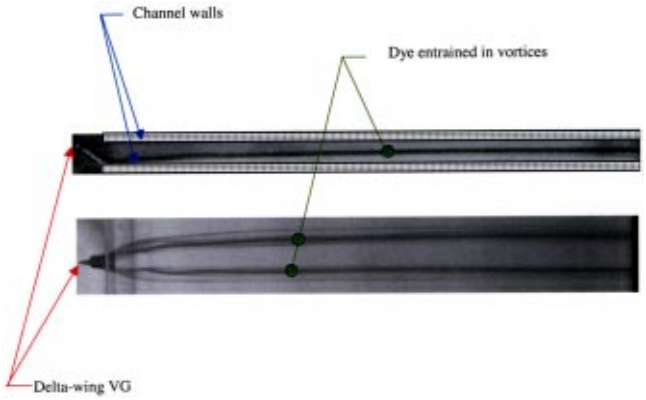

Fig. 10 Two views of an image recorded using dye-in-water visualization, showing vortices generated by a delta-wing VG at the leading edge of the channel, with $\Lambda=1.25$, $\alpha=35$ deg, and $Re_{dh}=1200$

center of the channel. This general character of the trajectory is evident in the flow visualization shown in Fig. 10. The instability and vortex waviness observed for flat-plate flows was never observed in the channel flows. Using the flow visualization and numerical calculations of the developing velocity profile, it can be shown that for the entire experimental range the vortex cores remained outside the boundary layer of the developing flow [15]; i.e., the vortices reach their equilibrium position along the centerline of the channel before the boundary layers grow to the channel centerline. Vortex breakdown was never observed in the developing channel flows in the parameter space considered. Even at the largest Reynolds numbers, the strongest vortices remained well defined and coherent throughout the entire channel.

Vortex circulation, from the vortex meter and trajectory data, are presented in Fig. 11. These data were obtained at a position 1 cm downstream from the leading edge of the channel. Again, the two methods for measuring circulation show good agreement. In most cases, the vortex meter measures a slightly lower vortex circulation than the trajectory measurement, perhaps due to friction in the device or higher-order contributions in the potential flow model. Nevertheless, the two measurements agree to within 20 percent over the entire parameter space. As in the flat-plate flow, vortex circulation in the developing channel flow increases with Reynolds number, wing aspect ratio, and wing attack angle. Comparing the channel-flow to a flat-plate flow, the vortex circulations are within about 10 percent for a wing with $\Lambda=1.25$ and $\alpha=35$ deg at $Re_c=1300$ and 800. Aside from confirming the repeatability of the vortex measurements, these results show that the initial strength of a tip vortex depends mostly on the approach velocity and wing geometry. The bounding channel did not vitiate the generation of tip vortices by the delta wing VG in this experimental range. Unfortunately, no data on vortex decay in the channel flow as a function of streamwise location were obtained in this study. We anticipate that vortex circulation will decay more rapidly in the channel flow due to the added ''viscous braking'' effect of the bounding surface.

In the channel flow, the vortices affect convection on both bounding channel walls. Results for the entire channel, accounting for the effects on both walls, are shown as surface plots of R_{Sh} in Fig. 12. The trends in these data are similar to those for the flat-plate flow. For all Reynolds numbers tested, the largest enhancement ratio was found at the largest attack angle and aspect ratio ($\alpha=55$ deg and $\Lambda=2$), and R_{Sh} increases with Re_{dh}. Significant enhancements of $R_{Sh}=1.2$, 1.4, and 1.5 were found for $Re_{dh}=400$, 1200, and 200 respectively. As in the flat-plate case, it is interesting to consider a varying channel length by integrating the local mass transfer data over a variable flow length. The results are shown in Fig. 13 for a typical case, where data are presented

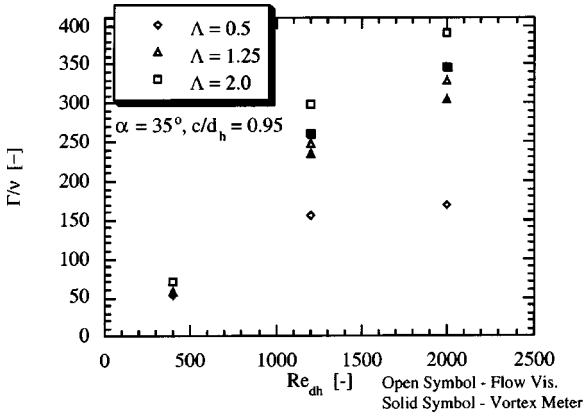

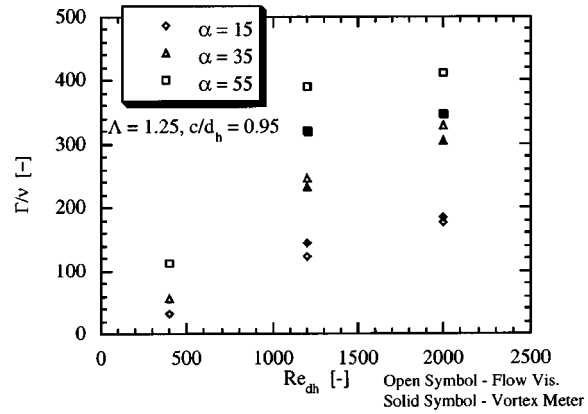

Fig. 11 Dimensionless vortex circulation as a function of Re_{dh} for a delta wing in a channel flow with $\Lambda=1.25$ and $\alpha=15$ deg, 35 deg, and 55 deg. Solid symbols were obtained using the vortex meter, and open symbols were obtained with the potential flow model. Ratio $c/d_h=0.95$.

for both the wall with the wing and the opposing surface as well as the channel. Results for the surface with the wing are qualitatively similar to the single plate results: at the entrance where the boundary layer is thin, the vortex has a little impact, and as the flow length increases, the enhancement ratio goes through a maximum to finally decrease as the vortices weaken. The behavior of the enhancement ratio for the surface without the vortex generator is quite different. For this case, the enhancement increases monotonically over the entire flow length. Near the channel entrance, R_{Sh} is small because the vortices are far from the surface, and the boundary layer is thin. As the flow length increases, the vortices move closer to the surface without the vortex generator as they weaken. These two competing features—closer proximity acting to increase the enhancement and weakening circulation acting to reduce the enhancement—result in an R_{Sh} that is nearly constant as the flow length increases for the surface without the wing. Overall, the channel shows an increasing enhancement ratio for small flow lengths. As Gz^{-1} increases, the vortices weaken and the enhancement decreases slightly. The results presented in Fig. 13 clearly demonstrate that the vortices continue to be effective for flow lengths longer than those considered in this research.

Measurements of local Sherwood number for $\Lambda=1.25$, and $\alpha=35$ deg are presented for several Reynolds numbers in Fig. 14. On the surface with the wing near the channel entrance, the vortices are at their strongest and are located close to the wall. The local effect of the vortices is the most pronounced in this region. As with the flat-plate data, there are areas of decreased mass trans-

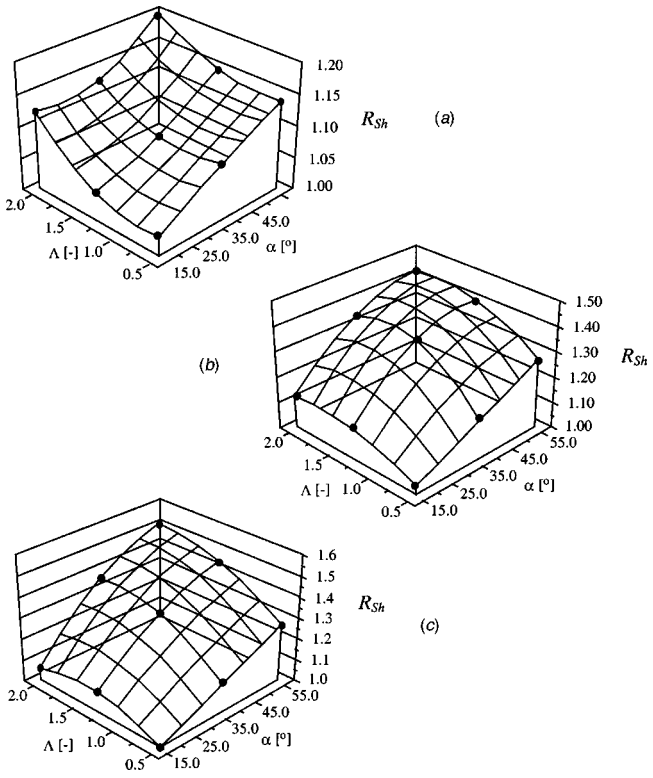

Fig. 12 Sherwood number enhancement for a channel flow as a function of VG aspect ratio and attack angle at (*a*) Re_{dh} =400, (*b*) Re_{dh}=1200, (*c*) Re_{dh}=2000. The data are averaged over both sides of the complete channel.

fer near the leading edge, where the vortex-induced flow is away from the wall. At downstream locations, the enhancement of local mass transfer occurs in nearly parallel lines. Contrasting these results with the flow visualization data, the regions of enhancement are found to correspond to regions where the vortices induce a surface-normal flow toward the channel wall. This finding is easy to see by comparing the local distribution of the wing surface to the opposite channel wall. At the leading edge and just downstream of the wing, the mass transfer rate is low because the flow is away from the surface. Farther downstream, the effect of the

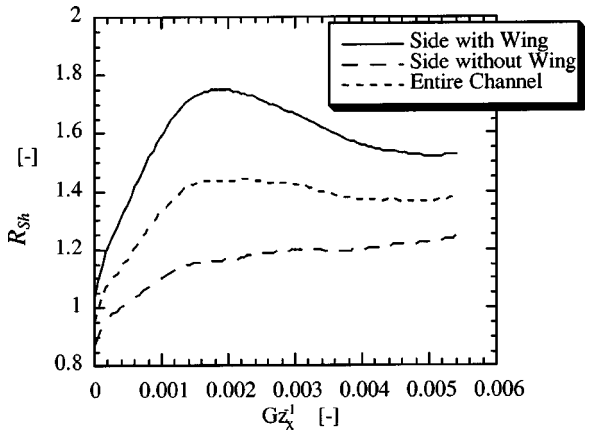

Fig. 13 Spatially averaged enhancement ratio for the channel flow as a function inverse Graetz number based on integration length, with Λ=1.25, α=35 deg, and Re_{dh}=2000. Data are presented for both surfaces of the channel and the channel as a whole.

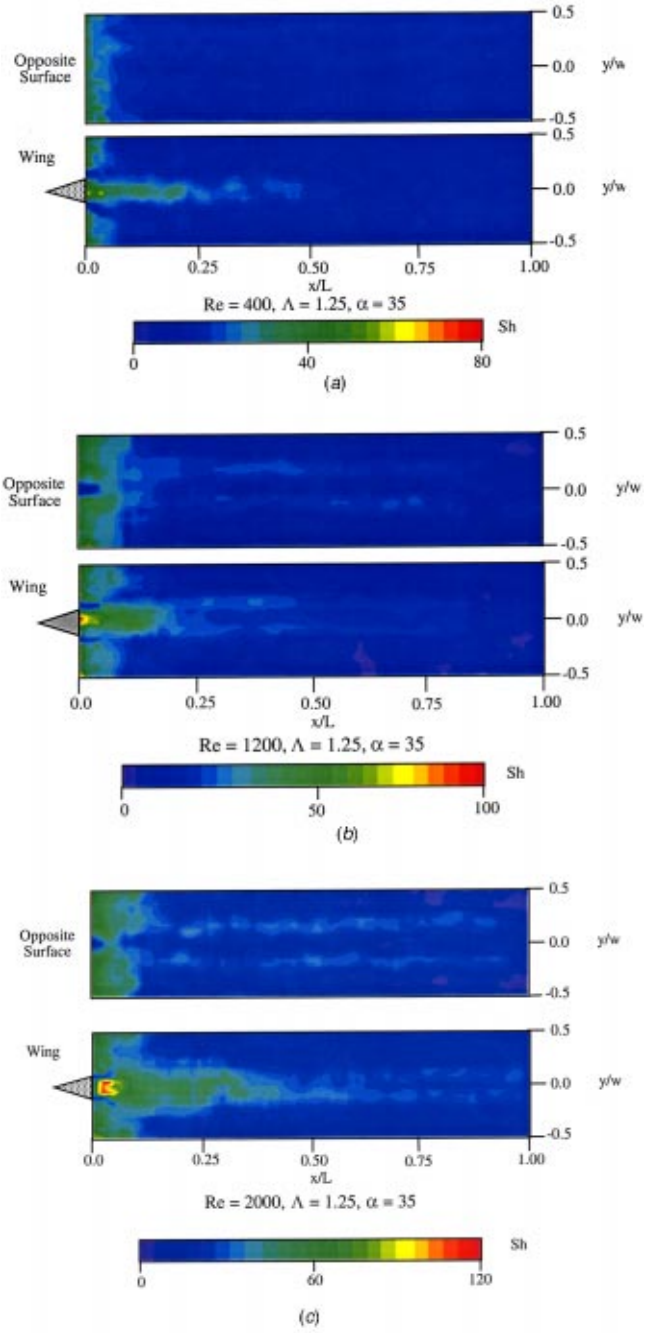

Fig. 14 Local Sherwood number distribution for a delta wing in a developing channel flow, with Λ=1.25, α=35 deg (c/d_h =0.95, L/c=11.43): (*a*) Re_{dh}=400, (*b*) Re_{dh}=1200, and (*c*) Re_{dh} =2000.

vortices mirrors that of the wing surface, but spacing between the enhanced regions is larger—a behavior congruent with enhancement corresponding to the surface-normal inflow. The character of the flow is essentially the same over the Reynolds number range of these experiments; however, the features discussed above are more pronounced at higher Re_{dh}, where the vortices are stronger.

The pressure drop in the channel with delta wing vortex generators was measured as described earlier, and the results are given in Fig. 15 as R_p versus Re_{dh} for wings with a range of aspect ratios and attack angles. For each aspect ratio, R_p increases with Reynolds number and angle of attack. For Re_{dh}=2000, and

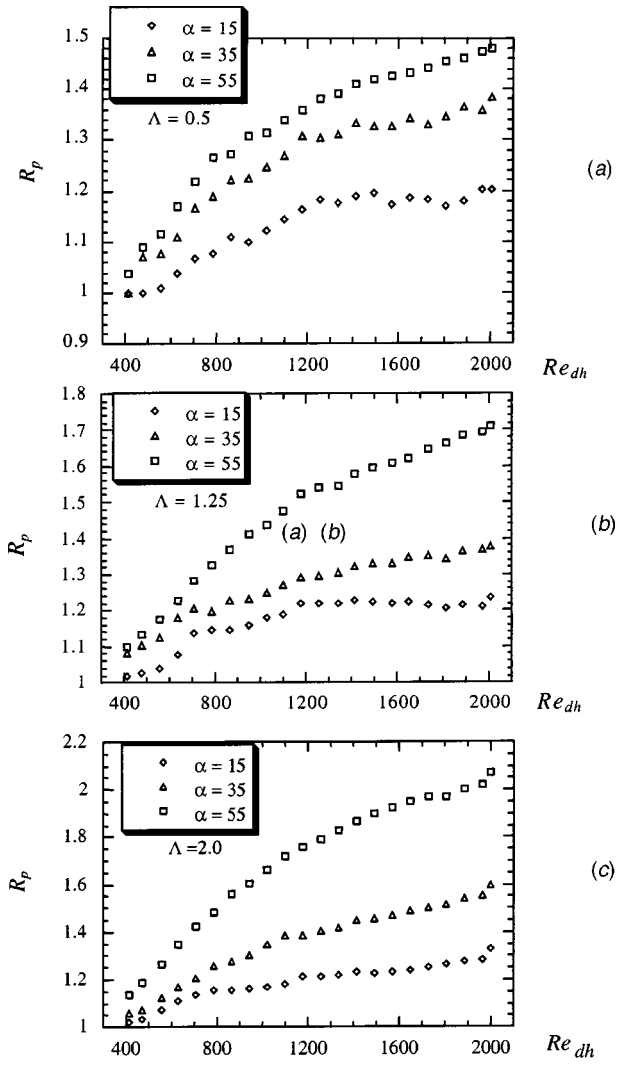

Fig. 15 Pressure-drop penalty for VG enhanced channel flow, over a range of aspect ratio, attack angle and Reynolds number: (*a*) Λ=0.5; (*b*) Λ=1.25; and (*c*) Λ=2.0 (c/d_h=0.95, L/c =11.43).

α=55 deg, R_p increases from 1.5 to 1.7 to 2.1 as the wing aspect ratio increases from 0.5 to 1.25 to 2.0. For the smallest aspect ratio, R_p is less dependent on the attack angle than for larger aspect ratios. For example, at Λ=0.5, the difference between the pressure drops for α=35 deg and α=55 deg is approximately 10 percent at Re_{dh}=2000; in contrast, for Λ=1.25, the difference in these values is approximately 35 percent, and at Λ=2.0, the difference increases to over 50 percent. Similar changes are seen in the strength of the vortices generated at these conditions. The vortex circulation increases by 17 percent, 28 percent, and 55 percent as the angle of attack is increased from 35 deg to 55 deg for Re_{dh}=2000 and Λ=0.5, 1.25, and 2.0 respectively. There are two components to the pressure drop associated with flow over a delta wing in a channel. The first is the form drag over the wing. The second component of the pressure drop is the increased wall shear stress. A local thinning of the concentration boundary layer causes the enhancement of mass transfer. The velocity boundary layer is also thinned, and the steeper velocity gradient at the wall results in increased wall shear stress that, in turn, increases the pressure drop for the flow through the channel.

Conclusions

For a delta-wing VG at the leading edge of a flat plate, the two resulting tip vortices interact with each other such that they spread apart and move away from the surface as the flow advects them down stream. New observations of periodic waviness were obtained. This instability is manifest when the vortex core passes into the velocity boundary layer, and we offer conjecture that it is due to a buckling instability. Vortex breakdown was also observed in the strongest tip vortices at Re_c=800 and 1300, Λ=2.0, and α=35 deg and 55 deg. In general, the measured vortex strength increased with Re_c, Λ, and α for the parameter space considered. For Λ=1.25 and α=35 deg, the vortex strength increased approximately 200 percent when Re_c was increased from 300 to 1300. The vortex circulation decreased with streamwise distance from the leading edge because of viscous interactions. Local convection enhancements as high as 300 percent (compared to flat-plate flow with no vortex generator) were observed in locations where the vortex flow was toward the surface. Maximum spatially averaged enhancements of 35 percent, 60 percent, and 80 percent were observed for the area affected by the vortices for Re_c =300, 800, and 1300. The largest convective enhancements were observed for the strongest vortices, and apparently vortex strength is more important than location relative to the boundary layer.

For vortices in a developing channel flow, the vortices spread and travel away from the winged surface—much as in the flat-plate flow—near the channel entrance. Once the vortices reach the channel centerline, however, the symmetry in the channel flow causes the vortices to travel in parallel paths down the channel centerline. No periodic waviness was observed in the tip vortices for the experimental range studied. Vortex circulation was seen to increase with Re_c, Λ, and α as with the flat-plate flows. For a constant wing geometry, the dimensionless vortex strength increased by as much as 300 percent when Re_{dh} increased from 400 to 2000. The vortices had a significant local convective effect on both channel walls, and although not reported in prior research, the impact on the non-winged wall must be taken into account when considering the heat transfer enhancement of tip vortices in developing channel flows. Local enhancements as large as 150 percent (compared to a channel flow with no vortex generator) occurred where the vortex flow was directed toward the surface. Maximum average mass transfer enhancements of approximately 20 percent, 40 percent, and 50 percent were obtained for the entire channel for Re_{dh}=400, 1200, and 2000 respectively. The pressure drop penalty in the channel flow with a vortex generator increased with Re_c, Λ, and α. For Λ=2.0 and α=55 deg, the ratio of the pressure drop with the vortex generator to the pressure drop in the unenhanced channel flow was approximately 1.5, 1.7, and 2.1 for Re_{dh}=400, 1200, and 2000 respectively.

Application of these results might be realized by placing delta-wing vortex generators on the inlet face of a continuous-fin heat exchanger (see ElSherbini and Jacobi [25]). The current findings support earlier research identifying trends in heat transfer enhancement and pressure-drop penalty as a function of Reynolds number, attack angle and aspect ratio for wing-type vortex generators, and buttress earlier work showing promise for this enhancement strategy. The inclusion of development effects suggests the heat transfer engineer might use flow depth and face-area tradeoffs in seeking near-optimum, vortex-enhanced heat exchangers. Because of their relative geometric simplicity as flow manipulators, it might desirable to implement vortex generators with adaptive attack angles, so the heat transfer surface can respond to a demand for increased duty with a higher attack angle, and when heat duty is not required, the attack angle can be reduced for lower pressure drop operation.

Nomenclature

A = area, [m^2]
a = radius dividing the free and forced vortex regions, [m]
A_c = minimum free flow area, [m^2]
b = span of vortex generator, [m]
c = chord length of vortex generator, [m]

d_h = hydraulic diameter, $d_h = 4A_cL/A_T$ [m]
Gz = Graetz Number, $x/d_h \mathrm{Re}_{dh}\mathrm{Sc}$, [−]
h_m = local mass transfer coefficient, [m/s]
$\overline{h_m}$ = average mass transfer coefficient, [m/s]
k = thermal conductivity, [W/m·K]
L = plate length, [m]
m = mass of naphthalene specimen, [kg] or parameter specifying streamwise pressure gradient for boundary layer solution, [−]
N = rotation rate of vortex meter, [s^{-1}]
P = pressure, [kPa]
r = radial distance, [m]
r_v = radius of vortex tube, [m]
R = ratio of enhanced-to-unenhanced
Re = Reynolds number, UL/ν, [−]
s = one-half distance between vortex cores, [m]
Sc = Schmidt number, $\mu/\rho D_{AB}$, [−]
Sh = local Sherwood number, $h_m L_c/D_{AB}$
$\overline{\mathrm{Sh}}$ = average Sherwood number, $\overline{h_m} L_c/D_{AB}$, [−]
U = air velocity, [m/s]
$V_{a,b}$ = induced velocity of vortex a from vortex b, [m/s]
$V_{a,y}$ = induced velocity of vortex a in y direction, [m/s]
w = width of naphthalene strip on fin, [m]
x = streamwise coordinate, [m]
x_L = length of integration for average mass transfer results, [m]
y = transverse coordinate, [m]
z = coordinate normal to plate surface, [m]

Greek

α = wing angle of attack, [deg] or thermal diffusivity, [m^2/s]
δ = velocity boundary layer thickness, [m]
δ_c = core-to-plate distance, [m]
δ_s = concentration boundary layer thickness, [m]
δ_{sb} = local naphthalene sublimation depth, [m]
Γ = vortex circulation, [cm^2/s]
γ = ratio δ_c/s, [−]
Λ = wing aspect ratio (See Fig. 1), [−]
λ_w = characteristic wavelength of vortex tube waviness, [m]
ν = kinematic viscosity, [m^2/s]
ζ = ratio of δ_c/δ_{bl}, [−]

Subscript

dh = quantity defined with respect to the hydraulic diameter
L = quantity defined with respect to the plate length
p = pressure drop
v = property of vapor phase or property of vortex
Sh = Sherwood number
x_L = quantity defined with respect to the integration length
∞ = property evaluated in freestream

References

[1] Jacobi, A. M., and Shah, R. K., 1998, "Air-Side Flow and Heat Transfer in Compact Heat Exchangers: A Discussion of Enhancement Mechanisms," Heat Transfer Eng., **19**, pp. 29–41.
[2] Jacobi, A. M., and Shah, R. K., 1995, "Heat Transfer Surface Enhancement Through the Use of Longitudinal Vortices: A Review of Recent Progress," Exp. Therm. Fluid Sci., **11**, pp. 295–309.
[3] Fiebig, M., 1995, "Vortex Generators for Compact Heat Exchangers," J. Enhanced Heat Transfer, **2**, pp. 43–61.
[4] Fiebig, M., 1998, "Vortices, Generators and Heat Transfer," Chem. Eng. Res. Des., **76**(A2), pp. 108–123.
[5] Turk, A. Y., and Junkhan, G. H., 1986, "Heat Transfer Enhancement Downstream of Vortex Generators on a Flat Plate," *Heat Transfer 1986*, Proceedings of the Eighth International Heat Transfer Conference, San Francisco, California, August 17–22, **6**, Hemisphere Publishing Corp., pp. 2903–2908.
[6] Torii, K., Yanagihara, J. I., and Nagai, Y., 1991, "Heat Transfer Enhancement by Vortex Generators," *Proceedings of the ASME/JSME Thermal Engineering Joint Conference*, J. R. Lloyd, and Y. Kurosaki, eds., ASME Book No. I0309C, ASME, New York, pp. 77–83.
[7] Yanagihara, J. I., and Torii, K., 1993, "Heat Transfer Augmentation by Longitudinal Vortices Rows," *Proceedings of the Third World Conference on Experimental Heat Transfer, Fluid Mechanics, and Thermodynamics*, M. D. Kelleher et al., eds., **1**, pp. 560–567.
[8] Gentry, M. C., and Jacobi, A. M., 1997, "Heat Transfer Enhancement by Delta-Wing Vortex Generators on a Flat Plate: Vortex Interactions with the Boundary Layer," Exp. Therm. Fluid Sci., **14**, pp. 231–242.
[9] Eibeck, P. A., and Eaton, J. K., 1987, "Heat Transfer Effects of a Longitudinal Vortex Embedded in a Turbulent Boundary Layer," ASME J. Heat Transfer, **109**, pp. 16–24.
[10] Pauley, W. R., and Eaton, J. K., 1988, "Experimental Study of the Development of Longitudinal Vortex Pairs Embedded in a Turbulent Boundary Layer," AIAA J., **26**, pp. 816–823.
[11] Fiebig, M., Kallweit, P., and Mitra, N. K., 1986, "Wing Type Vortex Generators for Heat Transfer Enhancement," *Heat Transfer 1986*, Proceedings of the Eighth International Heat Transfer Conference, San Francisco, California, August 17–22, **5**, Hemisphere Publishing Corp., pp. 2909–2913.
[12] Fiebig, M., Kallweit, P., Mitra, N. K., and Tiggelbeck, S., 1991, "Heat Transfer Enhancement and Drag by Longitudinal Vortex Generators in Channel Flow," Exp. Therm. Fluid Sci., **4**, pp. 103–113.
[13] Brockmeier, U., Fiebig, M., Guntermann, T., and Mitra, N. K., 1989, "Heat Transfer Enhancement in Fin-Plate Heat Exchangers by Wing-Type Vortex Generators," Chem. Eng. Technol., **12**, pp. 288–294.
[14] Biswas, G., Torii, K., Fujii, D., and Nishino, K., 1996, "Numerical and Experimental Determination of Flow Structure and Heat Transfer Effects of Longitudinal Vortices in a Channel Flow," Int. J. Heat Mass Transf., **39**, pp. 3441–3451.
[15] Gentry, M. C., and Jacobi, A. M., 1998, *Heat Transfer Enhancement Using Tip and Junction Vortices*, ACRC TR-137, University of Illinois, Urbana, IL.
[16] Goldstein, R. J., and Cho, H. H., 1995, "A Review of Mass Transfer Measurements Using the Naphthalene Sublimation Technique," Exp. Therm. Fluid Sci., **10**, pp. 416–434.
[17] Souza Mendes, P. R., 1991, "The Naphthalene Sublimation Technique," Exp. Therm. Fluid Sci., **4**, pp. 510–523.
[18] Kearney, S. P., and Jacobi, A. M., 1995, *Local and Average Heat Transfer and Pressure Drop Characteristics of Annularly Finned Tube Heat Exchangers*, ACRC TR-69, University of Illinois, Urbana, IL.
[19] Ogawa, A., 1993, *Vortex Flow*, CRC Press, Boca Raton, FL.
[20] Batchelor, G. K., 1967, *An Introduction to Fluid Dynamics*, Cambridge University Press, Cambridge.
[21] Bejan, A., 1995, *Convection Heat Transfer*, John Wiley & Sons, New York, NY.
[22] Panton, R. L., 1996, *Incompressible Flow*, 2nd ed., John Wiley and Sons, New York, NY.
[23] Peace, A. J., and Riley, N., 1983, "A Viscous Vortex pair in Ground Effect," J. Fluid Mech., **129**, pp. 409–426.
[24] Pohlhamus, E. C., 1966, "A Concept of the Vortex Lift of Sharp-Edge Delta Wings Based on a Leading Edge Suction Analogy," TN D-3767, NASA.
[25] ElSherbini, A., and Jacobi, A. M., 2002, "The Thermal Hydraulic Impact of Delta-Wing Vortex Generators on the Performance of a Plain-Fin-and-Tube Heat Exchanger," International Journal of HVAC&R Research, (in press).

Miles Greiner
e-mail: greiner@unr.edu
ASME Member
Professor of Mechanical Engineering,
University of Nevada, Reno

Paul F. Fischer
e-mail: fischer@mcs.anl.gov
Mathematics and Computer Science Division,
Argonne National Laboratories

Henry Tufo
e-mail: tufo@cs.colorado.edu
Associate Professor,
Department of Computer Science,
University of Colorado at Boulder,
Boulder, CO 80302

Numerical Simulations of Resonant Heat Transfer Augmentation at Low Reynolds Numbers

The effect of flow rate modulation on low Reynolds number heat transfer enhancement in a transversely grooved passage was numerically simulated using a two-dimensional spectral element technique. Simulations were performed at subcritical Reynolds numbers of $\mathrm{Re}_m = 133$ *and 267, with 20 percent and 40 percent flow rate oscillations. The net pumping power required to modulate the flow was minimized as the forcing frequency approached the predicted natural frequency. However, mixing and heat transfer levels both increased as the natural frequency was approached. Oscillatory forcing in a grooved passage requires two orders of magnitude less pumping power than flat passage systems for the same heat transfer level. Hydrodynamic resonance appears to be an effective method of increasing heat transfer in low Reynolds number systems, especially when pumping power is at a premium.* [DOI: 10.1115/1.1517273]

Keywords: Augmentation, Enhancement, Heat Transfer, Instability, Unsteady

Introduction

Miniaturization of electronic components has increased circuit junction density and the associated heat loads that must be removed to maintain reliable operation. New technologies allow micro-scale coolant passages to be cut directly into a variety of silicon circuit substrates. This technique reduces the thermal resistance between junctions and coolant passageways compared to ''strap-on'' heat sink techniques. Moreover, the small dimensions of the passages lead to very large heat transfer coefficients even at low Reynolds numbers [1,2].

The small surface area and lack of convective mixing associated with micro-channels are a limitation to their heat transfer performance. Fins, offset strips and jet array impingement are routinely used to increase convection in full-sized devices [3]. However, these features are subject to fouling and manufacturability problems in micro-scale systems. Moreover, they require the use of more powerful prime movers, which may be problematic in micro-devices. Finally, these techniques are not specifically designed to enhance convective mixing.

In recent years, a number of researchers have considered passage configurations that enhance mixing and heat transfer by triggering flow instabilities. Transversely grooved channels [4–6], passages with eddy promoters [7,8], and communicating channels [9] all contain features whose sizes are roughly half the channel wall to wall spacing. These structures excite normally damped Tollmien-Schlichting waves at moderately low Reynolds numbers.

The current authors have presented a series of studies on flow destabilization in rectangular cross section channels with transverse grooves cut periodically into the walls. Visualizations in a range of passage geometries show that the critical Reynolds number Re_C where two-dimensional waves first appear decreases as the spacing between grooves is reduced [10]. For a sawtooth-shaped wall with no spacing between grooves, two-dimensional waves first appear at $\mathrm{Re}_C = 350$, followed by a rapid transition to three-dimensional mixing [11]. Fully developed heat transfer using air is enhanced relative to laminar flat channel flow by as much as a factor of 4.6 at equal Reynolds numbers and by a factor of 3.5 *at equal pumping powers* [12–15].

Numerical and experimental studies of hydrodynamic resonance show that Tollmien-Schlichting waves may also be triggered *below* the critical Reynolds number by modulating the flow rate at the natural frequency of the waves [4,5,16]. Experiments and simulations were performed for *sparsely* grooved passages in which two-dimensional waves first appeared at $\mathrm{Re}_C = 2000$ (the onset of three-dimensional mixing in a flat passage occurs at $\mathrm{Re}_m = 2800$ [17]. At a subcritical Reynolds number of $\mathrm{Re}_m = 1400$ ($\mathrm{Re}_m/\mathrm{Re}_C = 0.7$), a 20 percent flow rate modulation at the correct frequency more than doubled the heat transfer.

Problem Definition

The current work has two goals. The first is to determine if resonant heat transfer augmentation provides significant enhancement at the low Reynolds numbers where micro-channels typically operate [1,2]. The second goal is to compare the pumping power required to enhance heat transfer using resonant flow rate modulation with the power required to reach the same heat transfer level by simply increasing the flow rate. In this work, numerical simulations are performed in the rectangular cross section passage with sawtooth walls shown in Fig. 1. The minimum and maximum wall-to-wall spacing are $H_{\min} = 0.01$ m and $H_{\max} = 0.034$ m respectively, and the groove length is $L = 0.024$ m. This geometry was chosen because it has a critical Reynolds number of $\mathrm{Re}_C = 350$, which is the lowest value of any geometry examined by Greiner [10]. The large dimensions of the current study were chosen as a practical size for future bench-scale experiments that will be performed to validate the simulation results. Typical micro-scale dimensions are much smaller.

We choose the *mean* wall-to-wall spacing as the characteristic dimension for this passage, $H = (H_{\min} + H_{\max})/2$, with a corresponding hydraulic diameter of $D_h = 2H$. This allows the results of the current study to be directly compared to a flat passage whose wall-to-wall spacing is equal to the mean spacing of the current grooved passage. The volume of the flat passage is also equal to that of the grooved channel.

Contributed by the Heat Transfer Division for publication in the JOURNAL OF HEAT TRANSFER. Manuscript received by the Heat Transfer Division October 22, 2001; revision received August 12, 2002. Associate Editor: M. Faghri.

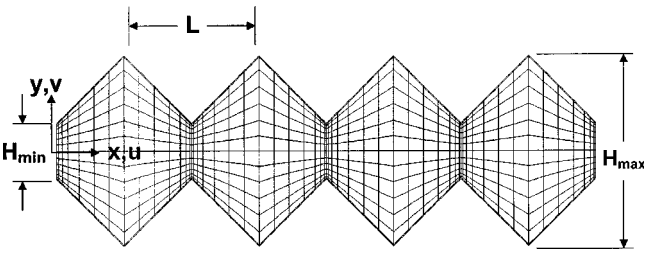

Fig. 1 Spectral Element Mesh. The flow is from left to right and periodic inlet/outlet conditions are employed.

The coolant for this study is modeled as constant-property room temperature air with thermal conductivity k, density ρ, thermal diffusivity α_t, molecular Prandtl number Pr, and kinematic viscosity ν. The working fluid flows from left to right in Fig. 1. Its volumetric flow rate per unit length normal to the plane of Fig. 1, $V_N(t)=\int u dy$, is modulated sinusoidally with time. The time dependent Reynolds number based on hydraulic diameter D_h is

$$\mathrm{Re}(t)=\frac{U_m(t)D_h}{\nu}=V_N(t)\frac{2}{\nu}=\mathrm{Re}_m[1+\eta\sin(2\pi Ft)] \quad (1)$$

In this expression, time dependent mean velocity is $U_m(t)=V_N(t)/H$, Re_m is the time mean Reynolds number, η is the oscillatory fraction, and F is the forcing frequency.

In this work, simulations are performed for two subcritical Reynolds numbers $\mathrm{Re}_m=133$ and 267, corresponding to ratios of mean to critical Reynolds numbers of $\mathrm{Re}_m/\mathrm{Re}_C=0.38$ and 0.76, respectively. The higher of these ratios is roughly the same as that studied by Ghaddar et al. [4] and Greiner [5] at $\mathrm{Re}_m=1400$. The lower Reynolds number is deeply in the subcritical range. Simulations are performed for oscillatory fractions $\eta=0$ (steady forcing), 0.2 and 0.4, and a range for forcing frequencies, F.

In the next section, linear stability results for a *flat* passage are used to estimate the forcing frequency that maximizes the heat transfer in the current *grooved* channel. We perform numerical simulations for a range of forcing frequencies centered about the predicted natural frequencies and determine the effect on time average heat transfer and pumping power.

Linear Stability of Plane Poiseuille Flow

Linear stability analysis of flat passage flow is generally used to determine if certain infinitesimal perturbations grow, decay, or remain unchanged with time [18]. Linear perturbations to plane Poiseuille flow are generally composed of traveling waves with a range of wavelengths λ. All *two*-dimensional perturbations to laminar flat passage flow decay below a critical Reynolds numbers of $\mathrm{Re}_C=U_mD_h/\nu=15{,}392$ (the well-known Orr-Sommerfeld value of $\mathrm{Re}_{C,OS}=U_{\max}h/\nu=5772$ is based on the channel half height $h=H/2$ and the maximum fluid velocity $U_{\max}=(3/2)U_m$, so that $\mathrm{Re}_{C,OS}=3/8\ \mathrm{Re}_C$). However, *three*-dimensional *finite*-amplitude perturbations first grow at a lower Reynolds number of $\mathrm{Re}_m=2800$ and this begins the transition to turbulence.

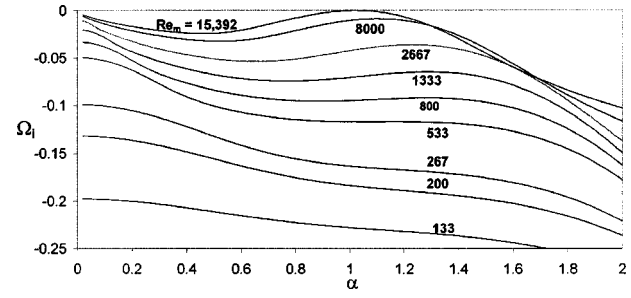

Fig. 2 Orr-Sommerfeld growth rate versus wavenumber and Reynolds number

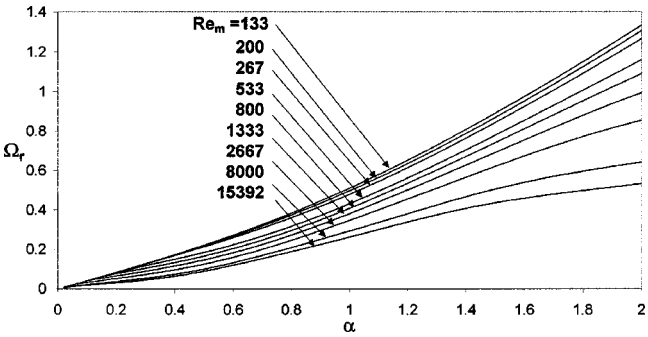

Fig. 3 Orr-Sommerfeld frequency versus wavenumber and Reynolds number

At any location within a plane passage the amplitude of each perturbation wave varies with time t according to $e^{Gt}\sin(2\pi Ft)$, where G is its dimensional growth rate and F is its dimensional natural frequency. The values of G and F for different perturbation wavelengths and Reynolds numbers are found from solutions to the Orr-Sommerfeld linearized equation of motion. Figures 2 and 3 show dimensionless growth rate $\Omega_i=2\pi GH/(3U_m)$ and dimensionless natural frequency $\Omega_r=2\pi FH/(3U_m)$ versus dimensionless wavenumber $\alpha=\pi H/\lambda$ for a range of Reynolds numbers.

Figure 2 shows that at the critical Reynolds number $\mathrm{Re}_C=15{,}392$ and $\alpha=1.03$, the dimensionless growth rate is $\Omega_i=0$. This indicates that perturbations of wavelength $\lambda=\pi H/\alpha=3.05\,H$ are neutrally stable (neither grow nor decay). All disturbances for $\mathrm{Re}_m<\mathrm{Re}_C$ decay with time since they have negative growth rates. However, for $\sim 533<\mathrm{Re}_m<\mathrm{Re}_C$, each Reynolds number exhibits a maximum growth rate at wavenumbers between $1.03\leqslant\alpha\leqslant 1.3$. This indicates that certain wavelengths decay more slowly than the rest.

Ghaddar et al. [4] and Greiner [5] both studied resonant heat transfer enhancement at $\mathrm{Re}_m=1400$. This Reynolds number is in the range that exhibits a peak in the growth rate curve. The Reynolds numbers of interest in the current paper are $\mathrm{Re}_m=133$ and 267. Figure 2 shows that there are no peaks in the growth rate curves at these low Reynolds numbers. However, both curves are inflected (zero curvature) at $\alpha\cong 1.3$, and this appears to be the only remnant of the peaks observed at higher Reynolds numbers. This wavenumber corresponds to perturbation wavelength of $\lambda=\pi H/\alpha=2.4\,H$. The periodicity length of the current grooved passage $L=2.4\ H_{\min}$, was chosen to be compatible with this wavelength ($H_{\min}$ was chosen instead of H because the external channel flow with steady forcing moves essentially parallel to the x-direction, similar to an ungrooved passage). Figure 3 shows that at $\mathrm{Re}_m=133$ and 267, the dimensionless frequency for waves with $\alpha\cong 1.3$ are $\Omega_r=0.73$ and 0.69, respectively. The corresponding dimensional natural frequencies at $\mathrm{Re}_m=133$ and 267 are therefore $F_N=(3\Omega_r/2\pi)(U_m/H_{\min})=3\nu\Omega_r\,\mathrm{Re}/(4\pi H_{\min}^2)=4.24$ and 8.04 Hz, respectively.

Numerical Methods

Figure 1 shows the two-dimensional spectral element mesh employed in this work. The upper and lower boundaries are no-slip solid walls, and the flow is form left to right (in the positive x-direction). The domain consists of four grooves with a domain length $L_d=4\,L$. Periodic inlet/outlet conditions are employed to model fully developed flow. Multiple grooves are employed so that long wavelength modes, which may exist at low Reynolds numbers, will be observed. Heat transfer for constant temperature walls is modeled.

In the spectral element method [19,20] the velocity, data and geometry are expressed as tensor-product polynomials of degree

N in each of K spectral elements, corresponding to a total grid point count of roughly KN^2. Numerical convergence is achieved by increasing the spectral order N. The present calculations were carried out at a base resolution of $K=782$, $N=5$. Resolution tests with $N=7$ indicated a 0.096 percent change in Nusselt number at the resonant forcing condition for $\mathrm{Re}_m=267$.

The present simulations use consistent approximation spaces for velocity and pressure, with pressure represented as polynomials of degree N-2 [20,21]. The momentum equations are advanced by first computing the convection term, followed by a linear Stokes solve for the viscous and pressure terms. The decoupling allows for convective Courant numbers greater than unity while maintaining third-order accuracy in time. Full details of the method can be found in [21]. The flow is driven from left to right in the periodic domain by a time-varying body force per unit mass $f_x=(-dp/dx)/\rho$. This forcing is determined so that the mass flow rate through the domain varies sinusoidally with time [22].

The thermal problem for the periodic domain requires careful treatment. If one simply specifies zero-temperature conditions on the walls then the solution eventually decays to zero. To produce the desired spatially fully-developed state requires that the temperature profiles at the inlet and outlet be self-similar, that is, $T(x=L_d,y,t)=CT(x=0,y,t)$, with $T\geqslant 0$ and $C<1$. The solution technique for computing the fully developed temperature field for constant temperature boundary conditions follows the analysis of Patankar et al. [23]. The energy equation and associated initial and boundary conditions are

$$\frac{\partial T}{\partial t}+\overline{U}\cdot\nabla T=\alpha\cdot\nabla^2 T \tag{2a}$$

$$T(x,y,t=0)=T_{\mathrm{init}}(x,y) \tag{2b}$$

$$T(x,y,t)=0 \quad \text{on the walls} \tag{2c}$$

$$T(x=L_d,y,t)=e^{-cL_d}T(x=0,y,t) \tag{2d}$$

where $\overline{U}=(u,v)$ is the convecting velocity field determined by the hydrodynamic part of the computation. Equation (2*d*) corresponds to the fully developed condition where the temperature profile is self-similar in each successive domain in the periodic sequence, that is $T(x+L_d,y,t)=e^{-cL_d}\cdot T(x,y,t)$ for all (x,y,t), where $e^{-cL_d}=C$. The decay constant c is determined as part of the computation and is proportional to the log-mean Nusselt number. The fact that each domain independently satisfies the homogeneous Eq. (2) and that we are considering fully developed solutions that are independent of T_{init} implies that the solution to Eq. (2) for each domain would yield the same value of c. Hence, c cannot be a function of x. Moreover, since the log-mean Nusselt number is constant, c cannot be a function of time even when the flow is itself unsteady.

Any function satisfying the above self-similar condition has the unique decomposition $T(x,y,t)=e^{-cx}\theta(x,y,t)$, where $\theta(x+L_d,y,t)=\theta(x,y,t)$ is a periodic function. Thus, the computation of T is reduced to the computation of the periodic temperature function θ, and the constant c. Substituting this decomposition into Eq. 2 yields:

$$\frac{\partial\theta}{\partial t}+\overline{U}\cdot\nabla\theta-\alpha\cdot\nabla^2\theta=(\alpha\cdot c^2+uc)\theta-2\alpha\cdot c\frac{\partial\theta}{\partial x} \tag{3a}$$

$$\theta(x,y,t=0)=\theta_{\mathrm{init}}(x,y) \tag{3b}$$

$$\theta(x,y,t)=0 \quad \text{on the walls} \tag{3c}$$

$$\theta(x=L_d,y,t)=\theta(x=0,y,t) \tag{3d}$$

Since the fully developed solution is independent of the initial condition we may arbitrarily assign θ_{init}, which is typically set to unity when starting from rest, or to a prior converged result when starting from an existing flow-field. Equation (3*a*) is solved using a semi-implicit time-stepping procedure similar to that for our Navier-Stokes solver. The diffusive terms are treated implicity while the convective terms are treated explicitly. In addition, all terms on the right of Eq. (3*a*) are treated explicitly using the latest available value for c.

In the steady state case ($\partial/\partial t=0$), Eq. (3) constitutes an eigenproblem for the eigenpair (c,θ). The constant c corresponds to the decay rate of the mean temperature in the x-direction. As such, a larger value of c implies more rapid decay and more effective heat transfer (larger log-mean Nusselt number). In the convection-dominated limit where the Peclet number U_mD_h/α_t is large, Eq. (3*a*) becomes a linear eigenvalue problem. In this case, standard iterative methods for computing the lowest value of c (corresponding to the most slowly decaying mode in x) can be used even when the nonlinear (c^2) term in Equation (3*a*) is not identically zero. We find that this method accurately computes the decay rate and Nusselt numbers for steady flows in square and round ducts [24].

For steady-periodic flows with period τ, the temperature is periodic in time, implying $T(x,y,t+\tau)=T(x,y,t)$. Since c is independent of time, this implies that $\theta(x,y,t+\tau)=\theta(x,y,t)$. If the value of c is not chosen correctly, this condition will not be satisfied. A robust approach to computing c is obtained by multiplying Eq. (3*a*) by θ, integrating over the domain Ω, and simplifying to yield:

$$\frac{1}{2}\frac{d}{dt}\int_\Omega\theta^2 dV=\int_\Omega[(\alpha c^2+uc)\theta^2-\alpha\nabla\theta\cdot\nabla\theta]dV \tag{4}$$

While we do not expect the time derivative of the average temperature (represented by the left-hand side of Eq. (4)) to be identically zero, it will in general be less than the time derivative of θ at any one point in the domain. Moreover, if we integrate the right-hand side of Eq. (4) from time t to $t+\tau$, the resultant quantity must be zero due to the temporal periodicity.

This suggests a two-tier strategy for computing c in the unsteady case. Initially, we determine c such that the right hand side of Eq. (4) is identically zero at each time step. This permits a relatively coarse but quick determination of c and θ. We use this value of c to advance θ for one or more periods, and monitor the decay or growth of $\int\theta^2 dV$. At the end of each trial period, we adjust c until convergence is attained. Once the decay constant c has converged (typically about 15–20 periods), averages are taken over a single period. Simulation times for a single period are roughly 45 min on a two-processor 500 MHz DEC Alpha cluster.

The current numerical technique has been used to simulate highly unsteady three-dimensional flows at $\mathrm{Re}=1600$ in the same grooved passage under investigation in the present study [14]. The local and spatially averaged results from that study were in excellent agreement with experimental data. No experimental data for unsteadily forced flow in the current passage geometry are available to validate the results. However, because the Reynolds number is well below the values considered in our previous work, we are reasonably confident of the numerical technique's ability to accurately simulate the heat transfer in these flows.

Results

Figure 4 shows streamlines for $\mathrm{Re}_m=267$ and $\eta=0$ (no unsteady forcing). The critical Reynolds number for this passage is

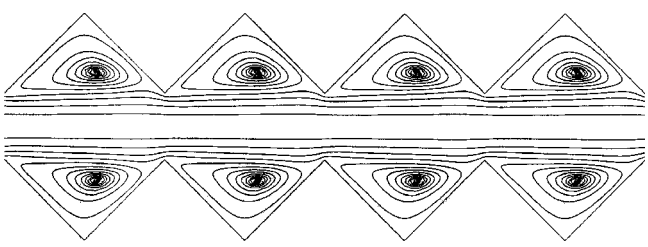

Fig. 4 Streamlines for Re=267, steady forcing

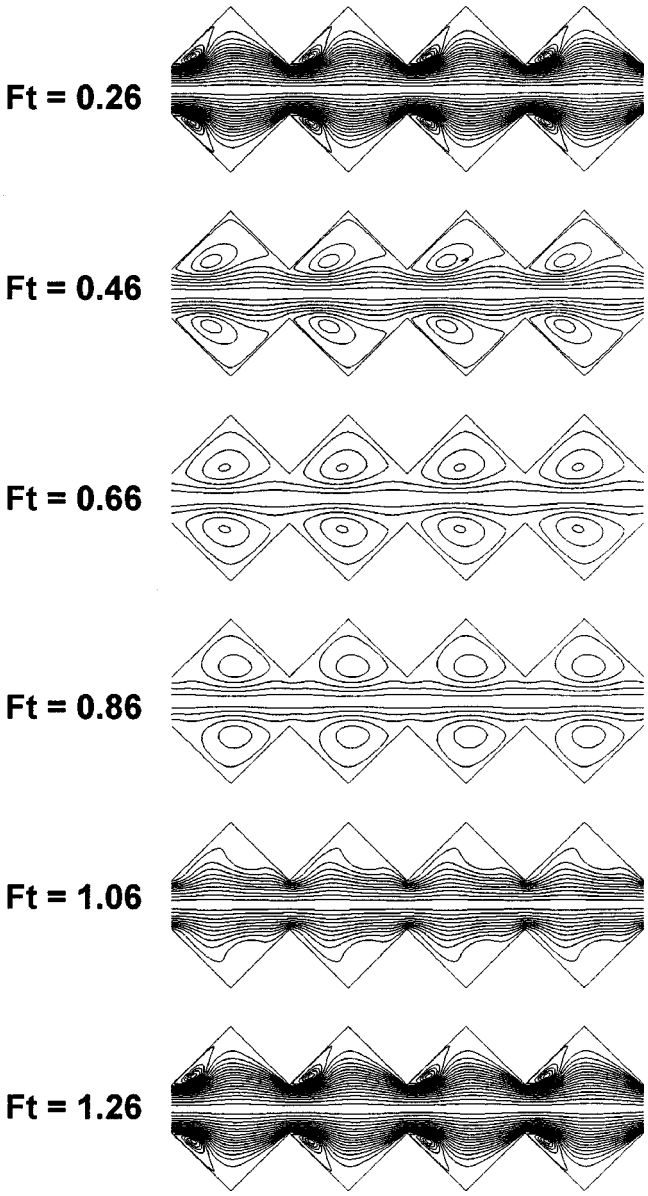

Fig. 5 Streamlines for Re=267, η=0.4, F=5.53 Hz at dimensionless times Ft=0.26, 0.46, 0.66, 0.86, 1.06, and 1.26

Re_C=350, and the flow field at this subcritical Reynolds number is steady. The flow field is identical from groove to groove. The outer channel flow moves essentially parallel to the x-direction with no significant transverse motion. Finally, the grooves are filled with slowly turning vortices.

Figure 5 shows streamlines for unsteadily forced flow at Re_m =267, η=0.4, and F=5.53 Hz. Streamlines are shown at six equally spaced dimensionless times, Ft=0.26, 0.46, 0.66, 0.86, 1.06, and 1.26 (see Eq. (1)) after periodic flow is established. The streamlines at each time are essentially symmetric about the channel centerline, and the flow field is identical from groove to groove. The flow in the grooves is not strongly separated at Ft =0.26, which is just after the maximum flow rate is reached. It exhibits only small vortices on the leeward surface of each groove. For $0.26<Ft<0.86$ the flow rate decelerates and then begins to re-accelerate. During this period the vortices grow and their centers move downstream. The vortices essentially disappear at Ft=1.06 when the flow begins to strongly accelerate. We see that modulating the flow rate under these conditions clears away the slowly turning groove vortices observed in Fig. 4.

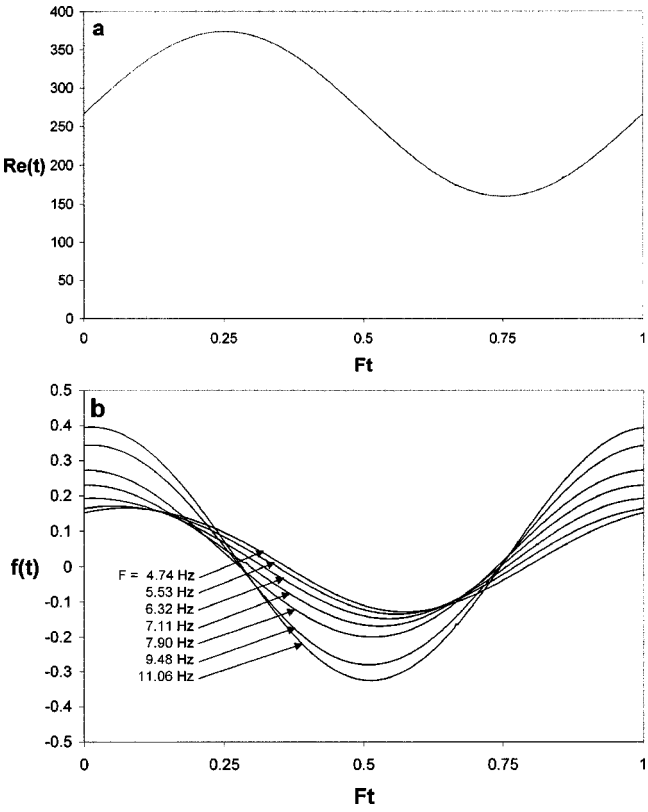

Fig. 6 (*a*) Reynolds number and (*b*) fanning friction factor versus dimensionless time for Re=267, η=0.4

Figures 6(*a*) and 6(*b*) show the time dependent Reynolds number and Fanning friction factor versus dimensionless time for Re_m=267, η=0.4 and a range of forcing frequencies 4.74 Hz $\leq F \leq$ 11.06 Hz. The time dependent Reynolds number versus dimensionless time varies sinusoidally and is identical for all seven forcing frequencies. The friction factor based on time dependent pressure gradient is defined as

$$f(t)=\left[-\frac{dp}{dx}(t)\right]\frac{D_h}{2\rho\overline{U_m^2}}=f_x(t)\,\frac{D_h^3}{2\,\mathrm{Re}_m^2\nu^2} \tag{5}$$

In this expression, $\overline{U}_m$ is the time average value of U_m, and $f_x(t)=(-dp/dx)/\rho$ is the time dependent body force, which is determined within the simulation so that the flow rate will follow the prescribed variation. The variation of the friction factor is nearly sinusoidally with time. The amplitude of the friction factor oscillation clearly increases with forcing frequency. Careful examination of Fig. 6(*b*) shows that the time mean value also increases with F. The phase shift between the friction factor and Reynolds number (flow rate) increases with forcing frequency as well. For $F \geq$ 6.32 Hz, the phase shift is nearly one quarter of the oscillatory period, corresponding to a phase angle of nearly $\pi/2$.

Because the flow rate varies with time, the pumping power required to modulate the flow also varies during the forcing cycle. The pumping power per unit volume is $(U_m)(-dp/dx)$. Figure 6(*b*) shows that $f(t)$ (and hence the pressure gradient $-dp/dx$) is positive and negative during different portions of the oscillatory period. Power must be supplied *to* the flow during periods when $(-dp/dx)>0$, and may be extracted *from* the flow when $(-dp/dx)<0$. The dimensionless *time-average* pumping power quantifies the *net* power input required from an external prime mover. This quantity is defined as:

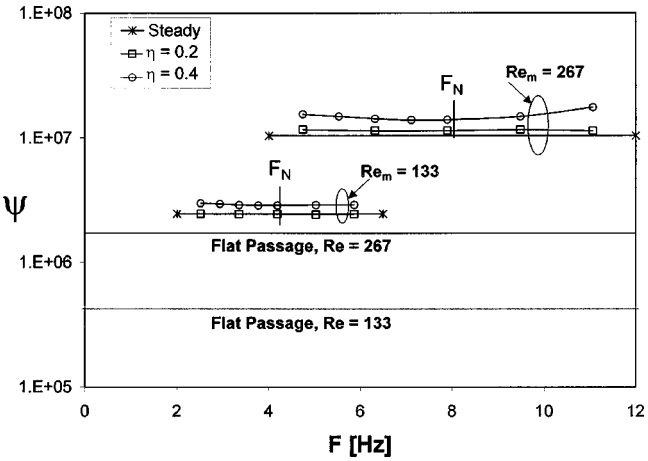

Fig. 7 Dimensionless pumping power versus forcing frequency, Reynolds number and oscillatory fraction

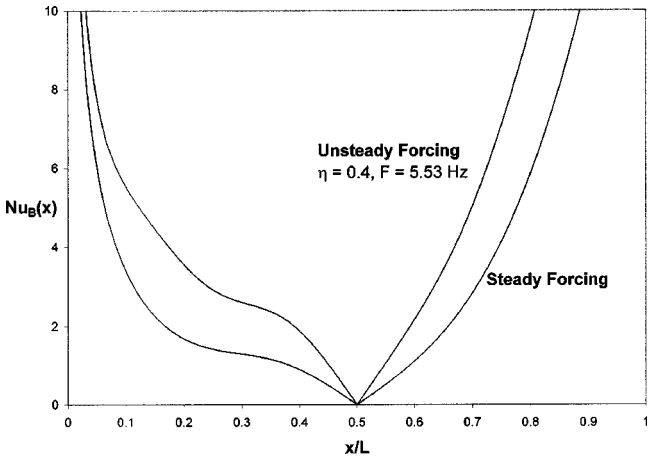

Fig. 8 Spatial variation of local bulk Nusselt number at Re_m =267 with steady and unsteady forcing

$$\Psi = -\frac{F}{\rho}\left(\frac{D_h}{v}\right)^3 \int_0^{1/F} \frac{dp}{dx}(t) V_N(t)\, dt$$

$$= \mathrm{Re}_m^2 \int_0^{Ft=1} f(Ft)\,\mathrm{Re}(Ft)\, d(Ft) \qquad (6)$$

The second equality in this expression shows that the dimensionless pumping power may be evaluated by time integrating the product of the friction factor and Reynolds number data presented in Fig. 6. The phase shift between Re(t) and $f(t)$ therefore affects the integration.

Figure 7 shows the dimensionless time-average pumping power versus forcing frequency at Re_m=133 and 267. Results are presented for η=0 (steady forcing), 0.2 and 0.4. Results are also presented for a flat passage (using f=24/Re_m in Eq. (6)). For steadily forced flow (η=0) the grooved passage pumping power is roughly six times larger than the flat passage level for both Re_m=133 and 267. The smaller minimum wall-to-wall spacing in the grooved channel causes this.

At Re_m=267, the pumping power at η=0.4 is roughly 40 percent higher than that for steady flow. However, the pumping power is minimized at $F \cong 7.5$ Hz. Figure 6 showed that both the amplitude and mean value of $f(t)$ increase with forcing frequency. However, the *phase shift* between $f(t)$ and Re(t) causes the net power requirement to decrease as F increases for $F<7.5$ Hz, and then increase at higher forcing frequencies. At Re_m=267 and η =0.2, the net pumping power is roughly 11 percent higher than for steadily forced flow, but it is minimized at $F \cong 6.3$ Hz. The forcing frequencies that minimize the pumping power are somewhat smaller than the predicted resonant frequency of F_N =8.04 Hz. Nonlinear effects at finite oscillatory fractions may cause the lower frequency.

At Re_m=133, the pumping power at η=0.4 is roughly 20 percent higher than that for steadily forced flow. The minimum pumping power is at F=4 Hz, which is also somewhat lower than the predicted value of F_N=4.24 Hz. For η=0.2 the pumping power is within 1 percent of that for steady forcing.

The pumping power data presented in Fig. 7 represent the minimum input from a prime mover if *all* the work extracted during periods of $(-dp/dx)<0$ is delivered back to the flow during periods of $(-dp/dx)>0$. A flexible bladder or cylinder/flywheel device may be able to extract some energy from the flow and deliver it back at appropriate times in the cycle. However, friction and finite speed will not allow this device to operate reversibly. The net energy input for a real device will depend on the design of an energy storage and return system. The net pumping power levels reported in Fig. 7 represent a lower limit for a reversible system.

Figure 8 shows the spatial variation of the local Nusselt number for Re_m=267 for steady forcing η=0 and for unsteady forcing with η=0.4 and F=5.53 Hz. Results from all four grooves are plotted in the figure but essentially overlap. The local Nusselt number is based on the hydraulic diameter and projected surface area and defined as:

$$\mathrm{Nu}(x) = \frac{-\dfrac{dT_m}{d\hat{n}}(x)}{T_b(x)} \frac{D_h}{s} \qquad (7)$$

In this expression, the temperature gradient is evaluated in the direction normal to the wall and the wall direction cosine is s =0.7071. The local bulk temperature is

$$T_b(x) = \frac{\int u_m(x,y) T_m(x,y)\, dy}{\int u_m(x,y)\, dy} \qquad (8)$$

where $u_m(x,y)$ and $T_m(x,y)$ are the local velocity and temperature time averaged over one forcing cycle, and both integrals are evaluated from the top to the bottom of the domain.

The heat transfer on the windward surface of the groove ($0.5 \leqslant x/L \leqslant 1$) is significantly greater than that on the leeward face ($0 \leqslant x/L \leqslant 0.5$) for both steady and unsteady forcing. This is caused by the rotation direction of the groove vortex. The inflection at x/L=0.3 is caused by the impingement of the groove vortex at that location. The strong clearing of the fluid from the groove at η=0.4 and F=5.53 Hz (seen in Fig. 5) causes the heat transfer at all locations to be significantly higher than for steady forcing.

Figure 9 shows the log-mean Nusselt number versus forcing frequency at Re_m=133 and 267. Grooved channel results are presented for η=0 (steady forcing), 0.2 and 0.4. The flat passage Nusselt number Nu_{LM}=7.54 is based on laminar flow ($\mathrm{Re}_m \leqslant 2800$). The natural frequencies predicted from linear stability theory are also shown. The log-mean Nusselt number is based on the projected surface area and the mean hydraulic diameter and is defined as

$$\mathrm{Nu}_{LM} = \frac{QD_h}{A_p T_{LM} k} = \mathrm{Re}_m \mathrm{Pr} \frac{Hc}{2} \qquad (9)$$

In this expression, the total heat transfer rate per unit length normal to the plane of Fig. 1 is $Q = \rho V_N [T_{B(x=0)} - T_{B(x=Ld)}]$, the projected surface area per unit length normal to the plane is $A_p = 2L_d$, and the log mean temperature difference is T_{LM}

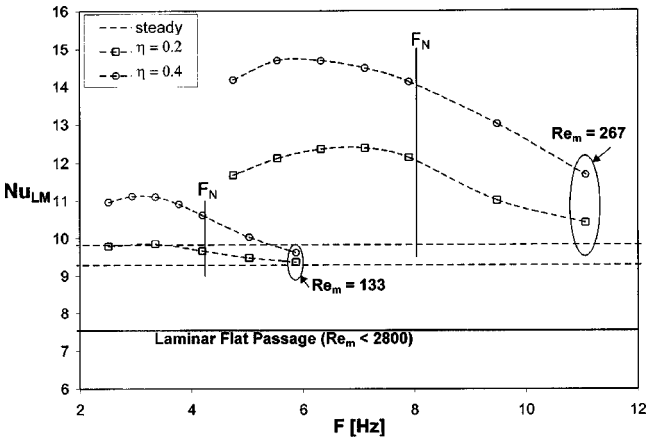

Fig. 9 Log-mean Nusselt number versus forcing frequency, Reynolds number and oscillatory fraction

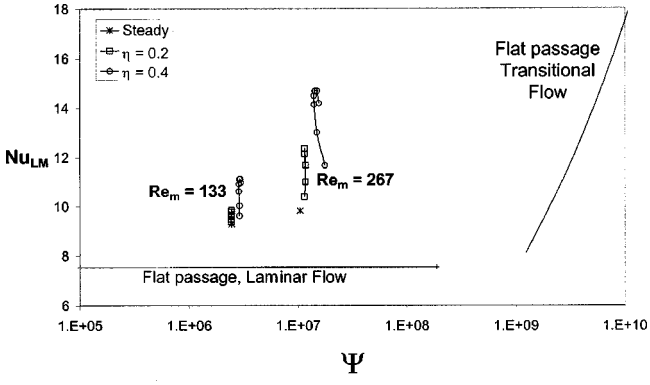

Fig. 10 Log-mean Nusselt number versus dimensionless pumping power

$=[T_{B(x=0)}-T_{B(x=Ld)}]/\ln[T_{B(x=0)}/T_{B(x=Ld)}]=[T_{B(x=0)}-T_{B(x=Ld)}]/cL_d$, (note that $T_{B(x=0)}/T_{B(x=Ld)}=e^{cL_d}$, where c is the eigen decay rate constant described in the numerical methods section).

For steady forcing ($\eta=0$) the grooved passage Nusselt number increases with Reynolds number even though the laminar flat passage value is constant. The steadily forced grooved channel Nusselt numbers at Re=133 and 267 are 23 percent and 30 percent above the flat passage value, respectively.

The heat transfer exhibits a resonant response to oscillatory forcing and peaks at forcing frequencies that are somewhat below the values predicted from Orr-Sommerfeld theory. Table 1 summarizes the peak enhancement factors for different unsteady forcing conditions. For Re=267, the peak heat transfer with $\eta=0.4$ is at $F=6$ Hz and is 50 percent above the steadily forced value. The peak with $\eta=0.2$ is at $F=6.7$ Hz and is 26 percent above the steadily force case. For Re=133, the peak heat transfer with $\eta=0.4$ is 20 percent above the steadily forced value and is at $F=3.1$ Hz. The peak with $\eta=0.2$ is 6 percent above and is at $F=3.3$ Hz. By comparison, resonance in a sparsely grooved passage at $\mathrm{Re}_m=1400$ with $\eta=0.2$ increases the heat transfer by 100 percent [4,5]. These data show that the maximum heat transfer enhancement factors increase with Reynolds number and with oscillatory fraction.

Figure 10 shows the log-mean Nusselt number versus net reversible pumping power for $\mathrm{Re}_m=133$ and 267. Results at each Reynolds number are given for $\eta=0$ (steadily forced flow), 0.2 and 0.4. Comparisons are also made to flat passage results in the laminar and transitional regimes. For a flat passage the flow is laminar up to $\mathrm{Re}_m=2800$ and the fully developed Nusselt number is independent of Reynolds number. At $\mathrm{Re}_m=2800$ the dimensionless pumping power is $\Psi=\mathrm{Re}_m^3 f=1.88\times10^8$ (where $f=24/\mathrm{Re}_m$). In the transition region $\mathrm{Re}_m>3000$, the Nusselt number increases with Reynolds numbers and hence with pumping power [25].

Grooved passage heat transfer levels are significantly higher than those in flat passages for the same pumping power. Since the flat passage laminar Nusselt number is independent of Reynolds number, a plane channel needs to operate in the transitional regime to reach the Nusselt numbers calculated for a steadily forced ($\eta=0$) grooved channel. Figure 10 shows that a flat passage operating in the transitional regime requires significantly more pumping power than a grooved passage operating at a low Reynolds number. Oscillatory forcing greatly increases the grooved passage heat transfer with only minor changes in the pumping power. At $\mathrm{Re}_m=267$, oscillatory forcing with $\eta=0.4$ nearly doubles the heat transfer compared to flat passage flow with no increase in net reversible pumping power costs. Alternately, to reach a heat transfer level of $\mathrm{Nu}_{LM}=10$, oscillatory flow in a grooved passage required *two orders of magnitude* less pumping power that a flat passage system. This conclusion is based on a reversible energy extraction and delivery system. Oscillatory forcing requires special plumbing systems and increases the complexity of the prime mover. However, it appears to be a very effective method of increasing heat transfer in low Reynolds numbers systems such as micro-channels, especially if prime mover pumping power is limited.

Table 1 Peak enhancement factors for different mean Reynolds numbers and oscillatory fractions

Re_m	η	$\mathrm{Nu}_{max}/\mathrm{Nu}_{\eta=0}$
267	0.4	1.50
267	0.2	1.26
133	0.4	1.20
133	0.2	1.06

Conclusions

The effect of flow rate modulation on hydrodynamic resonance and heat transfer enhancement in a transversely grooved passage was numerically simulated using a two-dimensional spectral element technique. Linear stability theory was used to estimate the natural frequency that maximizes the effect on transport. Simulations were performed at moderately low mean Reynolds numbers of $\mathrm{Re}_m=133$ and 267, with 20 percent and 40 percent flow rate oscillations.

The pumping power required to modulate the flow rate at given oscillatory amplitude was *minimized* as the forcing frequency approached the natural frequency. However, the flow mixing and heat transfer levels both *increased* as the natural frequency was approached. Hydrodynamic resonance enhances heat transfer at Reynolds numbers as low as $\mathrm{Re}_m=133$, which is applicable to micro heat transfer devices. However, as the Reynolds number decreases, the oscillatory fraction required for a given enhancement factor increases.

Flat passages need to operate in the transitional regime ($\mathrm{Re}_m>3000$) to achieve the heat transfer levels calculated for grooved passages at Re=133 or 267. As a result, oscillatory forcing in a grooved passage requires two *orders of magnitude* less pumping power than flat passage systems for the same heat transfer level. Oscillatory forcing may require special plumbing systems and increase the complexity of the prime mover. However, it appears to be an effective method of increasing heat transfer in low Reynolds number systems such as micro channels, especially when the pumping power is limited.

Acknowledgments

This work was supported in part by the Mathematical, Information, and Computational Sciences Division subprogram of the Office of Advanced Scientific Computing Research, U.S. Department of Energy, under Contract W-31-109-Eng-38.

Nomenclature

c = decay constant
D_h = hydraulic diameter, $2H$
F = dimensional frequency
F_N = dimensional natural frequency predicted from linear stability theory
f = fanning pressure gradient
f_x = fluid body force per unit mass in the x-direction
G = dimensional growth rate
H = mean channel wall-to-wall spacing
$H_{\max}$ = maximum channel wall-to-wall spacing
$H_{\min}$ = minimum channel wall-to-wall spacing
k = fluid thermal conductivity, 0.0263 W/m° C
K = number of spectral elements
L = groove length
L_d = domain length
N = spectral element order
Nu_b = bulk Nusselt number based on projected area
Pr = fluid molecular Prandtl number, 0.70
$\mathrm{Re}(t)$ = time dependent Reynolds number, $U_m(t)D_h/\nu$
Re_C = critical Reynolds number
Re_m = time mean Reynolds number
t = time
T = temperature
T_b = bulk temperature
u, v = velocity components in the x and y-directions
$U_m(t)$ = time dependent mean x-velocity at the mean channel cross-section
$\overline{U_m}$ = time average value of U_m
$U_{\max}$ = maximum x-velocity at the mean cross-section
V_N = volumetric flow rate per unit channel width

Greek

α = dimensionless wave number
α_t = thermal diffusivity, 2.63×10^{-5} m^2/s
ν = fluid kinematic viscosity, 1.84×10^{-5} m^2/s
η = oscillatory fraction
ψ = dimensionless pumping power per unit volume
θ = periodic temperature
ρ = fluid Density, 1.006 kg/m^3
τ = period of local time variations
Ω = computation domain
Ω_i = dimensionless growth rate
Ω_r = dimensionless natural frequency

References

[1] Peng, X. F., and Peterson, G. P., 1996, ''Convective Heat Transfer and Flow Friction for Water Flow in Microchannel Structures,'' Int. J. Heat Mass Transf., **39**, pp. 2599–2608.
[2] Rao, P., and Webb, R. L., 2000, ''Effects of Flow Mal-Distribution in Parallel Micro-Channels,'' *Proceedings of the ASME 34th National Heat Transfer Conference*, Pittsburgh Pa, August 20–22, Paper Number NHTC-2000 12102.
[3] Webb, R. L., 1994, *Principles of Enhanced Heat Transfer*, John Wiley and Sons, New York.
[4] Ghaddar, N. K., Korczak, K., Mikic, B. B., and Patera, A. T., 1986, ''Numerical Investigation of Incompressible Flow in Grooved Channels. Part 1: Stability and Self-Sustained Oscillations,'' J. Fluid Mech., **168**, pp. 541–567.
[5] Greiner, M., 1991, ''An Experimental Investigation of Resonant Heat Transfer Enhancement in Grooved Channels,'' Int. J. Heat Mass Transf., **24**, pp. 1383–1391.
[6] Roberts, E. P. L., 1994, ''A Numerical and Experimental Study of Transition Processes in an Obstructed Channel Flow,'' J. Fluid Mech., **260**, pp. 185–209.
[7] Kozlu, H., Mikic, B. B., and Patera, A. T., 1988, ''Minimum-Dissipation Heat Removal by Scale-Matched Flow Destabilization,'' Int. J. Heat Mass Transf., **31**, pp. 2023–2032.
[8] Karniadakis, G. E., Mikic, B. B., and Patera, A. T., 1988, ''Minimum-Dissipation Transport Enhancement by Flow Destabilization: Reynolds Analogy Revisited,'' J. Fluid Mech., **192**, pp. 365–391.
[9] Amon, C. H., Majumdar, D., Herman, C. V., Mayinger, F., Mikic, B. B., and Sekulic, D. P., 1992, ''Experimental and Numerical Investigation of Oscillatory Flow and Thermal Phenomena in Communicating Channels,'' Int. J. Heat Mass Transf., **35**, pp. 3115–3129.
[10] Greiner, M., 1987, ''Flow Field Destabilization and Heat Transfer Enhancement in Grooved Channels,'' *Forum on Unsteady Flow Separation*, ASME Applied Mechanics, Bioengineering, and Fluids Conference, Cincinnati, Ohio, June 14–17, FED-Vol. 52, ASME, New York, pp. 131–138.
[11] Greiner, M., Chen, R.-F., and Wirtz, R. A., 1990, ''Heat Transfer Augmentation Through Wall-Shaped-Induced Flow Destabilization,'' ASME J. Heat Transfer, **112**, pp. 336–341.
[12] Greiner, M., Chen, R.-F., and Wirtz, R. A., 1991, ''Enhanced Heat Transfer/Pressure Drop Measured From a Flat Surface in a Grooved Channel,'' ASME J. Heat Transfer, **113**, pp. 498–500.
[13] Greiner, M., Spencer, G., and Fischer, P. F., 1998, ''Direct Numerical Simulation of Three-Dimensional Flow and Augmented Heat Transfer in a Grooved Channel,'' ASME J. Heat Transfer, **120**, pp. 717–723.
[14] Greiner, M., Faulkner, R. J., Van, V. T., Tufo, H. M., and Fischer, P. F., 2000, ''Simulations of Three-Dimensional Flow and Augmented Heat Transfer in a Symmetrically Grooved Channel with Constant Temperature Walls,'' ASME J. Heat Transfer, **122**, pp. 653–660.
[15] Wirtz, R. A., Huang, F., and Greiner, M., 1999, ''Correlation of Fully Developed Heat Transfer and Pressure Drop in a Symmetrically Grooved Channel,'' ASME J. Heat Transfer, **121**, pp. 236–239.
[16] Lee, B. S., Kang, I. S., and Lim, H. C., 1999, ''Chaotic Mixing and Mass Transfer Enhancement by Pulsatile Laminar Flow in an Axisymmetric Wavy Channel,'' Int. J. Heat Mass Transf., **42**, pp. 2571–2581.
[17] Fox, R. W., and McDonald, A. T., 1985, *Introduction to Fluid Mechanics*, 3rd ed., John Wiley and Sons, New York.
[18] Drazin, P. G., and Reid, W. H., 1981, *Hydrodynamic Stability*, Cambridge University Press, London.
[19] Patera, A. T., 1984, ''A Spectral Element Method for Fluid Dynamics; Laminar Flow in a Channel Expansion,'' J. Comput. Phys., **54**, pp. 468–488.
[20] Maday, Y., and Patera, A. T., 1989, ''Spectral Element Methods for the Navier-Stokes Equations,'' *State of the Art Surveys on Computational Mechanics*, A. K. Noor and J. T. Oden, eds., ASME, New York, pp. 71–143.
[21] Fischer, P. F., 1997, ''An Overlapping Schwarz Method for Spectral Element Solution of the Incompressible Navier-Stokes Equations,'' J. Comput. Phys., **133**, pp. 84–101.
[22] Fischer, P. F., and Patera, A. T., 1992, ''Parallel Spectral Element Solutions of Eddy-Promoter Channel Flow,'' *Proceedings of the European Research Community on Flow Turbulence and Computation Workshop*, Lausanne, Switzerland, Cambridge University Press, pp. 246–256.
[23] Patankar, S. V., Liu, C. H., and Sparrow, E. M., 1977, ''Fully Developed Flow and Heat Transfer in Ducts Having Streamwise Periodic Variations of Cross-Sectional Area,'' ASME J. Heat Transfer, **99**, pp. 180–186.
[24] Kays, W. M., and Crawford, M. E., 1993, *Convection Heat and Mass Transfer*, third ed., McGraw-Hill, New York.
[25] Incropera, F. P., and DeWitt, D. P., 1996, *Introduction to Heat Transfer*, 3rd ed., John Wiley and Sons, New York.

Computation of Sub-Micron Thermal Transport Using an Unstructured Finite Volume Method

J. Y. Murthy
School of Mechanical Engineering,
Purdue University,
West Lafayette, IN 47907
e-mail: jmurthy@ecn.purdue.edu

S. R. Mathur
Fluent Inc.,
10 Cavendish Court,
Lebanon, NH 03766
e-mail: sm@fluent.com

An unstructured finite volume scheme is applied to the solution of sub-micron heat conduction problems. The phonon Boltzmann transport equation (BTE) in the relaxation time approximation is considered. The similarity between the radiative transfer equation (RTE) and the BTE is exploited in developing a finite volume scheme for the BTE. The spatial domain is divided into arbitrary unstructured polyhedra, the angular domain into control angles, and the frequency domain into frequency bands, and conservation equations for phonon energy are written. The unsteady wave propagation term, not usually present in thermal radiation problems, is differentiated using a fully implicit scheme. A sequential multigrid scheme is applied to solve the nominally linear set. Isotropic scattering due to a variety of mechanisms such as impurity and Umklapp scattering is considered. The numerical scheme is applied to a variety of sub-micron conduction problems, both unsteady and steady. Favorable comparison is found with the published literature and with exact solutions. [DOI: 10.1115/1.1518495]

Keywords: Computational, Conduction, Heat Transfer, Microscale, Modeling

Introduction

Heat conduction at very small scales is becoming increasingly important in the development of microelectronics, thin films, superlattices, nanomaterials and in short-pulse laser heating [1]. In silicon-on-insulator (SOI) devices, for example, a thin layer of silicon is supported by a thick low-conducting silicon dioxide layer. Lateral conduction in the silicon layer is critical in maintaining device temperature at acceptable levels. As device dimensions fall further, and the silicon layer thickness falls below the phonon mean free path Λ ($\approx$300 nm at room temperature), subcontinuum effects are expected to become increasingly important. Phonon confinement effects due to boundary scattering have been shown to decrease the effective conductivity of thin silicon layers [2] with deleterious effects on the thermal control of microelectronics. When the size of heat sources becomes comparable to Λ, again, sub-micron effects must be accounted for [3,4]. Subcontinuum interface effects become very important in superlattices and periodic thin film structures [5]. Since measurements are difficult to make at sub-micron scales, simulation is playing an increasingly critical role in understanding sub-continuum heat transfer. However, general purpose simulation methodologies remain to be developed.

Heat transfer in semiconductors and dielectrics occurs by phonon transport. At very small length and time scales conventional analyses using the Fourier law can yield erroneous results [6,7]. If $L/\Lambda \leqslant 1$ but $\lambda/L \ll 1$ and phase/coherence effects can be neglected, phonons can be treated as particles and the Boltzmann Transport Equation (BTE) may be used [6,7,8,5,3,4]. An analogy between the photon BTE in the relaxation time approximation and the radiative transfer equation (RTE) in thermal radiation has long been recognized [6]. This similarity has been exploited by researchers in developing numerical methods for solving the BTE. Kumar et al. [9] developed a differential discrete ordinates method whereby the angular domain was discretized using techniques similar to the conventional discrete ordinates method [10]; standard NAG and IMSL routines were used for the spatial operators. Majumdar and co-workers [6,7] also used a discrete ordinates method with an explicit Euler scheme for unsteady terms and an upwind differencing of spatial derivatives. These studies were used to study the conduction behavior of one-dimensional layers in the presence of various scattering mechanisms, both gray and frequency-dependent. Sverdrup et al. [4] developed a similar methodology to study the problem of electro-static discharge (ESD) in microelectronics. Here, the interest was in delineating the effect of a small unsteady heat source due to electron-phonon scattering on the predicted temperature field. Chen [5] considered the effective conductivity of layers of sub-micron thin films using a semi-analytical solution to the RTE. A semi-analytical approach was also taken in predicting non-equilibrium heat conduction in the vicinity of spherical nanoparticles in [8].

Nearly all published work in this area is for simple canonical geometries, and there exist few broadly applicable general purpose methods for predicting sub-micron conduction in real applications. In recent years, efficient unstructured solution-adaptive finite volume methods for the solution of the RTE have been developed [11] to address a variety of complex thermal radiation problems. In this paper, we extend this class of finite volume method to the solution of both steady state and transient phonon Boltzmann transport equation. Both gray and frequency-dependent problems are addressed. Conjugate heat transfer between sub-continuum and Fourier conduction regions is considered. Results using the method are compared to previously published solutions and are shown to be satisfactory.

Governing Equations

We consider a domain consisting of both sub-continuum and continuum regions. For the purposes of this paper, a sub-continuum region is defined as one for which the ratio $\Lambda/L \geqslant O(1)$. For such regions, heat conduction is described by the phonon Boltzmann transport equation. Continuum regions are those for which $\Lambda/L \ll O(1)$. For such regions, the Fourier law for heat conduction is assumed to hold.

Contributed by the Heat Transfer Division for publication in the JOURNAL OF HEAT TRANSFER. Manuscript received by the Heat Transfer Division December 14, 2001; revision received July 22, 2002. Associate Editor: D. Poulikakos.

The phonon Boltzmann transport equation may be written in the relaxation time approximation in terms of the phonon distribution $f_\omega(x,y,z,t,\omega,\mathbf{v})$ as [7]:

$$\frac{\partial f_\omega}{\partial t}+\mathbf{v}\cdot f_\omega=\frac{f_\omega^0-f_\omega}{\tau_\omega} \tag{1}$$

Here, ω denotes a dependence on the phonon frequency, which ranges from zero to ω_d, the Debye cutoff frequency [12]. τ_ω is the relaxation time, which typically depends on the frequency and temperature. $\mathbf{v}$ is the velocity vector in the direction s and is given by:

$$\mathbf{v}=v\mathbf{s}=v(\sin\,\theta\,\sin\,\phi\mathbf{i}+\sin\,\theta\,\cos\,\phi\mathbf{j}+\cos\,\theta\mathbf{k}) \tag{2}$$

Here v is the phonon group velocity. The angles θ and ϕ are the polar and azimuthal angles defined with respect to the global Cartesian system (x,y,z). For clarity, we assume a single group velocity independent of frequency. More complex dispersion relationships are easily incorporated if necessary. We assume that $\theta_d/T\gg 1$ for simplicity; this restriction is also easily relaxed.

Similar to [6], we define a phonon intensity as

$$I_\omega=\frac{1}{4\pi}\sum_p v f_\omega \hbar\omega\mathcal{D}(\omega) \tag{3}$$

Here the summation p is over the three phonon polarizations. $\mathcal{D}$ is the Debye density of states and $\hbar=h/2\pi$. Similar to Majumdar [6], we may write the equation of phonon radiative transfer (EPRT) as

$$\frac{1}{v}\frac{\partial I_\omega}{\partial t}+\nabla\cdot(\mathbf{s}I_\omega)=\frac{I_\omega^0-I_\omega}{v\tau_\omega} \tag{4}$$

I_ω^0 is given by

$$I_\omega^0=\frac{1}{4\pi}\int_{4\pi} I_\omega d\Omega \tag{5}$$

where Ω denotes solid angle.

Boundary Conditions

Though a variety of interface conditions may present themselves in micro-scale applications [5], we consider the following boundary conditions on the phonon intensity in the present paper.

Thermalizing Boundaries. Thermalizing boundaries are boundaries at which the temperature may be assumed given. Such boundaries are assumed to be perfectly absorbing. They correspond to black given-temperature boundaries in radiative transfer. Here, for directions outgoing from the boundary $(\mathbf{s}\cdot\mathbf{n}<0)$, the intensity I_ω in a frequency range $(\omega_1-\omega_2)$ about ω is given by

$$\int_{\omega_1}^{\omega_2} I_\omega(\mathbf{s})d\omega=(F(\lambda_1 T_b)-F(\lambda_2 T_b))\sigma T_b^4/\pi \tag{6}$$

Here $\lambda=2\pi v/\omega$. $F(\lambda T)$ is the emissive power fraction associated with the phonon equilibrium distribution function and is given by

$$F(\lambda T)=\frac{15}{\pi^4}\int_{C_2/\lambda T}^{\infty}\frac{\xi^3 d\xi}{e^\xi-1} \tag{7}$$

Here, $C_2=hv/k_B$, where k_B is the Boltzmann constant. The Stefan-Boltzmann constant for phonons is taken to be [6]

$$\sigma=\frac{\pi^2 k_B^4}{40\hbar^3 v^2}$$

Specularly Reflecting or Symmetry Boundaries . At a specularly reflecting boundary with an outward-pointing normal $\mathbf{n}$ the intensity in the outgoing directions is given by

$$I_\omega(\mathbf{s})=I_\omega(\mathbf{s_r})$$

where

$$\mathbf{s_r}=\mathbf{s}-2(\mathbf{s}\cdot\mathbf{n})\mathbf{n}$$

For continuum regions, the corresponding condition on the temperature is

$$-k\nabla T\cdot\mathbf{n}=0$$

Interfaces Between Continuum and Sub-Continuum Regions. Here, the net phonon energy impinging on the interface from the sub-continuum region is balanced by the conduction heat flux in the continuum region. If the interface normal $\mathbf{n}$ points into the continuum region, we may write

$$\int_0^{\omega_d}\int_{4\pi} I_\omega \mathbf{s}\cdot\mathbf{n}d\Omega d\omega=-k\nabla T\cdot\mathbf{n} \tag{9}$$

Equation (9) determines the interface temperature T_b of the continuum region. The condition on the outgoing phonon intensity is given by Eq. (6).

Recovery of Temperature

In sub-continuum regions, an equivalent equilibrium temperature may be recovered from the phonon intensity field. If phonon frequencies in the range $(\omega_1-\omega_2)$ are considered, the equivalent temperature is found from

$$[F(\lambda_1 T)-F(\lambda_2 T)]\frac{\sigma T^4}{\pi}=\frac{1}{4\pi}\int_{\omega_1}^{\omega_2}\int_{4\pi} I_\omega d\Omega\; d\omega \tag{10}$$

If the range $\omega_1-\omega_2$ does not cover the range $(0-\infty)$, Eq. (10) represents an implicit equation in T and iteration is required to recover it.

Numerical Method

A detailed description of the basic method is available in our previously published papers [11,13]. The treatment of continuum regions is described in our previous publications [14]. We briefly summarize the main ideas behind the discretization of the BTE below.

Discretization. The spatial domain is discretized into arbitrary convex polyhedral control volumes. The angular space 4π at any spatial location is discretized into discrete non-overlapping control angles Ω_i, the centroids of which are denoted by the direction vector $\mathbf{s_i}$, and the polar and azimuthal angles θ_i and ϕ_i. Each octant is discretized into $N_\theta\times N_\phi$ solid angles. The angles θ and ϕ are measured with respect to the global Cartesian system (x,y,z). The angular discretization is uniform; the control angle extents are given by $\Delta\theta$ and $\Delta\phi$. The frequency domain $(0-\omega_d)$ is discretized in N_b frequency bands of extent $\Delta\omega$; these bands need not be equal in extent, but for simplicity, they are assumed so in the development that follows.

For each discrete direction i Eq. (4) is integrated over the frequency band $\Delta\omega$, the volume $\Delta\mathcal{V}_0$ of the control volume $C0$ in Fig. 1, the solid angle Ω_i and the time step Δt to yield

$$(I_{ik}-I_{ik}^{n-1})\frac{\Delta\mathcal{V}_0\Delta\Omega}{v\Delta t}+\sum_f |\mathbf{A}|J_f I_{ik,f}=(I_k^0-I_{ik})\frac{\Delta\mathcal{V}_0\Delta\Omega}{v\tau_k} \tag{11}$$

Here, I_{ik} is the band-integrated cell centroid intensity in the direction i and the frequency band k and is given by

$$I_{ik}=\int_{\Delta\omega_k} I_\omega d\omega$$

and is used as the solution variable. The variable I_k^0 is the angular average of I_{ik} at the cell centroid and is given by

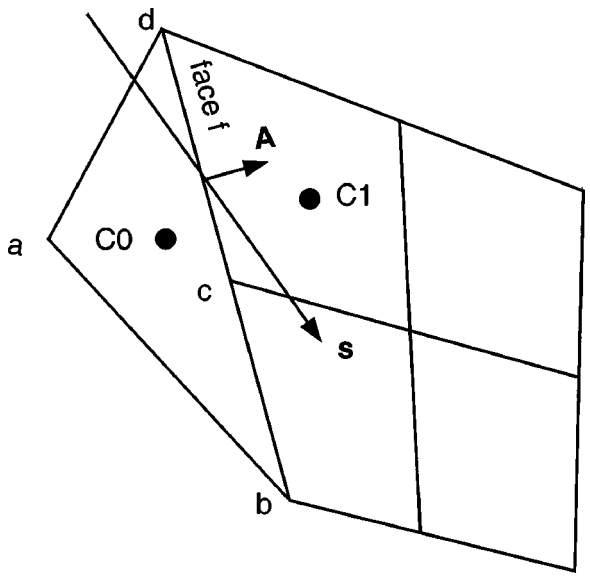

Fig. 1 Control volume for phonon energy conservation in direction *s*

$$I_k^0 = \frac{1}{4\pi} \sum_i I_{ik} \Delta\Omega \tag{13}$$

Variables at the previous time are superscripted $(n-1)$; values at the current time are un-superscripted. A fully implicit scheme is used in Eq. (11); consequently, the transport and scattering terms are evaluated at the present time. $I_{ik,f}$ is the intensity associated with the direction i and the frequency band k at the face f of the control volume. The quantity τ_k is scattering time constant in the frequency band k. J_f is a geometric factor defined below.

For unstructured meshes, cell faces are arbitrarily oriented with respect to the angular discretization, and control angle overhang results [11]. For directions with no control angle overhang, we write

$$J_f = \hat{\mathbf{e}}_\mathbf{n} \cdot \int_{\Delta\theta} \int_{\Delta\phi} \mathbf{s} \sin\theta \, d\theta \, d\phi \tag{14}$$

where $\hat{\mathbf{e}}_\mathbf{n}$ is

$$\hat{\mathbf{e}}_\mathbf{n} = \frac{\mathbf{A}}{|\mathbf{A}|} \tag{15}$$

Using a standard "step" approximation for $I_{ik,f}$ [10]

$$I_{ik,f} = I_{ik,\text{upwind}}$$

Here $I_{ik,\text{upwind}}$ is the value of I_i in the "upwind" cell. Higher-order reconstruction of the face value is also possible [13]. For directions with control angle overhang, a pixelation approach, described in Murthy and Mathur [11] is used. Each control angle is pixelated into $N_{\theta_1} \times N_{\phi_1}$ pixels which are used to compute the fraction of control angle overhang, which in turn determines the fraction of the neighbor cell values used to write $I_{ik,f}$.

Solution Procedure. The intensity equations result in a set of coupled nominally linear algebraic equations at each discrete time instant. An implicit time marching scheme is adopted. Intensities in each band k are coupled through the I_k^0 term. For the boundary conditions considered here cross-band coupling occurs only at conjugate boundaries when phonon energy is redistributed across frequency. At any given time step, the intensities in each direction in each band are solved sequentially and iteratively, using prevailing values to resolve nonlinearities. An algebraic multigrid scheme is used to solve each nominally linear set, as described in Mathur and Murthy [13].

Results

Ballistic Transport. The numerical method presented above has been validated for several steady state cases by applying it to the solution of the RTE [11,15,16]. In order to validate the method for transient cases, we first consider the ballistic transport limit of the BTE for heat transfer between parallel plates separated by length L. Assuming gray behavior, the governing equation is

$$\frac{1}{v}\frac{\partial I}{\partial t} + \nabla \cdot (\mathbf{s}I) = 0 \tag{17}$$

The left boundary is held at $T_1 = 30$ K and the right boundary at $T_2 = 300$ K. The medium is at $T = T_2$ at $t = 0$.

The exact solution for this problem can be easily determined. For $t^* < 1$, the net irradiation G defined as

$$G = \frac{1}{4}\int_{4\pi} I d\Omega \tag{18}$$

is given by

$$G(x^*, t^*) = \begin{cases} G_2(1-\xi) + G\xi & \text{if } x^* < t^* \\ G_2 & \text{otherwise} \end{cases} \tag{19}$$

where $\xi = 0.5(1 - x^*/t^*)$, $x^* = x/L$, $G_1 = \sigma T_1^4$ and $G_2 = \sigma T_2^4$. We define an equivalent temperature, $T = (G/\sigma)^{1/4}$ and its nondimensionalized value as $T^* \equiv (T - T_2)/(T_1 - T_2)$. Numerical results for the variation of T^* along x^* are compared with the exact solution at two time instants in Fig. 2.

As indicated by Eq. (18), G is composed of the solution of the BTE over all directions. For any given direction **s**, the solution for the intensity I in that direction is a step function, moving with a speed v. In other words, the profile for G is composed of an infinite number of step solutions. Thus, even though the exact G profile is linear, this problem is quite challenging from a numerical solution point of view. Good spatial as well as temporal accuracy is required to minimize the numerical diffusion that tends to smear the step solution in any given direction. Even more importantly, the *combination* of intensity profiles in all directions must be correctly represented or else unphysical wiggles in the G solution result. This combination of effects can be observed in Fig. 2. At $t^* = 0.1$, the coarse solution (obtained using a 40 cell mesh, 2×1 angular discretization and $\Delta t^* = 1/40$) is much more diffuse compares to the fine solution (obtained with a 160 cell mesh, 8×1 angular discretization and $\Delta t^* = 1/400$). At $t^* = 1.0$, the coarse solution exhibits wiggles in the profile. This results from

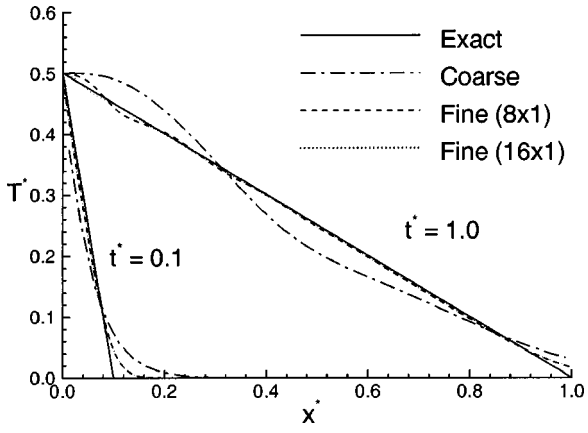

Fig. 2 Ballistic transport: comparison with exact solution

the coarse angular discretization. The intensity in a given solid angle is convected with the same speed; when the solid angle is large, gross errors in the combined speed of the thermal wave result. Thus, in addition to fine spatial and temporal discretization, fine angular discretization is also required. With 8×1 and 16×1 discretizations the solution is significantly better. Since many micro- and nano-scale thermal problems operate close to the ballistic limit, this example points to the need for sufficient angular resolution in any unsteady computation of phonon transport.

Unsteady Conduction in a Thin Diamond Film. We consider here the case of unsteady heat conduction in a diamond film of width L, similar to the problem considered by Majumdar and co-workers [6,7]. The film is initially at $T_2=300$ K. At $t=0$, the left boundary is raised to $T_1=301$ K. The objective is to compute the time evolution of the equivalent temperature defined in Eq. (10). Two phonon scattering processes are considered, impurity scattering and Umklapp scattering [7]. For impurity scattering, the relaxation time τ_i is taken to be:

$$\tau_i=\frac{1}{\alpha\Phi\,\eta v}$$

Here, R is the radius of the lattice imperfections, α is a constant that is approximately unity, and η is the number density of impurities. The scattering cross-section Φ is taken to be

$$\Phi=\pi R^2\frac{\xi^4}{\xi^4+1}$$

where

$$\xi=\frac{\omega R}{v}$$

Values of the constants used are given in Table 1. For Umklapp scattering, the relaxation time is taken to be

$$\tau_u=A\frac{T}{\theta_d\omega}\exp\left(\frac{\theta_d}{\gamma T}\right)$$

Values of the constants A, γ and Debye temperature θ_d are given in Table 1. Mathiessen's rule is used to obtain the combined time constant of the two scattering processes:

$$\frac{1}{\tau_\omega}=\frac{1}{\tau_i}+\frac{1}{\tau_u}$$

Frequency-dependent calculations are done using three different film thicknesses, $L=0.1$, 1.0 and 10.0 μm. At the frequency corresponding to the dominant energy ($\omega_{\rm dom}=k_BT/\hbar$), the acoustic thickness $L/v\,\tau_{\rm dom}$ for these three values ranges from 0.224 to 22.4. A mesh of 80 cells is used. An angular discretization $N_\theta\times N_\phi$ of the octant of 2×1 is used for all but the lowest acoustic thickness, for which an angular discretization of 4×1 is used. The frequency domain $(0-\omega_d)$ is divided into 29 equal frequency bands and the relaxation time τ_ω in each band is evaluated at the mid-point frequency. A dimensionless time step $\Delta t/(L/v)$ of 0.01 is chosen. Numerical experiments varying these discretizations were done for $\tau=2.24$ and indicate that the maximum error in the equivalent temperature with respect to finer discretization is well under 1%.

Table 1 Physical properties of diamond

Property	Symbol	Value
Impurity number density	η	$0.154\times10^{26}\ (\frac{1}{m^3})$
Radius of lattice imperfection	R	1.785 Å
Phonon velocity	v	1.2288×10^4 m/s
Umklapp scattering constant A	A	163.94
Umklapp scattering constant	γ	1.58
Debye temperature	θ_d	1860 K
Stefan-Boltzmann constant	σ	50.47 W/m^{2}K^4

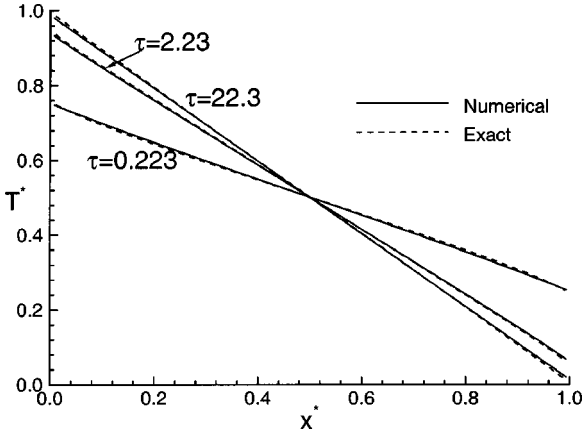

Fig. 3 Conduction in diamond thin film: comparison with exact steady-state solution

Steady State. The exact solution to one-dimensional gray absorption in a plane slab in radiative equilibrium is given by [10]:

$$\Phi_b(\tau)=\frac{T^4-T_2^4}{T_1^4-T_2^4}=\frac{1}{2}\left[E_2(\tau)+\int_0^{\tau_L}\Phi_b(\tau')E_1(|\tau-\tau'|)d\tau'\right] \tag{25}$$

The exact steady state solution to the non-gray scattering problem may be constructed by using Eq. (25) on a band basis. For a frequency band spanning the range $(\omega_k-\omega_{k+1})$, the band equivalent irradiation $G_k/\sigma=T_k^4$ may be found by interrogating Eq. (25) with boundary temperatures $(F(\lambda_kT_1)-F(\lambda_{k+1}T_1))^{1/4}T_1$ and $(F(\lambda_kT_2)-F(\lambda_{k+1}T_2))^{1/4}T_2$. The acoustic thickness τ is based on the band relaxation time τ_k. The overall equivalent temperature may be found by

$$T^4=\sum_k T_k^4$$

Figure 3 shows a comparison of the computed finite volume solution at steady state with the exact nongray solution for three acoustic thicknesses. The comparison is found to be good. Temperature jumps are seen at the boundaries for low acoustic thicknesses, similar to those found in thermal radiation problems; these jumps would not be present in corresponding Fourier conduction solutions.

Unsteady State. Results for unsteady state for the three acoustic thicknesses are shown in Figs. 4(*a*)–(*c*). Corresponding plots for Fourier conduction are also shown. The latter are computed using the methods outlined in [14]. For acoustic thickness $\tau=0.224$, the wave nature of transport is clearly visible, though scattering tends to spread the wavefront somewhat. The Fourier solutions tend to reach steady state too quickly for low acoustic thicknesses, and do not exhibit the temperature jump at the boundaries either during the time-evolution or at steady state. For larger τ, the discrepancies between the BTE and Fourier solutions decrease, but substantial differences in the evolution speed exist even at $\tau=22.4$.

Equivalent Conductivity of Array of Sub-Micron Rods. To demonstrate the geometric flexibility of our scheme, we consider a periodic array of rods embedded in a matrix of interstitial material as shown in Fig. 5. The array is four rods deep, and has lateral periodicity as shown. Adjacent rows of rods are displaced randomly with respect to each other; we present here results from

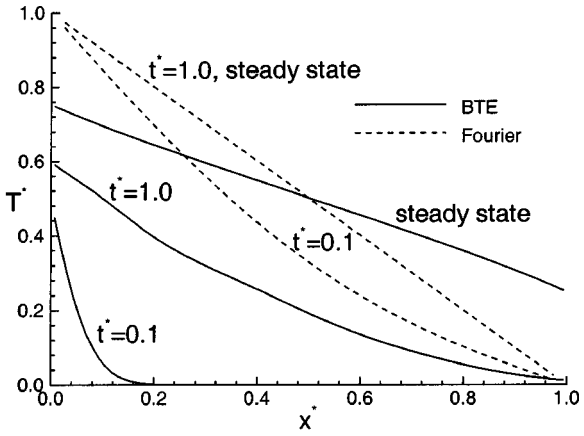

(a) $\tau = 0.224$

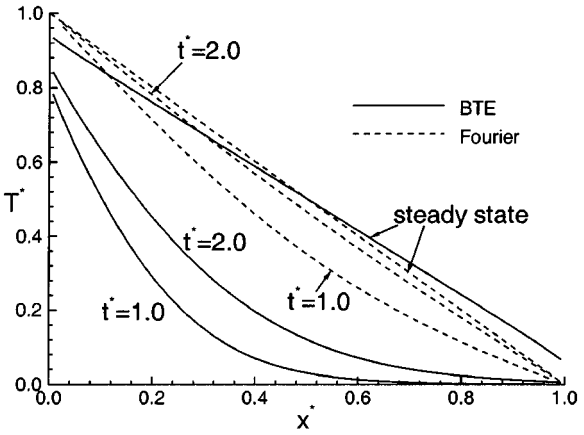

(b) $\tau = 2.24$

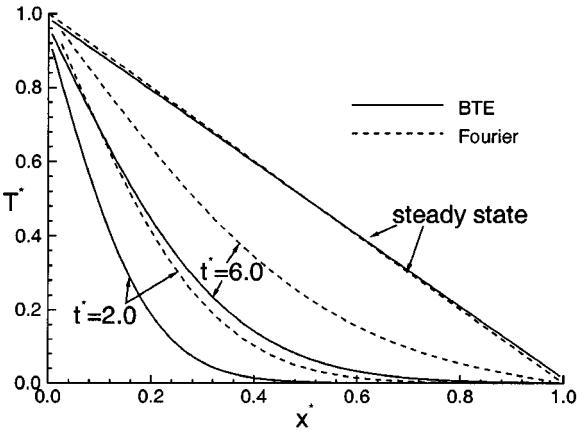

(c) $\tau = 22.4$

Fig. 4 Conduction in diamond thin film: unsteady state

a single realization where the rows starting from the top are displaced by 0.236928*l* 0.633978*l* and 0.139087*l* respectively with respect to the bottom row where *l* is the width of one module. The top and bottom boundaries are held at $T_1 = 300$ K and $T_2 = 301$ K respectively, yielding an emissive power ratio of 1.013; this has been kept deliberately small to yield thermal conductivities that are constant with respect to temperature. Both boundaries are assumed to be diffuse emitters and are completely absorbing.

The Fourier law is assumed to hold within the rods; this is valid if $(d/\Lambda) \gg 1$. The interstitial region is considered to consist of a material which may be acoustically thin. Thus, the BTE is solved in the interstices, while Fourier conduction is solved in the rods. The interface is assumed diffuse and completely absorbing. The aspect ratio of the bed depth to the rod diameter (L/d) is assumed to be 5.333. All computations are gray and steady. Mixed BTE/Fourier computations are done for a range of acoustic thicknesses $l/(v\tau)$. Details of the treatment of translationally periodic boundary conditions used here may be found in [16]. In addition, computations are also done for the case when Fourier conduction is valid in both the interstices and in the rods. The interstitial conductivity is deduced from kinetic theory [12].

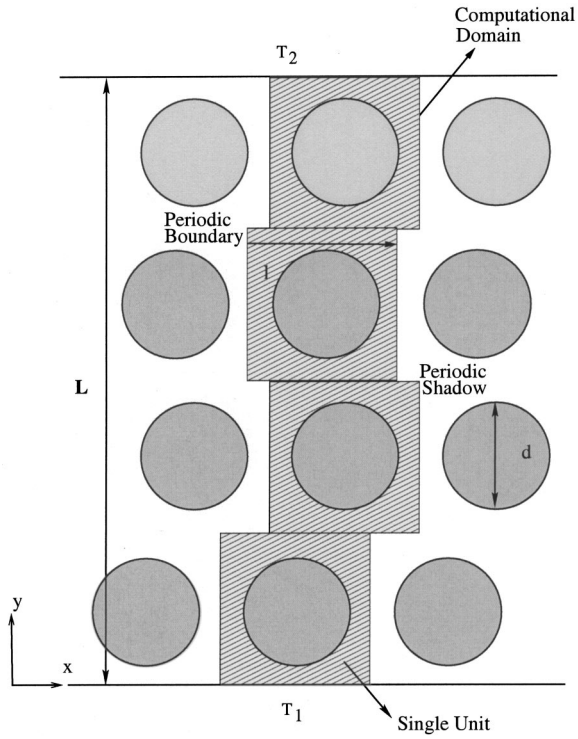

Fig. 5 Rod array embedded in matrix

$$k_i = \frac{1}{3} \overline{C} v^2 \tau$$

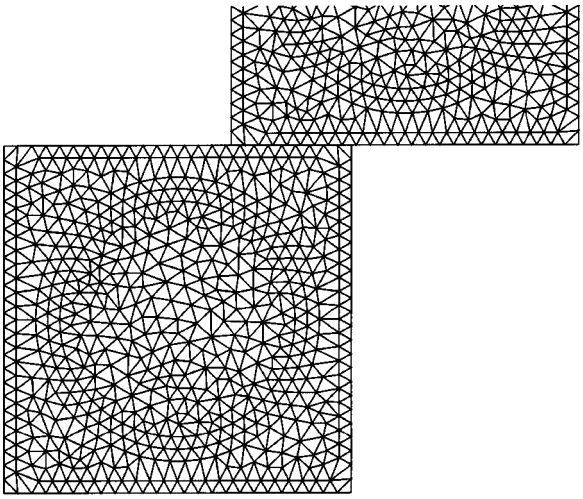

Fig. 6 Detail of mesh

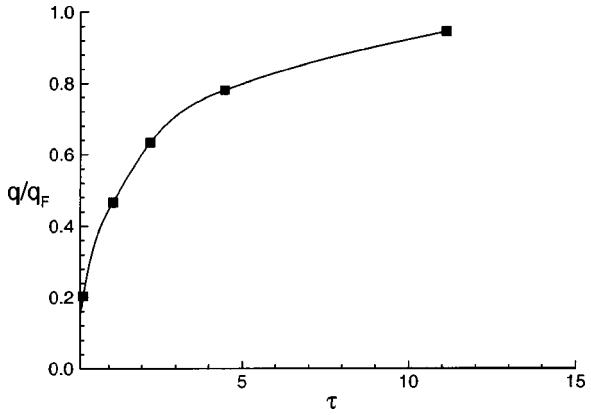

Fig. 7 Heat flux ratio

A dimensionless conductivity ratio $k_s 1/3\bar{C}v^2\tau = 0.1$ is chosen, corresponding to a Planck number of $k_s/(v\tau)/(4\sigma T_1^3)$ of 0.1364.

A fine mesh of 18592 triangular cells is used in the calculation, with a 4×4 angular discretization of the octant with 1×10 pixelation to address the non-orthogonal mesh. A detail of a typical mesh is shown in Fig. 6; nonconformal interfaces between the modules are admitted in the finite volume formulation. We also did computations with both finer and coarser triangular meshes; for the mesh used here, the overall boundary heat flux is accurate to better than 1%.

Figure 7 shows the ratio of the boundary heat fluxes obtained from the mixed BTE/Fourier computations and the pure Fourier cases; this ratio is also the ratio of equivalent bed conductivities for the two cases. The dimensionless Fourier flux $qL/k_i\Delta T$ is an invariant. For high acoustic thicknesses, the Fourier and the mixed BTE/Fourier computations yield the same heat flux, and the ratio tends to unity. For lower acoustic thicknesses, however, the BTE/Fourier computations yield a lower heat flux. This is primarily a result of absorption and diffuse re-radiation in the rods; since the emission is diffuse, phonon energy is radiated back to the cold boundary at lower acoustic thicknesses.

Closure

The unstructured finite volume method has been applied to the computation of steady and unsteady microscale heat transfer using the phonon Boltzmann transport equation. The method has been applied to unsteady and steady phonon transport problems, both gray and non-gray. The method has been shown to address both continuum and sub-micron heat conduction in an integrated fashion within the same finite volume framework. It ensures energy conservation in mixed continuum/sub-continuum domains. Since it admits geometric complexity easily, it forms the basis of a viable tool for computing microscale heat conduction problems. More complex models based on the BTE, including multiple phonon branches and phonon dispersion, may be incorporated within this framework.

Acknowledgments

We wish to acknowledge the use of Fluent Inc.'s solver FLUENT/UNS, and its mesh generators PreBFC and TGrid, in this work.

$\underline{\mathbf{A}}$ = area vector
C = volumetric specific heat
E_1, E_2 = exponential integrals
f_ω = phonon distribution function
F = emissive power fraction
h = Planck constant
I_ω = intensity in frequency band ω
I_ω^0 = equilibrium intensity
k_B = Boltzmann constant
k_i = interstitial conductivity
k_s = solid conductivity
L = domain length
$\mathbf{n}$ = unit normal vector
N_θ, N_ϕ = polar and azimuthal control angles per octant
q = heat flux
q_F = Fourier heat flux
$\mathbf{s}$ = ray direction vector (dimensionless)
t = time
t^* = dimensionless time tv/L
T = temperature
T_1, T_2 = boundary temperatures
$\mathbf{v}$ = phonon velocity vector
x_j = coordinate direction
$\Delta\mathcal{V}$ = volume of control volume
Λ = phonon mean free path
λ = phonon wavelength
Ω = solid angle
Ω_i = discrete solid angle associated with direction i
θ = polar angle
θ_d = Debye temperature
τ_ω = frequency-dependent relaxation time
τ_i = relaxation time scale for impurity scattering
τ_u = relaxation time scale for Umklapp scattering
ϕ = azimuthal angle
σ = Stefan Boltzmann constant

References

[1] Tien, C., and Chen, G., 1994, "Challenges in Microscale Radiative and Conductive Heat Transfer," ASME J. Heat Transfer, **116**, pp. 799–807.
[2] Asheghi, M., Touzelbaev, M., and Goodson, K., 1997, "Phonon-Boundary Scattering in Thin Silicon Layers," Appl. Phys. Lett., **71**, pp. 1798–1800.
[3] Sverdrup, P., Ju, Y., and Goodson, K., 1998, "Sub-Continuum Simulations of Heat Conduction in Silicon-on-Insulator Devices," ASME J. Heat Transfer, **120**, pp. 30–36.
[4] Sverdrup, P., Banerjee, K., Dai, K., Shih, W., Dutton, R., and Goodson, K., 2000, "Sub-Continuum Simulations of Deep Sub-Micron Devices under ESD Conditions," *Proceedings of the International Conference on Simulation of Semiconductor Processes and Devices*, IEEE, pp. 54–57.
[5] Chen, G., 1997, "Size and Interface Effects on Thermal Conductivity of Superlattices and Periodic Thin Film Structures," ASME J. Heat Transfer, **119**, pp. 220–229.
[6] Majumdar, A., 1993, "Microscale Heat Conduction in Dielectric Thin Films," ASME J. Heat Transfer, **115**, pp. 7–16.
[7] Joshi, A., and Majumdar, A., 1993, "Transient Ballistic and Diffusive Phonon Heat Transport in Thin Films," J. Appl. Phys., **74**, pp. 31–39.
[8] Chen, G., 1996, "Nonlocal and Nonequilibrium Heat Conduction in the Vicinity of Nanoparticles," ASME J. Heat Transfer, **118**, pp. 539–545.
[9] Kumar, S., Majumdar, A., and Tien, C., 1990, "The Differential Discrete-Ordinates Method for Solutions of the Equation of Radiative Transfer," ASME J. Heat Transfer, **112**, pp. 424–429.
[10] Modest, M. F., 1993, *Radiative Heat Transfer, Series in Mechanical Engineering*, McGraw Hill, New York, NY.
[11] Murthy, J., and Mathur, S., 1998, "Finite Volume Method for Radiative Heat Transfer Using Unstructured Meshes," J. Thermophys. Heat Transfer, **12**(3), pp. 313–321.
[12] Kittel, C., 1996, *Introduciton to Solid State Physics*, John Wiley & Sons, New York.
[13] Mathur, S., and Murthy, J., 1997, "A Pressure Based Method for Unstructured Meshes," Numer. Heat Transfer Part B, **31**(2), pp. 195–216.
[14] Murthy, J., and Mathur, S., 1998, "A Conservative Numerical Scheme for the Energy Equation," ASME J. Heat Transfer, **120**, pp. 1081–1085.
[15] Murthy, J. Y., and Mathur, S. R., 1998, "Radiative Heat Transfer in Axisymmetric Geometries Using an Unstructured Finite Volume Method," Numer. Heat Transfer, Part B, **33**(4), pp. 397–416.
[16] Mathur, S., and Murthy, J., 1998, "Radiative Heat Transfer in Periodic Geometries Using a Finite Volume Scheme," ASME J. Heat Transfer, **121**, pp. 357–364.

Modeling the Cooling Process Path of a Dehumidifying Coil Under Frosting Conditions

P. J. Mago
e-mail: pmago@ufl.edu
Department of Mechanical Engineering,
Universidad de Oriente,
Puerto La Cruz, Venezuela

Dr. S. A. Sherif
Fellow ASME
e-mail: sasherif@ufl.edu
Department of Mechanical
and Aerospace Engineering,
University of Florida,
228 MEB, P.O. Box 116300,
Gainesville, FL 32611-6300

Whenever humid air comes in contact with a cooling coil whose temperature is below both the dew-point of water vapor in air and the freezing point, frost will form. The nature of the frost forming on the coil will depend to a large measure on the psychrometric conditions prevailing inside the freezer and whether the air around the coil is subsaturated or supersaturated. Psychrometric theory and the apparatus-dew-point calculating procedure assume that the cooling process path as the air passes through the coil is a straight-line on the psychrometric chart. The actual path is however a result of a much more complex series of processes and is therefore a curve. While researchers have calculated the actual process path on a dehumidifying coil, none has attempted to do the same for a frosted, multi-row coil. It is believed that determining the actual conditions leaving a given row in a multi-row freezer coil is a crucial step in identifying the coil location in the vicinity of which the transformation from the subsaturated zone to the supersaturated zone occurs. This will prove a key step in identifying a demarcation line between the unfavorable snow-like frost and the more traditional (and more favorable) frost formation patterns. Thus, the objective of this paper is to calculate the air path on an actual industrial-size finned-tube, multi-row coil utilizing experimentally derived data and correlate the shape of the path with the prevailing psychrometric conditions in the freezer in the hope of identifying the demarcation line in question. [DOI: 10.1115/1.1494451]

Keywords: Dehumidification, Cooling, Energy, Heat Transfer, Mass Transfer, Frost Formation

Introduction

In a recent paper by the authors (Sherif et al. [1]), observations highlighting the importance of applying psychrometric theory in the design and operation of freezers were made. The authors argued that without proper understanding of the theory, freezer operation could be dominated by the presence of unwanted ice crystal formation, snow-like frost accumulation, and severe degradation in the coil heat transfer performance. A typical example that illustrates how the lack of understanding of psychrometric theory can be detrimental to freezer operation has to do with the proper choice of the so-called coil ''TD.'' The coil ''TD'' is a term used in the industrial refrigeration community to designate the difference between the coil entering air temperature and the coil refrigerant temperature. Prolonged freezer operation under less-than-optimum conditions typically results in a steady reduction in the refrigerating capacity. This is primarily caused by a steady build-up of snow-like frost on the freezer coil as well as on the suction line of the compressor. In attempting to correct for the loss of cooling capacity, inexperienced freezer operators are tempted to decrease the temperature in the suction line of the compressor. While this may seem like an intuitive remedy, nothing can be further from the truth. Decreasing the suction line temperature decreases the refrigerant temperature inside the freezer coil and hence increases the coil ''TD.'' Increasing the coil ''TD'' makes it more likely for the cooling process line to cross the saturation curve into the supersaturated zone of the psychrometric chart as was shown by Sherif et al. [1], thus contributing to the creation of airborne ice crystals and the subsequent formation of snow-like frost. Formation of snow-like frost further exacerbates the problem.

Despite the fact that the frosting problem has been extensively researched (see Sherif et al. [2]), very few looked into the formation mechanism under supersaturated conditions while accounting for psychrometric effects. These effects have been routinely ignored by refrigeration system engineers and designers, which prompted the current investigation. Among the large amount of work reported for frost formation in the subsaturated zone, gaps and inconsistencies still exist. These gaps and inconsistencies have been articulated in detail in Sherif et al. [2]. One of the problems that seems to have been under investigation deals with the frost-air interface temperature and how it evolves both spatially and temporally on a frosted surface. Both Padki et al. [3] and Sherif et al. [4] demonstrated that most of the relevant frost parameters depend in whole or in part on the interface temperature. However, more recent studies, such as those of Thomas et al. [5], Chen et al. [6,7] and Besant [8], have provided new experimental data on the frost surface temperature. Results of those studies should prove useful in developing a better overall understanding of the frost formation process at low temperatures. For finned heat exchangers, which are the subject of the present investigation, we can find the works of Notestine [9], Gates et al. [10], Huffman [11], Huffman and Sepsy [12], Gatchilov and Ivanova [13], Kondepudi [14], Kondepudi and O'Neal [15–22], Senshu et al. [23], Rite and Crawford [24], Ogawa et al. [25], Tao et al. [26,27], Al-Mutawa [28], Sherif et al. [29], Besant [8], Thomas et al. [5], Chen et al. [6], Al-Mutawa et al. [30–33], and Al-Mutawa and Sherif [34].

As was observed by Sherif et al. [2], the nature of the frost forming on a cold surface depends to a large measure on the psychrometric conditions prevailing inside the freezer and whether the air around the coil is subsaturated or supersaturated. Psychrometric theory and the apparatus-dew-point calculating procedure assume that the cooling process path as the air passes through the coil is a straight-line process on the psychrometric chart. In our continuing effort to provide more insight into the frost formation mechanism and how it relates to the prevailing

Contributed by the Heat Transfer Division for publication in the JOURNAL OF HEAT TRANSFER. Manuscript received by the Heat Transfer Division July 31, 2001; revision received March 20, 2002. Associate Editor: G. P. Peterson.

psychrometric conditions, we will attempt to calculate the path on an actual industrial-size finned-tube, multi-row freezer coil. This will be done employing basic heat and mass transfer principles. The model will then be validated employing measured data on the same coil. Development of a systematic mechanism for calculating the cooling process path on a finned freezer coil will prove very significant towards enhancing our understanding of the frost formation process and its relationship to the psychrometric theory of moist air. Determining the actual conditions leaving a given row in a multi-row freezer coil is a crucial step in identifying the coil location in the vicinity of which the transformation from the subsaturated zone to the supersaturated zone occurs. This is a key step in identifying a demarcation line between the unfavorable snow-like frost and the more traditional (and more favorable) frost formation patterns. Thus the objective of this paper is to calculate the air path on an actual industrial-size finned-tube, multi-row coil utilizing experimentally derived data and correlate the shape of the path with the prevailing psychrometric conditions in the freezer in the hope of identifying the demarcation line in question.

Experimental Program

The experimental facility utilized in this program is shown schematically in Fig. 1. The figure shows a laboratory-size freezer with an industrial-size freezer coil (having four fins per inch) located at the center and a water-vapor generator (WVG) facing the coil. Each of the freezer doors has good rubber seals to protect the freezer and the test results from the effect of air infiltration. The heat transfer rate of the test enclosure was determined experimentally while it was clean, dry, and empty.

The finned-tube freezer coil is a liquid overfeed recirculating evaporator with an overfeed ratio of three. This coil has a refrigerating capacity of about two tons at a coil suction temperature of $-40°C$ and is part of a complete refrigeration system discussed in detail in Al-Mutawa et al. [30–32]. Coil details are provided in Fig. 2. The coil finned tubes are arranged in eight rows in the direction of airflow and in a staggered pattern of 38 mm $\times$33 mm, where the tube material is copper having 15.9 mm outside diameter and 0.46 mm thickness. The fins are made of aluminum and have a flat pattern with flat edges. The fins have a thickness of 0.25 mm, and their spacing is four fins per inch. The coil has a finned height of 533 mm and a finned length of 737 mm, where its outside dimensions are 1016 mm $L\times$610 mm $W\times$627 mm H. The hot-gas defrosting method is used with this coil when the coil is operating in the defrosting mode. The finned-tube freezer coil is classified as a draw-through unit since the fan draws the air against the refrigerant in a crossflow direction where each fluid flows at right angle to the other. However, the tubes are circuiting in a manner that the two fluids will approach in a counterflow type heat exchanger arrangement. The freezer coil is employed with one fan that has a diameter of 508 mm and a speed of 18 rev/s and is operated by a 186 W motor. The unit has a face area of 0.39 m^2 and a face velocity of 3.81 m/s, while its capacity is 1.5 m^3/s.

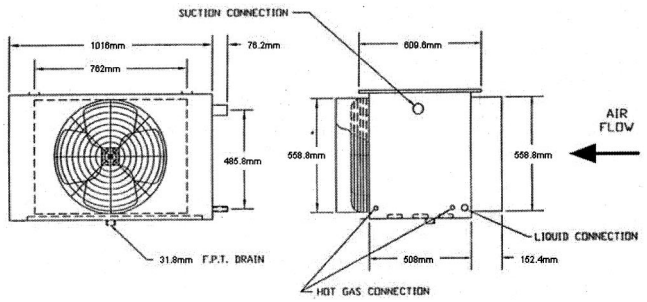

Fig. 2 Schematic of the Test Fan-Coil Unit (FCU-T)

The artificial load generation system is probably one of the most critical systems in the experimental program (see Fig. 3). It is designed to provide the freezer with the required latent heat load in order to be able to manipulate the moisture content inside the freezer during the testing period. This latent heat load is generated by the water-vapor generator (WVG) located outside the freezer. City water is allowed to flow into the WVG through an electronic diaphragm metering pump in order to control the mass flow rate of the steam to be injected inside the freezer. The metering pump capacity ranges from 0.01 to 1 mm/s, where its maximum capacity per day is 0.091 m^3. The pump's maximum injection pressure is 758 kPa. This metering pump has an adjustable speed, which ranges from 5 to 100 strokes per minute, while it also has an adjustable stroke length that ranges from 0 to 100 percent. The metering pump can be operated manually and by a computer. This WVG is a liquid-injection type water-vapor generator equipped with three heating elements strapped to its side and bottom. The vaporizer is insulated with a 25.4 mm thick high temperature insulation enclosed in a galvanized steel housing. The WVG is also equipped with a thermometer, a thermostat, and a pressure relief valve. The bi-metal dial thermometer is accurate to within 0.5°C and has a reading range of 10 to 288°C. The thermostat adjusting screw was used to obtain the desired set point. The pressure relief valve has a cracking pressure range of 0 to 138 kPa. The cracking pressure can be adjusted to the desired set point using the valve's adjustment screw. The water injected into the WVG is heated to the desired temperature inside the vaporizer and is allowed to leave the WVG as steam through a copper tube that passes through the freezer wall to the steam outlet inside the artificial load generator. To prevent steam from freezing inside the copper tube, an electric heating cable is wrapped around the cop-

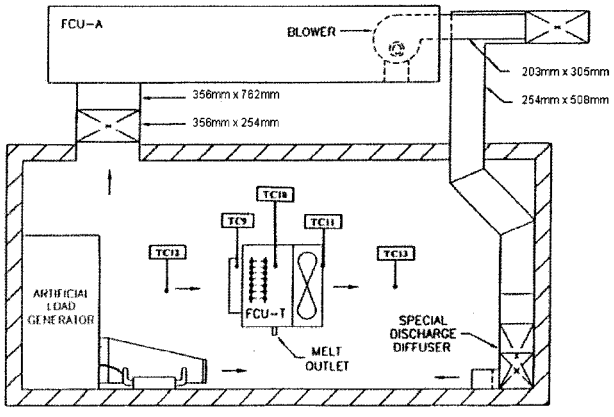

Fig. 1 Schematic of the freezer showing the test and auxiliary coils, the artificial load generator, and the location of thermocouples for temperature measurements

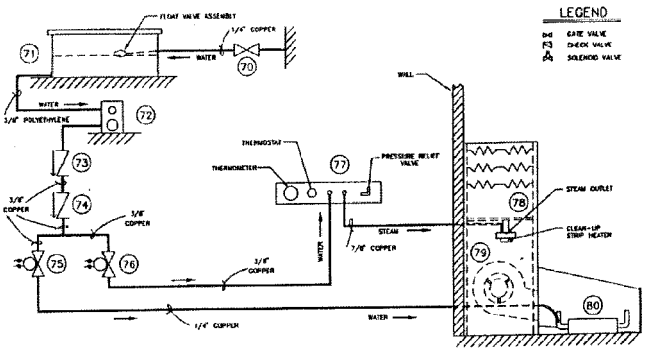

Fig. 3 Schematic of the artificial sensible and latent load generator

per tube inside the freezer. The copper tube and the heating cable are both covered by a 19 mm thick Armaflex insulation. A ''clean-up'' strip heater of 150 W is also attached to the bottom of the steam outlet in order to prevent the steam from freezing at the outlet that will then stop the flow of steam to the freezer. The artificial load generation system is employed with a direct-drive blower that is used to distribute the steam inside the freezer. The blower has a capacity of 0.73 m^3/s at 0.025 m static pressure when its motor is operating at a speed of 17.5 rev/s.

Temperatures have been measured at twenty locations using copper-constant (type-T) thermocouples with an uncertainty of ± 0.2°C. This type is suitable for low temperature applications as well as up to 370°C. All thermocouples have been calibrated using a constant-temperature water bath (model Polyscience-80). Locations of some of the thermocouples employed can be seen in Fig. 1. Temperature measurement using thermocouple TC9 is identified as coil entering air temperature, while temperature measurement using thermocouple TC10 is identified as coil leaving air temperature. Temperature measurement of thermocouple TC3 during the Test Fan-Coil Unit (FCU-T) refrigeration mode is identified as the coil refrigerant temperature.

The relative humidity (RH) of the air inside the freezer was measured both upstream and downstream of the test coil. Relative humidity measurements were performed using a Mamac humidity transducer (HU-224) connected to a remote probe hung inside the freezer. The two humidity transducers have a humidity range of 0 to 100 percent and are accurate to ± 2 percent of the full-scale. They utilize a DC power supply of 12–28 Volts to operate, while they send output signals of 4–20 mA. All measurements have been recorded using a computer equipped with a state-of-the-art data acquisition system.

Analysis

The primary purpose of the analysis described in this section is calculating the air path as it passes through a finned-tube, multi-row dehumidifying coil under frosting conditions. In order to achieve that goal, the slope of the enthalpy-humidity ratio curve on the psychrometric chart must be determined. In order to calculate this slope, several other quantities such as the overall heat transfer coefficient and the frost-air interface temperature have to first be computed. These quantities are determined according to what follows.

External Heat Transfer Coefficient. To determine the external heat transfer coefficient a staggered array is considered. For this configuration, the maximum velocity may occur at either the transverse plane or the diagonal plane. Here we use the diameter of the frosted tube (D_f) instead of the outside tube diameter. The maximum velocity occurs at the diagonal plane if

$$S_D = \left[S_L^2 + \left(\frac{S_T}{2} \right)^2 \right]^{1/2} < \frac{S_T + D_f}{2}$$

In this case, the maximum velocity is given by

$$u_{\max} = \frac{S_T}{2(S_D - D_f)} u_a \tag{1}$$

If the maximum velocity occurs at the transverse plane A_1, it can be expressed as

$$u_{\max} = \frac{S_T}{S_T - D_f} u_a \tag{2}$$

The Reynolds number based on the maximum fluid velocity occurring within the tube bank is given by

$$\mathrm{Re}_o = \frac{u_{\max} D_f}{\nu_a} \tag{3}$$

Table 1 Constants C_1 and m for a staggered arrangement Eq. (4) for air flow over a tube bank of ten or more rows (Incropera and DeWitt [40])

	S_T/D_f							
	1.25		1.50		2.00		3.00	
S_L/D_f	C_1	m	C_1	m	C_1	m	C_1	m
0.60	-	-	-	-	-	-	0.213	0.636
0.90	-	-	-	-	0.446	0.571	0.401	0.581
1.00	-	-	0.497	0.558	-	-	-	-
1.25	0.518	0.556	0.505	0.554	0.519	0.556	0.552	0.562
1.50	0.451	0.568	0.460	0.562	0.452	0.568	0.488	0.568
2.00	0.404	0.572	0416	0.568	0.482	0.556	0.449	0.570
3.00	0.310	0.592	0356	0.580	0.440	0.562	0.428	0.574

The Nusselt number for a unfinned tube bank composed of ten or more rows ($N_L \geq 10$) can be determined using the correlation proposed by Grimison [35]

$$\mathrm{Nu}_o = 1.13 C_1 \mathrm{Re}_0^m \mathrm{Pr}_a^{1/3} \quad \begin{bmatrix} N_L \geq 10 \\ 2000 < \mathrm{Re}_0 < 40{,}000 \\ \mathrm{Pr}_a > 0.7 \end{bmatrix} \tag{4}$$

If the number of rows (N_L) is less than ten a correction factor may be applied such that

$$\mathrm{Nu}_o|_{(N_L<10)} = C_2 \mathrm{Nu}_o|_{(N_L>10)} \tag{5}$$

where C_1 and m are listed in Table 1 while C_2 is listed in Table 2. The external heat transfer coefficient is then expressed by

$$h_{c,o} = \mathrm{Nu}_0 \frac{k_a}{D_f} \tag{6}$$

Internal Heat Transfer Coefficient. The properties are evaluated at the mean refrigerant temperature between the tube inlet and outlet

$$T_{R,m} = \frac{T_{R,i} + T_{R,o}}{2}$$

The Reynolds number for a flow in a circular tube is given by

$$\mathrm{Re}_i = \frac{\rho_R u_m D_i}{\mu_R} \tag{7}$$

where u_m is the mean velocity inside the tube, and D_i is the inside tube diameter. The mean velocity is defined by

$$u_{m,i} = \frac{\dot{m}_R}{\rho_R A_c} \tag{8}$$

where A_c is the cross-sectional area of the tube and m_R is the mass flow rate. The Reynolds number can be reduced to

$$\mathrm{Re}_i = \frac{4\dot{m}_R}{\pi D_i \mu_R} \tag{9}$$

For turbulent flow, the Nusselt number can be calculated using the Dittus-Boelter correlation [36]

$$\mathrm{Nu}_i = 0.023 \mathrm{Re}_i^{0.8} \mathrm{Pr}_R^{0.4} \tag{10}$$

The internal heat transfer coefficient is then given by

$$h_{c,i} = \mathrm{Nu}_i \frac{k_R}{D_i} \tag{11}$$

Frost Surface Temperature. Referring to Fig. 4, the heat transfer rate can be expressed by

Table 2 Correction factor C_2 for a staggered arrangement as provided for in Eq. (5) (Incropera and DeWitt [40])

N_L	1	2	3	4	5	6	7	8	9
C_2	0.68	0.75	0.83	0.89	0.92	0.95	0.97	0.98	0.99

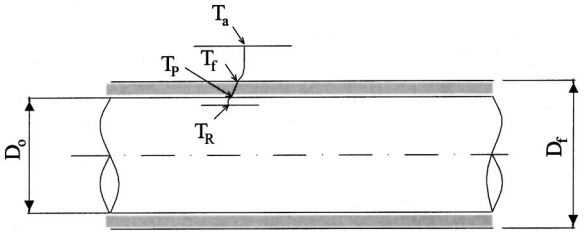

Fig. 4 Physical model of pipe

$$\dot{Q} = h_{c,o}(\pi D_f \lambda)(T_a - T_f) \tag{12}$$

as well as by

$$\dot{Q} = \frac{2\pi k_f \lambda (T_f - T_P)}{\mathrm{Log}_e(D_f/D_o)} \tag{13}$$

which if combined can give the following expression for the frost surface temperature

$$T_f = \frac{h_{c,o} D_f \mathrm{Log}_e(D_f/D_o) T_a + 2k_f T_p}{h_{c,o} D_f \mathrm{Log}_e(D_f/D_o) + 2k_f} \tag{14}$$

where k_f is the thermal conductivity of the frost in W/(m K).

Several empirical and theoretical correlations, relating the frost thermal conductivity and density to the frost surface temperature, exist. In this paper, the correlation by Yonko and Sepsy [37] will be used to calculate the frost thermal conductivity, while that by Hayashi et al. [38–39] will be used to compute the frost density. This gives the following equations, respectively:

$$k_f = 0.024248 + 0.00072311\rho_f + 0.000001183\rho_f^2 \tag{15}$$

$$\rho_f = 650 e^{(0.227 T_f)} \tag{16}$$

where T_f in Eq. (16) must be in (°C) and ρ_f in kg/m^3. Equation (16) is valid for a frost surface temperature in the range $-25°\mathrm{C} < T_f < 0°\mathrm{C}$ and for an air stream velocity between 2 and 6 m/s. In this analysis, the temperature of the frost is calculated twice for the purpose of calculating the overall heat transfer coefficient, one time at the entrance and another time at the exit of the coil.

Overall Heat Transfer Coefficient for a Frosted Finned-Tube Coil. In this section we will determine the overall heat transfer coefficient for the case when the fins and tubes are frosted. To achieve this we assume that the thermal resistance of the tube is negligible, that the tube mean surface temperature is T_P and that the refrigerant mean temperature is T_R. It will also be assumed that a thin layer of frost having an average thickness equal to y_f covers the fins and tubes. The local rate of heat transfer inside the tube can be written as

$$\dot{Q} = h_{c,i} A_{P,i} (T_P - T_R) \tag{17}$$

The enthalpy of saturated moist air can, in general, be expressed as $i_s = a + bT_s$ for a small temperature range, such as 5°C. The term b is the slope of the saturated enthalpy-temperature curve (i.e., $b = \Delta i_s / \Delta T_s$).

Thus, a quantity b' can be defined according to the equation

$$b'_R = \frac{i_{s,P} - i_{s,R}}{T_p - T_R} \tag{18}$$

Here, the subscripts P and R indicate conditions pertaining to the pipe surface and refrigerant mean temperatures, respectively.

From Equations (17) and (18) we get

$$\dot{Q} = h_{c,i} A_{P,i} \frac{(i_{s,P} - i_{s,R})}{b'_R} \tag{19}$$

The rate of heat transfer from the tube and fins to the air can be expressed by

$$\dot{Q} = \frac{h_{c,o,f}}{b_{f,P}} A_{P,o}(i - i_{s,P}) + \frac{h_{c,o,f}}{b_{f,m}} A_F (i - i_{F,m}) \tag{20}$$

where $b_{f,P}$ and $b_{f,m}$ are the slopes of the saturated enthalpy-temperature curve evaluated at the frost temperature on the tube surface and on the fin, respectively. Both of these quantities can be evaluated employing moist air tables. The quantity $i_{F,m}$ is the enthalpy of saturated air at the mean fin temperature. The term $h_{c,o,f}$ is the external heat transfer coefficient for a frosted surface and is given by

$$h_{c,o,f} = \frac{1}{\left(\frac{C_{p,a}}{b_f h_{c,o}}\right) + \left(\frac{y_f}{k_f}\right)} \tag{21}$$

where k_f is calculated by Equation (15).

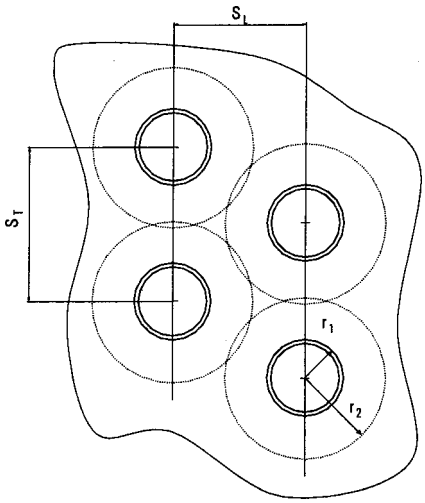

Fig. 5 Approximation method for treating a rectangular-plate fin of uniform thickness in terms of a flat circular-plate fin of equal area

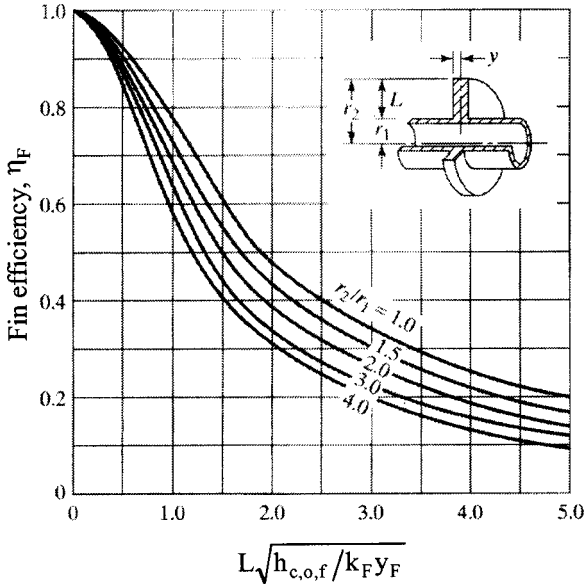

Fig. 6 Efficiency for a circular-plate fin of uniform thickness (Kuehn et al. [41])

The overall heat transfer coefficient can be expressed in terms of the fin efficiency. To compute the fin efficiency, it is necessary to compute the following quantity:

$$L\left[\sqrt{\frac{h_{c,o,f}}{k_F y_F}}\right] \tag{22}$$

where y_F is half of the fin thickness, $L=r_2-r_1$, and k_F is the thermal conductivity of the fin material.

To approximate a rectangular-plate fin of uniform thickness in terms of a flat circular-plate fin of equal area (Fig. 5), the outer radius of the circular fin is determined according to the following equation:

$$r_2=\sqrt{\frac{S_L S_T}{\pi}} \tag{23}$$

With the knowledge of r_2/r_1 and the quantity $L[\sqrt{h_{c,o,f}/k_f y_F}]$, the fin efficiency can be determined using Fig. 6. The efficiency of a frosted fin is defined as

$$\eta_F=\frac{i-i_{F,m}}{i-i_{F,B}} \tag{24}$$

where $i_{F,m}$ and $i_{F,B}$ are the enthalpies of saturated air evaluated at the mean fin temperature and fin base temperature, respectively.

Assuming that the temperature of the frost surface for the part of the frost on the tube to be approximately the same as the surface temperature of the frost for the part of the frost on the fin base, the term $b_{f,P}$ can be made equal to the term $b_{f,m}$. Furthermore, the temperature of the pipe surface can be assumed equal to the temperature of the fin base, thus resulting in the following two enthalpy terms being equal: $i_{s,P}=i_{F,B}$. This simplifies Eq. (20) to the following form after incorporating Eq. (24):

$$\dot{Q}=\frac{h_{c,o,f}}{b_{f,m}}(A_{P,o}+\eta_F A_F)(i-i_{s,P}) \tag{25}$$

By definition, the overall heat transfer coefficient, $U_{o,f}$, based on the enthalpy difference may be expressed as

$$\dot{Q}=U_{o,f}A_o(i-i_{s,R}) \tag{26}$$

Employing Equations (19), (25), and (26) we get

$$U_{o,f}=\frac{1}{\dfrac{b'_R A_o}{A_{P,i}h_{c,i}}+\dfrac{b_{f,m}(1-\eta_F)}{h_{c,o,f}(A_{P,o}/A_F+\eta_F)}+\dfrac{b_{f,m}}{h_{c,o,f}}} \tag{27}$$

The overall heat transfer coefficient for a frosted finned tube coil based on the enthalpy difference is calculated using the above procedure at two locations, one at the entrance and the other at the exit of the coil. An average value is then computed.

Calculated Path of the Cooling and Dehumidifying Process. As has been explained earlier, when simultaneous cooling and dehumidification occurs, the overall heat transfer coefficient, $U_{o,f}$, is defined in terms of an enthalpy (and not a temperature) driving force. Furthermore, the enthalpy "i" is the true air enthalpy. This is to be contrasted with the quantity $i_{s,R}$ which can be thought of as a fictitious saturated air enthalpy evaluated at the refrigerant temperature. The mean enthalpy difference Δi_m is defined by the equation

$$\dot{Q}=U_{o,f}A_o\Delta i_m \tag{28}$$

The mean enthalpy difference Δi_m is given by (modified from Incropera and Dewitt [40])

$$\Delta i_m=\frac{(i_1-i_{s,R,2})-(i_2-i_{s,R,1})}{\mathrm{Log}_e\left(\dfrac{i_1-i_{s,R,2}}{i_2-i_{s,R,1}}\right)} \tag{29}$$

where i_1 and i_2 are the true enthalpy values of the entering and leaving air conditions, respectively, and $i_{s,R,1}$ and $i_{s,R,2}$ are the fictitious enthalpies of saturated air calculated at the refrigerant entering and leaving conditions, respectively.

After calculating the inlet air conditions, the inlet refrigerant state, the various heat transfers coefficients, and the cooling coil surface data, the path of the cooling process can be determined. To get the enthalpy of saturated air at the mean frost surface temperature, we use the following equation:

$$i-i_{F,m}=\eta_F(i-i_{s,P})=\frac{b_{f,m}h_{c,o}}{h_{c,o,f}C_{p,a}}(i-i_{s,f,m}) \tag{30}$$

And from Equations (19) and (26),

$$i-i_{s,P}=\left(1-\frac{b'_R U_{o,f}A_o}{h_{c,i}A_{p,i}}\right)(i-i_{s,R}) \tag{31}$$

Using Equations (30) and (31), the enthalpy of saturated air evaluated at the mean frost surface temperature can be expressed by

$$i_{s,f,m}=i-\frac{C_{p,a}h_{c,o,f}\eta_F}{b_{f,m}h_{c,o}}\left(1-\frac{b'_R U_{o,f}A_o}{h_{c,i}A_{P,i}}\right)(i-i_{s,R}) \tag{32}$$

For a given coil entering air condition, the quantity $i_{s,f,m,1}$ can be calculated. This determines State "$s,f,m,1$" on the psychometric chart. This allows us to compute the quantity $(i_1-i_{s,f,m,1})/(W_1-W_{s,f,m,1})$. The slope at the coil entering air state, $(di/dW)_1$, can then be calculated according to the equation (Kuehn et al. [41])

$$\left(\frac{di}{dW}\right)_1=\mathrm{Le}\frac{i_1-i_{s,f,m,1}}{W_1-W_{s,f,m,1}}+(i_{g,1}-i_g^o\mathrm{Le}) \tag{33}$$

where Le is the Lewis number, $i_{g,1}$ is the enthalpy of saturated water vapor at the air dry-bulb temperature, and h_g^o is the enthalpy of saturated water vapor at a reference temperature (such as 0°C). With the aid of the chart, we draw a short segment of direction $(di/dW)_1$ through State 1. With an arbitrary value of enthalpy we can locate a new point on this segment. Then the procedure is repeated until the condition line meets with the state of saturated air at the coil apparatus dew-point temperature (approximately equal to the coil refrigerant temperature). Having determined the path of the actual cooling process, we can predict the condition downstream of any row using the following equation (Kuehn et al. [41]):

$$i_2=\frac{i_{s,R,1}(1-e^{-(1-C_3)C_4})+i_1(1-C_3)e^{-(1-C_3)C_4}}{1-C_3e^{-(1-C_3)C_4}} \tag{34}$$

where $C_3=\dot{m}_a b_R/\dot{m}_R C_{p,R}$ and $C_4=U_{o,f}A_o/\dot{m}_a$. In computing the quantity C_4, it should be kept in mind that the numerical value of A_o encompasses the areas of the row being calculated as well as all rows upstream of that row.

Results and Discussion

As was reported earlier, the objective of this paper was to calculate the path the air would take as it passes through an industrial-size, finned-tube, multi-row freezer coil. The calculated path is to be then compared to the path obtained from the straight-

Table 3 Geometrical data of the finned coil

Tube outside diameter, mm	15.88
Tube inside diameter, mm	14.968
Tube spacing between rows, mm	38.10
Tube spacing across coil-face, mm	32.80
Thickness of fins, mm	0.254
Net outside surface area m^2	6.23
Inside surface area, m^2	6.09
Fin surface area, m^2	43.37
Total outside surface area, m^2	49.59

Table 4 Parameter values employed in the model

Air inlet temperature, °C	0
Air inlet relative humidity, %	75
Air face velocity, m/s	3.81
Pipe surface temperature at the inlet, °C	-10
Pipe surface temperature at the outlet, °C	-2.2
Pipe mean surface temperature, °C	-6.1
Frost thickness, mm	1
Frost temperature at the coil inlet, °C	-6.05
Frost temperature at the coil outlet, °C	-1.83
Frost mean temperature, °C	-3.94
Fin efficiency, %	85

line principle of applied psychrometrics in order to assess the goodness of the theoretical model. The dimensions and other characteristics of the test coil have been described in the section entitled ''Experimental Program.''

Table 3 provides a summary of the geometrical data of the coil under study, whereas the values of the parameters employed in the model are given in Table 4. Table 5 gives a summary of the numerical results obtained by applying the equations used to compute the overall heat transfer coefficient.

In order to determine the calculated path for the conditions shown in Table 4, the surface area of the coil analyzed is arbitrarily divided into nine segments, thus producing ten state points through the coil. A summary of the conditions of these ten points is provided in Table 6. Figure 7 compares both the calculated and the straight-line dehumidifying paths. It is obvious that a path based on a straight-line process is in error to varying degrees, depending on the location of the point of interest relative to the coil. This can be easily demonstrated by comparing the relative humidity values of both the straight-line and calculated paths at a specific dry-bulb temperature.

Figure 8 displays both the calculated path showing the outlet conditions from successive rows in the coil as well as the entering and leaving air conditions based on experimental measurements. For example, experimental results for the leaving air conditions are: DBT $=-8.2$°C and RH $=97\%$, while calculated leaving conditions are: DBT $=-8.4$°C and RH $=97.4\%$, as is evident from examining Fig. 8. Thus, there is a slight difference of 0.2°C in the dry-bulb temperature and 0.4 percent in the relative humidity. The differences in both temperature and humidity are insignificant and lie within the uncertainty bounds of both variables. As can be observed, the outlet conditions become more closely spaced towards the last rows of the coil, implying that more cooling is performed in the first half of the coil. This is because the enthalpy driving force assumes smaller values as the air passes through the coil rows.

Table 5 Heat transfer coefficients using Eqs. (6), (11), (21), and (27)

Internal heat transfer coefficient, W/(m^2 K)	13471
External heat transfer coefficient, W/(m^2 K)	107.8
Heat transfer coefficient for a frosted surface, W/(m^2 K)	71.48
Overall heat transfer coefficient for a frosted finned-tube coil based on an enthalpy driving force, (kW kg)/(m^2. kJ)	0.075

Table 6 Calculated air path through the cooling coil

Point	T °C	RH %	W kg_w/kg_a	i kJ/kg	$i_{s,fm}$ kJ/kg	(di/dW)
1	0	65.0	0.00240	6.04	-1.35	21310.36
2	1	70.0	0.00235	4.92	-1.79	19340.68
3	2	74.2	0.00229	3.76	-2.24	16783.44
4	3	78.5	0.00223	2.60	-2.69	14823.96
5	4	82.6	0.00216	1.40	-3.16	14094.55
6	5	86.2	0.00206	0.18	-3.63	13675.00
7	6	89.8	0.00198	-1.06	-4.11	11942.40
8	7	92.8	0.00188	-2.32	-4.61	11427.26
9	8	95.8	0.00178	-3.58	-5.10	9790.76
10	9	97.5	0.00163	-4.88	-5.60	-

Now that the cooling process path has been found, the coil location in the vicinity of which the transformation from a subsaturated state to a supersaturated state occurs, can be determined. In order to achieve this goal, we will assume that the percentage of the energy removed by a given row of the coil relative to the total energy removed remains the same whether the air exists in a subsaturated state or a supersaturated state. Employing Fig. 8, it is relatively easy to observe that the total amount of cooling per unit mass performed by the coil is 10.1 kJ/kg. In Table 7, the amount of cooling per unit mass performed by each row and the percentage that amount represents relative to the total amount of cooling are provided. As reported earlier, more cooling is performed in the first row relative to subsequent rows. Carrying these cooling percentages to the supersaturated zone, the coil location in the vicinity of which transformation from a subsaturated condition to a supersaturated condition occurs can be calculated.

An experiment has been performed to verify the validity of the aforementioned assumption. In the experiment, the entering air temperature was kept constant at -8.3°C, while the relative humidity was steadily increased from 64 percent to 99 percent. The apparatus dew-point was kept constant at -18.3°C throughout the experiment. The apparatus dew-point is the lowest temperature that the air can achieve during the cooling and dehumidifying process and is, thus, approximately equal to the coil refrigerant temperature. Results of this experiment are shown on the psychrometric chart of Fig. 9 for both the straight-line theory and the calculated path. As can be seen, four scenarios were examined. For Scenario 1, the cooling process line falls completely in the subsaturated zone. For Scenario 2, transformation to the supersaturated zone using the straight-line theory occurs at Point 3a (DBT $=-15.1$°C), while it occurs at Point 3a′ (DBT $=-12.3$°C) using the calculated path. For this scenario, the amount of cooling achieved using the straight-line theory represents 84 percent of the total cooling performed by the coil. This means that at Point 3a the air was leaving the fifth row supersaturated. However, the amount of cooling achieved using the calculated path represents only 50 percent of the total cooling performed by the coil. This means that at Point 3a′ the air was leaving the third row supersaturated (as opposed to the fifth row for the straight-line theory). For Scenario 3, supersaturated conditions using the straight-line theory began at Point 3b (DBT $=-11.3$°C) and using the calculated path at Point 3b′ (DBT $=-10.3$°C). For this scenario, the amount of cooling achieved using the straight-line theory represents 37 percent of the total cooling performed. This means that transformation to the supersaturated zone occurred between the second and third rows (Point 3b). However, the amount of cooling achieved using the calculated path represents only 24 percent of the total cooling performed. This means that at Point 3b′ the air was leaving the first row supersaturated. For Scenario 4, supersaturated conditions started at Point 3c (DBT $=-8.7$°C) for both the straight-line theory and the calculated path. For this scenario, the amount of cooling achieved from Points 1c to 3c or from Points 1c to 3c′ represents 5 percent of the total cooling performed. This means that transition to the supersaturated state occurred in the vicinity of the first row. Obviously, as the relative humidity of the entering air increases, transition to a supersaturated state occurs quicker and at a more upstream location of the coil. This phenomenon has also been confirmed by other investigations performed by the authors (see Sherif et al. [2]).

As was pointed out before, the procedure employed in this paper is based on the premise that the percentage of cooling achieved between two consecutive rows of the coil will remain the same whether the air exists in the subsaturated or the supersaturated zone. In order to determine the percentage of cooling referred to above, the state of the air in the vicinity of two consecu-

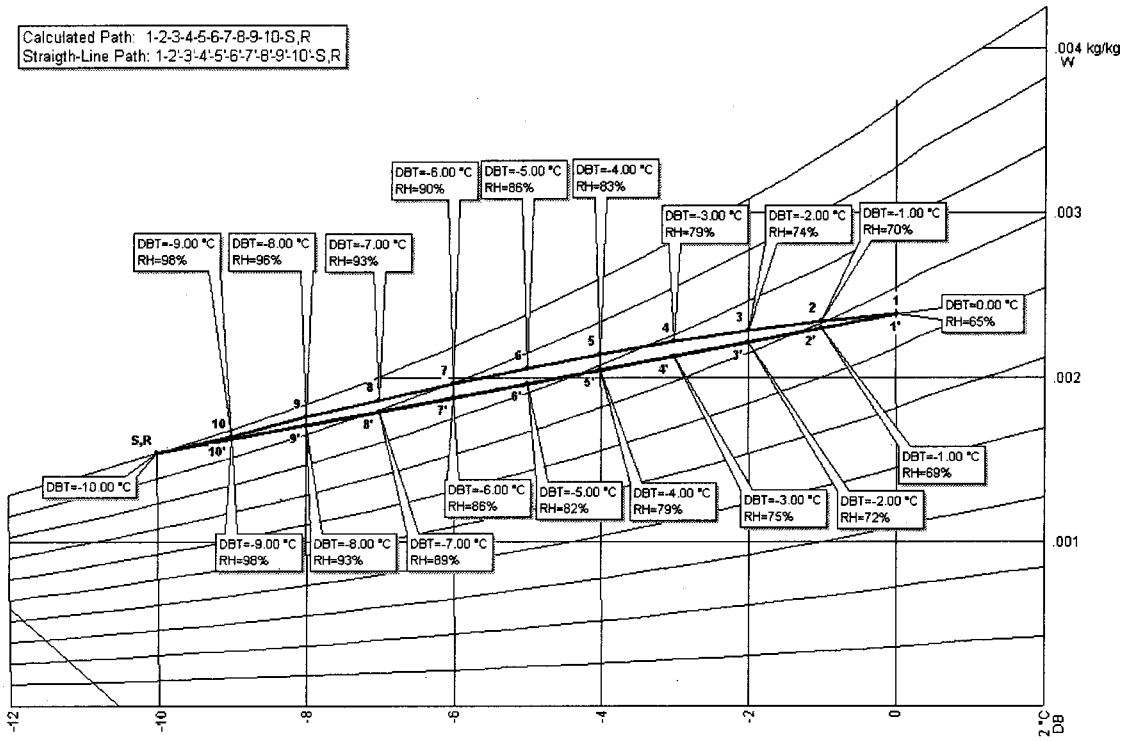

Fig. 7 Representation of the calculated and the straight-line dehumidifying paths through the dehumidifying coil (points on the chart are arbitrarily chosen for purposes of calculating the path)

tive rows has to be known. The procedure described for determining the enthalpy at the exit of a given row is thus necessary for computing the percentage of cooling. Employing this procedure necessarily produces a curved path for the air passing through the coil. While the bulk of the air paths lie in the subsaturated zone for all four processes shown, the procedure outlined is inherently capable of handling both supersaturated and subsaturated conditions. Using the straight-line theory to determine the air enthalpy in the vicinity of a given row produces results that are significantly less accurate than the ones produced using the

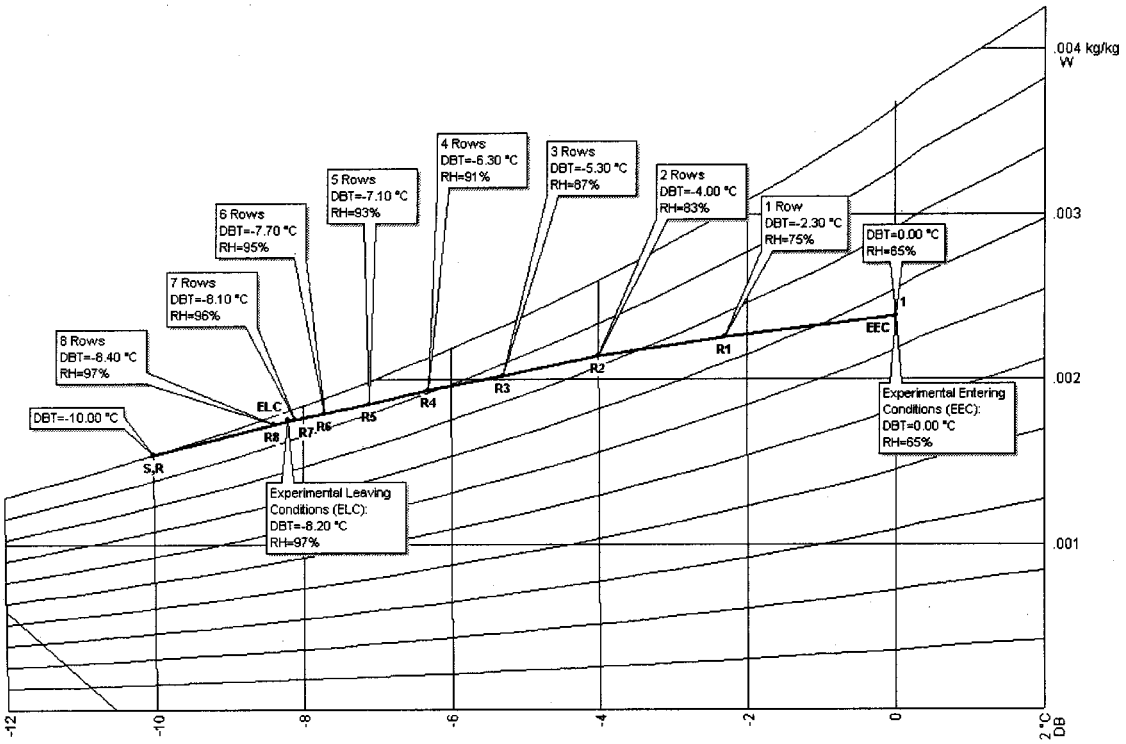

Fig. 8 Representation of the calculated cooling air path through the dehumidifying coil showing the calculated leaving air conditions from each row as well as the measured coil inlet and outlet states

Table 7 Amount of cooling and percentage of the total cooling for each row

Row	Δi kJ/kg	Percentage of total cooling %
R1	2.64	26.14
R2	2	19.80
R3	1.61	15.94
R4	1.23	12.18
R5	1.02	10.10
R6	0.74	7.33
R7	0.49	4.85
R8	0.37	3.66

curved-path. Figure 9 illustrates this point. While the straight-line theory and the calculated path approach agree reasonably well at the entrance and exit of the coil, significant differences between the two methods exist in the middle section of the coil. For example, Fig. 9 shows a 34 percent deviation in the percentage of cooling calculated for Scenario 2 employing both methods. This is manifested in the differences between paths 1a–3a and 1a–3a′, where, in the former, the straight-line theory predicts 84 percent cooling achieved between Rows 5 and 6, whereas the corresponding value for Path 1a–3a′ is only 50 percent.

Conclusions

This paper described a calculation procedure as well as an experiment for determining the air path on an actual industrial-size finned-tube, multi-row coil operating under frosting conditions. A calculated path based on the analysis presented and a path based on the straight-line theory of applied psychrometrics were correlated with the prevailing psychrometric conditions in the freezer. Determining the calculated path enabled accurate calculation of the conditions leaving a given row in a multi-row coil. This, in turn, helped identify the coil location in the vicinity of which the transformation from the subsaturated zone to the supersaturated zone occurred. This is crucial in identifying a demarcation line between the unfavorable snow-like frost and the more traditional and more favorable frost formation patterns. Calculated results were verified against experimental results at the entrance and exit of the coil with typical differences falling well within the uncertainty ranges of both temperature and humidity. In the middle section of the coil, on the other hand, significant deviations (up to 34 percent) between the calculated and the straight-line paths were observed. This underscores the significance of using the method outlined in this paper if reasonably accurate prediction of the location of the demarcation line between snow-like and conventional frost is to be determined.

Nomenclature

A = surface area; A_o is the total outside surface area including the finned surface, m^2

A_P = surface area of the pipe; $A_{P,i}$ is for the inside surface; $A_{P,o}$ is for the outside surface, m^2

b = slope of the saturated enthalpy-temperature curve ($b = \Delta i_s / \Delta T_s$); b_f evaluated at frost surface temperature; $b_{f,P}$ evaluated at the frost surface temperature for the part of the frost collecting on the pipe; $b_{f,m}$ evaluated at the mean frost surface temperature for the part of the frost collecting on the fin; b_R evaluated at the refrigerant temperature, kJ/(kg°C)

$C_{p,a}$ = air specific heat at constant pressure, kJ/(kg°C)

$C_{p,R}$ = refrigerant specific heat at constant pressure, kJ/(kg°C)

D_f = diameter of the frosted tube, m

D_i = inside diameter of the tube, m

D_o = outside diameter of the tube, m

h_c = film coefficient of convective heat transfer, $W/(m^2K)$

$h_{c,i}$ = convection heat transfer coefficient for inside of tube, $W/(m^2K)$

$h_{c,o}$ = convection heat transfer coefficient for outside surface, $W/(m^2K)$

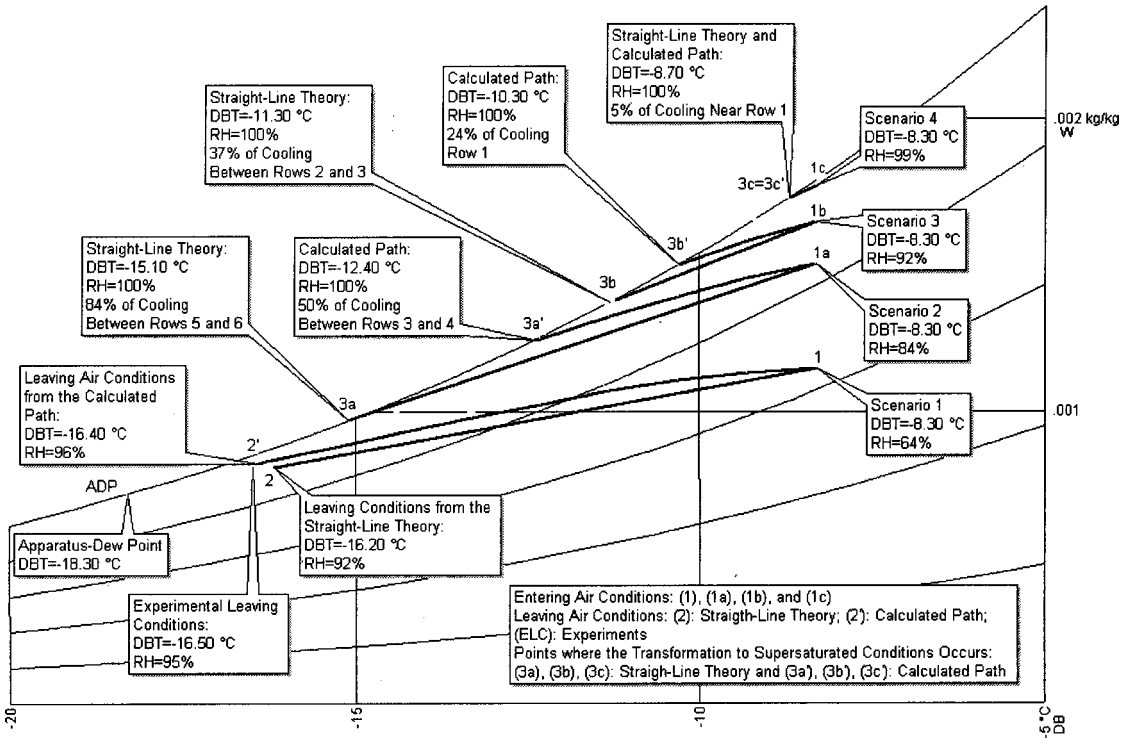

Fig. 9 Representation of processes on the psychrometric chart showing where the transition to a supersaturated state occurs by keeping the same entering air temperature (−8.3 °C) and gradually increasing the entering air relative humidity

$h_{c,o,f}$ = heat transfer coefficient for a frosted surface, W/(m^{2}K)
h_v = mass transfer coefficient, kg/(m^{2}s)
i = enthalpy, kJ/kg
i_F = enthalpy of moist air in the vicinity of the fin surface; $i_{F,m}$ evaluated at mean fin temperature; $i_{F,B}$ evaluated at the fin base temperature, kJ/kg
i_g = enthalpy of saturated water vapor, kJ/kg
i_s = enthalpy of saturated moist air; $i_{s,P}$ evaluated at pipe surface temperature, $i_{s,R}$ evaluated at refrigerant temperature, $i_{s,f,m}$ evaluated at the mean frost surface temperature, kJ/kg
k = thermal conductivity; k_F for the fin material; k_f for the frost, W/(mK)
Le = Lewis number, $h_c/(h_v C_{p,a})$, dimensionless
$\dot{m}_R$ = refrigerant mass flow, kg/s
$\dot{m}_a$ = air mass flow rate, kg/s
Nu = Nusselt number, dimensionless
N_L = number of tube rows, dimensionless
Pr = Prandlt number, dimensionless
$\dot{Q}$ = total heat transfer rate, kW
r_1 = internal radius of the fin, m
r_2 = external radius of the fin, m
Re = Reynolds number, dimensionless
S_L = longitudinal pitch, m
S_T = transverse pitch, m
T_a = air temperature, °C
T_f = frost surface temperature, °C
T_P = pipe surface temperature, °C
T_R = refrigerant temperature, °C
u = velocity
$U_{o,f}$ = overall heat transfer coefficient for a frosted finned tube coil based on an enthalpy driving force, (kW kg)/(m^2 kJ)
W = humidity ratio, kg_w/kg_a
y_F = half of fin thickness, m
y_f = frost thickness, m

Greek Symbols

η_f = fin efficiency, dimensionless
λ = length, m
μ = dynamic viscosity, kg/(m s)
ρ = density, kg/m^3

Subscripts

a = air
B = fin base
F = fin
f = frost
i = inside of tube
m = mean
max = maximum
o = outside of tube
P = pipe
p = constant pressure
R = refrigerant
s = saturated

References

[1] Sherif, S. A., Mago, P. J., Al-Mutawa, N. K., and Theen, R. S., 2001, ''Psychrometric Theory Under Supersaturated Frosting Conditions.'' *Proceedings of the 37th Heat Transfer and Fluid Mechanics Institute*, Reardon, F.H. and Thinh, N. D., eds., California State University at Sacramento, School of Engineering and Computer Science, Sacramento, California, pp. 177–188.

[2] Sherif, S. A., Mago, P. J., Al-Mutawa, N. K., Theen, R. S., and Bilen, K., 2001, ''Psychrometrics in the Supersaturated Frost Zone.'' ASHRAE Trans., **107**(2), pp. 753–767.

[3] Padki, M. M., Sherif, S. A., and Nelson, R. M., 1989, ''A Simple Method for Modeling Frost Formation in Different Geometries,'' ASHRAE Trans., **95**(2), pp. 1127–1137.

[4] Sherif, S. A., Raju, S. P., Padki, M. M., and Chan, A. B., 1993, ''A Semi-Empirical Transient Method for Modelling Frost Formation on a Flat Plate,'' Int. J. Refrig., **16**(5), pp. 321–329.

[5] Thomas, L., Chen, H., and Besant, R. W., 1999, ''Measurement of Frost Characteristics on Heat Exchanger Fins—Part I: Test Facility and Instrumentation,'' ASHRAE Trans., **105**(2), pp. 283–293.

[6] Chen, H., Thomas, L., and Besant, R. W., 1999, ''Measurement of Frost Characteristics on Heat Exchanger Fins—Part II: Data and Analysis,'' ASHRAE Trans., **105**(2), pp. 294–302.

[7] Chen, H., Besant, R. W., and Tao, Y. X., 1999, ''Frost Characteristics and Heat Transfer on a Flat Plate Under Freezer Operating Conditions: Part II, Numerical Modeling and Comparison with Data,'' ASHRAE Trans., **105**(2), pp. 252–259.

[8] Besant, R. W., 1999, ''Characterization of Frost Growth and Heat Transfer at Low Temperatures,'' Final Report, ASHRAE RP-824, The American Society of Heating, Refrigerating and Air-Conditioning Engineers, Atlanta, Georgia.

[9] Notestine, H. E., 1966, ''The Design, Fabrication, and Testing of an Apparatus to Study the Formation of Frost from Humid Air to an Extended Surface in Forced Convection,'' M.S. thesis, The Ohio State University, Columbus, OH.

[10] Gates, R. R., Sepsy, C. F., and Huffman, G. D., 1967, ''Heat Transfer and Pressure Loss in Extended Surface Heat Exchangers Operating Under Frosting Conditions—Part I: Literature Survey, Test Apparatus and Preliminary Results,'' ASHRAE Trans., **73**(2), pp. I.2.1–I.2.13.

[11] Huffman, G. D., 1966, ''Heat Transfer and Pressure Loss in an Extended Surface Heat Exchanger Operating Under Frosting Conditions,'' M.S. thesis, The Ohio State University, Columbus, OH.

[12] Huffman, G. D., and Sepsy, C. F., 1967, ''Heat Transfer and Pressure Loss in Extended Surface Heat Exchangers Operating Under Frosting Conditions—Part II: Data Analysis and Correlations,'' ASHRAE Trans., **73**(2), pp. I.3.1–I.3.16.

[13] Gatchilov, T. S., and Ivanova, V. S., 1979, ''Characteristics of the Frost Formed on the Surface of Finned Air Coolers,'' *15th International Congress of Refrigeration*, Paper B2-71, Venice, France, pp. 997–1003.

[14] Kondepudi, S. N., 1988, ''The Effects of Frost Growth on Finned Tube Heat Exchangers Under Laminar Flow,'' Ph.D. dissertation, Texas A&M University, College Station, TX.

[15] Kondepudi, S. N., and O'Neal, D. L., 1987, ''The Effects of Frost Growth on Extended Surface Heat Exchanger Performance: A Review,'' ASHRAE Trans., **93**(2), pp. 258–274.

[16] Kondepudi, S. N., and O'Neal, D. L., 1988, ''Performance of Triangular Spine Fins Under Frosting Conditions,'' Heat Recovery Syst. CHP, **8**(1), pp. 1–7.

[17] Kondepudi, S. N., and O'Neal, D. L., 1989, ''Effect of Frost Growth on the Performance of Louvered Finned Tube Heat Exchangers,'' Int. J. Refrig., **12**(3), pp. 151–158.

[18] Kondepudi, S. N., and O'Neal, D. L., 1989, ''The Effects of Frost Formation on the Thermal Performance of Finned Tube Heat Exchangers,'' *AIAA 24th Thermophysics Conference*, AIAA Paper No. 89–1741, Buffalo, New York.

[19] Kondepudi, S. N., and O'Neal, D. L., 1989, ''The Performance of Finned Tube Heat Exchangers Under Frosting Conditions,'' *Collected Papers in Heat Transfer-1989*, HTD-Vol. 123, ASME, New York, pp. 193–200.

[20] Kondepudi, S. N., and O'Neal, D. L., 1990, ''The Effects of Different Fin Configurations on the Performance of Finned-Tube Heat Exchangers Under Frosting Conditions,'' ASHRAE Trans., **96**(2), pp. 439–444.

[21] Kondepudi, S. N., and O'Neal, D. L., 1991, ''Frosting Performance of Tube Heat Exchangers with Wavy and Corrugated Fins,'' Exp. Therm. Fluid Sci., **4**(5), pp. 613–618.

[22] Kondepudi, S. N., and O'Neal, D. L., 1991, ''Modeling Tube-Fin Heat Exchangers Under Frosting Conditions,'' *18th International Congress of Refrigeration*, Paper No. 242, Montreal, Quebec, Canada.

[23] Senshu, T., Yasuda, H., Oguni, K., and Ishibane, K., 1990, ''Heat Pump Performance Under Frosting Conditions: Part I—Heat and Mass Transfer on Cross-Finned Tube Heat Exchangers Under Frosting Conditions,'' ASHRAE Trans., **96**(1), pp. 324–329.

[24] Rite, R. W., and Crawford, R. R., 1991, ''A Parametric Study of the Factors Governing the Rate of Frost Accumulation on Domestic Refrigerator-Freezer Finned-Tube Evaporator,'' ASHRAE Trans., **97**(2), pp. 438–446.

[25] Ogawa, K., Tanaka, N., and Takeshita, M., 1993, ''Performance Improvement of Plate Fin-and-Tube Heat Exchanger Under Frosting Conditions,'' ASHRAE Trans., **99**(1), pp. 762–771.

[26] Tao, Y. X., Besant, R. W., and Rezkallah, K. S., 1993, ''A Mathematical Model for Predicting the Densification and Growth of Frost on a Flat Plate,'' Int. J. Heat Mass Transf., **36**(2), pp. 353–363.

[27] Tao, Y. X., Besant, R. W., and Mao, Y., 1993, ''Characteristics of Frost Growth on a Flat Plate During the Early Growth Period,'' ASHRAE Trans., **99**(1), pp. 739–745.

[28] Al-Mutawa, N. K., 1997, ''Experimental Investigations of Frosting and Defrosting of Evaporator Coils at Freezer Temperatures,'' Ph.D. dissertation, University of Florida, Gainesville, FL.

[29] Sherif, S. A., Al-Mutawa, N. K., Mathur, G. D., Steadham, J. M., Tiedeman, J. S., MacFarlane, S., Urlaub, J., West, J., and Harker, R. A., 1997, ''A Study to Determine Heat Loads Due to Coil Defrosting,'' Final Technical Report No. UFME/SEECL-9701, Contract No. ASHRAE-622-RP, the American Society of Heating, Refrigerating and Air-Conditioning Engineers, Atlanta, GA.

[30] Al-Mutawa, N. K., Sherif, S. A., Mathur, G. D., West, J., Tiedeman, J. S., and Urlaub, J., 1998, ''Determination of Coil Defrosting Loads: Part I—Experimental Facility Description (RP-622),'' ASHRAE Trans., **104**(1A), pp. 268–288.

[31] Al-Mutawa, N. K., Sherif, S. A., Mathur, G. D., Steadham, J. M., West, J., Harker, R. A., and Tiedeman, J. S., 1998, ''Determination of Coil Defrosting Loads: Part II—Instrumentation and Data Acquisition Systems (RP-622),'' ASHRAE Trans., **104**(1A), pp. 289–302.
[32] Al-Mutawa, N. K., Sherif, S. A., and Mathur, G. D., 1998, ''Determination of Coil Defrosting Loads: Part III—Testing Procedures and Data Reduction (RP-622),'' ASHRAE Trans., **104**(1A), pp. 303–312.
[33] Al-Mutawa, N. K., Sherif, S. A., and Steadham, J. M., 1998, ''Determination of Coil Defrosting Loads: Part IV—Refrigeration/Defrost Cycle Dynamics (RP-622),'' ASHRAE Trans., **104**(1A), pp. 313–343.
[34] Al-Mutawa, N. K., and Sherif, S. A., 1998, ''Determination of Coil Defrosting Loads: Part V—Analysis of Loads (RP-622),'' ASHRAE Trans., **104**(1A), pp. 344–355.
[35] Grimison, E. D., 1937, Trans. ASME, **59**, pp. 583.
[36] Dittus, F. W., and Boelter, L. M. K., 1930, *Publications in Engineering* **2**, University of California, Berkeley, CA, pp. 443.
[37] Yonko, J. D., and Sepsy, C. F., 1967, ''An Investigation of the Thermal Conductivity of Frost While Forming on a Flat Horizontal Plate,'' ASHRAE Trans., **73**(2), pp. I.1.1–I.1.10.
[38] Hayashi, Y., Aoki, A., Adachi, S., and Hori, K., 1977, ''Study of Frost Properties Correlating With Frost Formation Types,'' ASME J. Heat Transfer , **99**(2), pp. 239–245.
[39] Hayashi, Y., Aoki, K., and Yuhara, H., 1977, ''Study of Frost Formation Based on a Theoretical Model of the Frost Layer,'' Heat Transfer-Jpn. Res., **6**(3), pp. 79–94.
[40] Incropera, F. P., and DeWitt, D. P., 1996, *Fundamentals of Heat and Mass Transfer*, Fourth Edition, John Wiley & Sons, Inc., New York.
[41] Kuehn, T. H., Ramsey, J. W., and Therelkeld, J. L., 1998, *Thermal Environment Engineering*, Third Edition, Prentice Hall, Upper Saddle River, NJ.

The Relationship Between Information, Sampling Rates, and Parameter Estimation Models

A. F. Emery
e-mail: emery@u.washington.edu
Dept. Mechanical Engineering,
University of Washington,
Seattle, WA 98195

B. F. Blackwell
e-mail: bfblack@sandia.gov

K. J. Dowding
e-mail: kjdowdi@sandia.gov

Validation and Uncertainty Quantification,
Sandia National Laboratory,[1]
Albuquerque, NM 87185-0828

To estimate parameters from experiments requires the specification of models and each model will exhibit different degrees of sensitivity to the parameters sought. Although experiments can be optimally designed without regard to the experimental data actually realized, the precision of the estimated parameters is a function of the sensitivity and the statistical characteristics of the data. The precision is affected by any correlation in the data, either auto or cross, and by the choice of the model used to estimate the parameters. An informative way of looking at an experiment is by using the concept of Information. An analysis of an actual experiment is used to show how the information, the optimal number of sensors, the optimal sampling rates, and the model are affected by the statistical nature of the signals. The paper demonstrates that one must differentiate between the data needed to specify the model and the precision in the estimated parameters provided by the data. [DOI: 10.1115/1.1513581]

Keywords: Information, Parameter Estimation, Correlated Data, Uncertainty

Introduction

Experiments are often performed to prove the accuracy or validity of models or to determine the parameters to be used in such models. The parameters are then often reported in a statistical form. For example suppose that the heat flux and the temperature difference are measured for a thin slab of material. For one dimensional steady state heat transfer, the conductivity of a material can be estimated from $k = q\Delta x/\Delta T$. Suppose that the experiment is run over a long period of time yielding N sets of repeated measurements, and thus N estimates of k, k_i, $i = 1..N$, are obtained. Then one usually reports the estimate of the average value of k, $\bar{k} = \Sigma k_i / N$, and its standard deviation $\sigma_{\bar{k}} = \sigma_k / \sqrt{N}$ using formulas familiar from an elementary course in statistics for statistically independent measurements.

With a limited number of estimates taken over a reasonable time, such statistics are usually sufficient. If the accuracy of the estimate is insufficient, then one usually increases the number of measurements, N, to reduce $\sigma_{\bar{k}}$. It would appear then that increasing N sufficiently would yield any desired accuracy. But if N is increased by increasing the frequency of sampling often the readings are no longer independent and the simple equations are no longer correct. If instead of using one sensor to measure ΔT, suppose that M sensors are used. It would appear that we have a total of NM estimates, but in fact the data from the M sensors may not be independent—in fact it is highly probable that they will be strongly correlated. The question is then how to appropriately use all of the data and what are the statistics which reflect the precision of the estimated conductivity.

Assumptions of independence are appropriate when the sampling rates are low and instrument accuracy is high. Under these conditions, if $\mathcal{I}_i$ is the information contributed by a datum point, then the total information from N points is simply $N\mathcal{I}_i$. If, on the other hand, the data from a single sensor are autocorrelated, or data from multiple sensors are cross-correlated, then the information per measurement is reduced. For example, if the correlation is perfect then an additional datum point contributes no information at all. It is known that data sampled at uniform intervals and reasonably high rates of sampling or with linearization often shows a high degree of autocorrelation [1]. The correlation typically reduces as the sampling rate decreases and data taken at slow rates can approach statistical independence. Thermocouple data is particularly suspect for inherent correlation when obtained with modern data acquisition systems in which the reference temperature is generated electronically and thus may introduce a high degree of both cross and auto-correlation between the data points.

Analysis of this type of data is best accommodated through a Bayesian approach to probability. In the following sections we present a short review of parameter estimation and Bayesian statistics and probability and demonstrate their application to the estimation of conductivity from the measurement of transient temperatures.

The Experiment

Blackwell et al. [2] estimated the conductivity of stainless steel by measuring the transient temperatures in a thin hollow tube of length $2L$. Full details are given in Ref. [2] but a brief description is given here. The tube was installed in an evacuated chamber and space insulation covered the outer surface of the tube and filled the hollow interior to minimize losses from the surfaces and to create a one dimensional temperature field. The ends of the tube were heated by a fluid which flowed through serpentine channels in copper end blocks. Temperatures were measured at 14 equally spaced axial locations each with 4 thermocouples equally spaced about the circumference. Figure 1(*a*) is a schematic of the experiment showing the thermocouple locations.

A candidate thermal model of this system by which the thermal conductivity can be estimated would have the circulating fluid temperature as the boundary conditions and would include the thermal characteristics of the copper end blocks, the convection coefficients in the serpentine channels and the contact resistance between the end blocks and the hollow tube. But lacking full details of these characteristics means that the system cannot be modeled. If a heat flux gauge were mounted at the ends of the tube, or if the flux could be estimated, then the problem could be considered as having a known flux history as the boundary conditions. Alternatively one could view the inverse problem as the simultaneous estimation of both the heat flux history and the ther-

[1]Sandia is a multiprogram laboratory operated by Sandia Corporation, a Lockheed Martin Company, for the United States Department of Energy under Contract DE-AC04-94AL85000.

Contributed by the Heat Transfer Division for publication in the JOURNAL OF HEAT TRANSFER. Manuscript received by the Heat Transfer Division August 24, 2001; revision received July 2, 2002. Associate Editor: A. F. Emery.

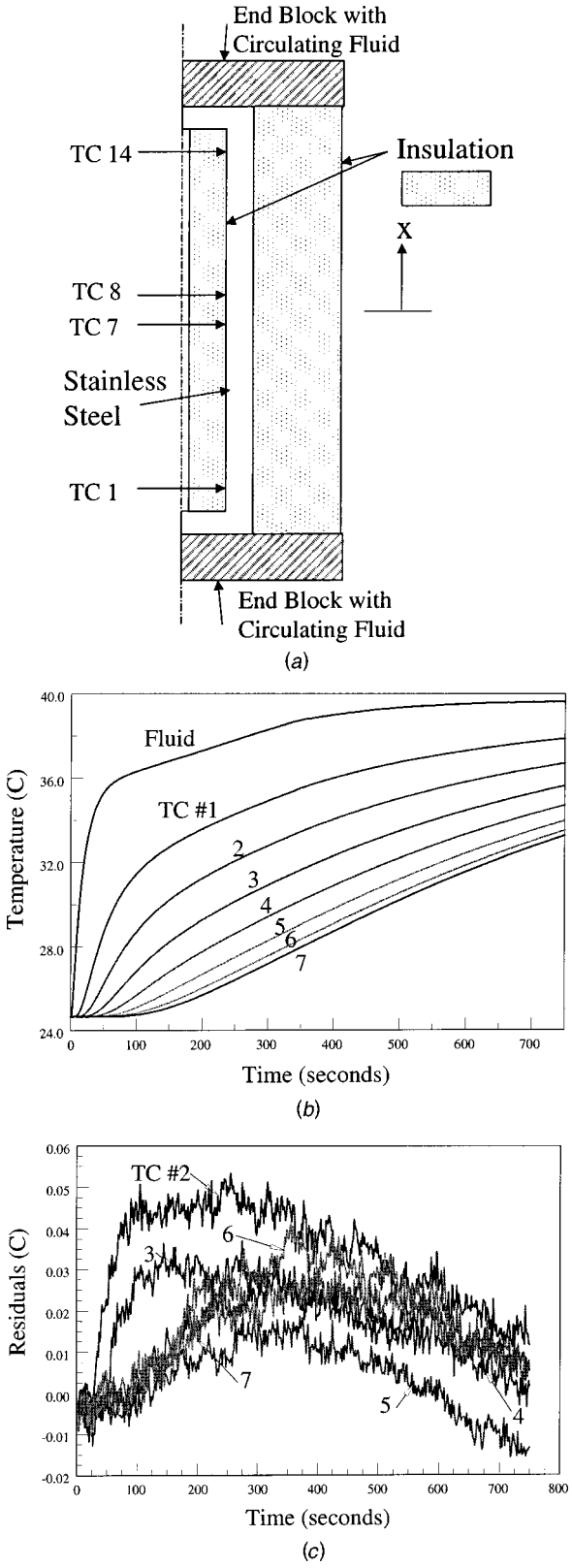

Fig. 1 (*a*) Schematic of the experiment; (*b*) Measured temperatures from Ref. [2]; and (*c*) residuals form Ref. [2].

mal conductivity. Because the time history of the fluxes is difficult to obtain, as demonstrated in by Beck [3,4], Blackwell et al. developed a novel approach in which the time varying temperatures measured at the ends, $x=\pm L$ were taken to be the prescribed boundary conditions and the temperature histories computed using a finite volume code. The measured transient temperatures were then fitted to the numerically computed temperatures as a function of k, x, and t and the conductivity estimated using the usual least squares equations

$$\text{choose } k \text{ to minimize } \sum_{i=1}^{N} (T_i - F(k,t_i,x))^2 \qquad (1a)$$

giving

$$k = k_0 + \frac{\sum_{i=1}^{N} \left(\frac{\partial F}{\partial k}\right)\Big|_{k_0,t_i,x} (T_i - F(k_0,t_i,x))}{\sum_{i=1}^{N} \left(\frac{\partial F}{\partial k}\right)^2\Big|_{k_0,t_i,x}} \qquad (1b)$$

where T_i are the measured temperatures and $F(k,t_i,x)$ are the predicted temperatures for a specific value of k. The conductivity was assumed to be a constant, independent of temperature, over the range of temperatures measured. Eq. (1*b*), which is obtained from Eq. (1*a*) by expanding $F(k,x,t_i)$ in a Taylor series and retaining only the 1st order term, was iterated to convergence. Figure 1(*b*) shows the first 750 seconds of the temperature history and Figure 1(*c*) the residuals $T_i - F(k,t_i,x)$ based upon the average of the four circumferentially located thermocouples whose standard deviation was of the order of 0.08 °C.

The residuals, which represent the combined effects of measurement errors and uncertainties in the system behavior which were not included in the model, were based upon model temperatures, $F(k,t_i,x)$, computed with a time step of 0.25 seconds or approximately six times the sampling rate. A grid refinement study was performed in Ref. [2] and the grid errors were found to be roughly an order of magnitude less than the temperature measurement errors. The computed and measured values cannot be differentiated on Figure 1(*a*) where the maximum differences (i.e., the residuals) are of the order of 0.05 °C or approximately 0.5 percent of the temperature change.

Using the maximum standard deviation of the measured temperatures, 0.13 °C, in conjunction with the equation for the propagation of errors [5] to estimate the standard deviation of y where y is a function of x_1 and x_2 and x_1 and x_2 are independent variables

$$\sigma_y^2 = \left(\frac{\partial y}{\partial x_1}\right)^2 \sigma_{x_1}^2 + \left(\frac{\partial y}{\partial x_2}\right)^2 \sigma_{x_2}^2 \qquad (2)$$

they determined the standard deviation of the average temperature at each axial position to be 0.08 °C, and of the estimated conductivity due to noisy temperature signals of $5.3\,10^{-4}$ W/m-K. In fact, the experiment actually serves to determine the thermal diffusivity, $k/\rho c$, and including the uncertainty in ρc through the use of Eq. 2 leads to an overall standard deviation of k of 0.6 W/m-K.

The temperatures shown on Fig. 1(*a*) are only for 1/2 of the tube, $-L \geqslant x \leqslant 0$ and are the average of the four circumferential sensors. Over the 750 sec, 500 measurements were made on each of the 56 thermocouples giving a total number of data points for use in Eq. 1 of 24,000 since the data from the end sets of thermocouples were used as prescribed boundary conditions and thus assumed to have no error.

If the constant conductivity model of the system $F(k,x,t_i)$ were exact and the measurements had no error, then only one measurement at one time and one location would be sufficient to estimate k. In reality, models never can precisely simulate the system because of inhomogeneities, heat losses, imprecisely specified temperature variations of properties, etc. and measurement systems are never without error. For this reason multiple temperatures are measured and each one contributes information and improves the precision of the estimated property.

Depending on the behavior of the system some of the temperatures may be correlated and will contribute less information than

if they were independent. In the case of this experiment it is likely that the measured temperatures at the four circumferentially located thermocouples at each axial station are correlated.

At this point it is important to clearly differentiate between the two uses of sensor data: (*a*) for defining the model and (*b*) for estimating parameters. Because of interdependence, i.e., correlation, not all of the measured temperatures will contribute equally to the precision with which the conductivity is estimated. Likewise, if the sampling rate is too high, some of the time data may contain less information. Thus it may appear that equally precise estimates may be achieved with less instrumentation if all data were independent. However, no parameter can be estimated without a model. In this study we have assumed that the temperature field is one dimensional and symmetric about $x=0$. Confirmation of one dimensionality, that is dependence only on x and not on the circumferential position, requires that thermocouples be placed at several circumferential positions. Assurance of axial symmetry requires that both halves of the tube, $-L \leqslant x \leqslant 0$ and $0 \leqslant x \leqslant L$ be instrumented. Examination of these temperatures will then confirm the validity of the model.

In this paper we examine the data to judge the effect of correlations in time and space and to test the applicability of the model which is based upon prescribed temperature boundary conditions. We will do this through the use of the Bayesian probabilities and we begin with a short review to orient the reader.

Parameter Estimation

Let the temperature be expressed in terms of position, time, boundary conditions, initial conditions and properties by $T=F(x,t,bc,ic,k,\rho c)$ where F is the solution of the appropriate field equation. Let all of the arguments of F be referred to as parameters. Those parameters which are to be estimated from the measured temperatures will be represented by P and the remaining parameters by θ. θ can include spatial location as well as properties, source strengths, etc. For simplicity of exposition we will estimate only one parameter, although the method can easily be extended to a vector of parameters, and we will consider only one axial position.

Assuming that the model is an accurate representation of the system, the measured temperatures will differ from F by measurement noise (and potentially by model error), ϵ, according to

$$T_i = F(P,\theta,t_i) + \epsilon_i \tag{3}$$

Estimation is usually done through the Least Squares approach in which we choose P to be such that the weighted sum of the squares of the errors, S, is minimized where

$$S = \sum_{i=1}^{N} w_i \epsilon_i^2 = \sum_{i=1}^{N} w_i (T_i - F(P,\theta,t_i))^2 \tag{4}$$

where the weights are usually taken to be $w_i = 1/\sigma_i^2$ [1]. The problems with this approach are: (*a*) it gives no estimate of σ_P and (*b*) it is not intuitively clear how to handle correlated errors. These questions are best answered through a probabilistic analysis.

Let the mean and standard deviation of T be represented by

$$E[T] = \int T f(T)\, dt \tag{5a}$$

$$\sigma_T^2 = \int (T - E[T])^2 f(T)\, dT \tag{5b}$$

where $f(T)$ is the probability density distribution of T. Let $\overline{P}$ be the true value of P and expand $T(P)$ in a Taylor series about $\overline{P}$ and retain only the 1st order terms

$$T(P) = T(\overline{P}) + \left(\left. \frac{\partial F}{\partial P} \right|_{\overline{P}} \right) (P - \overline{P}) \tag{6}$$

Substituting Eq. 6 into Eq. 5 and using the relationship between probability density distributions [6,7], $f(T)|dT| = f(P)|dP|$, yields

$$\sigma_T^2 = \left(\left. \frac{\partial F}{\partial P} \right|_{\overline{P}} \right)^2 \sigma_P^2 \tag{7}$$

Looking at Eq. (3) we see that the probability of finding a temperature in the range dT is simply the probability of ϵ being in the range $d\epsilon$, i.e., $f(T) = f(\epsilon)$ so that Eq. (7) can be written as

$$\sigma_P^2 = \left(\left. \frac{\partial F}{\partial P} \right|_{\overline{P}} \right)^{-2} \sigma_\epsilon^2 \tag{8}$$

Eq. (8) emphasizes that it is not the relationship of one data point, T_i, to another, T_j, that determines the precision of P but the distribution of the errors, $f(\epsilon)$, their statistics, σ_ϵ, and the sensitivity of the model to P, $\partial F/\partial P$. The equation makes it very clear that increased precision comes about from having large values of $\partial F/\partial P$ in conjunction with small values of σ_ϵ. The question remaining is how to estimate $\overline{P}$.

Bayesian Probability and Maximum Likelihood. Let $f(T|P)$ represent the probability of obtaining a specific set of data T given a value of the parameter P and $f(P|T)$ be the probability that a specific value of P will occur given a set of data T. Bayes' rule for relating these conditional probabilities [6,7] is

$$f(P|T) f(T) = f(T|P) f(P) \tag{9a}$$

or

$$f(P|T) \propto f(T|P) f(P) \tag{9b}$$

In Eq. (9*a*) $f(P)$ is the prior probability of P which reflects our initial estimate of the distribution of P. $f(T|P)$ is called the likelihood and denoted by $l(T)$.

In the Bayesian approach, $\hat{P}$, the estimate of P, is chosen to be the value of P which maximizes $f(P|T)$ or some measure of it. Sivia [8] and Lee [9] give very good summaries and practical applications of the Bayesian approach. The beauty of Eq. 9 is that it permits the use of *priors* which reflect our existing knowledge about P. For example since conductivity must be positive, $f(k) = 0,\ k \leqslant 0;\ f(k) > 0,\ k > 0$. A state of maximal ignorance would be if all that we knew about P was that it was limited by $P_{min} \leqslant P \leqslant P_{max}$, leading to the uniform *prior* $f(P) = 1/(P_{max} - P_{min})$. As long as the prior is relatively flat near $\hat{P}$, then $f(P|T)$ will be maximum when $l(T)$ $(= f(T|P))$ is maximum. It proves easier to deal with $L = \ln(l(T))$ than with $l(T)$, since their maxima occur at the same value of $\hat{P}$. Thus Bayes' approach reduces to

$$\hat{P} \text{ is defined by } \left(\left. \frac{\partial L(T)}{\partial P} \right) \right|_{\hat{P}} = 0 \tag{10}$$

which is called the *Principle of Maximum Likelihood* (ML). Substituting $f(\epsilon)$ for $f(T)$ in Eq. (9) and assuming that the errors are Gaussian with zero mean and a covariance matrix of Σ gives [7] (note that non-Gaussian distributions will give approximately the same results [1])

$$L(T) = \ln(f(T|P) = \ln(f(\epsilon)) \tag{11a}$$

$$= -\ln(\sqrt{2\pi}) - \ln(\det(\Sigma)) - \{T_i - F(P,\theta,t_i)\}^T \Sigma^{-1} \{T_i - F(P,\theta,t_i)\} \tag{11b}$$

where $\{T_i - F(P,\theta_i)\}$ is a column vector of ϵ_i. Maximizing $L(T)$ is equivalent to minimizing

$$S_L = \{T_i - F(P,\theta,t_i)\}^T \Sigma^{-1} \{T_i - F(P,\theta,t_i)\} \tag{12}$$

Comparing Eqs. (12) and (4) shows that the Maximum Likelihood Principle with normally distributed independent errors, i.e., Σ is a diagonal matrix with elements $\sigma_{\epsilon_i}^2$, is simply the weighted Least Squares method with $w_i = 1/\sigma_{\epsilon_i}^2$.

Maximizing $L(T)$ may be quite difficult for complicated functions F. If F is expanded in a Taylor series about an initial guess P_0 and only the first-order term is kept,

$$T_i = F(P_0, \theta, t_i) + H_i(P - P_0) \tag{13a}$$

where $H_i = \partial F(P, \theta, t_i)/\partial P|_{P_0}$ is the sensitivity of F to P. Then it can be shown [10,11] that if both the parameters and the data have Gaussian distributions or if the parameters are linear functions of the data that $\hat{P}$ has the normal distribution $N(\mu, \sigma_{\hat{P}}^2)$ where

$$\mu = P_0 + \sigma_{\hat{P}}^{-2}\mathbf{H}^T\Sigma^{-1}\{T_i - F_i(P_0)\} \tag{14b}$$

$$\sigma_{\hat{P}}^{-2} = \mathbf{H}^T\Sigma^{-1}\mathbf{H} \tag{14c}$$

If our prior for P assumes that P is normally distributed with $N(\eta, \phi)$, then maximizing $f(P|T)$, Eq. (9*a*), yields

$$\hat{P} = P_0 + \sigma_{\hat{P}}^{-2}\left[\mathbf{H}^T\Sigma^{-1}\{T_i - T_i(P_0)\} + \frac{\eta}{\phi}\right] \tag{15a}$$

$$\sigma_{\hat{P}}^{-2} = \mathbf{H}^T\Sigma^{-1}\mathbf{H} + \frac{1}{\phi} \tag{15b}$$

Eqs. (14*b*) and (15*a*) are iterated to convergence. Eqs. (15*a* and *b*) reduce to Eqs. (14*b* and *c*) if $\phi = \infty$, the condition for no prior knowledge about P.

The maximum likelihood principle typically gives rise to biased estimators, i.e., $E[\hat{P}] \neq \overline{P}$. If a sufficient number of data points are available, then the ML estimator is asymptotically unbiased. Probably the most commonly encountered biased estimator is the estimate of the standard deviation, $\Sigma_{i=1}^{N}(T_i - E[T])^2/N$. The correct value is $\Sigma_{i=1}^{N}(T_i - E[T])^2/(N-1)$ and as $N \to \infty$ the bias disappears.

Information and Correlated Errors. The Cramer-Rao theorem [6,10] gives a lower bound to $\sigma_{\hat{P}}$ for unbiased estimators of

$$\sigma_{\hat{P}}^2 \geqslant \frac{1}{E\left[-\dfrac{\partial^2 L}{\partial P^2}\right]} \tag{16a}$$

The inverse of $\sigma_{\hat{P}}^2$, called the *Information* $\mathcal{I}$, by Fisher [6] or sometimes referred to as the *precision* is

$$\mathcal{I} = \sigma_{\hat{P}}^{-2} = E\left[-\frac{\partial^2 L}{\partial P^2}\right] \tag{16b}$$

If one performed enough independent experiments, evaluating L for each, it would be possible to determine the expected value, and thus $\mathcal{I}$. Using only one experiment leads to an estimated value of $\mathcal{I}$ given [11] by

$$\hat{\mathcal{I}} = -\frac{\partial^2 L}{\partial P^2} \tag{17a}$$

By evaluating $\hat{\mathcal{I}}$ it is possible to optimally design an experiment in terms of where to place sensors, what to sense, the duration of the experiment, and the sampling rate to estimate desired parameters [12,13]. Expanding T in a *one* term Taylor series when evaluating L leads to

$$\hat{\mathcal{I}} = \mathbf{H}^T\Sigma^{-1}\mathbf{H} \tag{17b}$$

which is a function of the sensitivities, H_i, and the statistics of the error. If the errors are independent (not correlated) and of equal standard deviation, σ_ϵ, the total information is

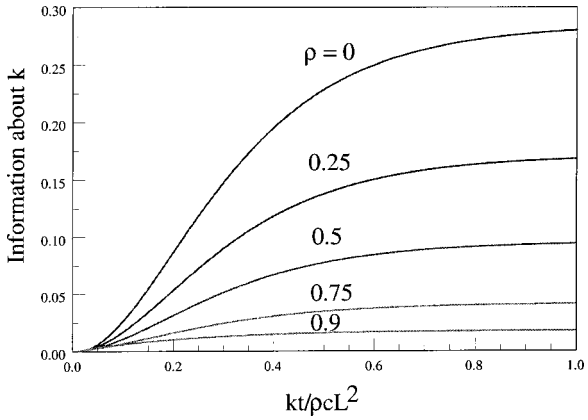

Fig. 2 Effect of correlated errors on the information from Eq. 18 for a prescribed heat flux at $x = L$ and an insulated boundary at $x = 0$ for $\sigma_\epsilon = 1$

$$\hat{\mathcal{I}} = \frac{1}{\sigma_{\hat{P}}^2} = \frac{1}{\sigma_\epsilon^2}\sum_{i=1}^{N}\left(\frac{\partial F_i}{\partial P}\right)^2 \tag{18}$$

and the reasoning behind Fisher's choice of the term *information* becomes clear since the more readings or the more accurate the readings, the smaller $\sigma_{\hat{P}}$ will be, i.e., the more we know about $\hat{P}$. If the errors are correlated, the situation is very different. Consider an experiment in which H_i is a constant, for example unity, and the errors of each successive data point are correlated such that

$$\Sigma = \sigma_\epsilon^2\begin{pmatrix} 1 & \rho & \rho^2 & \cdots & \rho^N \\ \rho & 1 & \rho & \cdots & \rho^{N-1} \\ \vdots & \vdots & \vdots & \ddots & \vdots \\ \rho^N & \rho^{N-1} & \vdots & \cdots & 1 \end{pmatrix} \tag{19a}$$

(which is representative of a sensor with a damped response). This matrix is easily inverted [14] and the increase in $\mathcal{I}$ due to an additional data point, i.e., the increment of information per reading $\Delta\mathcal{I}$, is found to be

$$\Delta\hat{\mathcal{I}} = \frac{1}{\sigma_\epsilon^2}\left(\frac{1-\rho}{1+\rho}\right) \tag{19b}$$

Thus independent errors, $\rho = 0$, add $1/\sigma_\epsilon^2$ information per additional reading; perfectly positively correlated errors, $\rho = 1$, give no additional information; and perfectly negatively correlated errors, $\rho = -1$, give an infinite amount of information and thus an absolutely precise value of $\hat{P}$. This last result may appear paradoxical, but it only means that two readings have errors which are exactly opposite in sign and thus averaging the two readings gives the true value. Figure 2 illustrates how the degree of correlation affects the information computed from Eq. (18) for a one dimensional transient conduction problem with a constant heat flux applied at $x = L$, an insulated boundary at $x = 0$, and temperatures read at $x = 0$. The figure clearly demonstrates the impact that any auto-correlation of the measured temperatures has on the information content.

From Eq. (19*b*) we can define an effective standard deviation which gives an approximate measure of the effects of correlation

$$\sigma_\epsilon^{eff} = \sigma_\epsilon^2\left(\frac{1+\rho}{1-\rho}\right) \tag{19c}$$

Analysis of the Experiment

With these fundamentals in mind it is possible to examine the conductivity experiment of Ref. [2] from the point of view of cross and auto-correlated errors. In addition, we will analyze the

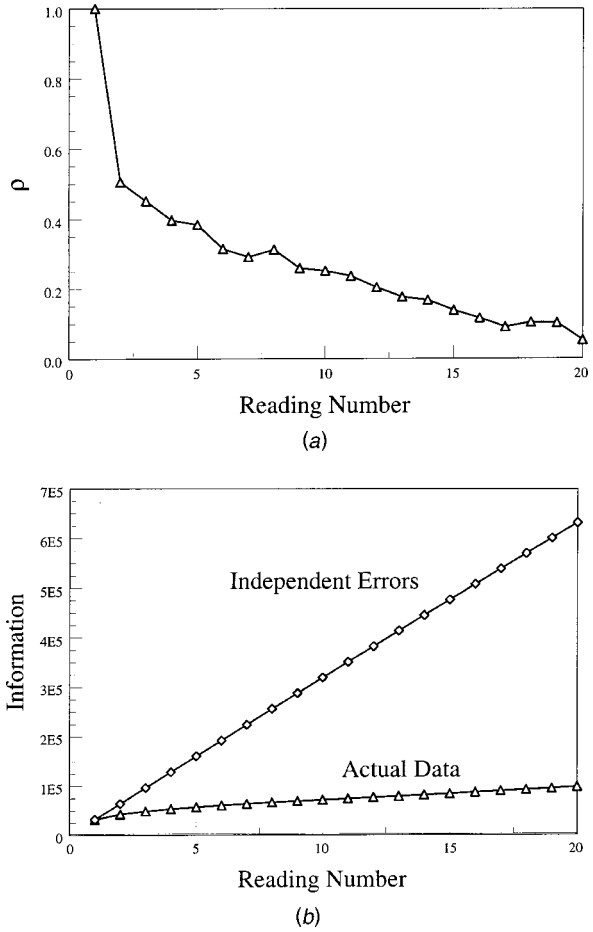

Fig. 3 (*a*) Correlation coefficients for a data trace at station 7 from the experiment of Ref. [2], sampled at ≈1.5 sec; and (*b*) Information content for a data trace at station 7 from the experiment of Ref. [2].

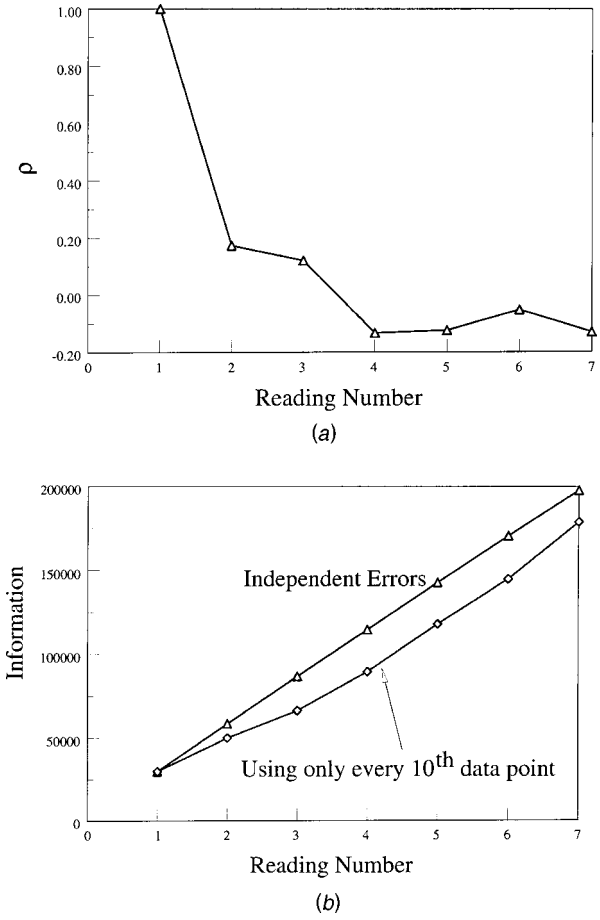

Fig. 4 (*a*) Auto-correlation when using every 10th data point to estimate the conductivity; (*b*) Information when using every 10th data point to estimate the conductivity.

effect of using different simulation models, i.e., the use of a prescribed heat flux versus a prescribed temperature boundary conditions model, on the estimated precision.

AutoCorrelated Signals. Figure 1(*b*) displays the residuals $T_i - F(k,t_i)$ as a function of time. That the mean of residuals is not zero is an indication that the model is not an exact simulation of the experiment. In this case, we speculate that errors are either the lack of accounting for any surface heat losses or errors in the temperature measurements due to either inexactness in knowing the location of the thermocouples or to data acquisition errors. The noise in the residuals is attributed to random noise (error) in the measured temperatures. To study the characteristics of the errors, the residuals have been fitted by a smooth curve, which would represent the response of an improved model, and the differences between the residuals and the smooth curve is taken as the error. The analysis of a single sensor's response is usually referred to as ''time series'' analysis and procedures are described in Bendat and Piersol [15] and Dhrymes [16]. The fundamental requirements are that errors have a zero mean and constant standard deviation and be normally distributed. The errors have been examined statistically following the recommendations of Bendat and Piersol [[15], pp. 386–388] regarding stationarity, trend removal, and the number of data points to be analyzed and found to satisfy these conditions and thus the methods of ''time series'' analysis can be applied to determine the autocorrelation.

The autocorrelation of the errors from the sensor nearest the plane of symmetry, station 7, is shown on Fig. 3(*a*). The auto correlation coefficient, ρ, between two successive readings is quite high, ≈0.5 and drops slowly as the data points are further separated.

Using the correlation matrix based upon the data of Figure 3(*a*, *b*) shows that the information gained when using a sequence of 20 consecutive readings is equivalent to that obtained from only three independent readings. Although every reading gives some additional information, the reduction in each increment due to the auto-correlation of the data yields a reduced level of precision.

If every 10th data point is used in estimating the conductivity, the corresponding results are shown in Fig. 4. Here we see that we have achieved essentially as much information as a set of independent readings would provide.

Multivariate Analysis. In the actual experiment data were taken at 56 locations. Each sensor's time history can be considered to be a vector of measurements and the set of such vectors treated as multivariate data. Details about multivariate analysis can be found in [17]. The basic requirement is that the standard deviation of the vectors be approximately equal.

At each axial position thermocouples were deployed around the circumference every 90 deg. At a given axial position the readings from each circumferential sensor were found to have approximately equal standard deviations and so could be treated as multivariate data. The readings at the 2nd axial position were found to be correlated with a correlation matrix of

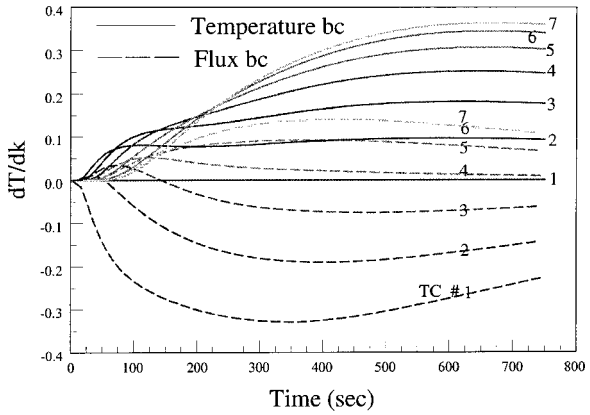

Fig. 5 Sensitivities $\partial T/\partial k|k_0,t_i,x$ for the PT and PF models

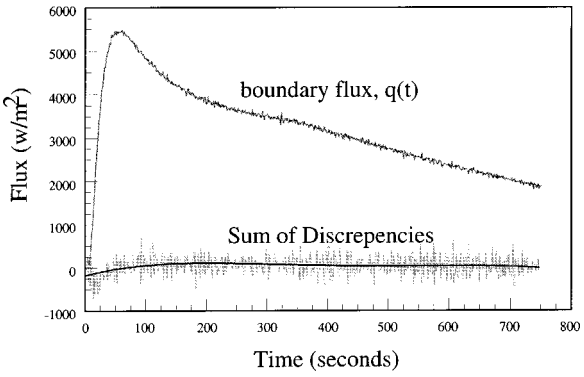

Fig. 6 Estimated boundary flux for the PF model

$$\text{Cor}=\begin{pmatrix} 1.0 & 0.9993 & 0.9986 & 0.9994 \\ 0.9993 & 1.0 & 0.9993 & 0.9993 \\ 0.9986 & 0.9993 & 1.0 & 0.9987 \\ 0.9994 & 0.9993 & 0.9987 & 1.0 \end{pmatrix}$$

This degree of correlation gives a total information from the four sensors of 1.0087 instead of the value of four that would be expected from four independent readings. Thus there is no gain in precision from including data from other than one of these sensors. A principal component analysis [17]—a technique to determine how to combine data to simplify the analysis by linearly combining data—reveals that 99 percent of the information is contained in the arithmetic average of the four circumferential temperatures, thus validating the use of the average temperature at each axial station as used in Ref. [2] in estimating k.

Comparing the measurements from the symmetric set of readings, stations 8–13, showed a correlation with their corresponding sensors, stations 2–7, greater than 0.98. Each pair of axial stations thus gave a total information of 1.02 compared to the value of two for independent data.

On the other hand, analyzing the data from sensors 2–7, showed a correlation coefficient less than 0.2 between each pair and an information content which was comparable to independent readings.

PF Versus PT Models. In the following discussion PF will refer to the prescribed heat flux model and PT to the prescribed surface temperature model used in the initial analysis for estimating the conductivity from this experiment.

If there are no measurement errors in the temperature measured at the first axial station and the fluxes were known exactly, both models will predict the same temperature histories at a given location, x. Because of this, both models predict approximately the same estimate of the conductivity, 14.58 W/m-K for the PT model and 14.62 for the PF model. The reason for this agreement can be seen from Eq. (1*b*). If the measurements had no error, then the iterative process will drive k to a value for which the residuals are exactly zero with the sensitivities $\partial F/\partial k|_{k_0,t_i,x}$ serving simply as weighting factors. In the real case with measurement errors, the differing sensitivities of the two models focus the attention of the estimation process on different sensors, leading to slightly different values of k, but driving the average weighted residuals to zero. Since both models produce the same values of temperature, it is not surprising that the estimated conductivities are quite close.

On the other hand, the precision of the estimate for a constant level of noise, Σ, as given by Eq. (14*c*), is seen to be a function only of the sensitivity. Figure 5 shows the sensitivities for both models. Initially the PF model has greater sensitivities, but as time progresses the PT model sensitivities are greater. In addition, the PF model sensitivities near the midpoint of the specimen are consistently near zero. Because the PT model sensitivity to a sensor at $x=L$ is zero (the temperature is prescribed there) while the sensitivity of the PF model is high for this sensor, the early time information of the PT model is less than that of the PF. However, as time progresses its information content soon exceeds that of the PF model.

If one is uncertain about the heat flux, $q(t)$, to be used as a boundary condition in the model of the experiment, then there are three possible approaches: (*a*) treat $q(t)$ as another parameter to be estimated; (*b*) evaluate $f(k|T)$ as a marginal distribution and find the value of k which maximizes this distribution; (*c*) consider $q(t)$ as an uncertain parameter. The difficulties with the first method have already been pointed out. The second approach using a marginal distribution requires evaluating the joint distribution $f(k,q|T)$, integrating over all values of q and maximizing the probability with respect to k [6,7].

$$f(k|T)=\int f(k,q|T)dq \tag{23a}$$

which, following the development of information leads to

$$\hat{\mathcal{I}}=\frac{\partial^2 L}{\partial k^2}=\frac{\partial^2}{\partial k^2}\left(\ln\left(\int f(k,q|T)dq\right)\right) \tag{23b}$$

However, determining $f(k,q(t)|T)$ for the actual experiment and integrating over all possible values of $q(t)$ for each time, t, is virtually impossible.

Instead let us estimate the boundary heat flux, $q(t)$, by using an initial guess for the conductivity, the measured temperatures, and a finite volume model for the experiment. This can then be used in the PF model to yield an improved value of k. Iterating gives a reasonable estimate of the heat flux history and of the information of the PF model.

Figure 6 shows the estimated time history of the flux, $q(t)$, and the error in satisfying the overall heat balance. The errors are presumed to be primarily surface losses. These estimated overall losses were found to be uncorrelated with a mean of approximately 1 percent of the applied flux. Using this estimated flux and the measured temperatures, Fig. 7(*a*) depicts the information content of the PF and PT models computed using values of σ_T of 0.08 °C in both models and assuming that the prescribed boundary conditions for both models have no error. The PT model yields about five times as much information as the PF model. When the auto-correlation of the temperatures is included, both models show a reduction of about a factor of ten.

The information content of the PT model, with or without considering the correlation, is seen to exceed that of the PF model by approximately a factor of five suggesting that the precision of the conductivity estimated from the PT model is approximately twice that estimated from the PF model. In fact the boundary conditions used in the models, the heat flux, $q(t)$, in the PF model and the

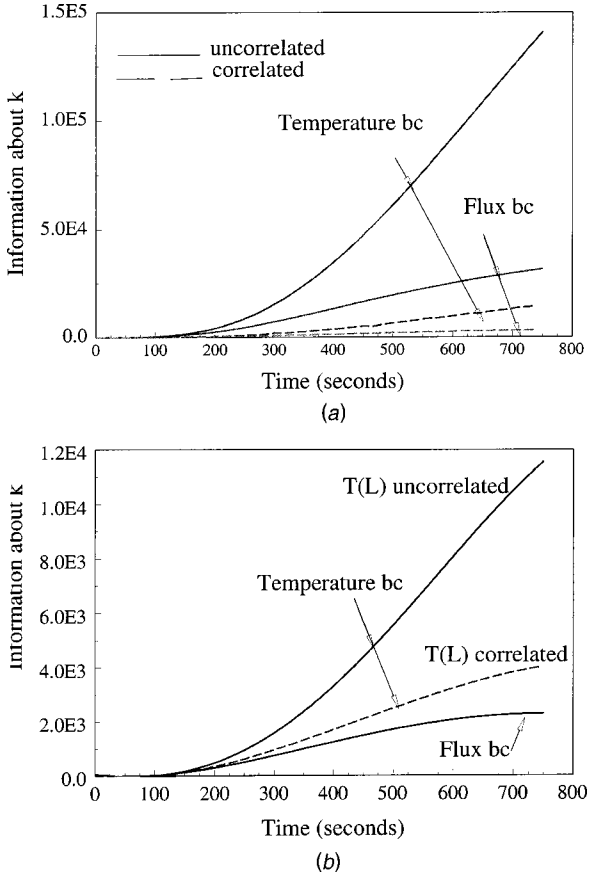

Fig. 7 (*a*) Information content of the PF and PT models with no uncertainty in the boundary conditions; (*b*) Information content of the PF and PT models with uncertainty in the boundary conditions and correlation in time.

measured temperature, $T(L)$, in the PT model, have statistical variations, i.e., they are uncertain and auto-correlated. Reference [18] has investigated how to consider such uncertainties and shown that their effect is to augment the covariance Σ of Eq. (18) to give an effective covariance matrix of

$$\Sigma + \left[\frac{\partial T}{\partial bc}\right] \mathrm{cov}(bc) \left[\frac{\partial T}{\partial bc}\right]^T \tag{24}$$

where $\mathrm{cov}(bc)$ is the covariance of the boundary conditions. The temperature history, $T(k,t_i,x)$, computed at N times, t_i, is based upon the N values of the boundary conditions, bc_j. This means that in Eq. (24) $[\partial T/\partial bc]$ is a $N\times N$ matrix. Likewise, $\mathrm{cov}(bc)$ is an $N\times N$ matrix reflecting the auto-correlation of the boundary conditions.

An analysis of the boundary conditions yields an estimate of σ_q of 42 W/m^2 and σ_T of 0.08 °C. Including these uncertainties in Σ, through Eq. (24), yields the results shown by the solid lines in Fig. 7(*b*). While the boundary flux was determined to be essentially uncorrelated in time, the temperature used for the PT model boundary condition was correlated as shown in Fig. 3(*a*). Including this correlation in $\mathrm{cov}(bc)$ then reduced the information content of the PT model to that depicted by the dashed line on Figure 7(*b*).

When the uncertainty in the boundary conditions and the auto-correlations are included, the PT model yields only 1.7 more information than the PF model compared to the 4.5 when these are ignored (solid lines of Figure 7*a*).

Conclusions

Reference ([2]) reported a standard deviation of the estimated thermal conductivity of

$$\left(\frac{\sigma_k}{k}\right)^2 = \frac{1}{\mathcal{I}_{PT}} + \left(\frac{\sigma_\rho}{\rho}\right)^2 + \left(\frac{\sigma_c}{c}\right)^2$$

where the last terms represent the uncertainty in the density, ρ, and the specific heat, c. The appropriate numerical values from Eq. (2) are

$$\left(\frac{\sigma_k}{k}\right)^2 = 1.3\times 10^{-9} + 5.2\times 10^{-6} + 4.0\times 0^{-4}$$

indicating that the uncertainty due to the measurement noise and errors was negligible in comparison to the other uncertainties. From the discussion regarding the effect of uncertainties in the boundary conditions and the correlation of the errors, the actual information should be reduced by a factor of 30 because of the auto-correlation and the uncertain boundary conditions, a factor of four because the circumferential readings contribute no additional information and a factor of two because the use of pairs of symmetrical sensors, e.g., stations 7 and 8, adds no additional information to that obtained from one of the sensors. The total reduction in information is thus by a factor of 240, yielding a first term of 0.3×10^{-6}. If only the effects of the temperatures were considered, i.e., the estimated parameter were the thermal diffusivity not the conductivity, the effect of this reduction in information would be a increase in the standard deviation by a factor of 15 (i.e., $\sqrt{240}$). However, when estimating the conductivity, not the diffusivity, the uncertainty in the specific heat dominates.

The results of the correlation analyses indicate that equal precision could be obtained by using fewer sensors and a slower sampling rate. If this same apparatus were employed for estimating other properties, for example the contact resistance between the end blocks and the tube, these results can be used to simplify the operation of the experiment and the resulting analysis.

The comparison of the PF and PT models illustrates that parameters should be estimated using models which provide the greatest sensitivities to the parameters sought. But the estimation must consider all uncertainties and statistical properties if the estimated precision is to accurately reflect the uncertainty in the estimated parameters.

The methods described are generally applicable to transient and steady state problems with data taken at arbitrary sampling rates. While for strongly correlated data, the effect of the correlations usually outweighs that of numerical errors in solving for $F(k,t_i,x)$ it is important to ensure that the solutions are independent of grid resolution and time steps.

Finally, it must be recognized that the statistical analysis presented here could only have been carried out because a large amount of data from multiple sensors was available. Of particular importance was the knowledge of the absence of a cross-correlation between the sensors at the different axial positions and the strong cross-correlation between sensors at the four circumferential positions. Because of these effects: (*a*) circumferential averages at each axial position could be used; (*b*) data from each axial position could be treated independently. Without this knowledge, all data would have had to be considered simultaneously and the covariance matrix, Σ, would have been of order 14,000 $\times$14,000 instead of 500×500, rendering the analysis impossible.

Equally important, the choice of the simulation model and the estimate of the conductivity depended upon the data from those extra sensors whose data was highly correlated, e.g., the circumferential sensors justified the use of a one-dimensional analysis. The number of sensors and their deployment must be carefully considered in order to justify the model used. These results demonstrate that one must differentiate between the data needed to specify the model and the precision in the estimated parameters provided by the data.

Nomenclature

Roman

bc = boundary condition
$E[x]$ = expected value of x
$f(x)$ = probability density function of
F = predicted temperature
$\mathbf{H}$ = sensitivity matrix
ic = initial condition
$\mathcal{I}$ = information
k = thermal conductivity
N = number
$N[\mu,\gamma]$ = normal distribution with a mean of μ and a variance of γ
P = parameter to be estimated
q = heat flux
t = time
T = temperature
w_i = weight
x = position

Greek and Mathematical Symbols

ϵ = error
Δ = difference
ρ = correlation coefficient, density
ρc = product of density and specific heat
σ_x = standard deviation of x
σ_x^{eff} = effective standard deviation of x
Σ = covariance matrix of ϵ
$\overline{\theta}$ = fixed parameter
$\overline{P}$ = true value of P
$\hat{P}$ = estimate of P
$\{x\}$, x = vector
$\{x\}^T$,x^T = transpose of vector

References

[1] Gans, P., 1992, *Data Fitting in the Chemical Sciences*, J. Wiley and Sons, New York, NY.
[2] Blackwell, B. F., Gill, W., Dowding, K. J., and Easterling, R. G., 2000, "Uncertainty Estimation in the Determination of Thermal Conductivity of 304 Stainless Steel," *Proc. IMECE 2000*, HTD Vol. 366-2, ASME, New York, pp. 147–154.
[3] Beck, J. V., and Arnold, K. J., 1977, *Parameter Estimation in Engineering and Science*, J. Wiley and Sons, New York, NY.
[4] Beck, J. V., Blackwell, B., and Haji-Sheikh, A., 1996, "Comparison of Some Inverse Heat Conduction Methods Using Experimental Data," Int. J. Heat Mass Transf., **39**, pp. 3649–3657.
[5] Coleman, H. W., and Steele Jr., W. G., 1989, *Experimentation and Uncertainty Analysis for Engineers*, J. Wiley and Sons, New York, NY.
[6] Papoulis, A., 1991, *Probability, Random Variables, and Stochastic Processes*, McGraw-Hill, New York, NY.
[7] Stark, H., and Woods, J. W., 1994, *Probability, Random Processes and Estimation Theory for Engineers*, Prentice Hall, New York, NY.
[8] Sivia, D. S., 1996, *Data Analysis, A Bayesian Tutorial*, Clarendon Press, Oxford, England.
[9] Lee, P. M., 1997, *Bayesian Statistics*, J. Wiley and Sons, New York, NY.
[10] Sorenson H. W., 1980, *Parameter Estimation: Principles and Problems*, Marcel Dekker, Inc., New York, NY.
[11] Cowan, G., 1998, *Statistical Data Analysis*, Oxford Press, Oxford, England.
[12] Emery, A. F., and Nenarokomov, A. V., 1998, "Optimal Experiment Design," Meas. Sci. Technol., **9**, pp. 864–876.
[13] Emergy, A. F., and Fadale, T. D., 1996, "Design of Experiments Using Uncertainty Information," ASME J. Heat Transfer, **118**, pp. 532–538.
[14] Savin, N. E., and White, K. J., 1978, "Estimation and Testing for Functional Form and Autocorrelation—A Simultaneous Approach," J. Econometr., **8**, pp. 1–12.
[15] Bendat, J. S., and Piersol, A. G., 2000, *Random Data: Analysis and Measurement Procedures*, J. Wiley and Sons, New York, NY.
[16] Dhrymes, P. J., 1981, *Distributed Lags: Problems of Estimation and Formulation*, North-Holland Publ., New York, NY.
[17] Johnson, D. E., 1998, *Applied Multivariate Methods for Data Analysis*, Duxbury Press, Brooks-Cole Publ., Pacific Grove, CA.
[18] Emery, A. F., 2001, "Using the Concept of Information to Optimally Design Experiments With Uncertain Parameters," ASME J. Heat Transfer, **123**, pp. 593–600.

Journal of Heat Transfer

Technical Notes

This section contains shorter technical papers. These shorter papers will be subjected to the same review process as that for full papers.

Heat Transfer Coefficients in Concentric Annuli

Jaco Dirker
Department of Mechanical Engineering, Rand Afrikaans University, Johannesburg, South Africa

Josua P. Meyer
Department of Mechanical and Aeronautical Engineering, University of Pretoria, Pretoria, 0002, South Africa
e-mail: jmeyer@up.ac.za

The geometric shape of a passage's cross-section has an effect on its convective heat transfer capabilities. For concentric annuli, the diameter ratio of the annular space plays an important role. The purpose of this investigation was to find a correlation that will accurately predict heat transfer coefficients at the inner wall of smooth concentric annuli for turbulent flow of water. Experiments were conducted with a wide range of annular diameter ratios and the Wilson plot method was used to develop a convective heat transfer correlation. The deduced correlation predicted Nusselt numbers accurately within 3 percent of measured values for annular diameter ratios between 1.7 and 3.2 and a Reynolds number range, based on the hydraulic diameter, of 4 000 to 30,000. [DOI: 10.1115/1.1517266]

Keywords: Annular Flow, Experimental, Forced Convection, Heat Transfer, Heat Exchangers

Introduction

Since the early nineteen hundreds many researchers have investigated heat transfer in annuli, particularly in order to find correlations that can describe the Nusselt number and convective heat transfer for a wide range of flow conditions and annular diameter ratios. Most of the proposed equations for calculating annular Nusselt numbers are functions of the annular diameter ratio, the Reynolds number and the Prandtl number and correspond with the Dittus-Boelter type form. Table 1 contains some correlations [1–10] cited in literature. Most correlations predict an almost linear increase in the Nusselt number with an increase in the Reynolds number.

When comparing the various correlations, applicable to the flow of water, over a wide range of annular diameter cases and Reynolds numbers, it is found that large differences, in the region of 25 percent in terms of the average, exist between predicted values.

Contributed by the Heat Transfer Division for publication in the JOURNAL OF HEAT TRANSFER. Manuscript received by the Heat Transfer Division March 13, 2002; revision received July 8, 2002. Associate Editor: C. Amon.

No literature was found that indicates the existence of an accurate heat transfer correlation for concentric annuli. It was thus the purpose of this investigation to deduce a correlation with which accurate predictions could be made of average Nusselt numbers at the inner annular wall under turbulent flow conditions of water.

Experimental Facility and Data

Eight different concentric tube-in-tube heat exchangers, each with a different annular diameter ratio, were used during the experimental investigation. Each heat exchanger had an effective heat transfer length of about 6 m and was operated in a counter-flow arrangement with hot water in the inner tube and cold water in the annulus. The heat exchangers were constructed from hard-drawn refrigeration copper tubing and were operated in a horizontal configuration.

The inner tubes were kept in concentric positions by employing sets of radial supporting pins along the length of each heat exchanger at different intervals. The size and position of the supporting pins were carefully calculated to minimize possible sagging of the inner tube. The supporting structures occupied between 3.9 percent and at most 6.5 percent of the cross-sectional areas of the various test sections [11].

Volumetric flow rates were measured by using semi-rotary circular-piston-type displacement flowmeters with a measuring accuracy of greater than 98 percent. Hot water supplied by an on-site hot-water storage tank ($1000l$), fitted with an electric resistance water heater, was pumped through the inner tube by means of a positive displacement pump and then returned to the storage tank. The hot-water flow rates were controlled with a hand-operated bypass system. Similarly, cold water was supplied from a cold-water storage tank ($1000l$) connected to a chiller and pumped through the annulus by means of two series connected centrifugal pumps to ensure high flow rates before being returned to the storage tank.

Temperature measurements were facilitated by means of K-type thermocouples fixed on the outside surfaces of entry and exit regions of the heat exchangers. Temperature errors were usually less than 0.1 K. Measuring points were sufficiently insulated from the ambient.

A high level of accuracy in the experimental data was maintained. More than 90 percent of all data points exhibited an energy balance error of less than 1 percent between the inner tube and annular heat transfer rates. A Reynolds number range, based on the annular hydraulic diameter, of 2 600 to 35,000 was covered.

Processing of Data

It was assumed from previous work (Table 1) that the internal and annular Nusselt numbers can be written in a Sieder-Tate [12] format, respectively:

$$\mathrm{Nu}_i = \frac{h_i D_i}{k_i} = C_i \,\mathrm{Re}_i^{0.8}\,\mathrm{Pr}_i^{1/3}\left(\frac{\mu}{\mu_w}\right)_i^{0.14} \tag{1}$$

Table 1 Equations available from literature describing the Nusselt number in a smooth concentric annulus during forced convection

Author(s)	Correlation	Diameter Ratio Range	Reynolds Number Range	Medium
Davis [1]	$*\mathrm{Nu}_{D_h} = 0.038a^{0.15}(a-1)^{0.2}\,\mathrm{Re}_{D_h}^{0.8}\,\mathrm{Pr}^{\frac{1}{3}}\left(\frac{\mu}{\mu_w}\right)_o^{0.14}$	1.18-6 800	Not specified	All mediums
McAdams [2]	$\mathrm{Nu}_{D_h} = 0.03105a^{0.15}(a-1)^{0.2}\,\mathrm{Re}_{D_h}^{0.8}\,\mathrm{Pr}^{\frac{1}{3}}\left(\frac{\mu}{\mu_w}\right)^{0.14}$	1.18 - 6 800	Not specified	All mediums
Foust and Christian [3]	$*\mathrm{Nu}_{D_h} = \frac{0.04a}{(a+1)^{0.2}}\,\mathrm{Re}_{D_h}^{0.8}\,\mathrm{Pr}^{0.4}$	1.2 - 1.84	3 000 - 60 000	Water
McAdams [2]	$\mathrm{Nu}_{D_h} = 0.023\,\mathrm{Re}_{D_h}^{0.8}\,\mathrm{Pr}^{\frac{1}{3}}\left(\frac{\mu}{\mu_w}\right)^{0.14}$	Not specified	Not specified	Not specified
Monrad and Pelton [4]	$\mathrm{Nu}_{D_h} = 0.023\left[\frac{2\ln a - a^2 + 1}{a - \frac{1}{a} - 2a\ln a}\right]\mathrm{Re}_{D_h}^{0.8}\,\mathrm{Pr}^{n}$	1.65, 2.45, 17	12 000 - 220 000	Water Air
Wiegand *et al.*[5]	$\mathrm{Nu}_{D_h} = 0.023a^{0.45}\,\mathrm{Re}_{D_h}^{0.8}\,\mathrm{Pr}^{n}\left(\frac{\mu}{\mu_w}\right)^{0.14}$	1 – 10	Not specified	Fluids: $\mu_{material} \le 2\mu_{water}$
Kays and Leung [6]	Results listed in tables for various conditions.	1 - 4	10^4 - 10^6	Not specified
Petukhov and Roizen [7]	$*\mathrm{Nu}_{D_h} = \frac{0.06759a^{0.16}}{(a+1)^{0.2}}\zeta\,\mathrm{Re}_{D_h}^{0.8}$ with $\zeta = 1 + 7.5\left(\frac{a-5}{(a+1)\mathrm{Re}_{D_h}}\right)^{0.6}$ for $a \ge 5$; $\zeta = 1$ for $a \le 5$	1 - 14.3	10^4 - $3\cong10^5$	Air
Dittus-Boelter [8]	$\mathrm{Nu}_{D_h} = 0.023\,\mathrm{Re}_{D_h}^{0.8}\,\mathrm{Pr}^{n}$	Not specified	Not specified	Not specified
Stein and Begell [9]	$\mathrm{Nu}_{D_h,f} = 0.0200a^{0.5}\mathrm{Re}_{D_h,f}^{0.8}\,\mathrm{Pr}_f^{\frac{1}{3}}$	1.232 , 1.463, 1.694	30 000 – 390 000	Water
Crookston *et al.* [10]	$\mathrm{Nu}_{D_h} = 0.023a^{\frac{1}{4}}\,\mathrm{Re}_{D_h}^{\frac{3}{4}}\,\mathrm{Pr}^{\frac{1}{3}}$	10, 16, 31	17 000 – 100 000	Air
* Original equations were rewritten as to have the Reynolds and Nusselt numbers based on the annular hydraulic diameter:				

$$\mathrm{Nu}_o = \frac{h_o D_h}{k_o} = C_o\,\mathrm{Re}_{o,D_h}^{P}\,\mathrm{Pr}_o^{1/3}\left(\frac{\mu}{\mu_w}\right)_o^{0.14} \qquad (2)$$

P, C_i, and C_o are added to account for geometry influences. The modified Wilson plot method developed by Briggs and Young [14] was used to determine these values for the different annular diameter ratios while for the inner tube the exponent of the Reynolds number was kept at 0.8 as suggested in literature [13,14].

More than 95 percent of all data points were predicted within a 3 percent accuracy by the Wilson plot obtained correlations for the different heat exchangers. All Wilson plot correlations exhibited a median error of less than or in close proximity to 1 percent. Standard deviances for error values were less than 2 percent.

Derivation of Correlation

P and C_o, from Eq. 2, showed a dependence on the annular diameter ratio. Figures 1 and 2 illustrate the general trends of P and C_o in terms of the diameter ratio. The value of P exhibited a downward trend when the annular diameter ratio was increased. On the other hand, the value of C_o had an upward trend for an increasing annular diameter ratio.

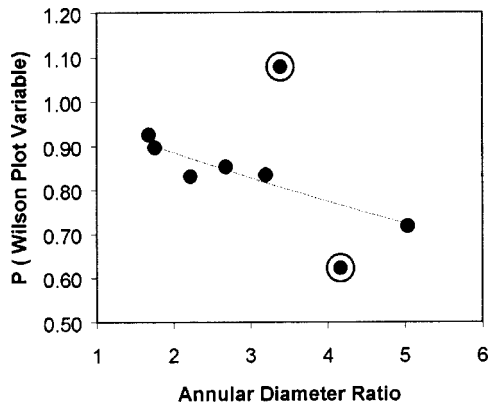

Fig. 1 P values obtained from Wilson plot analyses

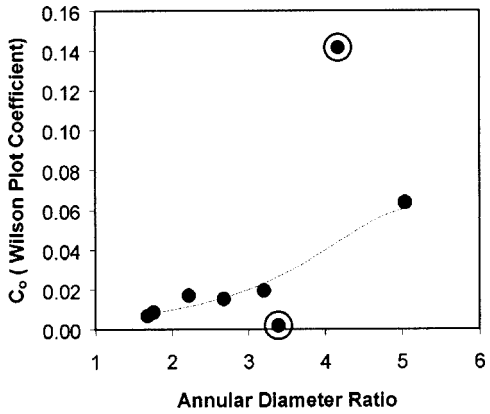

Fig. 2 C_o values obtained from Wilson plot analyses

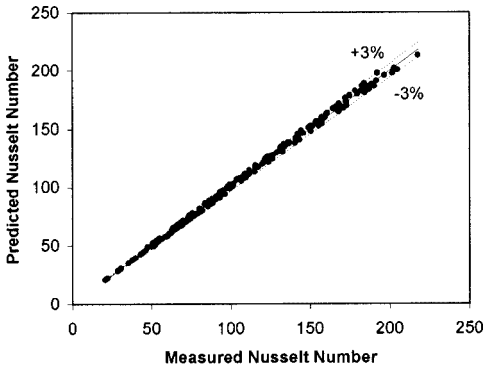

Fig. 3 Comparison between predicted Nusselt numbers and measured Nusselt numbers

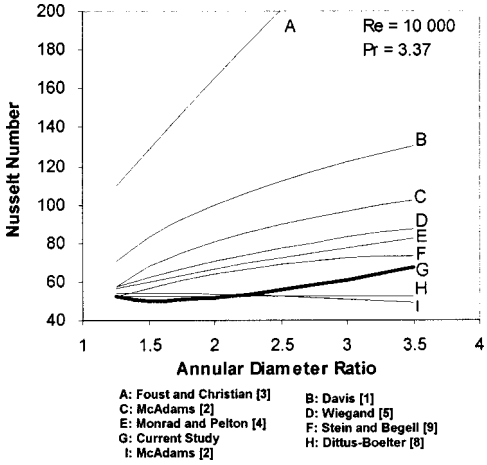

Fig. 4 Comparison between the derived correlations and correlations from literature for a wide range in annular diameter ratios

Results obtained for annular diameter ratios of 4.17 and 3.39 do not agree with the general trend of the rest of the heat exchangers which are encircled in Figs. 1 and 2.

These heat exchangers were rebuilt and the experimental tests repeated. The values of P and C_o were reaffirmed. From the experimental results, the behavior of P and C_o can be described relatively precisely for annular diameter ratios below 3.2. For ratios greater than this, it is unfortunately not the case and more experimental data are needed. Data points between annulus ratios of 3.2 and 5 are difficult to obtain as tube sizes which would give these ratios are not readily available.

Using results for annular ratios of below 3.2, it was possible to describe the trend mathematically by evaluating different curve fits. Equations (3) and (4) exhibited the best accuracies and are indicated in Figs. 1 and 2 as dotted lines.

$$P = 1.013e^{-0.067a} \tag{3}$$

$$C_o = \frac{0.003a^{1.86}}{0.063a^3 - 0.674a^2 + 2.225a - 1.157} \tag{4}$$

By substituting Eqs. (3) and (4) into Eq. (2) a correlation for the prediction of the Nusselt number is produced.

The validity of the resulting correlation for the prediction of Nusselt numbers was tested with experimental data from all heat exchangers having an annular diameter ratio of less than 3.2. All predictions were within 3 percent of experimentally obtained values (Fig. 3).

The correlation was also compared to correlations in literature (Table 1) for an arbitrary thermal condition over a wide range of annular diameter ratios and Reynolds numbers. For a case where the Reynolds number is 8 000 and the Prandtl number is 3.36, the result is shown in Fig. 4. This trend was found to be true for a wide range in Reynolds numbers and Prandtl numbers.

For small annular diameter ratios, up to about 2.5, the predictions correspond well with the correlation by Dittus and Boelter [8], and an equation by McAdams [2]. In the region of an annular ratio of 3.5, a close agreement exists with the correlation of Stein and Begell [9].

Conclusion

As was expected, it was found that the convective heat transfer correlation for an annulus is dependent on the annular diameter ratios. A correlation was deduced from experimental results that predicts Nusselt numbers accurately for water within 3 percent from the measured values for diameter ratios between 1.7 and 3.2 and a Reynolds number range of 4 000 to 30,000.

Nomenclature

a = annular diameter ratio $[D_2/D_1]$
C_i = inner tube convective heat transfer correlation coefficient (Wilson plot)
C_o = annulus convective heat transfer correlation coefficient (Wilson plot)
D_1 = diameter of outer wall of inner tube, m
D_2 = diameter of inner wall of outer tube, m
D_h = hydraulic diameter of annulus $[D_2 - D_1]$, m
D_i = inner diameter of inner tube, m
h = convective heat transfer coefficient, W/m^2K
k = thermal conductivity, W/mK
Nu = Nusselt number
P = exponent of Reynolds number in Wilson plot function
Pr = Prandtl number
Re = inner tube Reynolds number
Re_o = Reynolds number
μ = viscosity, Ns/m^2

Subscripts

D_h = based on the hydraulic diameter of the annulus
i = inner tube side
o = annulus side
w = wall

References

[1] Davis, E. S., 1943, "Heat Transfer and Pressure Drop in Annuli," Trans. ASME, **Oct**, pp. 755–760.
[2] McAdams, W. H., 1954, *Heat Transmissions*, 3rd ed., McGraw-Hill, New York, pp. 241–244.
[3] Foust, A. S., and Christian, G. A., 1940, "Non-Boiling Heat Transfer Coefficients in Annuli," American Institute of Chemical Engineers, **36**, pp. 541–554.
[4] Monrad, C. C., and Pelton, J. F., 1942, "Heat Transfer by Convection in Annular Spaces," American Institute of Chemical Engineers, **38**, pp. 593–611.
[5] Wiegand, J. H., McMillen, E. L., and Larson, R. E., 1945, "Discussion on: Annular Heat Transfer Coefficients for Turbulent Flow," American Institute of Chemical Engineers, **41**, pp. 147–153.
[6] Kays, W. M., and Leung, E. Y., 1963, "Heat Transfer in Annular Passages—Hydrodynamically Developed Turbulent Flow with Arbitrarily Prescribed Heat Flux," Int. J. Heat Mass Transf., **6**, pp. 537–557.
[7] Petukhof, B. S., and Roizen, L. I., 1964, "Generalized Relationships for Heat Transfer in Turbulent Flow of Gas in Tubes of Annular Section," High Temp., **2**, pp. 65–68.
[8] Dittus, F. W., and Boelter, L. M. K., 1930, "Publications on Engineering," **2**, University of California, Berkeley, pp. 443.
[9] Stein, R. P., and Begell, W., 1958, "Heat Transfer to Water in Turbulent Flow in Internally Heated Annuli," American Institute of Chemical Engineers Journal, **4**(2), June, pp. 127–131.
[10] Crookston, R. B., Rothfus, R. R., and Kermode, R. I., 1968, "Turbulent Heat Transfer with Annuli with Small Cores," Int. J. Heat Mass Transf., **11**, pp. 415–426.
[11] Dirker, J., 2002, "Heat Transfer Coefficient in Concentric Annuli," Master's degree dissertation, Department of Mechanical Engineering, Rand Afrikaans University, Johannesburg, South Africa.

[12] Sieder, E. N., Tate, G. E., 1936, ''Heat Transfer and Pressure Drops of Liquids in Tubes,'' Ind. Eng. Chem., **28**, pp. 1429.
[13] Wilson, E. E., 1915, ''A Basis for Rational Design of Heat Transfer Apparatus,'' Trans. ASME, **37**, pp. 47–82.
[14] Briggs, D. E., and Young, E. H., 1969, ''Modified Wilson Plot Technique for Obtaining Heat Transfer Correlations for Shell and Tube Heat Exchangers,'' Chemical Engineering Progress Symposium, **65**, pp. 35–45.

A Thermocapillary Mechanism for Lateral Motion of Bubbles on a Heated Surface During Subcooled Nucleate Boiling

Paul J. Sides
e-mail: ps7r@andrew.cmu.edu
Department of Chemical Engineering, Carnegie Mellon University, Pittsburgh, PA 15213

Both thermocapillary flow and the concerted motion of bubbles toward each other in subcooled nucleate boiling have been mentioned in the literature on boiling phenomena, but never associated with each other. Also, it has been shown in previously unrelated contributions that thermocapillary flow around bubbles of sparingly soluble gas can cause those bubbles to aggregate on a warm surface. The conjunction of these observations leads to the hypothesis that mutual entrainment in thermocapillary flow might drive bubbles toward each other during nucleate boiling of a subcooled liquid. An approximate equation for estimating the observability of such motion is presented. The effect would be especially important in cases where the bubble release rate is low such as boiling on horizontal down-facing surfaces and boiling in microgravity. [DOI: 10.1115/1.1517268]

A Thermocapillary Mechanism for Lateral Motion of Bubbles

A hypothesis about a transport mechanism that promotes coalescence of bubbles during subcooled nucleate boiling is presented. The hypothesis is that adjacent bubbles entrain each other in thermocapillary flow surrounding them during nucleate boiling of subcooled liquids. The entrainment manifests itself as motion of the bubbles toward each other, which promotes their coalescence. The discussion and calculations provided in this contribution are offered in support of the hypothesis.

Consider the circumstances appearing in Fig. 1(*a–c*). In all cases a growing bubble is immersed in liquid and either attached to- or very near a warm surface. We assume for simplicity that the process is occurring in microgravity, so natural convection is not included. It is also assumed for clarity that an adjacent ''tracer'' bubble is mobile; *i.e.*, that its contact line is either nonexistent or sufficiently small not to affect any lateral bubble motion. The bubble is growing either because of vaporization of liquid or diffusion of dissolved gas to the interface.

The bubble on the left of Fig. 1(*a*) is entirely immersed in saturated liquid heated by the solid surface; the vapor/liquid interface is an isotherm. Consequently, the only flow associated with these bubbles is due to the expanding interface. There are no thermal gradients on the vapor/liquid interface, so the contribution of thermocapillary flow is zero in this instance and there is no reason for the tracer bubble on the right to move as a whole toward the bubble on the left.

The bubble on the left of Figure 1(*b*) consists primarily of sparingly soluble gas such as hydrogen or oxygen produced during electrolysis; the bubble grows by diffusion of dissolved gas through the liquid to the gas/liquid interface. If the bubble is on a warm surface, there is an overall temperature gradient normal to the solid surface both in the liquid and at the gas/liquid interface. Since the surface tension of the liquid depends on temperature, a gradient of the latter engenders a gradient of the former; the mobile interface of the bubbles cannot sustain the shear stress and hence thermocapillary flow exists in the region around each bubble. This is the thermal version of the well-known Marangoni effect. [1,2] A few streamlines showing the upward flow near the bubble and circulation are provided. Since the flow is upward away from the heated surface in its vicinity the bubble pumps the liquid out from around it. A mobile tracer bubble shown on the right side of Fig. 1(*b*) is entrained in this flow. Of course in reality flow fields exist about both bubbles; they entrain each other.

This motion has been observed in electrolytic gas evolution and in model experiments. Sides and Tobias [3] observed lateral motion of oxygen bubbles on transparent tin oxide electrodes in electrolytic gas evolution; Sides and co-workers [4] formulated the thermocapillary pumping hypothesis and investigated the thermocapillary pumping mechanism theoretically and experimentally in a model system [5] where only viscous transport of momentum was allowed. Figure 2 is an example of their results. [5] Two bubbles adjacent to each other come together when the surface is warm and separate upon reversal of the temperature gradient. The mechanism of thermocapillary driven aggregation of two bubbles of sparingly soluble gas is well established where purely viscous flow is a good assumption.

The subject of the hypothesis of the present work is Fig. 1(*c*), the case where bubbles are produced by boiling into subcooled liquid. While superficially similar, in that both electrolysis and boiling result in growth of a much less dense phase within a more dense phase, the phenomena of electrolysis and boiling are quite different in many ways, such as in the origin of the less dense phase, the resulting size of the bubbles, and the speed of events. These differences make any new correlation between the two phenomena worthy of exploration. In fact the application of the concept of thermocapillary induced aggregation only applies to a subset of boiling phenomena, i.e., nucleate boiling into subcooled liquid. It is counterintuitive to apply thermocapillary flow concepts to boiling at all because in most cases the vapor liquid interface is an isotherm; it is only in the special case of nucleate boiling into subcooled liquid that the hypothesis has potential for being true.

The heated surface of Fig. 1(*c*) is above the boiling point, but the bulk liquid is subcooled. The liquid consists primarily of a pure compound such as water but also contains a sparingly soluble gas. The bubble of Fig. 1(*c*) in this case grows principally by vaporization but it extends into subcooled liquid. If a temperature gradient likewise exists (even if transiently) along their interfaces, the bubble on the left entrains a tracer bubble in its vicinity, as shown in Fig. 1(*c*).

The question is the extent to which this phenomenon might be apparent during boiling. Evidence both of thermocapillary flow and of boiling bubble motion driven by forces other than buoyancy exists in the literature. McGrew et al. [6] heated a suspension of small particles in n-butanol and other liquids. The particles traced the flow in the vicinity of bubbles that appeared during nucleate boiling of the test liquid. Their comments are worth quoting [6]:

''When boiling was established, we consistently observed a streamline type of flow and a rapid circulation of liquid around

Contributed by the Heat Transfer Division for publication in the JOURNAL OF HEAT TRANSFER. Manuscript received by the Heat Transfer Division October 10, 2001; revision received July 11, 2002. Associate Editor: C. Thomas Avedisian.

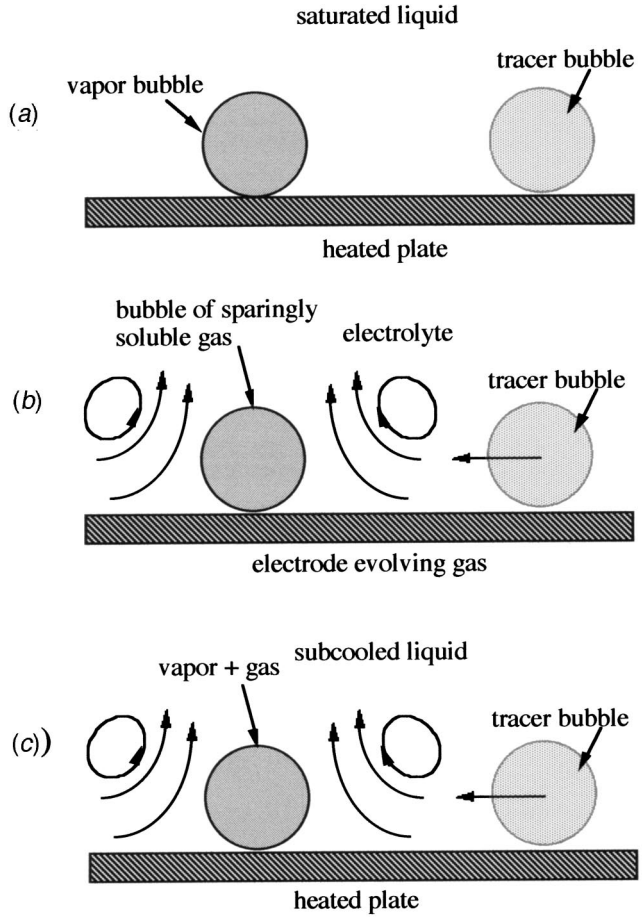

Fig. 1 (*a*) **A bubble in saturated boiling. The bubble is immersed entirely in superheated liquid. The fluid flow is due to the expanding interface because the vapor liquid interface is an isotherm. The tracer bubble does not move toward the other bubble.** (*b*) **A bubble of sparingly soluble electrolytically evolved gas near an electrode that is the source of the gas and is itself warm with respect to the electrolyte. The low thermal conductivity of the bubble relative to the thermal conductivity of the liquid supports a temperature gradient at the gas/liquid interface, which causes the liquid to flow away from the electrode and to entrain a tracer bubble.** (*c*) **A bubble being generated by vaporization at a heated surface, and consisting primarily of vapor with some amount of sparingly soluble gas immersed in subcooled liquid. Thermocapillary flow ensues because there is a temperature gradient along the surface of the bubble; as in** (*b*) **the temperature gradient engenders a surface tension gradient that pumps liquid in the vicinity of each bubble away from the heated surface. Adjacent bubbles entrain each other and consequently move toward each other.**

the bubbles. . . . The liquid moved along the heated surface toward the bubbles from all sides, and then traveled downward around the bubble periphery . . . .''

This was one of the earliest observations of thermocapillary flow during boiling. Elsewhere in this article, the authors record the following observation:

''Some of the bubbles could be observed moving along the heating surface, and a tendency for the bubbles to move toward each other was apparent.''

McGrew et al. [6] ascribed the aggregation to thermophoretic motion along the *horizontal* temperature gradients that exist because the low conductivity bubbles disturb the heat flux paths that would otherwise be normal to the heated surface. Ervin et al. [7] observed that bubbles moved on the surface of their heater and coalesced. They noted that they met at the warmest part of the heater, which echoes the lateral thermophoresis argument of McGrew et al. [6]. Qiu et al. [8] observed coalescence of bubbles grown side by side from prepared nucleation sites on silicon, but the aggregation of bubbles seemed to depend more on proximity and size than on directed motion toward each other.

The identification of thermocapillary flow in boiling of subcooled liquids led primarily to investigation of both its enhancement of heat transfer and its mechanism. Previously, the substantial improvement of heat transfer by boiling was ascribed to the agitation associated with bubble growth, coalescence, and departure, but investigators have turned their attention to the consequences of thermocapillary flow for heat transfer by boiling in subcooled liquids. Marek and Straub [9] describe this effect. Their vision of nucleate boiling into subcooled liquid in the presence of noncondensibles appears in Fig. 3. The heater superheats liquid adjacent to it. The liquid, bearing both a primary component and dissolved noncondensibles, vaporizes. The vapor condenses in the subcooled zone at the top of the bubble leaving behind the gas which accumulates. If the system is isobaric, equilibrium at the bubble interface sustains a negative temperature gradient along the bubble wall. The bubble can even collapse in some circumstances.

Recent reporting [10–12] on visual observation of growing bubbles during boiling has provided additional evidence both for the concerted motion of small bubbles to coalesce with large ones and for the aggregation of equal-sized bubbles, evidence that is strikingly similar to the observations of Sides and Tobias [3]. Kim et al. [10,11] flew a micromosaic heater in a reduced gravity environment and found that the large bubble that formed was ''fed by smaller satellite bubbles that surround it.''

Thus the phenomenon of thermocapillary driven aggregation of bubbles during boiling is plausible but it remains to examine whether it might be observable for the relatively large bubbles produced in that process. The circumstances are quite different since the small bubbles of electrolysis of aqueous solutions allowed assumption of flow dominated by low Reynolds number flow, while that assumption is clearly not appropriate for boiling. Second, it is not clear whether the possible thermocapillary flow velocities would be sufficient to generate an observable flow.

Estimation of Flow Rate Due to the Thermocapillary Mechanism

We perform a scaling analysis of the equations of motion including both diffusion and convection of momentum for the purpose of estimation of the strength of the flow and hence the potential lateral migration velocity of the bubble. Consider a vertical mobile interface in cartesian coordinates, as shown in Fig. 4; the direction along the interface is the z direction and the direction away from the interface is the x direction. For simplicity, the y direction is infinite. The length scale along the interface is taken as a. The characteristic velocity along the bubble surface is the thermophoretic velocity [13]

$$v_{zo}=\frac{d\gamma}{dT}\frac{\Delta T}{2\mu} \tag{1}$$

in which $d\gamma/dT$ is the variation of surface tension with temperature, ΔT is the temperature difference over the length scale a, and μ is the liquid viscosity. The z component of the steady equation of motion and the continuity equation appropriate for this case are

$$v_x\frac{\partial v_z}{\partial x}+v_z\frac{\partial v_z}{\partial z}=\nu\frac{\partial^2 v_z}{\partial x^2}+\nu\frac{\partial^2 v_z}{\partial z^2} \tag{2}$$

$$\frac{\partial v_z}{\partial z}+\frac{\partial v_x}{\partial x}=0 \tag{3}$$

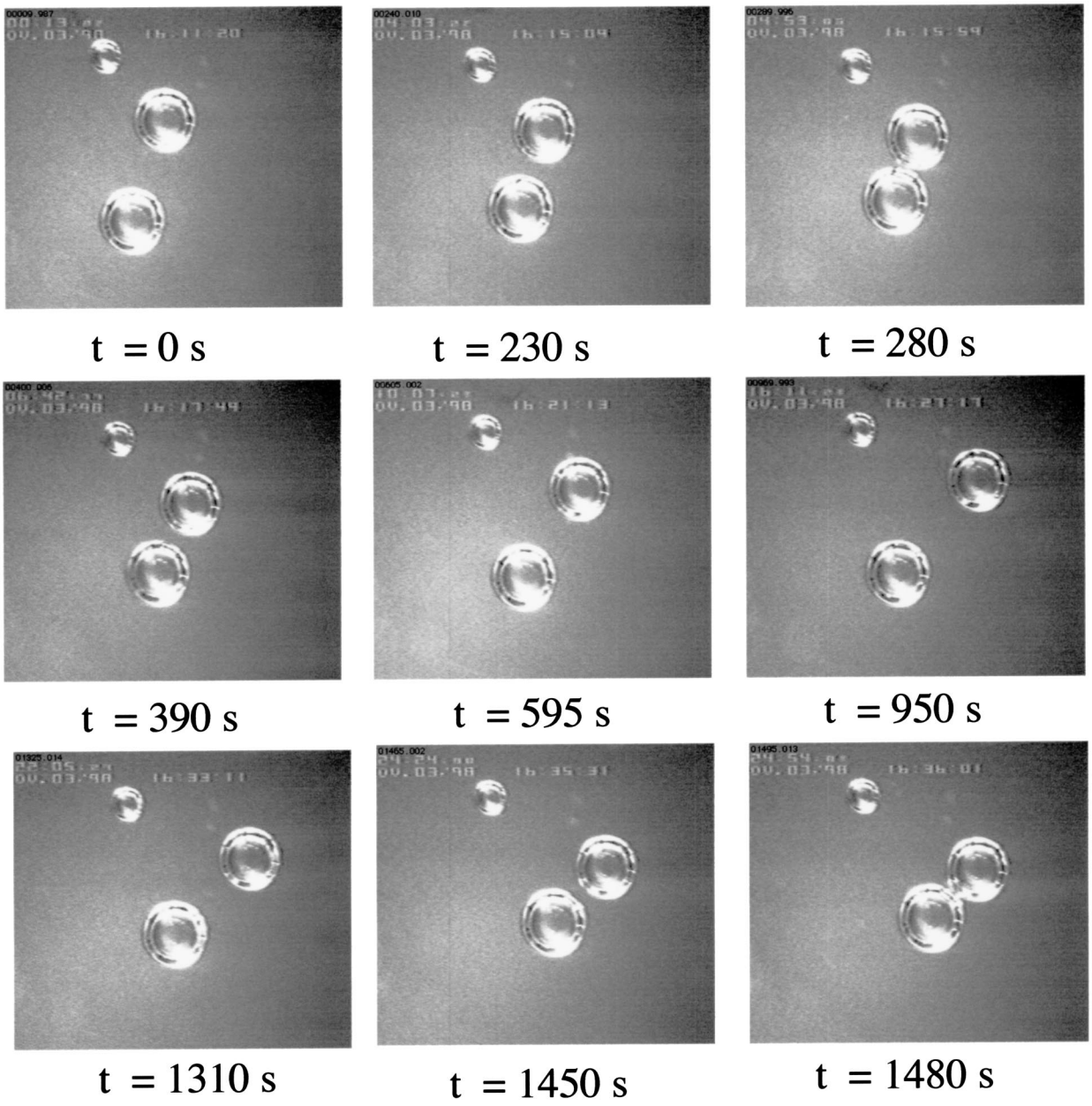

Fig. 2 Experimental observation of the thermocapillary pumping effect. Bubbles move together, apart, and back toward each other as the surface on which they rest is first heated, then cooled, then heated. Air in silicone oil. The bubbles are 1 mm in diameter. See Kasumi et al. [5] for details of the experiments and theory.

where v denotes velocity, x and z are cardinal directions, and υ is the kinematic viscosity. Unlike the analysis for electrolysis [4,5], the flow equation above includes convective terms.

The goal is to scale these equations appropriately and in the process deduce a characteristic velocity in the x direction. Defining x_o, v_{xo} as characteristic length and velocity normal to the interface, we substitute them into Eq. [2] along with a and v_{zo}.

$$\frac{v_{xo}v_{zo}}{x_o}\phi_x\frac{\partial\phi_z}{\partial\eta}+\frac{v_{zo}^2}{a}\phi_z\frac{\partial\phi_z}{\partial\zeta}=\nu\frac{v_{zo}}{x_o^2}\frac{\partial^2\phi_z}{\partial\eta^2}+\nu\frac{v_{zo}}{a^2}\frac{\partial^2\phi_z}{\partial\zeta^2} \quad (4)$$

where ϕ is velocity and $\eta=x/x_o$ and $\zeta=z/a$ are dimensionless distance in the x and z directions, respectively. Convection of momentum in the direction parallel to the interface is obviously an important term, so we scale it to $O(1)$ by dividing the equation through by the coefficient of the second term on the lhs, which gives

$$\frac{av_{xo}}{x_ov_{zo}}\phi_x\frac{\partial\phi_z}{\partial\eta}+\phi_z\frac{\partial\phi_z}{\partial\varsigma}=\frac{\nu a}{v_{zo}x_o^2}\frac{\partial^2\phi_z}{\partial\eta^2}+\frac{\nu}{v_{zo}a}\frac{\partial^2\phi_z}{\partial\zeta^2} \quad (5)$$

The thermocapillary flow at the interface is extended into the bulk fluid by diffusion of momentum, so the first term on the rhs is important. Scaling it to $O(1)$, one obtains a formula for a characteristic distance in the lateral direction, $x_o\equiv\sqrt{\nu a/v_{zo}}$. The coefficient of the second term on the rhs is $O(10^{-4})$ so diffusion of momentum in the z direction can be neglected. The reference velocities and distances are now inserted into the continuity equation.

$$\frac{v_{zo}}{a}\frac{\partial\phi_z}{\partial\varsigma}+\frac{v_{xo}}{\sqrt{\nu a/v_{zo}}}\frac{\partial\phi_x}{\partial\eta}=0 \quad (6)$$

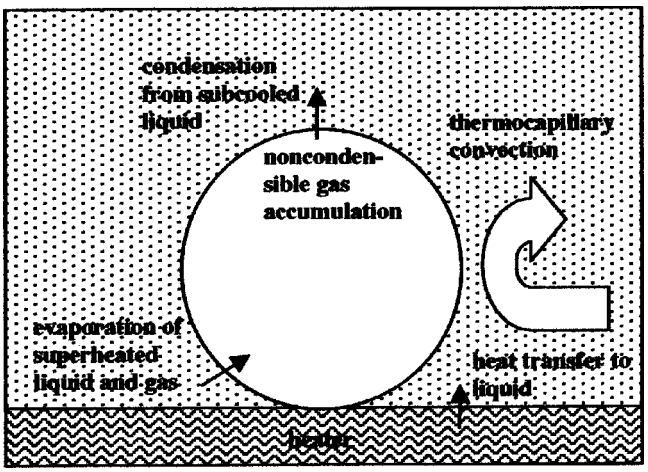

Fig. 3 Phenomena occurring during evolution of a bubble from an evaporating liquid containing dissolved noncondensible gases. Heat evaporates the liquid; dissolved gases also enter the vapor phase but accumulate at the top of the bubble as the vapor condenses. The accumulation of gas inside the bubble requires the temperature of the liquid at the top to decrease, which enhances the thermocapillary motion (After Marek and Straub [9]).

The terms balance if $v_{xo} \equiv \sqrt{\nu v_{zo}/a}$. Using (1), one obtains from this process an estimate of the lateral velocity to be expected for a given temperature difference over the distance a. Taking the distance a to represent the radius of the bubble and ΔT to represent the temperature difference between the base of the bubble and its apex, we obtain an estimate of the lateral velocity of the liquid, where ρ is its density.

$$v_{xo} = \sqrt{\frac{\nu}{a}\frac{d\gamma}{dT}\frac{\Delta T}{2\mu}} = \sqrt{\frac{\Delta T}{2a\rho}\frac{d\gamma}{dT}} \tag{7}$$

Equation (7) indicates that liquid flows toward the interface of Fig. 4, and similarly toward a single bubble of radius a, at a rate proportional to the square root of the temperature gradient in the direction of flow. The velocity is independent of viscosity because viscosity both produces and impedes the secondary flow toward the bubble.

The meaning of Eq. (7) is that two bubbles within a few radii of each other experience an attractive force due to the lateral flow along the heated surface. The bubbles aggregate in response to this force when at least one bubble of a pair is mobile. If both bubbles are mobile, they respond to each other's flow field and thus move toward a point between them. If both bubbles of a pair are attached to the surface, issues of the movement of contact lines come into play, which is beyond the scope of this analysis. This analysis also does not include any representation of the purely hydrodynamic hindrance of a detached bubble due to a nearby wall, but neither does it include a substantial increase of velocity due to intensification of thermal gradients between bubbles whose centers are less than 3 radii apart.

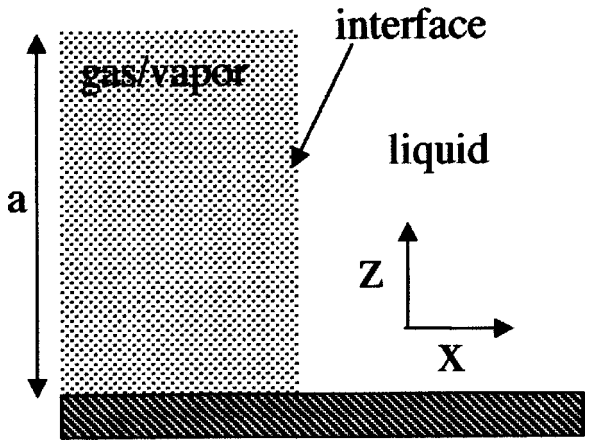

Fig. 4 A sketch of the simplified geometry for scaling analysis. The bubble is modeled as a block of vapor for use of Cartesian coordinates. The vertical length scale of the block corresponds to a bubble radius *a*.

The observability of motion due to thermocapillary pumping is given by the ratio of the time scale for bubble release divided by the time scale for motion of the bubble. Its meaning is that an observer can hope to record the lateral motion of bubbles due to the proposed thermocapillary mechanism before the bubble departs from the surface.

$$\text{observability} \equiv \frac{\tau_{\text{release}}}{\tau_{\text{motion}}} = \frac{\tau_{\text{release}} v_{xo}}{a} = \tau_{\text{release}} \sqrt{\frac{d\gamma}{dT}\frac{\Delta T}{2\rho a^3}} \tag{8}$$

As an example of the use of this equation, consider the results of Ibrahim and Judd [14] who boiled water on a copper surface and recorded a bubble growth time of 6 ms for bubbles that grew to 1.8 mm in radius in liquid subcooled by 10 K. Using $-1.8 \cdot 10^{-4}$ N/(m·K) as the derivative of surface tension for water near the boiling point [15], one calculates the observability to be 0.12, which means that thermocapillary motion was not obvious in their experiment performed in 1 g. The observability calculated above is not so far from unity that bubble motion due to mutual thermocapillary entrainment must always be negligible; instances where bubbles remain on surfaces, such as downward facing surfaces in earth gravity or any heated surface in microgravity, might reveal the effect.

Closure

The principal contributions of this note are the statement of a hypothesis concerning a possible thermocapillary pumping mechanism for lateral bubble motion on a heated surface during nucleate boiling, and the presentation of equations for estimating the strength of the effect. The phenomenon will be most evident in circumstances where bubbles are retained on surfaces, such as nucleate boiling from subcooled liquids in microgravity or on the underside of horizontal heaters.

Acknowledgment

This work was supported under the microgravity fluid physics program of NASA, Grant NAG3-2159

References

[1] Marangoni, C. G. M., 1871, "Ueber die Ausbreitung der tropfen einer flüssigkeit auf der oberfläche einer anderen," Poggendorf's Ann. d. Phys. u Chemie, **143**, p. 337.
[2] Sternling, C. V., and Scriven, L. E., 1959, "Interfacial Turbulence: Hydrodynamic Instability and the Marangoni Effect," AIChE J., **5**, p. 514.
[3] Sides, P. J., and Tobias, C. W., 1985, "A Close View of Gas Evolution From the Back Side of a Transparent Electrode," J. Electrochem. Soc., **132**, p. 583.
[4] Guelcher, S. A., Solomentsev, Y. E., Sides, P. J., and Anderson, J. L., 1998, "Thermocapillary Phenomena and Bubble Coalescence During Electrolytic Gas Evolution," J. Electrochem. Soc., **145**, p. 1848.
[5] Kasumi, H., Solomentsev, Y., Guelcher, S., and Anderson, J. L., 2000, "Bubble Aggregation due to Thermocapillary Flow," J. Colloid Interface Sci., **232**, p. 111.
[6] McGrew, J. L., Bamford, F., and Rehm, T., 1966, "Marangoni Flow: An Additional Mechanism in Boiling Heat Transfer," Science, **153**, p. 1106.
[7] Ervin, J., Merte, H., Keller, R., and Kirk, K., 1992, "Transient Pool Boiling in Microgravity," Int. J. Heat Mass Transf., **35**, p. 659.
[8] Qui, D., Dhir, V. K., Hasan, M., and Chao, D., 2000, "Single and Multiple Bubble Dynamics During Nucleate Boiling Under Low Gravity Conditions," *Proc. 34th National Heat Transfer Conf.*, ASME, New York, **1**, p. 865.
[9] Marek, R., and Straub, J., 2001, "The Origin of Thermocapillary Convection in Subcooled Nucleate Pool Boiling," Int. J. Heat Mass Transf., **44**, p. 619.

[10] Kim, J., Benton, J. F., and Wisniewski, D., 2002, "Poolboiling Heat Transfer on Small Heaters: Effect of Gravity and Subcooling," Intl. J. Heat and Mass Trans., **45**, p. 3919.
[11] Kim, J., and Benton, J. F., 2002, "Highly Subcooled Pool Boiling Heat Transfer at Various Gravity Levels," Intl. J. Heat and Fluid Flow, **23**, p. 497.
[12] Betz, J., and Straub, J., 2001, "Numerical and Experimental Study of the Heat Transfer and Fluid Flow by Thermocapillary Convection Around Gas Bubbles," Heat and Mass Transfer, **37**, p. 215.
[13] Young, O. N., Goldstein, J. S., and Block, M., 1959, "The Motion of Bubbles in a Vertical Temperature Gradient," J. Fluid Mech., **6**, p. 350.
[14] Ibrahim, E. A. and Judd, R. L., 1985, "An Experimental Investigation of the Effect of Subcooling on Bubble Growth and Waiting Time in Nucleate Boiling," ASME J. Heat Transfer, **107**, p. 168.
[15] *Handbook of Chemistry and Physics*, 1985, 66th edition, CRC Press, Boca Raton, FL, p. F32.

Vapor Phase Measurements in Subcooled Boiling Flow

S. Kang
Post-Doctoral Research Associate,
Department of Mechanical and Aerospace Engineering,
Arizona State University, Tempe, AZ 85287

R. P. Roy
Professor,
Fellow ASME,
Department of Mechanical and Aerospace Engineering,
Arizona State University, Tempe, AZ 85287

Measurements of vapor fraction and bubble axial velocity were carried out in subcooled boiling flow using a newly designed two-sensor fiber-optic probe. The sensors encountered the axial motion of the vapor bubbles essentially head-on. The new measurements were more repeatable and had less scatter in the outer low vapor fraction region of the boiling layer compared to our earlier measurements. [DOI: 10.1115/1.1517269]

Keywords: Boiling, Flow, Heat Transfer, Two-Phase

Introduction

In a recent paper, Roy et al. [1], we reported local measurements in the liquid and vapor phases of turbulent subcooled boiling flow. The vapor residence time fraction and vapor bubble time-mean axial velocity (taken to be the mean propagation velocity in the axial direction of the front interface of the bubble) were among the quantities measured at six different experimental conditions. A two-sensor fiberoptic probe (Photonetics) with 50 μm sensor tip size, Fig. 1(*a*), was used. However, the horizontal orientation of each sensor in a flow whose mean direction was vertical was deemed to have been a possible source of measurement error because of some ambiguity in the bubble piercing action of the sensor tip. To investigate this, we designed a new two-sensor fiberoptic probe which was then constructed by RBI Sarl, France. In this paper, we briefly describe the new probe and report its measurement of vapor fraction and bubble time-mean axial velocity.

Contributed by the Heat Transfer Division for publication in the JOURNAL OF HEAT TRANSFER. Manuscript received by the Heat Transfer Division March 13, 2002; revision received July 24, 2002. Associate Editor: D. B. R. Kenning.

The New Two-Sensor Fiber Optic Probe

Figure 1(*b*) shows this probe schematically. The orientation of the sensors is somewhat similar to the dual resistive probe sensors described by Herringe and Davis [2] and Revankar and Ishii [3]. The two fiberoptic sensors encounter the axial motion of the vapor bubbles essentially head-on, rendering the bubble piercing action more sharply defined. The optical fiber is of 200 μm diameter with 50 μm tip. Most of the bubbles in the flow being in the 0.4–1.5 mm diameter range (based on our earlier study), the sensor tip size is adequately small. A smaller tip size may be prefer-

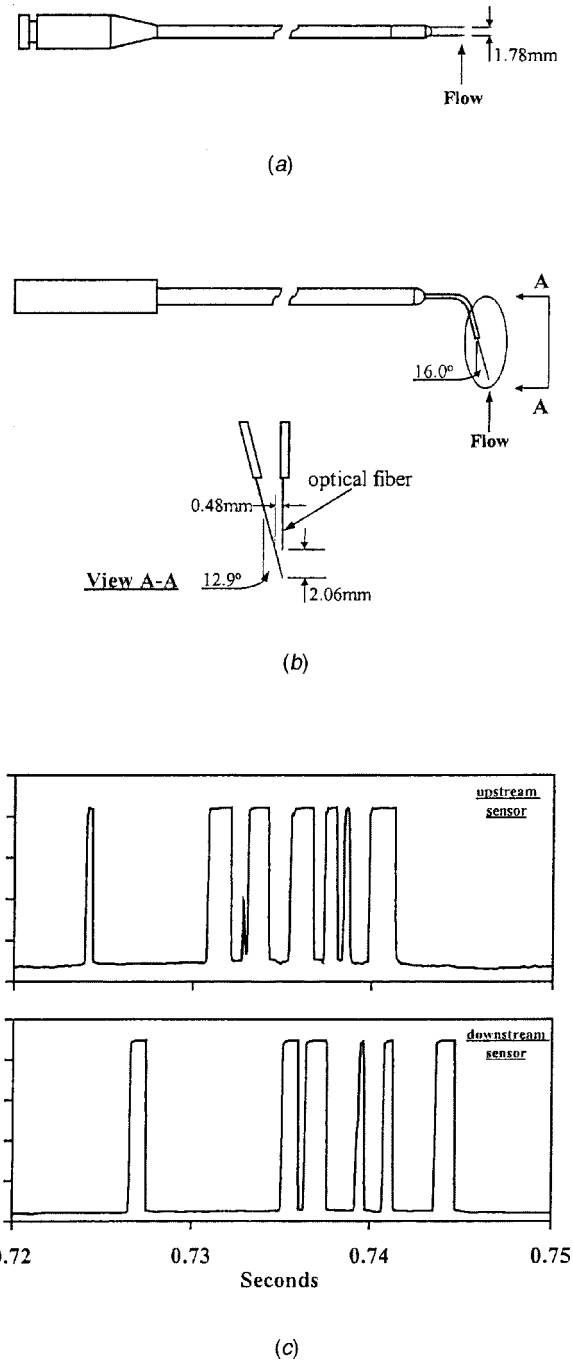

Fig. 1 The two-sensor fiber-optic probes: (*a*) earlier FOP probe; (*b*) new FOP probe; and (*c*) typical sensor outputs—new probe

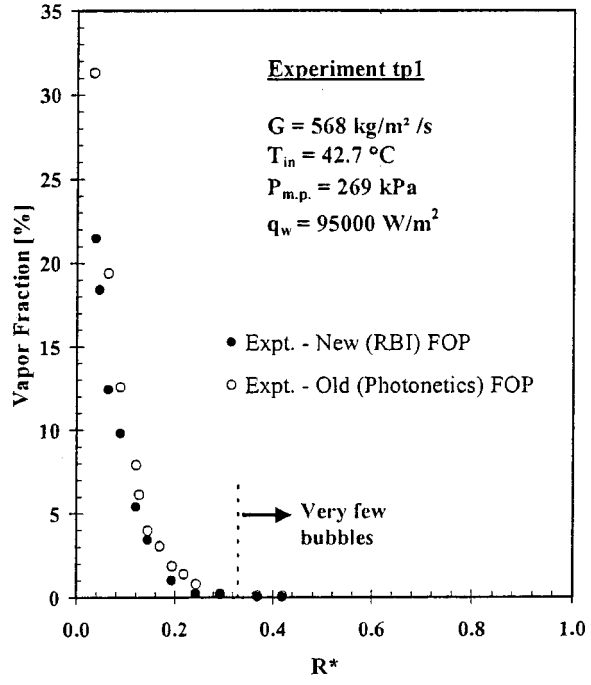

(*a*)

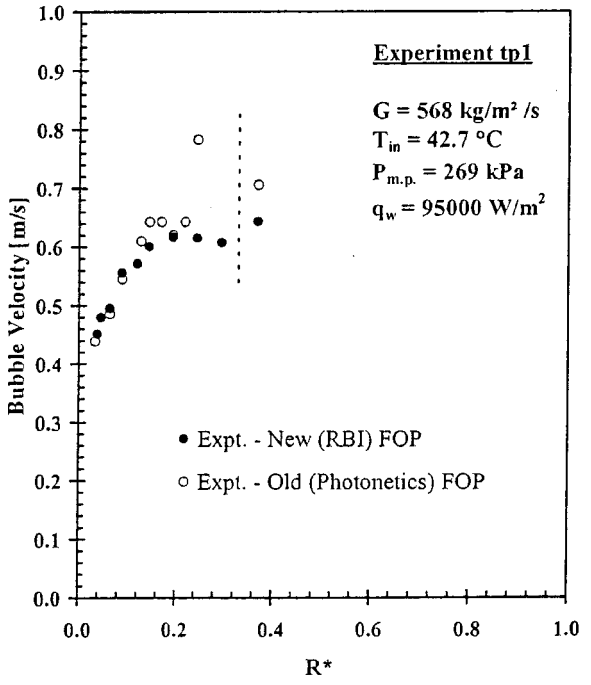

(*b*)

Fig. 2 Vapor fraction and time-mean bubble axial velocity distributions for experiment tp1

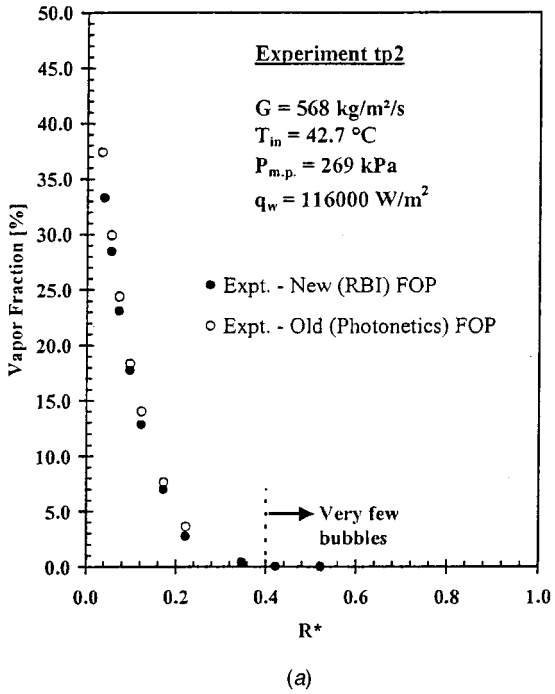

(*a*)

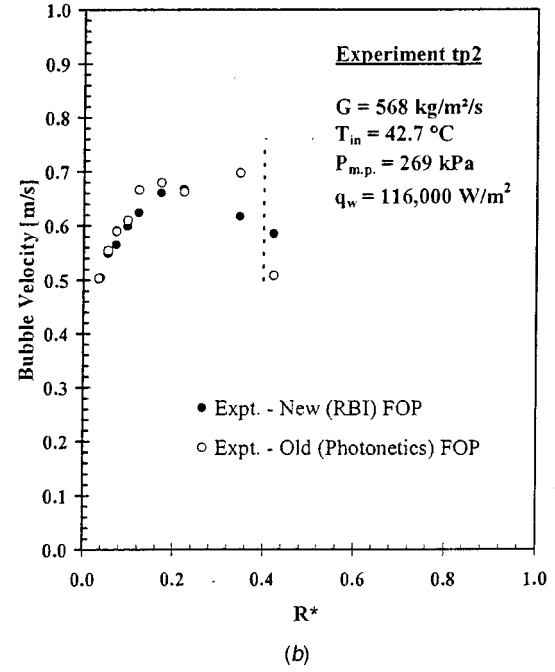

(*b*)

Fig. 3 Vapor fraction and time-mean bubble axial velocity distributions for experiment tp2

able but was decided against because of structural strength consideration. The probe was operated by a two-channel optoelectronic module (RBI Sarl).

Figure 1(*c*) shows typical outputs from the two sensors when in the bubbly flow boiling region. For each sensor signal, the sampling time interval was 50 μs and the record length 6 sec. A description of the signal analysis method for obtaining α_G and U_G can be found in [4]. The vapor fraction was based on the upstream sensor signal because the downstream sensor was likely to have been affected by the upstream sensor wake.

Results

The six experiments (tp1 through tp6) reported in [1] were repeated with the new probe. For brevity, we show the results of only three experiments (tp1, tp2, and tp5). Data from the other

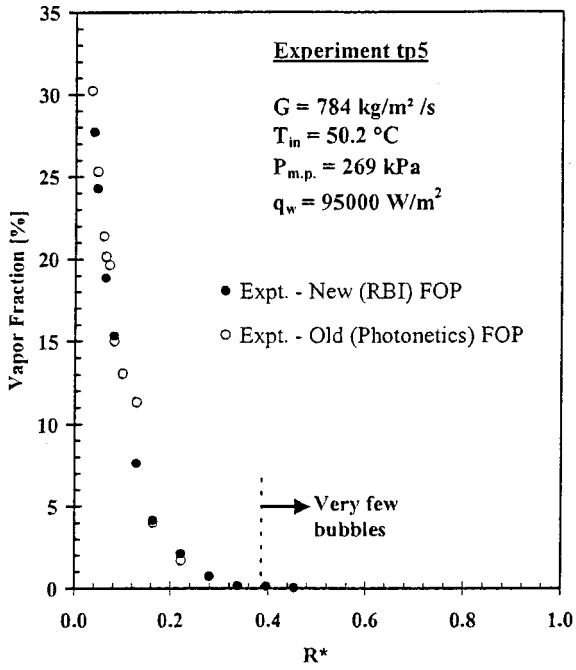

(a)

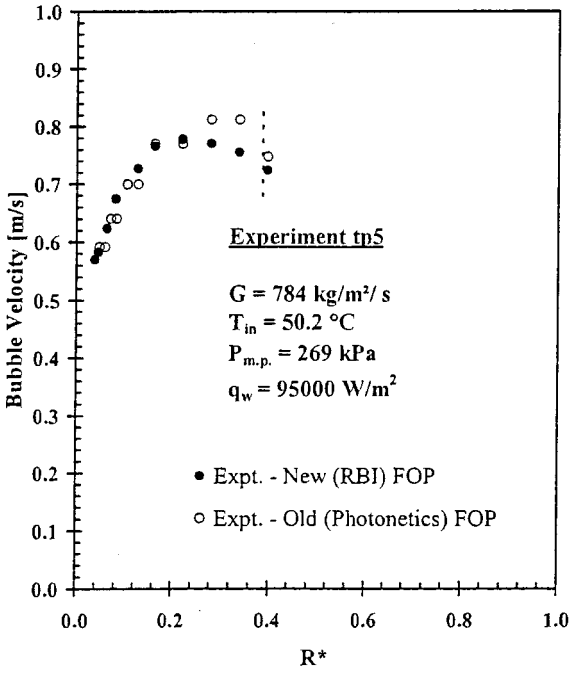

(b)

Fig. 4 Vapor fraction and time-mean bubble axial velocity distributions for experiment tp5

three experiments are of similar consistency. With the exception of the radially outermost bubble axial velocity, the measurement uncertainties are as follows:

$$\alpha_G \ \pm 1 \text{ percent } \alpha_G \text{ when } <15 \text{ percent}$$

$$\pm 2 \text{ percent } \alpha_G \text{ when } >15 \text{ percent}$$

$$U_G \ \pm 4 \text{ percent of value}$$

The uncertainty in bubble axial velocity at the outermost location was larger (±10% of value) mainly because very few bubbles were present. Furthermore, these bubbles were smaller in size and more susceptible to turbulent velocity fluctuations of the liquid phase than the larger bubbles.

Figures 2–4 show the results. The experimental conditions are given in the figures. Included in each figure are the new data and the earlier data [1]. The new α_G data are, in general, slightly lower—this trend was not influenced by uncertainty in locating the upstream sensor which was minimal, the sensor tip having been positioned accurately by two intersecting laser beams. The new U_G data were generally more repeatable and had noticeably less scatter in the low vapor fraction region ($R^*>0.2$) of the boiling layer. We note that the measurement location closest to the heated inner wall in the new experiments ($r-r_i=0.42$ mm) is slightly farther from the wall compared with the experiments reported in [1] ($r-r_i=0.37$ mm). This was in order to provide an additional safety margin for the sensor tips of the new probe when approaching the inner wall.

Numerical simulation results for α_G and U_G were presented in [1] and are not shown here.

Concluding Remarks

The altered orientation of the sensors in the new two-sensor fiberoptic probe yielded measurements of the bubble time-mean axial velocity that were more repeatable and with less scatter in the outer low vapor fraction region of the boiling layer compared to our earlier [1] measurements. In our opinion, this is because of the more sharply defined bubble piercing action of the sensor tips.

Acknowledgment

This work was partially funded by Electricité de France.

Nomenclature

D_h = channel hydraulic diameter, $=2(r_o-r_i)$
r = radial coordinate
r_i, r_o = dimensionless radius, $=(r-r_i)/(r_o-r_i)$
Re_{in} = Reynolds number at channel inlet, $=U_{b,in}D_h/\nu_L$
$U_{b,in}$ = time-mean bulk axial velocity of liquid at channel inlet
U_G = time-mean axial velocity of vapor bubble
z = axial coordinate
α_G = vapor residence time fraction
ν_L = liquid kinematic viscosity

References

[1] Roy, R. P., Kang, S., Zarate, J. A., and Laporta, A., 2002, "Turbulent Subcooled Boiling Flow—Experiments and Simulation," ASME J. Heat Transfer, **124**, pp. 73–93.
[2] Herringe, R. A., and Davis, M. R., 1976, "Structural Development of Gas-Liquid Mixture Flows," J. Fluid Mech., **73**(1), pp. 97–123.
[3] Revankar, S. T., and Ishii, M., 1992, "Local Interfacial Area Measurement in Bubbly Flow," Int. J. Heat Mass Transf., **35**(4), pp. 913–925.
[4] Roy, R. P., Velidandla, V., Kalra, S. P., and Peturaud, P., 1994, "Local Measurements in the Two-Phase Region of Turbulent Subcooled Boiling Flow," ASME J. Heat Transfer, **116**, pp. 660–669.

Numerical Study of Buoyant Plane Parallel Jets

Robert E. Spall
e-mail: spall@fluids.me.usu.edu
Department of Mechanical and Aerospace Engineering,
Utah State University, Logan, UT 84322-4130

A numerical study was performed to assess the influence of buoyancy on plane, parallel jets. Results indicate that, relative to isothermal jets, the location along the vertical symmetry plane at which the two jets merge (the merge point) decreases with increasing jet inlet temperature. This decrease is attributed to higher entrainment rates for the heated jet relative to the isothermal jet. It was also found that for sufficiently high values of the Archimedes number, the merge point becomes nearly independent of the initial jet spacing. [DOI: 10.1115/1.1501088]

Keywords: Heat Transfer, Jets, Mixed Convection.

Introduction

Single turbulent plane and offset wall jets are of great engineering importance, and consequently have been studied extensively [1–3]. Applications include burners and boilers, film-cooling of lining walls within gas turbine combustors, fuel-injection systems, and heating and air-conditioning systems. However, far fewer investigations into the behavior of multiple parallel jets appear in the literature. In addition to the applications mentioned above, the study of multiple jets may be particularly important in the design of pollutant exhaust stacks. Specifically, relative to a single exhaust stack, the close grouping of stacks to form parallel jets may be employed as a means to increase the exhaust plume trajectory and consequently decrease the impact of exhaust pollutants [4].

Flow patterns for two parallel plane jets have previously been reported in the literature [c.f. [5–11]]. The earliest studies were those of Tanaka [5,6] in which the basic flow patterns and entrainment mechanisms of parallel jets were described. In particular, Tanaka identified three relevant regions of the flowfield in the axial direction. The first may be termed the converging region, which begins at the nozzle exit and extends to the point where the inside shear layers of the jets merge (denoted the merge point). The merging of the jets is due to the asymmetric nature of the entrainment rates which results in a region of sub-atmospheric pressure between the jets. The jets are consequently deflected toward each other; at their merge point the velocity on the symmetry plane is equal to zero. The intermediate, or merge region is that existing between the merge point and the combine point, where the combine point is defined as that point along the symmetry plane at which the velocity is a maximum. Finally, the combined region is that downstream of the combine point where the two jets begin to resemble a self-similar single jet. The general characteristics of the flow field are illustrated in Fig. 1.

Anderson and Spall [11] recently presented experimental and numerical results for isothermal, plane parallel jets at spacings $S/d=9$, 13, and 18.25 (where S is the spacing between jet centerlines and d is the jet width). Values of the merge and combine points computed using both the standard $k-\varepsilon$ and a differential Reynolds stress model were compared with experimentally measured values. Good agreement between numerical and experimental results was obtained. Furthermore, no significant differences between the results of the two turbulence models was observed.

The author has found no published literature concerning the behavior of buoyant, plane parallel jets. However, experiments for free convection over two parallel heat sources were first carried out by Rouse et al. [12] in the early 1950s. They observed that the two plumes quickly merged so that the maximum velocities were located along the vertical symmetry plane. Subsequently, Pera and Gebhart [13] looked at both plane, parallel plumes and axisymmetric plumes, and observed that the plane, parallel plumes interacted more strongly than did the axisymmetric plumes at the same spacing. Gebhart et al. [14] further investigated the interaction of unequal plane plumes.

In the present work, the findings of Anderson and Spall [11], and the work of Rouse et al. [12] are extended by investigating numerically the evolution of buoyant, plane parallel jets.

Mathematical Model and Numerical Method

The governing equations consist of the incompressible Reynolds averaged momentum, continuity and energy equations, and equations for turbulence closure. The equations were solved using the pressure-based, structured-grid, finite-volume code Fluent (Version 4.4, Fluent, Inc., Lebanon, NH). The governing equations are well known, and hence for purposes of brevity are not listed. However, a brief description of the modeling assumptions regarding density variations and turbulence closure follow.

Density variations were taken into account using the Boussinesq approximation for which the density was treated as a constant value in all solved equations except for the buoyancy term in the momentum equations, which was treated as

$$(\rho-\rho_0)\overline{g}=-\rho_0\beta(T-T_0)\overline{g} \tag{1}$$

where ρ_0 and T_0 are the far field reference density and temperature respectively, β is the thermal expansion coefficient, and $\overline{g}$ is the gravity vector.

Results presented in Anderson and Spall [11] revealed little difference between the merge points obtained using $k-\varepsilon$ or differential Reynolds stress turbulence models. Consequently, for this study a $k-\varepsilon$ model was employed for turbulence closure. The transport equations solved for the turbulence kinetic energy k and dissipation rate ε in the present work are given as

$$\frac{\partial}{\partial t}(\rho k)+\frac{\partial}{\partial x_i}(\rho u_i k)=\frac{\partial}{\partial x_i}\left(\frac{\mu_t}{\sigma_k}\frac{\partial k}{\partial x_i}\right)+G_k+G_b-\rho\varepsilon \tag{2}$$

$$\frac{\partial}{\partial t}(\rho\varepsilon)+\frac{\partial}{\partial x_i}(\rho u_i\varepsilon)=\frac{\partial}{\partial x_i}\left(\frac{\mu_t}{\sigma_\varepsilon}\frac{\partial\varepsilon}{\partial x_i}\right)+C_{\varepsilon 1}\frac{\varepsilon}{k}(G_k+(1-C_{\varepsilon 3})G_b)-C_{\varepsilon 2}\rho\frac{\varepsilon^2}{k}. \tag{3}$$

The rate of production of turbulence kinetic energy, G_k, is defined as

$$G_k=\mu_t\left(\frac{\partial u_j}{\partial x_i}+\frac{\partial u_i}{\partial x_j}\right)\frac{\partial u_j}{\partial x_i} \tag{4}$$

and the generation of turbulence due to buoyancy, G_b, as

$$G_b=-g_i\frac{\mu_t}{\rho\sigma_h}\frac{\partial\rho}{\partial x_i}. \tag{5}$$

Contributed by the Heat Transfer Division for publication in the JOURNAL OF HEAT TRANSFER. Manuscript received by the Heat Transfer Division August 14, 2001; revision received June 6, 2002. Associate Editor: T. Y. Chu.

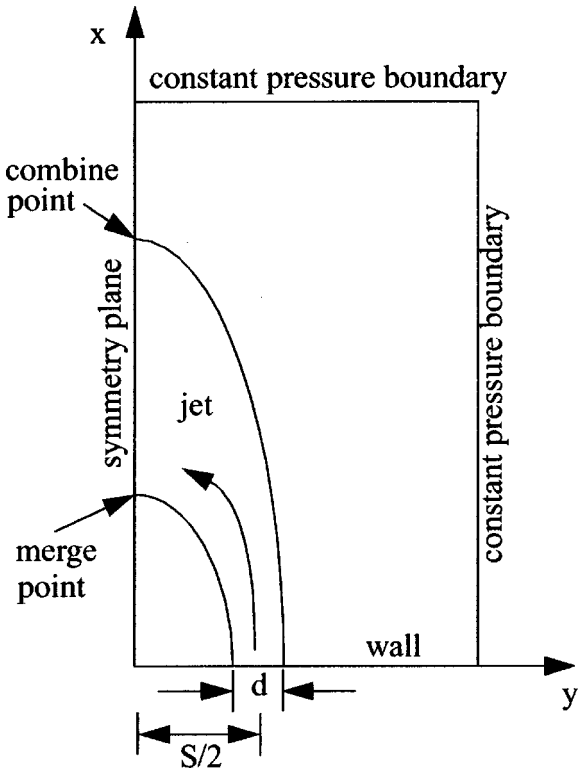

Fig. 1 Description of parallel jet geometry

The empirical constants in the model were taken as $C_{\varepsilon 1}=1.44$, $C_{\varepsilon 2}=1.92$, $C_{\varepsilon 3}=1.0$, $C_{\mu}=0.09$, $\sigma_k=1.0$, $\sigma_{\varepsilon}=1.3$, and $\sigma_h=0.85$. Note that σ_h is defined as $\mu_t C_p/k_t$ (where k_t is the effective thermal conductivity and C_p is the specific heat).

In terms of the solution procedure, interpolation to cell faces for the convection terms was performed using a bounded QUICK scheme [15]; second-order central differencing was used for viscous terms. Pressure-velocity coupling was based on the SIMPLEC procedure [16]. Solutions obtained using the segregated solver were considered converged when residuals for each of the equations (based on an L2 norm) were reduced by a minimum of four to five orders of magnitude. Additional iterations were then performed to confirm iterative convergence.

Geometry and Boundary Conditions

The computational domain is identical in size to that employed in Anderson and Spall [11], defined by a rectangular region discretized using a Cartesian grid covering one half of the flow field. A symmetry boundary condition was defined along the $y=0$ plane, whereas constant pressure boundary conditions were specified on the $y=y_{\max}$ and $x=x_{\max}$ planes (see Fig. 1). The domain was bounded on the $x=0$ plane by an adiabatic wall along which nonequilibrium wall functions were specified. An opening of width d in the wall defined the location of the jet inlet over which a uniform velocity profile was set. The inlet was centered at $y/d=4.5$, 6.5, or 9.125, providing the three jet spacings studied herein. Depending upon the S/d ratio, $x_{\max}$ ranged from $100d$ to $120d$; whereas $y_{\max}$ ranged from $20d$ to $30d$. (Note that numerical tests for several cases performed by further increasing the extent of the domain in each direction by 50 percent did not produce in any significant changes in the results.)

The relevant Reynolds number for the problem was defined as $\mathrm{Re}=(\rho V d)/\mu$ (where ρ is the density, V the inlet velocity, and μ is the dynamic viscosity). Air was employed as the working fluid, and the variables defining the Reynolds number were chosen such that Re=75,000. (We note that experimental data from previous isothermal studies indicates that the location of the merge and combine points are nearly independent of the Reynolds number.)

The turbulence intensities at the inlet were set to 5 percent, from which the turbulence kinetic energy distribution was obtained. The dissipation rate inlet boundary condition was derived from the relationship $C_{\mu}k^{1.5}/L$ where the turbulence length scale L was taken as $0.07d$.

Three different grid resolutions were employed for each S/d spacing. For the cases defined by $S/d=9$ and 13, grids consisting of 71×152, 140×300 and 278×597 cells were used, whereas for the case $S/d=18.25$ the three grids contained 91×152, 180×300, and 358×597 cells. Across the jet inlet, the coarse, medium, and fine grids contained 10, 20, and 40 cells, respectively. In all cases, cells were clustered toward the $(y=0)$ symmetry plane and the $(x=0)$ wall.

The importance of buoyancy in mixed convection flows is indicated by the ratio of the Grashof number to the square of the Reynolds number as $(\Delta\rho g d)/(\rho V^2)$. In general, when this ratio approaches unity, one may expect strong contributions from buoyancy. This ratio is also referred to as the Archimedes number (Ar), and when the density variation is accounted for by the Boussinesq approximation may be expressed as

$$\mathrm{Ar}=(\beta g d\Delta T)/V^2. \tag{6}$$

where $\Delta T=T_{\mathrm{inlet}}-T_0$. (Note that fluid at temperature T_0 may be entrained across the $x=x_{\max}$ and $y=y_{\max}$ constant pressure boundaries.) Parameters were set to provide values of Ar=0, 1/16, 1/8, 1/4, and 1/2. The maximum value of ΔT was limited to $\sim$15°C so that the assumption of small temperature variations inherent in the Boussinesq approximation would not be violated.

Results

Shown in Fig. 2 are contour plots of velocity magnitude which display the jet trajectory for cases defined by Ar=0 (left side) and Ar=1/2 (right side), at jet spacing $S/d=13$. Contours range from

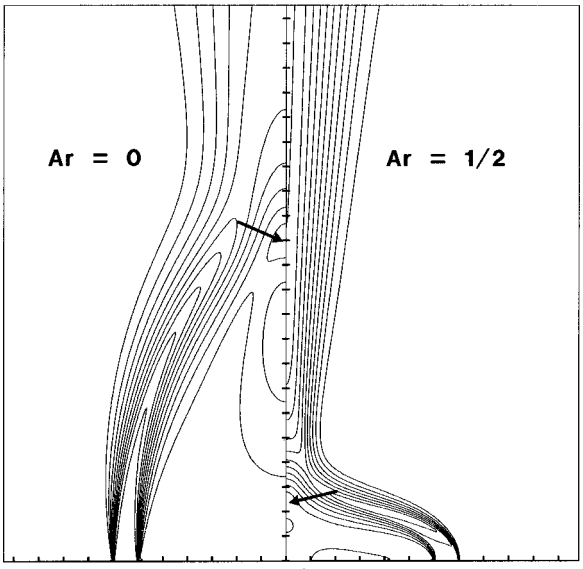

Fig. 2 Contour plot of constant velocity magnitude for values of Ar=0 (left side) and Ar=1/2 (right side) at a jet spacing of $S/d=13$. Contour intervals for the Ar=0 case range from 0.1 to 1.0 in intervals of 0.1. Contours for the Ar=1/2 case range from 0.2 to 2.2 in intervals of 0.2.

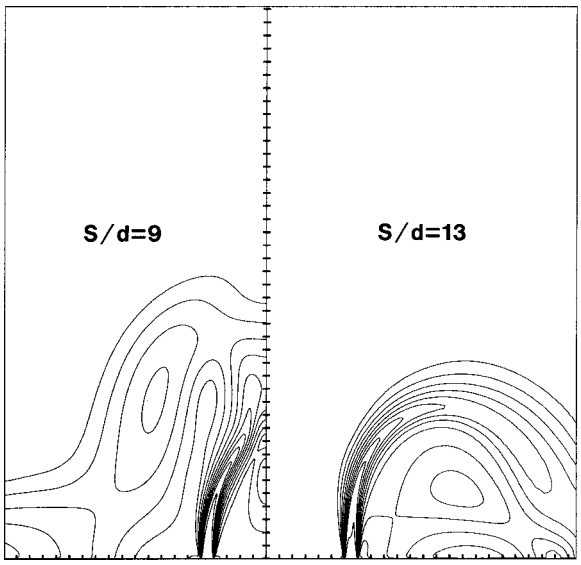

Fig. 3 Contour plot of constant velocity magnitude for cooled jet with Ar=1/64 at jet spacings $S/d=9$ (left side) and $S/d=13$ (right side). Contours range from 0.1 to 1.0 in intervals of 0.1.

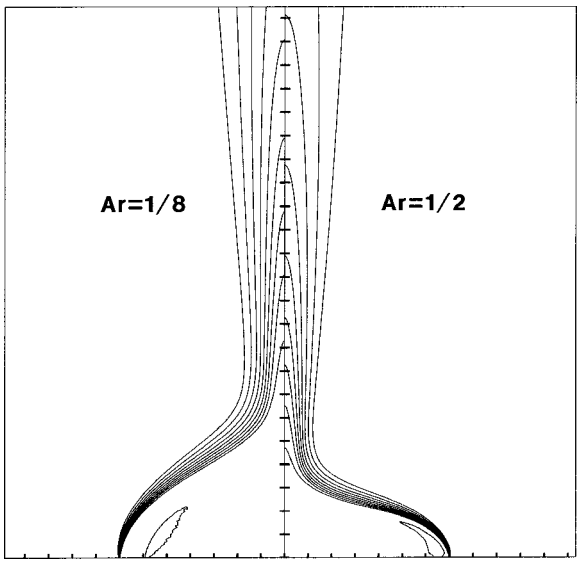

Fig. 4 Contours of constant dimensionless temperature $((T-T_0)/(T_{inlet}-T_0))$ for Ar=1/8 (left side) and Ar=1/2 (right side) at a jet spacing of $S/d=13$. Contour levels range from 0.1 to 1.0 in intervals of 0.1.

0.1 to 1.0 in intervals of 0.1 for the Ar=0 case, and from 0.2 to 2.2 in intervals of 0.2 for the Ar=1/2 case. (Note that only the region in the vicinity of the jet inlets is shown, not the entire computational domain.) For this and all subsequent contour plots, tic marks on the ordinate and abscissa appear in increments of $1d$. The merge points, the location of which are defined by a stagnation point along the axis, are identified on each side of the figure by the arrows. Consequently, the regions below the merge point constitute recirculation zones. Whereas the maximum velocity for the case Ar=0 occurs at the jet inlet, the maximum velocity occurring for the case Ar=1/2 is $2.28V$, and occurs downstream of the merge point. Examination of the contours for the case Ar=1/2 reveal that the jet velocity increases as the fluid leaves the inlet. This leads to greater local entrainment rates, and as a result (and perhaps contrary to intuition) the location of the merge point decreases relative to the isothermal case by a factor of approximately 5.5. The results also show that the width of the isothermal jet downstream of the merge points is larger than that of the heated jet. For instance, at $x/d=20$ (near the top of the figure) the width of the isothermal jet is approximately 50 percent greater than that of the heated jet. For purposes of brevity, results for other cases defined by $S/d=9$ and 18.25, and at intermediate values of the Archimedes number, are not shown. However, the trends inherent in those results are consistent with the results shown in Fig. 2.

Shown in Fig. 3 are contours of constant velocity magnitude for the case of a cooled jet at spacings $S/d=9$ (left side) and $S/d=13$ (right side). If ΔT is redefined as T_0-T_{inlet}, the Archimedes number for these results is then 1/64. For the spacing $S/d=13$, the resulting flow pattern is considerably different than for the isothermal and heated jets. The jet trajectory is away from the symmetry plane and no merging of the parallel jets takes place. Consequently merge and combine points are not defined. The direction of the flow here is dictated by continuity—the fluid within the cooler jet is denser than the surrounding fluid, and hence has a tendency to drop. Continuity dictates that the drop be directed away from the symmetry plane. However, for the case $S/d=9$ the forces drawing the cooled jets together (due to asymmetric entrainment) are sufficiently larger than the buoyancy force such that the jets still merge, with the merge point occurring at $x/d=9.23$. Nevertheless, slightly downstream from the merge point the jet trajectory is directed away from the symmetry plane as the vertical momentum is eventually diminished due to the influence of buoyancy. An additional cooled jet calculation for the $S/d=9$ spacing at Ar=1/16 revealed that the jets did not merge, but behaved in a manner similar to the $S/d=13$ results shown in Fig. 3.

Contours of constant dimensionless temperature $((T-T_0)/(T_{inlet}-T_0))$ are shown in Fig. 4 at a jet spacing of $S/d=13$ for Ar=1/8 (left side) and Ar=1/2 (right side). The temperature contours provide information that is qualitatively similar to velocity contours. The figure clearly reveals that the jets merge at lower values of x/d for the Ar=1/2 case than for the Ar=1/8 case. In addition, it is clear that the temperature distribution within the recirculation zone is essentially constant, a result of the adiabatic wall condition.

Shown in Fig. 5 is a line plot of the merge point (x/d) as a function of Archimedes number for the three jet spacings defined by $S/d=9$, 13, and 18.25. This figure serves to summarize the trends inherent as the Archimedes number is increased from the isothermal (Ar=0) cases. The results indicate a dramatic decrease

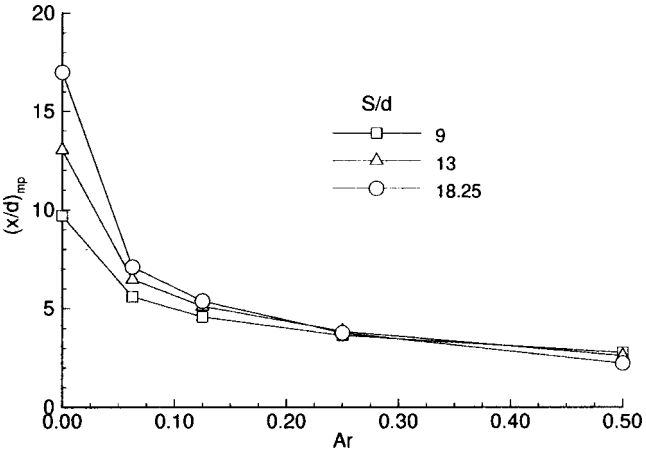

Fig. 5 Location of merge point as a function of Ar for jet spacings $S/d=9$, 13, and 18.25

in distance to the merge point (and consequently, the size of the recirculation zone) as the Archimedes number is increased only modestly from zero. In addition, the results indicate that for Ar $\geqslant 1/4$, the location of the merge point becomes nearly independent of the jet spacing, S/d.

Results shown in Fig. 5 were computed on the finest grids. Locations of the merge points computed on the intermediate and coarse level grids ranged from 1 percent to 6 percent lower than those computed on the fine grids. Several cases were then computed by doubling the grid resolution of the finest grid in the streamwise direction, and revealed essentially no change in the merge point. Consequently, for the purposes of the present study the fine grid calculations were thus considered to be adequately resolved.

Conclusions

The results reveal that the trajectory of plane parallel jets is strongly influenced by what may be considered as moderate levels of the ratio of buoyancy to inertial forces. This conclusion has implications in areas such as the ganging of smoke stacks, in which the close grouping of stacks may be utilized to combine non-manifolded exhausts into a single jet. The results also indicate that cooled jets are not prone to merging unless the Archimedes number is quite small. Although this is not likely to present itself as an application in the ganging of smoke stacks, it may be of significance in other engineering applications. The author plans to consider in future work the fully three-dimensional interaction between arrays of both isothermal and buoyant round jets.

References

[1] Thomas, F. O., 1991, ''Structure of Mixing Layers and Jets,'' Appl. Mech. Rev., **44**(3), pp. 119–153.

[2] Everitt, K. W., and Robins, A. G., 1978, ''The Development and Structure of Turbulent Plane Jets,'' J. Fluid Mech., **88**, pp. 563–568.

[3] Gutmark, E., and Wygnanski, I., 1976, ''The Planar Turbulent Jet,'' J. Fluid Mech., **73**, pp. 465–495.

[4] *ASHRAE Handbook of Fundamentals*, 1997, American Society of Heating, Refrigerating and Air Conditioning Engineers, Atlanta, GA, pp. 15–10.

[5] Tanaka, E., 1970, ''The Interference of Two-Dimensional Parallel Jets (1st report, Experiments on Dual Jet),'' Bull. JSME, **13**(56), pp. 272–280.

[6] Tanaka, E., 1974, ''The Interference of Two-Dimensional Parallel Jets (2nd Report, Experiments on the Combined Flow of Dual Jet),'' Bull. JSME, **17**(109), July, pp. 920–927.

[7] Elbanna, H., Gahin, S., and Rashed, M. I. I., 1983, ''Investigation of Two Plane Parallel Jets,'' AIAA J., **21**(7), pp. 986–990.

[8] Lin, Y. F., and Sheu, M. J., 1990, ''Investigation of Two Plane Parallel Unventilated Jets,'' Exp. Fluids, **10**, pp. 17–22.

[9] Lin, Y. F., and Sheu, M. J., 1991, ''Interaction of Parallel Turbulent Plane Jets,'' AIAA J., **29**, pp. 1372–1373.

[10] Nasr, A., and Lai, J. C. S., 1997, ''Comparison of Flow Characteristics in the Near Field of Two Parallel Plane Jets and an Offset Plane Jet,'' Phys. Fluids, **9**(10), Oct. pp. 2919–2931.

[11] Anderson, E. A., and Spall, R. E., 2001, ''Experimental and Numerical Investigation of Two-Dimensional Parallel Jets,'' ASME J. Fluids Eng., **123**, pp. 401–406.

[12] Rouse, H., Baines, W. D., and Humphreys, H. W., 1953, ''Free Convection Over Parallel Sources of Heat,'' Proc. Phys. Soc. London, Sect. B, **66**, pp. 393–399.

[13] Pera, L., and Gebhart, B., 1975, ''Laminar Plume Interactions,'' J. Fluid Mech., **68**, pp. 259–271.

[14] Gebhart, B., Shaukatulla, H., and Pera, L., 1976, ''The Interaction of Unequal Laminar Plane Plumes,'' Int. J. Heat Mass Transf., **19**, pp. 751–756.

[15] Leonard, B. P., 1979, ''A Stable and Accurate Convective Modeling Procedure Based on Quadratic Upstream Interpolation,'' Comput. Methods Appl. Mech. Eng., **19**, pp. 59–98.

[16] Ferziger, J. H., and Peric, M., 1999, *Computational Methods for Fluid Dynamics*, 2nd edition, New York, Springer-Verlag.

Numerical Solution for Transient Conjugate Two-Phase Heat Transfer With Heat Generation in the Pipe Wall

Yuri V. Fairuzov
Professor
Mem. ASME
e-mail: fairuzov@servidor.unam.mx

Hector Arvizu
Graduate Student,
Assoc. Mem. ASME

Institute of Engineering, P.O. Box 70-472, National Autonomous University of Mexico, Mexico City 04510, Mexico

A method developed earlier for modeling conjugate two-phase heat transfer in flashing flows was used to obtain a numerical solution for transient boiling flow in heated pipes or channels. Two criteria of applicability of the solution obtained were proposed and numerically tested using a more rigorous model, which accounts for the effects of heat conduction with heat generation in the wall and forced convective boiling. The solution obtained provides a simple and reliable alternative to more rigorous methods for modeling transient two-phase flow in heated channels when the material of the wall bounding the flow has a high thermal conductivity and the wall superheat is small.

[DOI: 10.1115/1.1470170]

Keywords: Boiling, Conjugate, Heat Transfer, Transient, Two-Phase

Introduction

Many existing and emerging multiphase technologies require simple and reliable methods for predicting transient conjugate two-phase heat transfer. In the petroleum industry, for instance, electrical heating is being currently considered as one of the effective methods to prevent wax and hydrate formation in subsea multiphase flowlines during very low production rates [1]. Several types of heating systems have been proposed: direct heating, induction heating and heat tracing [2]. Modeling of transient multiphase flow and heat transfer is an important stage in designing such systems. Problems involving conjugate two-phase heat-transfer also arise in the analysis of instabilities in two-phase systems [3]. Flow instabilities in heated channels are undesirable, because they can cause mechanical vibrations of components, oscillatory wall temperatures and induce boiling crisis (dryout). The analysis performed to predict the threshold of flow instability, in particular the analysis of dynamic instability, requires a correct description of the thermal interaction between the boiling flow and the heated wall.

A review of the existing techniques for predicting conjugate two-phase heat transfer is presented in a previous article [4] and shows that a rigorous approach to the problem requires numerical modeling of heat conduction within the wall and calculating the heat-transfer coefficient for convective flow boiling. Heated chan-

Contributed by the Heat Transfer Division for publication in the JOURNAL OF HEAT TRANSFER. Manuscript received by the Heat Transfer Division June 5, 2001; revision received December 18, 2001. Associate Editor: T. Y. Chu.

nels are usually made of steel or some other metal. When the heat generation rate is low, the transverse temperature gradient in the wall is small because of a high thermal conductivity of metals. Such situations cause difficulties in the numerical analysis of unsteady heat conduction inside the wall. Temperature differences between grid points of the numerical model of heat conduction in the pipe wall are so small that the problem becomes sensitive to round-off errors. Under these circumstances, it is very difficult to achieve the heat balance at the wall-fluid interface. It is important to note that in most such cases the problem considered yet should be treated as a conjugate heat transfer problem since the wall thermal capacity effect cannot be neglected.

In the present paper, a method proposed in the previous work [5] for modeling of conjugate heat transfer in flashing flows is used to obtain a simplified numerical solution for transient boiling flow in heated pipes or channels. The solution obtained is verified using a more rigorous model, in which the effects of the wall superheat and heat conduction with heat generation, are taken into account. Criteria of applicability of the simplified solution are proposed.

Problem Formulation

The problem to be considered in this study is shown schematically in Fig. 1. A two-phase gas-liquid mixture flows through a pipe of internal diameter D and length L. The thickness of the pipe wall is δ. Initially, the system comprising the flowing fluid and the pipe wall is at steady state. At $t=0$, an electrical current is passed through the pipe to provide heating of the wall. The heat generation rate within the wall is uniform over the whole length of the pipe. The problem is to predict the response of the system to heat input to the pipe wall.

The following assumptions are made in the derivation of governing equations:

1 The fluid flow is one-dimensional.

2 The phases are in thermal equilibrium. In slow transients, the effect of thermal non-equilibrium is negligible, because there is sufficient time for thermal equilibrium to be achieved.

3 The two-phase flow is homogeneous ($V_l=V_g$). This assumption is made here just to simplify the derivation of the combined energy equation. If the slip phenomenon is important, the proposed approach can be readily applied to other two-phase flow model formulations, for example, the drift-flux or two-fluid models.

4 The fluid and the pipe wall are in local thermal equilibrium. This assumption is applicable when the overall temperature drop in the transverse direction, the sum of temperature differences across the wall and the fluid flow, is negligible

$$\Delta T=\Delta T_w+\Delta T_f \ll \Delta T_{\mathrm{sys}} \tag{1}$$

where ΔT_{sys} is the temperature variation experienced by the fluid in the system (the difference between fluid temperatures at the pipeline inlet and outlet).

The temperature difference across the pipe wall is small when internal heat generation and changes of conditions at the wall-fluid interface do not produce large temperature gradients within the pipe wall. The maximum temperature rise induced by the internal heat sources can be estimated using solutions obtained for one-dimensional steady conduction with heat generation. For boundary conditions in which temperature is specified at the wall-fluid interface and the external pipe surface is insulated, the maximum-source-induced temperature rise can be calculated using the following relationships.

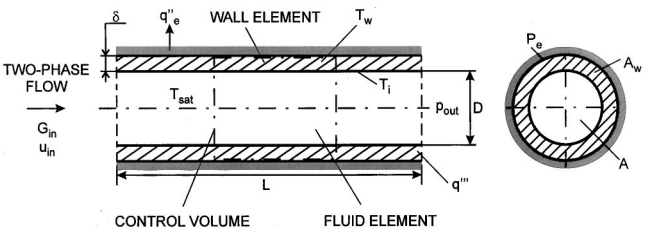

Fig. 1 Two-phase conjugate heat transfer with heat generation in the wall

Thin Wall

$$\Delta T_w=\frac{q'''\delta^2}{2k} \tag{2}$$

•Thick Wall

$$\Delta T_w=\frac{q'''r_e^2}{4k}\left\{\frac{r_i^2}{r_e^2}+2\ln\frac{r_e}{r_i}-1\right\} \tag{3}$$

Changes of the local conditions at the wall-fluid interface also may produce large temperature gradients within the wall. This occurs when the characteristic time of temperature or heat flux variation at the wall-fluid interface is much smaller than the time during which temperature perturbations reach the external wall surface (the transition time $t_{c,w}\sim\delta^2/\alpha_w$ [6]). In such a case, the transient temperature behavior is similar to that observed in the early stage of unsteady conduction in a body (the ''early'' regime [6]), and therefore the wall temperature is a function of both time and space. In slow fluid transients the characteristic time of local fluid temperature variation greatly exceeds the transition time. Therefore, the temperature gradients inside the wall decay rapidly and the instantaneous temperature has practically the same value throughout the wall (the ''late'' regime [6]). This condition is fulfilled when the characteristic time of the process during which the fluid flow parameters vary significantly (the time required to reach a new steady state in the system) is much greater than the transition time

$$t_{c,f}\gg t_{c,w}\sim\frac{\delta^2}{\alpha_w} \tag{4}$$

The characteristic time of the fluid transient, $t_{c,f}$, depends on many factors (geometry, operating conditions, fluid properties, etc.) In most practical cases the fluid particle residence time in the pipeline can be used to estimate the characteristic time of the fluid transient.

The difference between the local wall temperature and the local fluid temperature (the wall superheat) can be estimated using the following relationship:

$$\Delta T_f=\frac{q_i''}{h} \tag{5}$$

The heat flux in Eq. (5) can be obtained based on the known volumetric heat generation rate. However in some cases the amount of heat transferred to the fluid may be greater than the amount of heat generated in the wall. Therefore an additional verification of applicability of assumption 4 should be done after performing numerical simulations. This will be discussed in more detail in the next section.

5 The heat conduction in axial direction in the wall is negligible. In long pipes, the heat-transfer area in axial direction is much smaller than that in radial direction. Therefore, the effect of axial heat conduction inside the wall is negligible.

Under these assumptions, the governing equations can be written in the following form.

Continuity Equation

$$\frac{\partial\rho}{\partial t}+\frac{\partial}{\partial x}(\rho V)=0 \tag{6}$$

Momentum Equation

$$\frac{\partial V}{\partial t}+V\frac{\partial V}{\partial x}=-\frac{1}{\rho}\frac{\partial p}{\partial x}-KV|V| \tag{7}$$

Energy equation for the control volume comprising a wall element and a fluid element [5] Fig. 1:

$$\frac{\partial(\rho u)}{\partial t}+Fa\frac{\partial p}{\partial t}+\frac{\partial}{\partial x}(\rho uV)+p\frac{\partial V}{\partial x}=q \tag{8}$$

where

$$Fa=\frac{\rho_w c_w T v_{fg} A_w}{h_{fg} A} \tag{9}$$

The source term q in Eq. (8), the rate of heat transfer to the control volume per unit fluid volume, describes two effects: the heat input to the system due to heat generation in the pipe wall and the heat transfer of the system with the surroundings. This term can be expressed in the following form

$$q=q'''\frac{A_w}{A}+q_e''\frac{P_e}{A} \tag{10}$$

State Equation

$$\rho=\rho(p,u) \tag{11}$$

The initial condition is

$$\text{at}\quad t=0:$$

$$\rho,u,V=\text{known}\quad f(x) \tag{12}$$

The boundary conditions are $(t>0)$

$$\text{Inlet}\quad (x=0):$$

$$G=G_{\text{in}}$$
$$u=u_{\text{in}} \tag{13}$$

$$\text{Outlet}\quad (x=L):$$

$$p=p_{\text{out}} \tag{14}$$

The pipeline is assumed to be thermally insulated from the surroundings, hence, $q_e''=0$.

The set of equations (1), (2), and (8) was solved numerically using a semi-implicit finite-difference method. A detailed description of the method is given in [4]. A systematic mesh convergence testing was performed in order to achieve the required numerical accuracy. A uniform mesh comprising 100 cells has been found to be adequate to keep the relative discretization errors under 1 percent in all numerical simulations presented in this paper. The time step was 0.4 s.

Results and Discussion

Transient heating of a long pipeline carrying a two-phase hydrocarbon mixture was modeled. The pipeline geometry, the operating condition and the properties of the wall material are shown in Table 1.

Table 1 Pipeline geometry and operating conditions

Internal diameter, D	0.1317 m
Length, L	5,000 m
Wall thickness, δ	0.0182 m (δ/D=0.14)
Roughness of the pipe wall	0.05 mm
Fluid	Propane
Thermal capacity of steel, c_w	400 J/kgK
Density of steel, ρ_w	7,800 kg/m^3
Thermal conductivity of steel, k_w	60.5 W/mK
Mixture mass velocity, G	75 kg/s m^2
Quality at the pipeline inlet	0.05
Pressure at the pipeline outlet, p_{out}	8 bar
Heat generation rate in the pipe wall, q'''	7 kW/m^3

The overall temperature drop for given pipe geometry, wall material properties and volumetric heat rate (Table 1) is 0.021 K according to Eq. (3). The transition time in this case is $t_{c,w}\sim\delta^2/\alpha_w=17$. The time required to reach a steady fluid flow in the pipeline, $t_{c,f}$, can be estimated from the ratio of the pipeline length to the average mixture velocity at the initial steady state. This time scale is $\sim 10^4$ s for the mixture mass velocity, conditions at the pipeline inlet and outlet presented in Table 1. Thus, both criteria for applicability of the simplified model, Eq. (1) and Eq(4) are satisfied in this case. Figure 2 shows the temperature response on the sudden heat input to the wall at three different locations in the pipeline, $x/L=0$, 0.5 and 1 (more accurately, at center of the first mesh cell, the cell at the middle of the pipeline and the last cell). This prediction was made using the simplified model. As can be seen the local wall and fluid temperatures at $x/L=0$ and 0.5 increase during some period of time, and then decrease until a new steady state is reached (at $t\approx 18000$ s). Temperature at the pipeline outlet does not change because the outlet pressure is fixed. Figure 2 also shows the results of predictions in which the wall effect on the flow behavior is not accounted for, i.e., the factor of adiabaticity, Eq. (9) equals zero (this was achieved by setting $\delta=0$). As can be seen the temperature response in this case is very different from that observed in the previous case. Local temperatures reach their corresponding maximum values in a shorter time period and the maximum local temperatures produced during the transient are higher. The wall effect can be disregarded when the factor of adiabaticity, Fa, the ratio of energy stored in the pipe wall to energy required to vaporize liquid, is small (<1 in most practical applications) or the local fluid pressure does not change (see Eq. 8). In the considered case, $Fa=90.9$ at $x/L=0$, $Fa=91.7$ at $x/L=1$, and the pressure is constant only at the pipeline outlet, therefore the process of energy accumulation in the pipe wall must be included in the analysis.

To access the accuracy associated with using the numerical solution obtained in the present note, a more rigorous model of conjugate two-phase heat transfer has been used. This model is much more complex than that presented here. It consists of two parts: a model of unsteady heat conduction in the wall (the thermal model), and a model describing the dynamics of two-phase flow (the hydrodynamic model). It requires a correlation for predicting wall-to-fluid heat transfer under two-phase flow conditions and an iteration procedure to couple the thermal model with the hydrodynamic model. A detailed description of the ''rigorous'' model formulation is given in [4]. Some modifications have been made to the rigorous model. The heat generation term has been included in the heat conduction equation and the Gungor and Win-

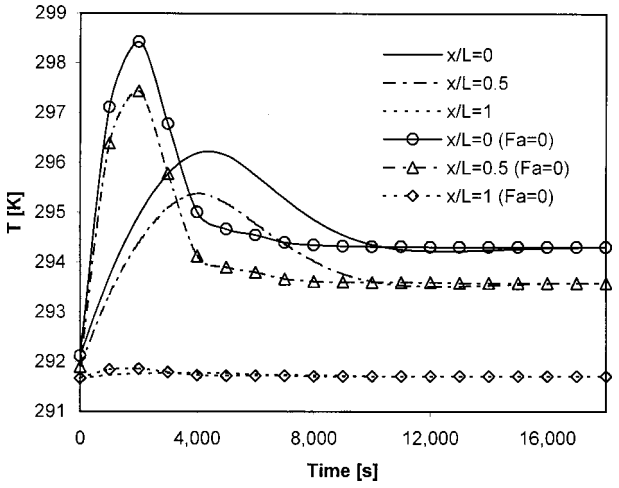

Fig. 2 Variation of temperature with time at the inlet ($x/L=0$), middle ($x/L=0.5$), and the outlet ($x/L=1$) of the pipeline

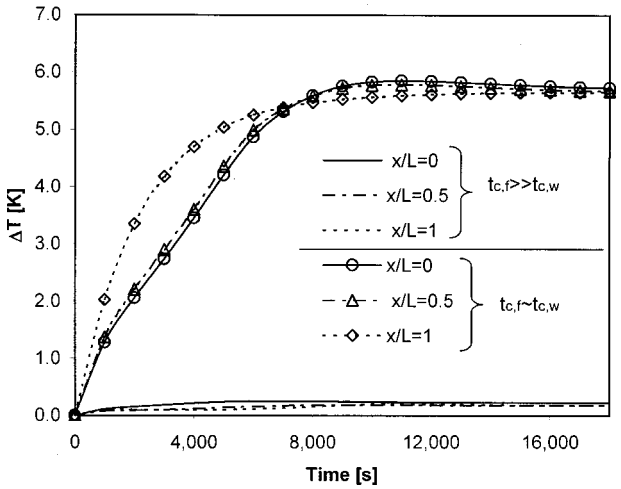

Fig. 3 Variation of the overall temperature difference with time at the inlet ($x/L=0$), middle ($x/L=0.5$), and the outlet ($x/L=1$) of the pipeline predicted by the rigorous model ($N=100$, $N_w=10$)

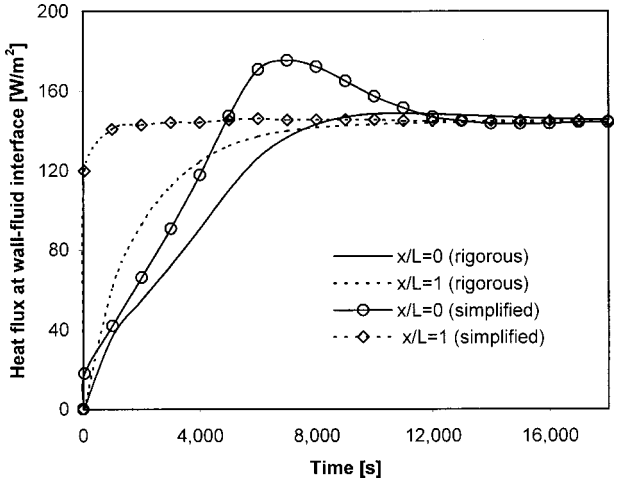

Fig. 5 Variation of the heat flux at the wall-fluid interface with time at the inlet ($x/L=0$) and the outlet ($x/L=1$) of the pipeline ($t_{c,f}\sim t_{c,w}$)

terton correlation [7] has been employed to predict the heat-transfer coefficient in flow boiling. This correlation has the advantage of simplicity and in many cases performs better than some of the more complex correlations for horizontal two-phase flow [8].

Figure 3 shows the variations of overall temperature drop (Eq. 1) at $x/L=0$, 0.5 and 1 predicted by the rigorous model. The temperature drop does not exceed 0.3 K. Local fluid temperature variations shown in Fig. 2 were also predicted by the rigorous model. They are not shown in Fig. 2, because the temperature histories predicted by the rigorous model coincided with those predicted by the simplified model.

Additional computations were performed for the case in which one of the criteria of applicability of the simplified model (the second condition, Eq. 4) is not satisfied. To achieve this, the wall conductivity was assumed to be of 0.25 W/mK in these calculations, and therefore $t_{c,f}\sim t_{c,w}$. All other conditions are the same as in the previously analyzed case (Table 1). As can be seen in Fig. 3 the overall temperature drop in the transversal direction at three locations increases with time and becomes very large (more than temperature difference between the pipeline inlet and outlet) at the new steady state. Therefore, the simplified model is not appropriate to describe the transient process of pipeline heating in such cases because it assumes local thermal equilibrium within the pipe wall and an infinite wall-to-fluid heat transfer rate.

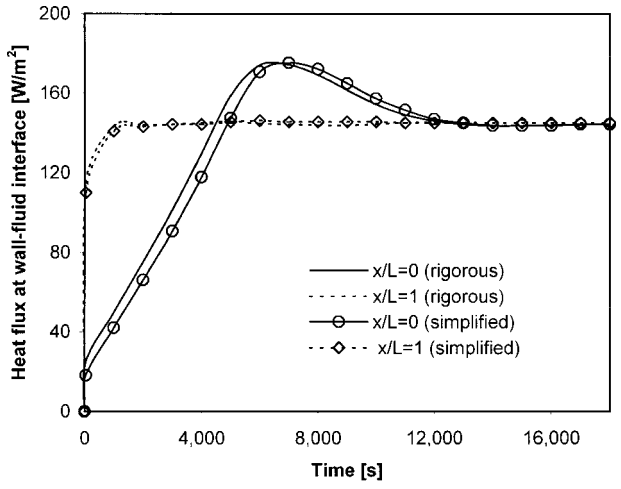

Fig. 4 Variation of the heat flux at the wall-fluid interface with time at the inlet ($x/L=0$) and the outlet ($x/L=1$) of the pipeline ($t_{c,f}\gg t_{c,w}$)

The predicted heat fluxes through the wall-fluid interface at the pipeline inlet and outlet are shown in Fig. 4. In the simplified model, the heat flux at the internal pipe surface is calculated from the energy balance in the pipe element that can be written in the following form

$$q_i''=\frac{q'''(r_e^2-r_i^2)}{2r_i}-\frac{\rho_w c_w(r_e^2-r_i^2)\Delta T}{2r_i\Delta t} \tag{15}$$

where the first term on the right-hand side in Eq. (15) is the internal heat generation rate per unit internal surface area of the pipe; the second term is the storage rate of energy in the wall element per unit internal surface area of the pipe. The heat flux in the rigorous model is predicted by solving coupled equations describing temperature fields both in the pipe wall and the fluid flow [4]. As can be seen in Fig. 4 the (relative) difference between the heat flux values predicted by these two models is less than 10 percent. The anticipated errors in heat flux predictions based on forced convective boiling correlations proposed in the literature are at least 20 percent. Thus, the simplified model predicts heat flux within the uncertainty range of existing heat transfer correlations.

It is interesting to note that initially (up to $t=4{,}500$ s) the heat generation rate in the wall is larger than the rate of wall-to-fluid heat transfer at the pipeline inlet. Therefore, the wall is heated up (Fig. 2). At $t=4{,}500$ s the inlet temperature reaches the maximum and then decreases, i.e., the wall is cooled by the fluid flow. This can occur only if the amount of heat transferred to the fluid is greater than the amount of heat generated in the wall. The simplified model correctly describes this phenomenon (Fig. 4). It is seen in Figs. 2 and 4 that the maximum local temperature is reached at the instant of time ($\sim$4500 s) when the heat fluxes to and from the wall become equal. After that the wall-to-fluid heat transfer rate is greater than the internal heat generation rate. Local temperatures decrease until the system comes to the new steady state. Thus, the results presented in Figs. 2 and 4 clearly show that transient phenomena occurring in the system during heating of the pipeline are controlled by conjugate heat transfer.

Figure 5 compares the heat flux predictions at the inlet and outlet of the pipeline for the case in which the second criterion of the simplified method is not satisfied. As can be seen the error associated with using the simplified model to predict wall-to-fluid heat transfer is large.

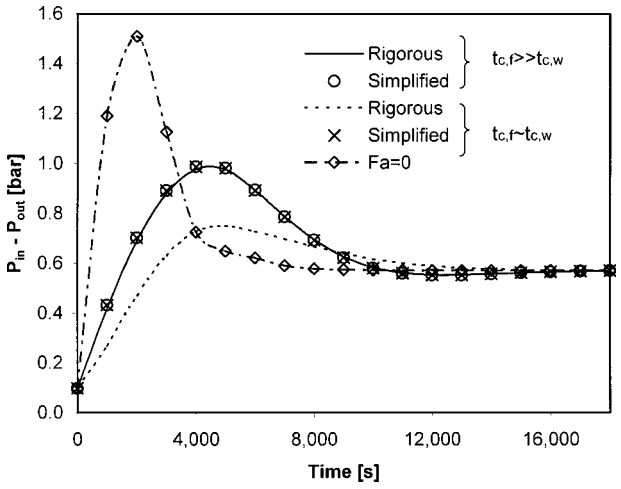

Fig. 6 Variation of the pressure drop with time

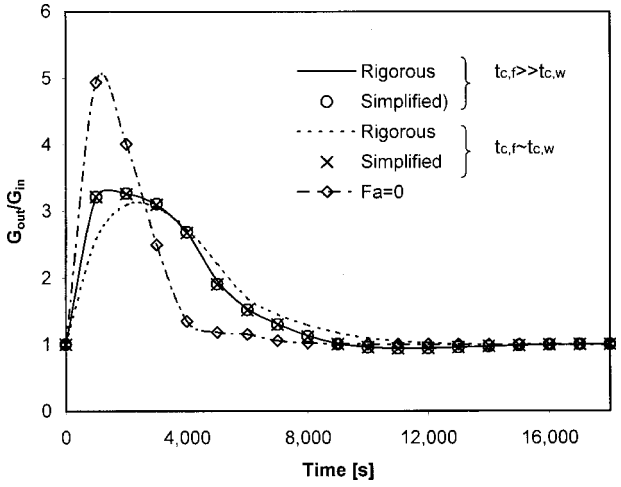

Fig. 7 Variation of the mass velocity at the pipeline outlet with time

Figures 6 and 7 show the predicted pressure drop and mass velocity at the pipeline outlet, respectively. These results are shown for three cases discussed above: two criteria for applicability of the simplified method are satisfied, the second criterion is not satisfied, and the effect of the wall is neglected.

When the simplified solution is applicable, the agreement between the simplified and rigorous models is good. The curves representing the pressure drop and mass velocity responses practically coincide (the departure of simplified model from predictions of the rigorous model does not exceed 1 percent). Beyond the range of applicability of the simplified model (when $t_{c,f} \sim t_{c,w}$) predictions differ significantly from those of the rigorous model. The simplified solutions for $t_{c,f} \gg t_{c,w}$ and $t_{c,f} \sim t_{c,w}$ in Figs. 6 and 7 coincide because the only difference between these two cases was that different thermal conductivities of the pipe wall (60.5 W/mK and 0.25 W/mK) were used in the numerical computations carried out for two conditions considered. A completely different flow behavior is observed when the wall thermal capacity is neglected (the prediction for zero adiabaticity factor, $Fa=0$).

Conclusions

A numerical solution for transient conjugate two-phase heat transfer in pipelines with heat generation in the pipe wall has been obtained using a method developed previously for modeling flashing flows. This method is based on the energy equation applied to a control volume comprising a fluid element and an adjacent wall element, in which heat is generated. Two criteria of applicability of the method have been proposed. The solution has been verified using a model that takes the radial heat conductance and forced convective boiling effects into account. The effect of the wall thermal capacity on the behavior of basic flow parameters has been studied. It has been shown that in situations when the material of the wall bounding the flow has a high thermal conductivity and the wall superheat is small, the solution obtained provides a simple and reliable alternative to more rigorous methods for modeling transient two-phase flow in heated channels.

Nomenclature

A = area
D = pipe internal diameter
c = thermal capacity
Fa = factor of adiabaticity, Eq. (9)
G = mass velocity
h_{fg} = latent heat of vaporization
K = wall friction coefficient
k = thermal conductivity
L = length
N = total number of mesh cells
P = perimeter
p = pressure
q = heat flux per unit volume of fluid
$\mathbf{q}''$ = heat flux
$\mathbf{q}'''$ = heat generation rate in the pipe wall
r = radius
t = time
$t_{c,f}$ = time required to reach a steady fluid flow in the pipeline
$t_{c,w}$ = transition time, a time scale used in the analysis of unsteady heat conduction in the pipe wall
T = temperature
u = specific internal energy
U = internal energy
v = specific volume
V = mixture velocity
x = axial coordinate
$\Delta \mathbf{T}$ = temperature difference
α = thermal diffusivity
δ = wall thickness
δ = density

Subscripts

e = external
f = fluid flow
fg = difference between properties of vapor (gas) and liquid
i = internal
in = inlet
out = outlet
sat = saturation
w = wall

References

[1] Vanvik, T., and Moe, R., 1998, "Direct Heating of Multiphase Flowlines for Hydrate Control on Asgard," *Multiphase Technology, Technology from the Arctic to the Tropics*, J. P. Brill and G. A. Gregory, eds., BHR Group, pp. 207–216.

[2] Aarseth, F., 1997, "Use of Electrical Power in Control of Wax and Hydrates," *Offshore Technology Conference*, Annual Proceedings, **4**, Richardson, TX, USA, p. 13.

[3] Bergles, A. E., 1981, "Instabilities in Two-Phase Systems," *Two-Phase Flow and Heat Transfer in the Power and Process Industries*, J. G. Collier, J. M. Delhaye, G. F. Hewitt, and F. Mayinger, eds., Hemisphere Publishing Corporation, pp. 383–423, Chap. 13.

[4] Fairuzov, Y. V., 2000, "Modeling of Conjugate Two-Phase Heat Transfer During Depressurization of Pipelines," ASME J. Heat Transfer, **122**, pp. 99–106.

[5] Fairuzov, Y. V., 1998, "Numerical Solution for Blowdown of Pipeline Containing Flashing Liquid," AIChE J., **44**, pp. 2124–2128.
[6] Bejan, A., 1993, *Heat Transfer*, John Wiley & Sons, New York.
[7] Gungor, A. E., and Winterton, R. S. H., 1987, "Simplified General Correlation for Saturated Flow Boiling and Comparisons of Correlations With Data," Chem. Eng. Res. Des., **65**, pp. 148–156.
[8] Hewitt, G. F., 1998, *Boiling, Handbook of Heat Transfer*, Third Ed., W. M. Rohsenow, J. P. Hartnett, and Y. I. Cho, eds. McGraw-Hill Handbooks, New York, pp. 15.97–15.103.

The Optimal Shape of the Interface Between Two Conductive Bodies With Minimal Thermal Resistance

J. V. C. Vargas and A. Bejan
Department of Mechanical Engineering and Materials Science, Duke University, Box 90300, Durham, NC 27708-0300

This paper considers the fundamental problem of optimizing the geometry of the interface between two conductive bodies, with the objective of minimizing the thermal resistance. The interface geometry is free to change. For simplicity, the geometry is assumed to be two-dimensional with equidistant tooth-shaped features. The tooth shape varies from triangles, to trapezoids and rectangles. The aspect ratio (height/width) of the tooth also varies. The third degree of freedom of the interface architecture is the volume fraction of the higher-conductivity tooth material that is present in the interface region. It is shown that the interface geometry can be optimized with respect to tooth shape. The global thermal resistance minimized with respect to tooth shape varies monotonically with the tooth aspect ratio and volume fraction. The optimized geometry and performance are reported graphically as functions of the physical properties and geometric parameters of the interface region. [DOI: 10.1115/1.1497355]

Keywords: Constructal, Contact Resistance, Geometry, Roughness

1 Constructal Theory and Design

It was shown recently that the geometric form of natural flow systems can be anticipated on the basis of a principle of design optimization subject to constraints [1]. Briefly stated, the deterministic mechanism that generates architecture in morphing flow systems is constructal design. The thought that the same principle accounts for flow shape and structure in natural systems is constructal theory. For a more detailed description of constructal design and theory, the reader should consult a recent book [1].

The first examples of constructal design dealt with the optimization of tree-shaped paths for minimum-time travel [2] and minimum-resistance cooling of electronics [3]. The heat transfer applications are stimulated by the push toward higher density, greater complexity, compactness and miniaturization. This is the trend everywhere, from packages of electronics [4–10] to heat exchangers [11,12]. Applications in other fields such as physiology, boiling, crystal growth, urban hydraulics, geophysics, transportation and business are reviewed in [1,13].

In the original tree-shaped path for conduction [3], the objective was to minimize the resistance to heat transfer between a heat generating volume (an infinity of points) and a concentrated heat sink (one point). The tree emerged as the optimal volume-point flow solution—the necessary structure that empowers the system to meet its global objective under constraints. The tree-shaped paths consisted of high-conductivity material, which was distributed optimally on the background of low-conductivity heat-generating material.

In a more recent example of constructal design [14], we minimized the thermal resistance across a conducting slab without heat generation. The two phases of the slab were maintained at different temperatures. A finite amount of high-conductivity material could be distributed through the slab volume. We found that an optimal distribution of such material exists: the optimal structure consists of optimally spaced needles and blades of high-conductivity material. This discovery led to the speculation [14] that the rough contact between two conductive bodies can be optimized for minimum heat transfer. The objective of this paper is to investigate this possibility.

2 Model

Consider the problem of connecting, with minimum thermal resistance, two slabs made from different materials. One of the slabs has a low thermal conductivity (k_0), and the other a high thermal conductivity (k_p). Figure 1 shows this two-dimensional configuration. The temperatures of the two extremities are assumed known: the hot end, T_h, and the cold end, T_c. The side walls are adiabatic, $\partial T/\partial y = 0$. The question is whether there is an optimal interface geometry, shape, or roughness, such that the heat transfer rate between the two slabs is maximized.

The problem defined in Fig. 1 is one of two-dimensional steady heat conduction. The shaded region at the interface (thickness L) is assumed to be small with respect to the total length of the two slabs put together (Z). The geometry of the L region is the subject of this study. The conduction in the entire domain is ruled by the energy conservation equation

$$\frac{\partial}{\partial x}\left[k(x,y)\frac{\partial T}{\partial x}\right]+\frac{\partial}{\partial y}\left[k(x,y)\frac{\partial T}{\partial y}\right]=0 \tag{1}$$

subject to the boundary conditions shown in Fig. 1, namely, $T=T_h$ at $(0,y)$, $T=T_c$ at (L,y), and $\partial T/\partial y=0$ at $(x,0)$ and (x,H).

The geometry of the interface is modeled according to Fig. 2, in which x is oriented vertically. Two limits can be distinguished.

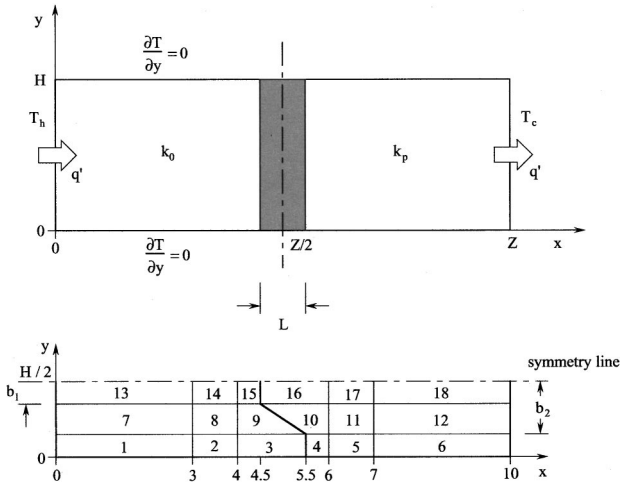

Fig. 1 Two-dimensional configuration consisting of two solids that make contact over a finite-thickness interface. The bottom figure shows the blocks of the grid used in the numerical work (Table 1).

Contributed by the Heat Transfer Division for publication in the JOURNAL OF HEAT TRANSFER. Manuscript received by the Heat Transfer Division November 26, 2001; revision received May 21, 2002. Associate Editor: G. Dulikravich.

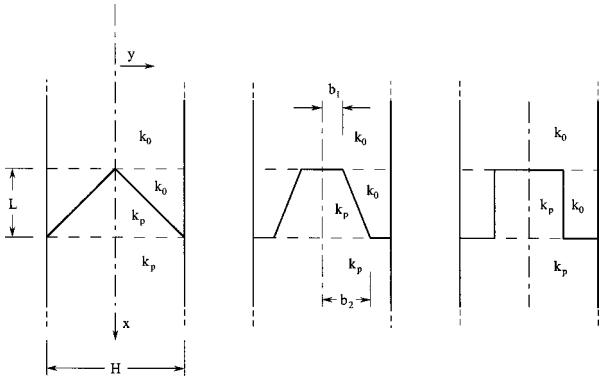

Fig. 2 Family of tooth-shaped interfaces that have the same volume fraction ϕ

The first limit (not shown in Fig. 2) is a perfectly smooth contact surface dividing the total length at $x=Z/2$, such that conduction is unidirectional and the heat flux can be calculated analytically as

$$q'_{\text{ref}}=\frac{2Hk_0k_p}{Z(k_p+k_0)}(T_h-T_c) \tag{2}$$

The second limit is represented by the rectangular shape shown on the extreme right of Fig. 2. The mathematical domain of interest can be reduced to half of each of the domains shown in Fig. 2, because of symmetry in the y direction. The volume fraction of the k_p material that is present in the interface region is

$$\phi=\frac{b_1+b_2}{H} \tag{3}$$

where $b_1=0$ represents the triangular pattern (Fig. 2, left) and $b_1=b_2$ the rectangular pattern (Fig. 2, right). Note further the geometric relations $b_1\leqslant b_2$ and $b_2\leqslant H/2$.

The nondimensional version of this problem is based on using Z as length scale and k_0 as reference thermal conductivity. It is convenient to introduce the dimensionless variables

$$\tilde{k}=\frac{k(x,y)}{k_0},\quad \theta=\frac{T-T_c}{T_h-T_c},\quad (X,Y)=\frac{(x,y)}{Z} \tag{4}$$

The nondimensional problem statement becomes

$$\frac{\partial}{\partial x}\left(\tilde{k}(X,Y)\frac{\partial\theta}{\partial x}\right)+\frac{\partial}{\partial y}\left(\tilde{k}(X,Y)\frac{\partial\theta}{\partial y}\right)=0 \tag{5}$$

$$\theta=1 \quad \text{at } (0,Y) \quad \text{and} \quad \theta=0 \quad \text{at } (1,Y) \tag{6}$$

$$\frac{\partial\theta}{\partial y}=0 \quad \text{at } (X,0) \quad \text{and} \quad \left(X,\frac{H}{Z}\right) \tag{7}$$

where, according to Fig. 1, $\tilde{k}=1$ on one side of the interface, and $\tilde{k}=\tilde{k}_p$ on the other side.

3 Numerical Formulation

The objective of the numerical work is to calculate and then maximize the heat flux at one of the two ends of the assembly, $X=0$ or $X=1$. The calculated heat flux is referenced to the limiting heat flux calculated in Eq. (2), q'_{ref}. The ratio of the two heat fluxes is

$$\tilde{q}=\frac{q''_{x=0}H}{q'_{\text{ref}}}=\frac{\tilde{k}_p+1}{2\tilde{k}_p}\frac{\partial\theta}{\partial X}\bigg|_{X=0}=\frac{\tilde{k}_p+1}{2}\frac{\partial\theta}{\partial X}\bigg|_{X=1} \tag{8}$$

The value $\tilde{q}=1$ corresponds to the reference case where teeth of any shape are absent, i.e., a perfectly idealized smooth contact surface at $X=0.5$. We will show that the presence of teeth at the interface leads to heat transfer enhancement, $\tilde{q}>1$.

Table 1 The number of elements in the grid shown in Fig. 1

	Elements			Elements	
Block	x	y	Block	x	y
1	16	8	10	48	8
2	16	8	11	16	8
3	48	8	12	16	8
4	48	8	13	16	8
5	16	8	14	16	8
6	16	8	15	48	8
7	16	8	16	48	8
8	16	8	17	16	8
9	48	8	18	16	8

The interface geometry has three degrees of freedom, the ratios b_1/b_2 and H/L, and the volume fraction ϕ. The first degree of freedom investigated is the tooth shape (the ratio b_1/b_2) for a fixed set of design parameters: the size of the contact region (L/Z), the materials (k_p/k_0), the tooth aspect ratio (H/L), and the volume fraction ϕ.

The conduction problem defined by Fig. 1 and Eqs. (5)–(7) was solved by the finite element method, using the code Finite Element Analysis Program (FEAP), originally written by Zienkiewicz and Taylor [15]. The elements were isoparametric, 4-noded quadrilaterals, i.e., with linear shape functions. The grid was nonuniform and more refined in the vicinity of the interface, where the highest gradients are expected. Mesh refinements were performed for all the tested shapes that are presented in Fig. 2. The convergence criterion consisted of monitoring the change in $\tilde{q}$ that resulted from successive mesh refinements [16]. The $\tilde{q}$ value resulting from a less refined mesh (mesh 1) was compared with the result of a more refined mesh (mesh 2), and the refinements stopped when the following relative error criterion was satisfied

$$\varepsilon=\frac{|\tilde{q}(\text{mesh 1})-\tilde{q}(\text{mesh 2})|}{\tilde{q}(\text{mesh 2})}\leqslant 0.01 \tag{9}$$

The converged mesh had 4025 nodes. This mesh satisfied criterion (9) for all the cases analyzed in this study, when it was compared with a mesh with 5957 nodes.

The grid was built as shown in the lower part of Fig. 1. The slab was divided into quadrilateral blocks. For the converged mesh, the elements were distributed among the blocks so that their density was greater near the interface between the two materials (Table 1).

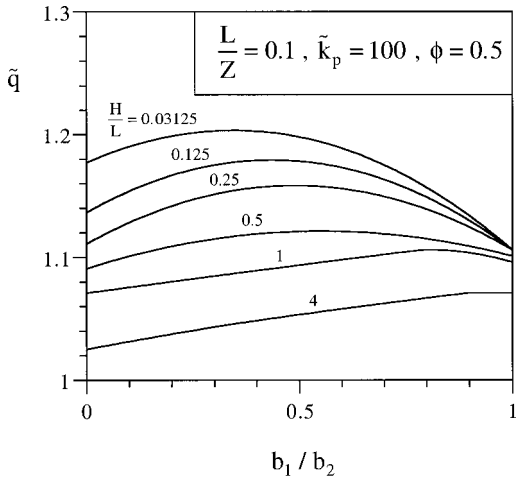

Fig. 3 The maximization of the global thermal conductance by selecting the tooth aspect ratio b_1/b_2

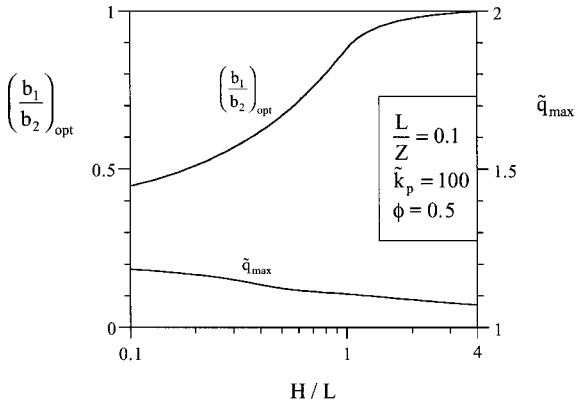

Fig. 4 The optimal tooth aspect ratio and the corresponding global thermal conductance

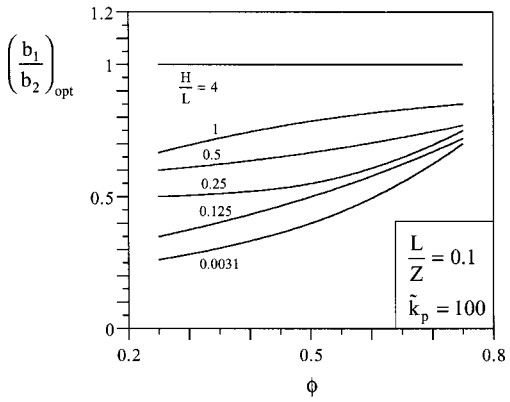

Fig. 6 The effect of H/L and ϕ on the optimized ratio b_1/b_2

4 Results

Figure 3 shows that when $H/L<1$ the global thermal conductance $\tilde{q}$ can be maximized with respect to the tooth shape ratio b_1/b_2. The optimized shape (b_1/b_2) and the maximized $\tilde{q}$ values are summarized in Fig. 4. The second degree of freedom—the aspect ratio H/L—has a significant effect, especially on the optimized ratio $(b_1/b_2)_{opt}$.

In the case of the rectangular interface (Fig. 2, right) with teeth that are thin enough such that $H/L \leqslant 0.5$, conduction is unidirectional and the temperature is practically independent of y. Under these circumstances the dimensionless heat flux becomes (e.g., [17])

$$\tilde{q}_{rect} = \frac{\tilde{k}_{eff}}{\left(1 - \frac{L}{Z}\right)\tilde{k}_{eff} + \frac{\tilde{k}_p}{\tilde{k}_p + 1}\frac{L}{Z}} \tag{10}$$

where

$$\tilde{k}_{eff} = 1 + \phi(\tilde{k}_p - 1) \tag{11}$$

When $H/L \gtrsim 0.5$, conduction in the assembly is no longer unidirectional even in the limit of rectangular teeth. See Fig. 5, which was drawn for $H/L=4$. The $\tilde{q}$ value obtained numerically based on Eq. (8) is smaller than the $\tilde{q}_{rect}$ value furnished by Eq. (10). The same observation can be made by looking at $b_1/b_2=1$ and $H/L=4$ in Fig. 3, where $\tilde{q}$ was calculated based on Eq. (8). When $b_1/b_2=1$, the $\tilde{q}$ value furnished by Eq. (10) is nearly the same as the $\tilde{q}$ value obtained based on Eq. (8). This is true up to $H/L \sim 0.5$. The $\tilde{q}$ estimate based on Eq. (10) is higher than the actual $\tilde{q}$ value when $H/L>0.5$.

We repeated the optimization work of Fig. 4 for many other combinations of H/L and ϕ values. The results for $(b_1.b_2)_{opt}$ are summarized in Fig. 6. The corresponding results for $\tilde{q}_{max}$ are reported in Fig. 7. These results are important because they show that after the optimization with respect to b_1/b_2, the maximized global conductance $\tilde{q}_{max}$ varies monotonically with respect to the

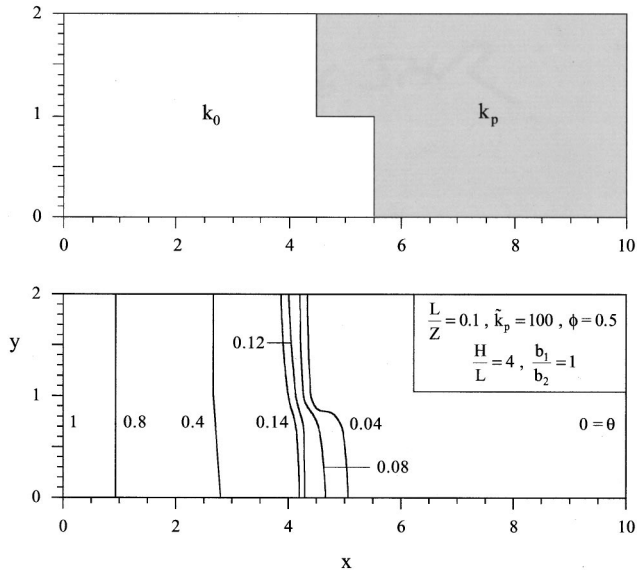

Fig. 5 The temperature field when the tooth shape is rectangular with $H/L=4$

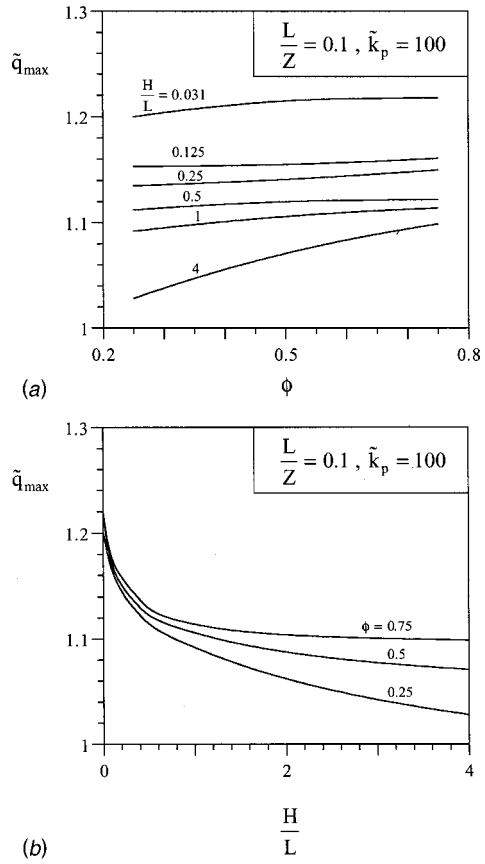

Fig. 7 The effect of H/L and ϕ on the maximized global conductance

remaining geometric parameters, H/L and ϕ. High conductances are achieved when H/L is small, and ϕ large. This finding is intuitively correct, as the thermal resistance of the interface is minimized with a shorter length L, wider cross-section H, and higher conductivity (large ϕ). The effect of ϕ is weak when H/L is smaller than 1.

The conductivity ratio $\tilde{k}_p$ was held fixed at a value greater than 1, in order to illustrate the effect of changing the interface geometry when the two solids are highly dissimilar. In the opposite extreme, $\tilde{k}_p = 1$, the conductivity does not change across the interface, and the geometry of the interface loses its effect on the global thermal resistance. In applications with $\tilde{k}_p$ values greater than 100, the effect of changing the interface geometry is expectedly greater than in the cases illustrated in this note. The interface geometry and $\tilde{k}_p$ influences the global thermal resistance because of the continuity of heat flux at the interface, $k_p(\partial T/\partial n)_p = k_0(\partial T/\partial n)_0$, requires information on $\tilde{k}_p$ and the position of the interface.

5 Conclusion

In summary, the geometry of the interface between two different conducting bodies can be ''designed'' such that the thermal contact resistance is minimal. Not every geometrical feature of the interface can be optimized. In the present study we considered a two-dimensional tooth-shaped interface and found that the contact resistance can be minimized by selecting the tooth shape, which is represented by the ratio b_1/b_2 in Fig. 2. The thermal conductance minimized with respect to b_1/b_2 varies monotonically with respect to the other degrees of freedom of the interface, the ratio H/L and the volume fraction ϕ.

The design optimization opportunity described in this paper deserves to be pursued in more complicated settings, for example, in thermal contacts with three-dimensional interface geometries. At a more basic level, the present paper illustrated once more the constructal method: the generation of optimal geometric form in a 'morphing' system, such that the global performance is maximized subject to constraints [1].

There is a clear and working analogy between the conceptual search for optimal distributions of maximal stresses, which leads to smooth (animal-bone, custom made) shapes in structural mechanics, and the search for paths with less and less resistance to flow (heat, fluid, electricity, goods, etc). In both fields, the result is geometric form—geometry as a mechanism by which the system achieves its global objective under constraints. Maximal stresses and peak temperatures and pressures (high resistances) represent peaks of imperfection, which must be smoothed, if not avoided. Optimal distribution of imperfection is the constructal principle that generates architecture in systems with purpose, in engineering and nature [1].

Acknowledgment

This work was supported by a grant from the National Science Foundation.

Nomenclature

$b_{1,2}$ = dimensions, *m*, Fig. 2
H = height, *m*, Fig. 2
k = thermal conductivity, $\mathrm{W\,m^{-1}\,K^{-1}}$
k_p = high thermal conductivity, $\mathrm{W\,m^{-1}\,K^{-1}}$
k_0 = low thermal conductivity, $\mathrm{W\,m^{-1}\,K^{-1}}$
$\tilde{k}$ = ratio of thermal conductivities, k_p/k_0
L = length, *m*, Fig. 2
q' = heat transfer rate per unit length, $\mathrm{W\,m^{-1}}$
q'' = heat transfer rate per unit area, $\mathrm{W\,m^{-2}}$
$\tilde{q}$ = overall thermal conductance, dimensionless
T = temperature
x,y = Cartesian coordinates, *m*, Fig. 1
X,Y = dimensionless coordinates
Z = overall size, *m*, Fig. 1

Greek Symbols

ε = error criterion
θ = dimensionless temperature
ϕ = volume fraction of k_p material

Subscripts

c = cold
h = hot
rect = rectangle
ref = reference

References

[1] Bejan, A., 2000, *Shape and Structure, from Engineering to Nature*, Cambridge University Press, Cambridge, UK.
[2] Bejan, A., 1996, ''Street Network Theory of Organization in Nature,'' J. Adv. Transp., **30**(**7**), pp. 85–107.
[3] Bejan, A., 1997, ''Constructal-Theory Network of Conducting Paths for Cooling a Heat Generating Volume,'' Int. J. Heat Mass Transf., **40**, pp. 799–816.
[4] Bar-Cohen, A., and Rohsenow, W. M., 1984, ''Thermally Optimum Spacing of Vertical, Natural Convection Cooled, Parallel Plates,'' ASME J. Heat Transfer, **106**, pp. 116–123.
[5] Peterson, G. P., and Ortega, A., 1990, ''Thermal Control of Electronic Equipment and Devices,'' Adv. Heat Transfer, **20**, pp. 181–314.
[6] Knight, R. W., Goodling, J. S., and Hall, D. J., 1991, ''Optimal Thermal Design of Forced Convection Heat Sinks—Analytical,'' ASME J. Electron. Packag., **113**, pp. 313–321.
[7] Anand, N. K., Kim, S. H., and Fletcher, L. S., 1992, ''The Effect of Plate Spacing on Free Convection Between Heated Parallel Plates,'' ASME J. Heat Transfer, **114**, pp. 515–518.
[8] Kakac, S., Yüncü, H., and Hijikata, K., eds., 1994, *Cooling of Electronic Systems*, Kluwer, Dordrecht, The Netherlands.
[9] Kraus, A. D., and Bar-Cohen, A., 1995, *Design and Analysis of Heat Sinks*, Wiley, New York.
[10] Kraus, A. D., Aziz, A., and Welty, J., 2001, *Extended Surface Heat Transfer*, Wiley, New York.
[11] Shah, R. K., and Mueller, A. C., 1985, ''Heat Exchangers,'' in *Handbook of Heat Transfer Applications*, 2nd ed., W. M. Rohsenow, J. P. Hartnett, and E. N. Ganic, eds., McGraw-Hill, New York, Chap. 4.
[12] Hesselgreaves, J. E., 2001, *Compact Heat Exchangers: Selection, Design and Operation*, Pergamon, Amsterdam.
[13] Bejan, A., 1997, *Advanced Engineering Thermodynamics*, 2nd ed., John Wiley and Sons, New York, Chap. 13.
[14] Neagu, M., and Bejan, A., 2001, ''Constructal Placement of High-Conductivity Inserts in a Slab: Optimal Design of Roughness,'' ASME J. Heat Transfer, **123**, pp. 1184–1189.
[15] Zienkiewicz, O. C., and Taylor, R. L., 1989, *The Finite Element Method*, **1**, McGraw-Hill, London.
[16] Editorial, 1994, ''Journal of Heat Transfer Editorial Policy Statement on Numerical Accuracy,'' ASME J. Heat Transfer, **116**, pp. 797–798.
[17] Bejan, A., 1993, *Heat Transfer*, Wiley, New York, p. 76.